Tourbilons et sillages dans les fluides géophysiques

Patrice Meunier

UNIVERSITÉ DE PROVENCE AIX-MARSEILLE I
Institut de Recherche sur les Phénomènes Hors Équilibre

Mémoire présenté pour obtenir

l'Habilitation à Diriger des Recherches

Discipline : Mécanique

par **Patrice MEUNIER**

le 10 juillet 2009

Tourbillons et sillages dans les fluides géophysiques

JURY :

M. Friedrich BUSSE, Institute of Physics, University of Bayreuth,
M. Jean-Marc CHOMAZ, LADHYX, Ecole Polytechnique, Paris,
Mme Elisabeth GUAZZELLI, IUSTI, Universités Aix-Marseille,
M. Michel RIEUTORD, Observatoire Midi-Pyrénées, Toulouse,
M. Joël SOMMERIA, LEGI, Université Joseph-Fourier, Grenoble,
M. Emmanuel VILLERMAUX, IRPHE, Universités Aix-Marseille,

Table des matières

1 Curriculum Vitæ

Patrice MEUNIER
35 ans, Né le 11 mars 1974 à Aix-en-Provence, Français, Célibataire.
Chargé de Recherche de première classe au CNRS
Institut de Recherche sur les Phénomènes Hors Equilibre,
UMR 6594, 49 rue Joliot-Curie, 13384 Marseille Cedex 13.
Tél : 04 96 13 97 69 Fax : 04 96 13 97 09
Mél : meunier@irphe.univ-mrs.fr

FORMATION

1991-1994	Mathématiques Supérieures et Mathématiques Spéciales (M')
1994–1998	**Élève de l'École Normale Supérieure de Lyon.**
1994–1998	**Magistère des Sciences de la Matière (Lyon 1).** *Mention Bien.*
1995	– Stage de Licence (2 mois) au LEGI (Grenoble).
1996	– Stage de Maîtrise (4 mois) à l'Université de York, Toronto (Canada).
1997–1998	DEA de Physique et Modélisation des Systèmes Complexes (Université d'Aix-Marseille I). *Mention Très Bien.*
1998	– Stage de DEA (3 mois) à l'IRPHE (Marseille).
1997	**Agrégation de Physique (option phys.)**. *Rang : 10ème.*
1998-2001	**Doctorat de l'Université Aix-Marseille I**. *Mention Très Honorable* Titre : *Étude expérimentale de deux tourbillons corotatifs* Soutenance le 17 décembre 2001 Spécialité : Mécanique des Fluides Directeur de thèse : T. Leweke Jury : E. J. Hopfinger, P. Huerre, L. Jacquin, S. Le Dizès, T. Leweke, K. Moffatt (Prés.), G. J. F. van Heijst (Rapp.), E. Villermaux, C. H. K. Williamson (Rapp.). Laboratoire : Institut de Recherche sur les Phénomènes Hors Équilibre
1998–2001	Moniteur en Physique à l'Université Aix-Marseille I.
2002	Études post-doctorales à l'Aerospace and Mechanical Engineering Department, University of Southern California Los Angeles, Etats-Unis.
depuis 2003	**Chargé de recherche à l'IRPHE**

2 Enseignement, encadrement et diffusion de la culture scientifique

2.1 Enseignement

1998-2000 : Travaux dirigés d'Electromagnétisme en Deug deuxième année, Université de Provence Aix-Marseille I, 128 heures.
2000-2001 : Travaux dirigés d'Electrocinétique en Deug première année, Université de Provence Aix-Marseille I, 50 heures.
2000-2001 : Travaux dirigés de Techniques mathématiques pour la physique en Deug première année, Université de Provence Aix-Marseille I, 14 heures.
2004-2008 : Cours au Master 2ème année recherche " Mécanique, Physique et Modélisation " de l'Université de Provence, sur le thème de la " Dynamique de Tourbillons ". 12 heures par an.

2.2 Encadrement de thèse

- Nicolas Boulanger en 2003-2006 (co-encadrement à 50% avec Stéphane Le Dizès) : *Dynamique d'un tourbillon incliné dans un fluide stratifié*. Soutenance le 5 décembre 2006.
- Romain Lagrange en 2007-2009 (Autorisation Ponctuelle à dirigier des recherches de l'Université de Provence, co-encadrement à 50% avec Christophe Eloy) : *Instabilité d'un fluide dans un cylindre en précession*. Soutenance prévue en novembre 2009.
- Xavier Riedinger en 2007-2009 (co-encadrement à 50% avec Stéphane Le Dizès) : *Rayonnement d'ondes par un tourbillon vertical dans un fluide stratifié*. Soutenance prévue en septembre 2009.
- Aldo Figueroa en 2008 : ce doctorant de l'UNAM (Université de Mexico) a effectué un stage de 8 mois à l'IRPHE sous ma direction grâce au programme d'échange SCAT (ALFA).

2.3 Encadrement de stages

- Stage de Master du M2 Techniques de l'Air et de l'Espace (Uniméca) de Benoit Van Aughem,
- Stage de 2ème année de l'Ecole Polytechnique de Francois Strina,
- Stage de l'EGIM / M2 Physique et Modélisation des Sytèmes Somplexes de Laurie Devesvres,
- Stage de 2ème année de l'ENSTA de Chao Wang.

2.4 Organisation de séminaires et écoles d'été

- Organisateur du séminaire de l'IRPHE depuis 2003.
- Co-organisateur de l'école d'été "Vortices and vortex sheets", Porquerolles, 4-10 juin 2007.
- Co-organisateur du workshop "Waves and instabilities in geophysical and astrophysical flows", Porquerolles, 25-31 mai 2009.

2.5 Autres activités d'intérêt collectif

- Membre de la commission de spécialistes "Université du Sud Toulon-Var" en 2003-2007
- Membre de la commission de spécialistes "Université de Provence Aix-Marseille I" en 2007-2008
- Responsable de la PIV (Particle Image Velocimetry) au laboratoire IRPHE : le logiciel DPIVsoft mis au point pendant ma thèse est utilisé dans tout le laboratoire et a été récemment modifié pour traiter la stéréo-PIV.
- Rapporteur pour Journal of Fluid Mechanics, Physics of Fluids, European Journal of Mechanics B, Exp. Fluids, Flow Turbulence and Combustion, Dynamics of Atmosphere and Oceans.

3 Liste de publications

3.1 Revues à comité de lecture

1 P. Meunier & T. Leweke (2001). "Three-dimensional instability during vortex merging", *Phys. Fluids* **13** (10), pp. 2747-2750.

2 P. Meunier (2001). "Etude expérimentale de deux tourbillons corotatifs", *Thèse de Docteur de l'Université de Provence, Marseille, France.*

3 P. Meunier, U. Ehrenstein, T. Leweke & M. Rossi (2002). "A merging criterion for two-dimensional co-rotating vortices", *Phys. Fluids* **14** (8), pp. 2757-2766.

4 P. Meunier & E. Villermaux (2003). "How vortices mix", *J. Fluid Mech.* **476**, pp. 213-222.

5 P. Meunier & T. Leweke (2003). "Analysis and optimization of the error caused by high velocity gradients in Particle Image Velocimetry", *Exp. Fluids* **35** (5), pp. 408-421.

6 P. Meunier & G. R. Spedding (2004). "A loss of memory in stratified momentum wakes", *Phys. Fluids* **16 (2)**, pp. 298-305.

7 P. Meunier & T. Leweke (2005). "Elliptic instability of a co-rotating vortex pair", *J. Fluid Mech.*, **533**, pp. 125-159.

8 P. Meunier, S. Le Dizès & T. Leweke (2005). "Physics of Vortex Merging", *C. R. Physique*, **6**, pp. 431-450.

9 P. Meunier & G. R. Spedding (2006). "Stratified Propelled Wakes", *J. Fluid Mech.*, **552**, pp. 229-256.

10 S. Gallet, P. Meunier & G. R. Spedding (2006). "Empirical scaling of antisymmetric stratified wakes", *J. Fluids & Structures*, **22**, pp. 941-947.

11 P. Meunier, P. Diamessis & G. R. Spedding (2006). "Self-preservation in stratified momentum wakes", *Phys. Fluids* **18** (10).

12 P. Meunier & E. Villermaux (2007). "Van Hove singularities in Probability Density Functions of scalars", *C. R. Mecanique*, **335**, pp. 162-167.

13 N. Boulanger, P. Meunier & S. Le Dizès (2007). "Structure of a stratified tilted vortex", *J. Fluid Mech* **583**, pp. 443-458.

14 N. Boulanger, P. Meunier & S. Le Dizès (2008). "Tilt-induced instability of a stratified vortex", *J. Fluid Mech* **596**, pp. 1-20.

15 P. Meunier, Ch. Eloy, R. Lagrange & F. Nadal (2008). "A rotating fluid cylinder subject to weak precession", *J. Fluid Mech* **599**, pp. 405-440.

16 R. Lagrange, P. Meunier, Ch. Eloy, & F. Nadal (2008). "Instability of a fluid inside a precessing cylinder", *Phys. Fluids* **20** (8).

17 X. Riedinger, S. Le Dizès & P. Meunier (2009). "Viscous stability properties of a Lamb-Oseen vortex in a stratified fluid", *soumis à J. Fluid Mech.*

18 P. Meunier & E. Villermaux (2009). "The Diffusive Strip Method as a tool for scalar mixing in two-dimensions", *en prép pour J. Fluid Mech.*

3.2 Actes de colloque à comité de lecture

1 P. Meunier & T. Leweke (1999). “Merging and three-dimensional instability in a co-rotating vortex pair”, Vortex Structure and Dynamics, A. Maurel & P. Petitjean (Éds.), Lecture Notes in Physics, vol. 555, Springer Verlag, Berlin, Allemagne, pp. 241-251.

2 P. Meunier, T. Leweke & M. Abid (2000). “Three-dimensional instability of two merging vortices”, Advances in Turbulence VIII, C. Dopazo (Éd.), Barcelona, Spain, pp. 15-18.

3 R. Lagrange, C. Eloy, F. Nadal & P. Meunier (2008). “Instability of a fluid inside a precessing cylinder”, Actes du 22nd International Congress of Theoretical and Applied Mechanics, 24-29 août 2008, Adelaide, Australie.

3.3 Publication dans des revues sans comité

1 P. Meunier & T. Leweke (1999). ”Etude expérimentale de la fusion de deux tourbillons corotatifs”, Visualisation et Traitement d’Images en Mécanique des Fluides, P. Hébrard (Éd.), ISBN 2-951-4015-X, ENSICA, Toulouse, pp. 183-188.

2 P. Meunier & T. Leweke (1999, 2000). ”Merging of a pair of co-rotating vortices”, Album of Visualisation 16, pp. 1-2 (1999) et 17, page de couverture (2000).

3 P. Meunier & T. Leweke (2000). ”Optimisation d’un algorithme de Vélocimétrie par Images de Particules pour l’étude d’une paire de tourbillons”, Actes du 7ème Congrès Francophone de Vélocimétrie Laser, Marseille, pp. 319-326.

4 P. Meunier & T. Leweke (2000). ”Unstable Vortex Merger”, Phys. Fluids 12 (9) Gallery of Fluid Motion, p. S6.

5 P. Meunier & T. Leweke (2000). ”Influence d’une instabilité tridimensionnelle sur la fusion de deux vortex”, Actes des Rencontres du Non-Linéaire 2000, Pomeau & Ribotta (Éds.), Paris Onze Edition, Orsay, pp. 67-72.

6 P. Meunier & T. Leweke (2000). ”Influence of a three-dimensional instability during vortex merging”, Actes de 4th European Fluid Mechanics Conference, 19-23 nov. 2000, Eindhoven, Pays-Bas.

7 P. Meunier & T. Leweke (2001).. ”Secondary structures in a corotating vortex pair”, J. Visualization 4 (2), p. 115.

8 P. Meunier, T. Leweke, S. Le Dizès & F. Laporte (2001). ”Elliptic instability in co-rotating vortex pairs”, Bull. Am. Phys. Soc., 46 (10), p. 127.

9 P. Meunier & G. R. Spedding (2002). ”Memory of initial conditions in stratified wakes at late times”, Bull. Am. Phys. Soc., 47 (10), p. 161.

10 P. Meunier & G. R. Spedding (2003). ”A signature of a bluff body in the internal wave field ?”, Actes de 5th European Fluid Mechanics Conference, 24-28 août 2003, Toulouse, France.

11 G. R. Spedding & P. Meunier (2003). "The effect of initial conditions in far wakes of different-shaped objects in a linearly-stratified fluid", Actes de 5th European Fluid Mechanics Conference, 24-28 août 2003, Toulouse, France.

12 P. Meunier, G. R. Spedding & L. G. Redekopp (2003). "Prediction and measurement of body-generated waves by submerged bodies in a stratified fluid", Bull. Am. Phys. Soc., 48 (10), p. 177.

13 G. R. Spedding & P. Meunier (2003). "Momentumless and almost-momentumless wakes in a stratified fluid", Bull. Am. Phys. Soc., 48 (10), p. 77.

14 P. Meunier & E. Villermaux (2004). "Enhanced mixing in vortices", Actes du 21st International Congress of Theoretical and Applied Mechanics, 15-21 août 2004, Varsovie, Pologne.

15 G. R. Spedding & P. Meunier (2004). "Self-propelled wakes in a stratified fluid", Bull Am. Phys. Soc., 49 (10), p. 204.

16 J. W. Rottman, D. Broutman, G. R. Spedding & P. Meunier (2004). "The internal wave field generated by the body and wake of a horizontally moving sphere in a stratified fluid", Bull Am. Phys. Soc., 49 (10), p. 60.

17 N. Boulanger, P. Meunier & S. Le Dizès (2005). "Dynamics of a tilted vortex in a stratified fluid", Bull Am. Phys. Soc., 50 (9), p. 68.

18 P. Meunier & C. Eloy (2005). "Instabilities inside a precessing cylinder", Bull Am. Phys. Soc., 50 (9), p. 172.

19 C. Eloy, P. Meunier, R. Lagrange & F. Nadal (2007). "Rotating fluid cylinder submitted to a weak precession", Bull Am. Phys. Soc., 52 (17), p. 42.

20 P. Meunier, N. Boulanger & S. Le Dizès (2007). "Tilt-induced instability of a vortex in a stratified fluid", Bull Am. Phys. Soc., 52 (17), p. 178.

3.4 Communication à des congrès, symposiums

1 T. Leweke, C. H. K. Williamson & P. Meunier (1999). "Experimental study of elementary vortex interactions : reconnection and merging", Symposium on Turbulence Structure, 15-19 mars 1999, Cambridge, Royaume-Uni.

2 P. Meunier & T. Leweke (1999). "Etude expérimentale de l'interaction entre deux tourbillons corotatifs", 8ème Colloque National de Visualisation et de Traitement d'Images en Mécanique des Fluides, 1-4 juin 1999, Toulouse, France.

3 T. Leweke & P. Meunier (1999). "Experimental study of the interaction of two co-rotating vortices", Vortical Structures in Rotating and Stratified Fluids, 22-25 juin 1999, Cortona, Italy.

4 P. Meunier & T. Leweke (1999). "Merging vs. three-dimensional instability of co-rotating vortices", 52nd APS-DFD Annual Meeting, 21-23 nov. 1999, New-Orleans, Lousiana, Etats-Unis.

5 P. Meunier & T. Leweke (2000). "Influence d'une instabilité tri-dimensionnelle sur la fusion de deux vortex", 3ème Rencontres du Non-Linéaire, 9-10 mars 2000, Paris, France.

6 P. Meunier & T. Leweke (2000). "The effect of a three-dimensional instability on vortex merging", 25th General Assembly of the European Geophysical Society, 25-29 avril 2000, Nice, France.

7 P. Meunier, T. Leweke & M. Abid (2000). "Three-dimensional instability of two merging vortices", 8th European Turbulence Conference, 27-30 juin 2000, Barcelone, Espagne.

8 P. Meunier & T. Leweke (2000). "Optimisation d'un algorithme de PIV pour l'étude de deux tourbillons corotatifs", 7ème Congrès Francophone de Vélocimétrie Laser, 19-22 sept. 2000, Marseille, France.

9 P. Meunier & T. Leweke (2000). "Influence of a three-dimensional instability during vortex merging", 4th European Fluid Mechanics Conference, 19-23 nov. 2000, Eindhoven, France.

10 T. Leweke, P. Meunier, F. Laporte & D. Darracq (2001). "Controlled interaction of co-rotating vortices", 3rd Onera DLR Aerospace Symposium (ODAS 2001), 20-22 juin 2001, Paris, France.

11 P. Meunier, T. Leweke, S. Le Dizès & F. Laporte (2001). "Elliptic instability in co-rotating vortex pairs", 54th APS-DFD Annual Meeting, 18-20 nov. 2001, San Diego, California, Etats-Unis.

12 G. R. Spedding & P. Meunier (2002). "Turbulent Wakes", Meeting of Hydrodynamics : Approaches from Russia and West, 12 juin 2002, Directed Technologies, Arlington, Etats-Unis.

13 G. R. Spedding & P. Meunier (2002). "Recent Progress in Turbulent Wakes Research", Remote Anthropogenic Sensing Project, Hydrodynamics Meeting II, 13 oct. 2002, Scripps Institute of Oceanography, La Jolla, California, Etats-Unis.

14 P. Meunier & G. R. Spedding (2002). "Memory of initial conditions in stratified wakes at late times", 55th APS-DFD Annual Meeting, 24-26 nov. 2002, Dallas, Texas, Etats-Unis.

15 P. Meunier & G. R. Spedding (2003). "A signature of a bluff body in the internal wave field ?", 5th European Fluid Mechanics Conference, 24-28 août 2003, Toulouse, France.

16 G. R. Spedding & P. Meunier (2003). "The effect of initial conditions in far wakes of different-shaped objects in a linearly-stratified fluid", 5th European Fluid Mechanics Conference, 24-28 août 2003, Toulouse, France.

17 P. Meunier, G. R. Spedding & L. G. Redekopp (2003). "Prediction and measurement of body-generated waves by submerged bodies in a stratified fluid", 56th APS-DFD Annual Meeting, 23-25 nov. 2003, New Jersey, Etats-Unis.

18 G. R. Spedding & P. Meunier (2003). "Momentumless and almost-momentumless wakes in a stratified fluid", 56th APS-DFD Annual Meeting, 23-25 nov. 2003, New Jersey, Etats-Unis.

19 J. W. Rottman, D. Broutman, G. R. Spedding & P. Meunier (2004). "Internal wave generation by a horizontally moving sphere at low Froude number", 25th Symp. on Naval Hydrodynamics, 8-13 août 2004, St. John's, Newfoundland, Canada.

20 P. Meunier & E. Villermaux (2004). "Enhanced mixing in vortices", 21st International Congress of Theoretical and Applied Mechanics, 15-21 août 2004, Varsovie, Pologne.

21 P. Meunier & E. Villermaux (2004). "Accelerated diffusion by vortices", Euromech Conference 448 : "Vortex Dynamics and Field Interactions", 6-10 sept. 2004, Paris, France.

22 J. W. Rottman, D. Broutman, G. R. Spedding & P. Meunier (2004) "The internal wave field generated by the body and wake of a horizontally moving sphere in a stratified fluid", 15th Australasian Fluid Mechanics Conference, 13-17 décembre 2004, University of Sydney, Australia.

23 G. R. Spedding & P. Meunier (2004). "Self-propelled wakes in a stratified fluid", 57th APS-DFD Annual Meeting, 21-23 nov. 2004, Seattle, Etats-Unis.

24 J. W. Rottman, D. Broutman, G. R. Spedding & P. Meunier (2004). "The internal wave field generated by the body and wake of a horizontally moving sphere in a stratified fluid", 57th APS-DFD Annual Meeting, 21-23 nov. 2004, Seattle, Etats-Unis.

25 P. Meunier & G. R Spedding (2005). "Stratified of Propelled and Towed Bluff Bodies", 4th Symposium on Bluff Body Wakes and Vortex Induced Vibrations, 21-24 juin 2005, Santorin, Grèce.

26 N. Boulanger, P. Meunier & S. Le Dizès (2005). "Dynamics of a tilted vortex in a stratified fluid", 58th APS-DFD Annual Meeting, 20-22 nov. 2005, Chicago, Etats-Unis.

27 P. Meunier & C. Eloy (2005). "Instabilities inside a precessing cylinder", 58th APS-DFD Annual Meeting, 20-22 nov. 2005, Chicago, Etats-Unis.

28 P. Meunier, P. Diamessis & G. R. Spedding (2006). "A general theory for stratified wakes", Ocean Sciences Meeting, 20-24 fev. 2006, Honolulu, Etats-Unis.

29 N. Boulanger, P. Meunier & S. Le Dizès (2006). "Stability of a stratified tilted vortex", 6th European Fluid Mechanics Conference, 26-30 juin 2006, Stockholm, Suède.

30 P. Meunier, G. R. Spedding & P. Diamessis (2006). "A general theory for stratified wakes", 6th European Fluid Mechanics Conference, 26-30 juin 2006, Stockholm, Suède.

31 F. Nadal, P. Meunier & C. Eloy (2006). "Resonances inside a precessing cylinder", 6th European Fluid Mechanics Conference, 26-30 juin 2006, Stockholm, Suède.

32 N. Boulanger, P. Meunier & S. Le Dizès (2006). "Dynamics of a stratified tilted vortex", 6th International Symposium on Stratified Flows, 11-14 décembre 2006, Perth, Australie.

33 N. Boulanger, P. Meunier & S. Le Dizès (2007). "Tilt-induced instability of a vortex in a stratified fluid", 60th APS-DFD Annual Meeting, 18-20 nov. 2007, Salt-Lake City, Etats-Unis.

34 C. Eloy, P. Meunier, R. Lagrange & F. Nadal (2007). "Rotating fluid cylinder submitted to a weak precession", 60th APS-DFD Annual Meeting, 18-20 nov. 2007, Salt-Lake City, Etats-Unis.

35 R. Lagrange, C. Eloy, F. Nadal & P. Meunier (2008). "Instability of a fluid inside a precessing cylinder", 22nd International Congress of Theoretical and Applied Mechanics, 24-29 août 2008, Adelaide, Australie.

36 X. Riedinger, P. Meunier & S. Le Dizès (2008). "Instability of a stratified Lamb-Oseen vortex", 7th European Fluid Mechanics Conference, 14-18 sept.2008, Manchester, Angleterre.

37 R. Lagrange, P. Meunier, C. Eloy, F. Nadal (2008). "Dynamics of a fluid inside a precessing cylinder", 7th European Fluid Mechanics Conference, 14-18 sept.2008, Manchester, Angleterre.

38 P. Meunier (2008). "Instabilities of a columnar vortex in a stratified fluid", Rotating stratified turbulence and turbulence in the atmosphere and oceans. 8-12 décembre 2008, Newton Institute, Cambridge, Royaume-Uni.

3.5 Séminaires, workshops

1 P. Meunier & T. Leweke (1999). "Etude expérimentale de l'interaction entre deux tourbillons corotatifs", Workshop structure et dynamique de vortex, 27-28 avril 1999, Rouen, France.

2 P. Meunier (2000). "Effet d'une instabilité tridimensionnelle sur la fusion de deux tourbillons", Journées de Dynamique Non-Linéaire, mai 2000, Laboratoire de Physique des Interactions Ioniques et Moléculaires, Marseille, France.

3 T. Leweke & P. Meunier (2000). "Instabilité elliptique dans les paires de tourbillons", Séminaire invité au Laboratoire des Ecoulements Géophysiques et Industriels, mai 2000, Grenoble, France.

4 T. Leweke, F. Richez, P. Meunier & P. Le Gal (2000). "Enroulement d'une nappe de vorticité - Etude expérimentale", Réunion dans le cadre du Plan d'Etudes Amont militaire no 98 26 10 : Aérodynamique des avions de combat, 20 déc. 2000, Marseille, France.

5 T. Leweke & P. Meunier (2001). "Experiments on merging and 3D instability of corotating vortices", Réunion du contrat européen Wake Vortex Characterization and Control (C-Wake), 13-14 fév. 2001, Athènes, Grèce.

6 T. Leweke & P. Meunier (2001). "Instabilité tridimensionnelle des paires de tourbillons", Séminaire invité au Institut de Mécanique des Fluides de Toulouse, fév. 2001, Marseille, France.

7 T. Leweke & P. Meunier (2001). "Interactions entre tourbillons parallèles", Séminaire invité au Laboratoire J. A. Dieudonné, avril 2001, Nice, France.

8 T. Leweke, P. Meunier, P. Le Gal & F. Richez (2001). "Enroulement 2D et 3D d'une nappe de vorticité - Etude expérimentale", Réunion dans le cadre du Plan d'Etudes Amont militaire no 98 26 10 : Aérodynamique des avions de combat, 2 mai 2001, Palaiseau, France.

9 P. Meunier & T. Leweke (2001). "L'instabilité elliptique dans une paire de tourbillons corotatifs", Rencontres de la Mécanique à Jussieu, 28 mai 2001, Paris, France.

10 P. Meunier & T. Leweke (2001). "Instabilité et fusion de deux tourbillons corotatifs", Séminaire invité au Laboratoire d'Hydrodynamique de l'Ecole Polytechnique (LadHyX), juin 2001, Palaiseau, France.

11 G. R. Spedding & P. Meunier (2002). "Effect of Initial Conditions on Vortex and Wave Motions in Stratified Wakes : a Progress Report", RASP meeting for the ONR contract on Stratified Wakes, oct. 2002, ?, Etats-Unis.

12 P. Meunier (2003). "Interaction of two corotating vortices : elliptic instability and merging", Séminaire invité au Aerospace and Mechanical Engineering Department, University of Southern California, 19 fév. 2003, Los Angeles, Californie, Etats-Unis.

13 P. Meunier (2003). "Interaction of two corotating vortices : elliptic instability and merging", Séminaire invité au Environmental Fluid Dynamics Department, University of California Santa Barbara, 4 mars 2003, Santa Barbara, Californie, Etats-Unis.

14 P. Meunier (2003). "Interaction de deux tourbillons corotatifs : fusion et instabilité elliptique", Colloque "Tourbillons en Hydrodynamique", 18-24 mai 2003, Porquerolles, France.

15 P. Meunier (2004). "Accelerated mixing in vortices", Séminaire invité au Department of Aeronautics, Turbulence and Mixing Team, Imperial College, 8 novembre 2004, Londres, Royaume-Uni.

16 P. Meunier (2004). "Sillages lointains dans des fluids stratifiés", Séminaire invité aux Journées de Dynamique Non-Linéaire, Centre de Physique Théorique, 16 nov. 2004, Marseille, France.

17 P. Meunier (2004). "Tourbillons stratifiés : le pourquoi et le comment", Séminaire de formation des techniciens de l'IRPHE, 19 nov. 2004, Marseille, France.

18 N. Boulanger, P. Meunier & S. Le Dizès (2005). "Dynamics of a stratified tilted vortex", Geophysical Turbulence Program : Coherent Structures in Atmosphere and Oceans, 11-14 juillet 2005, Boulder, Etats-Unis.

19 P. Meunier, L. Devesvres & C. Eloy (2005). "Resonances inside a precessing cylinder", Geophysical Turbulence Program : Coherent Structures in Atmosphere and Oceans, 11-14 juillet 2005, Boulder, Etats-Unis.

20 G. R. Spedding & P. Meunier (2005). "Waves and vortex motions in stably-stratified fluids", Geophysical Turbulence Program : Coherent Structures in Atmosphere and Oceans, 11-14 juillet 2005, Boulder, Etats-Unis.

21 P. Meunier (2005). "Interaction of 2 co-rotating vortices", Séminaire invité au Department of Mechanics, UCSD, 16 sept. 2005, San Diego, Etats-Unis.

22 P. Meunier (2006). "Sillages dans des fluids stratifiés", Séminaire invité à l'IMFT, 14 juin 2006, Toulouse, France.

23 P. Meunier (2007). "Sillages lointains dans des fluids stratifiés", Séminaire invité à Centrale Lyon, 26 janv. 2007, Lyon, France.

24 P. Meunier (2007). "Application de la PIV à l'etude d'un écoulement de précession", GDR Turbulence, 21-22 mai 2007, Marseille, France.

25 N. Boulanger, P. Meunier & S. Le Dizes (2007). "Dynamics of stratified tilted vortex", Workshop "Vortices and vortex sheets", 4-10 juin 2007, Porquerolles, France.

25 X. Riedinger, P. Meunier & S. Le Dizes (2007). "Instability of Lamb-Oseen stratified vortex", Workshop "Vortices and vortex sheets", 4-10 juin 2007, Porquerolles, France.

26 R. Lagrange, P. Meunier, F. Nadal & C. Eloy (2007). "Instability of a fluid inside a precessing cylinder", Workshop "Vortices and vortex sheets", 4-10 juin 2007, Porquerolles, France.

27 P. Meunier (2007). "A physically-based numerical method for scalar mixing", SCAT meeting, 12-16 nov. 2007, Cozumel, Mexique.

28 P. Meunier (2008). "Sillages lointains dans des fluids stratifiés", Séminaire invité au LPMC, 22 fév. 2008, Nice, France.

29 P. Meunier (2008). "A new Lagrangian numerical method for scalar mixing", Euromech workshop : Mixing of coastal, estuarine and riverine shallow flows, 8-11 juin 2008, Ancona, Italie.

30 P. Meunier (2008). "Le mélange turbulent, une suite d'étirements et d'agrégations", Séminaire Dautreppe : Turbulence, aspects fondamentaux et applications, 20-24 oct 2008, Grenoble, France.

31 R. Lagrange, P. Meunier, C. Eloy & F. Nadal (2008). "Dynamics of a fluid inside a precessing cylinder", IUTAM symposium on "150 years of vortex dynamics", 12-16 oct. 2008, Copenhagen, Danemark.

4 Transfert technologique, relations industrielles et valorisation

J'ai participé à deux contrats européens C-Wake, et Far-Wake sur la réduction des tourbillons de sillage d'avion, soutenus par Airbus. Le but de ces contrats était de comprendre la génération des tourbillons dans le sillage des avions, et de tenter de détruire ces tourbillons le plus rapidement possible. En effet, ces tourbillons posent de graves dangers dans les aéroports car ils peuvent déstabiliser les avions suivants. L'industrie aéronautique tente ainsi de détruire ces tourbillons de sillage afin de réduire les délais obligatoires entre l'atterrissage de deux avions. Ces contrats ont été validés par un contrat industriel Awiator permettant d'appliquer les travaux de recherche aux avions actuels. Nous participons ainsi activement à cette activité au sein de notre équipe, en essayant d'amener les résultats fondamentaux jusqu'à une application directe.

D'autre part, j'ai obtenu deux contrats avec le CEA/CESTA pour travailler sur la précession d'un container tournant. Les applications directes concernent la stabilisation des satellites possédant des fluides carburants en rotation. Ces contrats d'une valeur de 15kEuros chacun ont permis de monter l'expérience de précession. Ces travaux sont menés en collaboration avec Christophe Eloy au laboratoire. Ces contrats ont donné lieu à une bourse de thèse BDI CNRS/Entreprise qui a débuté au 1er octobre 2006 sous ma direction. Cette bourse de thèse est accompagnée d'un contrat d'accompagnement d'un montant de 22kEuros, qui a permis de modifier les expériences de précession pour la thèse de Romain Lagrange.

De plus, j'ai participé à l'ACI Catastrophes Naturelles, dans le cadre de l'étude de la " Dynamique de Cyclones Intenses ", piloté par Jan-Bert Flor (LEGI, Grenoble). Le but de cette étude était de tenter d'expliquer la formation de cyclones intenses par des grosses structures cycloniques, au moyen de la déstabilisation du front. De plus, nous avons essayé de prédire la dynamique d'un tourbillon soumis à une stratification. Cette ACI a ainsi permis de monter le dispositif expérimental utilisé par Nicolas Boulanger au cours de sa thèse sur l'inclinaison d'un vortex stratifié.

Enfin, je suis reponsable au laboratoire d'une ANR Flowing obtenue pour l'étude des fronts météorologiques. Cette ANR 30kEuros) a permis de monter l'expérience sur les instabilités d'un tourbillon vertical stratifié et sur l'écoulement de Taylor-Couette dans un fluide stratifié. C'est dans le cadre de cette ANR que rentre la thèse que Xavier Riedinger effectue sous ma co-direction sur l'étude des ondes internes générées par un vortex stratifié.

5 Résumé des travaux de recherche

Dans les années qui ont suivi ma thèse de doctorat, je me suis tourné vers l'étude des fluides géophysiques. Les écoulements géophysiques peuvent être séparés en deux catégories : d'une part la dynamique des océans et de l'atmosphère sont regroupés dans la géophysique externe, et d'autre part la dynamique du manteau et du noyau terrestre sont regroupés dans la géophysique interne. On inclut parfois dans la géophysique interne le cas des autres planètes que la terre.

La spécificité de ces écoulements géophysiques est qu'ils sont soumis à l'influence de la stratification du fluide et à l'influence de la rotation de la planète. En effet, les océans et l'atmosphère sont soumis à une forte stratification qui confère au fluide une géométrie en couche mince. Ceci est un élément fondamental pour la modélisation des écoulements en géophysique externe. De plus, en géophysique interne et externe, les grandes échelles de l'écoulement sont très sensibles à la force de Coriolis issue de la rotation de la planète.

Au cours de mes 7 dernières années de recherche, je me suis concentré sur la modélisation expérimentale de tels écoulements géophysiques dans un laboratoire. Le but était de créer des expériences modèles qui soient suffisamment simples pour être expliquées de manière propre par des théories, mais qui contiennent des éléments tels que la stratification ou la rotation pour être suffisamment proches des écoulements géophysiques réels.

J'ai tout d'abord étudié l'influence d'une stratification sur un sillage. Puis je me suis intéressé à la dynamique d'un tourbillon dans un fluide stratifié. Enfin, j'ai regardé la dynamique d'un tourbillon (ou plus précisément d'un cylindre tournant) dans un repère tournant, ce qui m'a conduit à étudier les écoulements de précession. Enfin, j'ai regardé comment un scalaire passif (tel que le sel pour les océans, l'humidité pour l'atmosphère ou la température pour le noyau terrestre) est advecté par un écoulement géophysique. Je développe dans la suite de ce mémoire ces quatre thèmes de recherche de manière séparée.

5.1 Sillages d'objets non-profilés dans un fluide stratifié

J'ai effectué ces travaux de recherche au cours de mon post-doc entre avril 2002 et janvier 2003 puis sur de courtes périodes en mars 2003, en octobre 2003 et en aout 2005 pour finir les expériences en cours. Ces travaux ont été menés au sein de l'équipe "Geophysical Fluid Dynamics" du "Aerospace and Mechanical Engineering Department" de l' "University of Southern California" à Los Angeles (Etats-Unis). Ces recherches étaient dirigées par G. Spedding pour les expériences, et ont été comparées avec des résultats numériques obtenus par P. Diamessis. Ces résultats s'appliquent directement au sillage des montagnes et des îles dans l'atmosphère et dans l'océan, mais aussi au sillage des sous-marins, justifiant ainsi la présence de contrats américains avec l'Office of Naval Research au sein de l'University of Southern California. Ce contrat visait à déterminer la durée de vie et la possible détection d'un sillage dans un fluide stratifié, avec application aux

sillages de sous-marins. Ces travaux ont donné lieu à quatre papiers publiés dans des revues de rang A ainsi qu'à onze présentations dans des conférences internationales.

5.1.1 Objets non propulsés

Le sillage d'un objet non profilé dans un fluide stratifié est différent d'un sillage dans un fluide homogène. En effet, même pour de faibles stratifications, c'est à dire pour des faibles nombres de Froude (F=U/ND, U étant la vitesse de l'objet, D son diamètre et N la fréquence de Brunt-Väisälä du fluide stratifié), la vitesse du sillage diminue avec la distance rendant ainsi le sillage lointain fortement stratifié [19, 7]. Les stades ultimes du sillage sont ainsi bien décrits par une turbulence quasi-bidimensionnelle[35], comportant de nombreux vortex horizontaux et de faibles vitesses verticales. Des mesures quantitatives de vitesse 2D par Vélocimétrie par Images de Particules (PIV) ont permis de construire une loi empirique [38, 39] prédisant la largeur L_y et l'amplitude U_0 du sillage en fonction du temps. Ces résultats ont été obtenus pour différents nombres de Reynolds et de Froude, mais uniquement pour une sphère, et ne pouvaient pas se généraliser à des objets possédant des formes quelconques. Par des expériences sur des objets de différentes formes (cylindre, ellipsoïde, disque, demi-sphère et cube), j'ai étendu cette loi. En effet, si l'on utilise comme diamètre de l'objet un diamètre efficace $D_{\text{eff}} = D(C_D/2)^{1/2}$, basé sur le coefficient de traînée de l'objet C_D (dans un fluide non stratifié), tous les résultats se ramènent à une loi universelle pour la largeur L_y et pour l'amplitude U_0 du sillage[24]. Ceci peut se comprendre par le fait que ce diamètre effectif est en fait l'"épaisseur de quantité de mouvement", correspondant à la quantité de fluide entraînée derrière l'objet et responsable de la traînée. Grâce à ces mesures, il est possible de connaître la force d'un sillage stratifié aux temps longs, dès que l'on connaît le coefficient de traînée de l'objet (tabulé pour la plupart des formes standards).

5.1.2 Objets auto-propulsés

Pour des objets possédant un moyen de propulsion comme une hélice ou un jet, la quantité de mouvement derrière l'objet n'est plus reliée au coefficient de traînée. En effet, la masse de fluide entraînée derrière l'objet par la traînée est entièrement compensée par la masse d'eau éjectée dans l'autre sens par le système de propulsion, lorsque l'objet se déplace à vitesse constante. On s'attend ainsi à ce que la quantité de mouvement derrière un objet auto-propulsé soit nulle.

Cependant, si le fluide est stratifié, l'objet émet des ondes internes qui transportent de la quantité de mouvement en dehors du sillage, créant ainsi une force de traînée plus importante : le coefficient de traînée peut être augmenté jusqu'à 10%. Le sillage peut ainsi recouvrir de la quantité de mouvement dans un fluide stratifié.

Expérimentalement, nous avons tiré un objet possédant une hélice tournant à une vitesse donnée, mais avec différentes vitesses de translation de l'objet. Nous avons ainsi montré que le sillage est entièrement dominé par la quantité de mouvement résiduelle aux temps longs, si la différence entre la

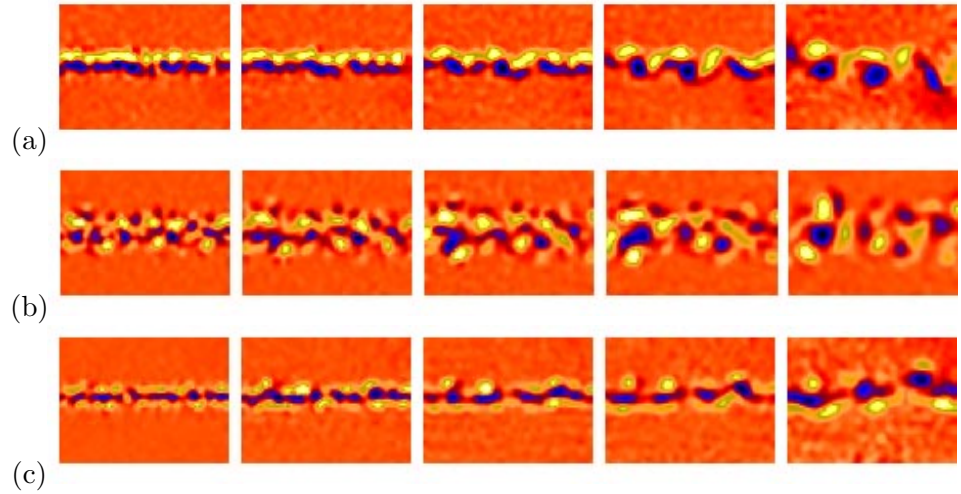

FIG. 1 – Champs de vorticité dans un plan horizontal du sillage d'un objet propulsé en accélération (a), en régime de croisière (b) et possédant un angle d'attaque (c).

vitesse de l'objet et la vitesse de croisière (qu'il aurait s'il n'était pas tracté) est supérieure à 2%. C'est ce que l'on observe sur la figure 1. Lorsque la vitesse de l'objet est suffisamment éloignée de sa vitesse de croisière, le sillage moyen présente un jet (une couche de vorticité positive à coté d'une couche de vorticité négative) qui contient de la quantité de mouvement. Cela correspond ainsi au sillage d'un objet non-propulsé ou au sillage d'un objet propulsé en accélération (Fig. 1a). Par contre, lorsque l'objet est tracté à sa vitesse de croisière, le jet devient turbulent et ne contient plus jet et donc de quantité de mouvement (Fig. 1b).

Théoriquement, il est possible de construire un modèle pour prédire la structure du sillage. En supposant que la quantité de mouvement expulsée par le système de propulsion ne dépend pas de la vitesse de l'objet, nous avons pu calculer la quantité de mouvement derrière un objet auto-propulsé. Grâce à la loi empirique générale obtenue pour des objets non propulsés (voir paragraphe précédent), il est alors facile de prédire la forme et l'amplitude du sillage d'un objet propulsé aux temps longs, ce qui est en bon accord avec les résultats expérimentaux. Ces travaux ont fait l'objet d'une publication[25].

5.1.3 Sillage d'un objet possédant un angle d'attaque

Nous avons regardé expérimentalement comment le sillage se comportait lorsque l'objet est exactement en régime de croisière. Nous avons vu que le sillage devient turbulent si l'angle d'attaque est nul. Cependant, le sillage peut devenir asymétrique si il existe un faible angle d'attaque comme le montre la figure 1(c). Ces travaux ont fait l'objet d'une publication à Journal of Fluids and Structures [10].

5.1.4 Théorie auto-similaire

Nous avons enfin réussi à expliquer ces résultats expérimentaux par une théorie auto-similaire, généralisant les théories classiques obtenues pour des fluides non-stratifiés. Pour ce faire, nous avons supposé que le sillage s'étend dans la direction verticale grâce à de la diffusion visqueuse uniquement et à de la diffusion turbulente dans la direction horizontale [28]. Grâce à cette théorie, nous avons retrouvé les différents stades du sillage stratifié, trouvés expérimentalement. Nous avons aussi découvert deux autres stades du sillage. Le premier stade doit être observé pour les nombres de Reynolds élevés, lorsque les effets visqueux interviennent plus tard. Le deuxième stade apparaît à de très grandes distances derrière l'objet. Il s'agit d'un régime complètement laminaire. Un conséquence intéressante de cette théorie est que le sillage stratifié dure plus longtemps lorsque son nombre de Reynolds est élevé. Ces prédictions théoriques sont en très bon accord avec tous les résultats expérimentaux et numériques obtenus depuis 30 ans et elles offrent donc une très bonne synthèse de la dynamique d'un sillage stratifié.

5.2 Instabilités d'un tourbillon dans un fluide stratifié

L'étude de l'interaction de deux tourbillons dans un fluide stratifié stable a révélé la présence d'une nouvelle instabilité "zigzag " [2]. Cependant, comme pour le cas de l'instabilité de Crow [8], cette instabilité repose sur la connaissance des modes de Kelvin d'un tourbillon stratifié. De plus, une nouvelle instabilité a été découverte par Cariteau & Flor [6, 5] sur un tourbillon stratifié unique. Il apparaissaît donc intéressant d'étudier la dynamique d'un tourbillon stratifié unique pour connaître les relations de dispersion de ses modes de Kelvin comme dans le cas précédent et pour identifier cette nouvelle instabilité.

5.2.1 Structure d'un vortex incliné par rapport à une stratification

Dans un premier temps, nous nous sommes intéressé au cas d'un tourbillon dont l'axe est incliné par rapport à la verticale. Pour cela, nous avons construit une expérience adaptée, dans laquelle le tourbillon est généré par une pale en rotation dans un fluide initialement stratifié. Nous pouvons faire varier l'angle du tourbillon avec la verticale pour connaître l'état de base (encore inconnu théoriquement) ainsi que ses instabilités. Ceci a constitué le travail de thèse de Nicolas Boulanger qui effectue sa thèse de doctorat sous la direction de Stéphane Le Dizès pour la partie théorique et sous ma direction pour la partie expérimentale. Ces travaux rentrent dans le cadre d'une ACI sur les Catastrophes Naturelles (CatNat), dont la section "Dynamique de Cyclones Intenses" est dirigée par Jan-Bert Flor au LEGI (Grenoble). Sur cette expérience, nous avons monté un système de visualisation par ombroscopie et par strioscopie. Quelques images typiques obtenues par cette technique sont montrées dans la figure 2. Cette méthode peut être rendue quantitative puisque l'intensité de l'image est reliée au Laplacien de la densité.

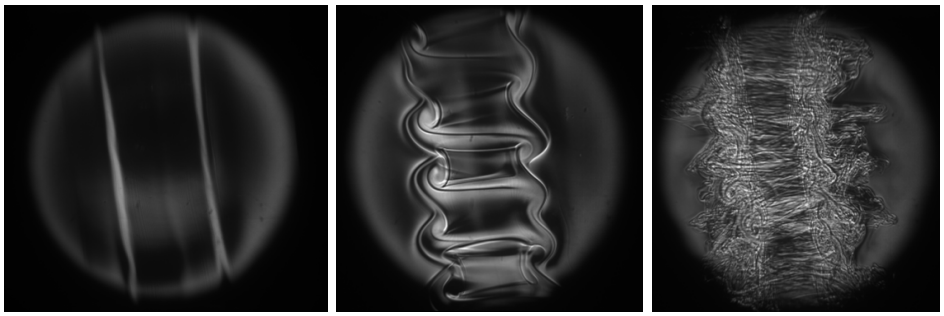

(a) (b) (c)

FIG. 2 – Visualisation par ombroscopie de l'instabilité d'un vortex incliné par rapport à une stratification ambiante du fluide

Nous avons montré expérimentalement et théoriquement que le vortex possède une couche critique au rayon où la vitesse angulaire du vortex est égale à la fréquence de flottaison du fluide stratifié. Cette couche critique est visible sur la photo de gauche de la figure ci-dessous. Ceci induit de fortes vitesses axiales à ce rayon critique, ainsi que de forts cisaillements [3].

Théoriquement, la couche critique a été lissée par les termes visqueux, montrant que l'amplitude de la vitesse axiale scale comme la racine du nombre de Reynolds et que l'épaisseur de la couche critique scale comme l'inverse de la racine du nombre de Reynolds. La solution théorique a été comparée avec un excellent accord aux résultats expérimentaux. De plus, nous avons lissé cette couche critique par des effets non-linéaires, montrant que l'amplitude scale alors comme la racine cubique de l'angle d'inclinaison.

Ces forts cisaillements au niveau de la couche critique semblent être la source d'une violente instabilité tri-dimensionnelle, sous la forme de rouleaux co-rotatifs de chaque côté du vortex[4]. Cette instabilité est visualisée dans la figure 2. Une théorie locale a été mise en place, qui prouve que le tourbillon est instable par rapport à une instabilité de Kelvin-Helmholtz de l'écoulement vertical dans la couche critique.

Cette instabilité rend le vortex extrêmement turbulent, sans pour autant détruire sa circulation. Elle crée un fort mélange au sein du vortex (voir Fig. 2c). Cette inclinaison du vortex augmente donc drastiquement le mélange dans la direction verticale, et pourrait être une source non négligeable de mélange dans les océans. Enfin, ces résultats s'appliquent aussi au cas des tornades par rapport à des applications météorologiques.

5.2.2 Modes instables d'un tourbillon vertical dans une fluide stratifié

Ces travaux constituent la suite de l'étude présentée au paragraphe précédent sur l'instabilité d'un vortex incliné. En l'absence d'inclinaison du vortex, on s'attend à ce que le vortex devienne stable. Cependant, des résultats théoriques récents [17] ont montré par une analyse WKB que le vortex possède des modes instables dans la limite des faibles nombres de Froude. Il apparaît donc nécessaire de trouver tous les modes instables en faisant une

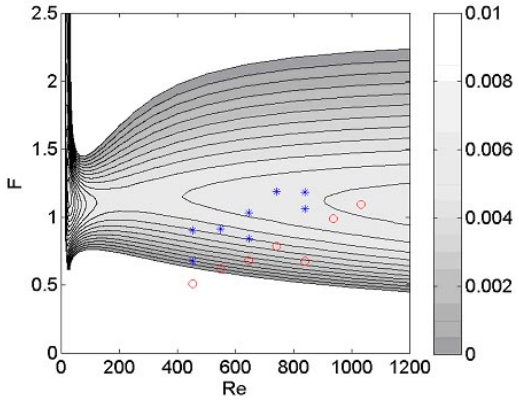

FIG. 3 – Taux de croissance des modes instables (de nombre d'onde azimutal m=1) pour un tourbillon vertical dans un fluide stratifié. Les contours correspondent aux résultats d'une analyse de stabilité linéaire numérique, les symboles indiquent les expériences pour lesquelles l'instabilité a été observée.

étude systématique pour différents nombres de Froude et nombres de Reynolds. Ceci constitue le travail de thèse de Xavier Riedinger, qui a débuté sa thèse au 1er octobre 2006 encadré par Stéphane Le Dizès pour la partie théorique et co-encadré par moi-même pour la partie expérimentale.

Il ressort de cette étude qu'un vortex placé dans un fluide stratifié est instable à n'importe quel nombre de Reynolds dans une bande de nombre de Froude autour de 1. Ceci est visible dans la figure 3 qui présente le taux de croissance du mode le plus instable en fonction du nombre de Froude et du nombre de Reynolds. Ces résultats ont été obtenus par une analyse de stabilité linéaire, réalisée numériquement pour un nombre d'onde axial et azimutal fixé. Tous les modes de nombre d'onde azimutal m supérieurs à 1 sont instables, mais c'est le mode $m = 1$ qui est le plus instable. La bande de longueur d'onde instable dépend fortement du nombre de Froude. Pour de faibles nombres de Froude, le mode instable apparaît pour une large bande de nombre d'onde axial. Lorsque le nombre de Froude augmente, l'instabilité se restreint à des bandes de nombre d'onde très étroites, qui correspondent à la résonance entre un mode de rayonnement du vortex et un mode de Kelvin du vortex non stratifié.

De plus, des expériences ont été effectuées sur un vortex généré par une pale mise en rotation dans un fluide stratifié. Nous avons observé que lorsque le vortex passe dans la zone instable du diagramme de stabilité, une ondulation apparaît sur le vortex, comme le montre la figure 4(a). Ceci correspond au mode instable du vortex, qui se superpose au vortex initial. Etant donné que la perturbation crée une ondulation du vortex, on peut en déduire que le mode instable contient deux lobes de vorticité de signe opposé placés de chaque coté du centre du vortex, tel que pour le mode de déplacement du vortex. C'est effectivement ce que l'on observe numériquement (4b) : dans une section du vortex, le mode instable contient deux lobes de vorticité opposés

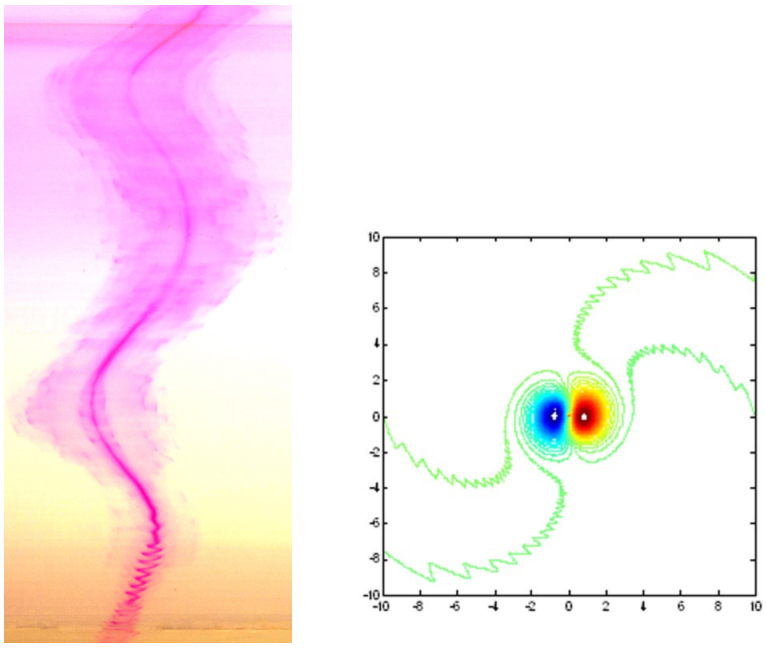

(a) (b)

FIG. 4 – Structure du mode instable d'un vortex dans un écoulement stratifié. L'instabilité est observée expérimentalement en vue de côté (a) et obtenue numériquement dans une section du vortex (b).

au cœur, puis des ailes de vorticité qui sont la signature d'ondes rayonnées par le vortex loin du cœur. C'est ainsi que l'on peut appeler ces modes, des modes rayonnants du vortex car ils sont oscillants loin du vortex. Ceci veut dire qu'un vortex, lorsqu'il est dans la zone instable du diagramme de stabilité, peut rayonner des ondes internes et perdre ainsi progressivement son énergie. Expérimentalement, ces ondes n'ont pu être observées car elles sont très faibles (comparé à la vorticité des deux lobes centraux). La décroissance du vortex n'a pas pu être observée non plus car les phénomènes visqueux sont plus importants. Cependant, on peut penser que dans des conditions gépohysiques réelles, à plus grand nombre de Reynolds, la décroissance du vortex peut être importante. Enfin, des comparaisons quantitatives sur la longueur d'onde instable ont été effectuées. La longueur d'onde observée expérimentalement est en moyenne plus élevée que la prédiction numérique, surtout pour les faibles stratifications.

Cette étude a donné lieu à 1 article en préparation, 1 article soumis et 2 présentations dans des conférences internationales.

5.3 Dynamique d'un fluide dans un cylindre en précession

Un des grands problèmes en géophysique interne consiste à comprendre comment est généré le champ magnétique terrestre. Même si l'on sait à l'heure actuelle que c'est le mouvement du fer liquide dans le noyau externe qui crée ce champ magnétique par effet dynamo, divers questions restent

sans réponse à ce sujet : quelle est la source d'énergie qui crée le mouvement du fer liquide, quel est l'écoulement moyen dans le noyau, et comment cet écoulement peut générer le champ magnétique par effet dynamo. Bien que la convection dans le noyau semble être la source d'énergie principale qui force l'écoulement dans le noyau, il existe deux autres candidats potentiels qui sont liés aux des phénomènes purement inertiels du fluide. D'une part, la précession de la terre pourrait générer un écoulement suffisamment intense s'il était turbulent pour compenser l'énergie disipée par le champ magnétique terrestre [21, 36, 12]. D'autre part, l'ellipticité des lignes de courant dans le noyau terrestre (liées au effets de marée), pourraient aussi créer une instabilité elliptique qui viendrait modifier l'écoulement dans le noyau terrestre. Il apparaît donc intéressant d'étudier précisément l'écoulement dans un objet en précession afin de pouvoir prédire l'effet de la précession sur le champ magnétique terrestre. Les premières études menées dans un cylindre en précession ont été faites par McEwan [23] et ont montré que les modes de Kelvin dans le cylindre pouvaient résonner lorsque la fréquence de précession correspondait à leur fréquence propre. Proche de ces résonances, l'écoulement devient fortement turbulent [22] et semble forcer un écoulement de rotation solide [14]. Bien que plusieurs théories aient été avancées pour la déstabilisation du fluide dans un cylindre en précession, il n'existait à l'heure actuelle aucune confirmation expérimentale.

Nous avons monté une expérience dans laquelle un cylindre en rotation autour de son axe est placé sur une plateforme tournante avec un faible angle de précession. En fonction du rapport des fréquence de rotation du cylindre et de la plateforme, différents modes propres (les modes de Kelvin) du fluide sont excités. Quelques exemples de modes propres sont montrés dans la figure 5. Nous avons mesuré expérimentalement la forme et l'amplitude de ces modes propres, et ainsi validé la théorie linéaire non-visqueuse.

L'amplitude de ces modes diverge lorsque la hauteur du cylindre est égale à un multiple impair de la demi-longueur d'onde du mode propre. Nous avons donc modifié la théorie afin de prendre en compte les effets non-linéaires et visqueux à la résonance. Nous avons ainsi montré que l'amplitude maximale du mode propre scale comme la racine du nombre de Reynolds dans le régime visqueux et comme la racine cubique de l'angle de précession dans le régime non-linéaire [29]. Cette théorie est en bon accord avec les résultats expérimentaux.

Cependant, il est bien connu que cet écoulement se déstabilise pour des nombres de Reynolds suffisamment élevés. Grace à des mesures PIV, nous avons montré que l'écoulement se déstabilise en créant 2 modes de Kelvin libres qui se superposent à l'écoulement de base qui contient un mode de Kelvin forcé [15]. Ceci est illustré dans la figure 6, dans laquelle la vorticité présente une structure de nombre d'onde azimutal m=6 (figure de gauche) dans une section du cylindre et un nombre d'onde azimutal m=5 superposé au mode de Kelvin forcé de nombre d'onde m=1 dans une autre section (figure de droite).

Ces mesures prouvent ainsi que l'instabilité est une résonance triadique entre ces trois modes de Kelvin, et une analyse de stabilité linéaire permet de prédire le taux de croissance de l'instabilité de manière analytique. En

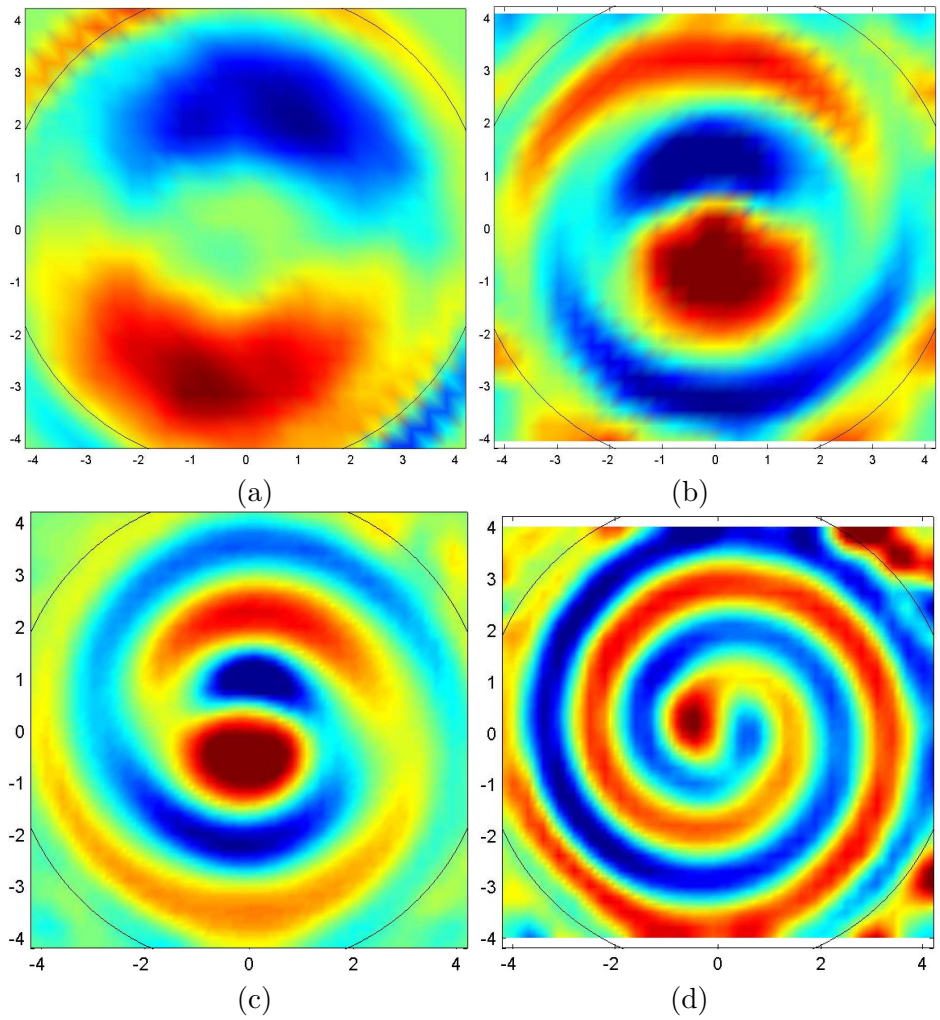

FIG. 5 – Mesure de la vorticité du 1er, 2ème, 3ème et 5ème mode propre du fluide dans un cylindre, excités par la précession du cylindre.

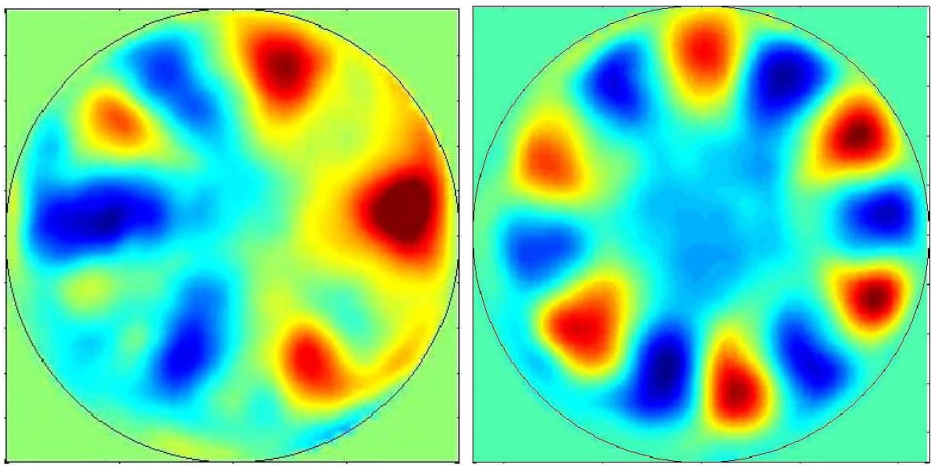

(a) (b)

FIG. 6 – Mesure dans deux sections différentes de la vorticité lors de l'instabilité du fluide dans un cylindre en précession, mettant en évidence la présence de deux modes de nombre d'onde azimutal m=6 et m=5.

rajoutant les effets visqueux, il est même possible de prédire théoriquement le diagramme de stabilité de l'écoulement dans un cylindre en précession (voir figure 7). Les résultats expérimentaux sont en excellent accord avec cette prédiction. Il est possible aussi d'inclure des effets de "detuning" lorsque la fréquence de précession varie, ce qui fait apparaître d'autres modes instables. Tout ceci a été confirmé expérimentalement.

De plus, en incluant des effets faiblement non-linéaires, il est possible de prédire la saturation des modes instables. Ces modes forcent un mode axisymétrique au travers des couches limites. Le mode axisymétrique limite alors l'instabilité en changeant la fréquence des modes instables. La théorie faiblement non-linéaire prédit non seulement la saturation de l'instabilité mais aussi des régimes d'intermittence, puis de chaos. Toutes ces prédictions sont en excellent accord avec les résultats expérimentaux, même pour des nombres de Reynolds une décade au dessus du seuil d'instabilité, dans un régime apparemment complètement turbulent. Il est donc intéressant de voir qu'une théorie faiblement non-linéaire permet de donner des prédictions quantitatives sur l'écoulement turbulent dans un cylindre en précession.

5.4 Mélange d'un scalaire passif

Une des questions actuelles en géophysique externe consiste à comprendre le mélange d'un scalaire passif tel que le dioxyde de carbone ou la température dans les océans. En effet, les mesures locales de diffusivité d'un scalaire dans les océans ne suffisent pas à expliquer la structure thermohaline aux grandes échelles[30, 18, 37]. Le mélange vertical dans les océans est extrêmement faible du fait de la stratification. Il est ainsi 10 plus faible que la valeur qui est prise en compte dans les modèles océaniques globaux. Ceci veut dire que 90% du mélange vertical dans les océans reste incompris. Or,

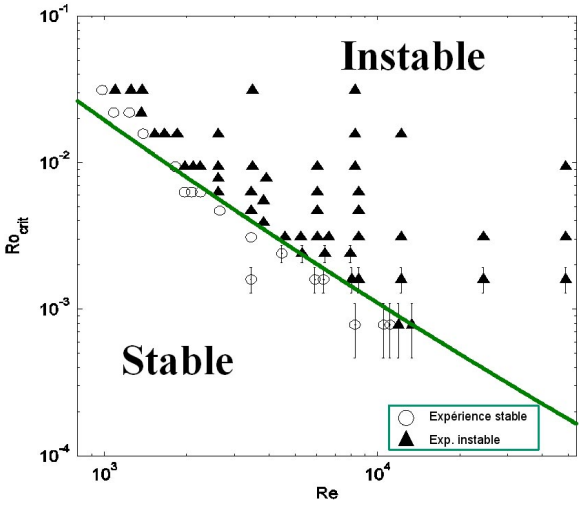

FIG. 7 – Mesure dans deux sections différentes de la vorticité lors de l'instabilité du fluide dans un cylindre en précession, mettant en évidence la présence de deux modes de nombre d'onde azimutal m=6 et m=5.

ce mélange est primordial dans les modèles climatiques car il intervient dans la modélisation des flux de chaleur entre les différentes latitudes et pour le stockage du dioxyde de carbone. Mais il est aussi important pour les modèles biologiques car il permet de faire remonter à la surface les nutriments dont le phytoplancton a besoin, et c'est donc un paramètre pris en compte dans les écosystèmes marins.

Les écoulements océaniques possèdent de forts tourbillons horizontaux et une faible vitesse verticale. Nous nous sommes donc intéressés à l'advection d'un scalaire passif dans un écoulement bi-dimensionnel, d'abord constitué d'un unique tourbillon, puis d'un écoulement modélisant la turbulence bi-dimensionnelle.

5.4.1 Mélange d'un scalaire dans un tourbillon

Cette étude a débuté de manière expérimentale et théorique à la fin de ma thèse par une collaboration avec E. Villermaux sur les problèmes de mélange. L'idée était de déterminer le mélange d'un scalaire passif dans le champ de vitesse d'un tourbillon. Malgré la présence de quelques résultats théoriques dans la littérature [34, 9, 1], il n'existait pas de résultats expérimentaux sur ce sujet. Cette expérience est assez délicate car le scalaire passif (ici, un colorant fluorescent) doit être injecté de manière uniforme et suffisamment rapidement dans le vortex. Une première technique consiste à introduire le colorant au moyen d'un tube parallèle à une pale. La mise en mouvement de la pale crée un tourbillon suffisamment rapidement pour que le colorant s'enroule autour du vortex. Cette évolution est présentée sur la figure 8. Une deuxième technique consiste à bouger verticalement un fil imbibé de fluorescéine dans un vortex déjà formé. Ceci donnait les mêmes résultats mais cela permettait d'utiliser un fluide stratifié afin que le vortex survive

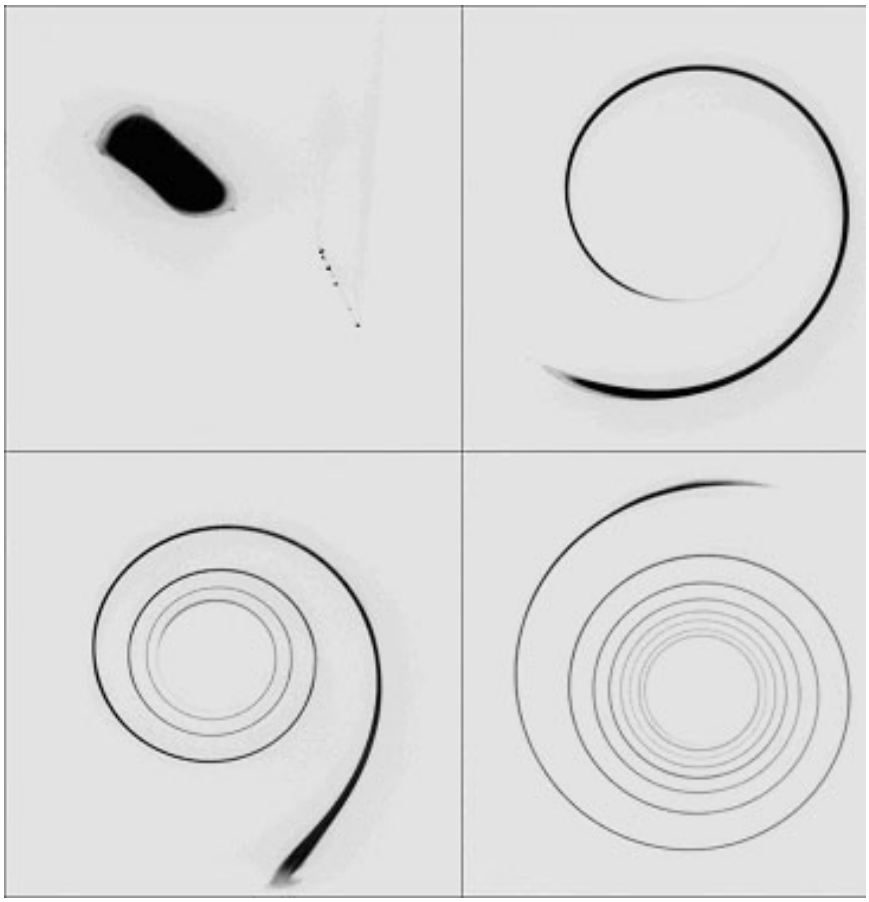

FIG. 8 – Visualisation de la spirale d'un colorant s'enroulant autour du centre d'un vortex.

pendant un temps très long.

Pour expliquer ces résultats expérimentaux, nous avons construit une théorie par une analyse locale de l'étirement du patch de scalaire. En poussant la théorie le plus loin possible, nous avons obtenu une prédiction pour la distribution spatiale et pour la PDF du scalaire, en excellent accord avec les résultats expérimentaux [26]. La diffusion est accélérée par l'étirement lié à la rotation différentielle du vortex, et il apparaît un cusp dans la PDF du scalaire lié à la présence d'un minimum d'étirement pour un rayon particulier [27]. Il est à noter que l'hypothèse (couramment utilisée en turbulence pour calculer des PDF) supposant que seuls les maximas locaux du scalaire suffisent à déterminer la PDF mène à un résultat en fort désaccord avec l'expérience et qu'il faut utiliser toute la distribution spatiale du scalaire pour obtenir un bonne prédiction de la PDF.

5.4.2 Mélange d'un scalaire passif dans un écoulement turbulent

Cette étude numérique est la suite de l'étude expérimentale et théorique sur le mélange d'un scalaire passif dans un vortex. Nous avions montré

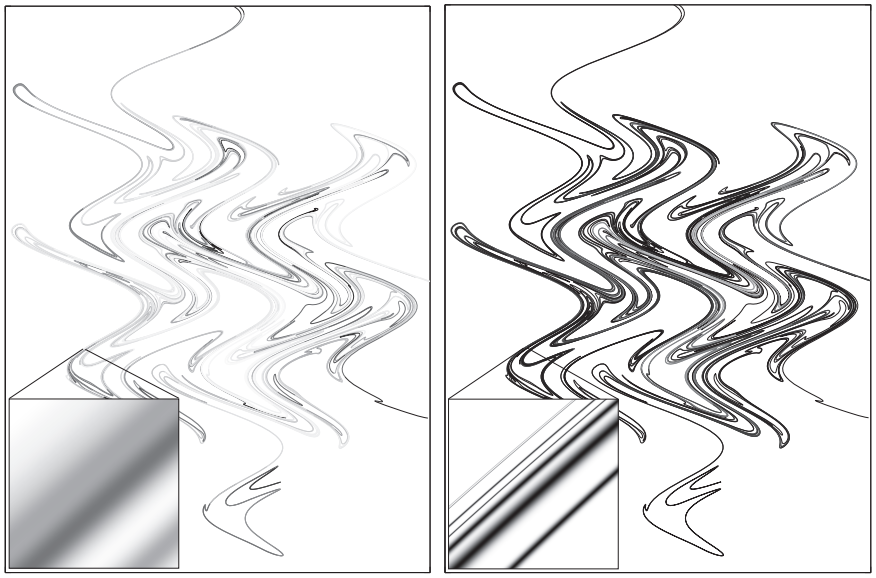

(a) (b)

FIG. 9 – Simulation numérique d'un filament de scalaire advecté par un écoulement de type 'Sine flow' pour deux diffusivités différentes : D=10-7 (gauche) et D=10-10 (droite).

qu'il est possible de prédire le champ de concentration et la densité de probabilité (PDF) d'un scalaire dans un vortex en faisant une analyse locale autour du filament de scalaire. En effet, une tache de scalaire se déforme rapidement en un filament de scalaire, qui se fait étirer par l'écoulement. L'effet de l'étirement tend à rétrécir l'épaisseur du filament et ainsi à augmenter l'effet de la diffusion. La plupart des études se sont restreintes à utiliser cette modélisation du scalaire pour des analyses théoriques dans des écoulements modèles tels qu'un jet [41], un vortex [26] ou une turbulence homogène [40]. Cependant, il est très facile d'utiliser cette modélisation dans un écoulement quelconque, en calculant numériquement la position et l'étirement du filament au cours du temps. Une analyse locale permet de prédire quantitativement la diffusion du scalaire autour du filament pour peu que l'étirement soit connu. Nous avons donc mis au point cette technique numérique et nous l'avons testée dans le cas d'un écoulement du type "Sine flow ". Les résultats sont présentés dans la figure ci-dessous. L'intérêt de cette technique est qu'elle s'applique à des diffusions tendant vers 0, puisque la méthode numérique ne diverge pas dans la limite non diffusive, contrairement aux méthodes classiques basées sur l'intégration des équations aux dérivées partielles sur un réseau carré. Cette méthode est extrêmement efficace pour les faibles diffusions (grand nombre de Péclet), et elle permet de connaître quantitativement l'épaisseur d'un filament et la concentration maximale du filament même pour des faibles diffusivités. Un exemple de résultat numérique est montré dans la figure 9. Bien que l'épaisseur du filament soit très fine, le code numérique reste stable, ce qui prouve l'efficacité de cette technique numérique.

De plus, en couplant cette étude aux résultats théoriques de Kalda (2000), nous avons obtenu un modèle pour la PDF d'un scalaire dans un écoulement turbulent 2D (dans le régime de Batchelor). Ce modèle est en très bon accord avec les résultats numériques, bien qu'il ne contienne aucun paramètre ajustable. Ces travaux ont donné lieu à un article en préparation.

6 Projet de recherche

Mes futures activités de recherche se situent d'une part dans la continuité des résultats déjà obtenus. En effet, je m'intéresse toujours aux instabilités liées à la présence de la stratification et de la précession. Et j'envisage aussi d'analyser l'influence d'une paroi sur la dynamique d'un tourbillon. Mais je compte aussi développer un nouveau thème de recherche, relié à la microfluidique, dans lequel je m'intéresserai au sillage d'une sphère proche d'un plan. Je détaille ci-dessous ces différents sujets de recherche.

6.1 Instabilité de Taylor-Couette dans un fluide stratifié

Il a été montré récemment que la présence d'une stratification stable du fluide peut provoquer la déstabilisation de l'écoulement de Taylor-Couette (obtenu entre deux cylindres tournants coaxiaux). Cette observation numérique [42] et expérimentale [16] a été obtenue dans un régime où l'instabilité centrifuge est absente et pour de faibles "gap", c'est à dire lorsque le rayon interne et externe sont proches. Dans cette géométrie, l'instabilité provient d'une résonance des ondes de gravité entre les deux cylindres. Elle est donc limitée à des bandes de nombre d'onde axiaux bien spécifiques. Cependant, cet écoulement semble être aussi instable dans une configuration où le rayon interne et le rayon externe sont très différents. Dans ce cas, l'instabilité provient d'un mode rayonnant instable, identique au mode de rayonnement d'un tourbillon Gaussien.

Expérimentalement, nous allons donc étudier l'instabilité de l'écoulement de Taylor-Couette en présence de stratification. Dans un premier temps, nous nous restreindrons au cas d'un rayon externe infini afin de faire le lien avec l'instabilité d'un tourbillon libre. Dans un deuxième temps, nous étudierons le cas d'un rapport fini entre le rayon interne et externe. Cet écoulement dépend de quatre paramètres (nombre de Reynolds, nombre de Froude, rapport des rayons et rapport des vitesses de rotation). Une étude systématique risquerait donc d'être fastidieuse. De plus, l'expérience ne permettra pas forcément d'atteindre tous les régimes instables. Ces études expérimentales seront donc comparées à une étude numérique extensive par analyse de stabilité linéaire.

6.2 Précession d'un ellipsoide

L'étude de l'écoulement de précession a été menée jusqu'à présent dans un cylindre. Afin de se rapprocher de l'écoulement géophysique réel, il serait intéressant de se placer dans une configuration ellipsoïdale. Diverses questions peuvent alors apparaître. Quel est l'écoulement de base dans un

ellipsoïde en précession ? Comment cet écoulement se déstabilise-t-il ? Quel est le taux de turbulence dans l'écoulement après déstabilisation ?

Il existe une solution laminaire pour un ellipsoïde en précession [33]. Cette solution décrit correctement la vitesse du fluide dans le cas laminaire et semble aussi bien représenter la vitesse moyenne du fluide dans le cas turbulent [31]. Mais il est bien connu[21, 31] que cette solution devient instable pour de forts taux de précession. Et on ne sait toujours pas si c'est une instabilité globale [13] ou des instabilités locales [20] qui sont à l'origine de la turbulence au sein du fluide. Il serait donc intéressant de pouvoir déterminer la nature de la transition vers la turbulence dans un ellipsoïde en précession. Il serait aussi intéressant de connaître le taux de turbulence et l'éventuelle présence d'ondes inertielles.

Enfin, il serait intéressant de rajouter un champ magnétique dans un tel écoulement de précession afin de voir quels sont les structures du champ magnétique. Cela pourrait donner des indications sur le possible effet dynamo dans une planète en précession.

6.3 Interaction d'un vortex avec une paroi

Bien que la structure d'un tourbillon soit bien comprise pour un tourbillon infini, les effets de bout viennent compliquer fortement l'analyse théorique. En effet, un tourbillon n'est plus stable lorsqu'on considère qu'il n'est pas d'extension axiale infinie. Un cas particulier consiste à couper le vortex par une paroi perpendiculaire à l'axe du vortex. L'écoulement est alors stable (aux faibles nombres de Reynolds) et génère une forte vitesse axiale qui résulte du pompage d'Ekman. Des études théoriques récentes ont montré que la structure du tourbillon peut devenir complexe lorsque le nombre de Reynolds est augmenté. En effet, le profil radial de vitesse axiale peut devenir oscillant, ce qui induit des vitesses vers la paroi au centre du vortex. Cette étude s'applique directement au cas d'un tornade qui est en générale attachée au sol.

Expérimentalement, nous nous proposons de générer un vortex en mettant en rotation une pale qui glisse le long du fond. Ceci crée un tourbillon qui descend jusqu'au fond, ce qui génère une forte vitesse axiale au coeur du tourbillon. Il serait donc intéressant de savoir si cette vitesse axiale est en accord avec les théories existantes et si on peut retrouver l'inversion de vitesse axiale pour de grands nombres de Reynolds.

6.4 Sillage d'une sphère le long d'une paroi

Lorsqu'une sphère glisse le long d'un plan, il existe un point de cisaillement infini entre la sphère et le plan. Cette singularité peut être résolue par des méthodes asymptotiques qui prédisent que la pression diverge en ce point lorsque la distance entre la sphère et le plan tend vers 0. Bien qu'il existe quelques théories contradictoires sur ce problème [32, 11], il existe peu d'expérience qui valide ces théories. Il apparaît donc intéressant de traiter ce problème de manière expérimentale.

Nous nous proposons donc d'étudier l'écoulement au voisinage du point de glissement pour une sphère en translation le long d'un plan. Ce problème

est intéressant pour de petites tailles de particules, pour lesquels l'écoulement reste laminaire. Nous nous restreindrons donc au cas des faibles nombres de Reynolds. Pour obtenir des nombres de Reynolds suffisamment faibles, nous utiliserons un fluide visqueux tel que la glycérine ou une huile silicone. Ceci permettra ainsi de faire de la micro-fluidique à taille humaine.

Ce projet fait partie d'un projet de subvention par l'ANR dirigé par Bernard Pouliny du CRPP à Bordeaux. Le but de ce projet est d'étudier l'effervescence dans les fluides saturés en gaz dissous en présence de cisaillement. Le dispositif d'une sphère glissant le long d'un plan permettrait de créer des petites échelles dans l'écoulement et de créer ainsi de forts gradients de vitesse, donc de fortes pressions, responsables de l'effervescence. C'est dans ce cadre que nous nous proposons de monter cette nouvelle expérience au laboratoire.

Références

[1] Bajer K., Bassom A. P. & Gilbert A. D. (2001) Accelerated Diffusion in the Centre of a Vortex. *J. Fluid Mech.*, **437**, 395–411. 5.4.1

[2] Billant P. & Chomaz J.-M. (2000) Experimental evidence for a new instability of a vertical columnar vortex pair in a strongly stratified fluid. *J. Fluid Mech.*, **418**, 167–188. 5.2

[3] Boulanger N., Meunier P. & Le Dizès S. (2007) Structure of a stratified tilted vortex. *J. Fluid Mech.*, **583**, 443–458. 5.2.1

[4] Boulanger N., Meunier P. & Le Dizès S. (2008) Tilt-induced Instability of a Stratified Vortex. *J. Fluid Mech.*, **596**, 1–20. 5.2.1

[5] Cariteau B. (2005) *Etude de la stabilité et de l'interaction de cyclones intenses en fluide stratifié*. Ph.D. thesis, Université Joseph Fourier, Grenoble. 5.2

[6] Cariteau B. & Flór J.-B. (2003) Instability of a columnar vortex in stratified fluid. *Bull. Am. Phys. Soc.*, **48**(10), 164. 5.2

[7] Chomaz J. M., Bonneton P. & Hopfinger E. J. (1993b) The Structure of the Near Wake of a Sphere Moving Horizontally in a Stratified Fluid. *J. Fluid Mech.*, **254**, 1–21. 5.1.1

[8] Crow S. C. (1970) Stability theory for a pair of trailing vortices. *AIAA J.*, **8**(12), 2172–2179. 5.2

[9] Flohr P. & Vassilicos J. C. (1997) Accelerated Scalar Dissipation in a Vortex. *J. Fluid Mech.*, **348**, 295–317. 5.4.1

[10] Gallet S., Meunier P. & Spedding G. R. (2006) Empirical scaling of antisymmetric stratified wakes. *J. Fluids and Struct.*, **22**, 941–947. 5.1.3

[11] Goldamn A. J., Cox R. G. & Brenner H. (1967) *Chemical Eng. Science*, **22**, 637–651. 6.4

[12] Kerswell R. R. (1996) Upper bounds on the energy dissipation in turbulent precession. *J. Fluid Mech.*, **321**, 335–370. 5.3

[13] Kerswell R.R. (1993) The instability of precessing flow. *Geophys. Astrophys. Fluid Dyn..*, **72**, 107–144. 6.2

[14] Kobine J. J. (1996) Azimuthal flow associated with inertial wave resonance in a precessing cylinder. *J. Fluid Mech.*, **319**, 387–406. 5.3

[15] Lagrange R., Meunier P., Eloy C. & Nadal F. (2008) Instabilit of a fluid inside a precssing cylinder. *Phys. Fluids*, **20**(8). 5.3

[16] Le Bars M. & Le Gal M. (2007) Experimental analysis of the stratorotational instability in a cylindrical couette flow. *Phys. Rev. Lett.*, **99**(6), 064502. 6.1

[17] Le Dizès S. & Billant P. (2009) Radiative modes of a stratified vortex. *soumis à Phys. Fluids*. 5.2.2

[18] Lewell J. R., Watson A. J. & Law C. S. (1993) Evidence for slow mixing across the pycnoclyne from an open-ocean experiment. *Nature*, **364**, 701–703. 5.4

[19] Lin J. T. & Pao Y. H. (1974) *Turbulent Wake of a Self-Propelled Slender Body in Stratified and Non-Stratified Fluids : Analysis and Flow Visualizations*. APL/JHU POR-3586 : Flow Research Report No. 11. 5.1.1

[20] Lorenzani S. & Tilgner A. (2001) Fluid instabilities in precessing spheroidal cavities. *J. Fluid Mech.*, **447**, 111–128. 6.2

[21] Malkus W.V.R. (1968) Precession of the Earth as the Cause of Geomagnetism. *Science*, **160**(3825), 259–264. 5.3, 6.2

[22] Manasseh R. (1992) Breakdown regimes of inertia waves in a precessing cylinder. *J. Fluid Mech.*, **243**, 261–296. 5.3

[23] McEwan A. D. (1970) Inertial oscillations in a rotating fluid cylinder. *J. Fluid Mech.*, **40**(3), 603–640. 5.3

[24] Meunier P. & Spedding G. R. (2004) A Loss of Memory in Stratified Momentum Wakes. *Phys. Fluids*, **16**(2), 298–305. 5.1.1

[25] Meunier P. & Spedding G. R. (2006) Stratified Propelled Wakes. *J. Fluid Mech.*, **552**, 229–256. 5.1.2

[26] Meunier P. & Villermaux E. (2003a) How Vortices Mix. *J. Fluid Mech.*, **476**, 213–222. 5.4.1, 5.4.2

[27] Meunier P. & Villermaux E. (2007) Van Hove Singularities in Probability Distribution Functions of Scalars. *C. R. Mecanique*, **335**, 162–167. 5.4.1

[28] Meunier P., Diamessis P. & Spedding G. R. (2006) Self-preservation in Stratified Momentum Wakes. *Phys. Fluids*, **18**(10), 106601. 5.1.4

[29] Meunier P., Eloy C., Lagrange R. & Nadal F. (2008) A rotating fluid cylinder subject to weak precssion. *J. Fluid Mech.*, **599**, 405–440. 5.3

[30] Munk W. & Wunsch C. (1998) Abyssal recipes II : energetics of tidal and wind mixing. *Deep Sea Research*, **45**, 1977–2010. 5.4

[31] Noir J., Jault D. & Cardin P. (2001) Numerical study of the motions within a slowly precessing sphere at low Ekman number. *J. Fluid Mech.*, **437**, 283–29. 6.2

[32] O'Neill M. E. (1964) *Mathematika*, **11**, 67. 6.4

[33] Poincaré H. (1910) Sur la précession des corps déformables. *Bull. Astro.*, **27**, 257–264. 6.2

[34] Rhines P. B. & Young W. R. (1983) How Rapidly is a Passive Scalar Mixed within Closed Streamlines. *J. Fluid Mech.*, **133**, 133–145. 5.4.1

[35] Riley J. R. & Lelong M. P. (2000) Fluid Motions in the Presence of Strong Stable Stratification. *Ann. Rev. Fluid Mech.*, **32**, 613. 5.1.1

[36] Rochester M. G., Jacobs J. A., Smylie D. E. & Chong K. F. (1975) Can precession power the geomagnetic dynamo ? *Geophys. J. R. Astron. Soc.*, **43**, 661–678. 5.3

[37] Rudnick D. L. (2003) From tides to mixing along the hawaiian ridges. *Science*, **301**, 355–357. 5.4

[38] Spedding G. R. (1997) The Evolution of Initially Turbulent Bluff-Body Wakes at High Internal Froude Number. *J. Fluid Mech.*, **337**, 283–301. 5.1.1

[39] Spedding G. R. (2002) The Streamwise Spacing of Adjacent Coherent Structures in Stratified Wakes. *Phys. Fluids*, **14**(11), 3820–3828. 5.1.1

[40] Villermaux E. & Duplat J. (2003) Mixing as an Aggregation Process. *Phys. Rev. Lett.*, **91**(18), 184501. 5.4.2

[41] Villermaux E. & Rehab H. (2000) Mixing in Coaxial Jets. *J. Fluid Mech.*, **425**, 161–185. 5.4.2

[42] Yavneh I., McWilliams J. C. & Molemaker M. J. (2001) Non-axisymmetric instability of centrifugally stable stratified Taylor-Couette flow. *J. Fluid Mech.*, **448**, 1–21. 6.1

Annexe 1

Articles sur les sillages d'objets non-profilés dans un fluide stratifié.

P. Meunier & G. R. Spedding (2004). "A loss of memory in stratified momentum wakes", *Phys. Fluids* **16 (2)**, pp. 298-305.

P. Meunier & G. R. Spedding (2006). "Stratified Propelled Wakes", *J. Fluid Mech.*, **552**, pp. 229-256.

S. Gallet, P. Meunier & G. R. Spedding (2006). "Empirical scaling of anti-symmetric stratified wakes", *J. Fluids & Structures*, **22**, pp. 941-947.

P. Meunier, P. Diamessis & G. R. Spedding (2006). "Self-preservation in stratified momentum wakes", *Phys. Fluids* **18** (10).

A loss of memory in stratified momentum wakes

Patrice Meunier[a] and Geoffrey R. Spedding
Department of Aerospace and Mechanical Engineering, University of Southern California, Los Angeles, California 90089-1191

(Received 29 April 2003; accepted 8 October 2003; published online 24 December 2003)

In this paper we compare the wakes of various bluff bodies in a stratified fluid at moderately high Froude numbers ($F \equiv 2U_B/ND > 8$) and Reynolds numbers (Re$\approx$5000). The size and amplitude of the long-lasting wakes clearly depend on the shape of the bluff body, the wake width being small for a streamlined object and large for an object with sharp edges. However, the wake width can be collapsed when it is normalized by an effective diameter based on the drag force, often called the momentum thickness. General laws for the wake width, the velocity defect, and the Strouhal number are thus deduced and fit the data well. Finally, the cross-fluctuations of the velocity and the turbulent kinetic energy are analyzed. Their amplitudes and widths are proportional to those of the mean profile. Thus, the wake remembers only the momentum flux given by the bluff body to the fluid and not any other aspects of its geometry. © *2004 American Institute of Physics.*
[DOI: 10.1063/1.1630053]

I. INTRODUCTION

Interest in stratified flows comes primarily from geophysical applications, due to the stratification of atmosphere and oceans. One focus concerns the effect of a stable stratification on homogeneous turbulence,[1–3] while another concentrates on the evolution of wakes in stratified flows,[4,5] especially for spheres.[6–8] All these results were obtained in the presence of a strong stratification, i.e., for small Froude numbers. For the wake flows, the Froude number is defined by $F \equiv 2U_B/ND$, where D is the diameter of the body, U_B the towing velocity, and $N=(g/\rho)^{1/2}(\partial\rho/\partial z)^{1/2}$ the buoyancy (or Brunt–Väisälä) frequency. For high Froude numbers, the effect of the stratification is negligible at early stages. However, since in wakes and in decaying turbulence the velocity decreases with time, the local Froude number will eventually approach 1 and the buoyancy effects can no longer be neglected. A global mechanism for weakly stratified wakes was proposed[9] for spheres at high Reynolds numbers (Re$>$4000) and can be decomposed into three stages.

In the first stage, the wake possess high velocities and creates a three-dimensional (3-D) flow, equivalent to that of a nonstratified fluid.[10–12] The velocity follows a power law in time scaling with a decay exponent $-2/3$ and the duration ($N\Delta t \approx 2$) of this stage is fairly independent of the type of wake, in agreement with the general results of stratified turbulence.[3] In units of downstream distance, the duration of this stage increases with F ($\Delta x/D \approx F$) and the second stage will never occur for infinite Froude numbers, leaving the wake in a three-dimensional state as in the case of nonstratified fluids.

The second stage starts as soon as the buoyancy cannot be neglected, which removes vertical velocities. The flow becomes more laminar and organizes into flat horizontal vortices. The fluctuations of density, created by the first stage, collapse since they are no longer maintained by vertical velocity fluctuations and potential energy is transformed back into kinetic energy. This mechanism limits the decay of the velocity defect, whose exponent has been determined experimentally to be close to -0.25. This stage is a nonequilibrium phase (NEQ), where the flow transitions from the initial 3-D regime to a last stage.

In the third stage, the wake begins to diffuse in the vertical direction again,[13] perhaps due to some kind of Ekman pumping. This enhances the decay of the velocity defect, although the wake is still very coherent. The decay exponent was found to be close to the 3-D case ($-2/3$) and not to the 2-D case ($-1/2$), although the flow is very close to two-dimensional. This regime is thus named quasi-two-dimensional (Q2-D).

The presence of the second stage slows the decay of the velocity defect and the stratified flows are thus known to preserve the wake for longer times than in the absence of stratification. In nonstratified flows, Bevilaqua and Lykoudis[10] have shown that there can be a memory of the initial conditions in turbulent bluff body wakes, i.e., that the structure of the flow depends on the shape of the bluff body. The objective of this paper is to examine the effect of body geometry on the intermediate and late wake structure. The goal is both to determine the possibility of a long-term memory in the stratified wake, and to determine one specific set of rescaling parameters if such parameters are found.

II. EXPERIMENT AND ANALYSIS

The experiment has been described in detail in previous papers,[8,9] and only the main features of the apparatus, and of the data acquisition and treatment are outlined here.

[a]Present address: Institut de Recherche sur les Phénomènes Hors Équilibre, 49 rue F. Joliot-Curie, B.P. 146, F-13384 Marseille Cedex 13, France.

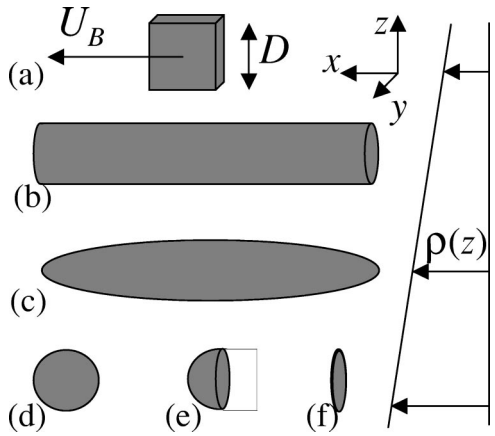

FIG. 1. Schematic of a cube (a), a 6:1 cylinder (b), a 6:1 prolate spheroid (c), a sphere (d), a hemisphere (e), and a disk (f) towed at a velocity U_B in a stably stratified fluid.

A. Experimental setup

The tank of dimensions 380×244 cm^2 is filled up to a height of 20 cm with stably stratified salted water, whose linear density gradient creates a buoyancy frequency $N=(-g/\rho_0)^{1/2}(\partial\rho/\partial z)^{1/2}\approx 2\ \mathrm{s}^{-1}$. A bluff body is towed at mid-height of the tank between three guide cables, using three thin towing cables under a strong tension. This setup prevents any oscillation of the body and the disturbances from the wire wakes are negligible. The bluff body is towed at a velocity U_B along the x axis, while the z axis is aligned with the vertical, as shown in Fig. 1. To investigate the influence of the shape of the body, several objects are used: a sphere for comparison with previous results, two slender objects such as a 6:1 cylinder and a 6:1 prolate spheroid, a disk perpendicular to the towing direction, a hemisphere whose flat face is turned backward and a cube with edges parallel to the axis (see Fig. 1). The diameter D of the bluff bodies (D being the size of the edges for the cube) was equal to 1.3 or 2.5 cm. These three quantities lead to two nondimensional parameters: the Froude number $F\equiv 2U_B/ND$ was equal to 8 or 32 and the Reynolds number $\mathrm{Re}\equiv U_B D/\nu$ (ν is the kinematic viscosity) was always close to 5000. In this paper we focus on the shape of the bluff body, which can be characterized by a third parameter A,[14] or by measuring its drag coefficient in a nonstratified fluid.

B. Definition of the flow characteristics

The evolution of the wake is analyzed by customized particle image velocimetry measurements, by introducing small reflecting particles with the density of the middle isopycnal. Digital images are analyzed by the correlation image velocimetry algorithm[15] to estimate instantaneous horizontal velocity fields (u,v) with dimensions 79×56 cm^2. The vertical component of the vorticity $\omega_z=\partial v/\partial x-\partial u/\partial y$ is shown in Fig. 2 for the prolate spheroid as a function of time. The vorticity fields are qualitatively similar for other objects (the case of the sphere being extensively shown[8,9]) and reveal the presence of coherent alternate vortices, whose size increases due to merging. Such a behavior has been already revealed by dye visualizations for various bluff bodies[4] and for a moving momentum source.[16]

Mean profiles are analyzed in Sec. III A. Second, the longitudinal distance λ_x between two vortices of the same sign defines a Strouhal number ($\mathrm{St}=D/\lambda_x$), which is compared to an extensive previous analysis on spheres.[17] The fluctuations of the velocity (u',v') are analyzed in Sec. IV.

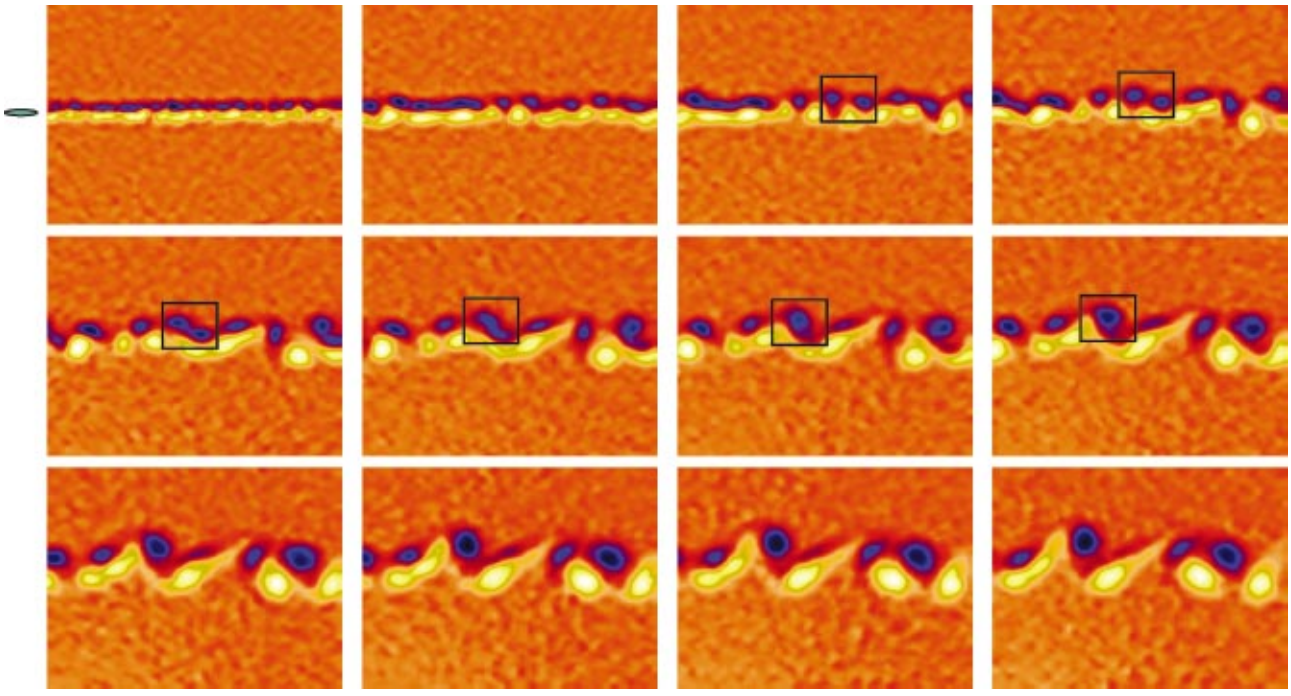

FIG. 2. (Color) The time series of the vertical vorticity distribution, $\omega_z(x,y,Nt)$ for the slender spheroid. $F=32$, $\mathrm{Re}=5.8\times10^3$, and the time steps are equally spaced from $Nt=5$ (top left) to $Nt=300$ (bottom right). The observation area has dimensions 61×43 D and the spheroid passed from right to left through it.

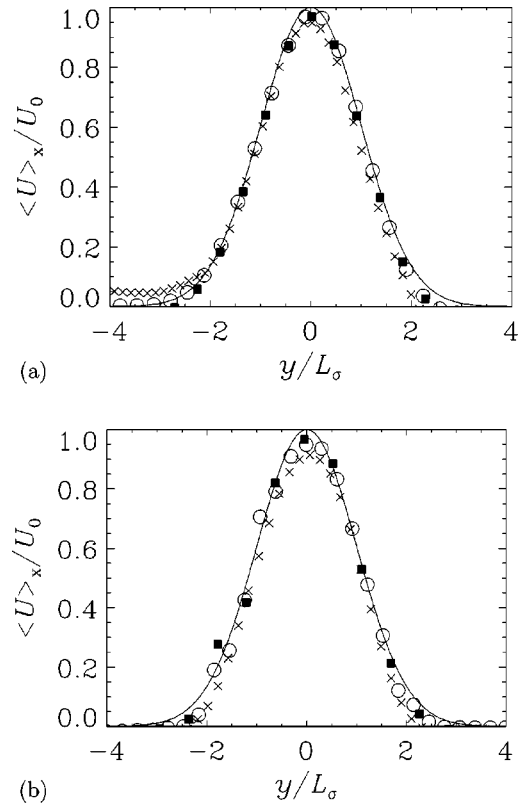

FIG. 3. Mean profiles of the streamwise velocity behind (a) the slender spheroid and (b) the cylinder. The averages are calculated on the global field of view for a downstream distance $x/D=170$ (■), $x/D=1000$ (○), and $x/D=5000$ (×). $F=32$ and Re≈5000. The solid lines correspond to the nondimensionalized Gaussian profile defined by Eq. (1).

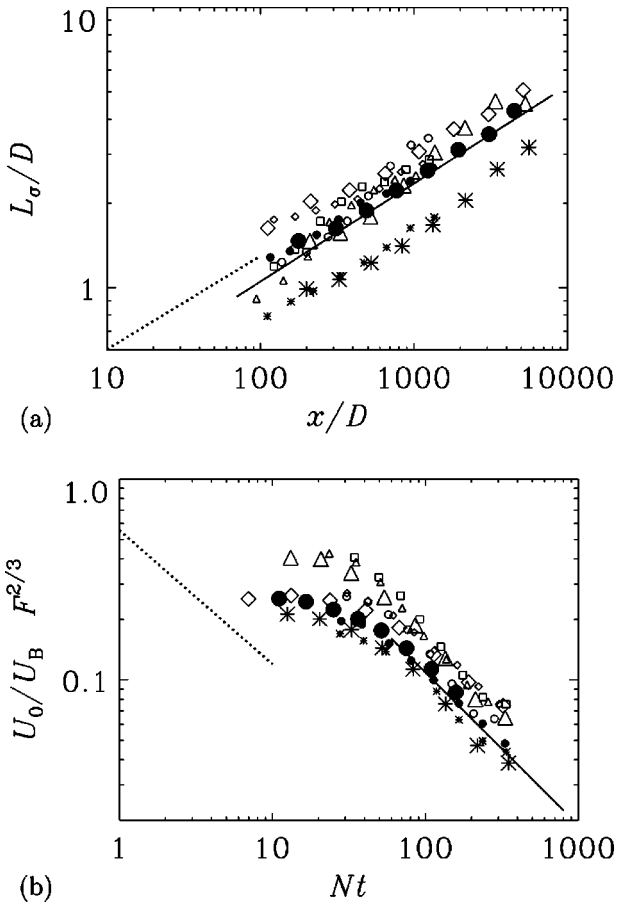

FIG. 4. Temporal evolution of the wake width L_σ (a) and of the velocity defect U_0 (b), defined by Eq. (1). The objects are a sphere (●), a slender spheroid (∗), a cylinder (△), a disc (◇), a cube (□), and a hemisphere (○). Small symbols correspond to $F=8$ and large symbols to $F=32$. Re≈5000. The solid line corresponds to the case of a sphere (Ref. 9) and the dotted line to a nonstratified sphere wake (Ref. 10).

In this towed configuration, mean quantities are obtained by averages over the streamwise direction and are plotted as a function of time Nt or as a function of the downstream distance x/D (they two are simply linked by $x/D=Nt\,F/2$).

III. A LOSS OF MEMORY?

Although the wakes are qualitatively similar, some quantitative differences have been observed and we will explain in this section how to collapse the results obtained on these various objects.

A. Mean profiles

Mean profiles of the streamwise velocity have been measured as a function of the downstream distance for each bluff body. They are shown in Fig. 3 for the slender spheroid and for the cylinder. The profiles are very close to Gaussian over a large band of downstream distances, in agreement with the theory of self preserving three-dimensional wakes.[18] They can be fitted by a Gaussian function,

$$U(y)=\langle u\rangle_x(y)=U_0 e^{-y^2/2L_\sigma^2}, \tag{1}$$

characterized by amplitude U_0 and wake half-width L_σ.

The wake width L_σ is plotted in Fig. 4(a) as a function of downstream distance for the various objects.

For the sphere, the growth has an exponent of $+0.35$ and is in very good agreement with the previous results[9] (solid line), also shown to be close to the nonstratified case. The magnitude of the wake width seems to be sensitive to the shape of the bluff body. For a streamlined object like the slender spheroid, the wake width is 30% smaller, but the growth rate is similar. On the contrary, for objects with sharp edges (open symbols in Fig. 4), the wake is slightly larger (up to 20%) while the growth rate is again very similar.

The same analysis can be performed for the amplitude U_0 of the mean profile, shown in Fig. 4(b). Spedding[9] has shown that the amplitude should be plotted as a function of time Nt to collapse all the results at different Froude numbers in the NEQ regime. Figure 4(b) shows that the results collapse for different Froude numbers in these coordinates and that they are in very good agreement with the results of Ref. 9. The velocity is much higher than in the absence of stratification due to the low decay in the NEQ regime. For a streamlined object such as the spheroid, the amplitude of the mean profile is smaller. The presence of sharp edges on the bluff body increases the amplitude. As for the wake width, the growth/decay rates appear to be independent of the shape of the bluff body.

The results indicate that the growth mechanism of the wake might be identical for all bluff bodies and that the

TABLE I. Values of the effective diameter D_{eff} for various bluff bodies defined by Eq. (2) using the drag force. The values for the drag force are taken from Blevins (Ref. 19).

Bluff body	Spheroid	Sphere	Hemisphere	Cylinder	Disk	Cube
D_{eff}/D	0.30	0.45	0.46	0.65	0.74	0.82

shape of the bluff body only changes the scaling of the flow. We thus seek to explain these differences by finding another length scale, which takes into account the shapes of the objects.

B. Toward universality

It seems intuitive that a streamlined object should have a narrower and slower wake than the sphere, since less fluid is entrained behind it. On the other hand, the presence of sharp edges modifies the vortex shedding and might create bigger vortices, leading to a thicker and more energetic wake. The appropriate length scale of the problem seems to be linked to the section of entrained fluid. The wakes of complex objects are not very well known in the literature and we would like to use a better defined quantity. Such a length scale has already been used theoretically by Tennekes and Lumley,[18] who showed that the momentum of the entrained fluid per unit time is exactly equal to the drag force on the object. If the entrained fluid has a section of diameter D_{eff}, also called the momentum thickness, inside which the velocity is U_B and zero outside, then the drag force is

$$F_{\text{drag}} = \rho_0 \frac{\pi D_{\text{eff}}^2}{4} U_B^2. \tag{2}$$

This definition of an effective diameter D_{eff} is very convenient since the drag force has been extensively studied in the literature.[19] It is thus easy to calculate the effective diameter for various shapes of bluff bodies, as shown in Table I, where the results of Blevins[19] are used. It can be noted that for axisymmetric bluff bodies the drag coefficient c_D is defined by

$$F_{\text{drag}} = \frac{1}{2} c_D \rho_0 \frac{\pi D^2}{4} U_B^2, \tag{3}$$

leading to a simplified definition of the effective diameter: $D_{\text{eff}} = D\sqrt{c_D/2}$. Figure 5(a) shows the wake width normalized by the effective diameter as a function of the downstream distance (similarly normalized). A reasonable collapse of the results is obtained [cf. Fig. 4(a)], indicating that the effective diameter is a more relevant length scale than the physical diameter of the bluff body. Moreover, the results for the amplitude U_0 also collapse when the Froude number is defined using the effective diameter ($F_{\text{eff}} = 2U_B/ND_{\text{eff}}$). It can be noted that the same collapse occurs when plotting U_0/U_B as a function of x/D_{eff}, since the two representations are equivalent in the Q2-D stage (but not in the NEQ regime).

The wake geometry depends only on the amount of entrained fluid and not on the real shape of the bluff body. The

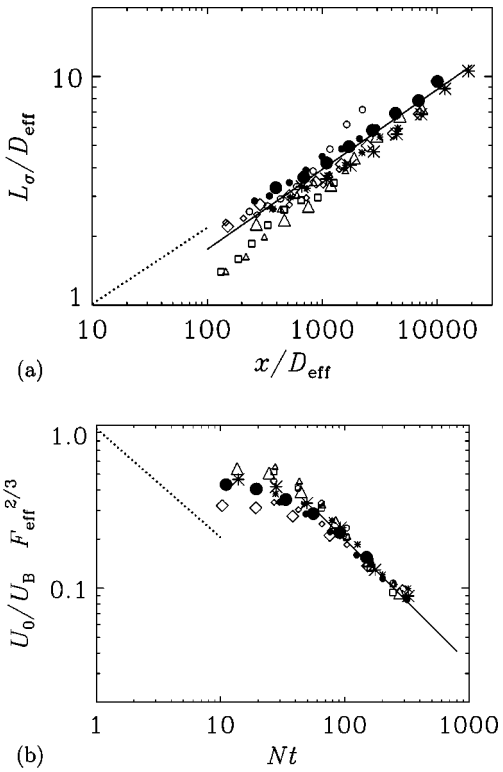

FIG. 5. Temporal evolution of the wake width L_σ (a) and of the velocity defect U_0 (b), defined by Eq. (1). Quantities are normalized using the effective diameter D_{eff} defined in Eq. (2) using the drag force. Symbols are as in Fig. 4. The solid line corresponds to the case of a sphere (Ref. 9) and the dotted line to a nonstratified sphere wake (Ref. 10).

same conclusion was recently obtained by Voropayev and Smirnov[16] in the case of a towed jet, by introducing the same length scale as in (2).

The collapse of the results allows a prediction of the wake width and amplitude for any bluff body, based only on its drag coefficient in a nonstratified fluid. Universal laws are found empirically to be

$$L_\sigma/D_{\text{eff}} = 0.35(x/D_{\text{eff}})^{0.35}, \tag{4}$$

$$U_0/U_B F_{\text{eff}}^{2/3} = 6.6(Nt)^{-0.76}. \tag{5}$$

The results collapse very well in these experiments since the bluff bodies were moderately modified. When the nature of the forcing from the body to the fluid is rather different, e.g., when a large force doublet or force quadruplet is added, the results might be affected more strongly. However, Voropayev *et al.*[20] studied a maneuvering self-propelled body, and found that even if the momentum is small compared to the force doublet, the final stage of the flow is mainly determined by the momentum, consistent with the differing decay rates derived theoretically for a laminar[21] or turbulent[18] nonstratified wake. Consequently, the relationships (4) and (5) might be quite general.

C. Strouhal number

The Strouhal number has been shown to decay with downstream distance due to merging of like-signed vortices[17] with constant exponent $-1/3$. This is the inverse of the

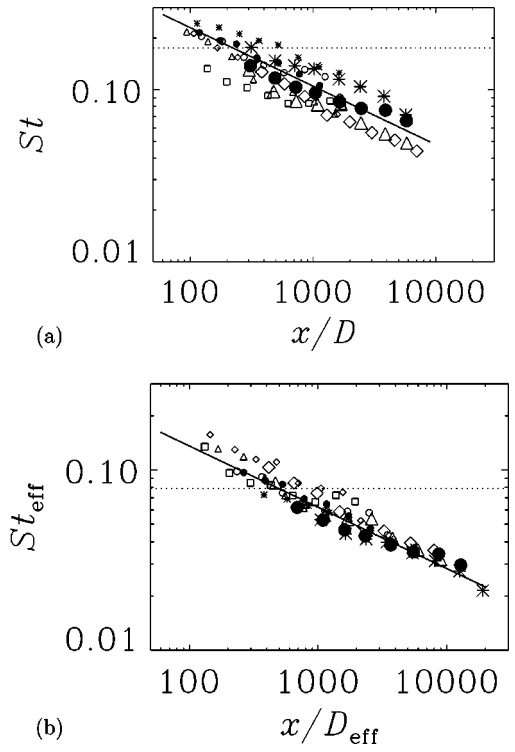

FIG. 6. The Strouhal number obtained by the mean streamwise distance between vortices. Quantities are normalized using (a) the real diameter D and (b) the effective diameter D_{eff} for a sphere (●), a slender spheroid (∗), a cylinder (△), a disk (◇), a cube (□), and a hemisphere (○). Small symbols correspond to $F=8$ and large symbols to $F=32$. Re≈5000. The solid line corresponds to the case of a sphere (Ref. 17) and the dotted line to a nonstratified sphere wake at early stages (Ref. 26).

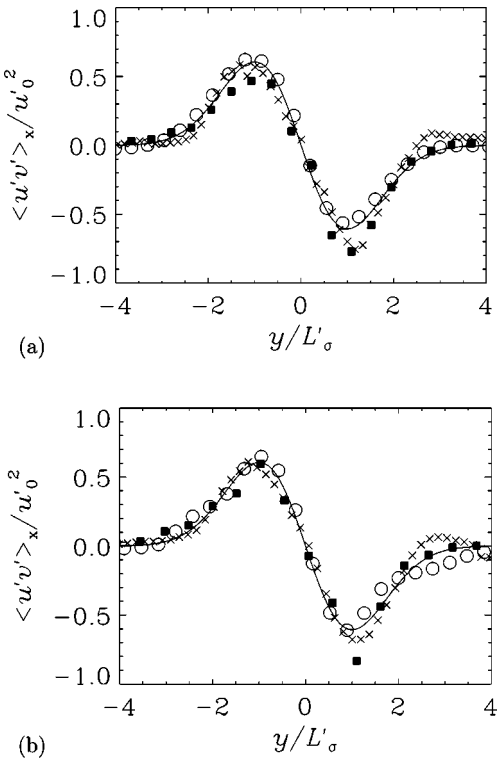

FIG. 7. Streamwise-averaged profile of the Reynolds stress $u'v'$ for the slender spheroid (a) and the cylinder (b) at three downstream distances: $x/D=170$ (■), $x/D=1000$ (○), and $x/D=5000$ (×). $F=32$ and Re≈5000. Solid lines correspond to the theoretical prediction (8) found in self-preserving wakes.

growth rate of L_σ, and can be explained by the fact that if the wake structure is self-preserved, λ_x is proportional to L_σ. Consequently, the Strouhal number should be larger for a streamlined object than for the sphere and slightly smaller for objects with sharp edges. This is clearly shown in Fig. 6(a) for the two different Froude numbers. Moreover, the results collapse very well when the Strouhal number is defined by the effective diameter ($\text{St}_{\text{eff}}=D_{\text{eff}}/\lambda$) instead of the diameter of the bluff body. Hence,

$$\text{St}_{\text{eff}}=0.65(x/D_{\text{eff}})^{-0.34}. \tag{6}$$

The results show that the global properties of the wake depend only on the amount of entrained fluid, which can be linked to the drag force. They are quite insensitive to the real shape of the bluff body and collapse very well using an effective diameter defined by (2) instead of the body's diameter. However, Bevilaqua and Lykoudis[10] have shown in a nonstratified wake that some memory could remain in the turbulent structure of the flow, even though the mean quantities follow the same evolution. The fluctuating quantities are examined in the next section.

IV. TURBULENT STRUCTURE OF THE WAKE

In three-dimensional turbulent wakes, Tennekes and Lumley[18] showed that the production of turbulence is due to the mean shear and can thus be modeled by an eddy viscosity, which should be independent of the bluff body. However, Bevilaqua and Lykoudis[10] showed that the amount of turbulence was three times smaller in the wake of a porous disk than in the wake of a sphere (of equal drag), at least for early stages ($x/D<110$). Their explanation was that the size of the turbulent eddies is smaller in the case of a porous disk, which would create a lower eddy viscosity.

In the theory of 3-D turbulence, the hypothesis of a constant eddy viscosity ν_T requires the cross-velocity fluctuations $\langle u'v'\rangle$ to be proportional to the mean shear:

$$\langle u'v'\rangle=\nu_T\frac{\partial U}{\partial y}. \tag{7}$$

The cross-fluctuation profile should thus be well fitted by the derivative of a Gaussian function:

$$\langle u'v'\rangle_x(y)=-u_0'^2\frac{y}{L_\sigma'}e^{-y^2/2L_\sigma'^2}, \tag{8}$$

characterized by an amplitude u_0' and a width L_σ'. If L_σ' is close to the mean wake width L_σ the amplitude u_0' defines a turbulent Reynolds number:

$$R_T=\frac{U_0L_\sigma}{\nu_T}=\frac{U_0^2}{u_0'^2}. \tag{9}$$

Figure 7 shows the cross-fluctuation profile for the cylinder and for the spheroid at three downstream distances. They are very well fitted by the function defined in Eq. (8) and Fig. 8(a) shows that the width of the fluctuations L_σ' is

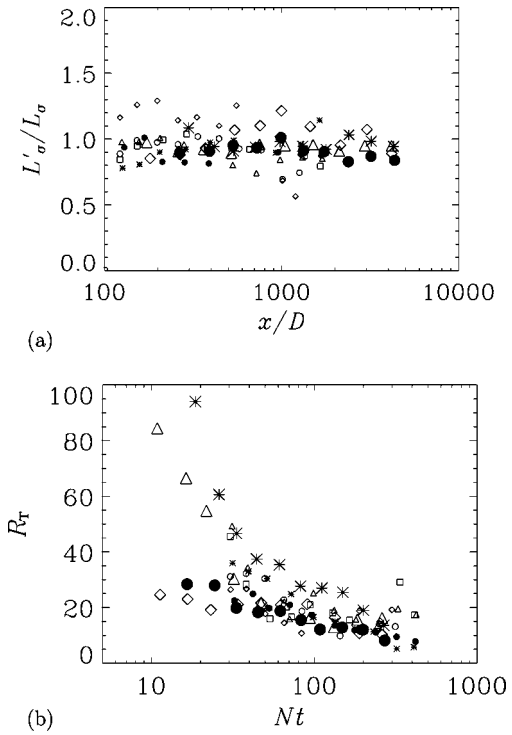

FIG. 8. Characteristics of the profile of the Reynolds stress $u'v'$ defined by Eq. (8). (a) Half-width L'_σ nondimensionalized by the wake width L_σ of the mean profile. (b) Turbulent Reynolds number $R_T=U_0^2/u_0'^2$. The objects are a sphere (●), a slender spheroid (∗), a cylinder (△), a disk (◇), a cube (□), and a hemisphere (○). Small symbols correspond to $F=8$ and large symbols to $F=32$. Re≈5000.

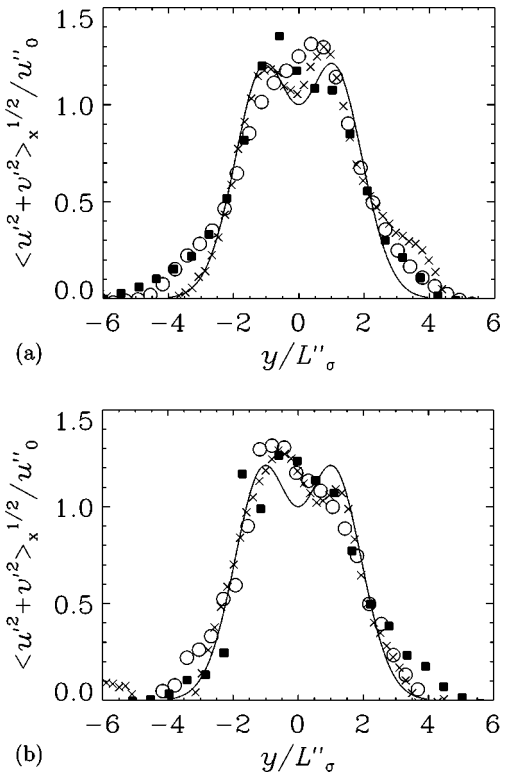

FIG. 9. Streamwise-averaged profile of the turbulent kinetic energy for the slender spheroid (a) and the cylinder (b) at three downstream distances: $x/D=170$ (■), $x/D=1000$ (○), and $x/D=5000$ (×). $F=32$ and Re≈5000. Solid lines correspond to the fitting function of Eq. (11).

very close to the mean wake width L_σ. This implies that the hypothesis of a constant eddy viscosity is valid not only at early stages, where the flow is close to two-dimensional, but also at late stages, where the structure of the flow is Q2-D.

To see if the eddy viscosity depends on the shape of the bluff body, Fig. 8(b) shows the turbulent Reynolds number for various objects. At early stages, R_T is three times higher for the cylinder and for the spheroid. This could be because the 3-D flows remember the shape of the bluff body, but it could also be because the flow is not yet at equilibrium, since this behavior is observed during the NEQ regime. Indeed, at late stages, all the results collapse to a constant value of the turbulent Reynolds number:

$$R_T \approx 15 \pm 5. \tag{10}$$

This value is in good agreement with the value $R_T \approx 20$ that can be deduced from the results of Spedding[22] and it is close to the values found for 3-D turbulent wakes, where R_T ranges from 5 to 30,[10] even though the physical mechanism might be slightly different. The memory of the initial shape of the bluff body is lost in the turbulent fluctuations, just as it was for the mean quantities.

A complete description of the fluctuating quantities must include the turbulent kinetic energy, which should be mainly contained in the horizontal components since, at late times ($Nt \gtrsim 50$), the vertical velocity is very small.[17] The horizontal turbulent kinetic energy can therefore be fit by a function characterized by an amplitude u''_0 and a width L''_σ:

$$(\langle u'^2+v'^2\rangle_x)^{1/2}(y)=u''_0\left(1+\frac{y^2}{L'^2_\sigma}\right)e^{-y^2/2L''^2_\sigma}. \tag{11}$$

Such a fitting function has been introduced by Dommermuth *et al.*,[23] to describe the results of Bevilaqua and Lykoudis[10] in the nonstratified sphere wake. The experimental profiles are shown in Fig. 9. The noise in the measurements is very high, and the profiles do not always present a double peak. However, the width of the fluctuating profile L''_σ is in good agreement with the width L_σ of the mean profile, as shown in Fig. 10(a). The amplitude u''_0 of the kinetic energy is shown in Fig. 10(b). As for the cross-fluctuations, the amplitude is slightly smaller for the cylinder and the spheroid at early stages, but at late stages, the amplitude of all bluff body data collapse onto

$$u''_0/U_0 \approx 0.25 \pm 0.05. \tag{12}$$

This value is in good agreement with values that can be derived from previous experimental ($u''_0/U_0 \approx 0.25$) and numerical ($u''_0/U_0 \approx 0.4$) results on the sphere.[22,23] Moreover, it is very close to the value found for the nonstratified wake of a porous disk ($u''_0/U_0 \approx 0.24$)[10] but smaller than for the case of a nonstratified sphere wake ($u''_0/U_0 \approx 0.6$).[10] However, this last result was obtained at relatively small downstream distances, where the equilibrium might not be settled yet.

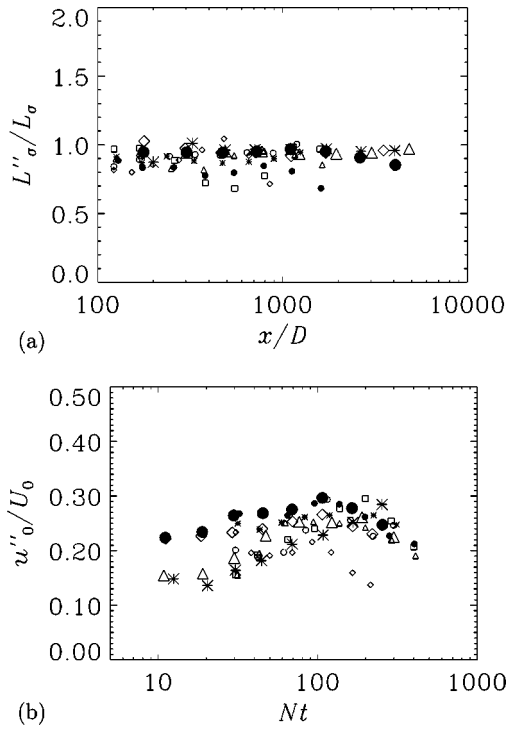

FIG. 10. Characteristics of the kinetic energy profile defined by Eq. (11). (a) Half-width L''_σ nondimensionalized by the wake width L_σ of the mean profile. (b) Amplitude u''_0 nondimensionalized by the velocity defect U_0. The objects are a sphere (●), a slender spheroid (*), a cylinder (△), a disk (◇), a cube (□), and a hemisphere (○). Small symbols correspond to $F=8$ and large symbols to $F=32$. Re≈5000.

V. DISCUSSION

Even though measurable differences have been observed in the wakes of different bluff bodies, the mean and fluctuating quantities can be easily collapsed using an effective diameter based on the drag coefficient. The wake does not remember the exact shape of the bluff body: it is only sensitive to the amount of fluid entrained behind the object. This idea suggests that the structure of the wake might be equivalent among objects and that its characteristics could be derived from this structure.

One may attempt to deduce the results of the previous sections from a simple 2-D model of the flow. The wake is imagined to be a row of alternate vortices of circulation Γ, with a Gaussian profile of vorticity $[\omega=\Gamma/\pi a^2 \exp(-r^2/a^2)]$ of core size a. Such a flow model and its stability has been studied in detail in the case of point vortices[24] and in the case of vortex patches,[25] but not in the case of Gaussian vortices. If the vortices are separated by λ_x in the x direction and by $2b$ in the y direction, using the periodicity of the flow, it can be shown that the mean profile is

$$U(y)=\frac{\Gamma}{2b}\left[\mathrm{erf}\left(\frac{y+b}{a}\right)-\mathrm{erf}\left(\frac{y-b}{a}\right)\right]. \tag{13}$$

This profile is close to a Gaussian for a/b close to 1 as is the case in the experiment, since a and b are of the order of the vortex sizes. The result, obtained by a two-dimensional model, is thus in good agreement with the global properties of the flow, although the flow is not two dimensional. This model does not predict the time evolution of wake width and velocity defect, which might be achieved by calculating the crossed fluctuations. However, a rough calculation shows that the crossed fluctuations vanish if the flow is exactly periodic. The model of the flow is therefore too simple to explain the velocity fluctuations and either some noise in the velocity field, or some aperiodicity of the flow should be taken into account.

ACKNOWLEDGMENTS

The support of ONR Grant No. N00014-96-1-0001 under Dr. L. P. Purtell and Dr. R. Joslin is most gratefully acknowledged.

[1] E. J. Hopfinger, "Turbulence in stratified fluids: A review," J. Geophys. Res. **92**, 5287 (1987).
[2] C. H. Gibson, "Internal waves, fossil turbulence, and composite ocean microstructure spectra," J. Fluid Mech. **168**, 89 (1986).
[3] J. R. Riley and M. P. Lelong, "Fluid motions in the presence of strong stable stratification," Annu. Rev. Fluid Mech. **32**, 613 (2000).
[4] J. T. Lin and Y. H. Pao, "Wakes in stratified fluids: A review," Annu. Rev. Fluid Mech. **11**, 317 (1979).
[5] Y. Xu, H. J. S. Fernando, and D. L. Boyer, "Turbulent wakes of stratified flow past a cylinder," Phys. Fluids **7**, 2243 (1995).
[6] Q. Lin, W. R. Lindberg, D. L. Boyer, and H. J. S. Fernando, "Stratified flow past a sphere," J. Fluid Mech. **240**, 315 (1992).
[7] J. M. Chomaz, P. Bonneton, and E. J. Hopfinger, "The structure of the near wake of a sphere moving horizontally in a stratified fluid," J. Fluid Mech. **254**, 1 (1993).
[8] G. R. Spedding, F. K. Browand, and A. M. Fincham, "Turbulence, similarity scaling and vortex geometry in the wake of a towed sphere in a stably stratified fluid," J. Fluid Mech. **314**, 53 (1996).
[9] G. R. Spedding, "The evolution of initially turbulent bluff-body wakes at high internal Froude number," J. Fluid Mech. **337**, 283 (1997).
[10] P. M. Bevilaqua and P. S. Lykoudis, "Turbulence memory in self-preserving wakes," J. Fluid Mech. **89**, 589 (1978).
[11] C. H. Gibson, C. C. Chen, and S. C. Lin, "Measurements of turbulent velocity and temperature fluctuations in the wake of a sphere," AIAA J. **6**, 642 (1968).
[12] M. S. Uberoi and P. Freymouth, "Turbulent energy balance and spectra of the axisymmetric wake," Phys. Fluids **13**, 2205 (1970).
[13] J. M. Chomaz, P. Bonneton, A. Butet, and E. J. Hopfinger, "Vertical diffusion in the far wake of a sphere moving in a stratified fluid," Phys. Fluids A **5**, 2799 (1993).
[14] S. I. Voropayev and I. A. Filippov, "Vortical track behind three-dimensional body moving in a stratified fluid," Morskoy Gydrofiz. Zhu. **6**, 62 (1985) (in Russian).
[15] A. M. Fincham and G. R. Spedding, "Low-cost high-resolution DPIV for turbulent flows," Exp. Fluids **23**, 449 (1997).
[16] S. I. Voropayev and S. A. Smirnov, "Vortex streets generated by a moving momentum source in a stratified fluid," Phys. Fluids **15**, 618 (2003).
[17] G. R. Spedding, "The streamwise spacing of adjacent coherent structures in stratified wakes," Phys. Fluids **14**, 3820 (2002).
[18] H. Tennekes and J. L. Lumley, *First Course in Turbulence* (MIT Press, Cambridge, MA, 1972).
[19] R. D. Blevins, *Applied Fluid Dynamics Handbook* (Van Nostrand Reinhold, New York, 1984).
[20] S. I. Voropayev, G. B. McEachern, H. J. S. Fernando, and D. L. Boyer, "Large vortex structures behind a maneuvering body in stratified fluids," Phys. Fluids **11**, 1682 (1999).
[21] S. A. Smirnov and S. I. Voropayev, "On the asymptotic theory of momentum/zero-momentum wakes," Phys. Lett. A **307**, 148 (2003).
[22] G. R. Spedding, "Anisotropy in turbulence profiles of stratified wakes," Phys. Fluids **13**, 2361 (2001).

[23]D. G. Dommermuth, J. W. Rottman, G. E. Innis, and E. A. Novikov, ''Numerical simulation of the wake of a towed sphere in a weakly stratified fluid,'' J. Fluid Mech. **473**, 83 (2002).
[24]P. G. Saffman, *Vortex Dynamics* (Cambridge University Press, Cambridge, 1992).
[25]D. Meiron, P. Saffman, and J. Schatzman, ''The linear two-dimensional stability of inviscid vortex streets of finite-cored vortices,'' J. Fluid Mech. **147**, 187 (1984).
[26]E. Achenbach, ''Vortex shedding from spheres,'' J. Fluid Mech. **62**, 209 (1974).

J. Fluid Mech. (2006), *vol.* 552, *pp.* 229–256.
doi:10.1017/S0022112006008676 Printed in the United Kingdom

Stratified propelled wakes

By PATRICE MEUNIER† AND GEOFFREY R. SPEDDING

Department of Aerospace and Mechanical Engineering,
University of Southern California, Los Angeles, CA 90007, USA

(Received 22 December 2004 and in revised form 12 October 2005)

This paper presents experimental results on the wake of a propelled bluff body towed at a constant horizontal speed in a linearly stratified fluid. Three regimes of the wake have been found, depending on the angle of attack and on the ratio of drag force to propeller thrust. Most of the experiments were obtained in a first regime where a strong momentum flux is created in the wake, which can be oriented backward or forward depending on the ratio of drag force to thrust of the propeller. The velocity amplitude, wake width and Strouhal number of the wake can be predicted by defining a momentum thickness based on the drag coefficient of the bluff body and the thrust of the propeller. A second regime is obtained for a narrow band of towing velocities, with a relative width of 4%, in which the momentum flux is found to vanish. The wake is characterized by the velocity fluctuations; the scaling exponents of the velocity, vorticity and width of the wake are measured. A third regime is obtained for wakes with a small angle of attack, with a null momentum flux. The mean profile of the wake is found to be asymmetric and its amplitude and wake width are measured. Finally, the relevance of these results to the case of a real self-propelled bluff body is discussed. The presence of weak internal waves or of weak fluctuations of background velocity would lead to a wake in the regime with momentum flux, and would allow prediction of the amplitude, width and Strouhal number of the wake.

1. Introduction

1.1. *Towed-body wakes*

Over a range of intermediate scales (1–100 m in the ocean, 100–1000 m in the atmosphere) geophysical flows are strongly influenced by the background density gradient, giving rise to numerous complex and interesting flow phenomena and numerous problems for large-scale modelling efforts for which these complex processes must appear as single coefficients modelling subgrid-scale processes. One of the canonical problems receiving much attention has been the decay of initially turbulent motions in a stably stratified environment. The review articles by Lin & Pao (1979) and Riley & Lelong (2000) indicate the range of theoretical, numerical and experimental approaches and progress over the years.

One such general problem involving decaying stratified turbulence is the bluff-body wake at moderate and high Reynolds number, which also has certain practical applications. The wakes of towed spheres are characterized by the persistence of large coherent structures, even at high internal Froude number when such order might not be expected to emerge and/or survive to late times (Lin & Pao 1979; Chomaz,

† Current address: Institut de Recherche sur les Phénomènes Hors Équilibre, UMR 6594 CNRS/Universités Aix-Marseille, 49 rue F. Joliot-Curie, F-13384 Marseille Cedex 13, France.

Bonneton & Hopfinger 1993; Spedding, Browand & Fincham 1996; Spedding 1997). Stratified fluids support internal wave motions and the waves emitted by both body and wake have been studied in experiment and theory (Gilreath & Brandt 1985; Bonneton, Chomaz & Hopfinger 1993; Spedding *et al.* 2000; Voisin 1991). Since the coherent wake structures organize in a very ordered fashion (resembling a von Kármán street), the pattern of wave packets emitted by them reflects that order. Indeed if one characteristic were to be specified as diagnostic it is likely to be the coherent structures themselves, and Spedding (2002) proposed that the spacing and lengthscales of these structures, which could be rescaled over all experimentally accessible Reynolds and Froude numbers, could be viewed this way. Voropayev & Smirnov (2003) argued similarly based on experiments on low-Reynolds-number jets in stratified fluids, deriving the same scaling law based on the momentum flux from the jet source.

1.2. *Computations and generalization*

If all towed-sphere wakes are similar in mean and turbulent length and velocity scales, and if the same scaling laws could be derived for objects that were not spheres (essentially point momentum sources), then it seems plausible that the observed characteristics are quite general and applicable to many cases of decaying flows in a stratified fluid (Spedding 1997). It is reasonable to enquire whether the body geometry has any influence at all in the far wake, and Meunier & Spedding (2004) showed that all late wakes with a momentum defect can be rescaled by the momentum flux, regardless of body geometry, for bluff, streamlined and sharp-edged bodies. As a practical matter, the appropriate scaling can be looked up from published drag coefficients for the different body shapes in non-stratifed flows.

The unimportance of initial conditions can also be inferred from the successful simulation of the stratified wake by DNS (Gourlay *et al.* 2001) and LES computations (Dommermuth *et al.* 2002; Diamessis, Domaradzki & Hesthaven 2005) where there is no body, only a mean profile with turbulence superimposed upon it as a starting condition for the flow. The simulations clearly show the emergence of the large-scale (in the horizontal) coherent structures from the initially turbulent initial condition. In the absence of the background density gradient, the same simulation conditions show no emergent coherence.

1.3. *Momentumless wakes*

It seems then that all drag wakes can be treated similarly. However, another class of application concerns the motion and disturbance field of underwater vehicles of various types, and in this case, since they are self-propelled, the drag is balanced by a local thrust, and the wake has no net momentum. The towed-sphere wake, where turbulence production is due to the mean shear, might after all be a special case, not only for naval applications, but also in geophysical flows, where different turbulence production mechanisms may also have, at least on average, zero net momentum.

Indeed, if one searches analytically for similarity solutions, as in Tennekes & Lumley (1972), Finson (1975) and Hassid (1980), then one finds scaling exponents for growth of lengthscales and decay of mean and turbulence quantities that differ significantly from the drag wake case. Using only the simplest eddy viscosity approximation, for example, Tennekes & Lumley (1972) find that while axisymmetric wakes with momentum show mean centreline velocities, $U_W \sim x^{-2/3}$, and wake thickness, $l_W \sim x^{1/3}$, the solutions for the momentumless case are $U_W \sim x^{-4/5}$, and $l_W \sim x^{1/5}$. Finson (1975) notes how the self-propelled wake represents a singular situation, requiring closure approximations in higher-order turbulence quantities. Since production is no longer

driven by a mean shear, it decays rapidly and does not balance the dissipation. Consequently the far wake never becomes independent of initial conditions.

It may not be unrelated that the literature on experimental results is characterized by some degree of scatter (Schooley & Stewart 1962; Naudascher 1965; Swanson, Schetz & Jakubowski 1974; Chieng, Jakubowski & Schetz 1974; Lin & Pao 1974; Schetz & Jakubowski 1975; Lin & Pao 1979; Higuchi & Kubota 1990; Sirviente & Patel 1999, 2000*a*, *b*, 2001) as a wide variety of geometries and mechanisms for production of the momentumless condition have been used. Higuchi & Kubota (1990) in particular noted that the matched case of exact zero-momentum was different in both mean and turbulence decay rates (they were significantly higher) and that a sensitivity to initial conditions (degree of wall roughness) could be detected down to $x/D \simeq 40$–100.

With the exception of Schooley & Stewart (1962), Lin & Pao (1974) and Lin & Pao (1979), none of the momentumless wakes have been in stratified conditions and none have been studied at truly late times. The stratified sphere data of Spedding *et al.* (1996), for example, extends to equivalent $x/D \geqslant 4000$. For most other studies, $x/D \leqslant 40$–100. In stratified fluids, evolution times are expressed in units of buoyancy frequency, N, and the data of Lin & Pao (1979) extend to $Nt \leqslant 60$, compared with $Nt \simeq 3000$ in Spedding *et al.* (1996). Focusing on the late-wake behaviour is not simply an experimental expedient; it also avoids some of the confusion that results when different wakes have different relaxation times to their asymptotic state, which may only be observable very far downstream, as noted by Johansson, George & Gourlay (2003).

Asymptotic theories for far wakes in both momentum and zero-momentum cases have been given by Smirnov & Voropayev (2003) and Afanasyev (2004) but make no statement on the appropriate form of the initial condition (in this case the distribution of localized force doublets) and contain no notion of turbulence modelling. However, such numerical modelling has been done recently by Chernykh, Demenkov & Kostomakha (2001) and Chernykh, Ilyushin & Voropayeva (2003).

1.4. *Objectives*

There is, therefore, considerable uncertainty concerning the extension of previous results from stratified, towed-body wakes to practical applications. Based on available theoretical and experimental work, one would not expect similar scaling laws to apply to either mean or turbulence quantities in the momentumless wake, and one might also not expect the same insensitivity to details of the initial conditions. Currently, there are no quantitative measurements to check these ideas for late wakes in stratified flows. The objective of this paper is to measure wakes at, or close to, the self-propelled point, under the same conditions as for the existing towed-body experiments. The parameters varied will allow systematic investigation of the effect of the strength of the background density gradient, the degree of thrust/under-thrust from the propeller, and the shape of the solid body. The results will be compared for consistency, or lack thereof, with the existing literature, and the relevance of such results to practical flows will be re-examined.

2. Experiment and data analysis

2.1. *Experimental devices*

The materials and methods are similar to those described in detail in Spedding *et al.* (1996). A bluff body with diameter $D \approx 3$ cm is towed at a velocity U_B along the

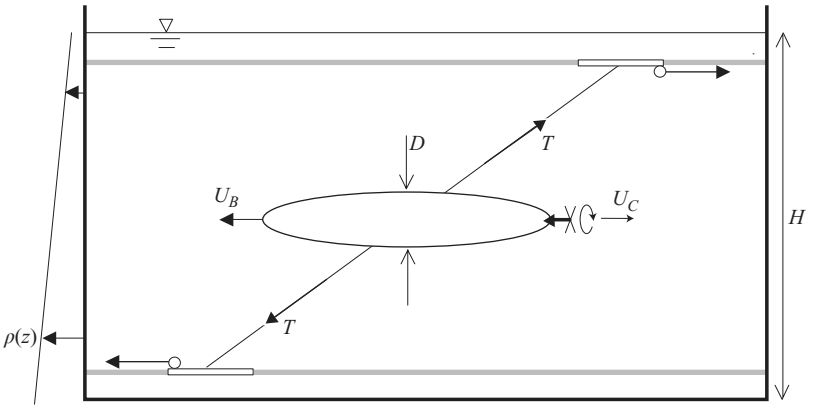

FIGURE 1. Experimental set-up.

x-direction, in a water tank with horizontal dimensions $380 \times 244\ \mathrm{cm}^2$. The bluff body is maintained by three thin wires ($d = 250\ \mu\mathrm{m}$) under strong tension T, as shown on figure 1. These tow wires slide along three guide cables with a minimum of vibration, up to a tow speed of $1\ \mathrm{m\ s}^{-1}$. The disturbances created by the wakes of the tow wires themselves (where $Re < 250$) are negligible in amplitude compared with the wake of the bluff body. Furthermore, the obliquely mounted wires do not intersect the measurement plane, which is at mid-body height in all experiments reported here.

The bluff body has a small propeller made of two flat plates with diameter close to 1 cm, which are fixed to a rotating axis with an angle of roughly 30° to the tow axis. When the propeller rotates, some momentum is expelled backwards, which creates a thrust on the bluff body. However, this does not change the velocity of the bluff body which is fixed through the towing wires. The propeller axis is rotated by a motor located inside the body, whose power comes from an external DC current generator. The current is stopped when the body reaches the end of the tank, to prevent a strong jet created by the propeller from impinging back upon the flow.

Two different bluff bodies have been studied, so the influence of the shape of the object can be determined. The first is a cylinder with diameter $D = 3.35$ cm and length of 15.6 cm. The sharp edges and the non-profiled shape create a very turbulent wake. The second object is a prolate spheroid with diameter $D = 2.54$ cm and length of 15.2 cm. The streamlined object creates a very weakly turbulent wake, and the comparison between these two different body types – streamlined and sharp-edged – can represent a range of possible initial conditions. The boundary layer remained laminar since it was not tripped.

The tank is filled with stably stratified salt water, whose linear density gradient creates a buoyancy frequency $N = (-g/\rho_0)^{1/2}(\partial\rho/\partial z)^{1/2} \approx 2\ \mathrm{rad\ s}^{-1}$. The water depth, $H = 26$ cm, is large compared to the diameter of the bluff bodies $D \approx 3$ cm, and will be considered infinite for the centreplane measurements described. Systematic variation of D/H in Spedding (1997) showed no dependence for such values.

The flow is analysed by measuring horizontal two-dimensional instantaneous velocity fields using particle image velocimetry. For flow seeding, small polystyrene beads with a mean diameter 600–800 μm are carefully sorted in an auxiliary tank to select a density of $\rho_{\mathrm{part.}} = 1.0510 \pm 0.0008$. When introduced in the stratified fluid, the particles settle at the specific height where the fluid has the same density $\rho_{\mathrm{part.}}$, marking an isopycnal with a thickness $\Delta z \approx 3$ mm. The height of the isopycnal can

be modified, by adding or removing small amounts of heavy fluid at the bottom of the tank, so that it is located precisely at the mid-height centreplane of the bluff body. The particles are illuminated by four 1 kW floodlights and their positions are recorded on a Pulnix TM9701 CCD camera positioned above the tank, over a field of view with dimensions $79 \times 56\,\mathrm{cm}^2$. The digital images are treated by a variant of the customized Correlation Image Velocimetry (CIV) algorithm described in detail in Fincham & Spedding (1997). At each grid point, the cross-correlation peak is estimated by a least-squares fit of a function constructed from an average of the two spline-interpolated autocorrelation functions from each image correlation box. The most serious contribution to peak-locking error is thus removed. The resulting velocity fields correspond, at late stages, to the horizontal velocities (u, v) at the mid-plane of the bluff body, since the vertical displacements vanish at late stages. The uncertainties in the individual velocity measurements are of the order of 1%. The vertical component of the vorticity $\omega_z = \partial v/\partial x - \partial u/\partial y$ is calculated by a smoothing spline interpolation of the velocity field with an uncertainty of less than 10%.

2.2. *Parameters of the flow*

Using the tow speed, U_B, the diameter, D, of the bluff body, the kinematic viscosity of the fluid $\nu = 1.02 \times 10^{-6}\ \mathrm{m^2\,s^{-1}}$ and the buoyancy frequency N, two non-dimensional parameters can be defined. The Reynolds number $Re \equiv U_B D/\nu$ is varied between 5000 and 33 000. It was shown in Spedding *et al.* (1996) and Spedding (1997) that the Reynolds number over this range has only a weak influence on late-time stratified wakes and its independence has not been studied in further detail here. More attention has been paid to the effect of the Froude number defined by $F \equiv 2U_B/N D$, where N is the buoyancy frequency. The Froude number is varied between 6 and 40, and for a set of experiments with fixed N, it is proportional to the Reynolds number, since D is not modified.

Meunier & Spedding (2004) demonstrated that for different shapes of bluff bodies, all the characteristics of the wake rescale when using an effective diameter (introduced as the momentum thickness by Tennekes & Lumley 1972, chapter 4) based on the drag coefficient:

$$D_{\mathrm{eff}} = D\sqrt{c_D/2}. \tag{2.1}$$

In this formula, c_D is the drag coefficient for an axisymmetric bluff body, based on the surface area $\pi D^2/4$ of the object in a plane normal to its axis. In this paper, D_{eff} is used to rescale the characteristics of the wakes with non-zero momentum. Since D_{eff} is the only relevant lengthscale in the late stages of the momentum wakes, an effective Froude number can be defined as $F_{\mathrm{eff}} = 2U_B/N D_{\mathrm{eff}}$.

The effective diameters of the bluff bodies were calculated from published measurements of the drag coefficient (Blevins 1984) in a non-stratified fluid. For the self-propelled cylinder, the drag coefficient of the cylinder alone is equal to 0.85, leading to an effective diameter $D_{\mathrm{eff}} = 0.65D$. The drag of the propeller is neglected, since it does not significantly alter the drag coefficient. The drag coefficient of a spheroid with aspect ratio 1:6 is equal to 0.176, for an effective diameter $D_{\mathrm{eff}} = 0.3D$. The drag of the propeller has again been neglected, which is a reasonable assumption when the propeller is rotating, i.e. when the towing velocity is close to the momentumless velocity. However, when the propeller is not rotating, it creates an additional drag which tends to increase D_{eff}. This willl be discussed in more detail in § 4.

2.3. *Instantaneous and mean measurements*

The non-dimensional downstream distance x/D, commonly used for non-stratified wakes in water channels and wind tunnels, is related here to the elapsed time t in the tow tank by $x/D = U_B t/D$. However, in stratified wakes, time scales with the buoyancy frequency at late stages, which defines a non-dimensional time Nt. The downstream distance is thus related to the non-dimensional time by

$$x/D = F/2\ Nt. \tag{2.2}$$

Mean quantities are obtained by averages along the streamwise direction x at a given time Nt and over the entire interrogation window length Δx. They will be denoted by $\langle\cdot\rangle_x$ and were measured on 60–80 velocity vectors. They correspond to temporal averages that would be obtained in a wind tunnel or a water channel configuration at late stages. Indeed both averages are identical when the downstream distance x is much larger than the interrogation window length Δx. This approximation is valid up to one order of magnitude for all cases here, when Nt is greater than 50.

The streamwise velocity is separated into mean and fluctuating parts,

$$(u, v) = (U, 0) + (u', v'), \tag{2.3}$$

and the following mean quantities are studied: the mean streamwise velocity $U = \langle u\rangle_x$, the quadratic fluctuations of velocity $u^* = \langle u'^2 + v'^2\rangle_x^{1/2}$ and the crossed fluctuations of velocity $\langle u'v'\rangle_x$. All of these quantities depend on the transverse coordinate y and on the non-dimensional time Nt.

3. Three regimes of the wake

Seven series of experiments were run, three with the propelled cylinder and four with the propelled spheroid. Each series was conducted in the same manner: the angular velocity of the propeller was fixed at a constant rate, the bluff body was towed with a constant velocity, and the velocity fields were estimated by CIV. From one experiment to the next, the tow speed was increased.

The patterns of the vertical vorticity fields are summarized in figure 2. The vertical component of the vorticity ω_z is shown as a function of time for three different tow speeds. The bluff bodies are always towed from right to left, i.e. in the positive x-direction.

For low tow speeds, the momentum flux expelled by the propeller is much higher than the momentum flux entrained by the bluff body due to the drag. The self-propelled body thus creates a jet of fluid toward the right (i.e. in the $-x$-direction), although the bluff body moves toward the left, as seen in figure 2(a), where the coherent structures move slowly toward the right. Since the wake is composed of two layers of opposite-signed vorticity, positive for y negative (y^-) and negative for y positive (y^+), net momentum is ejected backward by the bluff body. The jet then destabilizes into coherent vortices, which merge gradually, increasing the width of the wake.

On the contrary, for high tow speeds, there is more momentum flux created by the drag force than expelled by the propeller. Some fluid follows the bluff body and creates a leftward-moving jet. The vorticity fields look very similar to those of figure 2(a) except that the positive vorticity is found for y^+ and the negative vorticity for y^-. The wake is similar to that of a non-propelled bluff body, which is recovered when the drag force is much higher than the thrust of the propeller. In either of the two previous cases (high or low velocities), some momentum is created by the bluff

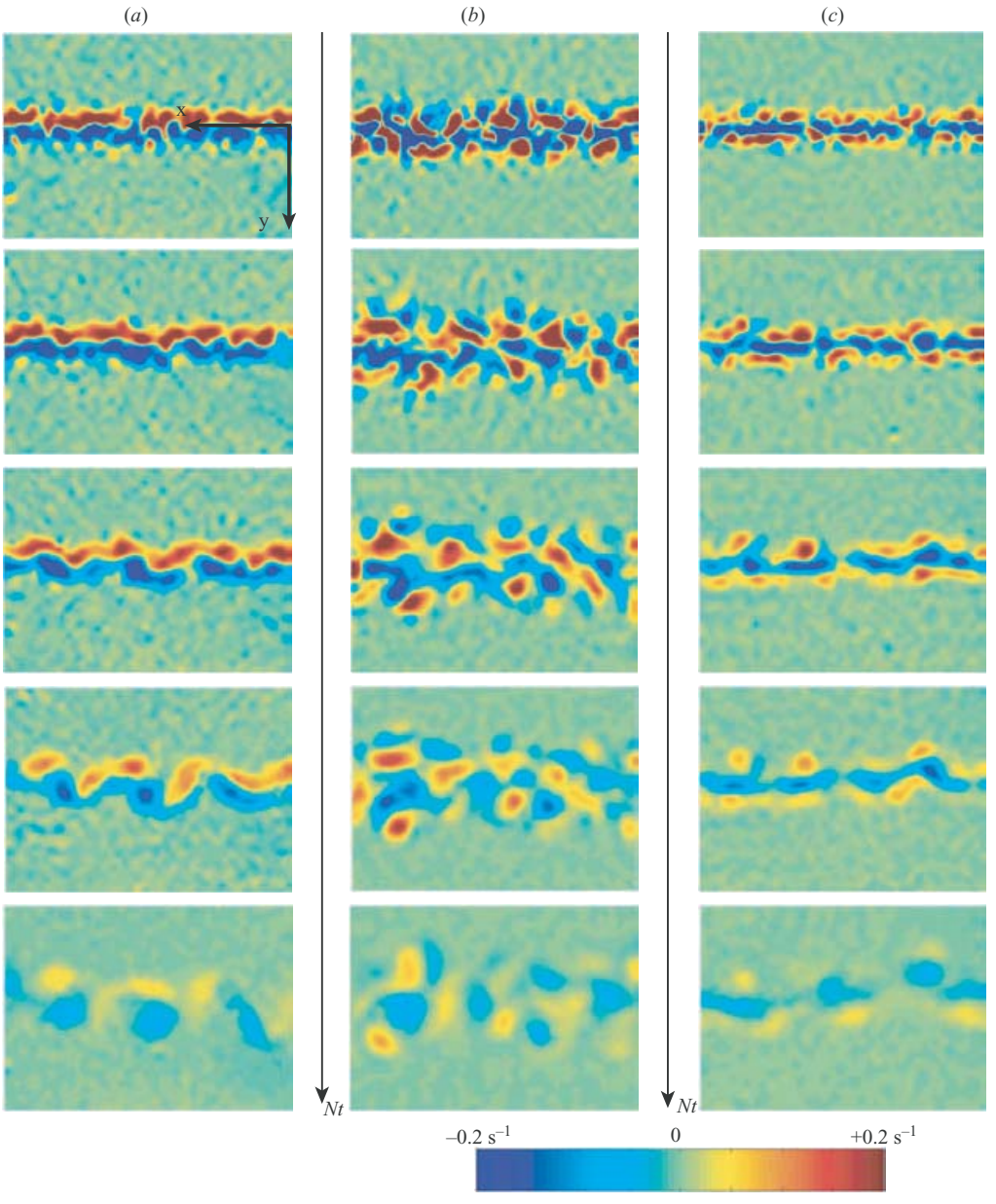

FIGURE 2. Vorticity fields of a towed body with a rotating propeller for $Nt =$ [12, 30, 60, 120, 300] from top to bottom. The bodies are towed from right to left at a speed (*a*) lower than the momentumless velocity, (*b*) equal to the mometumless velocity, and (*c*) equal to the momentumless velocity with an angle of attack. The bluff body is a prolate spheroid for (*a*) and (*c*) and a cylinder for (*b*). The field of view has dimensions $80 \times 60\,\mathrm{cm}^2$, corresponding to 32×23 diameters. $F \approx 20$; $Re \approx 15\,000$.

body and the treatment of the data is essentially the same, as described in detail in § 4, which focuses on this momentum regime.

Between the two previous cases with a backward jet at small U_B and a forward jet at high U_B, there is a limiting case where the jet eventually vanishes. It happens for

a particular (critical) value of the tow speed $U_B = U_C$, where no net momentum is created. Intuitively, its value is proportional to the angular velocity of the propeller. U_C is thus a way of measuring the angular velocity of the propeller, and to recalibrate it with no need to take into account the shape of the propeller and the bluff body. In the experiments, this critical momentumless velocity is defined by the criterion that the sum of the mean profile vanishes:

$$U_B = U_C \quad \text{when} \quad \int_{-\infty}^{\infty} \langle u \rangle_x \, \mathrm{d}y = 0. \tag{3.1}$$

This criterion defines U_C to within $\pm 2\%$, and if U_B is changed by more than 2%, the late stages of the wake resemble one of the cases mentioned above (high or low U_B). Only by careful matching of U_B to U_C was it possible to reach the momentumless regime, for which the mean profile of velocity vanishes in the incoherent fluctuations of the measurements. An example is shown in figure 2(*b*). The two layers of vorticity found in the momentum regime have disappeared and the vorticity field contains many vortices of both signs, with no organized longitudinal spatial structure. Like-signed vortices merge, leading to larger scales of motion, whose peak vorticity magnitude decreases gradually with time. This momentumless regime will be described in detail in § 5.

Finally, a third regime has been found incidentally. In the first experiments, a slight angle of attack was present between the axis of the bluff body and the towing direction. The angle of attack (measured between the guide cable and the axis of the propeller) was smaller than 1° and had no influence on the momentum regime. However, when the tow speed was close to the momentumless velocity U_C, the wake became asymmetric. Since the bluff body was oriented slightly toward y^+, the fluid expelled by the propeller was slightly to y^-. This leads to three layers of vorticity: two layers of positive vorticity surround a layer of negative vorticity, as can be observed in figure 2(*c*). This regime is very similar to the momentum regime except that there are three layers of vorticity instead of two. These three layers destabilize into vortices, as in the momentum regime, which merge into bigger vortices, thus increasing the wake width. This regime will be described in detail in § 6.

4. Momentum regime

4.1. *Mean profiles*

In the momentum regime (figure 2*a*), the mean velocity is larger than the fluctuations. Figure 3 shows the transverse profile of mean velocity $U(y) = \langle u \rangle_x(y)$ as filled symbols, together with the profile of the quadratic fluctuations of velocity $u^* = \langle u'^2 + v'^2 \rangle_x^{1/2}$ as open symbols. It is clear that the fluctuations are smaller than the mean velocity up to $Nt = 300$.

Figure 3 shows that the mean profiles of velocity can be fitted well by a Gaussian function (shown as a solid line on figure 3) with amplitude U_0 and half-width L_0,

$$U(y) = U_0 \, \mathrm{e}^{-y^2/2L_0^2}. \tag{4.1}$$

As time increases, the amplitude U_0 decreases and the wake width L_0 increases, as is found in both stratified and non-stratified wakes of non-propelled bodies.

In the case of propelled bodies, the amplitude U_0 of the wake can be either positive or negative, depending on whether the towing velocity U_B is larger or smaller than the critical velocity U_C. Indeed, when U_C is smaller than U_B, i.e. when the propeller rotates slowly, the bluff body is similar to a non-propelled body and the amplitude

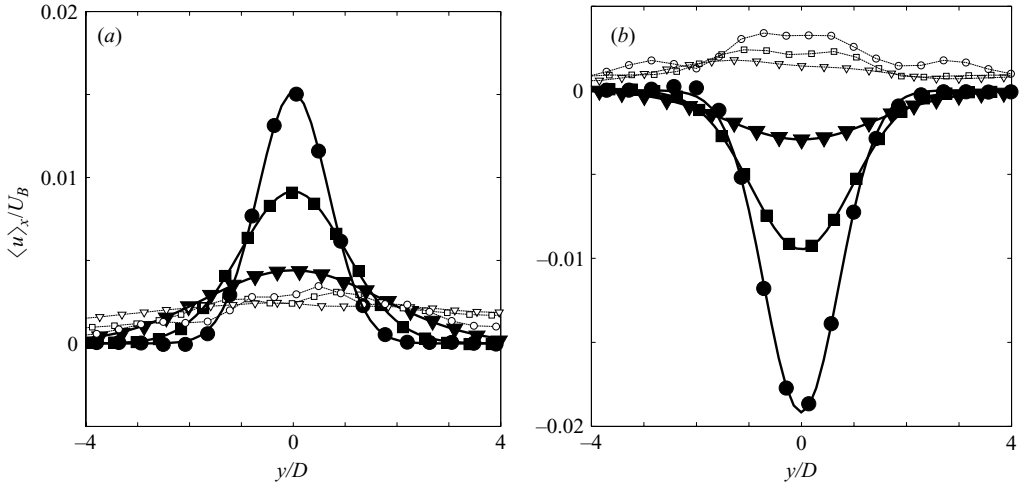

FIGURE 3. Profile of mean velocity (filled symbols) and quadratic fluctuations $\langle u'^2 + v'^2 \rangle_x^{1/2}$ (open symbols) at times $Nt = 20$ (●), $Nt = 100$ (■) and $Nt = 300$ (▼). The spheroid is towed at (*a*) a speed larger than the momentumless velocity ($U_B = 1.13U_C$) and (*b*) a speed smaller than the momentumless velocity ($U_B = 0.88U_C$). The Froude and the Reynolds numbers are: (*a*) $F = 14$, $Re = 11\,000$; (*b*) $F = 18$, $Re = 9000$.

of the wake U_0 is positive. This means that some fluid is entrained behind the body by the drag. On the other hand, when U_C is larger than U_B, i.e. when the body is towed slowly, some fluid is expelled backwards by the propeller, creating a jet in the $-x$-direction, which gives a negative amplitude U_0.

As U_C/U_B is increased (obtained in the experiments by decreasing U_B and keeping U_C constant), the amplitude of the wake decreases continuously from positive to negative values. This is shown in figure 4 where $U_0/U_B\ F_{\text{eff}}^{2/3}$ is plotted as a function of the ratio U_C/U_B for $Nt = 100$. All the results collapse well in these units. The curve has a steep gradient at $U_C = U_B$ so even a very small variation in U_B can create a large amplitude U_0 in the wake. This explains why it was very hard in the experiment to obtain a momentumless regime, and why most of the experiments were found to be in the momentum regime. When the tow speed U_B differs from the momentumless velocity U_C by more than 2%, the amplitude of the wake U_0 cannot be neglected and the wake is in the momentum regime.

4.2. *A new definition of the momentum thickness for propelled bluff bodies*

The absolute amplitude of a stratified wake depends strongly on the shape of the bluff body (see Meunier & Spedding 2004). However, the results were found to collapse when using an effective diameter based on the drag coefficient and defined by equation (2.1), leading to a universal law for non-propelled bodies:

$$\frac{U_0}{U_B} F_{\text{eff}}^{2/3} = 6.6(Nt)^{-0.76}, \tag{4.2}$$

where $F_{\text{eff}} = 2U_B/ND_{\text{eff}}$. In the case of propelled bodies, this law is expected to apply only when the propeller is not rotating, i.e. when $U_C = 0$, shown as a star in figure 4. It is 30% smaller than the experimental value for a spheroid, which can be explained quantitatively by the additional drag created by the non-rotating propeller.

The evolution of $U_0(Nt)$ is shown in figure 5(*a*) for varying tow speeds U_B. The dashed line shows the empirical curve for non-propelled bodies given by equation (4.2).

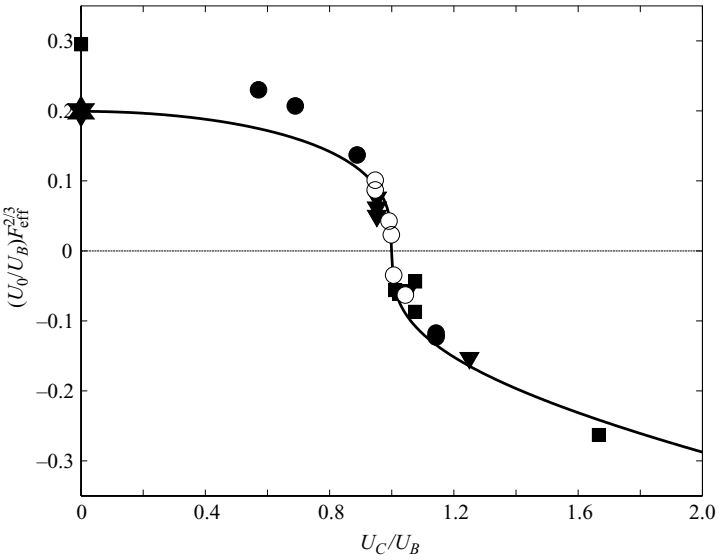

FIGURE 4. Amplitude of the mean profile of velocity as a function of the velocity of the propeller for a spheroid (closed symbols) and a cylinder (open symbols) at $Nt = 100$. The solid star represents the prediction given by Meunier & Spedding (2004) for non-propelled bodies. The solid line is from equation (4.5), developed in § 4.2.

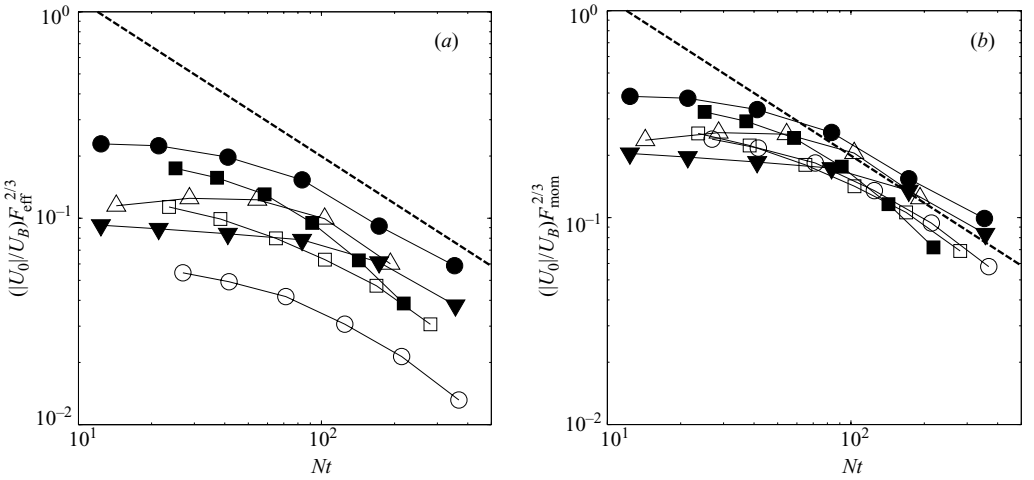

FIGURE 5. Amplitude of the mean profile of velocity for a cylinder (open symbols) and for a spheroid (closed symbols) using (*a*) the effective diameter defined by (2.1) and (*b*) the momentum thickness defined by (4.3). The ratios of U_B/U_C of towed and momentumless velocity are [0.994, 0.959, 1.063, 1.125, 0.930, 1.050] for [○, □, △, ●, ■, ▼]. $F = [15, 14, 27, 18, 23, 41]$ and $Re = [10.5, 10.1, 28.4, 11.4, 15.2, 26.6] \times 10^3$ respectively.

In all these experiments, the scaling exponent seems to be equal at late stages, but the curves always remain below the non-propelled case. The model must therefore be modified to take into account the action of the propeller.

In the case of non-propelled bodies, the dynamics of the wake are mainly governed by the momentum flux, which is a conserved quantity of the wake. Indeed, the effective

diameter $D_{\rm eff}$ is simply the momentum thickness, already introduced in non-stratified wakes by (Tennekes & Lumley 1972, chapter 4), and which is found by equating the momentum flux $J = \rho \frac{1}{4}\pi D_{\rm eff}^2 U_B^2$ and the drag force $F_{\rm drag} = c_D \frac{1}{2}\rho U_B^2 \frac{1}{4}\pi D^2$.

For propelled bodies, the momentum comes from fluid entrained by the drag, and also from fluid expelled by the propeller, which creates the thrust: $J = F_{\rm drag} - F_{\rm thrust}$. By definition of the momentumless velocity U_C, the thrust is equal to the drag for $U_B = U_C$, which leads to an expression for the thrust: $F_{\rm thrust} = c_D \frac{1}{2}\rho U_C^2 \frac{1}{4}\pi D^2$. A momentum thickness can thus be defined in the case of propelled bodies as $\rho \frac{1}{4}\pi D_{\rm mom}^2 U_B^2 = |J| = |F_{\rm drag} - F_{\rm thrust}|$, which can be simplified into

$$D_{\rm mom} = D\sqrt{c_D/2}\sqrt{|1 - U_C^2/U_B^2|}. \tag{4.3}$$

The universal law (4.2) found for non-propelled bodies should be modified to

$$\frac{|U_0|}{U_B} F_{\rm mom}^{2/3} = 6.6(Nt)^{-0.76}, \tag{4.4}$$

where the momentum Froude number is defined using the momentum thickness, $F_{\rm mom} = 2U_B/N D_{\rm mom}$. Equation (4.4) is plotted in figure 5(*b*) as a dashed line. All the results collapse onto this prediction to within 25%, even though they were initially as much as 6 times smaller. Furthermore, if the momentum Froude number in equation (4.4) is explicitly written with (4.3) one arrives at an expression for the amplitude U_0 as a function of the ratio U_C/U_B,

$$\frac{|U_0|}{U_B} F_{\rm eff}^{2/3} = 6.6(Nt)^{-0.76}|1 - (U_C/U_B)^2|^{1/3}. \tag{4.5}$$

This curve is plotted in figure 4 as a solid line. The vertical slope at $U_C = U_B$, observed in the experimental data, comes from the power 1/3 of the term $U_B - U_C$ in (4.5), and the dependence on $|U_B - U_C|^{1/3}$ explains the overall features of the curve.

4.3. *Wake width and Strouhal number*

The wake width L_0 of the mean profile of velocity, defined by equation (4.1), is plotted in figure 6 as a function of time. The wake width increases in time with a power law close to 0.3. For non-propelled bodies, it was shown in Meunier & Spedding (2004) that the wake width of different bluff bodies collapses when the lengthscale is defined as the effective diameter $D_{\rm eff}$, and can be written as

$$\frac{L_0}{D_{\rm eff}} F_{\rm eff}^{-0.35} = 0.275(Nt)^{0.35}. \tag{4.6}$$

This prediction is plotted in figure 6(*a*) as a dashed line. The experimental values obtained for propelled bodies are smaller than the theoretical prediction for non-propelled bodies, by a factor almost two. Recall that the wake is slower for propelled bodies, with a smaller amplitude U_0, and the wake width thus increases more slowly at early stages and remains smaller than for a non-propelled body.

To adapt the prediction made for non-propelled bodies to the case of propelled bodies, the wake width can be normalized by the momentum thickness $D_{\rm mom}$ defined in (4.3), rather than by the effective diameter $D_{\rm eff}$. If the Froude number is also defined using the momentum thickness $D_{\rm mom}$, (4.6) is modified to

$$\frac{L_0}{D_{\rm mom}} F_{\rm mom}^{-0.35} = 0.275(Nt)^{0.35}. \tag{4.7}$$

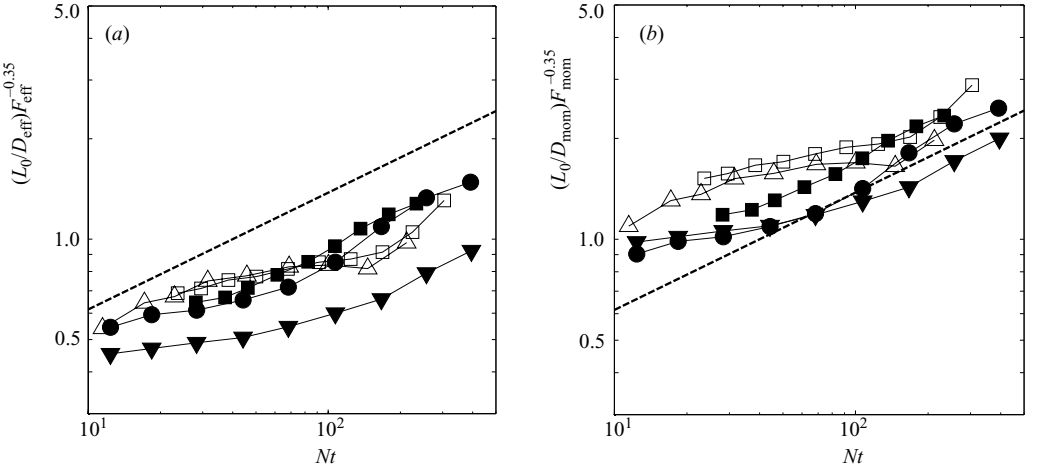

FIGURE 6. Wake half-width of the mean profile of velocity for a cylinder (open symbols) and for a spheroid (closed symbols) using (*a*) the effective diameter and (*b*) the momentum thickness. Symbols as in figure 5.

The modified prediction is shown in figure 6(*b*) by the dashed line. The experimental data collapse reasonably well onto this power law at late stages. The measurements are centred on the dashed line, although the variation in the measurements is relatively high (close to 30%). The scatter is due to the small amplitude of the wake U_0 compared to the towing velocity U_B of the bluff body: U_0/U_B can be as small as 0.1%. It is surprising to see that the simple rescaling using the momentum thickness $D_{\rm mom}$ is also efficient for the wake width, as it was for the velocity defect. It confirms the fact that the late stages are mainly governed by the momentum, without memory of the lengthscale of the bluff body. However, in the early stages, the wake width is slightly higher than the value given by the prediction (4.7). This might be due to a transient effect: when the towing velocity is close to the momentumless velocity, the wake motions are very slow and it takes a longer time (which could be rescaled by $D/(U_B - U_C)$ rather than D/U_B) for the wake to reach the asymptotic self-preserved state.

The Strouhal number can be measured from the instantaneous vorticity fields, as explained in Spedding *et al.* (1996) and Spedding (2002) for the stratified wake of a sphere. The Strouhal number can be defined as

$$St = D/\lambda_x, \tag{4.8}$$

where λ_x is the mean streamwise distance between two vortices of the same sign. It was shown in Meunier & Spedding (2004) that a general law for the Strouhal number can be found in the case of non-propelled bodies by defining the Strouhal number using the effective diameter,

$$St_{\rm eff} = D_{\rm eff}/\lambda_x. \tag{4.9}$$

With this definition all the measurements of different bluff bodies collapsed onto a universal law,

$$St_{\rm eff} F_{\rm eff}^{0.34} = 0.823(Nt)^{-0.34}, \tag{4.10}$$

plotted in figure 7(*a*) as a dashed line. The experimental values are twice as large, but decay at the same rate. Recall that propelled wakes develop more slowly than

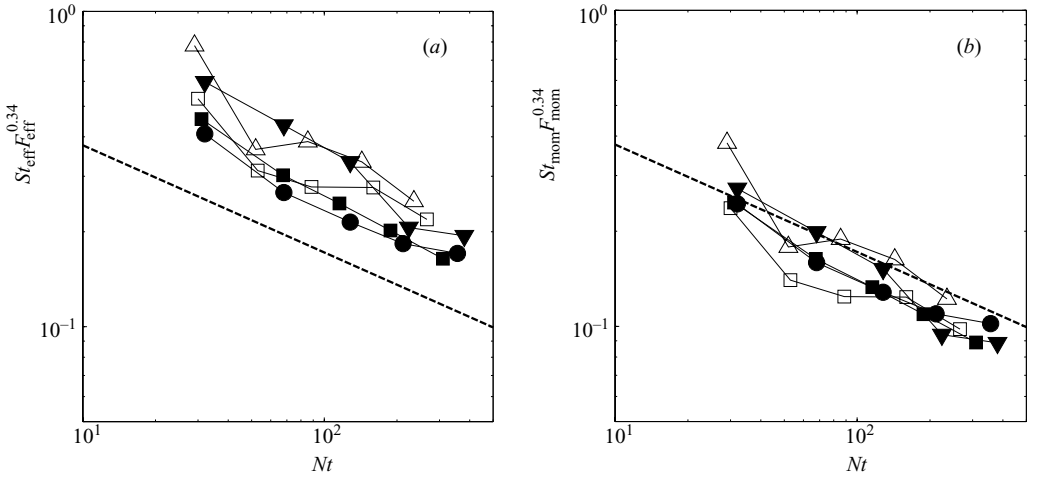

FIGURE 7. Strouhal number based on the distance between two vortices of the same sign for a cylinder (open symbols) and for a spheroid (closed symbols) using (*a*) the effective diameter and (*b*) the momentum thickness. Symbols as in figure 5.

non-propelled wakes (since U_0 is smaller), so the Strouhal number also decreases more slowly at early stages, and stays larger than for non-propelled bodies.

If the Strouhal number is defined using the momentum thickness $D_{\rm mom}$ defined in (4.3), and if the Froude number is also defined using the momentum thickness $D_{\rm mom}$, the prediction for non-propelled bodies is

$$St_{\rm mom}F_{\rm mom}^{0.34} = 0.823(Nt)^{-0.34}, \tag{4.11}$$

and is plotted as a dashed line in figure 7(*b*). The experimental data collapse onto the prediction, within 20%. This shows again that the wake is governed by the momentum flux at late stages.

4.4. *Fluctuating quantities*

In self-preserved, turbulent wakes, the mean profile of the wake diffuses due to the Reynolds stress, which is sustained by the mean shear. The hypothesis of a constant eddy viscosity can be checked for the case of stratified and propelled wakes, and if ν_T is constant, the profile of Reynolds stress may be supposed to be proportional to the mean shear,

$$\langle u'v'\rangle_x = \nu_T \frac{\partial U}{\partial y}. \tag{4.12}$$

Profiles of Reynolds stress, or velocity cross-fluctuations, are shown in figure 8 for tow speeds, U_B, close to the critical momentumless velocity, U_C. The Reynolds stress are very weak and $\langle u'v'\rangle^{1/2}$ is always smaller than 0.1% of U_B. When $U_B > U_C$, the mean profile has a positive amplitude U_0; the mean shear is thus positive for y^- and negative for y^+. Figure 8(*a*) shows that the cross-fluctuations follow the same trend for $U_B > U_C$, supporting the assumption that the profile of Reynolds stress is proportional to the mean shear, with a constant eddy viscosity. When the bluff body is towed at a velocity smaller than the momentumless velocity, the amplitude of the wake U_0 is negative, which gives negative Reynolds stress for y^- and positive Reynolds stress for y^+, as shown on figure 8(*b*), again proportional to the mean shear.

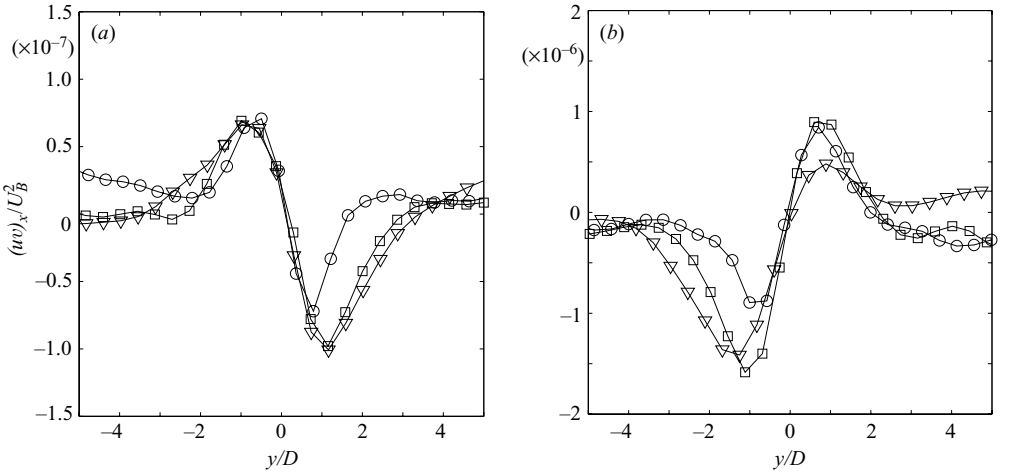

FIGURE 8. Profile of cross-fluctuation velocity $\langle u'v' \rangle_x$ at times $Nt = 60$ (○), $Nt = 120$ (□) and $Nt = 240$ (▽). The spheroid is towed at speed (*a*) larger than the momentumless velocity ($U_B = 1.05U_C$) and (*b*) smaller than the momentumless velocity ($U_B = 0.88U_C$). The Froude and the Reynolds numbers are: (*a*) $F = 41$, $Re = 26,000$; (*b*) $F = 14$, $Re = 9000$.

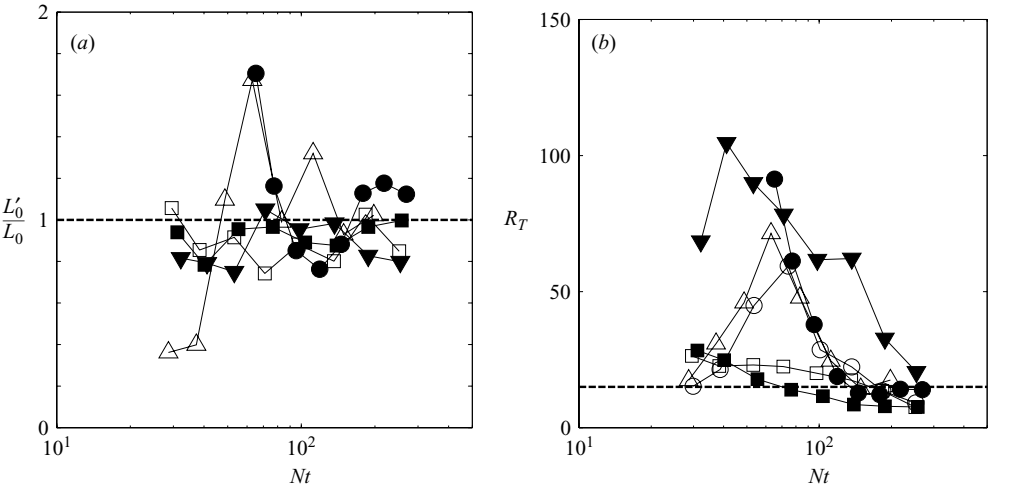

FIGURE 9. (*a*) Wake width of the profile of cross-fluctuations, and (*b*) turbulent Reynolds number, defined by (4.13) and (4.14). Symbols as in figure 5.

Since the mean profile of velocity is approximated well by a Gaussian (4.1) with amplitude U_0, the Reynolds stress profile should be fitted well by the derivative of a Gaussian function with an amplitude A and a width L_0':

$$\langle u'v' \rangle_x(y) = -A \frac{y}{L_0'} \mathrm{e}^{-y^2/L_0'^2}. \tag{4.13}$$

The amplitude A should be similar to $\nu_T U_0$ and the width L_0' should be similar to the wake width L_0. These two fitting constants have been measured and are shown in figure 9. The width of the cross-fluctuation profile L_0' is close to the wake width L_0 (figure 9*a*) although the variation in the measurements is large. This supports once again the hypothesis of a constant eddy viscosity. The amplitude A of the

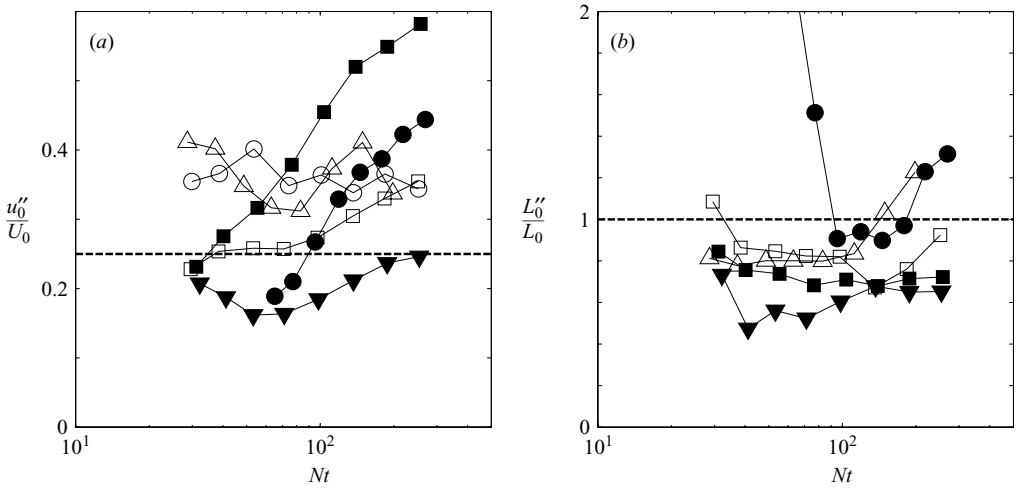

FIGURE 10. (*a*) Amplitude and (*b*) half-width of the profile of the quadratic fluctuations. Symbols as in figure 5.

cross-fluctuation profile is linked to the turbulent Reynolds number R_T by

$$R_T = \frac{|U_0|L_0}{\nu_T} = \frac{U_0|U_0|}{A}. \tag{4.14}$$

The turbulent Reynolds number is plotted in figure 9(*b*) as a function of time. The dashed line represents the value $R_T = 15$ found for non-propelled bodies at late times ($Nt > 100$). Initially, R_T can be significantly higher than its asymptotic value for $Nt > 100$, which is the same result as for towed bodies, suggesting that, just as in the non-propelled case for these body shapes, an equilibrium state is only reached at comparatively late times.

For a complete analysis of the turbulent fluctuations, the turbulent kinetic energy, equal to half the quadratic fluctuations of velocity $u^* = \langle u'^2 + v'^2 \rangle^{1/2}$ is measured. A profile of quadratic fluctuations of velocity was shown in figure 3, and seen to be very small compared to the mean profile. Moreover, the presence of large internal waves in the tank creates a background of velocity variations, which are of the order of the velocity fluctuations created by the wake. This background can be seen on figure 3 at the edges of the profile. The amplitude of the quadratic fluctuations was estimated by measuring the difference between the maximum and the minimum of the profile of quadratic fluctuations,

$$u_0'' = \max\left(\langle u'^2 + v'^2 \rangle^{1/2}\right) - \min\left(\langle u'^2 + v'^2 \rangle^{1/2}\right). \tag{4.15}$$

This amplitude is plotted in figure 10(*a*) as a function of time. The measurements are not very clean, but the ratio u_0''/U_0 is close to the value 0.25, which was found for non-propelled bodies and which is shown as a dashed line on figure 10(*a*).

Finally, the width of the profile of quadratic fluctuations was estimated by a fitting function introduced by Dommermuth *et al.* (2002):

$$\langle u'^2 + v'^2 \rangle^{1/2} = B + C\left(1 + y^2/L_0''^2\right)\mathrm{e}^{-y^2/2L_0''^2}. \tag{4.16}$$

L_0'' is normalized by the wake width L_0 and plotted in figure 10(*b*). The ratio L_0''/L_0 is slightly smaller than one, as in the case of non-propelled bodies. This may be due to transient effects, since the self-preserved state is only reached for very late stages.

5. Momentumless regime

As demonstrated in § 3, the wake presents a different structure when the towing velocity U_B of the bluff body is equal to the momentumless velocity U_C. The vorticity fields do not contain two layers of opposite-sign vorticity, as in the momentum regime ($U_B \neq U_C$), but they contain a disordered array of vortices of different signs. There seems to be no organized structure, except that the vortices are located in a compact domain that trails the body and widens with time.

The momentumless regime is only accessible when the relative difference between U_B and U_C is smaller than 2%. The primary difficulty in the experiments was in determining U_C, which was done by iteration for each angular velocity of the propeller, so that for each experiment, the mean velocity profile was measured and the towing velocity was then adjusted for the next experiment. Since at least 20 minutes waiting time (frequently many times this, depending on flow conditions) was required between two experiments for the fluid to be effectively at rest, a long time (usually a few days) was needed to determine the exact momentumless velocity for a given angular velocity of the propeller. Although this momentumless regime might represent the wakes of self-propelled bodies, it was evidently very hard to obtain in the experiments, and was very fragile compared with the momentum regime. The question of whether the wake of a real self-propelled body is in the momentum or in the momentumless regime will be discussed in § 7.

When $|U_B - U_C|/U_B < 2\%$ the signal:noise ratio is (by definition) small, and particular care was taken to repeat each experiment several times, and to remove all spurious results caused by contamination from wave motions or imperfect boundary conditions. All points shown are averages of the remaining two to four clean experiments.

5.1. *A null mean profile?*

When $U_B > U_C$, U_0 is positive and when $U_B < U_C$, U_0 is negative, so U_0 might be expected to vanish when $U_B = U_C$. However, in the constant turbulent eddy viscosity assumption of Tennekes & Lumley (1972), it is only the integral of the mean profile that vanishes, and not the mean profile itself. The mean profile is supposed to contain a central lobe with negative velocity, surrounded by two symmetric lobes of positive velocity. This shape of the mean velocity profile ensures that the turbulent fluctuations are still sustained by the mean shear. More sophisticated treatments (Finson 1975; Hassid 1980) invoke assumptions on higher-order closure of the fluctuating velocities, but some coherent form of the mean radial profile of the velocity differences is still required. Some kind of assumption like this is a necessary condition in order to impose self-similar solutions.

The measured mean velocity profiles are plotted in figure 11 as closed symbols, for the wake of a cylinder and the wake of a spheroid. The mean profile has no coherent shape, and seems to be smaller than the incoherent fluctuations in the measurements. It does not contain the features described in non-stratified wakes, with a positive lobe surrounded by two negative lobes. It is possible that such a structure of the wake could be recovered if the measurement resolution were higher (or, equivalently, at smaller x/D), or if the generating geometry were different. However, figure 11 shows that the quadratic fluctuations of velocity are larger than the mean velocity: they can be as much as five times larger in the case of the cylinder. This contradicts the assumption that the turbulent fluctuations are sustained by the mean shear. This regime is best described as a turbulent flow, with no mean shear, which diffuses and dissipates by self-induction. Such a description of the wake is consistent (of course)

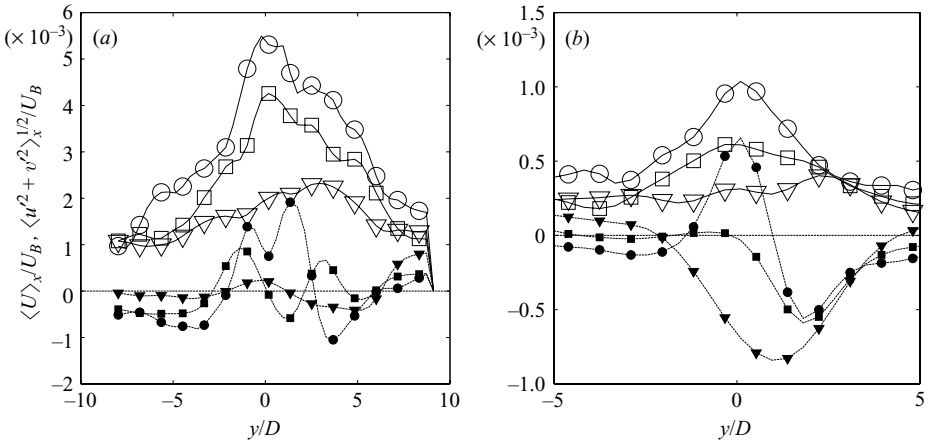

FIGURE 11. Profile of mean velocity (filled symbols) and quadratic fluctuations (open symbols) at times $Nt = 50$ (○), $Nt = 100$ (□) and $Nt = 300$ (▽) for (*a*) a cylinder with $F = 25$ and $Re = 27\,000$, (*b*) a spheroid with $F = 40$ and $Re = 25\,000$.

with the vorticity fields of figure 2(*b*), where no organized structure can be found. Now, the evolution of the wake should be governed by the fluctuations of the velocity rather than by the mean velocity of the wake.

5.2. *Quadratic fluctuations*

The profile of quadratic fluctuations of velocity $u^* = \langle u'^2 + v'^2\rangle^{1/2}$ is plotted in figure 11 as open symbols, for a cylinder and for a spheroid. The quadratic fluctuations are very small: between 0.1% and 0.5% of the towing velocity U_B. Moreover, the bluff body creates internal waves of large amplitude, propagating in the x-direction, which remain in the tank for a long time due to reflection on the walls. Their amplitude can be measured by the average of the streamwise velocity in the y-direction $\langle u\rangle_y(x)$ and they were removed from the velocity field before measuring the quadratic fluctuations of velocity. However, these internal waves also created some small-scale variations which cannot be averaged out in this way, especially far from the wake (for large $|y|$), which leads to a positive background in the profiles of quadratic velocity fluctuations. Consequently the width of the wake cannot be measured accurately using the profile of velocity fluctuations. It will be instead measured using the profile of vorticity flucuations (see § 5.3), which are not perturbed by the internal waves since the internal waves do not contain any vertical vorticity.

The maximum of the profile of velocity fluctuations can be relatively accurately measured. It is plotted in figure 12 for the five different configurations studied for this momentumless regime. Each curve is the average of two to four experiments. The variation in the measurements is represented by the size of the symbols.

The maximum of the quadratic fluctuations $u^*_{\max} = \max(\langle u'^2 + v'^2\rangle^{1/2})$ is plotted as $u^*_{\max}/U_B F^{0.75}$ so the results may be compared with the measurements obtained by Lin & Pao (1979) for a streamlined spheroid, plotted as a solid line on this figure. The current measurements are significantly smaller, the velocity being four times smaller at early stages. Moreover, assuming the quadratic velocity has a power law $u^*_{\max} \sim (Nt)^{\alpha_{u^*}}$, Lin & Pao measured a decay exponent of -0.76, whereas we find

$$\alpha_{u^*} = -0.40 \pm 0.04. \tag{5.1}$$

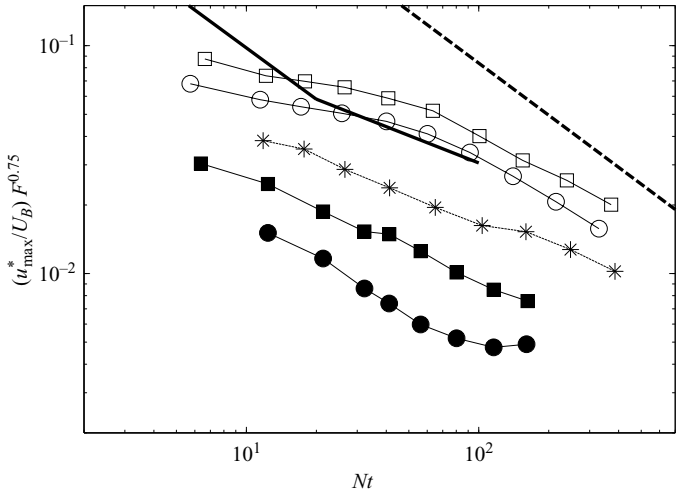

FIGURE 12. Amplitude of the quadratic fluctuations of velocity $u^* = \langle u'^2 + v'^2 \rangle_x^{1/2}$ for a slender spheroid (closed symbols), a cylinder with a small propeller (open symbols) and a cylinder with a large propeller (*). The solid line corresponds to the experimental fit given by Lin & Pao (1979), and the dashed line corresponds to the amplitude of the mean velocity of a towed slender body given by Meunier and Spedding (2004). $F = [15, 40, 12, 15, 25]$ for experiments [●, ■, *, ○, □] with $Re = [10, 25, 11, 13, 27] \times 10^3$ respectively.

The disagreement comes partly from the fact that the results of Lin & Pao (1979) were restricted to the early stages of the wake: their scaling is valid for $1 < Nt < 20$ while our results cover $10 < Nt < 300$. At the early stages, the flow is mainly three-dimensional, which might explain why they measure a decay exponent $\alpha_{u^*} = -0.76$, more in agreement with the theoretical prediction for a non-stratified self-propelled wake ($\alpha_u = -4/5$). Upon close inspection, their measurements even show that the quadratic fluctuations of velocity depart from the initial power law for $Nt > 20$, as the authors noted. A decay exponent for this latter regime can be roughly estimated to be $\alpha_u = -0.4$ for $20 < Nt < 60$, in close agreement with our value for $10 < Nt < 300$.

In figure 12, two experiments with the same bluff body (a cylinder) and with two different sizes of propeller have been reported: the case of a large propeller is plotted by stars and the case of a small propeller is plotted by open symbols. The velocity fluctuations are 60% higher in the case of a small propeller. Evidently the results cannot be collapsed by simply using the drag coefficient of the bluff body alone. The amplitude of the quadratic fluctuations depends on the shape of the bluff body and the propeller, and not only on the drag coefficient of the bluff body (here, the drag of the propeller is small compared to the drag of the cylinder). It is possible that the fluctuations depend on the shape of the bluff body close to the propeller, since the propeller draws the fluid inward and deforms the set of streamlines that would be created in the absence of a propeller. The small propeller may draw the fluid into a smaller cross-section, forcing streamlines closer to the edges of the cylinder, and so creating strong turbulence.

It can be noted that the measurements do not collapse with respect to the Froude number when the velocity fluctuation is multiplied by $F^{0.75}$. A better collapse of the measurements is obtained when the velocity fluctuation is multiplied by $F^{0.25}$. However, the Froude number was varied with a factor 3 only, and the measurements should be repeated on a larger range of Froude numbers for this result to be confirmed.

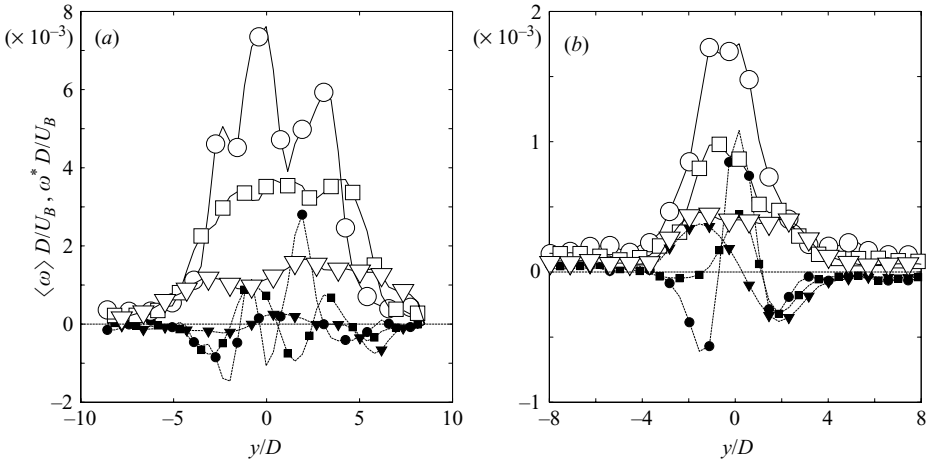

FIGURE 13. Profile of mean vorticity (filled symbols) and quadratic fluctuations of vorticity $\omega^* = \sqrt{\langle\omega^2\rangle_x}$ (open symbols) at times $Nt = 50$ (○), $Nt = 100$ (□) and $Nt = 300$ (▽) for (*a*) a cylinder with $F = 25$ and $Re = 27\,000$, (*b*) a spheroid with $F = 40$ and $Re = 25\,000$.

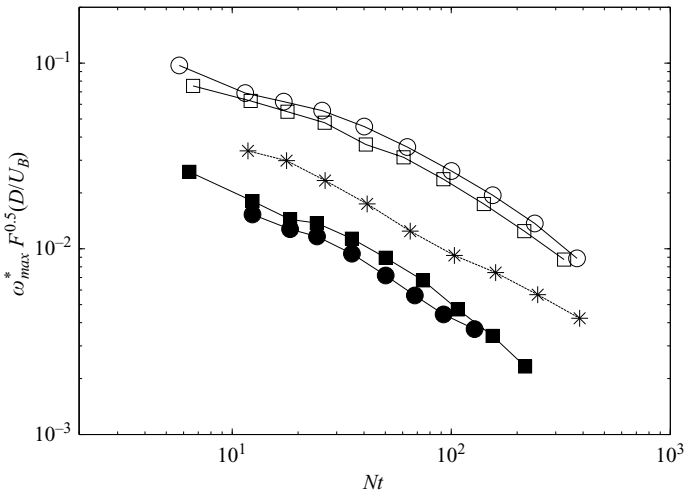

FIGURE 14. Amplitude of the maximum quadratic fluctuations of vorticity $\omega^* = \langle\omega^2\rangle_x^{1/2}$ for a slender spheroid (closed symbols), a cylinder with a small propeller (open symbols) and a cylinder with a large propeller (∗). Symbols as in figure 12.

5.3. *Vorticity fluctuations*

As noted in § 5.2, the vorticity profiles are not disturbed by internal waves which do not contain any vertical vorticity. The profiles of mean vorticity $\langle\omega\rangle$ and of the quadratic fluctations of vorticity $\omega^* = \sqrt{\langle\omega^2\rangle_x}$ are therefore less variable than the profiles of velocity. They are plotted in figure 13 for a cylinder and a spheroid. The mean vorticity is very small compared with the fluctuations. This shows again that the wake seems to be disordered, closer to a layer of free turbulence rather than to turbulence forced by the mean shear.

The maximum of the quadratic fluctuations of vorticity $\omega^*_{\max}$ is plotted in figure 14 as a function of time for a cylinder and for a spheroid. As previously noted, it is not possible to rescale the experiments by simply using the effective diameter of the bluff

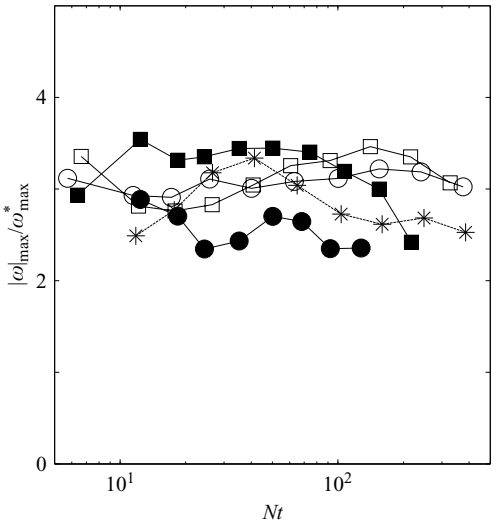

FIGURE 15. Maximum of the vorticity magnitude $|\omega|$ for a slender spheroid (closed symbols), a cylinder with a small propeller (open symbols) and a cylinder with a large propeller (*). Symbols as in figure 12.

body, since the size of the propeller strongly modifies the amplitude of the vorticity fluctuations. However, a reasonable collapse of the measurements has been obtained by multiplying the amplitude by the Froude number to the power 0.5. This empirical scaling (which has no external justification) needs to be verified since the Froude number was only varied with of a factor 3. Assuming the vorticity fluctuations follow a power law Nt^{α_ω}, the decay exponent α_ω can be estimated as

$$\alpha_\omega = -0.61 \pm 0.02. \tag{5.2}$$

Finally, the maximum of the absolute value of the vorticity $|\omega|_{\max}$ on the centreplane has been measured and is plotted as a function of time in figure 15; $|\omega|_{\max}$ is constant and roughly equal to three times the maximum of the quadratic fluctuations of vorticity, $\omega^*_{\max}$. This implies that some aspect of the spatial structure of the wake is constant, and that the wake may be self-similar in this measure.

5.4. *Wake width*

Since the profiles of quadratic fluctuations are relatively clean, it is possible to measure the width L_ω of the profile at mid-height, defined as the range for which the quadratic vorticity is larger than half the maximum quadratic vorticity:

$$\omega^*(y) > \frac{\omega^*_{\max}}{2} \text{ for } -\frac{L_\omega}{2} < y < \frac{L_\omega}{2}. \tag{5.3}$$

The width L_ω is plotted in figure 16 for five different set of experiments. In figure 16(*a*), the width is normalized using the effective diameter of the bluff body, as in the case of a momentum wake (see § 4.3). It seems that the experiments for a cylinder with a large (stars) and with a small propeller (open symbols) give the same result. This indicates that the wake width may be independent of the real shape of the bluff body and that it may be collapsed using the drag coefficient. Indeed, when plotting the wake width multiplied by the drag coefficient to the power −0.8, an excellent collapse is obtained for the case of both a spheroid and a cylinder, as is shown in figure 16(*b*).

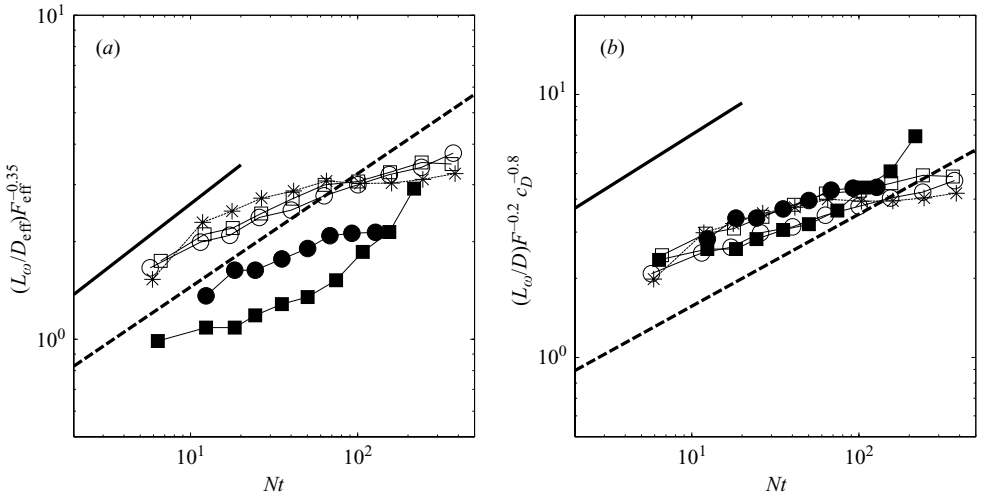

FIGURE 16. Width L_ω of the quadratic fluctuations of vorticity $\omega^* = \langle\omega^2\rangle_x^{1/2}$ for a slender spheroid (closed symbols), a cylinder with a small propeller (open symbols) and a cylinder with a large propeller (*), (*a*) normalized using the effective diameter and (*b*) multiplied by $c_0^{-0.8}$. The solid line corresponds to the experiments of Lin & Pao (1979) obtained through visualizations, and the dashed line corresponds to the mean velocity profile of a towed body (Meunier & Spedding 2004). Symbols as in figure 12.

The best fit for all the data is given by

$$\frac{L_\omega}{D} = 1.8(Nt)^{0.18} F^{0.2} c_D^{0.8}. \tag{5.4}$$

This wake width is three times smaller than the one measured by Lin & Pao (1979), plotted as a solid line on figure 16. However, this is not a real disagreement since they measured the width for which the wake appeared turbulent on the corresponding shadowgraph visualizations, which will be larger than the width at mid-height. The main disagreement comes from the fact that the exponent for their power law is equal to +0.4 whereas here it is

$$\alpha_{L_\omega} = +0.18 \pm 0.05. \tag{5.5}$$

Part of the discrepancy may again come from the fact that their measurements were obtained for early stages ($Nt < 20$) and do not extrapolate simply to the late stages ($10 < Nt < 300$) measured here, as noted previously.

An exponent for the wake width can also be estimated as follows. If the velocity fluctuations have an exponent α_{u^*} and if the vorticity fluctuations have an exponent α_ω, the wake width should have an exponent $\alpha_{L_\omega} = \alpha_{u^*} - \alpha_\omega$ since the vorticity scales as $\omega \sim u/L$. This formula together with the measurements of α_{u^*} in (5.1) and α_ω in (5.2) leads to a value of the exponent for the wake width $\alpha_{L_\omega} = +0.21 \pm 0.03$, in good agreement with (5.5).

6. Asymmetric momentumless regime

This section focuses on the flow obtained when a slight angle of attack is present between the axis of the bluff body and the towing velocity. This configuration was first obtained unintentionally, but it revealed interesting features of the flow, and is

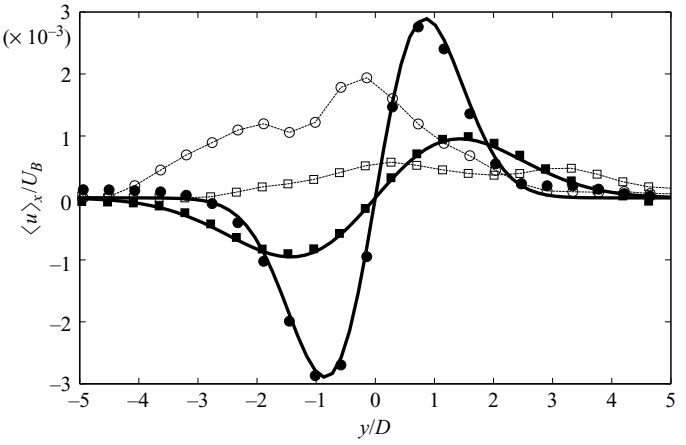

FIGURE 17. Profile of mean velocity (filled symbols) and quadratic fluctuations of velocity $u^* \equiv \langle u'^2 + v'^2 \rangle_x^{1/2}$ (open symbols) at times $Nt = 30$ (○) and $Nt = 200$ (□) for a spheroid with a slight angle of attack toward positive y. $F = 25$ and $Re = 16\,000$.

an example of the sensitive dependence on initial conditions that is a unique feature of the momentumless case.

As shown in figure 2(c), the vorticity fields obtained in the asymmetric regime are very organized, but differ from the ones obtained in the momentum regime (shown on figure 2a). The instantaneous vorticity fields contain three layers of vorticity in the asymmetric regime, whereas only two layers of vorticity are present in the momentum regime. In this experiment, the angle of attack was positive (toward the left), i.e. the nose of the bluff body was located at a small y^+. This leads to a layer of negative vorticity surrounded by two layers of positive vorticity. For such a distribution of vorticity, it can be deduced that the velocity profile must be asymmetric, as the data in figure 17 show. Although the angle of attack could not be measured accurately, it was estimated to be between 0.5° and 1°. The experiment was carried out for $U_B = U_C$, which means that the integral of the mean profile $\int U(y)\mathrm{d}y$ is equal to zero, as can be seen on figure 17. The towing velocity U_B had to be very close to the momentumless velocity for the profile to be asymmetric: a relative difference of 1% was sufficient to modify the profile from asymmetric to symmetric. In the asymmetric regime, the mean profile of velocity contains two lobes, a negative lobe of velocity for y^- and a positive lobe for y^+. This accords with the fact that the angle of attack is toward y^+: the propeller is located at a small y^-, and more fluid is expelled backwards at y^-, creating a negative velocity for y^-. On the other hand, for y^+, the jet of the propeller is weaker and more fluid is more entrained by the drag of the bluff body, creating a positive lobe of velocity for y^+.

Figure 17 also shows the quadratic fluctuations of velocity $u^* \equiv \langle u'^2 + v'^2 \rangle_x^{1/2}$ as open symbols. These fluctuations are slightly smaller than the mean profile, indicating that the wake may again be governed by the mean shear rather than by the turbulent fluctuations, as in the momentum regime. The measurements of the mean profile are clean enough and it is possible to fit the mean velocity by an odd function with an amplitude U_1 and a width L_1,

$$U(y) = U_1 \frac{y}{L_1} \mathrm{e}^{-y/2L_1^2}. \tag{6.1}$$

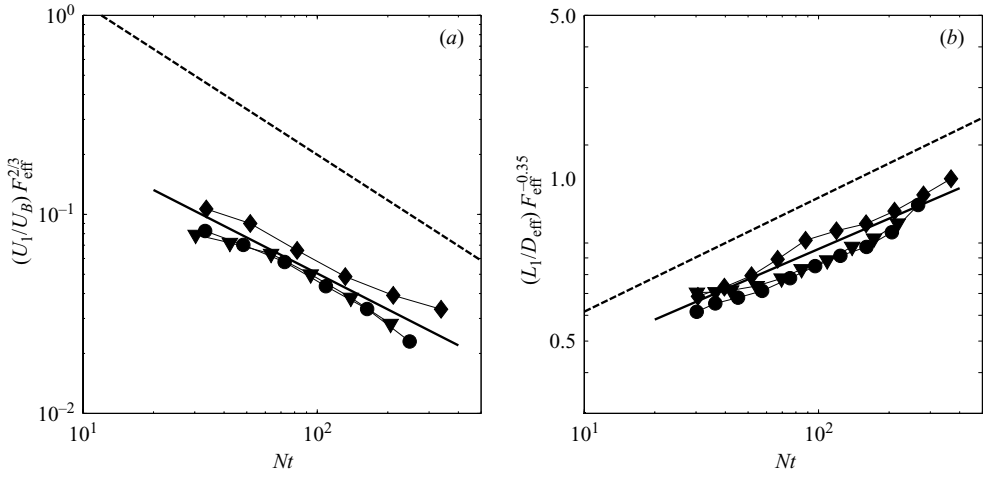

FIGURE 18. Amplitude (*a*) and wake width (*b*) of the mean profile of velocity for a spheroid with a Froude number $F = 25$ and $Re = 16\,000$.

This function is convenient because it is a self-similar solution of the diffusion equation $\partial U/\partial t = \nu_T \partial^2 U/\partial y^2$ which governs the wake in a non-stratified fluid. The fitting function is plotted in figure 17 as a solid line and shows a good fit to the experimental data, and hence a reasonable determination of the amplitude U_1 and the width L_1 of the wake as a function of time, which are plotted in figure 18 for three experiments in the same configuration (angle of attack, Froude number and Reynolds number).

The amplitude U_1 of the asymmetric mean profile is plotted in figure 18(*a*) and is compared with the prediction for a non-propelled bluff body given by equation (4.2), shown as a dashed line. The amplitude U_1 is four times weaker than in the non-propelled case, as expected since the experiments are conducted close to the momentumless velocity U_C and with a slight angle of attack. The amplitude should strongly depend on the angle of attack and it should vanish when the angle of attack vanishes. Hence, there was no attempt to predict the multiplying factor for the variation of U_1. However, it is possible that the scaling exponent may be universal in this regime, independent of the drag coefficient or the angle of attack. For this experiment, assuming the amplitude scales as $U_1 \sim Nt^{\alpha_{U_1}}$, the best fit (plotted as a solid line on figure 18*a*) is

$$\alpha_{U_1} = -0.6 \pm 0.06. \tag{6.2}$$

This value is smaller than the value $\alpha_U = -0.76$ found for momentum wakes, described in detail in § 4, but it is larger than the value $\alpha_{u^*} = -0.4$ found for the symmetric momentumless wakes, described in § 5. Further experiments would be required to confirm this result, and its possible dependence on Froude number and angle of attack.

Figure 18(*b*) shows the wake width normalized by the effective diameter. It is slightly smaller than in the case of a non-propelled wake, represented by the dashed line. This tendency was also obtained in the momentum regime – the propeller decreased the wake width (see figure 6*a*). However, in this case, it is not possible to use the momentum thickness $D_{\rm mom}$ defined by equation (4.3), since it is zero.

The wake width might be collapsed using a lengthscale based upon the (small but finite) angle of attack, but this was not feasible here since the angle of attack has not

been measured with sufficient precision. Nevertheless, assuming that the wake width scales as $L_1 \sim Nt^{\alpha_{L_1}}$, the scaling exponent of the wake width may yet be universal. A best fit of the results (shown as a solid line on figure 18*b*) gives

$$\alpha_{L_1} = +0.31 \pm 0.03, \tag{6.3}$$

which is indistinguishable from the value of $\alpha_L = +0.35$ obtained for momentum wakes but larger than the value of $\alpha_{L_\omega} = +0.18$ obtained for symmetric momentumless wakes.

To conclude, it seems that in the asymmetric momentumless regime, the scaling exponents are between the scaling exponents of the momentum regime and the scaling exponents of the momentumless regime. This may come from the fact that the mean profile of velocity is close to the quadratic fluctuations of velocity, meaning that the wake is governed by the mean shear but also by the turbulent fluctuations. This regime could be better analysed with a larger angle of attack and further experiments could be done in this regime, both on the grounds that a small angle of attack may not be that uncommon in practice and because the different balance between mean and turbulence-driven fluctuations might be instructive.

7. Discussion

7.1. *Momentumless wakes are not universal*

The true momentumless wake, where $|U_B - U_C| \leqslant 4\%$, has no coherent mean profile, and no obviously self-preserving form of the velocity fluctuations. The late-time wake decay exponents were found to depend on the initial conditions, as data for the cylinder with small and large propeller do not collapse. No drag wake, or any other case outside this particular limiting condition, has a measurable dependence on initial conditions in the late wake.

The lack of universal scaling laws in the momentumless wake is consistent with the observation that since, unlike drag wakes, there is no balance between turbulence production and dissipation, then turbulence parameters determined in near-wake initial conditions can continue to affect the far-wake similarity solutions (Finson 1975). It is also consistent with experimental observations in the literature for self-propelled bodies in non-stratified flows, showing measurable differences in the wakes of smooth and rough-walled bodies, and between wakes where the propulsion is provided by propellers or momentum jets (Swanson *et al.* 1974; Chieng *et al.* 1974; Higuchi & Kubota 1990; Sirviente & Patel 2000*a*, *b*).

It is important to note that this non-universality is measured here in the late wake. The data extend to $Nt = 500$ and $x/D = 10^4$ and appear to have reached their final, asymptotic state. There is experimental (e.g. Bevilaqua & Lykoudis 1978) and theoretical (Johansson *et al.* 2003) evidence showing that velocity fluctuations in particular may not reach a self-preserving form until far downstream, and many of the self-propelled results in the literature are for $x/D < 100$.

The ability of the current experiments to access and differentiate between almost and exactly self-propelled cases is due to the simultaneous operation of independent towing and thrust generation mechanisms. In this respect, the experiment is similar to that of Higuchi & Kubota (1990) where the thrust-producing central jet momentum flux was varied independently of the tunnel mean speed around a drag-producing body. In a similar systematic variation of the degree of propulsion, these authors also noted the unique characteristics of the precise self-propelled point.

The definition of momentumless here is different from other possible definitions, such as drag = thrust. Only the condition $\int_{-\infty}^{\infty}\langle u\rangle_x \mathrm{d}y = 0$ (equation (3.1)) is imposed and only at the horizontal centreplane. The fact that the self-propelled point defined this way ($U_B = U_C$) does lead to and correspond with a unique (almost singular in the sense of Finson 1975) flow field suggests that it is useful operationally, even if it does not account for all possible momentum fluxes (for example if surface or internal wave drag were significant; see next section).

7.2. *Momentumless wakes are unlikely*

The exact self-propelled point is rarely attained, because a number of conditions will pull the wake far enough away from it to enter a completely different regime. The possible perturbations include non-steady motion of the body, non-steady motion in the environment, and drag contributions from waves at boundaries, or (most likely in stratified flows) internally within the fluid.

The acceleration of a self-propelled body times its mass m is equal to the sum of the drag force and the thrust force. This can be rewritten, using the expressions for the drag force and the thrust force, as

$$m\frac{\mathrm{d}U_B}{\mathrm{d}t} = F_{\text{thrust}} - F_{\text{drag}} = c_D \tfrac{1}{2}\rho\left(U_C^2 - U_B^2\right)\frac{\pi D^2}{4}. \tag{7.1}$$

Here, U_B is the velocity of the bluff body and U_C is a velocity for which the momentum of the wake vanishes, proportional to the angular velocity of the propeller. When the bluff body reaches a constant speed, the acceleration is zero and the velocity of the bluff body equals the momentumless velocity U_C. The wake is thus in the momentumless regime. However, the time needed to reach this constant speed is infinite, and during the phase of acceleration, the wake will be better represented by the momentum regime.

We may estimate the time needed for the wake to reach the momentumless regime. By integrating the differential equation (7.1), the velocity U_B is governed by a law $U_B = U_C \tanh(t/\tau)$ with $\tau = 4L/c_D U_C$. For this result, the bluff body is assumed to be cylindrical, so that the mass m of the bluff body is equal to the density of the fluid ρ times the section of the bluff body $\pi D^2/4$ times the length L of the bluff body times a factor 2 to take into account the added mass. The velocity of the bluff body is thus equal to the momentumless velocity within 2% after a time $t = 2.3\tau$, which represents a distance close to $L_{\text{acc.phase}} \approx 1.6\tau U_C \approx 6.4L/c_D$. For example, a bluff body with a length of the order of 30 m leaves a momentum wake of a length close to one kilometre each time it changes the velocity of its propellers. It is only after this distance that the wake is in the momentum regime.

This calculation shows that the momentum regime may be representative of the wake of a real self-propelled body, if the velocity of the bluff body is not exactly constant. This is the case in the acceleration and deceleration phases. But it is also the case if the fluid has its own fluctuations of velocity, for example created by oceanic currents. If we assume that the length needed by the bluff body to reach its cruise velocity is much larger than the lengthscale of the currents, the bluff body will have a constant velocity and will experience variations in its momentumless velocity: the velocity of the currents is equal to the difference between the velocity of the bluff body U_B and the momentumless velocity U_C ($u_{\text{curr.}} = U_B - U_C$). Suppose the fluctuations $U_B - U_C$ are small compared to the velocity of the bluff body U_B, but big enough for the wake to be in the momentum regime. Then the mean absolute amplitude of the

wake can be obtained by taking the average of equation (4.5):

$$\langle |U_0| \rangle = 6.6(Nt)^{-0.76} F_{\text{eff}}^{-2/3} \frac{\langle |u_{\text{curr.}}|^{1/3} \rangle}{U_B^{1/3}} U_B. \tag{7.2}$$

If the fluctuations are of the order of 10% of the velocity of the bluff body, the mean absolute amplitude of the wake would be equal to 46% of the amplitude of the wake without a propeller. Thus, even if the fluctuations of velocity of the ambient fluid are small, the momentum can be high. We thus expect the wake to be in the momentum regime most of the time.

In the above analysis, the drag was imagined to be due only to the fluid entrained by the bluff body, as in a non-stratified fluid. However, in a stratified fluid, there is an additional drag due to the internal waves. This drag can be as high as 10% of the standard drag for Froude numbers between 2 and 10 (Lofquist & Purtell 1984). If $\lambda = F_{\text{int.waves}}/F_{\text{drag}}$ is the ratio between the drag due to the internal waves and the drag due to the entrained fluid, the thrust force can be calculated as $F_{\text{thrust}} = (1+\lambda)F_{\text{drag}}$ for a constant speed of the body. Since the internal waves propagate away very rapidly, the only momentum left in the wake at late stages is $J = F_{\text{drag}} - F_{\text{thrust}}$, which leads to a new definition of the momentum thickness,

$$D_{\text{mom}} = D\sqrt{\lambda c_D/2} = D_{\text{eff}}\sqrt{\lambda}. \tag{7.3}$$

The wake is now governed by the momentum created by the drag from the internal waves, in which case all the predictions made in § 4 remain valid if the momentum thickness is defined by (7.3). The value of the amplitude U_0 is easily found by introducing (7.3) into (4.4), so

$$\frac{U_0}{U_B} = -6.6(Nt)^{-0.76} F_{\text{eff}}^{-2/3} \lambda^{1/3}. \tag{7.4}$$

If the drag due to the internal waves is of the order of 10% of the drag due to the entrained fluid, the amplitude of the wake is still equal to 46% of the amplitude of the wake in the absence of the propeller. The stratified wake remains in the momentum regime even when the body is self-propelled, and moving at perfectly constant speed in a perfectly still environment.

8. Conclusions

Exactly momentumless wakes are very fragile and peculiar flows. They contain information from the initial conditions in the late wake: these include turbulence parameters, body/propeller geometry and angle of attack of the body. Unlike the drag wake, there is no single rescaling based only on wake momentum flux that will collapse measurements or predict, in a general way, the wake dynamics. In particular, the measurable turbulent fluctuations cannot be seen as being driven by some self-similar mean shear profile. This would bode ill for extrapolation of these kinds of results to practical applications, but for the fact that almost always some kind of momentum excess (positive or negative) will be present. That being the case, this paper establishes a set of universal scaling exponents that can be used to describe the mean flow, turbulence quantities and vortex geometry for all stratified (momentum) wakes, regardless of their origin. Some differences with literature results remain to be explained, but may be due in part to the difficulty of maintaining precise momentumless experiments, and partly to the fact that the experiments described

here apply to stages of the wake evolution that are an order of magnitude later than for other comparable data.

REFERENCES

Afanasyev, Y. D. 2004 Wakes behind towed and self-propelled bodies: Asymptotic theory. *Phys. Fluids* **16**, 3235–3238.

Bevilaqua, P. M. & Lykoudis, P. S. 1978 Turbulence memory in self-preserving wakes. *J. Fluid Mech.* **89**, 589–606.

Blevins, R. D. 1984 *Applied Fluid Dynamics Handbook*. Van Nostrand Reinhold.

Bonneton, P., Chomaz, J.-M. & Hopfinger, E. J. 1993 Internal waves produced by the turbulent wake of a sphere moving horizontally in a stratified fluid. *J. Fluid Mech.* **254**, 23–40.

Chernykh, G. G., Demenkov, A. G. & Kostomakha, V. A. 2001 Numerical modelling of a swirling turbulent wake behind a self-propelled body. *Russian J. Numer. Anal. Math. Model.* **16** (1), 19–32.

Chernykh, G. G., Ilyushin, B. B. & Voropayeva, O. F. 2003 Anisotropy decay of turbulence in a far momentumless wake in a linearly stratified medium. *Russian J. Numer. Anal. Math. Model.* **18** (2), 105–116.

Chieng, C. C., Jakubowski, A. K. & Schetz, J. A. 1974 Investigation of the turbulent properties of the wake behind self-propelled axisymmetric bodies. *VPI-Aero-025*. Virginia Polytechnic Institute, Blacksburg, Virginia.

Chomaz, J. M., Bonneton, P. & Hopfinger, E. J. 1993 The structure of the near wake of a sphere moving horizontally in a stratified fluid. *J. Fluid Mech.* **254**, 1–21.

Diamessis, P. J., Domaradzki, A. J. & Hesthaven, J. S. 2005 A spectral multidomain penalty method model for the simulation of high Reynolds number localized incompressible stratified turbulence. *J. Comput. Phys.* **202**, 298–322.

Dommermuth, D. G., Rottman, J. W., Innis, G. E. & Novikov, E. A. 2002 Numerical simulation of the wake of a towed sphere in a weakly stratified fluid. *J. Fluid Mech.* **473**, 83–101.

Fincham, A. M. & Spedding, G. R. 1997 Low-cost high-resolution dpiv for turbulent flows. *Exps. Fluids* **23**, 449–462.

Finson, M. L. 1975 Similarity behaviour of momentumless turbulent wakes. *J. Fluid Mech.* **71**, 465–479.

Gilreath, H. E. & Brandt, A. 1985 Experiments on the generation of internal waves in a stratified fluid. *AIAA J.* **23**, 693–700.

Gourlay, M. J., Arendt, S. C., Fritts, D. C. & Werne, J. 2001 Numerical modeling of initially turbulent wakes with net momentum. *Phys. Fluids* **13**, 3783–3802.

Hassid, S. 1980 Similarity and decay laws of momentumless wakes. *Phys. Fluids* **23**, 404–405.

Higuchi, H. & Kubota, T. 1990 Axisymmetric wakes behind a slender body including zero-momentum configurations. *Phys. Fluids* A **2**, 1615–1623.

Johansson, P. B. V., George, W. K. & Gourlay, M. J. 2003 Equilibrium similarity, effects of initial conditions and local Reynolds number on the axisymmetric wake. *Phys. Fluids* **15**, 603–617.

Lin, J. T. & Pao, Y. H. 1974 Turbulent wake of a self-propelled slender body in stratified and non-stratified fluids: analysis and flow visualizations. *APL/JHU POR-3586: Flow Research Rep. 11*.

Lin, J. T. & Pao, Y. H. 1979 Wakes in stratified fluids: a review. *Annu. Rev. Fluid Mech.* **11**, 317–338.

Lofquist, K. E. B. & Purtell, L. P. 1984 Drag on a sphere moving horizontally through a stratified liquid. *J. Fluid Mech.* **148**, 271–284.

Meunier, P. & Spedding, G. R. 2004 A loss of memory in stratified momentum wakes. *Phys. Fluids* **16**, 298–305.

Naudascher, E. 1965 Flow in the wake of self-propelled bodies and related sources of turbulence. *J. Fluid Mech.* **23**, 625–656.

Riley, J. R. & Lelong, M. P. 2000 Fluid motions in the presence of strong stable stratification. *Annu. Rev. Fluid Mech.* **32**, 613.

Schetz, J. A. & Jakubowski, A. K. 1975 Experimental study of the turbulent wake behind self-propelled slender bodies. *AIAA J.* **13**, 1568–1575.

Schooley, A. H. & Stewart, R. W. 1962 Experiments with a self-propelled body submerged in a fluid with vertical density gradient. *J. Fluid Mech.* **15**, 83–99.

Sirviente, A. I. & Patel, V. C. 1999 Experiments in the turbulent near wake of an axisymmetric body. *AIAA J.* **37**, 1670–1673.

Sirviente, A. I. & Patel, V. C. 2000*a* Wake of a self-propelled body, part 1: Momentumless wake. *AIAA J.* **38**, 611–619.

Sirviente, A. I. & Patel, V. C. 2000*b* Wake of a self-propelled body, part 2: Momentumless wake with swirl. *AIAA J.* **38**, 620–627.

Sirviente, A. I. & Patel, V. C. 2001 Turbulence in wake of a self-propelled body with and without swirl. *AIAA J.* **39**, 2411–2414.

Smirnov, S. A. & Voropayev, S. I. 2003 On the asymptotic theory of momentum/zero-momentum wakes. *Phys. Lett.* A **307**, 148–153.

Spedding, G. R. 1997 The evolution of initially turbulent bluff-body wakes at high internal froude number. *J. Fluid Mech.* **337**, 283–301.

Spedding, G. R. 2002 The streamwise spacing of adjacent coherent structures in stratified wakes. *Phys. Fluids* **14**, 3820–3828.

Spedding, G. R., Browand, F. K., Bell, R. & Chen, J. 2000 Internal waves from intermediate, or late-wake vortices. In *Stratified Flows I Proc. 5th Int. Symp. on Stratified Flows, Vancouver, Canada: UBC*. (ed. G. A. Lawrence, R. Pieters & N. Yonemitsu), pp. 113–118.

Spedding, G. R., Browand, F. K. & Fincham, A. M. 1996 Turbulence, similarity scaling and vortex geometry in the wake of a towed sphere in a stably stratified fluid. *J. Fluid Mech.* **314**, 53–103.

Swanson, R. C., Schetz, J. A. & Jakubowski, A. K. 1974 Turbulent wake behind slender bodies including self-propelled configurations. *VPI-Aero-024*. Virginia Polytechnic Institute, Blacksburg, Virginia.

Tennekes, H. & Lumley, J. L. 1972 *A First Course in Turbulence*. M.I.T. Press.

Voisin, B. 1991 Internal wave generation in uniformly stratified fluids. part 1. green's function and point sources. *J. Fluid Mech.* **231**, 439–480.

Voropayev, S. I. & Smirnov, S. A. 2003 Vortex streets generated by a moving momentum source in a stratified fluid. *Phys. Fluids* **15**, 618–624.

ELSEVIER

Journal of Fluids and Structures 22 (2006) 941–947

JOURNAL OF FLUIDS AND STRUCTURES

www.elsevier.com/locate/jfs

Empirical scaling of antisymmetric stratified wakes

S. Gallet[a], P. Meunier[b,*], G.R. Spedding[a]

[a]*Department of Aerospace & Mechanical Engineering, University of Southern California, Los Angeles, CA, USA*
[b]*Institut de Recherche sur les Phénoménes Hors Equilibre, 49, av. Joliot-Curie, F-13384 Marseille, France*

Received 4 October 2005; accepted 14 April 2006
Available online 25 July 2006

Abstract

Initially turbulent wakes of a propelled cylinder at nonzero angles of yaw to the mean flow were measured in the horizontal centerplane plane up to approximately 100 buoyancy times, where vertical velocities are very small. The profiles of mean velocity were found to be antisymmetric throughout their lifetime, with both width and maximum velocity decaying at the same rate as previously studied momentum wakes. The maximum velocity of the profile is proportional to the angle of yaw, but the width is constant. Both the mean flow and fluctuating quantities show that the late wake is self-similar, with scaling laws that are consistent with previous work on propelled and drag wakes.

1. Introduction

In a homogeneous fluid, the late stages of a turbulent bluff-body wake can be described by the theory of a self-preserved wake [see Tennekes and Lumley (1972)]. However, the presence of even a weak stable stratification can significantly modify this picture, imposing an anisotropy that must be accounted for and bringing internal wave motions into the dynamics. This is the case of the wakes of submarines and of mountains or islands, for which the ocean and the atmosphere are stably stratified.

Lin and Pao (1979) showed that the stratification diminishes the vertical velocities and thus prevents the growth of the wake in the vertical direction after a time $Nt \approx 2$ (N is the Brünt Vaisala frequency, $N^2 = (g/\rho_0)(\partial\rho/\partial z)$, where z is the vertical direction, ρ is the density and g is the gravitational acceleration), leading to coherent vortices that are small in the vertical compared with the horizontal direction. Since horizontal growth rates do not increase commensurately, the defect velocity decays more slowly, and can be as high as 10 times larger than in the absence of stratification. Spedding (1997) showed that this stage lasts up to $Nt \approx 50-100$, and that the defect velocity then decays again with the same exponent as in a homogeneous fluid. Most of the late-wake measurements have been obtained for spheres [e.g., Chomaz et al. (1993), Spedding et al. (1996), Spedding (1997)]. The effect of the shape of the bluff body was investigated by Meunier and Spedding (2004), who showed that all bluff-body wakes, regardless of body geometry, could be rescaled with parameters that depended only on the initial momentum flux in the wake. Meunier and Spedding (2006) described the wakes of propelled bodies, finding similarly general scaling behavior for all but a small class of wakes that were almost exactly momentumless. Furthermore, if the wakes were at this (almost singular) point, a third class of antisymmetric velocity profile was found behind a body having a small angle of yaw. This paper presents systematic and

*Corresponding author.
E-mail address: meunier@irphe.univ-mrs.fr (P. Meunier).

0889-9746/$ - see front matter © 2006 Elsevier Ltd. All rights reserved.
doi:10.1016/j.jfluidstructs.2006.04.017

quantitative experimental results of such wakes behind a propelled cylinder at small angle of yaw. The important parameters will be defined and quantified. Decay rates of velocity, turbulent Reynolds number and kinetic energy will be compared with the existing values in the literature.

2. Procedure

2.1. Experimental set-up

A cylinder of diameter $D = 2.7\,\text{cm}$ and length $L = 15.6\,\text{cm}$ is towed through a $2.4 \times 2.4\,\text{m}$ water tank filled to a height $H = 22\,\text{cm}$, as described in detail in Spedding et al. (1996). The tank is filled using the standard two-tank method, mixing between fresh water ($\rho_f = 1.0\,\text{kg/m}^3$) and salt water ($\rho_s = 1.1\,\text{kg/m}^3$), to yield a linear vertical density gradient so that $N = 1.8\,\text{rad/s}$; ρ_f and ρ_s are selected so polystyrene beads of diameter $d = 1\,\text{mm}$ and density $\rho = 1.04965 \pm 0.00005\,\text{kg/m}^3$ rest on an isopycnal at the horizontal centerline of the cylinder. The beads are illuminated using four 500 W floodlights, and a custom digital particle imaging velocimetry method (DPIV) (Fincham and Spedding, 1997) is used to determine velocity fields u, v in the x, y horizontal plane, together with their spatial gradients.

In order to accurately control the yaw angle, and in contrast to previous mounting methods, the cylinder is mounted on a streamlined carriage via a hollow sting (3 mm in diameter). A tight friction fit and set-screw to the carriage post provide convenient submergence and removal of the body, and allow yaw angles to be reliably and precisely set. The propulsion system inside the body consists of a small DC motor powered by a 4.8 V battery through a 4 channel 75 MHz FM RC transmitter and GWS ICS50 micro speed-control.

In the laboratory frame of reference, shown in Fig. 1, the body is towed steadily along the x-axis with speed U_b. An experiment consists of one towing of the body through the length of the tank, and digital image acquisition using a Pulnix TM9701 CCD camera mounted above the tank until $Nt = 300$, with $t = 0$ defined when the body center crosses the center of the $84 \times 61\,\text{cm}$ capture window. The propeller is started just before the body is towed and takes less than 0.5 s to reach the set angular velocity. It is shut off by the transmitter approximately 1–2 cm before the body comes to rest, to prevent a jet from impinging upon the wake at late times. Since the resolution of towing speed is higher than that of the propulsion system, the propeller angular velocity is held constant and experiments are conducted by systematically varying the tow speed until the measured momentum flux in the wake is zero. Once this momentumless speed, denoted U_c is known, experiments are repeated with $\alpha = 2^\circ, 3^\circ, 5^\circ$.

2.2. Flow definitions

Two nondimensional parameters are used to classify flows in a stratified medium: the Reynolds number $\text{Re} \equiv U_b D/\nu$, where ν is the kinematic viscosity, and a Froude number based on cross-section radius, $\text{F} \equiv 2U_b/ND$. Experiments were conducted for $\text{Re} = 6600$, $\text{F} = 10$, for which the inner wake is fully turbulent, and the late-wake centerline flowfield is not affected by the tank boundaries.

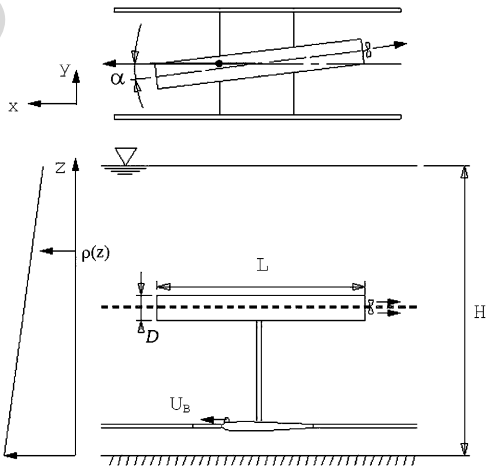

Fig. 1. Top and side views of the carriage and propelled cylinder. The black dotted line at the body centerline represents the bead sheet.

Because the inner wake is turbulent, the flow can be split into nonzero mean and fluctuating parts, $(u, v) = (U, V) + (u', v')$. Mean profiles plotted for each Nt value are obtained by averaging the u velocity components of one image along the x-axis (direction of travel) and are denoted $\langle u \rangle$. In these experiments, this is equivalent to a time average over $Nt = 6$, which is small compared to the total time span of the experiment. Consistent offsets in the profile tails (typically $u_{\text{off}} \leqslant 10\%$ of the peak defect magnitude) were removed by assuming that all averaged horizontal velocity components should be zero far ($y > 15D$), from the wake centerline. These offsets were mainly due to slow back and forth motion of the entire fluid in the tank caused by reflected internal waves. Apart from mean profiles, the cross-fluctuations, $\langle u'v' \rangle$ and the quadratic fluctuations $\langle u'^2 + v'^2 \rangle^{1/2}$ of velocity are used to compare this flow with self-preserved wakes found in the literature. It is useful to define the momentum thickness $D_{\text{mom}} = \text{D}\sqrt{(c_{\text{d}}/2)}$ of the bluff body and its corresponding Froude number $\text{F}_{\text{mom}} \equiv 2\,U_b/ND_{\text{mom}}$ in order to compare these results with the universal laws found in stratified momentum wakes (Meunier and Spedding 2004).

3. Results

3.1. Flow structure

Experimentally, three regimes have been distinguished behind propelled bodies in stratified flows depending on the ratio of tow-speed to the true self-propelled speed. These are shown in Fig. 2 in the form of instantaneous vertical vorticity fields (the body was towed from right to left). The first regime, called the momentum-regime and shown in Fig. 2(a), reveals two layers of opposite-signed vortices, which is equivalent to a mean Gaussian profile of velocity in the wake. Here the tow speed is slightly greater than U_c, creating a net positive mean flow in the wake on the order of 7% of U_c. Meunier and Spedding (2006) successfully re-scaled flow parameters of towed propelled bodies with those of simply towed bodies based on the difference between the tow speed and the momentumless speed U_c, for which the net momentum in the wake would be zero. Wakes of propelled bodies under such conditions are classified as within the momentum-regime.

The second regime, truly momentumless, cannot be re-scaled in the same fashion, as the tow speed is exactly equal to U_c. Attempts to quantify this flow regime in a general way have failed as there appears to be no organizing structure. This can be seen in Fig. 2(b), where opposite-signed vortices lie within a band, but with no apparent order.

The third regime is also momentumless, but involves a slight asymmetry of the body. This regime was discovered when the propelled body had a small angle of yaw. Fig. 2(c) shows the qualitatively different nature of this regime from the previous case with zero angle of yaw. The wake is composed of three layers of alternating opposed-sign vortices, whose pattern reverses for opposite angles of yaw. The organized layers lead to quantifiable mean profiles and fluctuating quantities.

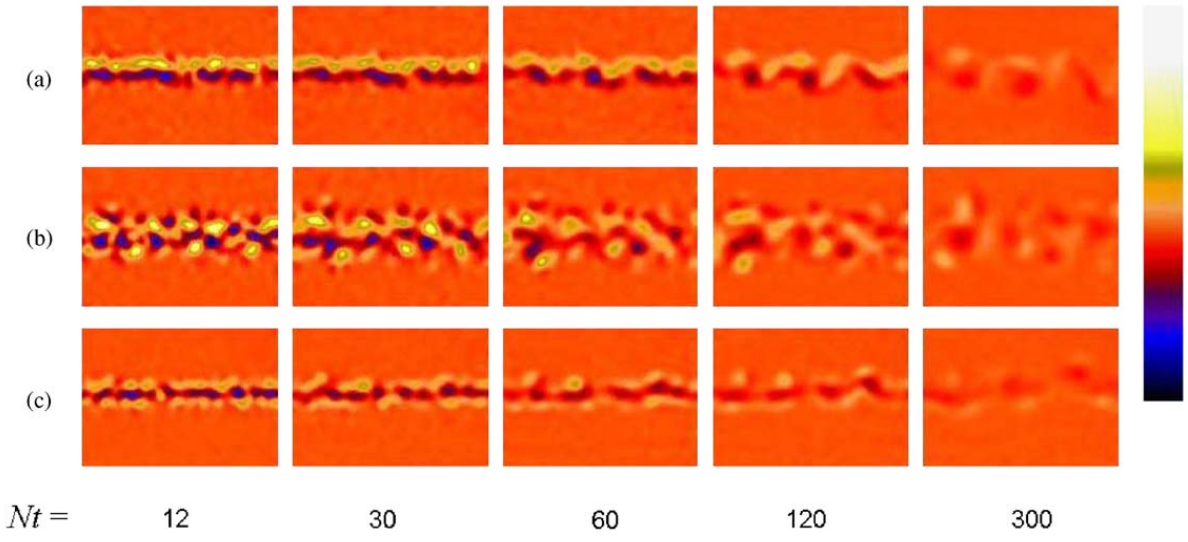

Fig. 2. Vertical in-plane vorticity ω_z revealing three wake structures for towed-propelled bodies: in (a) when the towing speed is different from the momentumless speed, in (b) when they are exactly equal, and in (c) for the same conditions as (b) but with a small angle of yaw. The color bar extremes are scaled at $0.02, 0.04$ and $0.02U_b/D$, respectively.

3.2. Mean flow

Using the Reynolds decomposition defined in Section 2.2, mean profiles can be plotted, for $4 < Nt < 300$, and are shown in Fig. 3. As can be seen in Fig. 3(a), these mean profiles are antisymmetric, and remain so throughout the measurable lifetime of the wake. This is in contrast to profiles of wakes in the momentum-regime, which can be described by Gaussian distributions. For propelled bodies at an angle of yaw, the resultant wake can be pictured as a linear combination of a drag wake with mean negative velocity and a thrust jet of mean positive velocity. As shown in Fig. 3(b), for increasing angles the negative peak (due to the drag) increases, and while the total momentum in the wake is zero for $\alpha = 2^0$, there is a small net momentum at $\alpha = 5^0$. The tow speed was not increased for each angle, even though it would correct for the increase in drag, because it would substantially increase the number of runs to yield one usable experiment. For increasing α, as shown in Fig. 3(b), the defect amplitude also increases though the direct correspondence to α is difficult to ascertain.

The profiles of $\langle U \rangle / U_b$ can be described as odd functions of y/D, whose maximum amplitude is $U_1 = \max(\langle U \rangle) - \min(\langle U \rangle)$ and inner wake width is $L_1 = y_{\max} - y_{\min}$, where $y_{\max}$ is the y/D position of the maximum value of the profile and $y_{\min}$ the position of the minimum.

The evolution of U_1 and L_1 as a function of Nt are plotted in Fig. 4, re-scaled with F to be comparable with previous data in the literature. The re-scaling is needed in the momentum-regime to collapse data with varying F. In Fig. 4(a),

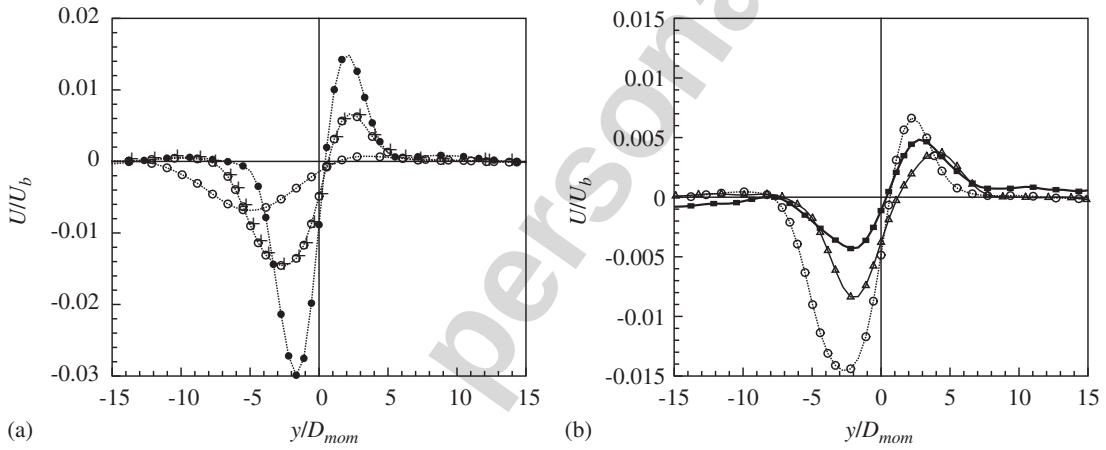

Fig. 3. Profiles of mean velocity. (a) For $\alpha = 5^\circ$: •, at $Nt = 20$; ⊕, $Nt = 100$; ○, $Nt = 300$. (b) At $Nt = 100$: ■, $\alpha = 2^\circ$; △, $\alpha = 3^\circ$; ○, $\alpha = 5^\circ$.

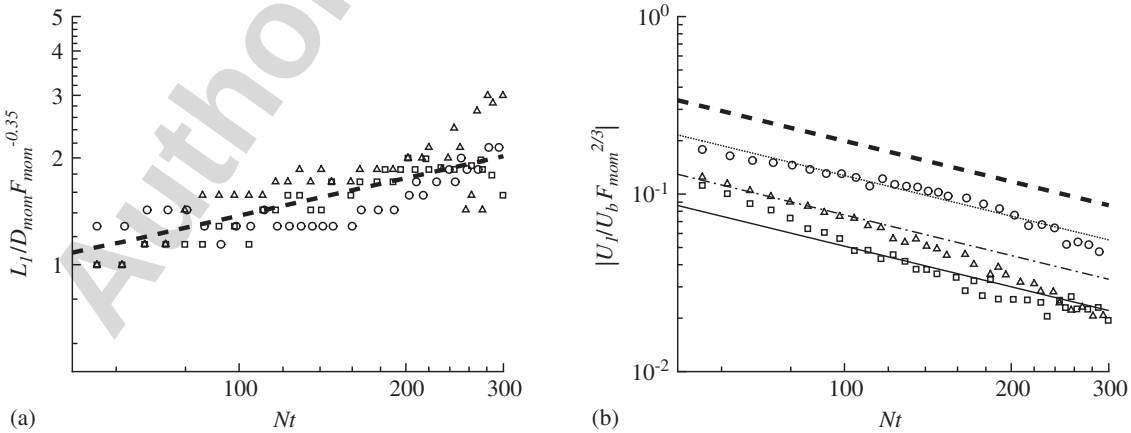

Fig. 4. (a) Wake width and (b) maximum amplitude of the mean velocity profiles for yaw angles $\alpha = 2^\circ(\square), 3^\circ(\triangle), 5^\circ(\circ)$. The thick dashed line represents Eq. (1) in (a) and Eq. (2) in (b) with $C = 6.6$. In (b) Eq. (2) is plotted with $C = \alpha \cdot (0.0055 \pm 0.0005)$: —, $\alpha = 2^\circ$; $- \cdot -$, $\alpha = 3^\circ$; …, $\alpha = 5^\circ$.

L_1 is seen to grow with Nt at a rate similar to the universal decay law for momentum wakes, defined as

$$\frac{L_1}{D_{\mathrm{mom}}}\mathrm{F}^{-0.35} = 0.275(Nt)^{0.35}, \tag{1}$$

where $D_{\mathrm{mom}} = D\sqrt{c_d/2}$ and plotted as a thick dashed line. c_d is the drag coefficient for the body with no stratification and can be looked up in reference texts; its use is appropriate at moderate to high F when the drag determined by the near wake is not strongly influenced by stratification. Here L_1 agrees well with the momentum case (the discrete jumps in L_1 are caused by the finite resolution of the original gridded data, which have not been further interpolated), and no dependence on angle is apparent, which is reasonable at least for small angles.

U_1 however, plotted in Fig. 4(b), shows a clear dependence on α. The decay law for the momentum-regime is shown with a thick dashed line, defined by

$$\frac{U_1}{U_B}\mathrm{F}^{2/3} = C(Nt)^{-0.76} \tag{2}$$

with $C = 6.6$. In the asymmetric regime, this simple model also predicts U_1 if we take $C(\alpha) = \alpha(0.0055 \pm 0.0005)$. This relationship is plotted in Fig. 4(b) for $\alpha = 2^\circ, 3^\circ, 5^\circ$, and agrees quite well with the experimental data in the sense that the *ad hoc* magnitude correction appears good and there are no systematic deviations from the straight lines over the three angles considered. Direct proportionality apparently occurs at small angles, but obviously breaks down theoretically at $\alpha = \pi/2$, and most probably earlier in experiments due to a more complex 3-D flow structure.

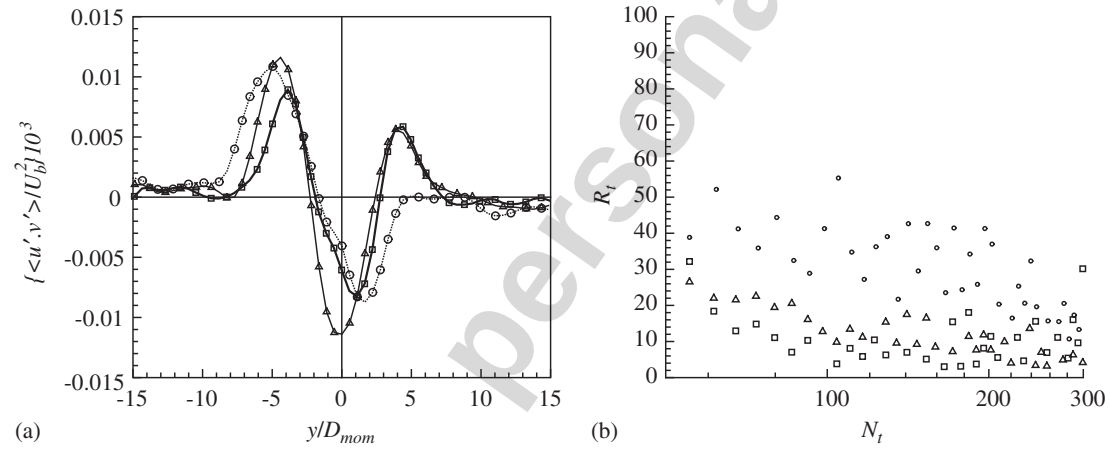

Fig. 5. (a) Profiles of cross-fluctuation velocity for yaw angles $\alpha = 2^\circ(\square), 3^\circ(\triangle), 5^\circ(\circ)$ at $Nt = 100$. (b) The turbulent Reynolds number defined in Eq. (4).

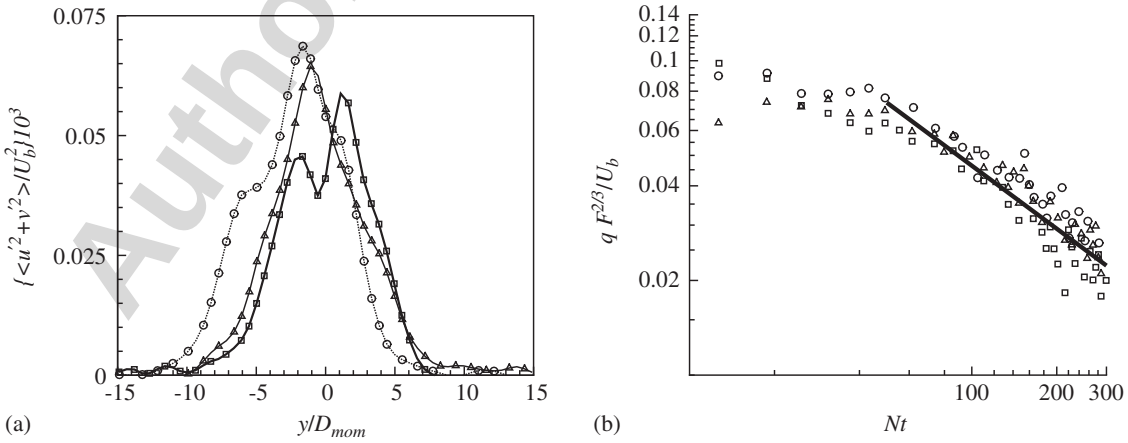

Fig. 6. (a) Mean profiles of turbulent kinetic energy and (b) its re-scaled peak value for yaw angles $\alpha = 2^\circ(\square), 3^\circ(\triangle), 5^\circ(\circ)$, compared to an $Nt^{-2/3}$ power-law decay rate (solid line).

3.3. Fluctuating quantities

In a turbulent flow, the cross-fluctuations of velocity can be related to the mean shear by

$$\langle u'v' \rangle = \nu_T \frac{\partial U}{\partial y}, \tag{3}$$

where ν_T is the turbulent eddy viscosity. The cross-fluctuation profiles are plotted in Fig. 5(a), and do seem proportional to the derivative of the mean profiles plotted in Fig. 3(b). The three peaks of fluctuations align with the three areas of maximum slope of the mean profile, and the signs are consistent. This supports the idea that the antisymmetric wake is also self-preserved, and diffuses by the action of the cross-fluctuations of velocity $\langle u'v' \rangle$, themselves driven by the mean shear $\partial U/\partial y$. This regime, just as the drag or momentum-regimes, may therefore be described under the assumption of a constant eddy viscosity ν_T. One can define a turbulent Reynolds number relating the mean flow magnitude to the cross-fluctuations magnitude,

$$R_t = \frac{|U_1|L_1}{\nu_T} = \frac{U_1^2}{\langle u'v' \rangle_{\max}}, \tag{4}$$

which in turn provides a check for the constant eddy-viscosity assumption. The results in Fig. 5(b), show R_t to be at best weakly dependent on α, though the values are scattered. Overall a constant R_t approximation is reasonable for the full range, and very good after $Nt = 100$. A mean value of the turbulent Reynolds number for $\alpha \leqslant 5^\circ$ lies around $R_t = 25 \pm 20$. For nonpropelled body experiments, Meunier and Spedding (2004) found a similar value of $R_t \simeq 15$, and concurred that it may not be considered constant until after $Nt = 100$.

As noted in Spedding et al. (1996) for the case of a towed sphere, the turbulent kinetic energy in the inner wake $q = \langle u'^2 + v'^2 \rangle_{\max}^{1/2}$, can be expected to scale as

$$\frac{q}{U_b} \mathrm{F}^{2/3} \sim (Nt)^{-2/3} \tag{5}$$

for self-similar evolution. The averaged profiles of quadratic fluctuations are plotted in Fig. 6(a). They are wedge-shaped, with a single peak in the center of the wake. The peak value can be used to compare the decay of the turbulent kinetic energy with the expected power-law decay rate for a self-preserved wake. Both parts of Eq. (5) are plotted in Fig. 6(b), and agree well for $Nt \geqslant 80$.

4. Discussion and conclusions

The wakes of propelled bodies in stratified fluids have previously been quantified both in the momentum and momentumless regimes, for axisymmetric conditions and now with an angle of yaw. At nonzero angles of yaw, the wakes are simpler to predict than for $\alpha = 0$.

The mean velocity profile is antisymmetric and decays stably. It can be described fully by L_1 and U_1 as a function of α. Both the cross-fluctuations of velocity and the kinetic energy show that some theory of self-preserved wakes is applicable, at least for $Nt \geqslant 100$. Since the antisymmetric profile can contain some momentum, the transition from a Gaussian momentum wake to an asymmetric zero-momentum wake is smooth, unlike for $\alpha = 0$ as shown by Meunier and Spedding (2006), though the asymmetric profile is quickly overtaken by the drag away from the zero-momentum point.

This work provides further evidence that wakes of submerged bodies will almost always be different from those discovered for the exactly momentumless case. It is rare that a body will travel at exactly zero degrees angle of attack, unless the specified route is exactly aligned with the mean flow, or unless the mean flow is negligible (and uniform, and steady). Moreover, almost any navigation or turning manoeuvre will put the flow into the small yaw angle regime described here. Thus, the family of robust scaling relationships for initially turbulent bluff-body wakes is expanded by those found in the small yaw angle regime, and they can be considered applicable to most practical situations.

Acknowledgment

The support of ONR Grant no. N00014-04-1-0034 administered by Dr R. Joslin is most gratefully acknowledged.

References

Chomaz, J.M., Bonneton, P., Hopfinger, E.J., 1993. The structure of the near wake of a sphere moving horizontally in a stratified fluid. Journal of Fluid Mechanics 254, 1–21.

Fincham, A.M., Spedding, G.R., 1997. Low-cost high-resolution dpiv for turbulent flows. Experiments in Fluids 23, 449–462.

Lin, J.T., Pao, Y.H., 1979. Wakes in stratified fluids: a review. Annual Review of Fluid Mechanics 11, 317–338.

Meunier, P., Spedding, G.R., 2004. A loss of memory in stratified momentum wakes. Physics of Fluids 16 (2), 298–305.

Meunier, P., Spedding, G.R., 2006. Stratified propelled wakes. Journal of Fluid Mechanics 552, 229–256.

Spedding, G.R., 1997. The evolution of initially turbulent bluff-body wakes at high internal froude number. Journal of Fluid Mechanics 337, 283–301.

Spedding, G.R., Browand, F.K., Fincham, A.M., 1996. Turbulence, similarity scaling and vortex geometry in the wake of a towed sphere in a stably stratified fluid. Journal of Fluid Mechanics 314, 53–103.

Tennekes, H., Lumley, J.L., 1972. A First Course in Turbulence. M.I.T. Press, Cambridge, MA.

Self-preservation in stratified momentum wakes

Patrice Meunier
IRPHÉ, CNRS, Univ. Aix-Marseille, 49 rue F. Joliot-Curie, F-13384 Marseille, France

Peter J. Diamessis
School of Civil and Environmental Engineering, Cornell University, Ithaca, New York 14853

Geoffrey R. Spedding
Department of Aerospace & Mechanical Engineering, University of Southern California, Los Angeles, California 90089-1191

(Received 14 March 2006; accepted 1 September 2006; published online 16 October 2006)

A general model is described for drag wakes in a linearly stratified fluid, based on the self-preservation of the flow. It is assumed that the buoyancy-controlled self-similar wake expands in the horizontal direction due to turbulent diffusion and in the vertical direction due to viscous diffusion. The mean characteristics of the wake (height, width and velocity defect) are analytically derived and show good agreement with existing data from experimental and numerical results. Moreover, the three regimes previously found in the literature that characterize different dynamical phases of the wake evolution are recovered, and two new regimes are found. The model allows for prediction of characteristic length and velocity scales at the high Reynolds numbers of large-scale applications of geophysical and naval origin. © *2006 American Institute of Physics*.
[DOI: 10.1063/1.2361294]

I. INTRODUCTION

Research on stratified wakes has both meteorological (flow over islands, mountains or sea-mounts) and naval applications (submerged bodies). In each case, the Reynolds number ($\mathrm{Re}=U_B D/\nu$, for an object of diameter D in a uniform freestream U_B) is several orders of magnitude higher than obtained in both laboratory experiments and numerical simulations. By contrast, the appropriate internal Froude number ($\mathrm{F}=2U_B/ND$, for a fluid of buoyancy frequency $N=\sqrt{-(g/\rho)(\partial\rho/\partial z)}$, which ranges from 10^{-1} to 10^3, can be readily obtained experimentally and numerically. At sufficiently large values of Reynolds number and Froude number, the initial (near) wake is fully turbulent in all three directions. Chomaz *et al.*[1] found the necessary criterion on F to be $\mathrm{F}\geqslant 4.5$, and a minimum value of $\mathrm{F}\simeq 4$ was shown in scaling arguments[2] and later in experiments,[3] where F and Re were varied independently. In Ref. 4, it was demonstrated that all wakes for $4\leqslant \mathrm{F}\leqslant 240$ have similar scaling behavior, provided Re is also sufficiently large (an approximate minimum value of 5×10^3 was suggested). Physically, the reason for the similar scaling is that since local wake velocities decrease, while local length scales increase, then a local Froude number based on these scales will decrease so that it becomes of order 1, and thus the late stages of even a weakly stratified wake are eventually dominated by buoyancy effects.

The observations were consistent with previous experiments, simulations and analysis of decaying stratified turbulence, where buoyancy forces start to act at $Nt\approx 1$ when the local dynamics experience the onset of buoyancy control (see Riley and Lelong[5] for a review). In experiments on self-propelled slender bodies, Lin and Pao[6] showed that buoyancy begins to affect the flow at $Nt=2$, suspending the expansion of the wake in the vertical direction. This was followed by the emergence of large coherent structures as shown by dye pictures, which also showed that their aspect ratio (horizontal length scale compared with vertical extent) was large. The origin of these structures was later traced[7] to Kelvin-Helmholtz free shear-layer instabilities generated at the edge of the near wake and the gradual suppression of vertical motions by the density gradient ensures that only these so-called pancake vortices persist into the late wake.

Reference 4 found that two different regimes could be distinguished in the velocity field of the intermediate and late wakes. Initially, decay rates of horizontal mean velocity were found to be surprisingly low, with $U\sim(Nt)^{-0.25}$ (instances where the defect velocity even increases have been reported[8]). There is then a transition to a steeper decay rate with exponents of approximately −0.76, with the transition time apparently constant in buoyancy time scales of $Nt\approx 50$. (While this transition time appeared to be independent of F for the towed sphere experiments, a survey of the literature suggested large variation from $Nt=10$ to $Nt=180$ in the transition time between different laboratory or numerical experiments.) The subsequent steeper decay rate was maintained for all measurable times up to $Nt\approx 2000$. The preceding intermediate regime is one where vertical velocities gradually become small, associated with radiation of internal waves from the wake to the ambient, and, it was conjectured, with conversion of potential to kinetic energy close to the wake center. This adjustment period was termed the nonequilibrium regime (NEQ). The subsequent, late wake is characterized by the relative insignificance of vertical velocities and largely horizontal motions account for almost all the remaining kinetic energy in the flow. The flow field however, is not two-dimensional (2D) (and its decay rate is not the

same as for a two-dimensional wake, which would have a −0.5 exponent) because there is significant variability in the vertical, and the horizontal vorticity marking the shearing between neighboring layers is stronger than the vertical vorticity.[9] This late wake regime was named the quasi-2D, or Q2D regime.

During both NEQ and Q2D, the wake width grows as $Nt^{1/3}$ (or $x/D^{1/3}$), which is the same as would occur in a fully three-dimensional, unstratified turbulent wake. Since growth rates of vertical scales are very slow during NEQ, and since the stratified wake does not grow laterally faster than its three-dimensional (3D) counterpart, momentum conservation requires that NEQ is associated with the observed low decay rates. Finally, it was argued in Ref. 4 that the very early wake at moderate to high F would most likely evolve with buoyancy forces playing little part, and thus a sequence of 3D-NEQ-Q2D was identified as characterizing stratified wakes.

The basic phenomenology of the NEQ and Q2D regimes has been replicated also in numerical simulations,[10,11] but agreement on vertical length scales has been more elusive. Chomaz *et al.*[12] found that the wake height increases very rapidly in the late wake, and a transition from almost zero growth to rapid growth (but different growth rates than in Ref. 12) of vertical length scales was reported in further experiments by Spedding.[9] Numerical simulations appeared to share similar features,[10,11] but the setting of the initial vertical length scales according to F was never resolved as the simulations would typically be run for only one finite value of F. This vertical growth of the wake is not yet well understood and precise measurements have been difficult to obtain, both experimentally and numerically.

The experimental results were obtained for the particular case of the wake of a sphere, but were successfully extended to the general case of other bluff bodies,[13] by considering the momentum thickness as the proper length scale rather than the body diameter. For an axisymmetric bluff body, the momentum thickness is defined as $D_m = D\sqrt{c_D/2}$, where c_D is the drag coefficient for the bluff body in an unstratified fluid. In fact, the very same wake scalings could be extended to almost all wakes generated by propelled bluff bodies[14] (including all those of practical interest), if the momentum thickness is defined as $D_m = D\sqrt{c_D/2}\sqrt{1-U_C^2/U_B^2}$, where U_C is the particular velocity of the self-propelled bluff body for which the wake becomes momentumless. The relevant nondimensional parameters become a momentum Reynolds number $\mathrm{Re}_m = U_B D_m/\nu$ and a momentum Froude number $\mathrm{F}_m = 2U_B/ND_m$.

The empirical scaling laws describing the velocity defect and wake width as developed in Refs. 3, 4, 13, and 14 apply to any bluff body wake or jet in a uniform, stable density gradient. However, they remain empirical findings, linked by incomplete arguments and a coherent theoretical framework has not been proposed. Moreover, compared with practical applications where Reynolds numbers are usually in the range of 10^6–10^8, the limited range of Re of the experiments upon which they are based makes the extrapolation of these scaling arguments to higher Re somewhat speculative. The laboratory experiments show no significant Re dependence over $\mathrm{Re} \in [5\times10^3, 2.8\times10^4]$ and the largest Re in numerical experiment was 10^5, indicating that the results might at least be only weakly Re dependent. On the other hand, high-Re, high-resolution, numerical simulations of a simple stratified flow geometry[15] have indicated that as Re increases, more small-scale instabilities of the vertical shear layers develop, becoming a continuous source of small-scale turbulence, and raising the idea that at sufficiently high Re, the large-scale coherent structures seen in laboratory experiment may never develop, or survive. However in the range of $\mathrm{Re}_l \in [800, 6400]$, where l is a numerically imposed initial length scale of the Taylor-Green vortices, the large scales were only weakly dependent on Re_l, a finding that is consistent with the increased fine structure of the higher Re wake simulations of Dommermuth *et al.*,[11] but which still produced large-scale structures in the late wake.

In this paper, some scaling relations are derived, based on the evolution of self-similar solutions of reduced equations of motion for stratified momentum wakes with high Reynolds number and high Froude number. Analytical results will be derived for the horizontal and vertical length scales, and for the mean and turbulence profiles. The agreement with existing data from laboratory and numerical experiment will be shown to be good, and the scaling behavior for high Reynolds number can be clearly shown.

II. A SELF-PRESERVING THEORY

A. General equations

We will suppose that the fluid is linearly stratified with a constant buoyancy frequency N and a density ρ_0 at the bluff body's height, and write the Navier-Stokes equations in the Boussinesq approximation

$$\frac{\partial \mathbf{u}}{\partial t} + (\mathbf{u}\cdot\nabla)\mathbf{u} = \frac{-\nabla p}{\rho_0} + \nu\Delta\mathbf{u} + \frac{\rho}{\rho_0}\mathbf{g} \tag{1}$$

together with the incompressibility condition

$$\nabla\mathbf{u} = 0 \tag{2}$$

and the equation for the evolution of the density

$$\frac{\partial \rho}{\partial t} + \mathbf{u}\cdot\nabla\rho = \kappa\Delta\rho. \tag{3}$$

Since the flow is stationary in the frame of reference moving with the bluff body, $U = U(y,z)$, the velocity can be decomposed as a temporal mean and a fluctuating part: $\mathbf{u} = U + \mathbf{u}'$. The mean velocity is equal to the bluff body velocity U_B in the far field, and the wake has a defect velocity of the order of U_0, as indicated schematically in Fig. 1. We then follow the standard analysis for the turbulent wake in a nonstratified flow, found for example in Tennekes and Lumley.[16] By averaging the streamwise component of the momentum equation (1), one arrives at

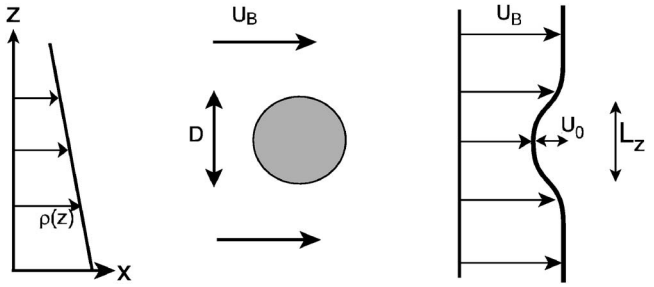

FIG. 1. Schematic of the wake created by a bluff body of diameter D translated horizontally at U_B in a linearly stratified fluid.

$$U\frac{\partial U}{\partial x}+V\frac{\partial U}{\partial y}+W\frac{\partial U}{\partial z}+\frac{\partial\langle u'^2\rangle}{\partial x}+\frac{\partial\langle u'v'\rangle}{\partial y}+\frac{\partial\langle u'w'\rangle}{\partial z}$$
$$=-\frac{1}{\rho_0}\frac{\partial P}{\partial x}+\nu\Delta U. \tag{4}$$

Note that on this component of velocity, stratification effects are in fact absent, except insofar as they would lead to nonzero mean values of $\langle u'w'\rangle$. This is a consequence of assuming w to be small at late times, and thus retaining only the streamwise momentum components. Now, following Ref. 16, we assume that the flow is nearly parallel, so the length scale l in the y and z directions is smaller than the length scale L in the x direction. Since the focus is on late wake evolution, we may also assume that the velocity amplitude U_0 is much smaller than the tow speed U_B, which is valid at least far from the bluff body. The second, third, and fourth terms in Eq. (4) can therefore be neglected since they are of order U_0^2/L, which is U_0/U_B smaller than the first term. The pressure term can be shown to be of the order of $\partial\langle v^2\rangle/\partial x$ by inspection of the leading order terms in the cross-stream momentum equation, which are again negligible with respect to the first term. At high Reynolds numbers, the viscous terms could be entirely neglected at early stages, but will be retained because they will reappear later, as the local Reynolds number decreases in time. Here though, the term $\partial^2U/\partial x^2$ is small compared with $\partial^2U/\partial y^2$ and may be omitted. Finally, the mean velocity U can be replaced by U_B in the first term, which leads to a simple form for the streamwise momentum equation

$$U_B\frac{\partial U}{\partial x}=-\frac{\partial\langle u'v'\rangle}{\partial y}-\frac{\partial\langle u'w'\rangle}{\partial z}+\nu\left(\frac{\partial^2U}{\partial y^2}+\frac{\partial^2U}{\partial z^2}\right). \tag{5}$$

It has been shown experimentally that mean profiles are close to Gaussian in both nonstratified wakes[16] and also in stratified wakes,[3,4] and an example of the latter is shown in Fig. 2(a) from Ref. 17. Thus, we may search for Gaussian solutions to Eq. (5), of the form

$$U=U_B-U_0\exp\left(-\frac{y^2}{2L_y^2}-\frac{z^2}{2L_z^2}\right), \tag{6}$$

where the velocity defect U_0, the wake width L_y and height L_z are functions of x only. Other solutions might be found,[18] but this Gaussian solution is convenient since it is the simplest self-similar solution for a momentum wake.

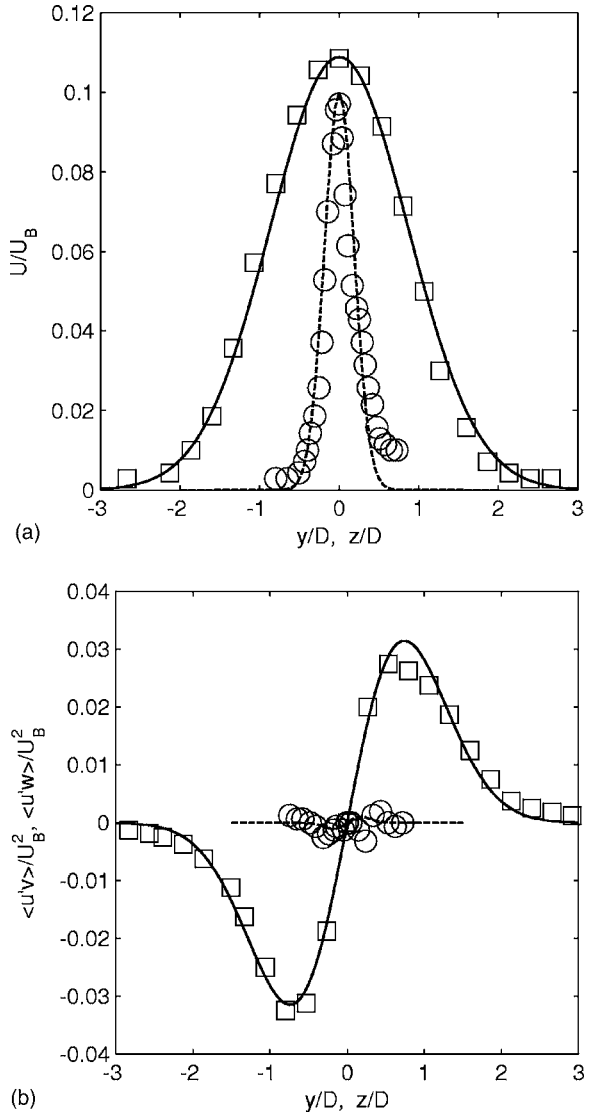

FIG. 2. Profile of (a) the mean velocity U and (b) the Reynolds stresses $\langle u'v'\rangle$ and $\langle u'w'\rangle$ for a sphere wake at $Nt=20$ for F=4 and $\mathrm{Re}=5\times10^3$. The data come from experimental results by Ref. 17 in the horizontal (□) and vertical centerplane (○). The solid lines show a Gaussian profile for the mean velocity and the derivative of a Gaussian profile for the Reynolds stresses.

Under the Boussinesq approximation, the momentum flux $J=\int\int\rho U_B(U-U_B)dydz$ is equal to $\rho_0\int\int U_B(U-U_B)dydz$. By integrating (5) on a transverse section, the mean momentum flux can be shown to be independent of the position x and equal to the drag force $\mathrm{F}_D=c_D\rho_0U_B^2\pi D^2/8$, where c_D is the body drag coefficient. Thus, by defining the momentum thickness as $D_m=D\sqrt{c_D/2}$, the integration of (6) leads to a relation between U_0, L_y and L_z:

$$U_0L_yL_z=U_BD_m^2/8. \tag{7}$$

B. Initial three-dimensional regime

At high Froude numbers, the stratification is negligible in the early stages and the flow may be expected to be three-dimensional and the mean velocity to be axisymmetric. It is common practice to suppose that the Reynolds stress is pro-

portional to the mean shear ($\langle u'v' \rangle = -\nu_3 \partial U/\partial y$), with an eddy viscosity ν_3 independent of y and z in the 3D regime. Partial experimental support for this notion has been found in[13,14] for stratified wakes. Based on the mixing length model, or based on dimensional grounds, the eddy viscosity should be proportional to $U_0 L_y$, which defines a turbulent Reynolds number $\mathrm{R}_3 = U_0 L_y/\nu_3$ for the 3D regime. Bevilaqua and Lykoudis[19] found

$$\mathrm{R}_3 = 4$$

in the case of the sphere, for the same definitions of the mean profile, and this value will be used in the following.

We will also assume that the Reynolds number is sufficiently high to neglect the viscous terms in the 3D stage (it will be shown to be true when $\mathrm{F} \ll \mathrm{Re}^3$). The momentum equation thus becomes a standard diffusion equation,

$$U_B \frac{\partial U}{\partial x} = \frac{U_0 L_y}{\mathrm{R}_3} \frac{\partial^2 U}{\partial y^2} + \frac{U_0 L_z}{\mathrm{R}_3} \frac{\partial^2 U}{\partial z^2}, \tag{8}$$

except that the diffusion coefficient $U_0 L_y/\mathrm{R}_3$ is now x dependent. Imposing a Gaussian form of the mean profile (6) into (8), leads to

$$\frac{\dot{U}_0}{U_0} + \frac{y^2}{L_y^2}\frac{\dot{L}_y}{L_y} + \frac{z^2}{L_z^2}\frac{\dot{L}_z}{L_z} = \frac{U_0}{\mathrm{R}_3 L_y U_B}\left(\frac{y^2}{L_y^2} - 1\right) + \frac{U_0}{\mathrm{R}_3 L_z U_B}\left(\frac{z^2}{L_z^2} - 1\right), \tag{9}$$

where the dot denotes the derivative with respect to the downstream distance ($\dot{U}_0 = dU_0/dx$).

The Gaussian form introduced in (6) is a solution of the Navier-Stokes equations if and only if Eq. (9) is valid for any y and z. Since this equation only contains three types of terms (terms in y^2, terms in z^2, and terms independent of y and z), (6) is a solution if and only if their three coefficients vanish, which leads to three independent equations:

$$\dot{L}_y = \frac{U_0}{\mathrm{R}_3 U_B}, \tag{10}$$

$$\dot{L}_z = \frac{U_0}{\mathrm{R}_3 U_B}, \tag{11}$$

$$\frac{U_0}{U_0} = -\frac{U_0}{\mathrm{R}_3 L_y U_B} - \frac{U_0}{\mathrm{R}_3 L_z U_B}. \tag{12}$$

Since there are three variables U_0, L_y, and L_z, a Gaussian solution can exist. By summing (10)/L_y+(11)/L_z+(12), we recover that $U_0 L_y L_z$ is constant, as was found using the momentum flux equation (7). Introducing this condition (7) into (10) and (11), we also recover the solution given by Tennekes and Lumley:[16]

$$L_y = L_z = D_m \left(\frac{3x}{8\mathrm{R}_3 D_m}\right)^{1/3}, \tag{13}$$

$$U_0 = \frac{U_B}{8}\left(\frac{3x}{8\mathrm{R}_3 D_m}\right)^{-2/3}. \tag{14}$$

This solution is valid when the local Froude number (defined as U_0/NL_y) is larger than one, which is met only close to the bluff body. Indeed, this local Froude number decreases as $1/x$ and reaches unity for $x_1/D_m = \mathrm{R}_3\mathrm{F}_m/6 \approx 0.66\mathrm{F}_m$. This transition distance is in good agreement with previous experimental results,[4,6] where it was shown, or inferred, that the wake is 3D until $Nt \approx 2$; i.e., until $x_1/D_m = \mathrm{F}_m$ in our units. We may also note that since the form of the reduced equations (5) and the presumed existence of self-similar solutions (6) requires that x/D is large, then the simultaneous requirement of large x/D and large local F limits this model system to flows with large initial F. Only then can a self-similar flow be imagined before the transition distance, x_1. In fact, the exact value of this transition distance very weakly influences the late stages and we will assume that the transition occurs for $x_1/D_m = \mathrm{F}_m$. The vertical width of the wake at this point is thus

$$L_v = D_m \left(\frac{3\mathrm{F}_m}{8\mathrm{R}_3}\right)^{1/3}. \tag{15}$$

This classical solution, with no stratification effects, will now be extended into the stratified regime, which occurs for x larger than x_1.

C. Stratified regime

In the late wake, vertical velocity fluctuations eventually subside as one component of the wake disturbance propagates away in the form of internal waves,[17] leaving residual motions whose time evolution is much slower.[20,21] Consequently, the vertical Reynolds stress $\langle u'w' \rangle$ becomes much smaller than the horizontal Reynolds stress $\langle u'v' \rangle$ in the far-wake, strongly stratified regime. The experimental results of Fig. 2(b) compare these two terms at $Nt = 44$ and show that the first term is about an order of magnitude smaller than the second. As a convenient simplifying assumption, valid at least for the far wake, we will therefore neglect the vertical Reynolds stress in the averaged momentum equation (5). However, we should note how neglecting $\langle u'w' \rangle$ removes much physics from this intermediate regime. All contributions from internal wave motions which lead to significant peaks in experimental measurements of $\langle u'w' \rangle$ as late as $Nt = 15$ (see Ref. 17) are omitted, as are any production terms where energy is drawn to the mean flow from the turbulent motions. Anisotropy of the dissipation rate tensor and of the velocity and vorticity energy balance has been noted and discussed in simulations of stratified turbulence[22,23] and specifically for direct numerical simulations of stratified wakes.[10,11] The analysis that follows must be considered one where such intermediate dynamics are ignored, valid at the latter stages of the wake evolution only when $w \approx 0$ and $\langle u'w' \rangle \ll \langle u'v' \rangle$. It will prove instructive to see how much (or how little) of the mean flow dynamics can be found with this strong simplification.

We may recall that one of the purposes of this model is to find simplified expressions that both respect current results from laboratory and computational work, and at the same time give explicit predictions on how decaying turbulence scales at the much higher Reynolds numbers characteristic of

ocean conditions. Higher Reynolds number simulations are just now becoming available, and some (see Ref. 15) raise the question as to whether the pancake vortices may be unstable with respect to the mean shear. [See also Fig. 5(c) of Waite and Bartello[24] for small-scale instabilities at moderate stratifications.] These instabilities (Kelvin-Helmholtz) could lead to nonzero vertical Reynolds stresses, and if this is shown to be the case then the strong assumption of $\langle u'w' \rangle \ll \langle u'v' \rangle$ will need to be modified.

The turbulent motion in the horizontal direction will continue to be modeled as a turbulent diffusion and so we will continue to assume that the horizontal Reynolds stress is proportional to the mean shear ($\langle u'v' \rangle = \nu_2 \partial U/\partial y$), consistent with available experimental evidence [see Fig. 2(b)]. The eddy viscosity is therefore now characterized by a two-dimensional Reynolds number ($\mathrm{R}_2 = U_0 L_y/\nu_2$). It is two-dimensional because the suppression of vertical velocities by the stratification at late times ($Nt \geqslant 40$, for example) has allowed us to assume that $\langle u'w' \rangle \ll \langle u'v' \rangle$. This flow regime is denoted "BC" for buoyancy-controlled, where the effect of the stratification is supposed to be sufficiently strong that the averaged equations of motion in a horizontal plane have no explicit buoyancy terms in them. Note that by neglecting the buoyancy terms entirely, this approach differs from the usual scaling expansion where $\mathrm{F} \ll 1$ (see, e.g., Refs. 20, 25, and 26).

In late wakes of towed bluff bodies in stratified fluids, R_2 was found to be close to 15, regardless of initial conditions (within 30%),[13] so this numerical value is retained in the following. By neglecting the vertical Reynolds stress while retaining the horizontal Reynolds stress in (5), we reach again a standard diffusion equation for the buoyancy-controlled flow:

$$U_B \frac{\partial U}{\partial x} = \left(\frac{U_0 L_y}{\mathrm{R}_2} + \nu \right) \frac{\partial^2 U}{\partial y^2} + \nu \frac{\partial^2 U}{\partial z^2}. \tag{16}$$

As in the 3D regime, a Gaussian solution is introduced (6) into (16), which leads to an equation with only terms in y^2, terms in z^2 and terms independent of y and z. The Gaussian form (6) is thus a solution if and only if the three coefficients of these terms vanish, corresponding to the three following equations:

$$L_y = \frac{U_0}{\mathrm{R}_2 U_B} + \frac{\nu}{U_B L_y}, \tag{17}$$

$$L_z = \frac{\nu}{U_B L_z}, \tag{18}$$

$$\frac{U_0}{U_0} = -\frac{U_0}{\mathrm{R}_2 L_y U_B} - \frac{\nu}{U_B L_y^2} - \frac{\nu}{U_B L_z^2}. \tag{19}$$

As before, the conservation of the momentum flux is recovered (7) by summing (10)/L_y+(11)/L_z+(12). The equation for the vertical wake width (18) is characteristic of a laminar diffusion and can be integrated by setting initial conditions $L_z = L_v$ at $x/D_m = \mathrm{F}_m$ to arrive at

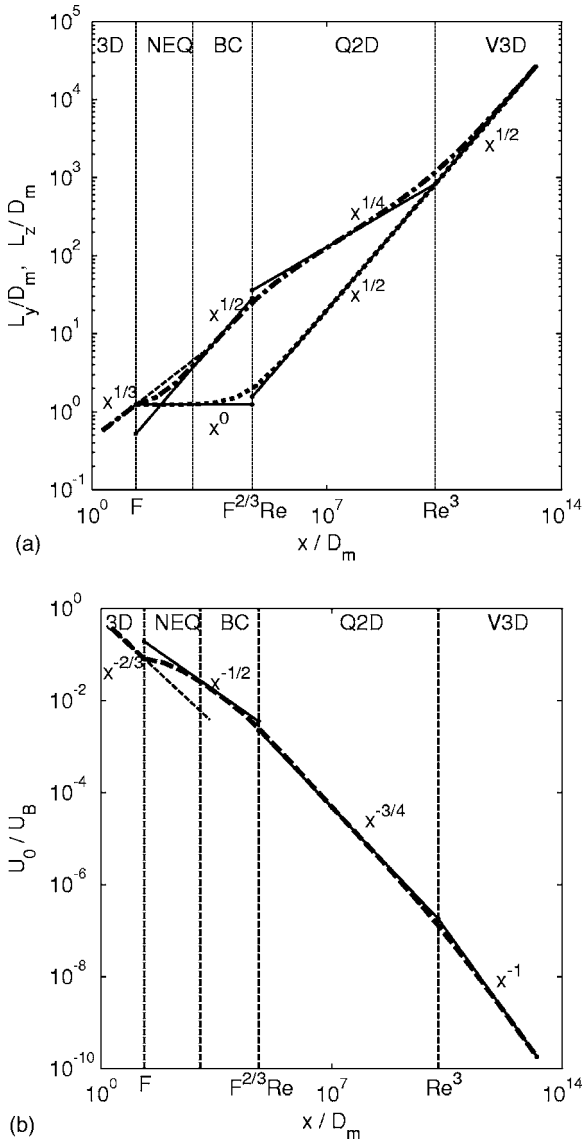

FIG. 3. Evolution of (a) the wake height L_z (dotted line) and wake width L_y (dash-dotted line), and of (b) the velocity defect U_0, given by the model; see Eqs. (20), (22), and (7), respectively. The thin solid lines correspond to the asymptotic predictions for each stage. The thin dashed line corresponds to the standard theory for a homogeneous fluid (13) and (14). $\mathrm{F}_m = 20$ and $\mathrm{Re}_m = 50 \times 10^3$.

$$L_z = \sqrt{L_v^2 + \frac{2D_m^2}{\mathrm{Re}_m}(x/D_m - \mathrm{F}_m)}. \tag{20}$$

This solution is plotted in Fig. 3(a) as a dotted line for $x/D_m > \mathrm{F}_m$, together with the nonstratified solution (13) for $x/D_m < \mathrm{F}_m$. For small x/D, $L_z \approx L_v$ in Eq. (20) and vertical growth is at first negligible. The second term eventually becomes larger than L_v^2 (i.e., at sufficiently large x/D), and when these two terms in the square root of Eq. (20) are of equal magnitude, a second transition point can be identified at a downstream distance of the order of the Reynolds number:

$$x_{\mathrm{II}}/D_m = \frac{\mathrm{Re}_m}{2}\left(\frac{3\mathrm{F}_m}{8\mathrm{R}_3} \right)^{2/3}. \tag{21}$$

The wake height then increases as $\sqrt{x}$ due to viscous diffusion as the wake enters the quasi-2D regime (Q2D). It can be

noted that for higher Reynolds numbers, the NEQ and buoyancy-controlled (BC) regimes will last longer. Since the NEQ regime in particular is associated with quite rich dynamics and complex interactions between internal waves and turbulence, the implication is that at full scale, these complex fields will assume even more importance in turbulence evolution in a stratified ambient. The possible consequences in geophysical and naval applications will be discussed in the conclusion.

To calculate the horizontal wake width, we introduce (7) into (17), which leads to

$$L_y \dot{L}_y = \frac{D_m^2}{8 L_z \mathrm{R}_2} + \frac{\nu}{U_B}.$$

This can be integrated by introducing the expression of the vertical wake width (20), with initial conditions $L_y = L_v$ at $x/D_m = \mathrm{F}_m$:

$$L_y = \left\{ L_v^2 + \frac{D_m \mathrm{Re}_m}{4\mathrm{R}_2} \left[\sqrt{L_v^2 + \frac{2D_m^2}{\mathrm{Re}_m}\left(\frac{x}{D_m} - \mathrm{F}_m\right)} - L_v \right] + \frac{2D_m^2}{\mathrm{Re}_m}\left(\frac{x}{D_m} - \mathrm{F}_m\right) \right\}^{1/2}. \quad (22)$$

The solution is plotted in Fig. 3(a) as a dash-dotted line. In the BC regime ($x_\mathrm{I} < x < x_\mathrm{II}$), the horizontal wake width increases asymptotically (when $\mathrm{F}_m \ll x/D_m \ll \mathrm{Re}_m$) as $\sqrt{x/L_v \mathrm{R}_2 D_m/2}$, with the same power law that was found theoretically for a two-dimensional nonstratified wake.[16] This regime is entered only after passing through the NEQ phase, which has been discovered experimentally.[4,8] It appears here not as a regime defined explicitly, but as a transient between 3D and BC stages (note however, that this is simply a consequence of modeling decisions made initially). This transient stage lasts until $x/D_m = 50\mathrm{F}_m$, independent of the Reynolds number. The BC regime ends at x_II defined previously, giving rise to the quasi-2D regime (Q2D), for which the wake width increases more slowly as $x^{1/4}$: $L_y \sim (\mathrm{Re}_m x/2D_m)^{1/4} D_m/\sqrt{2\mathrm{R}_2}$. This approximation can be obtained by a Taylor expansion of (22) assuming $x_\mathrm{I} \ll x_\mathrm{II} \ll x$. Finally, at very late stages, a new regime appears, which we denote the viscous 3D regime (V3D), since now the wake width also increases by viscous diffusion as $\sqrt{2\nu x/U_B}$. This regime starts for downstream distances larger than x_III, defined as

$$x_\mathrm{III}/D_m = \frac{\mathrm{Re}_m^3}{32\mathrm{R}_2^2}, \quad (23)$$

which is obtained when the second and third terms inside the square root of Eq. (22) are equal; i.e., when turbulent diffusion in the horizontal is accompanied by equal or greater molecular diffusion. The flow is expected to be laminar and axisymmetric, since the horizontal and vertical wake widths become equal again. It was assumed in the model that the stratified effects would occur before the viscous effects, which is valid if $x_\mathrm{I} \ll x_\mathrm{III}$; i.e., when $\mathrm{F} \ll \mathrm{Re}^3$, which is easily met even for moderate Reynolds numbers.

Finally, the theory gives a prediction for the velocity defect U_0, by introducing (20) and (22) into (7):

$$U_0 = \frac{U_B}{8}\left[\frac{L_v^2}{D_m^2} + \frac{2}{\mathrm{Re}_m}\left(\frac{x}{D_\mathrm{m}} - \mathrm{F}_m\right)\right]^{-1/2} \times \left\{ \frac{L_v^2}{D_m^2} + \frac{\mathrm{Re}_m}{4\mathrm{R}_2}\left[\sqrt{\frac{L_v^2}{D_m^2} + \frac{2}{\mathrm{Re}_m}\left(\frac{x}{D_\mathrm{m}} - \mathrm{F}_m\right)} - L_v \right] + \frac{2}{\mathrm{Re}_m}\left(\frac{x}{D_\mathrm{m}} - \mathrm{F}_m\right) \right\}^{-1/2}. \quad (24)$$

This solution is plotted in Fig. 3(b). In the BC stage, the velocity defect decreases as $U_B D_m \sqrt{\mathrm{R}_2/x L_v}/4$. This state is reached after a transient (at least in this framework) stage (the NEQ regime) in which the velocity decreases very slowly. The BC regime is followed by the Q2D regime, in which the velocity defect scales as $x^{-3/4}$: $U_0 \sim \sqrt{\mathrm{R}_2}(2\mathrm{Re}_m)^{1/4}(x/D_m)^{-3/4} U_B/8$. This regime ends at x_III/D_m, and the wake then enters the viscous 3D regime (V3D), in which the velocity defect decreases even faster: $U_0 \sim (U_B D_m)/(16\mathrm{Re}_m x)$. This regime has never been observed experimentally as it occurs for very far downstream distances.

The theory outlined above gives a universal prediction for wake width, height and velocity defect in a stratified wake given by (22), (20), and (24). The model recovers the approximate scaling behavior of the experimentally determined 3D-NEQ-Q2D progression from fully three-dimensional to quasi-two-dimensional (strongly stratified) flow. It also predicts a Reynolds number dependence in transition lengths between these regimes, and in particular, the NEQ regime extends into a strongly buoyancy-controlled (BC) regime, where the dominating influence of the stratification is to constrain the flow to evolve in two-dimensional layers, when the stratification then, paradoxically, has no direct influence. At the end of the Q2D regime there appears a viscous 3D regime (V3D), in which the wake becomes laminar and grows in all directions by diffusion only. Neither the BC nor the V3D regimes has been observed yet, because experiment Reynolds numbers and observation times have not been large enough. The model predictions can now be compared with laboratory and numerical experiment for specific values of the Reynolds and Froude number.

III. COMPARISON WITH EXPERIMENT

A. Variations with the downstream distance

The mean characteristics of the wake predicted by the model were plotted in Fig. 3 at a high Reynolds number, and for a large range of downstream distances. This was designed to define clearly the different regimes and to show their asymptotic behaviors. We will now focus on a common Froude number and Reynolds number pair encountered in the literature, to compare the model to data from both laboratory and numerical experiment. A momentum Froude number of 8.89, and a momentum Reynolds number of 2250 correspond to F=4 and Re=5000 for the canonical towed-sphere example, allowing comparisons with experimental results from three different facilities[4,8,12] and with numerical simulations that used three different methods.[10,11,27]

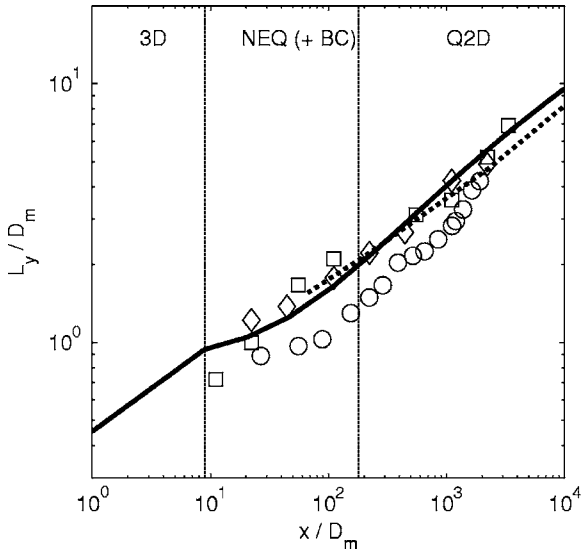

FIG. 4. Time evolution of the wake width L_y for a sphere at $F_m=8.9$ and $Re_m=2.25\times10^3$. The model predictions (solid line) are compared with the experimental results from Ref. 4 (dotted line). Numerical simulations (open symbols) from Ref. 11 (◇) for $F_m=8.9$, $Re_m=4.5\times10^3$, from Ref. 10 (□) for $F_m=22.2$, $Re_m=4.5\times10^3$ and from Ref. 27 (○) for $F_m=8.9$, $Re_m=2.25\times10^3$ are also shown. The uncertainties in the experimental results (Ref. 4) is of the order of 25%.

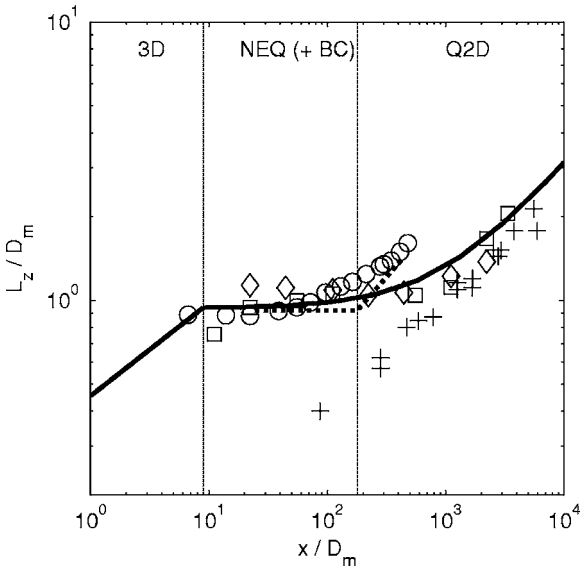

FIG. 5. Temporal evolution of the wake height L_z for $F_m=8.9$ and $Re_m=2.25\times10^3$. Same caption as in Fig. 4. Experimental results from Ref. 12 for $F_m\approx8.9$ and $Re_m\approx2.25\times10^3$ are also shown by + symbols. The uncertainties in the experimental results (Ref. 4) are of the order of 25%.

First, we compare the horizontal wake width L_y in Fig. 4. All experimental and numerical data fall on the model within 30%. The model is thus seemingly in good agreement with the data, even though it does not contain any fitting parameter. Note, however, that the experimental growth rates (over $4\leqslant F\leqslant240$ and $4.7\leqslant Re\leqslant10.6\times10^4$) have a constant power law exponent of 0.35 ± 0.03, which is different from both the early (NEQ/BC: $x^{1/2}$) and later (Q2D: $x^{1/4}$) time exponents of the model. The reason for the apparent agreement in Fig. 3 is Re is low enough for the NEQ and BC regimes to be barely distinguishable. The mixed result of exponents between the two (0.5 and 0.25, respectively), combined with the initial phase of Q2D in the theory gives a result that looks like the data. The prediction is that if Re is high enough (for example, in a field measurement), then the separate regimes will be observed.

The vertical wake height L_z is compared in Fig. 5. This measurement is hard to achieve experimentally, and there is an observed dependence of initial wake height on F, which is not taken into account in this figure. The results included here of Chomaz *et al.*[12] were re-analyzed and plotted by assuming that the mean profiles were Gaussian so as to calculate an equivalent quantitative value of the wake height. Although these particular results do not all fall within the agreement of the other experimental data (at least at moderate x/D), the slope is in fact quite consistent with a purely viscous diffusion growth process, and not significantly accelerated, as seemed to be the case when shown in their original form (see Ref. 12, Fig. 9). In general, both numerical and experimental results show a large plateau, followed by a steep increase at later stages. This corresponds to the NEQ and BC regimes in which the wake height is constant, followed by the Q2D regime, in which the wake height increases by viscous diffusion as $\sqrt{x}$. This basic phenomenon therefore requires no more complex an explanation than initial suppression of vertical growth by stratification, followed by viscous diffusion in the vertical at later times, as specified in the model problem. However, it is also important to note that considerable differences persist at late times (Q2D), and that any F dependence in NEQ/BC remains unaccounted for in this plot.

The mean velocity defect U_0 is compared in Fig. 6. In experiment (dotted line in Fig. 6), the initial decay rate is imagined to be $x^{-2/3}$ as for an unstratified wake, followed by the nonequilibrium period when measured decay rates are

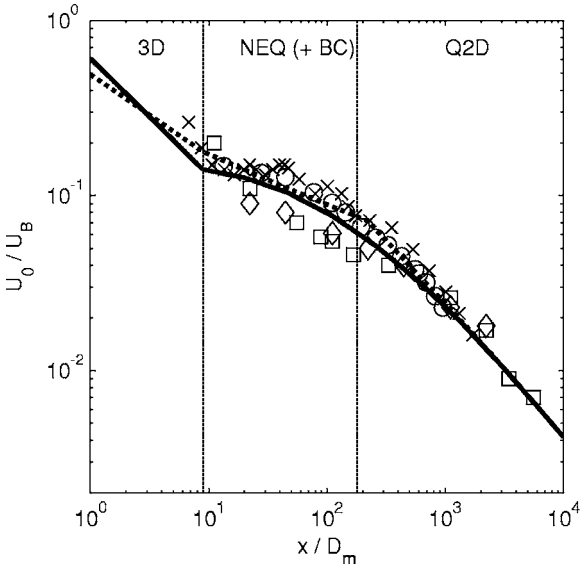

FIG. 6. Time evolution of the mean velocity defect U_0 for $F_m=8.9$ and $Re_m=2.25\times10^3$. Same caption as in Fig. 4. Experimental results from Ref. 8 for $F_m=13.3$ and $Re_m\approx3\times10^3$ are also shown as × symbols. The uncertainties in the experimental results (Ref. 4) is of the order of 40%.

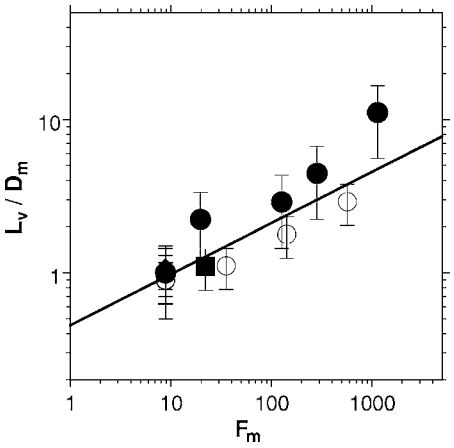

FIG. 7. Variation of the initial vertical wake height with Froude number. Experimental results (●) are taken from Ref. 9. Numerical results are from Ref. 10 (□), Ref. 11 (◇), and Ref. 27 (○). The solid line corresponds to Eq. (15).

significantly lower $x^{-0.25\pm0.04}$.[4] (Measurements by Bonnier and Eiff[8] in fact show a possible increase in U_0 at early-NEQ, as shown by the crosses for one of their experiments.) In the model, NEQ is supposed to last from $x/D_m = F_m$ to $x/D_m \approx 50F_m$. In experiment, NEQ was found to begin at $Nt \approx 2$ and end at $Nt \approx 50$ and the equivalent x/D varies with F (as $x/D = Nt\,F/2$). U_0 then decreases more rapidly, as $x^{-0.75}$, which is characteristic of the Q2D regime: in experiments, the decay exponent was found to be -0.76 ± 0.12. The agreement between model predictions (solid line) and laboratory (dotted line, crosses) and numerical (open symbols) experiment is good given that all numerical and experimental measurements fall within 50% of the model prediction. Again, the NEQ and BC regimes of the model are very close at this Re, and the net effect is to mimic the experimental results reasonably well. The collapse of points in the Q2D regime is also good. Figure 6 can be viewed as a consequence of momentum conservation, given Figs. 4 and 5, and just as any F dependence is omitted from Fig. 5, so it is also absent in Fig. 6.

The following section considers the F and Re dependence in the model and experimental data in more detail.

B. Dependence on the Froude and the Reynolds number

By varying the Froude number over almost two decades, Spedding[4] showed that the velocity defect scales as $(Nt)^{-0.76}\,F^{-2/3}$ at the beginning of the Q2D regime. This dependence on the Froude number can be recovered theoretically by looking at the velocity defect in the BC regime, where $U_0 \sim 1/\sqrt{xL_v} \sim (Nt)^{-1/2}\,F^{-2/3}$. The dependence differs slightly in the Q2D regime $[U_0 \sim (Nt)^{-3/4}\,F^{-3/4}]$, but such variations might be difficult to distinguish in practice.

The primary feature of stratified wakes is that the wake height saturates at a specific vertical length scale L_v, which can be readily deduced from experimental and numerical results by looking at the value of the initial plateau of the wake height. These values are compared in Fig. 7 with the theoretical prediction given by Eq. (15). The model predicts that

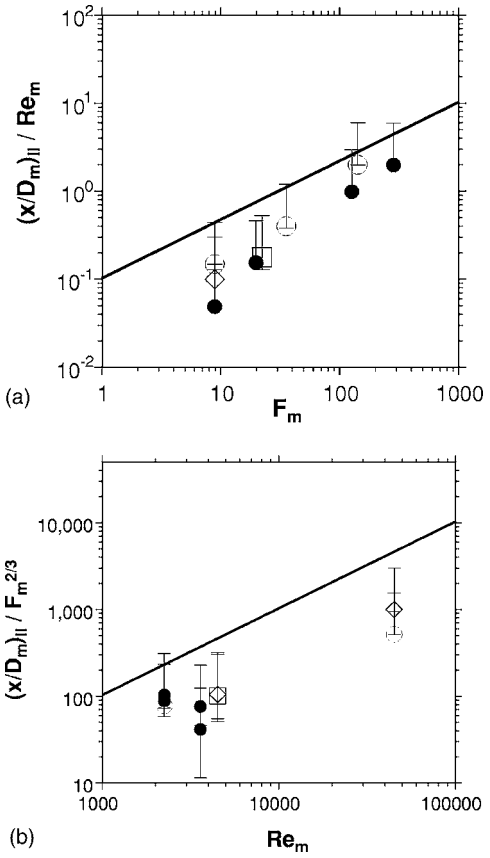

FIG. 8. Downstream distance x_{II} of the second transition, between a buoyancy-controlled (BC) regime and a quasi-2D regime (Q2D), as a function of (a) the Froude number and (b) the Reynolds number. Caption as in Fig. 7. The solid line corresponds to Eq. (21).

L_v scales as $F^{1/3}$, while it was found to vary as $F^{0.6}$ experimentally.[9] The discrepancy is perhaps unsurprising, given the complete neglect of physical mechanisms involving any correlation of vertical velocities, density field structure and internal wave dynamics. Further improvements in the model will be especially important at high Froude number, for example, where L_v is underestimated by a factor of 2. Although the numerical simulations show good agreement, they do not predict the variation of L_v with the Froude number, since they were always performed at low F. Moreover, it is far from a trivial matter knowing how a numerical simulation should be initialized with correct initial length scales where any L_v could be truly claimed to be an independent outcome of the model, rather than an input.

Finally, we can determine the downstream distance x_{II} at which the transition between the BC and the Q2D regime occurs. It is plotted in Fig. 8 as a function of the Froude and the Reynolds number. While the general dependence of x_{II} as $Re_m\,F_m^{2/3}$ is consistent with the data, for any given Re_m or F_m, the model always overestimates x_{II}, which again shows that the model might be improved. This might include improved modeling and/or higher order correction of terms leading to vertical transport, or some way of accounting for initial conditions whose effect could be felt out to x_{II}. Further experi-

ments and numerical simulations over a broad range of Re and run for long times might help to point out ways in which this can be done.

IV. CONCLUSIONS

The general theory developed here predicts the mean profile evolution of a drag wake in a linearly stratified fluid. The model is based on an assumption of eddy viscosity in the horizontal direction, which allows the mean momentum equations to be closed by assuming that the horizontal Reynolds stress is proportional to the mean shear. The (constant) value of the eddy viscosity is chosen from relevant experiments in stratified wakes, and not as an *a posteriori* fitting parameter. The evolution of the wake in the vertical is modelled by viscous diffusion alone for $Nt>1$, which is reasonable for the moderate Re in laboratory experiments and numerical simulations. In this respect, the approach is analagous to stratified dipole and turbulence evolution experiments where experimental data were quite closely matched by numerical models with turbulent and viscous diffusion in the horizontal and vertical, respectively.[28,29] The averaged equations of motion show that a Gaussian solution can be found and allow an analytical determination of the wake height, the wake width, and the velocity defect.

Existing results from the literature for wake height, wake width, and velocity defect, from both laboratory and numerical experiment, agree with the theoretical predictions within 50%. The three different regimes found in the literature that characterize decaying stratified flows (3D, NEQ, and Q2D regimes) are recovered, and two new regimes are proposed: a buoyancy-controlled (BC) regime which should be observed (as distinct from the NEQ regime) at very high Reynolds numbers, and a viscous 3D regime, which should be observed at very late stages. Note that since the formulation involves self-similar solutions of simplified equations of motion, transients at relatively small x/D, such as the acceleration phase noted by Ref. 8, are not accounted for.

These results apply to any self-similar shear flow in a stratified fluid, where a momentum thickness is defined by $D_m=D\sqrt{c_D/2}$. Such a model can even be extended to the majority of cases of self-propelled bodies,[14] whenever the wake momentum balance departs from zero by more than 2%; that will be the case for even small accelerations, whenever there is significant wave drag, and whenever the ambient is nonuniform.

The extension to high Reynolds numbers is of interest to many practical geophysical and naval applications. Examples include large-scale submerged bodies and atmospheric wakes of mountains or oceanic wakes of islands and sea-mounts. The mean characteristics of the wake are given analytically by the model in Eqs. (20), (22), and (24) and the previous experimental and numerical results can be extrapolated to high Reynolds numbers using the similarity laws of the model.

One of the principal consequences is that the Q2D regime appears later for higher Reynolds numbers (at $x/D=\mathrm{Re}\,\mathrm{F}^{2/3}$, or $Nt=\mathrm{Re}\,\mathrm{F}^{-1/3}$). Since the mean velocity decay rates in the intervening NEQ and BC regime are lower than in either the surrounding 3D or Q2D regimes, this scaling behaviour predicts that the high magnitude defect wakes that have been observed in laboratory experiment should be even more evident with higher Re. In this regard, the model described in this paper bears a certain similarity with another, spectrally based, theoretical model of localized stratified turbulence,[30] and despite fundamental differences in their formulation, both models identify a signature of the initial Re on the intermediate-to-late-time flow dynamics, which persists for longer times with increasing Re.

The model could be extended to more specialized cases, such as bluff body wakes with an angle of attack,[31] and to the particular case of exactly momentumless wakes. In both cases, the mean profiles are not simple Gaussians and it would be interesting to test other scaling functions.

ACKNOWLEDGMENTS

The support of ONR Grant No. N00014-04-1-0034 administered by Dr. R. Joslin is most gratefully acknowledged.

[1] J. M. Chomaz, P. Bonneton, and E. J. Hopfinger, "The structure of the near wake of a sphere moving horizontally in a stratified fluid," J. Fluid Mech. **254**, 1 (1993).
[2] G. R. Spedding, F. K. Browand, and A. M. Fincham, "The long-time evolution of the initially-turbulent wake of a sphere in a stable stratification," Dyn. Atmos. Oceans **23**, 171 (1996).
[3] G. R. Spedding, F. K. Browand, and A. M. Fincham, "Turbulence, similarity scaling and vortex geometry in the wake of a towed sphere in a stably stratified fluid," J. Fluid Mech. **314**, 53 (1996).
[4] G. R. Spedding, "The evolution of initially turbulent bluff-body wakes at high internal Froude number," J. Fluid Mech. **337**, 283 (1997).
[5] J. R. Riley and M. P. Lelong, "Fluid motions in the presence of strong stable stratification," Annu. Rev. Fluid Mech. **32**, 613 (2000).
[6] J. T. Lin and Y. H. Pao, "Wakes in stratified fluids: a review," Annu. Rev. Fluid Mech. **11**, 317 (1979).
[7] G. R. Spedding, "The streamwise spacing of adjacent coherent structures in stratified wakes," Phys. Fluids **14**, 3820 (2002).
[8] M. Bonnier and O. Eiff, "Experimental investigation of the collapse of a turbulent wake in a stably stratified fluid," Phys. Fluids **14**, 791 (2002).
[9] G. R. Spedding, "Vertical structure in stratified wakes with high initial Froude number," J. Fluid Mech. **454**, 71 (2002).
[10] M. J. Gourlay, S. C. Arendt, D. C. Fritts, and J. Werne, "Numerical modeling of initially turbulent wakes with net momentum," Phys. Fluids **13**, 3783 (2001).
[11] D. G. Dommermuth, J. W. Rottman, G. E. Innis, and E. A. Novikov, "Numerical simulation of the wake of a towed sphere in a weakly stratified fluid," J. Fluid Mech. **473**, 83 (2002).
[12] J. M. Chomaz, P. Bonneton, A. Butet, and E. J. Hopfinger, "Vertical diffusion in the far wake of a sphere moving in a stratified fluid," Phys. Fluids A **5**, 2799 (1993).
[13] P. Meunier and G. R. Spedding, "A loss of memory in stratified momentum wakes," Phys. Fluids **16**, 298 (2004).
[14] P. Meunier and G. R. Spedding, "Stratified propelled wakes," J. Fluid Mech. **552**, 229 (2006).
[15] J. R. Riley and S. M. deBruynKops, "Dynamics of turbulence strongly influenced by buoyancy," Phys. Fluids **15**, 2047 (2003).
[16] H. Tennekes and J. L. Lumley, *A First Course in Turbulence* (M.I.T. Press, Cambridge, MA, 1972).
[17] G. R. Spedding, "Anisotropy in turbulence profiles of stratified wakes," Phys. Fluids **13**, 2361 (2001).
[18] Y. D. Afanasyev, "Wakes behind towed and self-propelled bodies: Asymptotic theory," Phys. Fluids **16**, 3235 (2004).
[19] P. M. Bevilaqua and P. S. Lykoudis, "Turbulence memory in self-preserving wakes," J. Fluid Mech. **89**, 589 (1978).
[20] J. R. Riley, R. W. Metcalfe, and M. A. Weissman, in *Nonlinear Properties of Internal Waves*, edited by B. J. West (AIP, Melville, NY, 1981), pp. 79–112.

[21] M. J. Lighthill, "Internal waves and related initial-value problems," Dyn. Atmos. Oceans **23**, 3 (1996).
[22] E. Itsweire, J. Koseff, D. Briggs, and J. H. Ferziger, "Turbulence in stratified shear flows: Implications for interpreting shear-induced mixing in the ocean," J. Phys. Oceanogr. **23**, 1508 (1993).
[23] W. D. Smyth and J. N. Moum, "Anisotropy of turbulence in stably stratified mixing layers," Phys. Fluids **12**, 1343 (2000).
[24] M. L. Waite and P. Bartello, "Stratified turbulence dominated by vortical motion," J. Fluid Mech. **517**, 281 (2004).
[25] D. K. Lilly, "Stratified turbulence and the mesoscale variability of the atmosphere," J. Atmos. Sci. **40**, 749 (1983).
[26] P. Billant and J.-M. Chomaz, "Self-similarity of strongly stratified inviscid flows," Phys. Fluids **13**, 1645 (2001).
[27] P. J. Diamessis, A. J. Domaradzki, and J. S. Hesthaven, "A spectral multidomain penalty method model for the simulation of high Reynolds number localized incompressible stratified turbulence," J. Comput. Phys. **202**, 298 (2005).
[28] O. Praud, A. M. Fincham, and J. Sommeria, "Decaying grid turbulence in a strongly stratified fluid," J. Fluid Mech. **522**, 1 (2005).
[29] O. Praud and A. M. Fincham, "The structure and dynamics of dipolar vortices in a stratified fluid," J. Fluid Mech. **544**, 1 (2005).
[30] C. H. Gibson, in *Marine Turbulence*, edited by J. C. T. Nihoul (Elsevier, Amsterdam, 1980), pp. 221–258.
[31] S. Gallet, P. Meunier, and G. R. Spedding, "Empirical scaling of antisymmetric stratified wakes," J. Fluids Struct. **22**, 941 (2006).

Annexe 2

Articles sur les instabilités de tourbillon dans un fluide stratifié

N. Boulanger, P. Meunier & S. Le Dizès (2007). "Structure of a stratified tilted vortex", *J. Fluid Mech* **583**, pp. 443-458.

N. Boulanger, P. Meunier & S. Le Dizès (2008). "Tilt-induced instability of a stratified vortex", *J. Fluid Mech* **596**, pp. 1-20.

X. Riedinger, S. Le Dizès & P. Meunier (2009). "Viscous stability properties of a Lamb-Oseen vortex in a stratified fluid", *soumis à J. Fluid Mech.*

J. Fluid Mech. (2007), *vol.* 583, *pp.* 443–458.
doi:10.1017/S0022112007006416 Printed in the United Kingdom

Structure of a stratified tilted vortex

NICOLAS BOULANGER, PATRICE MEUNIER AND STÉPHANE LE DIZÈS

Institut de Recherche sur les Phénomènes Hors Équilibre, CNRS/Universités Aix-Marseille I&II, 49, rue F. Joliot-Curie, B.P. 146, F-13384 Marseille cedex 13, France

(Received 13 July 2006 and in revised form 8 March 2007)

The structure of a columnar vortex in a stably stratified fluid is studied experimentally and theoretically when the vortex axis is slightly tilted with respect to the direction of stratification. When the Froude number of the vortex is larger than 1, we show that tilting induces strong density variations and an intense axial flow in a rim around the vortex. We demonstrate that these characteristics can be associated with a critical-point singularity of the correction of azimuthal wavenumber $m = 1$ generated by tilting where the angular velocity of the vortex equals the Brunt–Väisälä frequency of the stratified fluid. The theoretical structure obtained by smoothing this singularity using viscous effects (in a viscous critical-layer analysis) is compared to particle image velocimetry measurements of the axial velocity field and visualizations of the density field and a good agreement is demonstrated.

1. Introduction

Small intense vortices, characterized by large Froude and Rossby numbers, are present in both the atmosphere and the ocean. The goal of the present paper is to determine their structure when the vortex axis is slightly tilted with respect to the direction of stratification.

In the atmosphere, the dynamics is often governed by large-scale motion induced by the baroclinic instability of thermal fronts. However, secondary instabilities have also been evidenced (Neiman, Shapiro & Fedor 1993) and they may lead to the formation of small intense cyclones (Polavarapu & Peltier 1993; Garnier, Métais & Lesieur 1996). These vortices are often too small to be described by meteorological models, but they can be very damaging during strong storms (Lesieur, Métais & Garnier 2000). Understanding the dynamics of these structures constitutes one of the motivations of this work. The most intense of these structures are columnar vortices with large Froude numbers (their maximum angular velocity is larger than the Brunt–Väisälä frequency of the fluid). We think that the analysis performed in this paper could provide some information on their dynamics, when their axis is tilted with respect to the direction of stratification.

Vortices are also observed in the ocean. For instance, they can form close to islands or near headlands by a barotropic instability of the flow generated by the tide. The resulting vortices are generally strongly tilted owing to the weak slope of coastal regions (Pawlak *et al.* 2003) and it has been argued that this could be the cause of intense vertical mixing (Farmer, Pawlowicz & Jiang 2002). Here, we shall see that, if the vortices are sufficiently intense, tilt angle need not be important in inducing strong vertical displacements.

The effect of a stable stratification on the dynamics and stability of vortices has been the subject of numerous works. The inviscid criteria for two-dimensional shear instability and centrifugal instability are not affected by stratification (see for instance Hopfinger & van Heijst 1993). However, other instabilities usually active when several vortices interact are modified: the elliptic instability is stabilized (Kerswell 2002) and the Crow instability is replaced by a new zigzag instability (Billant & Chomaz 2000) when the stratification is sufficiently strong. For a single vortex with a large Froude number, Cariteau & Flór (2003) also reported a new instability characterized by a rim region of strong vertical mixing, but they did not propose any instability mechanism (see Cariteau 2005). We shall argue below that this instability was probably due to a misalignment of the vortex axis with the direction of stratification.

As far as we know, the effects of vortex tilting have not been studied in the laboratory. When the vortex axis is tilted with respect to the direction of stratification, the azimuthal symmetry of the vortex is broken and non-axisymmetric corrections of azimuthal wavenumber $m = 1$ are created. For large Reynolds numbers and Froude numbers greater than 1, we shall see that these corrections are characterized by strong density variations and intense axial flow near a particular radial location. We shall associate this location with the critical-point singularity where the angular velocity of the vortex is equal to the Brunt–Väisälä frequency of the fluid. These singularities, which appear in the inviscid description of linear perturbations, are known to play an important role in shear instabilities (Drazin & Reid 1981; Maslowe 1986), and internal wave propagation (e.g. Booker & Bretherton 1967). They have also been shown to be present in the analysis of the deformation of a vortex by a rotating strain field (Le Dizès 2000). In this case, the critical-point singularity occurs in the $m = 2$ azimuthal correction at the location where the angular velocity of the vortex is equal to the angular frequency of the strain. Le Dizès (2000) showed that the singularity can be smoothed by introducing either viscous or nonlinear effects in the critical-layer region as for planar shear flows.

The theoretical description of the correction induced by tilting will be obtained by a similar method. We shall demonstrate that the characteristics obtained by smoothing the critical-point singularity with viscous effects allows the reproduction of the experimental observations and measurements.

The paper will be organized as follows. In § 2, the experimental set-up is presented and the characteristics of the vortices when the axis is not tilted are discussed. In § 3, experimental evidence for the critical-layer region is given and the theoretical framework is introduced. In § 4, the viscous critical-layer analysis is performed and the theoretical predictions for axial flow velocities are compared to particle image velocimetry (PIV) measurements. In the last section, the main results of the paper are briefly summarized. We also introduce the instability which develops in the critical-layer region and which is the subject of a companion paper (Boulanger, Meunier & Le Dizès 2007).

2. Experimental set-up and base flow

2.1. *Experimental details*

The experimental set-up is represented schematically in figure 1. The experiments are performed in a 1.50 m long, 0.75 m wide and 0.50 m high Plexiglas tank. The tank is filled with linearly stratified fluid up to a height of 0.45 m. The linear stratification is established by the two-tank method, using clear water in the first tank and salt water with a density varying between $1100\,\mathrm{kg\,m^{-3}}$ and $1190\,\mathrm{kg\,m^{-3}}$ in the second tank. The

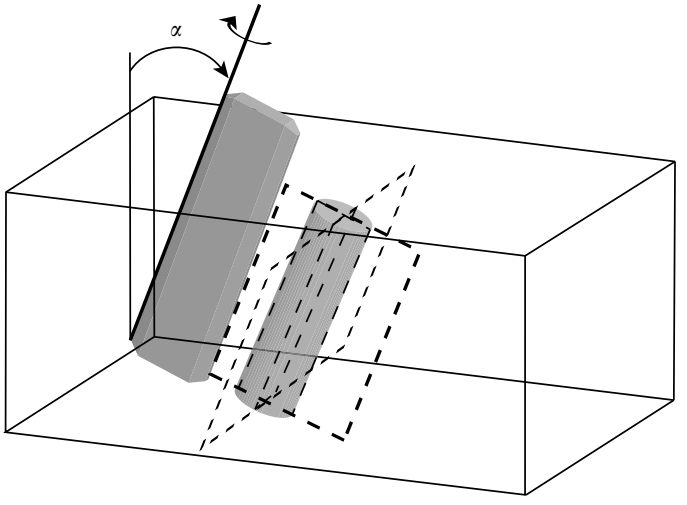

FIGURE 1. Experimental set-up. The rotation of the grey plate around its upper edge generates a vortex inclined at an angle α with respect to the vertical.

density gradient is deduced from density measurements of small samples of fluid every 5 cm, using a densitometer Anton Paar DMA 35N with an accuracy of $0.1\,\mathrm{kg\,m^{-3}}$. By varying the effective depth of fluid between 0.2 m and 0.45 m, we have been able to obtain a Brunt–Väisälä frequency ranging from $1.5\,\mathrm{rad\,s^{-1}}$ to $3\,\mathrm{rad\,s^{-1}}$. For small depth of fluid, a uniform layer of maximal density ($1190\,\mathrm{kg\,m^{-3}}$) and 0.10 m thickness was added under the linearly stratified fluid in order to avoid bottom effects.

The vortex is created by impulsively rotating a flap in the fluid initially at rest. This generates a two-dimensional shear layer detaching at the edge of the flap and rolling-up in a vortex. This method is convenient since it creates a laminar two-dimensional vortex. It has been used frequently for the study of three-dimensional instabilities (Crow, elliptic, zigzag or centrifugal) of vortices (see Leweke & Williamson 1998; Billant & Chomaz 2000; Meunier & Leweke 2005). In our set-up, the flap is made of aluminium and has dimensions $0.1 \times 0.6\,\mathrm{m^2}$, and is sharpened at its free edge, i.e. where the shear layer detaches. It is rotated by a computer-controlled step-motor as in Meunier & Leweke (2005). The motion of the flap has been chosen carefully, through empirical improvements, to create a nearly Gaussian vortex, and to avoid roll-up instabilities (Kelvin–Helmholtz instabilities of the shear layer) and stopping vortices. The motion profile (angular velocity as function of angle in degrees) that was finally adopted is

$$\dot{\Theta} = \dot{\Theta}_{max} \frac{0.42}{\Theta + 0.017} \left[1 + \mathrm{e}^{-(\Theta/0.26)^{5/4}}\right], \tag{2.1}$$

and consists of a rapid acceleration of the flap, followed by a gradual slow-down up to the angle of $\pi/2$ rad. The circulation of the vortex is varied by modifying the maximum angular velocity $\dot{\Theta}_{max}$ between 0.01 and $0.5\,\mathrm{rad\,s^{-1}}$. The inclination of the vortex is obtained by tilting the flap with respect to the vertical in the initial plane of the flap (see figure 1).

Quantitative measurements of velocity fields are obtained by PIV. The flow is seeded with particles of variable density so that they are homogeneously distributed through the whole depth. We have used Sphericel hollow glass spheres 110P8 (Potter Industries), with a density of approximately 1.1, and a diameter ranging from 11 to

18 μm. The particles are illuminated by a luminous sheet of 3–5 mm thickness, created by a continuous 5 W argon-ion lasr. Image pairs are recorded by a digital PIV camera (Kodak Megaplus Es 4.0) with a resolution of 2048×2048 pixels at a rate of 5 fields per second, and treated by a cross-correlation algorithm (Meunier & Leweke 2003).

Measurements have been made in three different planes. The first one is perpendicular to the vortex axis and provides the characteristics of the initial vortex. The other two planes correspond to two orthogonal longitudinal planes, one plane being vertical ($\theta = 0$) and the other being tilted ($\theta = \pi/2$) (figure 1). In the vertical longitudinal plane, the vortex appears tilted in the images, whereas in the tilted longitudinal plane, the vortex appears vertical in the images. The displacement of the flap also induces a weak background velocity field which slowly moves the vortex away from the flap. This slow translating movement is used to scan the complete vortex volume without moving the plane of measurement. It allows the determination of the axial component of the velocity field in the whole three-dimensional space.

Shadowgraph visualizations were also carried out, to observe the two-dimensional and three-dimensional spatial distribution of density inside the vortex. For this purpose, the stratified fluid is illuminated by a large beam of parallel light, created by an intense light placed behind a small diaphragm located 2 m from the tank. Since the refraction index of the fluid depends on its density, the rays are bent toward the larger densities. To first order, the rays are thus deviated toward the floor. To second order, they will be deviated according to the spatial distribution of density inside the vortex. By placing a large lens (of diameter 0.3 m and of focal distance 0.5 m) behind the tank, it is thus possible to obtain an image of the density distribution. These images are recorded by a 2000×2000 pixels grey-scale camera located behind the focal point of the lens. For better visualizations, a small disk of 1 mm diameter has been positioned exactly at the focal point of the lens. This process, called strioscopy, allows us to mask the rays which are not deviated by the density perturbations of the vortex, and enhances the contrast of the images. In strioscopy measurement, it can be shown that the intensity of the images is proportional to the Laplacian of the refraction index, i.e. of the density. However, this property will not be used. In our experiments, we will simply use strioscopy to reveal the qualitative features of the flow.

2.2. *Vortex characteristics*

Figure 2(*a*) shows a typical velocity field obtained by PIV measurements in a horizontal plane, when the vortex axis is exactly vertical. The velocity field is very close to axisymmetric. The spatial resolution is very high (approximatively 20 vectors within the vortex core) such that the uncertainties on the velocity field are small. In figure 2(*a*), the spatial resolution has been reduced by a factor 2 for visualization purposes. The uncertainties on the vorticity field are larger, but still remain lower than 5%. Figure 2(*b*) presents the velocity profiles obtained from an angular averaging of the velocity field shown in figure 2(*a*). The velocity profile is approximated well by the profile of a Gaussian vortex (Lamb–Oseen), whose angular velocity is given by:

$$\Omega_0(r) = \frac{v_\theta(r)}{r} = \frac{\Gamma}{2\pi r^2}\left(1 - \mathrm{e}^{-r^2/a^2}\right). \tag{2.2}$$

In our experiments, the circulation was varied between 17 and 42 $\mathrm{cm}^2\,\mathrm{s}^{-1}$. The core size a is slowly varying with time between 0.9 and 1.1 cm owing to viscous effects, but this dependency can be neglected on the time scale we are considering.

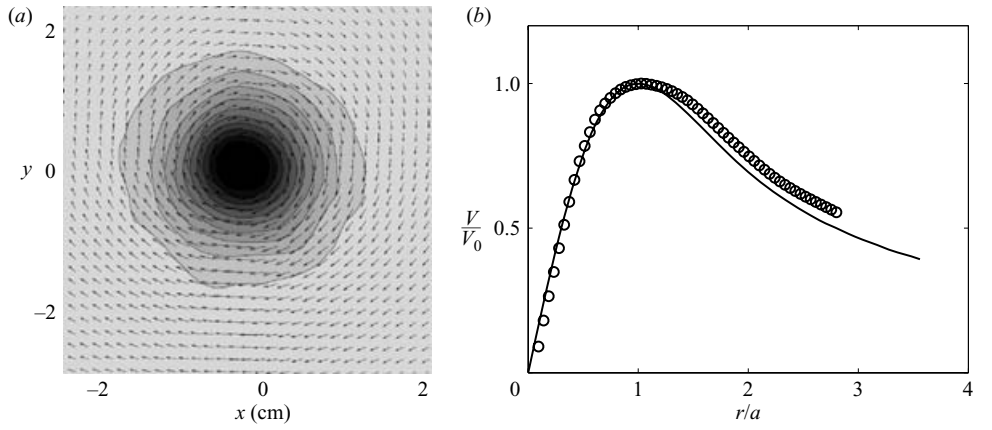

FIGURE 2. Velocity field of the vortex as obtained by PIV measurement in a horizontal cross-section. (*a*) Two-dimensional velocity field and vorticity contours. (*b*) Azimuthal velocity profile measured by PIV and fitted by (2.2) for a Gaussian vortex (solid line). Here, $Re = 370$.

We will non-dimensionalize lengths by the vortex core size a, since it is the only relevant length scale of the flow. Moreover, the inverse of the angular velocity at the centre of the vortex $\Omega_0(r=0) = \Gamma/2\pi a^2$ will be used as the time scale of the flow. This leads to non-dimensionalizing the velocity by $a\Omega_0(0)$. Finally, we will non-dimensionalize densities by the density of the fluid ρ_f at $z=0$.

Our system is characterized by five non-dimensional parameters α, Re, F, Sc and L. The first parameter α is the tilt angle between the vortex and the vertical. It was varied between 0 and 0.26 rad. The Reynolds number Re characterizes the strength of the vortex: it is defined from the circulation of the vortex by $Re = \Gamma/(2\pi\nu)$ (ν being the kinematic viscosity of the fluid) and ranges from 240 to 800. The stratified fluid is characterized by its Brunt–Väisälä frequency $N = \sqrt{-(g/\rho)(\partial\rho/\partial z)}$ from which we define the Froude number $F = \Omega_0(0)/N$. In our experiments, the Froude number ranges from 1.5 to 5. The Schmidt number $Sc = \nu/\kappa$ is the ratio between the viscous diffusivity and the diffusivity of the salt; it is roughly equal to 700 for salted water, which renders the diffusion of salt negligible. The last parameter L compares the vertical stratification length to the vortex core size: $L = \rho/(a\partial\rho/\partial z)$. In our experiments, this parameter ranges between 100 and 400.

3. A critical layer in tilted vortices

3.1. *Experimental evidence*

Figure 3(*a*) shows a side view of the vortex by strioscopic visualizations for an inclination angle $\alpha = 0.12$ rad. This photograph reveals two white strips going from the bottom to the top of the image, with the same angle $\alpha = 0.12$ rad. They are nearly symmetrically located around the vortex axis, which is a barely visible blurry bright line going through the centre of the image. These white strips appear progressively during the vortex formation, and become brighter and brighter as time evolves. After a saturation time of a few seconds they remain stationary during the whole experiment, if the Reynolds number is sufficiently small. These strips reveal a strong density variation (stronger than the radial variations induced by the vortex) concentrated in a

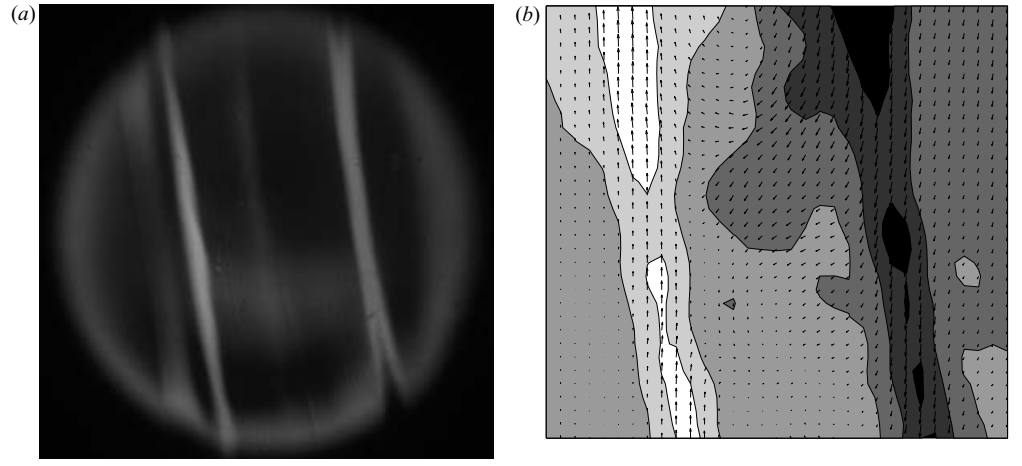

FIGURE 3. View of the vortex approximately five rotation periods after its formation, in a vertical longitudinal plane. (*a*) Density contrast visualized by strioscopy ($Re = 720$, $F = 5$, $\alpha = 0.12$ rad and $r_c = 2.2a$). (*b*) Instantaneous velocity field measured by PIV ($Re = 450$, $F = 3.2$, $\alpha = 0.07$ rad and $r_c = 1.7a$). The grey-scale contours correspond to the vertical velocity component.

thin region at the periphery of the vortex, which we shall see below can be attributed to a critical-layer singularity.

Figure 3(*b*) represents the velocity field superimposed on the axial velocity contours in the same vertical longitudinal plane as in figure 3(*a*), but with a smaller tilt angle $\alpha = 0.07$ rad. For a vertical vortex, the axial velocity is equal to zero. Here, for this small value of the tilt angle, we observe a strong axial velocity field. This axial velocity field is concentrated in two strips located symmetrically with respect to the vortex axis. The velocity is downward on the upper side of the vortex and upward on the lower side. These strips create a pattern similar to the density variation pattern observed in figure 3(*a*).

This strip-like pattern is not observed for a vertical vortex. For large Reynolds numbers, it appears as soon as the inclination angle is above 2°–3°. It is also observed for moderate Froude numbers between 1 and 5, only. It is possible to measure the radial position where these strips are located in both shadowgraph visualizations and PIV velocity fields. This position is indicated by symbols in figure 4 as a function of the inverse of the Froude number $1/F = N/\Omega_0(0)$. The solid curve gives the location of the critical-point singularity r_c at which the angular velocity $\Omega_0(r_c)$ is equal to the Brunt–Väisälä frequency N. As can be observed, the symbols are very close to the curve. This is the first indication that the strips could be associated with a critical-layer phenomenon. We shall see below that this observation will allow the construction of a theoretical model to describe the flow in the neighbourhood of the critical point.

This link between strips and critical points readily explains why strips have been observed only for moderate Froude numbers above 1. When the Froude number is smaller than unity, there is no critical-point singularity, so no strip is expected to appear. When the Froude number is increased above unity, the critical point moves away from the vortex centre and the strength of the singularity decreases. Density variations and axial flow generation are thus expected to become weaker and to move progressively outside the observation domain.

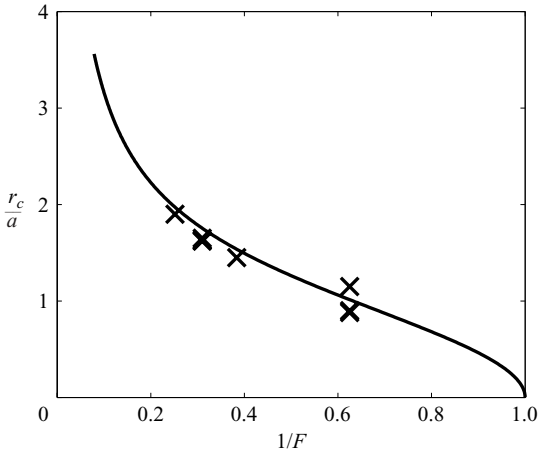

FIGURE 4. Theoretical prediction (solid line) and experimental measurements (×) of the position of the critical layer on shadowgraph visualizations, versus the inverse of the Froude number $1/F = N/\Omega_0(0)$ for a Gaussian vortex. Here, $\alpha = 0.07$ rad and Re varies between 240 and 560 with a fixed Brunt–Väisälä frequency $N = 1.5\,\mathrm{rad\,s^{-1}}$.

3.2. *Theoretical formulation of the problem*

Our goal is to provide the basic flow solution for a vortex in a stratified fluid, whose axis is tilted with an angle α with respect to the gravity (i.e. the density gradients). The flow is governed by the Navier–Stokes equations together with the density equation and the incompressibility condition, which are in dimensional form:

$$\frac{\mathrm{D}\boldsymbol{u}}{\mathrm{D}t} = -\frac{1}{\rho}\nabla p - g\boldsymbol{e}_z + \nu\Delta\boldsymbol{u}, \tag{3.1a}$$

$$\frac{\mathrm{D}\boldsymbol{\rho}}{\mathrm{D}t} = \kappa\Delta\rho, \tag{3.1b}$$

$$\nabla\cdot\boldsymbol{u} = 0. \tag{3.1c}$$

As was discussed at the end of § 2.2, the non-dimensional problem is defined by the angle α, the Froude number F, the length ratio L, the Reynolds number Re and the Schmidt number Sc. In particular, note that the dimensionless form of the acceleration due to gravity g is L/F^2.

To determine the tilted vortex solution, the main idea is to use the new variables:

$$x' = x - \tan\alpha z, \quad y' = y, \quad z' = z. \tag{3.2}$$

Equations (3.1) can then be written, in cylindrical coordinates, as:

$$\frac{\mathrm{D}u}{\mathrm{D}t} - \frac{v^2}{r'} - w\tan\alpha\frac{\partial u}{\partial x'} - w\frac{\tan\alpha\sin\theta'}{r'}v = -\frac{1}{\rho}\frac{\partial p}{\partial r'} + \frac{(\Delta'\boldsymbol{u})_r}{Re}, \tag{3.3a}$$

$$\frac{\mathrm{D}v}{\mathrm{D}t} + \frac{uv}{r'} - w\tan\alpha\frac{\partial v}{\partial x'} + w\frac{\tan\alpha\sin\theta'}{r'}u = -\frac{1}{\rho r'}\frac{\partial p}{\partial\theta'} + \frac{(\Delta'\boldsymbol{u})_\theta}{Re}, \tag{3.3b}$$

$$\frac{\mathrm{D}w}{\mathrm{D}t} - w\tan\alpha\frac{\partial w}{\partial x'} = -\frac{1}{\rho}\frac{\partial p}{\partial z'} + \frac{\tan\alpha}{\rho}\frac{\partial p}{\partial x'} - \frac{L}{F^2} + \frac{\Delta' w}{Re}, \tag{3.3c}$$

$$\frac{\mathrm{D}\rho}{\mathrm{D}t} - w\tan\alpha\frac{\partial\rho}{\partial x'} = \frac{\Delta'\rho}{Re\,Sc}, \tag{3.3d}$$

$$\frac{1}{r'}\frac{\partial(r'u)}{\partial r'} + \frac{1}{r'}\frac{\partial v}{\partial\theta'} + \left(\frac{\partial}{\partial z'} - \tan\alpha\frac{\partial}{\partial x'}\right)w = 0, \tag{3.3e}$$

with

$$\frac{\mathrm{D}}{\mathrm{D}t} = \left(\frac{\partial}{\partial t} + u\frac{\partial}{\partial r'} + \frac{v}{r'}\frac{\partial}{\partial\theta'} + w\frac{\partial}{\partial z'}\right), \quad \frac{\partial}{\partial x'} = \cos\theta'\frac{\partial}{\partial r'} - \frac{\sin\theta'}{r'}\frac{\partial}{\partial\theta'}.$$

In these equations, u and v are the radial and azimuthal components of the horizontal velocity field in the polar coordinate system (r', θ') deduced from (x', y') while w is the velocity component along the direction of the gravity field (z-axis). In the following, the primes are dropped.

When the vortex is not tilted ($\alpha = 0$), we recover the classical equations for the dynamics of a vertical stratified vortex. A stationary axisymmetric solution is known to exist in the form $(u, v, w, p, \rho) = (0, r\Omega_0(r), 0, p_0(r, z), \rho_0(r, z))$ provided that

$$r\Omega_0^2 = \frac{1}{\rho_0}\frac{\partial p_0}{\partial r}, \quad -\frac{1}{\rho_0}\frac{\partial p_0}{\partial z} = \frac{L}{F^2}. \tag{3.4a, b}$$

These two equations express the cyclostrophic and the hydrostatic equilibrium with no interaction between the density field and the velocity field. If we further assume that the stratification length L is independent of z, the general solution is found, for any angular velocity profile $\Omega_0(r)$ as:

$$\rho_0 = \mathrm{e}^{-z/L}\ \exp\left(\frac{F^2}{L^2}\int^r r'\Omega_0^2(r')\,\mathrm{d}r'\right), \tag{3.5a}$$

$$p_0 = N^2L^2\,\mathrm{e}^{-z/L}\exp\left(\frac{F^2}{L^2}\int^r r'\Omega_0^2(r')\,\mathrm{d}r'\right). \tag{3.5b}$$

This solution has been obtained in the absence of the Boussinesq approximation.

We now wish to solve these equations for a finite tilt angle α.

3.3. *Expansion for small tilt angles*

For small α, inclination is expected to modify the flow field only weakly. Thus, it is natural to use a perturbation approach. Velocity, pressure and density fields are thus expanded as:

$$\boldsymbol{u} = \boldsymbol{u}_0 + \tan\alpha\boldsymbol{u}_1 + \cdots, \tag{3.6a}$$

$$p = p_0(1 + \tan\alpha p_1(F/L)^2 + \cdots), \tag{3.6b}$$

$$\rho = \rho_0(1 + \tan\alpha\rho_1/L + \cdots), \tag{3.6c}$$

where $(\boldsymbol{u}_0, p_0, \rho_0)$ is the vertical solution and $(\boldsymbol{u}_1, p_1, \rho_1)$ is the non-dimensional first-order correction due to inclination with $\alpha \ll 1$ so that $\tan\alpha \sim \alpha$.

The introduction of (3.6) into (3.3) and linearizing with respect to α yields, at leading order, a solution (u_0, p_0, ρ_0) given by (3.5), as in the vertical case. At order α, equations (3.3) become:

$$\left(\frac{\partial}{\partial t} + \Omega_0\frac{\partial}{\partial\theta}\right)u_1 - 2\Omega_0 v_1 = -\frac{\partial p_1}{\partial r} - r\Omega_0^2\left(\frac{\rho_1}{L} - \frac{p_1F^2}{L^2}\right) + \frac{(\Delta\boldsymbol{u}_1)_r}{Re}, \tag{3.7a}$$

$$\left(\frac{\partial}{\partial t} + \Omega_0\frac{\partial}{\partial\theta}\right)v_1 + \omega_0 u_1 = -\frac{1}{r}\frac{\partial p_1}{\partial\theta} + \frac{(\Delta\boldsymbol{u}_1)_\theta}{Re}, \tag{3.7b}$$

$$\left(\frac{\partial}{\partial t}+\Omega_0\frac{\partial}{\partial\theta}\right)w_1=-\frac{\partial p_1}{\partial z}-\frac{\rho_1}{F^2}+r\Omega_0^2\cos\theta+\frac{p_1}{L}+\frac{\Delta w_1}{Re}, \tag{3.7c}$$

$$\left(\frac{\partial}{\partial t}+\Omega_0\frac{\partial}{\partial\theta}\right)\rho_1=w_1-\frac{r\Omega_0^2F^2u_1}{L}+\frac{\Delta\rho_1}{Re\,Sc}, \tag{3.7d}$$

$$\frac{1}{r}\frac{\partial(ru_1)}{\partial r}+\frac{1}{r}\frac{\partial v_1}{\partial\theta}+\frac{\partial w_1}{\partial z}=0, \tag{3.7e}$$

where $\omega_0=(1/r)(\mathrm{d}(r^2\Omega_0)/\mathrm{d}r)$ is the vorticity of the vortex. Note that the only forcing term in these equations corresponds to $r\Omega_0^2\cos\theta$, which is a buoyancy force generated by the inclination of the isolevels of pressure. This term can guide us to determine the form of the solution.

To simplify the analysis, we shall now apply the Boussinesq approximation. This approximation amounts to considering the limit $L\to\infty$ in the above equations. The first-order corrections induced by non-Boussinesq effects are provided in the Appendix. Under the Boussinesq approximation, a simple inviscid and stationary solution (that is if we assume also $Re\to\infty$) can be obtained as

$$u_1=v_1=p_1=0,\quad w_1=\frac{r\Omega_0^3}{\Omega_0^2-F^{-2}}\sin\theta,\quad \rho_1=-\frac{r\Omega_0^2}{\Omega_0^2-F^{-2}}\cos\theta. \tag{3.8a, b, c}$$

This solution shows that inclination affects the axial component of the velocity and the density field only. However, it can be noted that this solution diverges at the critical point where the angular velocity $\Omega_0(r)$ is equal to the Brunt–Väisälä frequency N. This singularity can be understood as a resonance of the forcing created by the tilt of the vortex with the natural oscillating frequency of the fluid. Note also that the axial velocity in the vertical longitudinal plane (i.e. for $\theta=0$) should always be zero. This is not what has been observed in the experiments (see figure 3*b*). We shall see below that this can be explained by considering viscous effects in the neighbourhood of the critical point.

4. Critical-layer region

4.1. *Viscous critical-layer analysis*

The critical-layer singularity which is observed in the linear inviscid solution (3.8) can be smoothed by introducing additional effects such as viscosity, diffusivity or nonlinearity. For small angles, it is natural to consider viscosity as the main effect (we shall provide a more precise justification below by estimating the first nonlinear terms). The structure of the solution near the critical-point singularity is thus provided in a viscous critical layer. Viscous critical layers have been studied for many years in shear flows (see Drazin & Reid (1981) for details and references).

The idea is to introduce a new local variable $\tilde r=(r-r_c)Re^{1/3}$ on which are captured the viscous variations. The critical-layer solution is then searched in the form

$$u_1=v_1=p_1=0,\quad w_1=Re^{1/3}\tilde w_1(\tilde r)\,\mathrm{e}^{\mathrm{i}\theta}+\text{c.c.} \tag{4.1a, b}$$

$$\rho_1=Re^{1/3}\tilde\rho_1(\tilde r)\,\mathrm{e}^{\mathrm{i}\theta}+\text{c.c.}, \tag{4.1c}$$

where the condition of matching with the inviscid solution (3.8) requires that for large $\tilde r$

$$\tilde w_1\sim\frac{r_c\Omega_{0c}^2}{2i\Omega'_{0c}\tilde r},\quad \tilde\rho_1\sim-\frac{r_c\Omega_{0c}}{2\Omega'_{0c}\tilde r}. \tag{4.2a, b}$$

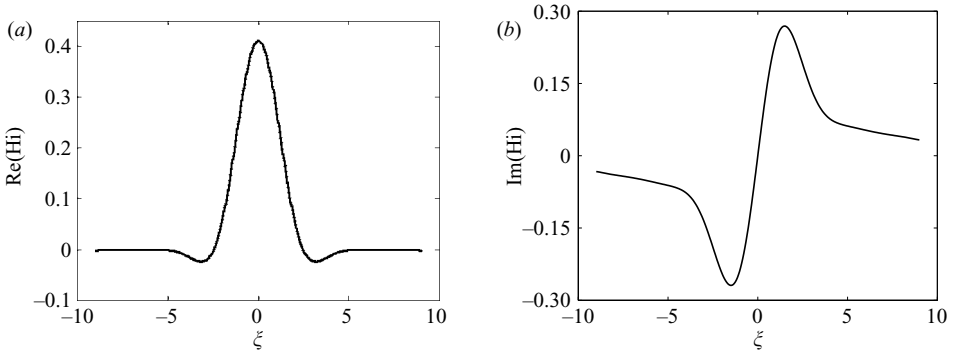

FIGURE 5. (*a*) Real part and (*b*) imaginary part of the critical-layer solution $\mathrm{Hi}(i\xi)$ versus ξ.

In the above expressions, the index c indicates values taken at r_c; Ω_{0c}' denotes the derivative of $\Omega_0(r)$ evaluated at r_c. Note that the critical-layer condition implies $\Omega_{0c} = 1/F$.

The equations for $\tilde{w}_1$ and $\tilde{\rho}_1$ are obtained by substituting (4.1) into (3.7) with $L = \infty$ and by considering the leading order in the power of $Re^{-1/3}$. This gives

$$\tilde{\rho}_1 = -\mathrm{i}\frac{\tilde{w}_1}{\Omega_{0c}}, \tag{4.3}$$

and

$$\left(1 + \frac{1}{Sc}\right)\frac{\mathrm{d}^2\tilde{w}_1}{\mathrm{d}\tilde{r}^2} - 2\mathrm{i}\Omega_{0c}'\tilde{r}\tilde{w}_1 = -r_c\Omega_{0c}^2. \tag{4.4}$$

Equation (4.4) is an inhomogeneous Airy equation. As explained in the Appendix of Drazin & Reid (1981), the solution of (4.4) which has the asymptotic behaviour (4.2*a*) is a 'balanced' generalized Airy function $B_k(K\tilde{r}, 1)$. This solution can also be expressed in terms of the Scorer's function $\mathrm{Hi}(\xi)$ (see Abramowitz & Stegun 1965, p. 448) which satisfies

$$\frac{\mathrm{d}^2\mathrm{Hi}}{\mathrm{d}\xi^2} - \xi\,\mathrm{Hi} = \frac{1}{\pi}, \tag{4.5a}$$

$$\mathrm{Hi}(\xi) \sim -\frac{1}{\pi\xi} \quad \text{as} \quad |\xi| \to \infty \quad \text{with} \quad |\arg(\xi)| > \frac{\pi}{3}. \tag{4.5b}$$

The axial velocity amplitude $\tilde{w}_1$ thus reads

$$\tilde{w}_1(\tilde{r}) = \frac{\pi r_c\Omega_{0c}^2}{|2\Omega_{0c}'|^{2/3}}\mathrm{Hi}\left(\mathrm{i}|2\Omega_{0c}'|^{1/3}\tilde{r}\right), \tag{4.6}$$

where we have implicitly assumed $Sc = \infty$. The same solution is also obtained when the diffusion of the density is taken into account by multiplying the Reynolds number by the factor $(1 + 1/Sc)^{-1}$.

Equation (4.3) tells us that the density amplitude $\tilde{\rho}_1$ exhibits the same variations as the axial velocity but with a $\pi/2$ phase shift. The Scorer function Hi with a complex argument has both a real and an imaginary part. Their variations with respect to its argument are shown in figure 5. These variations imply that contrarily to the inviscid outer solution, axial velocity and density are now expected to exhibit radial variations in all angular directions. In the vertical longitudinal plane ($\theta = 0$), the axial velocity varies as $\mathrm{Im}(\mathrm{Hi}(\mathrm{i}z))$ (figure 5*a*), while density varies as $\mathrm{Re}(\mathrm{Hi}(\mathrm{i}z))$ (figure 5*b*). In the

tilted longitudinal plane ($\theta = \pi/2$), it is the opposite. These typical variations do not depend on the vortex profile. However, the local value at the critical point r_c of the angular velocity and its radial derivative intervenes in the solution as scaling factors.

A few characteristic features of the solution in the vertical and tilted longitudinal planes can easily be provided. In the vertical longitudinal plane, the axial velocity has a jet-like profile. If we return to initial variables, the maximum velocity and the width at mid-height of the jet are given, respectively, by

$$w_{max}^{(jet)} = 0.81 \frac{r_c \Omega_{0c}^2}{|\Omega'_{0c}|^{2/3}} Re^{1/3} \tan\alpha, \tag{4.7a}$$

$$\delta^{(jet)} = \frac{2.3}{|Re\Omega'_{0c}|^{1/3}}. \tag{4.7b}$$

In the tilted longitudinal plane, the axial velocity has a shear-layer profile. The maximum absolute velocity and the distance between minimum and maximum velocities are, respectively,

$$w_{max}^{(shear)} = 0.56 \frac{r_c \Omega_{0c}^2}{|\Omega'_{0c}|^{2/3}} Re^{1/3} \tan\alpha, \tag{4.8a}$$

$$\delta^{(shear)} = \frac{2.65}{|Re\Omega'_{0c}|^{1/3}}. \tag{4.8b}$$

For instability considerations, it is also useful to compute the maximum vorticity of the jet and shear-layer profiles. They are given by

$$\omega_{max}^{(jet)} = 0.6 \frac{r_c \Omega_{0c}^2}{|\Omega'_{0c}|^{1/3}} Re^{2/3} \tan\alpha, \tag{4.9a}$$

$$\omega_{max}^{(shear)} = 0.74 \frac{r_c \Omega_{0c}^2}{|\Omega'_{0c}|^{1/3}} Re^{2/3} \tan\alpha. \tag{4.9b}$$

For large Reynolds numbers or important α, viscosity may not be the dominant effect in the critical layer. Nonlinearity may become more important. The importance of nonlinear effects in the viscous critical-layer can be estimated by introducing the viscous critical-layer solution into the governing equations (3.3) rewritten with the viscous critical-layer variable. Under the Boussinesq approximation, the radial velocity is deduced from (3.3*e*):

$$\tilde{u} = \alpha^2 Re^{1/3} \mathrm{Re}(\tilde{w}_1(\tilde{r})\, \mathrm{e}^{\mathrm{i}\theta}) + O(\alpha^2). \tag{4.10}$$

This expression permits us to show that the dominant convective term $\alpha w \partial_x$ simplifies with $u\partial_r$ such that the nonlinear terms in the (3.3*c*) for w are only $O(\alpha^3 Re^{2/3})$. These terms have to be compared to the viscous term $\Delta w/Re$ which is $O(\alpha)$. They are therefore negligible as long as $\alpha Re^{1/3} \ll 1$. In view of (4.7), this condition is equivalent to assuming that the amplitude of the axial velocity correction remains small. This condition is therefore not restrictive, as a fully nonlinear regime is expected for $O(1)$ amplitudes. It is worth mentioning that a different conclusion is reached in classical critical-layer studies (see for instance Maslowe 1986) where a nonlinear regime is obtained for small amplitudes of order $Re^{-2/3}$.

4.2. *Experimental measurements*

In this section, experimental measurements are compared to the theoretical profiles predicted by the viscous critical-layer analysis performed in the previous section.

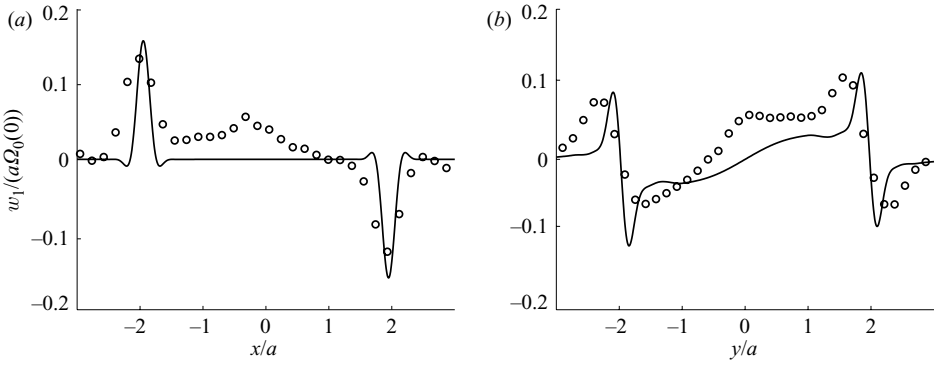

FIGURE 6. Theoretical (solid line) and experimental (circles) axial velocity profiles in two different longitudinal planes, (*a*) $\theta = 0$, (*b*) $\theta = \pi/2$. $Re = 560$, $F = 4.3$ and $\alpha = 0.07$ rad.

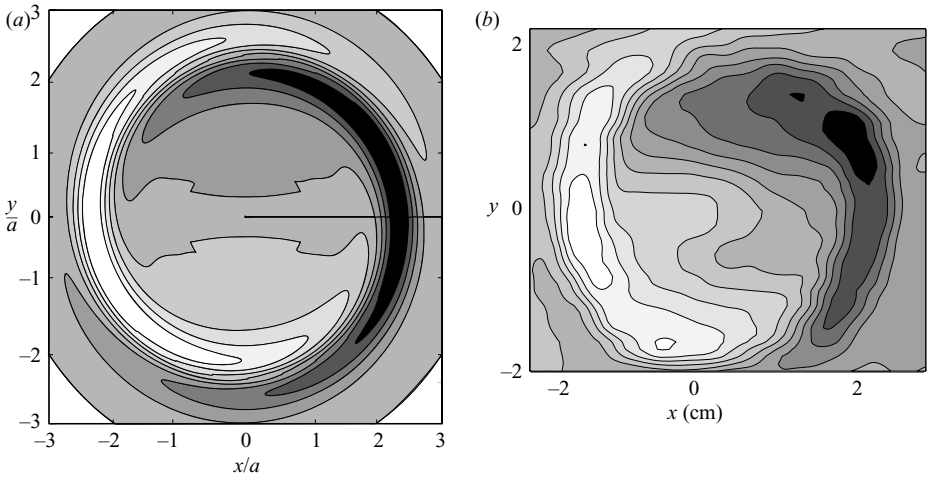

FIGURE 7. (*a*) Theoretical and (*b*) experimental axial velocity contours in a plane perpendicular to the vortex axis. $Re = 450$, $F = 3.2$ and $\alpha = 0.07$ rad.

As explained in § 2.1, visualizations and PIV measurements are made in two perpendicular longitudinal planes corresponding to the $\theta = 0$ and $\theta = \pi/2$ directions. Figure 6 shows the axial velocity profiles measured in these two planes. These profiles have been obtained by averaging the PIV measurements along the vortex axis. They are compared to theoretical profiles obtained from the critical-layer analysis for the experimental parameters. Both the jet and shear-layer profiles are observed in the critical-layer region in the $\theta = 0$ and $\theta = \pi/2$ planes, respectively, in qualitative agreement with the theory. The theory slightly underestimates the largest velocities, but it provides a good estimate of the widths of the jet and of the shear layer. However, note that between the two critical-layer regions, the experimental velocity profile is not as smooth as expected from the theory. We think that this is due to the strong diffraction of the luminous rays across the critical layer, which makes the PIV images blurred near the vortex centre and therefore less accurate. It is also worth mentioning that for the experimental data shown in figures 6 and 7, the parameter $\alpha Re^{1/3}$ which measures the strength of the nonlinear effects is not very small (it is

close to 0.5). The discrepancies in the critical layer could therefore also be due to nonlinear effects.

In figure 7, the isocontours of axial velocity in a plane perpendicular to the vortex axis are shown. The theoretical plot is obtained by using (4.1) and (4.6) for θ varying between 0 and 2π. The experimental plot has been obtained by constructing the data from measurements made in a longitudinal plane. We have used the properties that the vortex slowly moves away from the flap, so that the whole volume can be scanned by a fixed plane if this plane is placed perpendicular to the direction of displacement of the vortex. Measurements in this plane of the axial velocity have been made at a rate of 5 velocity fields per second. A total of 48 vertical velocity fields have been used to reconstruct the velocity field in figure 7(*b*). We have not been able to scan a larger volume because of lack of computer memory. Despite this limitation, the main features of the critical-layer solutions are clearly visible in the experimental measurements. Note, in particular, that the azimuthal dependency of the solution is reproduced well. This result, together with the good agreement observed for the radial profiles, validates the theoretical description in terms of the viscous critical-layer solution.

5. Conclusion

The dynamics of a vortex in a stratified fluid whose axis is slightly tilted with respect to the direction of stratification has been investigated theoretically and experimentally. For moderate Froude number $Fr \approx 1$–5 and large Reynolds numbers $Re = 240$–800, we have observed by using strioscopic visualizations and PIV measurements that strong density and axial flow variations are generated around the vortex near a particular radial location when the vortex is tilted by a few degrees. We have shown that this location corresponds to a critical point where the angular velocity of the vortex equals the Brunt–Väisälä frequency of the stratified medium.

A theoretical model has been constructed to describe these experimental observations. The critical point has been shown to correspond to a singularity of the linear inviscid correction to the vortex induced by tilting. A viscous critical-layer analysis has been performed to smooth the singularity and the critical-layer solution has been demonstrated to describe correctly the measured axial velocity profiles. The theory has also provided the main characteristics of the flow generated by tilting. In particular, we have shown that density variations can be deduced from axial velocity variations by a $\pi/2$ angular phase shift. The axial velocity variations exhibit a strong shear with a maximum vorticity of order $\alpha Re^{2/3}$ in the tilted longitudinal plane ($\theta = \pi/2$) and a jet-like structure in the vertical longitudinal plane ($\theta = 0$).

Note also that when the Froude number is smaller than 1, that is, the Brunt–Väisälä frequency is larger than any angular velocity of the vortex, there is no critical-point singularity and the linear inviscid solution (3.8) is expected to provide a description, at least for small angles, of the correction induced by tilting at any point.

It is important to remember that we have focused on small inclination angles and large Reynolds numbers. For large inclination angles, nonlinear effects should become important. For Froude numbers larger than 1, these effects are expected to appear first near the critical point where the correction amplitude is the largest. As explained above, the nonlinear transition should occur when $\alpha Re^{1/3}$ becomes large, that is when axial velocity corrections become $O(1)$.

The stability of the tilted stratified vortex solution we have obtained has not been addressed in this paper. Experimental observations do demonstrate that a

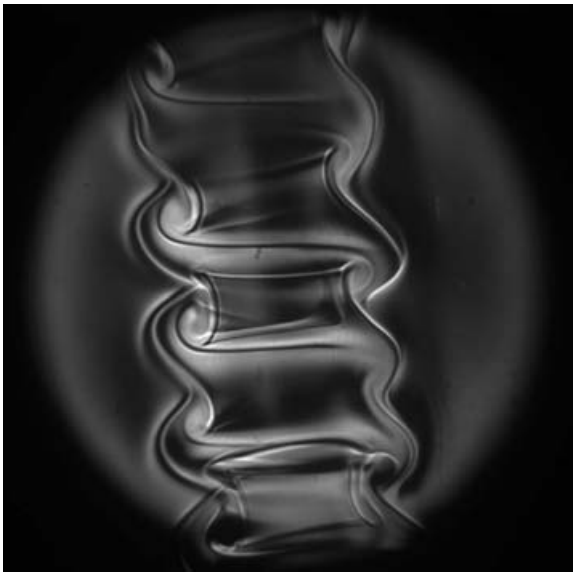

FIGURE 8. Instability of a stratified tilted vortex. Strioscopic visualization of the configuration shown in figure 3(*a*), 3.5 rotation periods later.

three-dimensional instability is indeed active under certain conditions. Figure 8 is a typical visualization by strioscopy of the density variations when instability is present. Coherent co-rotating vortical structures apparently develop in the critical-layer region. The characteristics of the critical-layer solution allow at least two possible instability mechanisms: the strong shear generated in the critical layer could be responsible for a Kelvin–Helmholtz-like instability whereas density variations coupled with the centrifugal force could be the source of a Rayleigh–Taylor instability. The comprehensive analysis of this instability is the subject of a companion paper (Boulanger *et al.* 2007).

We would like to stress that both the generation of the strong axial shear and density variation and its further destabilization occur for very small inclination angles. For this reason, we believe that this phenomenon is a generic feature affecting any intense vortex in a stratified fluid, provided its Froude number is larger than 1. The experiments performed by Cariteau (2005) have confirmed this point, as the same phenomenology has been observed although the vortex was not supposed to be tilted.

Appendix. Non-Boussinesq corrections

In this section, we provide the first-order correction to the tilted vortex solution induced by non-Boussinesq effects.

Outside the critical layer, the density and axial velocity perturbations are provided at leading order by (3.8*c*). These variations induced small perturbations of order $1/L$ for the radial and azimuthal velocity and the pressure. If we expand these components as

$$u_1 = \frac{u_1^{(1)} \sin\theta}{L} + O\left(\frac{1}{L^2}\right), \quad v_1 = \frac{v_1^{(1)} \cos\theta}{L} + O\left(\frac{1}{L^2}\right), \tag{A 1a, b}$$

$$p_1 = \frac{p_1^{(1)} \cos\theta}{L} + O\left(\frac{1}{L^2}\right), \tag{A 1c}$$

we obtain the following equations for $u_1^{(1)}$, $v_1^{(1)}$ and $p_1^{(1)}$:

$$\Omega_0 u_1^{(1)} - 2\Omega_0 v_1^{(1)} = -\frac{\mathrm{d}p_1^{(1)}}{\mathrm{d}r} + \frac{r^2\Omega_0^4}{\Omega_0^2 - F^{-2}}, \quad \Omega_0 v_1^{(1)} - \omega_0 u_1^{(1)} = -\frac{p_1^{(1)}}{r}, \tag{A 2a, b}$$

$$\frac{\mathrm{d}ru_1^{(1)}}{\mathrm{d}r} = v_1^{(1)}. \tag{A 2c}$$

This system can be reduced to a single equation for $u_1^{(1)}$:

$$\frac{\mathrm{d}^2u_1^{(1)}}{\mathrm{d}r^2} + \frac{3}{r}\frac{\mathrm{d}u_1^{(1)}}{\mathrm{d}r} - \left(\frac{3\Omega_0'}{r\Omega_0} + \frac{\Omega_0''}{\Omega_0}\right)u_1^{(1)} = -\frac{\Omega_0^3}{\Omega_0^2 - F^{-2}}. \tag{A 3}$$

Since $\Omega_0(r)$ is the solution to the homogeneous part of this equation, a general solution can be obtained by the variation of the constant as

$$u_1^{(1)} = -\Omega_0(r)\int_{c_1}^{r} \frac{1}{\Omega_0^2(x)x^3}\int_{c_2}^{x} \frac{\Omega_0^4(y)y^3}{\Omega_0^2(y) - F^{-2}}\,\mathrm{d}y\,\mathrm{d}x, \tag{A 4}$$

where c_1 and c_2 are constants. These constants may be different in the regions $(0, r_c)$ and $(r_c, +\infty)$. From the boundary conditions, we find that $c_1 = c_2 = 0$ in $(0, r_c)$ and $c_2 = +\infty$ in $(r_c, +\infty)$. The latter constant can be derived from a condition of matching with the critical-layer solution. The components $v_1^{(1)}$ and $p_1^{(1)}$ can be obtained using (A 2*b*, *c*) and similar arguments.

In the critical layer, pressure corrections and radial and azimuthal velocity corrections are also created by non-Boussinesq effects. These corrections can be calculated from (3.7) using the viscous radial variable $\tilde{r} = (r - r_c)Re^{1/3}$ and keeping first-order non-Boussinesq terms only. We find that the complex amplitude of pressure and radial and azimuthal velocities expand as

$$u_1 = \frac{\tilde{u}_1^{(1)}(\tilde{r})}{LRe^{1/3}}\,\mathrm{e}^{\mathrm{i}\theta} + O\left(\frac{1}{L^2}\right), \quad v_1 = \frac{\tilde{v}_1^{(1)}(\tilde{r})}{L}\mathrm{e}^{\mathrm{i}\theta} + O\left(\frac{1}{L^2}\right), \tag{A 5a, b}$$

$$p_1 = \frac{\tilde{p}_1^{(1)}(\tilde{r})}{L}\,\mathrm{e}^{\mathrm{i}\theta} + O\left(\frac{1}{L^2}\right), \tag{A 5c}$$

and satisfy the relations

$$\frac{\mathrm{d}\tilde{p}_1^{(1)}}{\mathrm{d}\tilde{r}} = -r_c\Omega_{0c}^2\tilde{\rho}_1, \quad \tilde{v}_1^{(1)} = -\frac{\tilde{p}_1^{(1)}}{r_c\Omega_{0c}}, \quad \frac{\mathrm{d}\tilde{u}_1^{(1)}}{\mathrm{d}\tilde{r}} = -i\frac{\tilde{v}_1^{(1)}}{r_c}, \tag{A 6a, b, c}$$

where $\tilde{\rho}_1$ is given by (4.3) and (4.6). Note that the non-Boussinesq corrections of order α may be smaller than Boussinesq corrections of order α^2. For instance, the radial velocity correction given by (4.10) is larger than the correction induced by non-Boussinesq effects as soon as $\alpha Re^{2/3}L$ is large.

REFERENCES

Abramowitz, M. & Stegun, I. A. 1965 *Handbook of Mathematical Functions*. Dover.

Billant, P. & Chomaz, J.-M. 2000 Experimental evidence for a new instability of a vertical columnar vortex pair in a strongly stratified fluid. *J. Fluid Mech.* **418**, 167–188.

Booker, J. R. & Bretherton, F. P. 1967 The critical layer for internal gravity waves in a shear flow. *J. Fluid Mech.* **27**, 513–539.

Boulanger, N., Meunier, P. & Le Dizès, S. 2007 Tilt-induced instability of a stratified vortex. *J. Fluid Mech.* (submitted).

Cariteau, B. 2005 Etude de la stabilité et de l'interaction de cyclones intenses en fluide stratifié. PhD thesis, Université Joseph Fourier, Grenoble.

Cariteau, B. & Flór, J.-B. 2003 Instability of a columnar vortex in stratified fluid. *Bull. Am. Phys. Soc.* **48** (10), 164.

Drazin, P. G. & Reid, W. H. 1981 *Hydrodynamic Stability*. Cambridge University Press.

Farmer, D., Pawlowicz, R. & Jiang, R. 2002 Tilting separation flows: a mechanism for intense vertical mixing in the coastal ocean. *Dyn. Atmos. Oceans* **36**, 43–58.

Garnier, E., Métais, O. & Lesieur, M. 1996 Instabilités primaire et secondaire d'un jet barocline. *C. R. Acad. Sci. Paris* B 323, 161–168.

Hopfinger, E. J. & van Heijst, G. J. F. 1993 Vortices in rotating fluids. *Annu. Rev. Fluid Mech.* **25**, 241–289.

Kerswell, R. R. 2002 Elliptical instability. *Annu. Rev. Fluid Mech.* **34**, 83–113.

Le Dizès, S. 2000 Non-axisymmetric vortices in two-dimensional flows. *J. Fluid Mech.* **406**, 175–198.

Lesieur, M., Métais, O. & Garnier, E. 2000 Baroclinic instability and severe storms. *J. Turb.* **1**, 1–17.

Leweke, T. & Williamson, C. H. K. 1998 Cooperative elliptic instability of a vortex pair. *J. Fluid Mech.* **360**, 85–119.

Maslowe, S. A. 1986 Critical layers in shear flows. *Annu. Rev. Fluid Mech.* **18**, 405–432.

Meunier, P. & Leweke, T. 2003 Analysis and optimization of the error caused by high velocity gradients in particle image velocimetry. *Exps. Fluids* **35**, 408–421.

Meunier, P. & Leweke, T. 2005 Elliptic instability of a co-rotating vortex pair. *J. Fluid Mech.* **533**, 125–159.

Neiman, P. J., Shapiro, M. A. & Fedor, L. S. 1993 The life cycle of an extratropical marine cyclone. Part ii: mesoscale structure and diagnostics. *Mon. Weather Rev.* **121**, 2177–2199.

Pawlak, G. MacCready, P., Edwards, K. A. & McCabe, R. 2003 Observations on the evolution of tidal vorticity at a stratified deep water headland. *Geophys. Res. Lett.* **30**, 2234.

Polavarapu, S. M. & Peltier, W. R. 1993 Formation of small-scale cyclones in numerical simulations of synoptic-scale baroclinic wave life cycles: secondary instability at the cusp. *J. Atmos. Sci.* **50**, 1047–1057.

J. Fluid Mech. (2008), *vol.* 596, *pp.* 1–20.
doi:10.1017/S0022112007009263 Printed in the United Kingdom

Tilt-induced instability of a stratified vortex

NICOLAS BOULANGER, PATRICE MEUNIER AND STÉPHANE LE DIZÈS

Institut de Recherche sur les Phénomènes Hors Équilibre, 49, rue F. Joliot-Curie, BP 146, F-13384 Marseille cedex 13, France

(Received 24 April 2007 and in revised form 31 August 2007)

This experimental and theoretical study considers the dynamics and the instability of a Lamb–Oseen vortex in a stably stratified fluid. In a companion paper, it was shown that tilting the vortex axis with respect to the direction of stratification induces the formation of a rim of strong axial flow near a critical radius when the Froude number of the vortex is larger than one.

Here, we demonstrate that this tilt-induced flow is responsible for a three-dimensional instability. We show that the instability results from a shear instability of the basic axial flow in the critical-layer region. The theoretical predictions for the wavelength and the growth rate obtained by a local stability analysis of the theoretical critical-layer profile are compared to experimental measurements and a good agreement is observed. The late stages of the instability are also analysed experimentally. In particular, we show that the tilt-induced instability does not lead to the destruction of the vortex, but to a sudden decrease of its Froude number, through the turbulent diffusion of its core size, when the initial Froude number is close to 1. A movie is available with the online version of the paper.

1. Introduction

The presence of intense and small vortices in geophysical flows is problematic for the oceanic and atmospheric models. These structures are unresolved when they become smaller than the mesh size used in the numerical codes, although they might influence the stability and mixing properties of larger scales. In this paper, we consider the stability and dynamics of such an intense vortex when its axis is slightly tilted with respect to the direction of stratification.

In the atmosphere, the large-scale structures (of a few thousand kilometres), created by the baroclinic instability, have a very small Froude number and a small Rossby number. These primary structures are mainly two-dimensional and not likely to be subject to a three-dimensional instability. However, they can be unstable with respect to two-dimensional instabilities (Nieman, Shapiro & Fedor 1993) and create secondary vortices with a smaller length scale (Polavarapu & Peltier 1993; Garnier, Métais & Lesieur 1996). These intense vortices can reach a size of 10 km, which gives a Rossby number of order 10 and a Froude number of order 1. This paper will focus on this type of intense vortex in which the stratified effects are comparable to advection, and in which the effect of the global rotation can be neglected. Our goal is to show that a weak inclination of the vortex can strongly affect its dynamics.

In oceans, vortices are often observed beyond coastal tips or behind islands. They are generated by the tide or strong currents. These vortices are usually inclined with respect to the stratification owing to the slope of coastal regions (see for instance Pawlak *et al.* 2003). When their Froude number is larger than 1, they will be subject

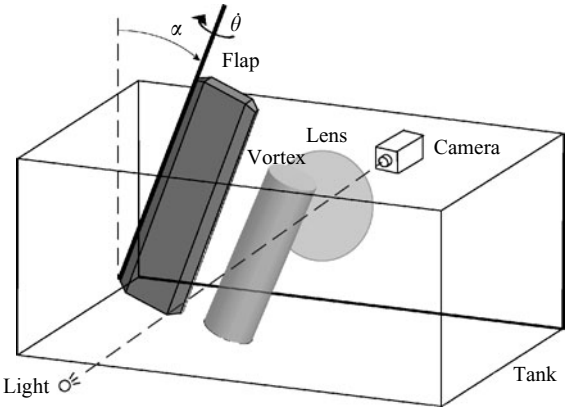

FIGURE 1. Schematic of the experimental set-up. The rotation of the grey plate around its upper edge generates a vortex inclined with respect to the vertical with an angle α. The light, lens and camera allow shadowgraph visualizations.

to the instability described in this paper. However, Coriolis effects might be expected for these vortices since the Rossby number is of order 1 here.

In Boulanger, Meunier & Le Dizès (2007), the structure of a tilted vortex was studied experimentally and theoretically in the limit of small inclination angles. When the Froude number is larger than 1, a critical layer was shown to appear at the radius where the angular velocity of the vortex equals the Brunt–Väisälä frequency. In the viscous regime, this creates a strong vertical motion of order $Re^{1/3}$ in a layer of thickness scaling as $Re^{-1/3}$.

As far as we know, no stability analysis of such a tilted vortex has been performed. However, the effect of a stable stratification on various instabilities has been extensively studied. In the case of several vortices, the stratification stabilizes the elliptic instability (Kerswell 2002) and transforms the Crow instability (Crow 1970) in a so-called zig-zag instability (Billant & Chomaz 2000). For a single vortex, the two-dimensional shear instability and the centrifugal instability are not affected by a stable stratification in the inviscid limit (Hopfinger & van Heijst 1993). However, Cariteau & Flór (2003) reported a new columnar instability of a stratified vortex, which creates some vertical motion in a thin rim around the vortex and leads to a three-dimensional instability. Although they did not add any intentional tilting of the vortex (Cariteau 2005), we will show that this instability is probably due to a weak misalignment of the vortex with the stratification. This previous experimental evidence indicates that this instability is very strong and can be effective even in the presence of very weak tilt angles.

The paper will be organized as follows. In § 2, we describe the experimental set-up and the two-dimensional base flow of a tilted vortex. In § 3, we show experimental evidence of this new instability, followed by a local theory in § 4. The late stages of the instability are considered in § 5, before the conclusion in § 6.

2. Experimental set-up and base flow

2.1. *Experimental details*

The experimental set-up (figure 1) is explained in detail in Boulanger *et al.* (2007) and only the main features are recalled here. The experiments are performed in a 150 cm

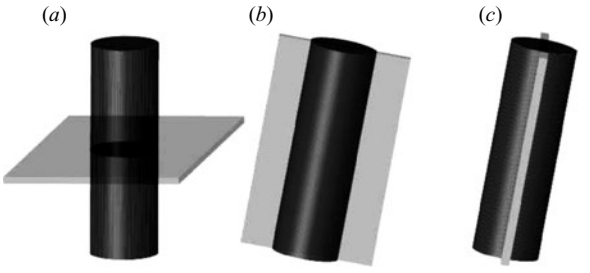

FIGURE 2. Location of PIV measurement planes. (*a*) Transverse plane (*b*) vertical longitudinal plane $\theta = 0$, and (*c*) tilted longitudinal plane, $\theta = \pi/2$.

long, 75 cm wide and 50 cm high Plexiglas tank, filled with a linearly stratified fluid (made using the two-tank method). The density gradient is deduced from density measurements of small samples of fluid every 5 cm, using a densitometer Anton Paar DMA 35N with an accuracy of 10^{-4} kg l^{-1}. By varying the effective depth of fluid between 20 cm and 45 cm and the maximal density between 1.1 and 1.19 kg l^{-1}, we have been able to obtain a Brunt–Väisälä frequency ranging from 1.5 to 3 rad s^{-1}.

The vortex is created by rotating impulsively a 10×60 cm^2 aluminium flap in the fluid initially at rest, using a computer controlled step-motor. This flap motion generates a two-dimensional shear layer around the flap which detaches at the sharpened edge of the flap, and rolls up into a very laminar vortex. The motion profile of the flap was chosen carefully to obtain a nearly Gaussian vortex and was defined by imposing the angular velocity of the flap as a function of its angle as:

$$\dot{\Theta} = \dot{\Theta}_{max} \frac{0.42}{\Theta + 0.017} [1 + \exp(-(\Theta/0.26)^{5/4})]. \tag{2.1}$$

It consists of a rapid acceleration of the flap, followed by a gradual slow-down up to the angle of $\pi/2$ rad. The circulation of the vortex is varied by modifying the maximum angular velocity $\dot{\Theta}_{max}$ between 0.01 and 0.5 rad s^{-1}. The inclination of the vortex is obtained by tilting the flap with respect to the vertical in the initial plane of the flap: it was varied in the range 0 to 0.38 rad.

Particle image velocimetry (PIV) measurements of velocity fields were obtained by seeding the tank with Sphericel hollow glass spheres 110 P8 (Potter Industries), whose diameter ranges from 11 to 18 μm and whose density is approximately 1.1. The particles are illuminated by a luminous sheet of 3–5 mm thickness, created by a continuous 5 W argon-ion laser. Image pairs are recorded by a digital PIV camera (Kodak Megaplus Es 4.0) with a resolution of 2048×2048 pixels and treated by a cross-correlation algorithm developed for flows with high-velocity gradients at the laboratory (Meunier & Leweke 2003). PIV measurements have been made in three different planes (figure 2). The first one is perpendicular to the vortex axis and provides the horizontal characteristics of the initial vortex. The two other planes correspond to two orthogonal longitudinal planes, one plane being vertical ($\theta = 0$) and the other being tilted ($\theta = \pi/2$). These instantaneous two-dimensional velocity fields are extremely useful for the study of the instability since they permit us to follow the evolution of the vortex in time, which would be impossible using a two-dimensional reconstruction of point measurements.

Shadowgraph visualizations were also carried out, to observe the two-dimensional and three-dimensionl spatial distribution of density inside the vortex. For this purpose, the stratified fluid is illuminated by a large beam of parallel light, created by an intense

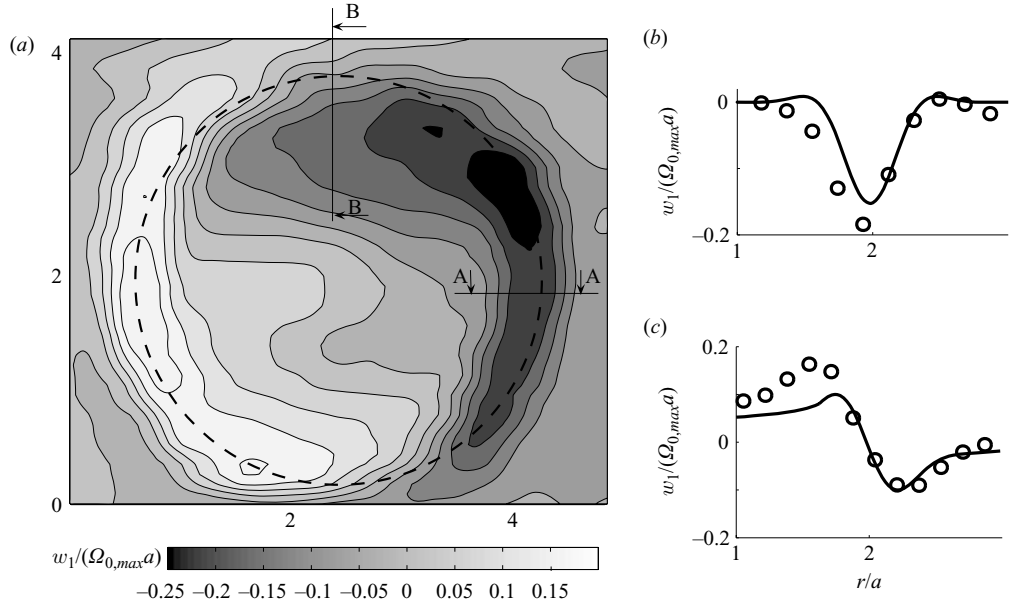

FIGURE 3. (*a*) Theoretical contours of the axial velocity of a tilted vortex in a transverse plane. (*b*, *c*) Theoretical (solid line) and experimental (circles) axial velocity profiles in two different longitudinal planes, (*b*) section A–A: $\theta = 0$, (*c*) section B–B: $\theta = \pi/2$. (*a*) The dashed line indicates the location of the critical layer. $Re = 450$, $F = 3.2$, $\alpha = 0.07$ rad.

light placed behind a small diaphragm located 2 m away from the tank. By placing a large lens (of diameter 30 cm and of focal distance 50 cm) behind the tank, it is thus possible to obtain an image of the density distribution. These images are recorded by a 2000×2000 pixel greyscale camera located behind the focal point of the lens. A small disk of 1 mm diameter was positioned exactly at the focal point of the lens, which enhances the contrast of the images.

2.2. *Characteristics of the tilted vortex*

The vortex is completely defined by its profile of angular velocity, which is very close in our experiments to the profile of a Gaussian (Lamb–Oseen) vortex:

$$\Omega_0(r) = \frac{v_\theta(r)}{r} = \frac{\Gamma}{2\pi r^2}(1 - \exp(-r^2/a^2)). \tag{2.2}$$

In our experiments, the circulation Γ was varied between 17 and 42 $\mathrm{cm^2\,s^{-1}}$. The core size a is slowly varying with time between 0.9 and 1.1 cm owing to viscous effects, but this dependency can be neglected on the time scale of the instability we shall describe below.

In Boulanger *et al.* (2007), it was shown that tilting the vortex with respect to the direction of stratification with an angle α creates a critical layer at the radius r_c where the angular velocity of the vortex $\Omega_0(r)$ is equal to the Brunt–Väisälä frequency. This critical layer is observed for moderate Froude numbers larger than 1 only, such that the critical radius r_c exists ($\Omega_0(r = 0) > N$) and is located not too far from the vortex centre ($\Omega_0(r = 0) < 5N$).

The axial velocity field created by tilting the vortex is plotted in figure 3(*a*) and compared with the viscous critical-layer profiles in figure 3(*b*, *c*). These figures are similar to those presented in Boulanger *et al.* (2007) with a minor modification to

the velocity profiles: they have been enlarged around the critical layer. This velocity field exhibits a complex spatial structure: in the vertical longitudinal plane ($\theta = 0$), the axial velocity has a jet-like profile (see figure 3*b*); in the tilted longitudinal plane, it looks like a shear layer (see figure 3*c*). There is a good agreement between theory and experiment on the structure and amplitude of the velocity field, although there are some large uncertainties (of the order of 50%) for $r < r_c$ owing to the deformation of the images by a strong refraction at the critical layer. The theory predicts that the size of the critical layer scales as $Re^{-1/3}$ and the amplitude of the density and the vertical velocity scale as $\alpha Re^{1/3}$. This leads to a scaling of the azimuthal vorticity as $\alpha Re^{2/3}$.

In the following, we will non-dimensionalize lengths by the vortex core size a. Moreover, the inverse of the angular velocity at the centre of the vortex $\Omega_0(r=0) = \Gamma/2\pi a^2$ will be used as the time scale of the flow. This leads to non-dimensionalize velocities by $\Gamma/2\pi a$. Finally, we will non-dimensionalize densities by the density of the fluid ρ_f at $z = 0$. Our system is thus characterized by five non-dimensional parameters. The inclination angle α is varied from 0 to 0.38 rad. The Reynolds number $Re = \Gamma/(2\pi\nu)$ (ν being the kinematic viscosity) is varied between 160 and 800. The Froude number $F = \Gamma/(2\pi a^2 N)$ ranges from 1.5 to 4.3. The Schmidt number $Sc = \kappa/\nu$ is close to 700. The last parameter L compares the vertical stratification length to the vortex core size: $L = \rho/(a\partial\rho/\partial z)$. In our experiments, this Boussinesq parameter ranges between 100 and 400, which justifies the use of the Boussinesq approximation obtained by assuming L infinite.

3. Three-dimensional instability

3.1. *Dye visualizations*

For high Reynolds numbers, the vortex was found to be unstable with respect to a three-dimensional perturbation. The time-sequence of figure 4 shows the temporal evolution of the tilted vortex by shadowgraph visualizations. The vortex is viewed from the side perpendicularly to the tilting plane. This view reveals the density structures in the vertical plane ($\theta = 0$). The vortex is thus tilted with an angle of 0.07 rad on the images.

At the beginning, just after the end of the flap motion (figure 4*a*), the vortex is cylindrical and contains two strips created by the critical layer. At $t = 1$ s, these strips are subject to a sinusoidal undulation (figure 4*b*), which breaks the invariance along the axis of the vortex. This perturbation is initially confined within the strips. At later stages (figure 4*c*, *d*), the perturbation grows and becomes visible all around the vortex. This is due to an increase of the contrast associated with the increase of $\partial^2\rho/\partial z^2$ and not to a propagation of the perturbation around the vortex, as is attested by other visualizations made from different view angles. The undulation of the two strips is then amplified and gives birth to structures characteristic of vortices rotating in the clockwise direction (figure 4*d*). The two alleys of vortices alternate on each side of the vortex and the vortex centres are linked by two strips which create a zigzag-like structure. This perturbation thus looks like a secondary spiral vortex which is rolled-up around the tilted vortex in a helical mode. However, this is not the case, because it would create vortices of opposite sign on each side of the vortex. On the contrary, it can be seen clearly in figure 4(*d*) that the vortices are clockwise (negative vorticity in this plane) on both sides of the vortex. It is thus a perturbation which grows almost independently on both sides of the vortex. All of this suggests that the instability is localized in the critical layer, and not influenced by the global

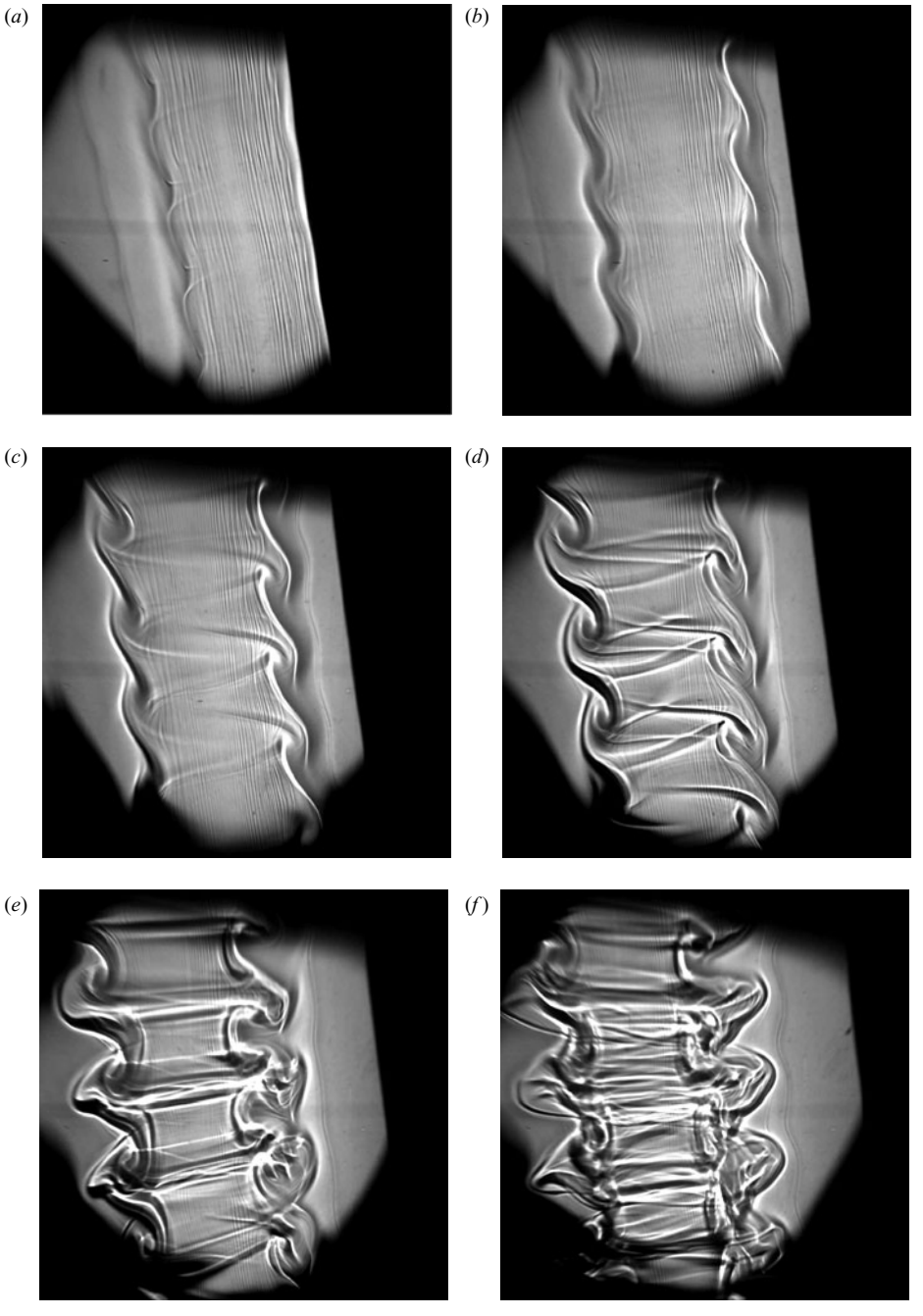

FIGURE 4. Shadowgraph sequence of the vortex instability in a vertical longitudinal plane ($\theta = 0$). The time interval is 1.1 rotation period. $F = 3$, $Re = 720$, $\alpha = 0.07$ rad. A movie of the same instability, obtained for slightly lower Reynolds and Froude numbers, is available with the online version of the paper.

structure of the vortex. These shadowgraph visualizations are very similar to the pictures presented by Cariteau (2005), and we suspect that it is the same instability that they observed although they did not tilt the generating plate.

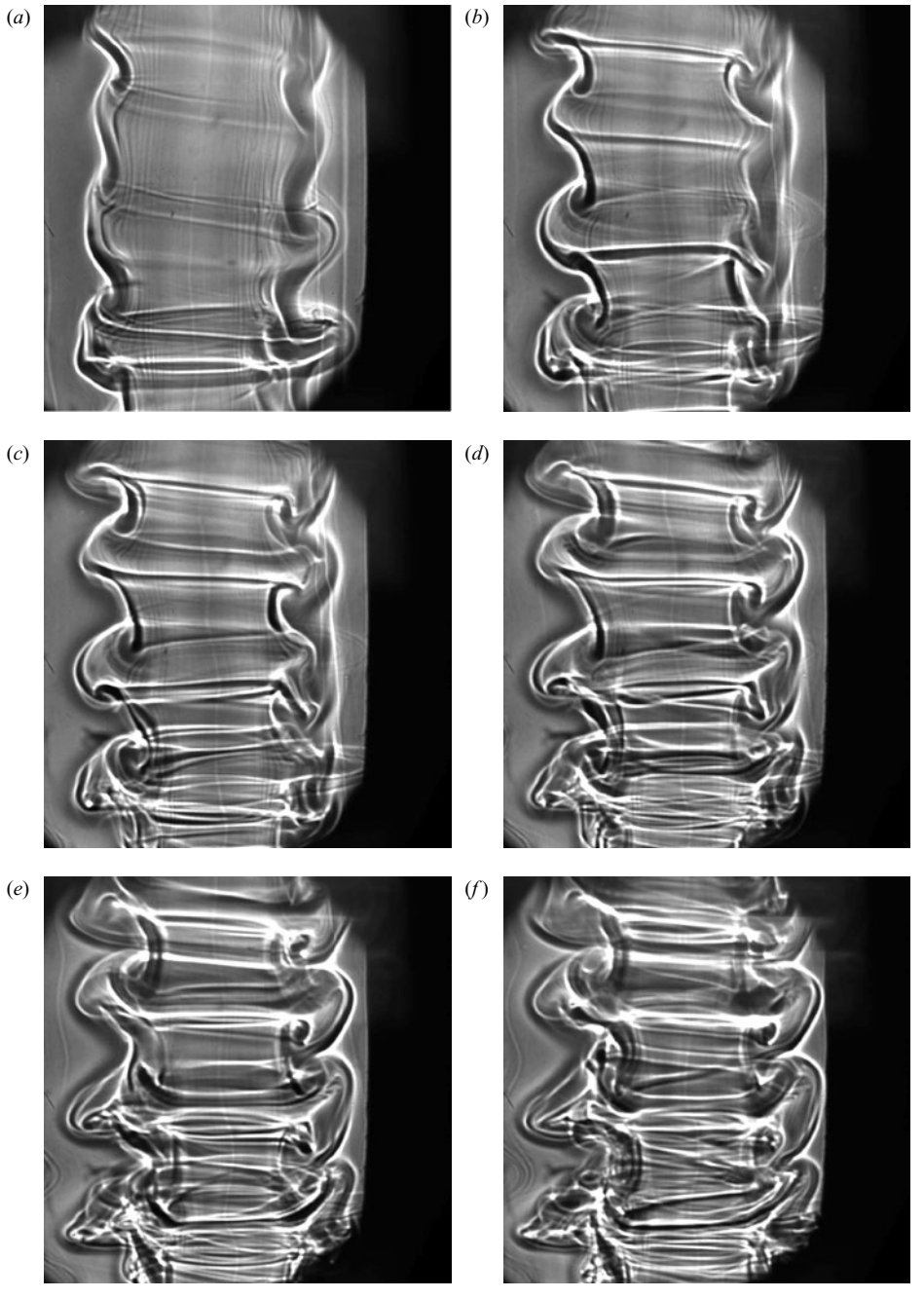

FIGURE 5. Shadowgraph sequence of the vortex instability in a tilted longitudinal plane ($\theta = \pi/2$). The time interval is 1.1 rotation period. $F = 3$, $Re = 720$, $\alpha = 0.07$ rad.

At late stages, the instability saturates and the co-rotating vortices finally break down, leading to a strong mixing, in which some coherent structures are still visible.

Figure 5 shows the temporal evolution of the vortex in the tilted plane ($\theta = \pi/2$). Although the perturbation starts as an undulation of the critical layer (figure 5*a*) as in figure 4, the perturbation is then rather different. It rapidly creates an alley of

alternate vortices on each side of the vortex (figures 5*b–d*). The instability thus looks like a centrifugal instability, although the vortex is stable with respect to the Rayleigh criterion. In fact, the structure of the instability is very similar to a von Kármán vortex street on each side of the vortex. This could be related to the presence of a jet in the critical layer.

In this section, the shadowgraph visualizations were used to reveal the spatial structure of the density field from which the velocity field was inferred. However, it is not clear that the density field is simply advected by the velocity field, and there might be a three-dimensional perturbation of the density without any perturbation of the velocity field. To confirm the validity of the previous arguments, we provide in the following sections some PIV measurements, which give directly the velocity field in these longitudinal planes.

3.2. *PIV measurements*

The time-sequence of figure 6 shows the temporal evolution of the azimuthal vorticity in the tilted plane (i.e. $\theta = \pi/2$) obtained by PIV measurements. In this plane, the tilted vortex creates two critical layers on each side of the vortex, containing some strong negative (black) vorticity (see figure 6*a*). This corresponds to the vorticity of the shear layer created by tilting (see figure 3*c*). In fact, each critical layer is made of one band of strong negative vorticity, surrounded by two smaller bands of weak positive vorticity which are hardly visible on figure 6(*a*, *b*). At the vortex centre, the vorticity field contains large errors, which are due to the presence of many spurious vectors. This is caused by the images being blurry at the vortex centre owing to large deviations of the luminous rays by the critical layer.

The perturbation appears at first as a periodic modulation of the negative vorticity layers on both sides of the vortex (figure 6*b*, *d*). The instability does not induce any motion in the vortex core: it is clearly localized in the critical layer. The perturbation then leads to the formation of co-rotating vortices of negative vorticity (figure 6*e*, *f*). The wavelength is similar on both sides and the two alleys of vortices are alternate, as was observed on the shadowgraph visualizations of figure 4. The positive layers are only slightly modified by the perturbation: they split into weak vortices under the influence of the negative-layer evolution. It can be noted that these vortices are created extremely rapidly, in approximately half a rotation period $2\pi/\Omega_0(r)$ between figures 6(*b*) and 6(*e*).

The presence of an alley of co-rotating vortices is characteristic of the shear instability leading to Kelvin–Helmholtz billows at late stages. This explains why the vortices rotate in the same direction on both sides of the vortex in the visualizations of figure 4. It is thus a possible explanation of the instability. However, it is curious to see that the structure observed on the velocity field of the tilted plane ($\theta = \pi/2$) is observed on the visualizations of the vertical plane ($\theta = 0$) and not on the visualizations of the tilted plane. In fact, the density structures are advected by the velocity field and the amplitude of the density perturbation is thus maximal at the end of the forcing by the velocity perturbation, i.e. a quarter of a turn later.

At late stages, the growth stops, and the structures lose their coherence, leading to a partial reformation of the vorticity layers (see figure 6*g*). This non-uniform vorticity layer sometimes creates again some isolated vortices, but the flow is found to be less organized and very turbulent.

Figure 7 shows the azimuthal vorticity obtained by PIV measurements in the vertical plane (i.e. $\theta = 0$). The temporal evolution of the vorticity could not be obtained because the vortex slowly moves inside the water tank and a fixed measurement plane

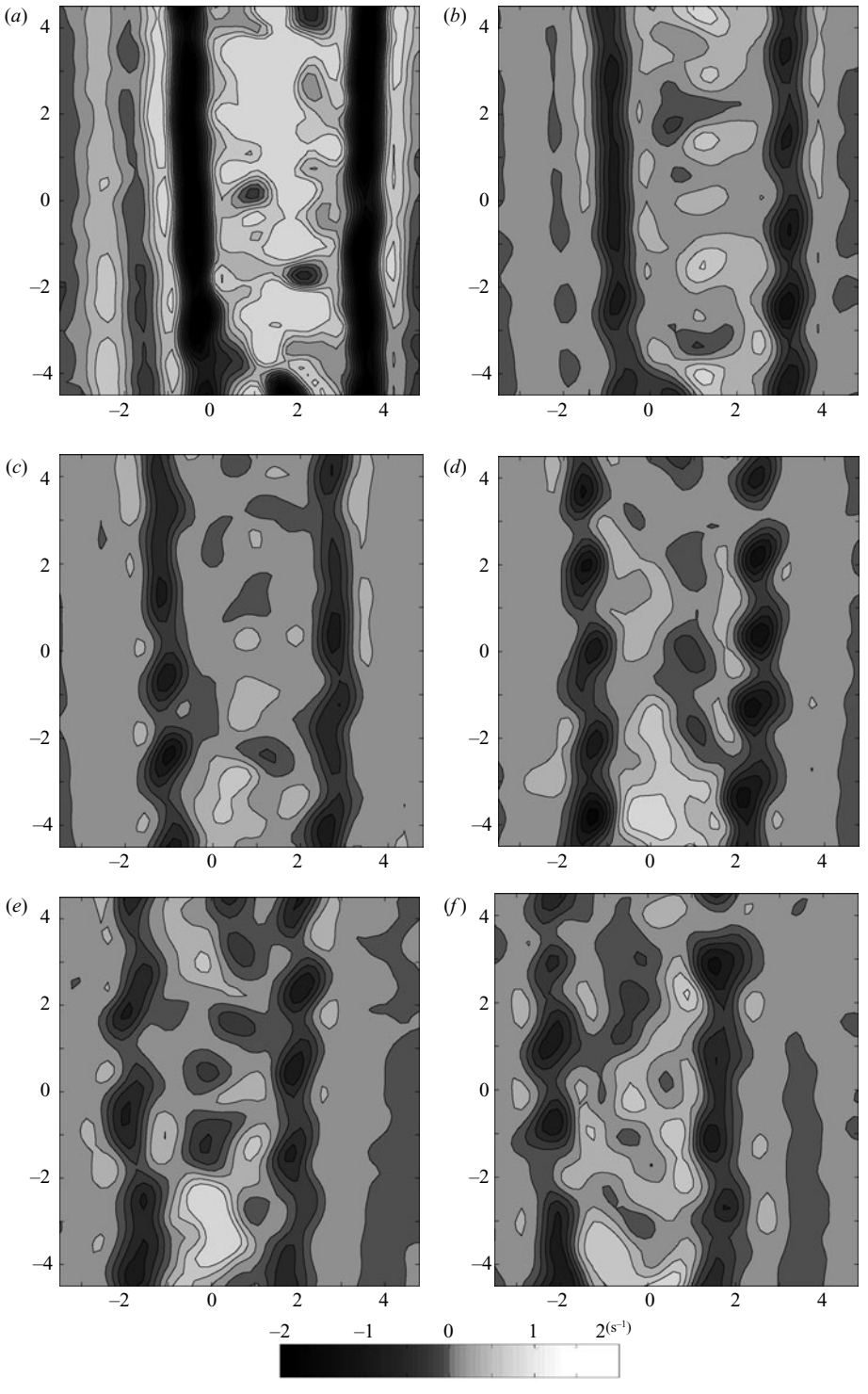

FIGURE 6. PIV sequence of the instantaneous azimuthal vorticity field in a tilted longitudinal plane ($\theta = \pi/2$), starting 10 rotation periods after the flap motion. The time interval is 0.5 rotation period. $F = 2.1$, $Re = 560$, $\alpha = 0.12$ rad.

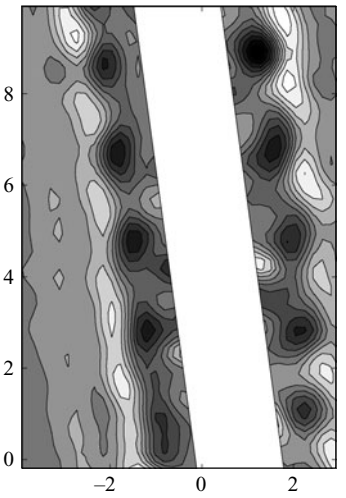

FIGURE 7. PIV measurement of the instantaneous azimuthal vorticity field in a vertical longitudinal plane ($\theta = 0$), approximately 12 rotation periods after the flap motion. $F = 2.1$, $Re = 560$, $\alpha = 0.12$ rad.

contains the axis of the vortex only at one instant in time. The centre of the vortex was masked because it contains many spurious vectors (as in figure 6), owing to the refraction of the luminous rays when they cross the critical layer.

In this vertical plane, the tilted vortex creates a jet on each side of the vortex. Each jet creates two vertical layers of opposite vorticity. Figure 7 shows that the perturbation is made of a periodic modulation of each vorticity layer, which creates an alley of alternate counter-rotating vortices. This is characteristic of the sinuous instability of a jet. This structure can be linked to the structure of the perturbation observed on the shadowgraph visualization of figure 5. However, it is again surprising to see that these structures are not observed in the same plane for the velocity field. As in the case of the Kelvin–Helmholtz instability, it can be explained by the density being advected by the vortex.

3.3. *A local instability*

The dye visualizations and the PIV measurements have shown that the instability is localized in the critical layer and that it does not modify the vortex core. Moreover, this instability appears rapidly compared to the advection time around the vortex. These two arguments mean that the instability is linked to the local properties of the critical layer rather than to the global structure of the vortex itself. This will justify the local stability analysis of the critical layer in the next section. Figure 8 shows the structure of the instability. The velocity profiles are plotted for each plane inside the critical layer and the secondary vortices are represented by spirals as would be obtained by the roll-up of a line of dye.

The critical layer has a complex structure and several instabilities are thus candidates. In the tilted plane ($\theta = \pi/2$), the velocity profile contains a strong shear and is subject to the Kelvin–Helmholtz instability. In the vertical plane ($\theta = 0$), the velocity profile is a jet-like profile and is subject to jet instabilities. Moreover, in the tilted plane, there is a strong density layer which, added to the centrifugal force, could lead to a Rayleigh–Taylor instability. This last instability would also lead to an undulation of the critical layer, as in the visualizations.

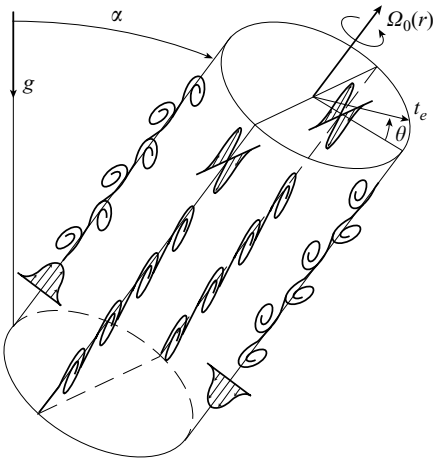

FIGURE 8. Schematic of the tilt-induced instabilities occurring in the critical layer of the vortex: a shear instability for $\theta = \pm\pi/2$ and a jet instability for $\theta = 0$ and $\theta = \pi$.

In order to determine which mechanism is responsible for the instability observed in the tilted vortex, we must evaluate the growth rate associated with each of these possible instabilities. Moreover, it is also important to quantify in which conditions the local instability can be sufficiently strong not to be affected by the mean angular advection around the vortex. The next section addresses these issues theoretically.

4. Stability analysis of the viscous critical-layer solution

In this section, we provide a theoretical analysis of the dynamics of the tilted vortex. As demonstrated in Boulanger *et al.* (2007), it is convenient to analyse the flow with new coordinates where x is modified into $x - \tan\alpha z$, and y and z are unchanged in such a way that in each horizontal plane $z = \text{const}$ the point $x = y = 0$ corresponds to the vortex centre. With these variables, the governing equations for the velocity $\boldsymbol{u} = (u, v, w)$, pressure p and density ρ are in cylindrical coordinates:

$$\frac{\mathrm{D}u}{\mathrm{D}t} - \frac{v^2}{r} - w\tan\alpha\frac{\partial u}{\partial x} - w\frac{\tan\alpha\sin\theta}{r}v = -\frac{1}{\rho}\frac{\partial p}{\partial r} + \frac{1}{Re}(\Delta\boldsymbol{u})_r, \tag{4.1a}$$

$$\frac{\mathrm{D}v}{\mathrm{D}t} + \frac{uv}{r} - w\tan\alpha\frac{\partial v}{\partial x} + w\frac{\tan\alpha\sin\theta}{r}u = -\frac{1}{\rho r}\frac{\partial p}{\partial\theta} + \frac{1}{Re}(\Delta\boldsymbol{u})_\theta, \tag{4.1b}$$

$$\frac{\mathrm{D}w}{\mathrm{D}t} - w\tan\alpha\frac{\partial w}{\partial x} = -\frac{1}{\rho}\frac{\partial p}{\partial z} + \frac{\tan\alpha}{\rho}\frac{\partial p}{\partial x} - \frac{L}{F^2} + \frac{1}{Re}\Delta w, \tag{4.1c}$$

$$\frac{\mathrm{D}\rho}{\mathrm{D}t} - w\tan\alpha\frac{\partial\rho}{\partial x} = 0, \tag{4.1d}$$

$$\frac{1}{r}\frac{\partial(ru)}{\partial r} + \frac{1}{r}\frac{\partial v}{\partial\theta} + \left(\frac{\partial}{\partial z} - \tan\alpha\frac{\partial}{\partial x}\right)w = 0, \tag{4.1e}$$

with

$$\frac{\mathrm{D}}{\mathrm{D}t} = \left(\frac{\partial}{\partial t} + u\frac{\partial}{\partial r} + \frac{v}{r}\frac{\partial}{\partial\theta} + w\frac{\partial}{\partial z}\right) \tag{4.2a}$$

$$\frac{\partial}{\partial x} = \cos\theta\frac{\partial}{\partial r} - \frac{\sin\theta}{r}\frac{\partial}{\partial\theta}\ . \tag{4.2b}$$

The problem is characterized by the angle α, the Froude number F, the length ratio L and the Reynolds number Re. The diffusion of density has been neglected. Note that the gravity g is given by L/F^2 in term of these parameters.

As shown in Boulanger *et al.* (2007), a basic flow solution can be obtained in the limit of small α, large Reynolds numbers and large L in the form

$$(u_b, v_b, w_b, p_b, \rho_b) = (0, V_0(r), 0, p_0(r,z), \rho_0(r,z)) + \alpha \left(\frac{u_1}{L}, \frac{v_1}{L}, w_1, \frac{p_1}{L}, \frac{\rho_1}{L}\right) \mathrm{e}^{\mathrm{i}\theta} + c.c., \tag{4.3}$$

where the first term represents an axisymmetric vortex, and the second term the first-order corrections in α and $1/L$ induced by tilting. This solution is singular at the critical point r_c defined by $\Omega_0(r_c) = 1/F$, and a specific approximation with a local viscous variable $\bar{r} = Re^{1/3}(r - r_c)$ was constructed in Boulanger *et al.* (2007) to describe the solution near this point. The viscous critical-layer solution was shown to exhibit strong shear which is believed to be responsible for the instability observed in the experiments. For this reason, we now perform a local stability analysis of the critical-layer solution.

As shown in Boulanger *et al.* (2007), the basic flow expands in the critical layer as:

$$u_b = \frac{\alpha}{LRe^{1/3}} \mathrm{Re}[\bar{u}_1(\bar{r}, \theta)], \tag{4.4a}$$

$$v_b = V_{0c} + \frac{\bar{r} V'_{0c}}{Re^{1/3}} + \frac{\alpha}{L} \mathrm{Re}[\bar{v}_1(\bar{r}, \theta)], \tag{4.4b}$$

$$w_b = \alpha Re^{1/3} \mathrm{Re}[\bar{w}_1(\bar{r}, \theta)], \tag{4.4c}$$

$$p_b = \frac{\rho_{0c} L^2 \mathrm{e}^{-z/L}}{F^2} \left(1 + \frac{\alpha F^2}{L^3} \mathrm{Re}[\bar{p}_1(\bar{r}, \theta)]\right), \tag{4.4d}$$

$$\rho_b = \rho_{0c} \mathrm{e}^{-z/L} \left(1 + \frac{\alpha Re^{1/3}}{L} \mathrm{Re}[\bar{\rho}_1(\bar{r}, \theta)]\right), \tag{4.4e}$$

where we have kept the first-order terms in α and $1/L$ only. In these expressions, V_{0c} and V'_{0c} are defined as the azimuthal velocity and its derivative at r_c. The functions $\bar{u}_1$, $\bar{v}_1$, $\bar{p}_1$ and $\bar{\rho}_1$ are connected to the critical-layer solution

$$\bar{w}_1(\bar{r}, \theta) = \frac{\pi r_c}{F^2 |2\Omega'_{0c}|^{2/3}} \mathrm{Hi}\left(\mathrm{i}|2\Omega'_{0c}|^{1/3} \bar{r}\right) \mathrm{e}^{\mathrm{i}\theta}, \tag{4.5}$$

via the relations

$$\bar{\rho}_1 = -\mathrm{i} F \bar{w}_1, \tag{4.6a}$$

$$\frac{\mathrm{d}\bar{p}_1}{\mathrm{d}\bar{r}} = -\frac{r c \bar{\rho}_1}{F^2}, \tag{4.6b}$$

$$\bar{v}_1 = -\frac{F \bar{p}_1}{r_c}, \tag{4.6c}$$

$$\frac{\mathrm{d}\bar{u}_1}{\mathrm{d}\bar{r}} = -\mathrm{i}\frac{\bar{v}_1}{r_c}. \tag{4.6d}$$

The function Hi appearing in (4.5) is the Scorer's function (see Abramowitz & Stegun 1965, p. 448) and Ω'_{0c} is the derivative of the angular velocity at r_c. The theoretical profiles plotted in figures 3(*b*) and 3(*c*) for $\theta = 0$ and $\theta = \pi/2$ correspond to the real part and imaginary part of (4.5), respectively.

As the base flow varies on a $Re^{-1/3}$ radial length scale in the critical layer, it is natural to search three-dimensional perturbations varying on a similar axial length scale and

thus to introduce a new axial variable $\bar{z} = Re^{1/3} z$. However, the angular variation of the base flow is weak and no high azimuthal wavenumber perturbation has been observed in the experiments. Therefore, we shall consider only small azimuthal wavenumber perturbations.

In the limit of small α, large Reynolds numbers and large length ratio L, the perturbation equations obtained by linearizing the system (4.1*a*)–(4.1*e*) around the local base flow (4.4*a*)–(4.4*e*) can then be reduced into the following form:

$$\left(\frac{\partial}{\partial t} + \frac{1}{F}\frac{\partial}{\partial \theta} + \mathrm{Re}(\bar{w}_1)\alpha Re^{2/3}\frac{\partial}{\partial \bar{z}}\right) u - 2\frac{v}{F} = -\frac{\partial p}{\partial \bar{r}}, \tag{4.7a}$$

$$\left(\frac{\partial}{\partial t} + \frac{1}{F}\frac{\partial}{\partial \theta} + \mathrm{Re}(\bar{w}_1)\alpha Re^{2/3}\frac{\partial}{\partial \bar{z}}\right) v + \omega_{0c} u = 0, \tag{4.7b}$$

$$\left(\frac{\partial}{\partial t} + \frac{1}{F}\frac{\partial}{\partial \theta} + \mathrm{Re}(\bar{w}_1)\alpha Re^{2/3}\frac{\partial}{\partial \bar{z}}\right) w + \alpha Re^{2/3}\mathrm{Re}(\bar{w}_1')u = -\frac{\partial p}{\partial \bar{z}} - \frac{\rho}{F^2}, \tag{4.7c}$$

$$\left(\frac{\partial}{\partial t} + \frac{1}{F}\frac{\partial}{\partial \theta} + \mathrm{Re}(\bar{w}_1)\alpha Re^{2/3}\frac{\partial}{\partial \bar{z}}\right) \rho + \alpha Re^{2/3}\mathrm{Re}(\bar{\rho}_1')u - w = 0, \tag{4.7d}$$

$$\frac{\partial u}{\partial \bar{r}} + \frac{\partial w}{\partial \bar{z}} = 0\ . \tag{4.7e}$$

The $O(Re^{-1/3})$ viscous forces, the $O(1/L)$ non-Boussinesq effects and the $O(\alpha Re^{1/3})$ advection terms of the base flow correction by the azimuthal velocity of the perturbation, are all negligible with respect to the dominant $O(1)$ or $O(\alpha Re^{2/3})$ advection terms associated with the main rotation or the axial velocity field induced by tilting. The $O(\alpha/L)$ radial buoyancy force induced by the radial variation of the density, which is responsible for the Rayleigh–Taylor instability, is also negligible.

The above system of equations is complicated because it is inhomogeneous with respect to both $\bar{r}$ and θ. Local perturbations are advected around the vortex and modified during their angular rotation owing to the dependency of $\bar{w}_1$ and $\bar{\rho}_1$ on θ. Yet, the experimental observations discussed in the previous section tend to demonstrate that the characteristics of the perturbations are mainly associated with the local axial velocity profile, and that its growth results from a local process. In other words, angular advection of the perturbation by the vortex is expected to be small during the growth of the perturbation. This amounts to neglecting the term $F^{-1}\partial_\theta$ in the (4.7*a*)–(4.7*d*) in front of $\alpha Re^{2/3}$. This hypothesis has several consequences. The terms $-2v/F$ in (4.7*a*), $\omega_{0c}u$ in (4.7*b*), ρ/F^2 in (4.7*c*) and w in (4.7*d*) also become negligible. This means that if the dynamics of the perturbations is not affected by the angular advection, it is neither affected by vertical stratification nor Coriolis effects in these dimensionless variables. However, the instability is indirectly related to the stratification through the position and amplitude of the critical layer (which define the dimensionless variables). The perturbation then follows the dynamics of two-dimensional perturbations in a parallel unstratified shear flow $\alpha Re^{2/3}\bar{w}_1(\bar{r}, \theta)$ where θ can be considered as a parameter.

If we normalize spatial and time variables by

$$\delta_c = \frac{1}{|\Omega_{0c}' Re|^{1/3}}, \tag{4.8a}$$

$$\tau_c = \frac{|\Omega_{0c}'|^{1/3} F^2}{r_c \alpha Re^{2/3}}, \tag{4.8b}$$

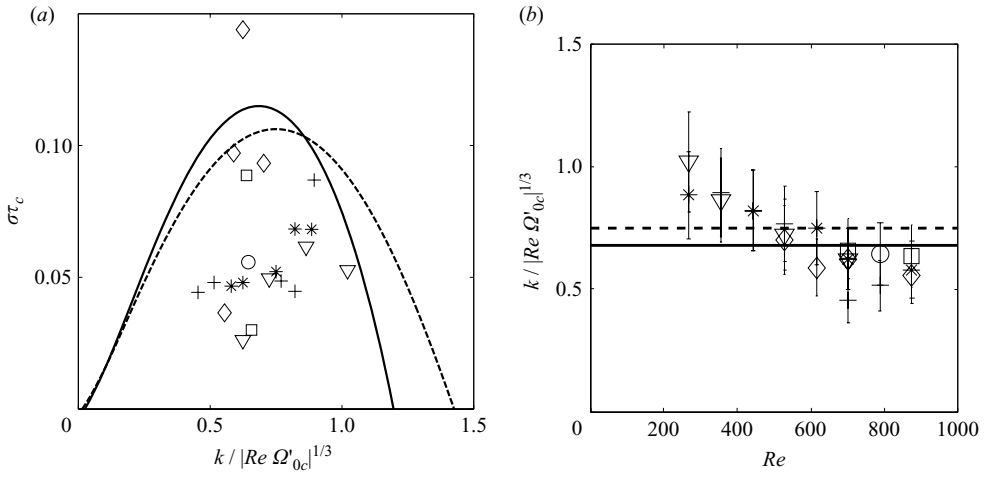

FIGURE 9. (*a*) Maximum growth rate versus the axial wavenumber of the most unstable mode. (*b*) Most unstable wavelength as a function of the Reynolds number. The theoretical lines correspond to a jet profile ($\theta = 0$) for a dashed line and to a mixing layer profile ($\theta = \pi/2$) for the solid line. Experimental data have been obtained for $\alpha =$ 0.03 rad ($\circ$), $\alpha = 0.07$ rad ($\square$), $\alpha = 0.14$ rad ($\diamond$), $\alpha = 0.23$ rad ($+$), $\alpha = 0.30$ rad ($*$), $\alpha = 0.38$ rad ($\triangledown$).

such that

$$\tilde{r} = \bar{r}|\Omega'_{0c}|^{1/3} = (r - r_c)/\delta_c, \tag{4.9a}$$

$$\tilde{z} = \bar{z}|\Omega'_{0c}|^{1/3} = z/\delta_c, \tag{4.9b}$$

$$\tilde{t} = t/\tau_c, \tag{4.9c}$$

$$\tilde{w}_1 = \alpha Re^{1/3}\bar{w}_1\tau_c/\delta_c = \mathrm{Re}\left(\frac{\pi}{2^{2/3}}\mathrm{Hi}\left(2^{1/3}\tilde{r}\right)\mathrm{e}^{\mathrm{i}\theta}\right), \tag{4.9d}$$

a familiar Rayleigh equation,

$$(-\mathrm{i}\tilde{\omega} + \mathrm{i}\tilde{k}\tilde{w}_1)\left(\frac{\partial^2}{\partial\tilde{r}^2} - \tilde{k}^2\right)\tilde{u} + \mathrm{i}\tilde{k}\tilde{w}_1''\tilde{u} = 0, \tag{4.10}$$

is obtained for the radial velocity amplitude $\tilde{u}$ of the normal mode $u(\tilde{r}, \tilde{z}, \tilde{t}) = \tilde{u}(\tilde{r})\mathrm{e}^{\mathrm{i}\tilde{\omega}\tilde{t} - \mathrm{i}\tilde{k}\tilde{z}}$.

The maximum growth rate $\mathrm{Im}(\tilde{\omega})$ versus $\tilde{k}$ of the perturbation to the profile $\tilde{w}_1$ is plotted in figure 9 for $\theta = 0$ and $\theta = \pi/2$. We recall that $\theta = 0$ corresponds to the vertical plane in which $\tilde{w}_1$ has a jet profile (figure 3*b*). The other value $\theta = \pi/2$ corresponds to the tilted plane in which $\tilde{w}_1$ has a mixing layer profile (figure 3*c*). As expected, the local mixing-layer profile is slightly more unstable than the jet, and classical results of stability are recovered (see Drazin & Reid 1981). The most unstable mode of the mixing layer is stationary with a growth rate

$$\mathrm{Im}\left(\tilde{\omega}_{ML}^{max}\right) = \sigma_{ML}^{max}\tau_c \approx 0.12, \tag{4.11}$$

reached for

$$\tilde{k}_{ML}^{max} = k_{ML}^{max}\delta_c \approx 0.68. \tag{4.12}$$

The most unstable mode of the jet is a sinuous mode with

$$\tilde{k}_J^{max} = k_J^{max}\delta_c \approx 0.75. \tag{4.13}$$

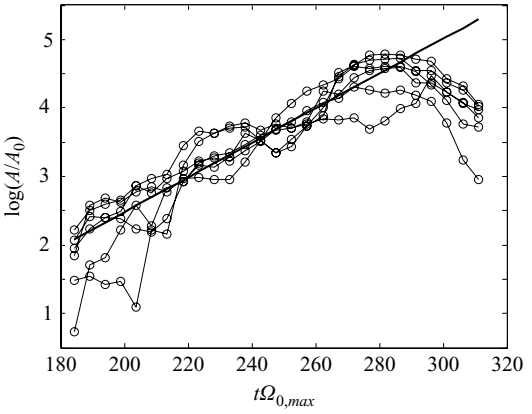

FIGURE 10. Evolution of the amplitude of the perturbations from shadowgraph visualizations for $Re = 700$, $F = 3.8$ and $\alpha = 0.23$ rad.

This mode has a growth rate

$$\mathrm{Im}\left(\tilde{\omega}_J^{max}\right) = \sigma_J^{max}\tau_c \approx 0.11, \tag{4.14}$$

and contrarily to the mixing-layer mode, it is propagating with a phase velocity

$$c_J \frac{\tau_c}{\delta_c} \approx 0.24\ . \tag{4.15}$$

Experimental estimates for the growth rate have also been added in figure 9. They have been obtained from shadowgraph visualizations in the vertical longitudinal plane. For this purpose, the amplitude of the sinusoidal undulation of the critical layer was measured manually on two wavelengths on each side of the vortex. This leads to 10 determinations of the amplitude of the perturbation as a function of time. They are plotted in figure 10 where the uncertainty can be as large as 20%. In this figure, the amplitude increases exponentially, which leads to the determination of the growth rate. However, these growth rate measurements contain a large uncertainty for various reasons. First, the advection of the structures around the vortex can drastically increase or decrease the growth of the amplitude if the perturbation is not homogeneous in θ. Secondly, there is a competition between several wavelengths, which makes it hard to follow exactly the same maximum and minimum of the undulation. All of this induces a large uncertainty in the determination of the growth rate, whose error can be as large as 50%.

Figure 9(a) shows that the growth rates measured experimentally are, in general, smaller than the theoretical predictions and can be as small as half the theoretical value. This is not surprising because the theory does not take into account the stabilizing viscous and advection effects. Moreover, as explained above, the presence of various wavelengths might introduce a small bias toward smaller values during the experimental determination of the growth rate. Figure 9(b) shows the measured wavelength as a function of the Reynolds number. It is very close to the theoretical value of the maximum growth rate. The results are apparently slightly dependent on the Reynolds number, showing that smaller wavelengths are obtained for larger values of the Reynolds number. This is surprising because viscosity is expected to damp preferentially the smaller wavelengths. Further data are required in order to confirm this slight dependency.

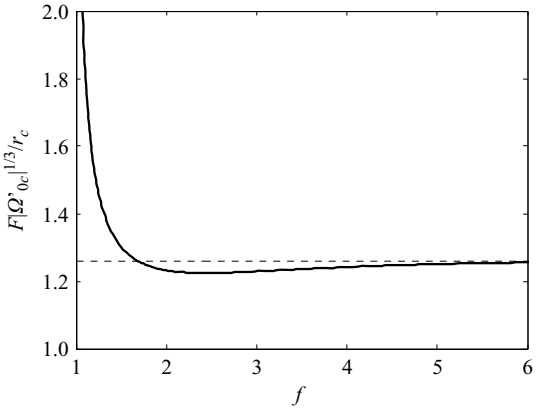

FIGURE 11. Variation of the amplitude factor of the local growth rate: $r_c/(F|\Omega'_{0c}|^{1/3})$ versus F. The dashed line is the asymptotic value $2^{1/3}$ obtained for large F.

For large Froude numbers, a theoretical estimate for τ_c can be obtained. In this limit, the critical layer is far from the vortex centre in a region where $\Omega_0(r) \sim 1/r^2$. The critical radius r_c and Ω'_{0c} can therefore be expressed in terms of F such that we obtain $(F|\Omega'_{0c}|^{1/3}/r_c) \approx 2^{1/3}$ for large F. By plotting $(F|\Omega'_{0c}|^{1/3}/r_c)$ versus F (see figure 11), we can see that this estimate applies approximatively as soon as $F > 1.5$. It follows that $\tau_c \sim F/(2^{1/3}\alpha Re^{2/3})$ for $F > 1.5$. The consequence is that the product $\sigma_{ML}^{max} F$, which compares the maximum growth rate to the angular advection frequency, becomes independent of the Froude number. It is given (for $F > 1.5$) by

$$\sigma_{ML}^{max} F \approx 0.1\alpha Re^{2/3}. \tag{4.16}$$

A priori, the theory requires that this product must be large, which means

$$\alpha Re^{2/3} \gg 10. \tag{4.17}$$

Figure 12 shows the experimental stability diagram of the tilt-induced instability. Three types of behaviour have been observed. For high Reynolds numbers and high tilt angles, the flow presents the instability described previously. The corresponding parameter region has been marked as light grey in figure 12. As predicted by the theory, this instability appears for Froude numbers larger than 1 and for $\alpha Re^{2/3}$ sufficiently large. When the Froude number is smaller than 1, the critical layer disappears and no instability was observed. When the parameter $\alpha Re^{2/3}$ becomes small (of the order of 5), we have observed that the critical-layer establishment is followed by the development of non-stationary and non-persistent disturbances. After the disappearance of the disturbances, the critical layer starts to beat at the Brunt–Väisälä frequency. This regime is indicated in dark grey in figure 12. It is found for $\alpha Re^{2/3}$ decreasing from 10 to 3 when the Froude number increases from 1 to 4. It is not clear whether this region tends to $\alpha Re^{2/3} = 0$ for larger Froude numbers. We have not been able to explore this domain of parameters because it corresponds to very small tilt angles which are too strongly affected by the remnant motions of the fluid in the tank.

5. Late stages

We have also analysed the evolution of the tilted vortex when the instability is strongly active. PIV measurements were made in a horizontal plane in order to study

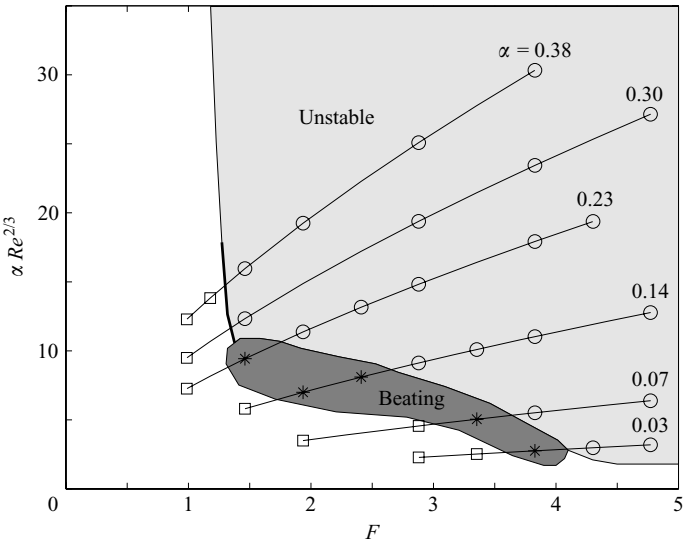

FIGURE 12. Experimental stability diagram of the tilt-induced instability for various inclination angles α of the vortex. Each experiment can present a stable flow (□), an unstable flow (○) or a beating of the perturbation (∗).

the two-dimensional characteristics of the final vortex. The two-dimensional velocity fields show that the vortex remains very close to axisymmetric and that the mean velocity profile is fitted very well by the profile of a Gaussian vortex defined by (2.2). The circulation and the core size were thus evaluated as a function of time for three different tilt angles and for two different Reynolds numbers by fitting the experimental data with the Gaussian vortex.

The circulation Γ of the vortex is shown in figure 13(a) as a function of time. The uncertainty is very small, but it may depend slightly on the method used for the fit of the experimental data. The overall error is smaller than 5%. The dotted symbols correspond to a vertical vortex (used as a reference), for which the circulation remains constant after a vortex formation time of approximately 5 s. Open symbols show the results of a vortex tilted with an angle $\alpha = 0.12$ rad. For this tilt angle, the three-dimensional perturbation appears around $t = 9$ s for both Reynolds numbers. The circulation is roughly constant, although it increases by about 30% for the smaller Reynolds number and decreases by about 15% for the larger Reynolds number. The vortex is not broken by the instability, even though the instability is very active. This is consistent with Kelvin's theorem predicting that the circulation should be conserved. The small variations of the circulation are probably due to slight modifications of the vortex profile during the instability.

The square of the core size a^2 is plotted in figure 13(b) as a function of time. The uncertainty for this parameter is slightly larger than for the circulation: the error can be as high as 10% for the tilted vortex owing to strong refractions in the turbulent regions. For a vertical vortex, it increases linearly with time owing to viscous diffusion, with a slope 4ν (shown as thick lines) corresponding to a non-stratified Gaussian vortex. For a vortex tilted with an angle $\alpha = 0.12$ rad, the initial evolution of the core size is similar, showing that the formation of the vortex is weakly influenced by the tilt angle. However, the core size jumps suddenly to a large value after the onset of the instability, when the Reynolds number is equal to 2000. This comes from the

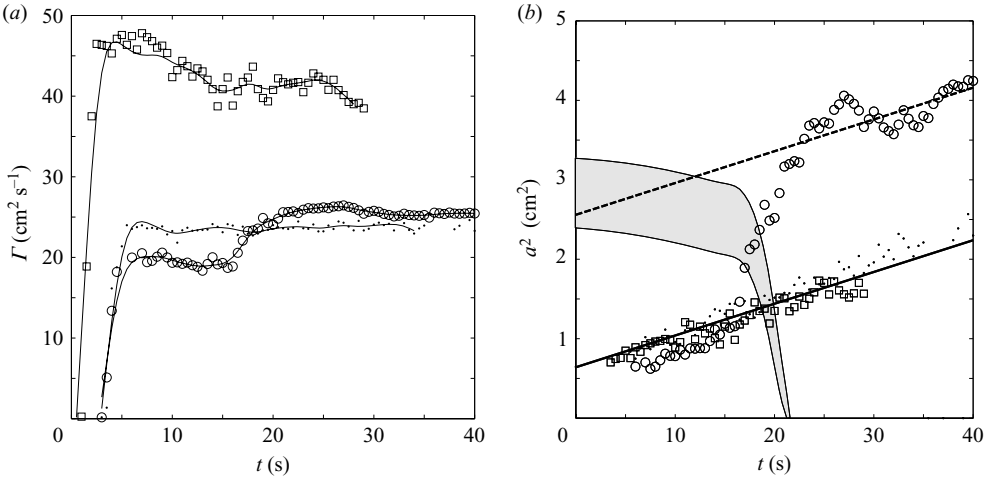

FIGURE 13. Temporal evolution of (*a*) the circulation and (*b*) the core size of a tilted vortex. Dotted symbols are the reference vertical vortex. Open symbols correspond to a tilt angle $\alpha = 0.12$ rad and a Reynolds number $Re = 2000$ (○) and $Re = 4200$ (□). (*a*) The solid lines are experimental data fits. (*b*) The slope of the lines is calculated from the viscous evolution of a Gaussian vortex and the grey area indicates the position and width of the critical layer for the $Re = 2000$ (○) experiment.

large dispersion caused by the instability which enhances the diffusion of the vorticity and creates an artificial growth of the core size. The final vortex has a core size 50% larger than in the absence of instability. Such a sudden increase of the core size has not been observed for a higher Reynolds number ($Re = 4200$) although the instability was more active there. This can be explained by the instability being located much farther from the vortex centre in that case, because the Froude number is twice as large. The position of the critical layer can be calculated for these two experiments. For the lower Reynolds number, it is indicated in figure 13(*b*) by the grey area. We can see that this region is close to the core radius when the instability develops. On the contrary, the grey area would be outside the figure for the higher Reynolds number, since it is located around $r_c^2 \approx 10\,\mathrm{cm}^2$. For the lower Reynolds number, the sudden increase of the core size induces a sudden decrease of the Froude number and a disappearance of the critical layer. This might explain why the instability saturates and creates only a beating of the flow, probably associated with the oscillation of a stable Kelvin mode. After the turbulence has slowed down, the core size seems to increase again as for a Gaussian vortex.

We can infer from these observations that at high Reynolds numbers, the instability of a tilted vortex will not break the vortex, but will increase its core size if its Froude number is close to 1.

6. Conclusion

In this paper, we have analysed the dynamics of a tilted vortex in a stratified fluid for small inclination angles, large Reynolds numbers and Froude numbers larger than 1.

In a previous paper (Boulanger *et al.* 2007), we showed that when $F > 1$, tilting induces a strong axial flow and important density variations in a cylindrical region located near a critical radius where the Brunt–Väisälä frequency is equal to the angular velocity of the vortex. Moreover, it was also shown that these corrections to

the rotating flow were captured well by a viscous critical-layer analysis: the axial flow was demonstrated to have an $m = 1$ azimuthal structure, and radial profiles which vary from jet in the vertical plane ($\theta = 0$) to mixing layer in the tilted plane ($\theta = \pi/2$). Here, we have demonstrated experimentally that the axial flow correction is responsible for a violent instability characterized by the formation of small co-rotating vortices on either side of the vortex. The growth rate and the spatial structure of the instability mode have been obtained using visualizations and PIV measurements, and compared to the theoretical predictions obtained from a local stability analysis of the radial profile of axial flow in the viscous critical layer.

A good quantitative agreement has been obtained for the wavelength of the modes supporting the hypothesis that the instability is mainly governed by the local stability characteristics for the experimental parameters we have considered. However, we have also observed that experimental estimates for the instability growth rate were up to a factor 2 below the local theoretical predictions. We have attributed this discrepancy to the large uncertainties found in the experimental measurements, to the possible bias due to the competition between several wavelengths and to neglected viscous and advection effects in the theory.

The theoretical description has permitted us to show that, as soon as $F > 1.5$, the condition for the validity of the local approach does not depend on the Froude number and only requires the product $\alpha Re^{2/3}$ to be large. This product is also expected to be the parameter controlling the stability of the tilted vortex: the dimensional growth rate is shown to be equal to $0.1\alpha Re^{2/3}N$, N being the Brunt–Väisälä frequency. When this product is small, the local instability is in competition with the angular advection of the vortex: the vortex becomes stable because local perturbations do not have time to grow sufficiently before being advected. In our experiments, we have observed that the stability threshold was slightly Froude-number dependent: it varied from $\alpha Re^{2/3} = 10$ to $\alpha Re^{2/3} = 3$ when the Froude number increases from 1 to 4.

We have also looked at the evolution of the vortex after the development of the instability. We have observed that the instability does not break the vortex and its circulation does not change significantly. However, the instability can increase the core size of the vortex by 50% and hence decrease its Froude number below the threshold for the instability. This effect is observed only when the Froude number is small enough (between 1 and 3), such that the critical layer is close to the vortex centre.

It is striking to see that this instability occurs for tilt angles as small as 0.03 rad (2°) at high Reynolds numbers, and is thus likely to happen in most situations. We have observed that the tilt angle of the vortex could vary from at least 1° owing to the remnant motions in the tank. We suspect that it was the case in the experiments of Cariteau (2005), who observed exactly the same instability without any intentional tilt of the vortex. We thus expect this instability to occur in real geophysical flows, where the Reynolds numbers are much higher than in laboratory experiments. A consequence would be that vortices with a Froude number close to 1 are subject to this instability and will thus decrease their Froude number below 1, where the instability disappears. Such a defect of vortices with Froude number close to 1 might be visible in oceanic and atmospheric data.

Finally, it is clear that this instability creates a strong vertical mixing of the stratified fluid. This mixing mechanism is different from the simple overturning mechanism which is often invoked in the ocean (Farmer, Pawlowicz & Jiang 2002). It will be now interesting to quantify its real contribution to the global mixing properties of the ocean.

We would also like to mention that Schecter, Montgomery & Reasor (2002) have examined a situation in which a local tilting was created by a three-dimensional linear Rossby wave. In their case, a critical layer is also present, but its role is to damp the linear Rossby wave and then favour the realignment of the vortex with the direction of stratification. It is not clear what the structure of the flow is in that critical layer and whether secondary instabilities such as the one described here could develop.

The support of ACI grant 'Prévention des catastrophes naturelles' by the French Ministry of Research is gratefully acknowledged.

REFERENCES

Abramowitz, M. & Stegun, I. A. 1965 *Handbook of Mathematical Functions*. Dover.

Billant, P. & Chomaz, J.-M. 2000 Experimental evidence for a new instability of a vertical columnar vortex pair in a strongly stratified fluid. *J. Fluid Mech.* **418**, 167–188.

Boulanger, N., Meunier, P. & Le Dizès, S. 2007 Structure of a stratified tilted vortex. *J. Fluid Mech.* **583**, 443–458.

Cariteau, B. 2005 Etude de la stabilité et de l'interaction de cyclones intenses en fluide stratifié. PhD thesis, Université Joseph Fourier, Grenoble.

Cariteau, B. & Flór, J.-B. 2003 Instability of a columnar vortex in stratified fluid. *Bull. Am. Phys. Soc.* **48** (10), 164.

Crow, S. C. 1970 Stability theory for a pair of trailing vortices. *AIAA J.* **8**, 2172–2179.

Drazin, P. G. & Reid, W. H. 1981 *Hydrodynamic Stability*. Cambridge University Press.

Farmer, D., Pawlowicz, R. & Jiang, R. 2002 Tilting separation flows: a mechanism for intense vertical mixing in the coastal ocean. *Dyn. Atmos. Oceans* **36**, 43–58.

Garnier, E., Métais, O. & Lesieur, M. 1996 Instabilités primaire et secondaire d'un jet barocline. *C. R. Acad. Sci., Paris* B **323**, 161–168.

Hopfinger, E. J. & van Heijst, G. J. F. 1993 Vortices in rotating fluids. *Annu. Rev. Fluid Mech.* **25**, 241–289.

Kerswell, R. R. 2002 Elliptical instability. *Annu. Rev. Fluid Mech.* **34**, 83–113.

Meunier, P. & Leweke, T. 2003 Analysis and optimization of the error caused by high velocity gradients in particle image velocimetry. *Exps. Fluids* **35**, 408–421.

Nieman, P. J., Shapiro, M. A. & Fedor, L. S. 1993 The life cycle of an extratropical marine cyclone. Part ii: mesoscale structure and diagnostics. *Mon. Weather Rev.* **121**, 2177–2199.

Pawlak, G., MacCready, P., Edwards, K. A. & McCabe, R. 2003 Observations on the evolution of tidal vorticity at a stratified deep water headland. *Geophys. Res. Lett.* **30** (24), 2234.

Polavarapu, S. M. & Peltier, W. R. 1993 Formation of small-scale cyclones in numerical simulations of synoptic-scale baroclinic wave life cycles: secondary instability at the cusp. *J. Atmos. Sci.* **50**, 1047–1057.

Schecter, D. A., Montgomery, M. T. & Reasor, P. D. 2002 A theory for the vertical alignment of a quasigeostrophic vortex. *J. Atmos Sci.* **59** (2), 150–168.

Viscous stability properties of a Lamb-Oseen vortex in a stratified fluid

By Xavier RIEDINGER, Stéphane LE DIZÈS and Patrice MEUNIER

Institut de Recherche sur les Phénomènes Hors Équilibre,
CNRS / Universités Aix-Marseille I&II,
49, rue F. Joliot-Curie, B.P. 146, F-13384 Marseille cedex 13, France.

(Received 4 March 2009)

In this work, we analyse the linear stability of a frozen Lamb-Oseen vortex in a fluid linearly stratified along the vortex axis. The temporal stability properties of 3D normal modes are obtained under the Boussinesq approximation with a Chebychev collocation spectral code for large ranges of Froude numbers and Reynolds numbers (the Schmidt number being fixed to 700). A specific integration technique in the complex plane is used in order to apply the condition of radiation at infinity. For large Reynolds numbers and small Froude numbers, we show that the vortex is unstable with respect to all non-axisymmetrical waves. The most unstable mode is however always a helical radiative mode ($m = 1$) which either resembles a displacement mode or a ring mode. The displacement mode is found to be unstable whatever the Reynolds numbers for moderate Froude numbers ($F \sim 1$). The radiative ring mode is by contrast unstable only for large Reynolds numbers above 10^4, and is the most unstable mode for large Froude numbers ($F > 2$). The destabilization of this mode for large Froude numbers is shown to be associated with a resonance mechanism which is analysed in detail. Explanations for the scaling and the spatial structure of the different unstable modes are also provided.

1. Introduction

Vortices such as the Lamb-Oseen vortex are often considered as robust coherent structures in homogeneous fluids. The goal of this work is to demonstrate that when such a vortex is placed in a stratified environment it becomes unstable.

Despite the important number of works, the linear stability of a Lamb-Oseen vortex in a homogeneous medium has been demonstrated only recently (Fabre *et al.*, 2006). Such a vortex, which has a Gaussian vorticity profile, is considered as more realistic than other discontinuous vortex models such as the Rankine vortex which have often been used in the literature. As shown by Fabre *et al.* (2006), the linear normal mode perturbations of the Lamb-Oseen vortex exhibit special properties owing to the continuous vorticity profile. In particular, many inviscid waves, termed Kelvin modes, become damped due to the appearance of a critical point singularity (Le Dizès, 2004; Le Dizès & Lacaze, 2005). In a homogeneous fluid, the Lamb-Oseen vortex is stable, and other effects have to be added in order to destabilize it such as axial flow (Lessen & Paillet, 1974; Fabre & Jacquin, 2004), strain field (Eloy & Le Dizès, 1999) or other vortices (Le Dizès & Laporte, 2002; Meunier & Leweke, 2005).

The effect of stratification has mainly been considered in the context of oceanography and atmospheric sciences under simplifying hypotheses. The first works have been performed in the context of shallow water flows (see for instance Satomura, 1981; Hayashi &

Young, 1987; Knessl & Keller, 1992). For vortices, the destabilizing role of stratification has been first demonstrated by Ford (1994). More recently, Schecter & Montgomery (2004) have analysed the stability of a family of Rankine-like vortices under an hydrostatic hypothesis and obtained a formal expression for the instability growth rate. Further studies have also been performed in a more applied context (Schecter & Montgomery, 2006; Schecter, 2008; Hodyss & Nolan, 2008). The stability of a strongly stratified Rankine vortex has also been considered in Billant & Le Dizès (2009). Asymptotic expressions in the small Froude number limit have been derived.

The analysis of stratified Lamb-Oseen vortex has started with the works of Miyazaki & Fukumoto (1991) and Le Dizès (2008) who demonstrate the existence of neutral radiative inviscid modes. The instability has been demonstrated only recently in Le Dizès & Billant (2009) (see also Le Dizès & Billant, 2006). By using a large wavenumber asymptotic approach (Le Dizès & Lacaze, 2005; Billant & Gallaire, 2005), Le Dizès & Billant (2009) have shown how the emission of internal gravity waves can become destabilising and obtained explicit formulae for the inviscid growth rate which compare very well with numerical results for small Froude numbers. In the present work, this theory will also be used to explain some of the characteristics of the instability for large Reynolds numbers. Interestingly, we shall demonstrate that the Lamb-Oseen vortex is also unstable for small Reynolds numbers and for large Froude numbers.

The effect of stratification on Taylor-Couette flows has been investigated for many years. It was first thought that stratification stabilizes the centrifugal instability (Withjack & Chen, 1974, 1975; Boubnov *et al.*, 1995). But, it was recently found that stratification can also have a destabilizing effect in particular regions of the parameter space (Molemaker *et al.*, 2001; Yavneh *et al.*, 2001; Le Bars & Le Gal, 2007). This so-called Strato-Rotational Instability is associated with a resonance of boundary modes. Such a resonance mechanism has been obtained in several other contexts. Satomura (1981), Hayashi & Young (1987) and Balmforth (1999) have demonstrated its occurrence in shallow water shear flows. Sakai (1989) and more recently Gula *et al.* (2009) have analysed the different types of resonance for a two-layer channel model. Interestingly, we shall demonstrate that in large Froude number regime, the Lamb-Oseen vortex is also unstable due to a resonance of Kelvin and radiative modes.

It is also worth mentioning the works on acoustic modes in jets (Luo & Sandham, 1997) and in vortices (Broadbent & Moore, 1979) and on accretion disks (Papaloizou & Pringle, 1984; Narayan *et al.*, 1987) where the instability is also due to either wave emission or wave resonance.

The paper is organised as follows. In section 2, the base flow and the linear stability equations are given. We also discuss the radiative boundary conditions to apply to the perturbations. We show that these boundary conditions can be implemented with a spectral code to weakly damped modes by performing the integration in the complex plane. The spectral collocation code is briefly presented in this section. In section 3, the stability results are presented for the most unstable modes which correspond to helical modes ($m = 1$). Two types of modes are shown to become the most unstable. Stability diagrams (growth rate contours) are obtained for each mode as functions of the Reynolds and Froude numbers. The structure of the eigenmodes is provided and the role of the critical points in the damping of the modes is also discussed. An important subsection is concerned with the mechanism of resonance which explains the instability for large Froude numbers. A criterion for its occurrence is in particular provided. Results for higher azimuthal wavenumbers $m \geq 2$ are presented in section 4. The last section provides a summary of the main results.

2. Framework and numerical method

2.1. *Base Flow and perturbation equations*

We consider an axisymmetrical Lamb-Oseen vortex in a viscous fluid of kinematic viscosity ν, stably stratified along the vortex axis. The stratification is assumed to be linear with a constant Brunt-Väisälä frequency $N = \sqrt{-g\partial_z\rho/\rho_0}$ and a mass diffusivity D. The vortex is characterized by its radius a and circulation Γ. It satisfies the Navier-Stokes equations under the Boussinesq approximation (Boulanger *et al.*, 2007) provided that the radius a increases in time according to $a = \sqrt{a_0^2 + 4\nu t}$. In this study, this weak diffusion is neglected such that the vortex is assumed "frozen" with a constant radius a.

Using a and $2\pi a/\Gamma$ as characteristic spatial and temporal scales respectively, the angular velocity profile of the vortex can be written as

$$\Omega(r) = \frac{1}{r^2}\left(1 - e^{-r^2}\right) \ . \tag{2.1}$$

Under the Boussinesq approximation, the base flow is then defined by the three parameters, the Reynolds number Re, the Froude number F and the Schmidt number Sc given by

$$Re = \frac{\Gamma}{2\pi\nu} \ , \tag{2.2a}$$

$$F = \frac{\Gamma}{2\pi N} \ , \tag{2.2b}$$

$$Sc = \frac{\nu}{D} \ . \tag{2.2c}$$

Whereas the Froude number and the Reynolds number will be varied in a large range of values, the Schmidt number will be fixed to 700, a value commonly used for salt water.

Infinitesimal disturbances of the velocity, pressure and density fields are considered in the form of normal modes

$$(u', v', w', p', \rho') = [u(r), v(r), w(r), p(r), \rho(r)] \exp(ikz + im\theta - i\omega t) \ , \tag{2.3}$$

where u', v' and w' are the radial, azimuthal and axial velocities, r the radial coordinate, k and m the axial and azimuthal wavenumbers and ω the complex frequency. The normal mode amplitudes satisfy the following equations obtained by linearizing the Navier-Stokes equations under the Boussinesq approximation:

$$i\phi u - 2\Omega v = -\frac{dp}{dr} + \frac{1}{Re}\left(\Delta u - \frac{u}{r^2} - \frac{2im}{r^2}v\right) \ , \tag{2.4a}$$

$$i\phi v + \left(2\Omega + r\frac{d\Omega}{dr}\right)u = -\frac{imp}{r} + \frac{1}{Re}\left(\Delta v - \frac{v}{r^2} + \frac{2im}{r^2}u\right) \ , \tag{2.4b}$$

$$i\phi w = -ikp - \frac{1}{F^2}\rho + \frac{1}{Re}\Delta w \ , \tag{2.4c}$$

$$i\phi\rho = w + \frac{1}{ReSc}\Delta\rho \ , \tag{2.4d}$$

$$\frac{1}{r}\frac{d(ru)}{dr} + \frac{imv}{r} + ikw = 0 \ . \tag{2.4e}$$

where $\Delta = \frac{\partial^2}{\partial r^2} + \frac{1}{r}\frac{\partial}{\partial r} - k^2 - \frac{m^2}{r^2}$ is the Laplacian operator written in cylindrical coordinates and

$$\Phi = -\omega + m\Omega \ . \tag{2.5}$$

This system can be further reduced by eliminating pressure and axial velocity to obtain a

third order system of the form $\omega A\mathbf{f} = B\mathbf{f}$ for $\mathbf{f} = [u(r), v(r), \rho(r)]$. This reduced system together with adequate boundary conditions at the origin and at infinity defines a generalized eigenvalue problem for the frequency ω, for fixed base flow parameters (Re, F, Sc) and fixed real axial wavenumber k and azimuthal wavenumber m. Our goal is to determine the unstable eigenmodes, that is those with a positive growth rate $\Im m(\omega)$, when all the parameters (except Sc) are varied. Because we want to provide the marginal curves of the unstable modes, we will also consider neutral and weakly damped eigenfrequencies.

2.2. *The boundary conditions and the numerical method*

The boundary conditions that we shall apply to the perturbations are prescribed by causality. Because the fluid is at rest at infinity, we should be able to form the perturbations from a compact initial condition. This condition implies that when the medium can sustain waves at infinity, these waves must propagate outward. The condition of causality is thus in that case a condition of radiation. The difficulty with this condition is that it does not necessarily imply vanishing of the solution at infinity, when the modes are neutral or damped ($\Im m(\omega) < 0$).

In order to express the condition of radiation, it is necessary to determine the possible behaviors of the perturbations at ∞. These can be easily derived by manipulating equations (2.4a-e) in the large r limit. We obtain 8 independent solutions with an asymptotic behavior of the form $r^{\alpha_j} e^{\pm i\beta_j r}$ where the radial wavenumbers β_j satisfy the equation:

$$\left[\left(\frac{(\beta^2+k^2)^2}{Re^2 Sc} - i\omega\frac{(\beta^2+k^2)}{Re} + \frac{1}{F^2} - \omega^2\right)(\beta^2+k^2)\right]\left(\frac{(\beta^2+k^2)}{Re} - i\omega\right) = 0\ . \quad (2.6)$$

Two of the solutions of this equation, say $\pm\beta_1$, can be considered as "non-viscous" and are such that $\beta_1 = k\omega/\sqrt{F^{-2}-\omega^2} + O(1/\sqrt{Re})$. The six others are associated with diffusion processes and depend on the Reynolds number at leading order. The condition of radiation means that the perturbations should be only composed of waves propagating outward at infinity. The property of these waves is that they are spatially damped as r increased when they correspond to a positive growth rate $\Im m(\omega) > 0$. The condition of radiation thus imposes that the solutions should behave near ∞ as

$$\mathbf{f} \sim \sum_{j=1}^{4} f_j r^{\alpha_j} e^{i\beta_j r} \quad (2.7)$$

where the radial wavenumbers β_j have been chosen such that $\Im m(\beta_j) > 0$ when $\Im m(\omega) > 0$. When $\Im m(\omega) \leq 0$, the β_j should be obtained by continuity from their definition for $\Im m(\omega) > 0$. When $\Im m(\omega) > 0$, the above condition is equivalent to the vanishing of the solution at ∞. But, this is not always the case for $\Im m(\omega) \leq 0$. In particular, if one $\Im m(\beta_j)$ has changed sign, the solution prescribed by the condition of radiation is no longer bounded but increases exponentially as r goes to infinity. In that case, the condition of radiation means that the inward wave corresponding to the exponentially decreasing behavior $r^{\alpha_j} e^{-i\beta_j r}$ should not be part of the solution near infinity. This is a priori a condition difficult to implement numerically with a spectral code. With the spectral code we shall use, the condition we shall implicitly apply is the vanishing of the solution at infinity. As a consequence, we will not be able to provide the eigenfrequencies in frequency domains where the physical condition of radiation is not equivalent to the vanishing of the solution.

To get round this difficult, we have used a trick. Our idea is to consider the problem on a complex path of the form $r = se^{i\theta}$, $s \in \Re$ with a small fixed value of θ. The

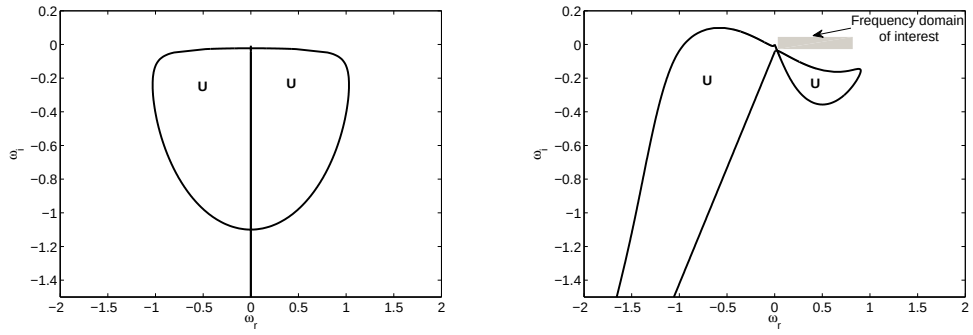

(a) (b)

FIGURE 1. Continuous spectrum (solid lines) and "unphysical" domain (indicated by the letter "U") for $Re = 200$, $F = 0.9$, $k = 3$. (a) Real path $\theta = 0$ (b) Complex path $\theta = \pi/10$.

boundary conditions are then implemented in the complex plane by assuming that the behavior prescribed by the condition of radiation is also valid along the complex path as s goes to ∞. By doing so, we modify the frequency domain where the condition of radiation is equivalent to the spectral condition of vanishing, and therefore change the frequency domain which can be resolved numerically. This domain of the complex ω plane is delimited by curves which define the so-called continuous spectrum. These curves can be obtained by solving (2.6) with respect to ω. They are defined by the parametric expressions:

$$\omega = -i\frac{\beta^2 + k^2}{Re} \,, \tag{2.8a}$$

$$\omega = -i\frac{\beta^2 + k^2}{2Re} \pm \sqrt{-\frac{(\beta^2 + k^2)^2}{4Re^2} + \frac{\beta^2}{F^2(\beta^2 + k^2)} + \frac{\beta^2 + k^2}{Re^2 Sc}} \,. \tag{2.8b}$$

When we stay on the real axis, the continuous spectrum is obtained by varying β with $\Im m(\beta) = 0$. On a complex path of the form $r = se^{i\theta}$, β should be varied with the condition $\Im m(\beta e^{i\theta}) = 0$. In figure 1, we have represented the continuous spectrum for typical parameters for a real path and for a complex path with $\theta = \pi/10$. As discussed above, these curves delimit the "unphysical" frequency domain where the vanishing of the solution does not correspond to the condition of radiation. This figure illustrates the interest of using a complex path. We clearly see the deformation of the continuous spectrum and the enlargement of the domain where the condition of radiation can be correctly prescribed by the spectral code. Note in particular that the frequency domain of interest indicated in gray is far from the unphysical domain only if the integration is performed in the complex plane.

On the real axis or on the complex path, the numerical resolution of the eigenvalue problem mainly follows the analysis which was performed by Fabre & Jacquin (2004) for a vortex in a non-stratified fluid. We use a similar Chebychev spectral collocation code, which was, for the present analysis, initially developed by Antkowiak & Brancher with Matlab© for non-stratified fluids. As in Fabre & Jacquin (2004), we have used the parity properties of the solutions and implemented these symmetries on the Chebychev decomposition to speed up the calculation. We have also used a similar mapping from $s \in [-\infty; \infty]$ to the Chebychev domain $\xi \in [-1; 1]$ to avoid the treatment of the regular singularity at the origin. With this mapping, the complex radial coordinate is connected

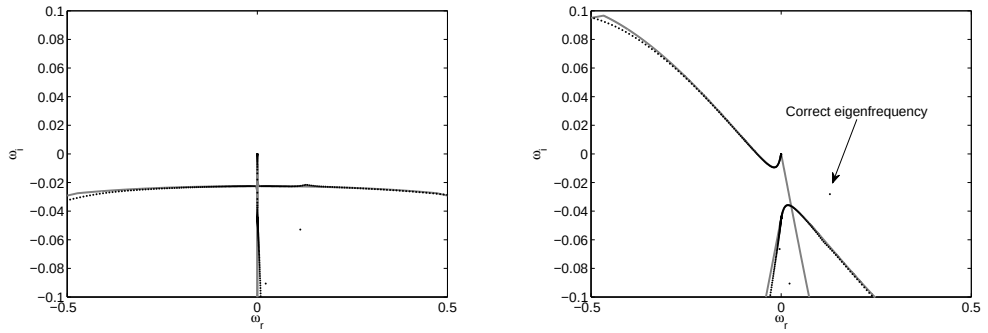

(a) (b)

FIGURE 2. Close view of the numerical spectrum (dots) and theoretical continuous spectrum (solid gray lines) near a correct damped eigenvalue (indicated by the arrow) for the parameters of figure 1, and $Np = 400$ and $H = 12$. (a) Real path $\theta = 0$ (b) Complex path $\theta = \pi/10$.

to the Chebychev variable by the relation

$$r = (H\xi/(1-\xi^2))e^{i\theta}. \tag{2.9}$$

We have usually taken values of H between 1 and 12 and of θ between 0 and $\pi/10$. Fabre & Jacquin (2004) have shown that the eigenvalues automatically satisfy the boundary conditions at the origin and we refer to their paper for more details. The number Np of polynomials was varying between 80 and 500. In practice, $Np = 80$ was often sufficient to describe correctly the modes. Larger values of Np were mainly used to test the convergence of the eigenvalues.

The numerical spectrum obtained with $Np = 400$ and $H = 12$ for the parameters of figure 1 is shown in figure 2. With these figures, we want to show that the genuine eigenfrequency $\omega \approx 0.128 - 0.028i$, indicated by an arrow in figure 2(b) can only be obtained with a complex path. With a real path, this frequency is behind the continuous spectrum and is not obtained by the code. It is also interesting to note that for both cases, most of the numerical eigenvalues align very well along with the curves of the theoretical continuous spectrum.

Before presenting the results, we would like to mention a second advantage in performing the integration along a complex path. In the inviscid limit, the perturbation equations possess critical point singularities where $-\omega + m\Omega(r) = 0$ or $-\omega + m\Omega(r) = \pm 1/F$. When ω is real, these singularities can be on the real axis. By integrating along the line $r = se^{i\theta}$ with $\theta = \pi/10$, these singularities are thus avoided. Moreover, for the eigenvalues that we will consider which will satisfy $0 < \omega_r < m$ for $m > 0$ [see gray region in figure 1(b)], the way they are avoided corresponds to the prescription obtained by causality. The critical points are indeed in the negative imaginary half-plane when $\Im m(\omega) > 0$: they should therefore be avoided in the positive imaginary half plane. In the presence of a small amount of viscosity, the singularities disappear but viscous scales appear close to the critical points, as well as in large domains of the complex plane (Le Dizès, 2004). By integrating in the complex plane, these viscous regions are avoided. The eigenmode structure then remains mainly non-viscous on the integration contour. It can therefore be better resolved with a small number of polynomials. The interest of such an approach has also been demonstrated by Fabre *et al.* (2006).

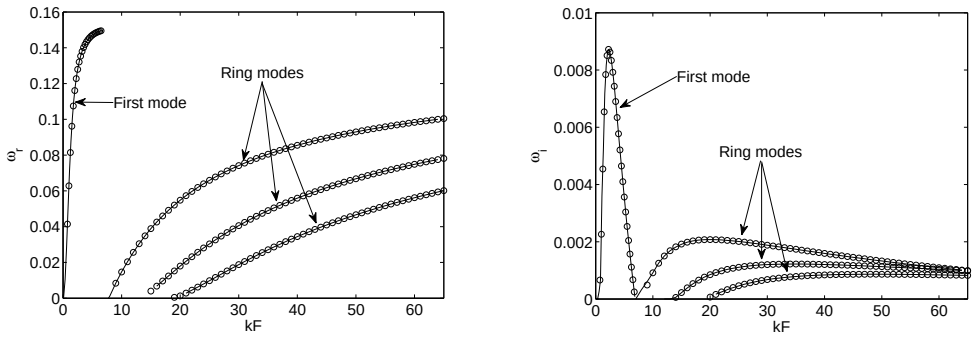

(a) (b)

FIGURE 3. Frequency ω_r (a) and growth rate ω_i (b) of the first four more unstable modes for $Re = \infty$, $F = 0.9$. Symbols: our results with $Np = 150$, $H = 3$, $\theta = \pi/10$. Lines: results obtained by the shooting method of Le Dizès & Billant (2009).

3. Instability of helical modes ($m = 1$)

Unstable modes have been obtained for $m = 1, 2, 3$ but not for $m = 0$. The helical modes ($m = 1$) have been found to be the most unstable. They are presented first.

3.1. *Unstable mode characteristics*

Results in the inviscid and strongly stratified limits have been obtained and discussed in Le Dizès & Billant (2009). They have used a shooting method to obtain the dispersion relation of the unstable helical modes ($m = 1$). For small Froude numbers, they have shown that the Lamb-Oseen vortex exhibits an infinite number of unstable inviscid modes and that the frequencies of these modes only depend on the product kF. Their results are compared to the present spectral code results for a Froude number $F = 0.9$ in figure 3. Only the first four unstable branches have been plotted. The good agreement with an error smaller than 1% constitutes a validation of the code.

The first mode, which is the most unstable for these parameters, is particular as it is unstable in a finite interval of kF ($kF \in [0, 8]$ in fig. 3). It also exhibits a special structure which, contrarily to the other modes, is mainly localized in the vortex core (see figure 4(a)). By contrast, all the other modes are unstable in an infinite wavenumber interval $[k_n, \infty[$. As shown in Le Dizès & Billant (2009), the properties of these modes, as well as the instability mechanism, can be understood by using a large wavenumber WKBJ analysis. They have demonstrated that all these modes exhibit the same structure. They are mainly localized in a ring region and discretized by the number of half-oscillations in this region. All modes exhibit a radiative part which extends to infinity and which is responsible for the destabilization. The density structure of the second mode, which corresponds to the first ring mode is plotted in figure 4(b). Both the localization in a ring and the radiative part are visible in this figure. Note also that the amplitude of the ring mode is negligible in the vortex core, contrarily to the first mode shown in figure 4(a).

The effects of the viscosity and of the stratification on the first two modes are shown in figures 5 and 7. In figure 5, inviscid characteristics are displayed for various Froude numbers. We clearly see that the frequency and the growth rate are mainly functions of kF for all F. For small F, this property is in agreement with the results of Le Dizès & Billant (2009). Note, however, that for moderate Froude numbers, the growth rate of the modes starts to be affected, especially the first mode. In particular, the growth rate of the first mode strongly decreases as F increases above 1, and becomes negative when

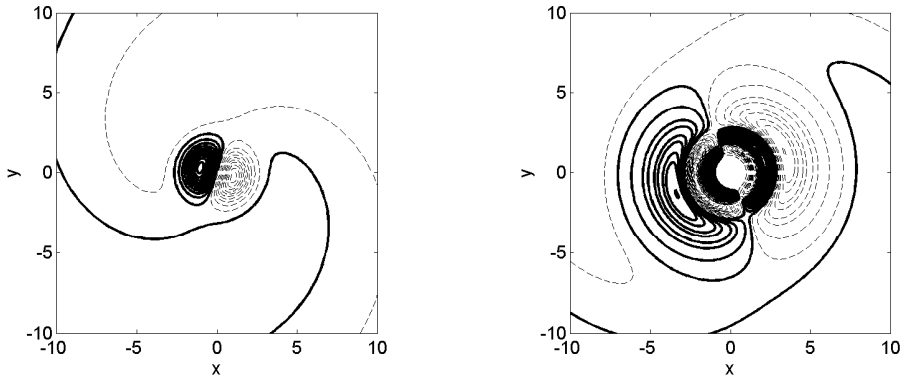

FIGURE 4. Density structure of the first two most unstable helical modes for $F = 0.9$ and $Re = \infty$. (a) First mode obtained for $k = 2.5$, $\omega = 0.126 + i0.0078$; (b) Second mode (first ring mode) obtained for $k = 22.1$, $\omega = 0.055 + i0.00206$.

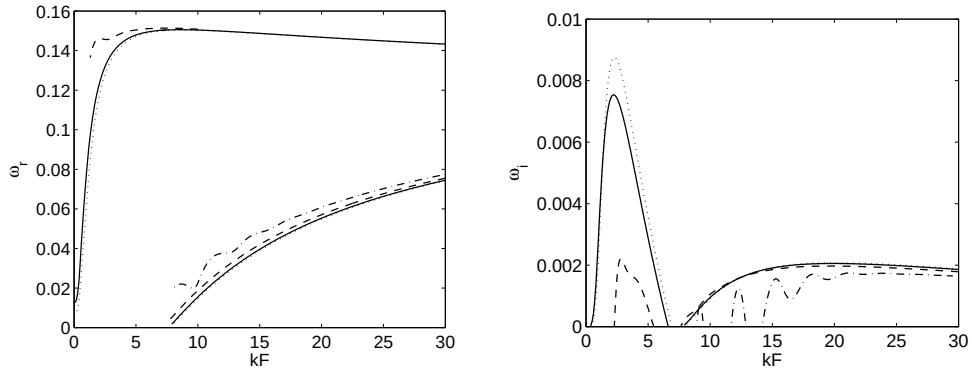

FIGURE 5. Variation of the first two branches with respect to the Froude number in the weakly stratified case for $m = 1$ and $Re = \infty$. (a) Frequency ω_r and (b) growth rate ω_i versus k, for $F = 0.1$ (dotted line), $F = 1$ (solid line), $F = 2$ (dash line), and $F = 3$ (dash-dotted line).

$F > 2.5$. The second mode is, by contrast, less damped by an increase of F. It becomes the dominant mode when $F > 2$. For $F = 3$, we can however note that the growth rate curve changes and exhibits oscillations. As we shall see below, these oscillations are associated with a phenomenon of resonance.

As mentioned above, the eigenmodes possess critical point singularities where either $-\omega + m\Omega(r) = 0$ (type I) or $-\omega + m\Omega(r) = \pm 1/F$ (type II). When the mode becomes neutral some of these singularities are on the real axis. They do not affect the numerical resolution because they remain far from the complex integration contour. For small F, only critical points I are present. The role of these critical points was discussed in Schecter & Montgomery (2004) in the limit of vanishing Froude numbers. For large F, both types of critical points can be present. Here, the critical points which tend to have a stabilizing effect are of type II. These critical points have actually the same effects than the regular critical points in non-stratified vortices (Le Dizès & Lacaze, 2005; Fabre *et al.*, 2006). By contrast, critical points of type I tend to have a destabilizing role (Le Dizès & Billant, 2009).

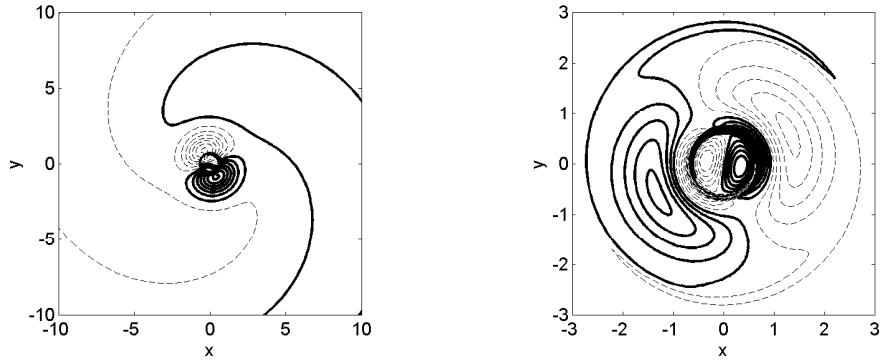

(a) (b)

FIGURE 6. (a) Density and (b) vorticity structure of the first helical mode ($m = 1$) for $F = 1.5$ $Re = 10^5$, $k = 1.6$, $\omega = 0.136 + 0.00538i$.

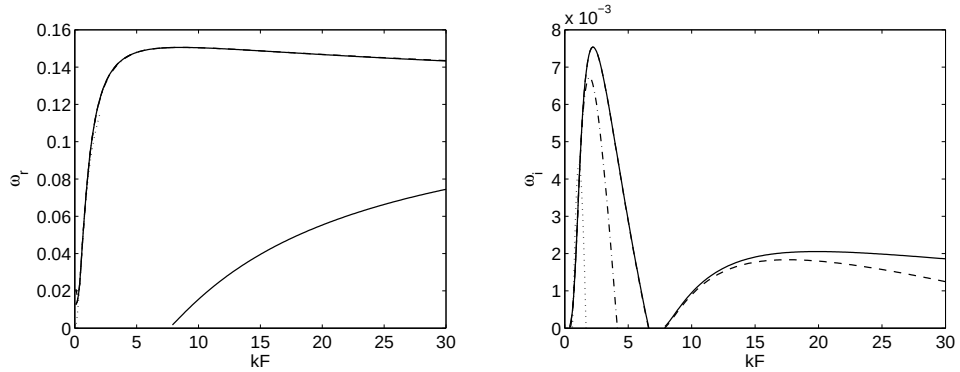

FIGURE 7. Variation of the first two branches with respect to the Reynolds number for $m = 1$, $F = 1$,. (a) Frequency ω_r and (b) growth rate ω_i versus kF for $Re = \infty$ (solid line), $Re = 10^6$ (dash), $Re = 3000$ (dash-dot), $Re = 200$ (dotted)

In the present study, it is the appearance of critical points II which can explain the progressive stabilisation of the eigenmodes when F is increased above 1. The trace of such a critical point is visible in the eigenmode structure, as illustrated in figure 6. Compare, in particular, the two figures 6(a) and 4(a) which display the density structure of the first mode with and without critical layer respectively. Note also the phase change of the vorticity structure across the critical layer [see figure 6(b)]. Such a phase change is typical of viscous critical layers.

A critical point of type II is also present in the second mode when F exceeds 1 but it has a weaker stabilizing effect. More precisely, its stabilizing effect is delayed to higher values of the Froude number. This difference is associated with the different structure of the second mode which is not localized in the vortex core. The critical point II indeed reaches the region where the second mode is localized for much larger values of F. We shall come back to this point in section 3.3 where the properties of the second mode will be analysed in more details.

The effect of the Reynolds number on the first two branches is shown in figure 7. As expected viscosity is stabilising and the larger the wavenumber the stronger the damping. Note for instance that for $Re = 3000$, the second mode is completely stable and the instability band of the first mode has moved to smaller wavenumbers. Surprisingly, we

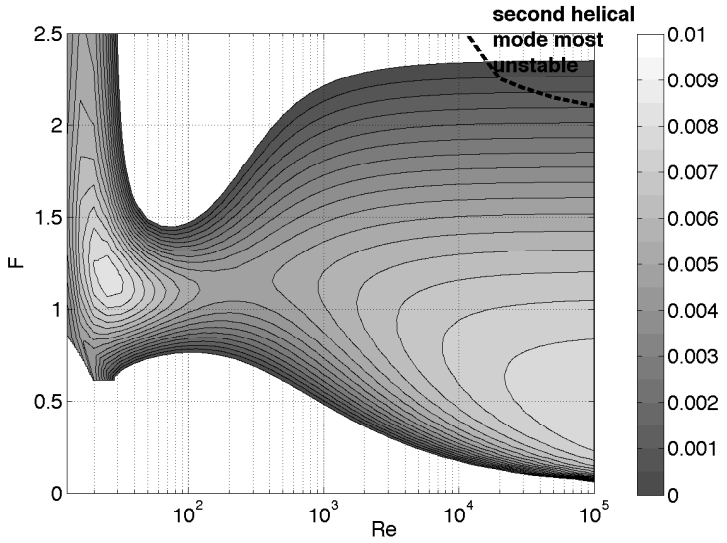

FIGURE 8. Maximum growth rate contours of the first helical mode ($m = 1$) as a function of the base flow parameters F and Re. The dashed curve delimits the unstable region where the first helical mode is not the most unstable mode.

shall see below that viscosity does not kill the instability and that the first mode remains unstable whatever small the Reynolds number. This small Reynolds number behavior is reminiscent of the Kelvin-Helmholtz instability which is also active for Reynolds numbers of order 1 (Esch, 1957). Note however that for small Reynolds numbers, viscous diffusion of the base flow is no longer negligible. The unstable character of the "frozen" base flow for small Reynolds numbers may not be useful in practice.

3.2. *Instability properties of the first helical mode*

We now detail how the properties of the first helical mode vary with F and Re when it is the most unstable mode. The maximum growth rate contours of the first helical mode in the (Re, F) plane are shown in figure 8. We have also indicated in this figure, the parameter region where the first mode is no longer dominant. Maximum growth rate curves for fixed Reynolds numbers are also shown in figure 9(b). The corresponding frequency ω_r and axial wavenumber of the most unstable mode are displayed in figures 9(a,c). A first point to note is that for $Re > 200$, the frequency of the most unstable mode does not vary much with respect to the Froude number and is always between 0.1 and 0.14. The plots of figures 9(d) confirm the scaling already mentioned above: the most unstable mode has a wavenumber which scales as $k_c^-(Re)/F$ for small Froude numbers and large Reynolds numbers $k_c^-(\infty) \approx 2.3$. Note, by contrast that for large Froude numbers, the most unstable wavenumber is mainly constant.

Figure 9(b) demonstrates that for large Reynolds numbers, the mode is most unstable for small Froude numbers. Its maximum growth rate $\omega_i^{max} = 8.75\ 10^{-3}$ is obtained in the inviscid limit for $F \to 0$. The scaling $k_{max} \sim k_c^-(Re)/F$ explains the stabilisation of the mode for small Froude numbers at a finite Reynolds number. This damping is a viscous effect which becomes more and more important as F decreases due to the divergence of the most unstable wavenumber for vanishing F. Whatever the Reynolds number, we therefore expect a stabilisation for sufficiently small Froude numbers. For instance, for $Re = 10^6$, the first helical mode becomes stable at $F = 0.015$. The stabilisation for large

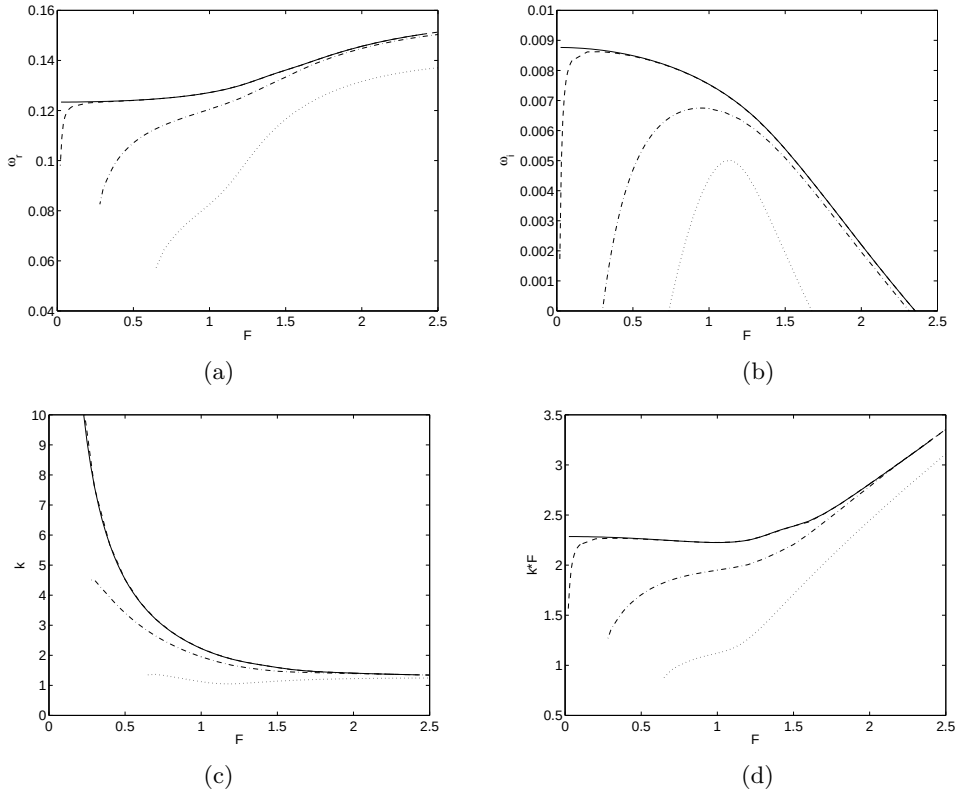

FIGURE 9. Characteristics of the most unstable first helical mode for $Re = \infty$ (solid line), $Re = 10^6$ (dash), $Re = 3000$ (dash-dot), $Re = 200$ (dotted) as a function of the Froude number F. (a) Frequency ω_r, (b) Growth rate ω_i, (c) Axial wavenumber k, (d) Product kF.

F is due to the appearance of a critical point of type II. As explained above, the first mode is more affected by this critical point because it appears when F is increased above 1 in the region where this mode is localized. This also explains why the second mode can become more unstable than the first mode for large Froude numbers. The region of the parameters where the second mode is the most unstable has been indicated in figure 8. More details on this mode are given below.

Figure 8 shows that the first mode is not stabilized by viscosity and remains unstable for small Reynolds numbers in a large domain of Froude numbers. The peak of instability of the Lamb-Oseen vortex is reached for a small Reynolds number $Re = 26$. The characteristics of the most unstable mode over all the parameters are the following: $\omega = 0.0198 + 0.00879i$, $k = 0.385$, $Re = 26$ and $F = 1.15$. The vorticity structure of this mode is given in figure 10(a). It is different from the most unstable mode obtained for infinite Reynolds number and the same Froude number [see figure 10(b)]. It has a simple dipolar structure and resembles a displacement mode. Interestingly, the modes structure changes continuously from 10(b) to 10(a) as the Reynolds number is decreased. This is illustrated in figure 10(c) where we have plotted the vorticity field of the eigenmode obtained at an intermediate Reynolds number $Re = 80$. The continuous variation is also visible in figure 11 where we have displayed the isocontours of the frequency and of the product kF of the most unstable first mode in the (F, Re) plane. We clearly see that

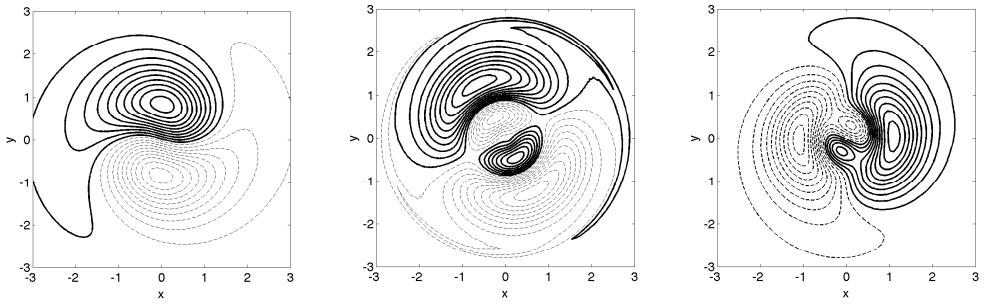

(a) (b) (c)

FIGURE 10. Axial vorticity contours in the plane of the first helical eigenmode for $F = 1.15$ (a) $Re = 26$, $k = 0.38$, $\omega = 0.0195 + i0.00878$ and (b) $Re = \infty$, $k = 1.95$, $\omega = 0.129 + i0.00706$, (c) $Re = 80$, $k = 0.8$, $\omega = 0.0682 + i0.00566$.

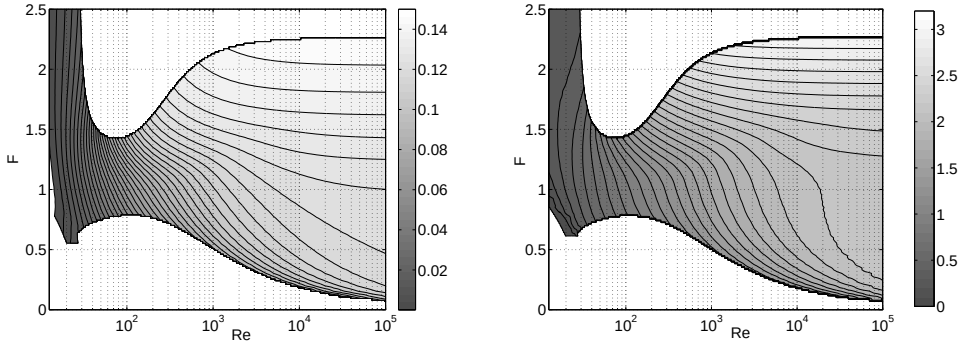

(a) (b)

FIGURE 11. Characteristics of the most unstable first helical mode as function of F and Re. (a) Isocontours of the frequency ω_r; (b) Isocontours of the product kF.

there is no discontinuity and therefore no jump from one mode to another when either the Reynolds number or the Froude number is varied.

When Re goes to 0, both the frequency and the wavenumber of the most unstable mode tend to zero as seen in figures 11. Because the numerical method is not adapted to compute very small wavenumber modes, we have stopped the calculation for $k = 0.05$. The right marginal curve obtained in figures 8 and 11 thus correspond to the marginal curve for a fixed wavenumber $k = 0.05$. We suspect that there is no critical Reynolds number if k is allowed to go to zero.

3.3. *Instability properties of the second helical mode*

As discussed in section 3.1, there is an infinity of unstable helical modes in the inviscid limit. In the previous section, we have given the property of the first mode which is the most unstable mode in a large range of parameters. However, we have also seen that the second mode, which is the first in the family of ring modes can become more unstable for large Froude numbers. In this section, we want to provide more information on this mode in this regime.

The maximum growth rate contours for this mode as function of the base flow parameters are shown in figure 12. This plot has to be compared with figure 8 which shows the characteristics of the first mode. Contrarily to the first mode, the second mode possesses

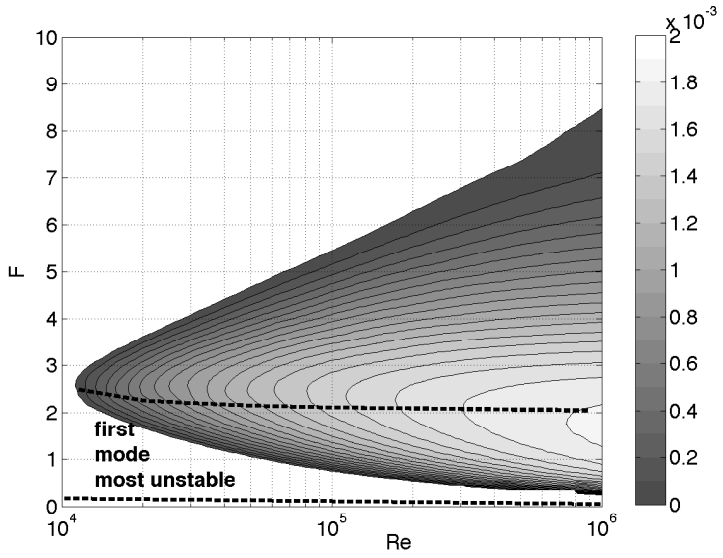

FIGURE 12. Maximum growth rate contours of the second helical mode ($m = 1$) as functions of the base flow parameters F and Re. The dashed curves delimit the unstable region where the first helical mode is more unstable.

a critical Reynolds number $Re_c \approx 10^4$ below which it is stable whatever the Froude number. The instability domain extends to much larger values of the Froude number than the first mode. A large domain of the parameters, which is above the dashed line in figure 12 is then dominated by the second helical mode.

As for the first mode, we have represented in figure 13, the frequency and the wavenumber of the most unstable mode for fixed values of the Reynolds number as a function of the Froude number. The first point to note is that the growth rate curves of the second mode shown in figure 13(b), though they extend to larger Froude numbers, are similar to those of the first mode for the same large Reynolds numbers [see figure 9(b)]. The maximum growth rate is also obtained in the inviscid limit as F goes to 0. It is equal to $\sigma \approx 0.002$. In this domain of parameters (small Froude, large Reynolds), the second mode is however always less unstable than the first mode.

The interesting aspect of the second mode is seen in figures 13(a,c) : the frequency and wavenumber curves exhibit discontinuities as F varies. No such behavior was observed for the first mode. These discontinuities are associated with mode jumps. They can be understood by looking at figure 14 where the growth rate of the second mode is plotted versus k for different Froude numbers. We see in this figure that the growth rate curves exhibit oscillations which become more and more pronounced as F increases. These oscillations are limited to small values of k but they become sufficiently important for large F to change qualitatively the form of the instability domain. For large F, the second mode becomes unstable in instability bands centred on fixed wavenumbers which are independent of the Froude number. Each discontinuity observed in the frequency and wavenumber curves in figure 13 corresponds to a change in the most unstable peak.

The origin of these instability peaks can be attributed to a phenomenon of resonance. In figure 15, we have considered a large Froude number case where this phenomenon is clearly visible. We have plotted in figure 15(a) the frequencies of the modes involved in the resonance. The almost vertical dotted lines correspond to damped Kelvin modes. The solid oscillating curve corresponds to the second helical mode. This radiative mode

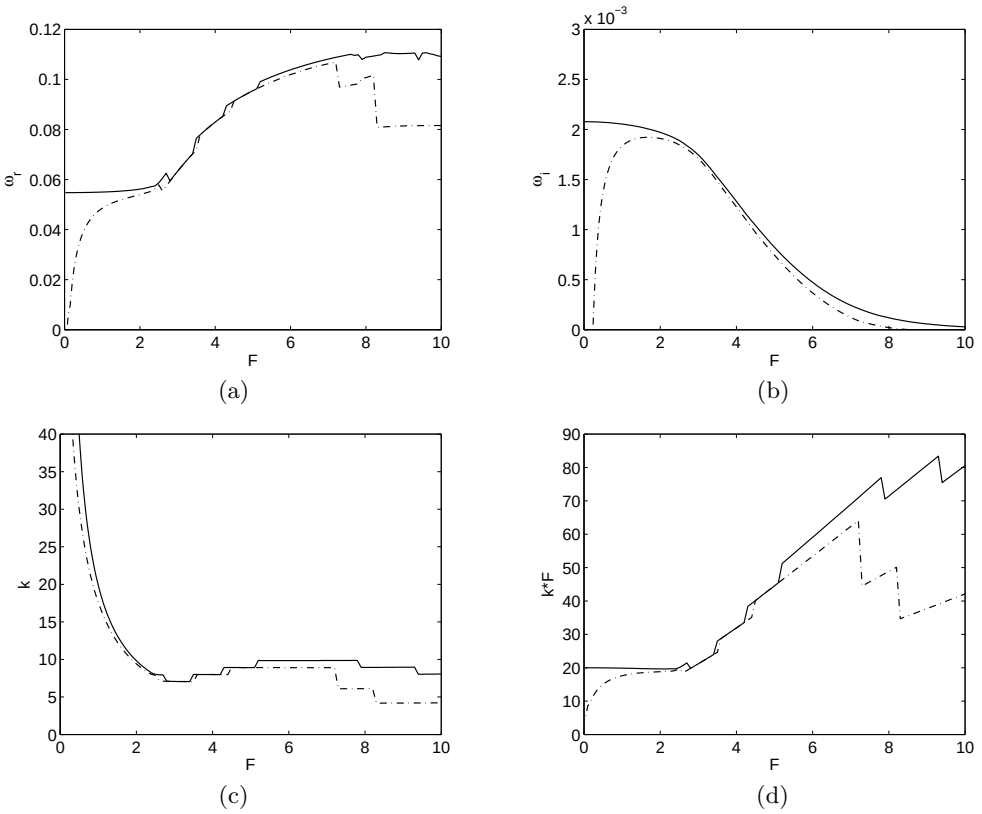

FIGURE 13. Characteristics of the most unstable second helical mode for $Re = \infty$ (solid line) and $Re = 10^6$ (dash) as a function of the Froude number F. (a) Frequency ω_r, (b) Growth rate ω_i, (c) Axial wavenumber k, (d) Product kF.

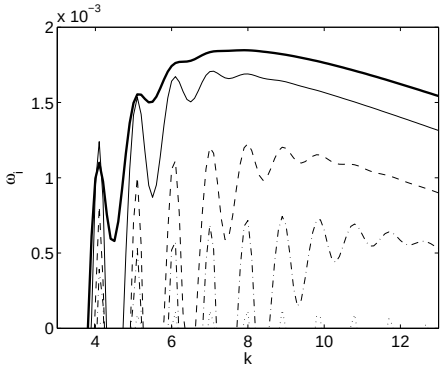

FIGURE 14. Maximum growth rate versus k of the second helical mode for $Re = \infty$. $F = 2.5$ (thick solid line), $F = 3$ (solid), $F = 4$ (dash), $F = 5$ (dash-dot), $F = 7$ (dotted)

is also damped except when its frequency matches the frequency of one of the Kelvin modes. This is a clear evidence of the mechanism of resonance. The Kelvin modes can also be destabilized by a resonance with the third helical mode (which is not plotted in fig. 15(a) because it is too strongly damped). This leads to the bands of instability plotted as dotted lines in fig. 15(b). The fact that the two types of modes do exist simultaneously can be understood by using the results of the asymptotic theory performed in Le Dizès &

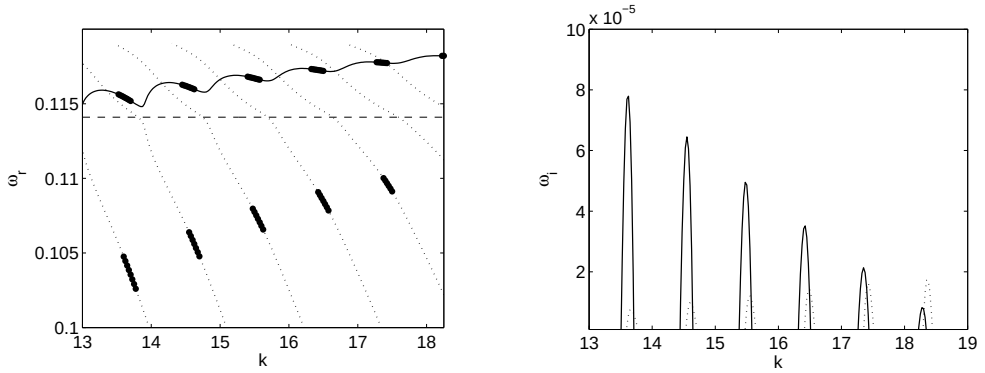

(a) (b)

FIGURE 15. Dispersion relation of the helical modes for $Re = \infty$ and $F = 8$. (a) Frequency ω_r and (b) growth rate ω_i. The modes shown in fig. (a) are damped expect on the thick part of the curve where the growth rate is given in fig. (b). Solid and dotted lines correspond to radiative and Kelvin modes respectively. Modes with a growth rate smaller than $-3\,10^{-2}$ have not been plotted in fig. (a). The horizontal dashed line in fig. (a) is the theoretical prediction of maximum resonance.

Lacaze (2005) and Le Dizès & Billant (2009). In Le Dizès & Lacaze (2005), it was shown that for infinite Froude number, inviscid Kelvin modes with frequencies $0 < \omega_r < 0.13$ do exist. These modes are localised in the vortex core between the centre and a (turning) point $r_t(\omega_r)$ defined by $\omega_r = \omega^-(r_t)$ with

$$\omega^-(r) = m\Omega(r) - \sqrt{2\Omega(r)(2\Omega + r\frac{d\Omega}{dr})}\ . \tag{3.1}$$

When stratification is introduced, these Kelvin modes are still present and not immediately affected by the critical point r_c of type II which appears in their structure. As explained in Le Dizès & Lacaze (2005), the Kelvin modes are expected to remain quasi-neutral as long as this critical point is outside the region where the mode is localized, that is as long as $r_t(\omega_r) < r_c(\omega_r, F)$. This is always the case when $F < 2.59$. However, when $F > 2.59$, this limits the frequency of the quasi-neutral Kelvin modes to an interval $(0, \omega_l(F))$, where $\omega_l(F)$ is defined by $r_t(\omega_l) = r_c(\omega_l, F)$ [see figure 16]. For the radiative modes, we have the opposite problem. As shown by Le Dizès & Billant (2009), these modes are known to be quasi-neutral in the strongly stratified case. In this limit, they possess similar frequencies $0 < \omega_r < 0.13$ as Kelvin modes in the non-stratified case and are localised in the ring region delimited by the two turning points where $\omega_r = \omega^-(r)$. The left turning point of this region corresponds to the turning point delimiting the Kelvin mode region. Therefore, both modes leave in different regions. As for the Kelvin modes, we expect the radiative modes to remain quasi-neutral as long as the critical point does not enter the region where the mode is localized. When $F > 2.59$, this provides a constraint on the allowed frequencies which must satisfy $\omega_l(F) < \omega_r < 0.13$. With these large wavenumber analysis arguments, both types of modes are thus expected to remain quasi-neutral in distinct frequency intervals having the frequency $\omega_l(F)$ as common boundary, [see figure 16]. It is therefore around this frequency that we expect a possible mechanism of resonance. This is in agreement with the numerical results obtained for $F = 8$. For this value of F, we have $\omega_l(8) \approx 0.114$, which is close to the value for which the mechanism of resonance is the most efficient [see figure 15]. Using these arguments, we predict that the mechanism of resonance is active on the helical ring modes for F satisfying $2.59 < F < 18.5$. Above $F = 18.5$, the critical point is within

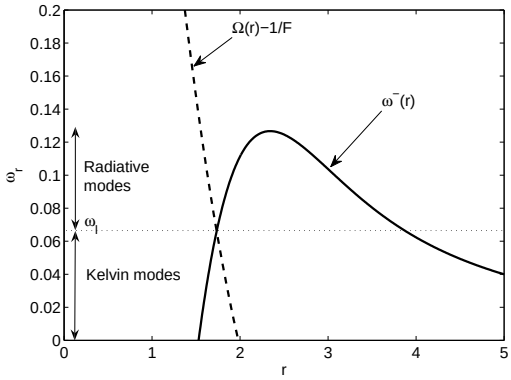

FIGURE 16. Theoretical predictions for the frequency domain of existence of quasi-neutral modes for $m = 1$ and $F = 4$. Dashed line: plot of $\Omega(r) - 1/F$ which defines the location of the critical point II; Solid line: plot of $\omega^-(r)$ which defines the location of the turning points.

the domain where the ring modes are localized whatever their frequency. The modes are therefore expected to be too strongly damped to be resonantly excited.

The resonance mechanism is also visible in the structure of the modes. In figure 17(b-d), we have plotted the density of the eigenmodes for two resonant wavenumbers (c,d) and one non-resonant wavenumber (b) for a particular set of parameters. The frequency of these modes has been indicated in figure 17(a). In order to plot these modes in the physical space, especially the stable mode (b), we have used a particular integration path which is real up to $r = 20$ and then complex on the line $r = 20 + se^{i\theta}$ to satisfy the condition of radiation. To facilitate the comparison of the different profiles, we have normalised the density of the eigenmodes such that its maximum amplitude in the radiative domain $r \in [5; 20]$ is equal to 1. By doing so, we can remark that the amplitude of the mode in the core region $r < 1.6$ is greater for the unstable cases. The stable mode is by contrast more localized in the critical layer. It is also interesting to compare the number of wavelength in the core region for the two successive resonant modes shown in figures 17(c) and (d). We can notice that there is one more half wavelength in figure 17(d) than in 17(c). This is in agreement with the fact that the resonance occurs with two successive Kelvin modes which possess this particular property (Le Dizès & Lacaze, 2005).

4. Instability of higher azimuthal wavenumbers: $m = 2, 3, ...$

For higher azimuthal wavenumbers ($m \geq 2$), unstable modes have also been obtained. Their structure and properties resemble those of the helical ring modes. In figures 18 and 19, we have plotted the first unstable branches for an inviscid and strongly stratified case for $m = 2$ and $m = 3$ respectively. As for the helical ring modes, there are an infinite number of unstable inviscid modes, which are all unstable in semi-infinite wavenumber intervals. The frequency of each mode increases from zero to a finite value which is 0.4 for $m = 2$ and 1 for $m = 3$ as the wavenumber increases. However, the growth rate of each mode reaches its maximum for a finite wavenumber. As for the case $m = 1$, we have also observed that, for small Froude numbers, the dependence with respect to the Froude number appears only via a rescaled wavenumber kF.

The density and vorticity structure of an unstable mode $m = 2$ has been illustrated in figure 20. We can notice in figure 20(a) the radiative zone which extends far from the

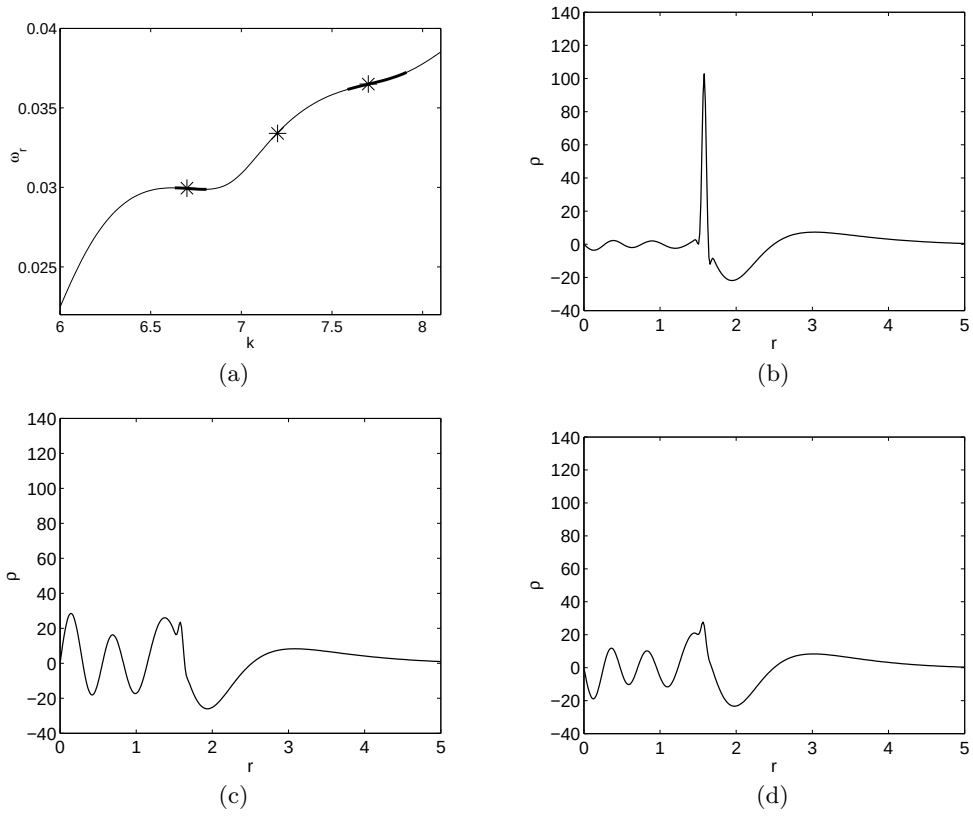

FIGURE 17. Structure of the resonant/non-resonant modes for $m = 1$, $F = 3$, $Re = 10^5$. (a) Frequency of the third helical mode (second ring mode). Thick line: unstable domain. The radial profile of the eigenmode density at the crosses is given in fig. (b-d). (b) $kF = 7.2$ (stable); (c) $kF = 6.7$ (unstable); (d) $kF = 7.7$ (unstable).

vortex. In the vorticity plot [figure 20(b)], we also observe near $r_c \approx 0.29$ the trace of a critical point of type I. Contrarily to the helical modes $m = 1$, the mode $m = 2$ extends in the core region. This property can be understood from the large wavenumber asymptotic theory already used above. Using this theory, we expect the eigenmodes to be localized between two turning points corresponding to zeroes of the function $\omega^-(r)$ defined in (3.1). As the left turning point is closer to the centre than for the modes $m = 1$, the extension of the mode towards the centre is thus more important. For higher azimuthal wavenumbers $m \geq 3$, the left turning point disappears, and all the mode becomes core modes. For $m = 2$, the two turning points merge for $\omega \approx 0.4$. For $m = 3$, the right turning point collapses to the centre for $\omega \approx 1$. We therefore do not expect eigenmodes above these frequencies in agreement with the numerical results shown in figures 18 and 19. With this argument, we can also predict that there exist radiative core modes for all $m \geq 3$ with frequencies between 0 to $m - 2$.

For the case $m = 2$, the most unstable mode is the first mode [see figure 18]. The instability diagram for this azimuthal wavenumber can therefore be obtained by considering the first mode only. In figure 21, we have plotted the maximum growth rate contours of this first mode as functions of Re and F. If we compare this diagram with the one obtained for the second helical mode [see figure 12], we can notice that the characteristics of the growth rate contours with respect to these parameters are similar. Note however

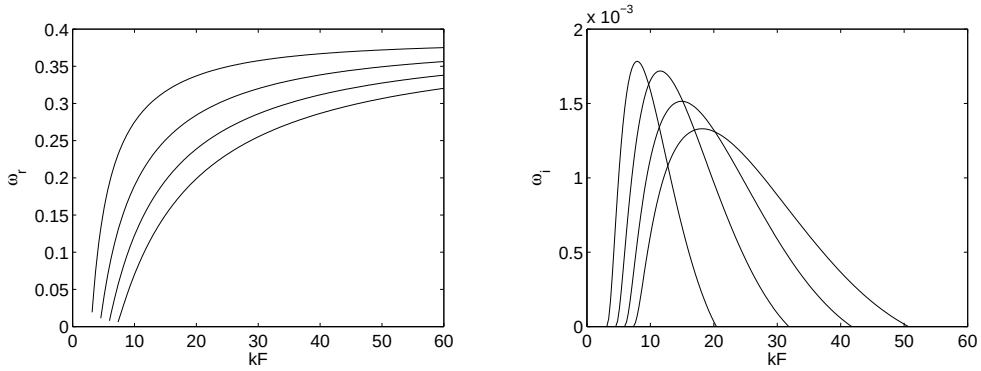

(a) (b)

FIGURE 18. (a) Frequency ω_r and (b) growth rate ω_i for $m = 2$, $Re = \infty$ and $F = 0.3$

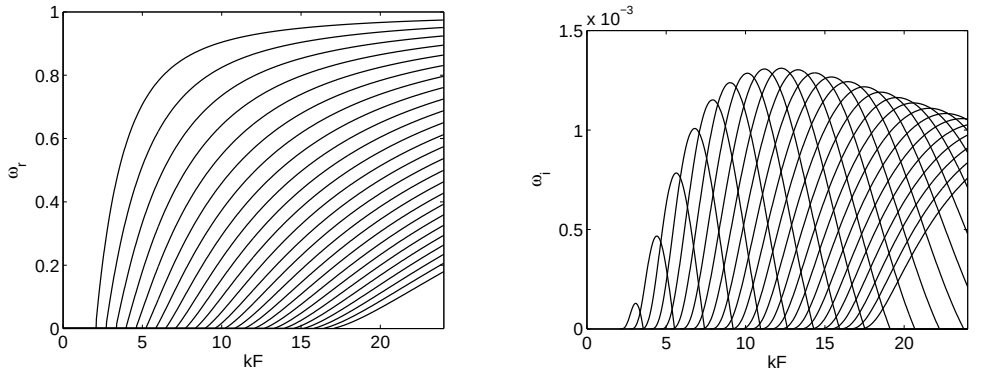

(a) (b)

FIGURE 19. (a) Frequency ω_r and (b) growth rate ω_i for $m = 3$, $Re = \infty$ and $F = 0.2$

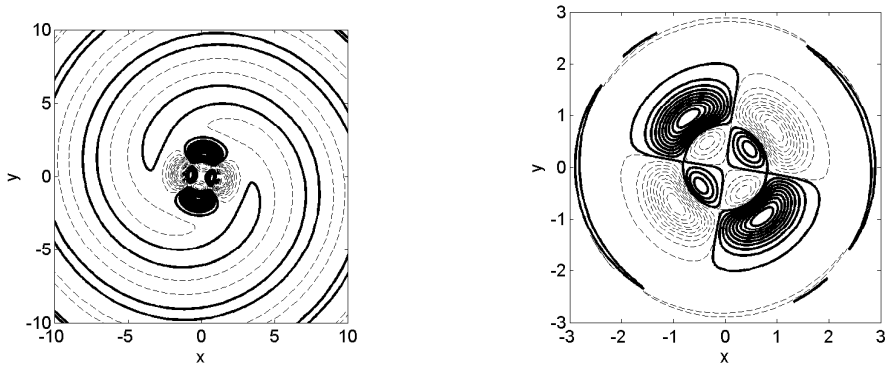

(a) (b)

FIGURE 20. Structure of the eigenmode $m = 2$, $k = 19.8$ and $\omega = 0.244 + i0.00173$ for $F = 0.4$ and $Re = \infty$. (a) Density contours, (b) Axial vorticity contours.

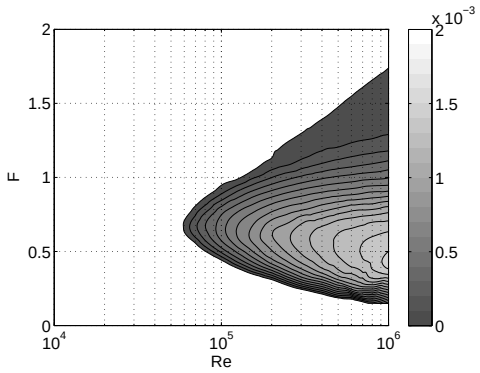

FIGURE 21. Maximum growth rate contours of the first mode $m = 2$ in the (Re, F) plane.

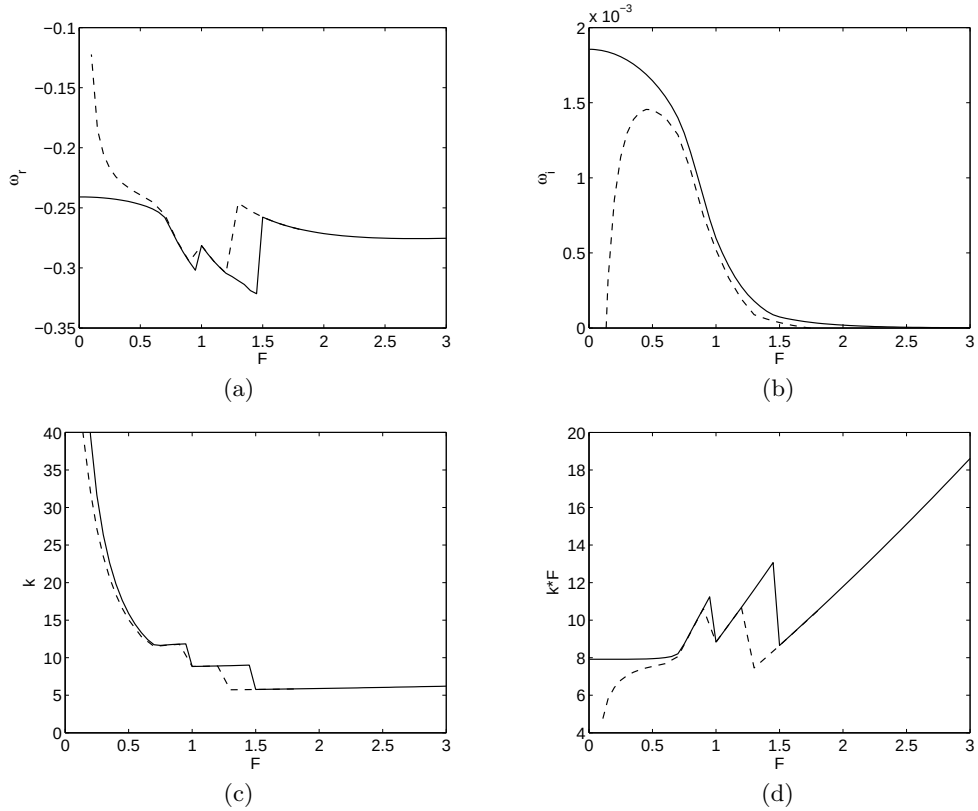

FIGURE 22. Characteristics of the most unstable mode $m = 2$ as a function of the Froude number for $Re = \infty$ (solid line), $Re = 10^6$ (dash). (a) Frequency ω_r, (b) Growth rate ω_i, (c) Wavenumber k, (d) Product kF.

that, for $m = 2$, the growth rate values are smaller, the critical Reynolds number is larger and the maximum growth rate tends to be reached for Froude number around 0.5 instead of 1 for the modes $m = 1$. Yet, in the inviscid limit, the maximum growth rate is also reached for vanishing Froude numbers [see figure 22(b)]. A similar scaling of the most unstable wavenumber with respect to the Froude number is obtained: k_{max} is constant for large F but proportional to $1/F$ for small F. The mechanism of resonance is also

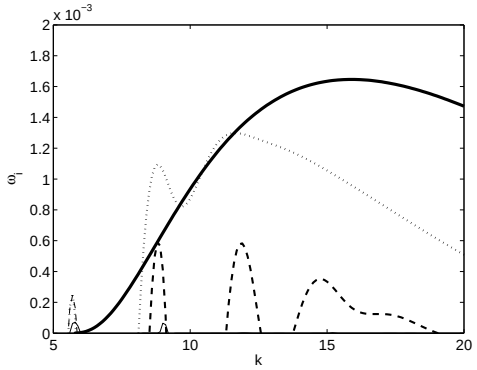

FIGURE 23. Maximum growth rate versus k of the first mode $m = 2$ for $Re = \infty$. $F = 0.5$ (thick solid line), $F = 0.75$ (dotted line), $F = 1$ (dash line), $F = 1.5$ (solid line)

active for the modes $m = 2$ as it can be seen in figure 23. This leads to discontinuities in the plots of the most unstable frequency and wavenumber [see figure 22(a,c,d)]. However, using the theoretical arguments mentioned above, we predict that resonance is possible for Froude numbers between 0.5 and 2.8 only.

For $m = 3$ and for larger m, similar characteristics are obtained but the modes are less unstable, and therefore destabilized for larger Reynolds numbers. The large wavenumber asymptotic theory also predicts that the unstable radiative modes are all core modes and that no phenomenon of resonance is possible whatever the Froude number.

5. Conclusion

In this work, we have obtained the stability characteristics of a Lamb-Oseen vortex stratified along its axis for a large range of Froude and Reynolds numbers. We have shown that for moderate Froude number the vortex is unstable, whatever the Reynolds number, with respect to a helical perturbation ($m = 1$) which resembles a displacement mode with a radiative structure. For large Reynolds numbers ($Re > 10^4$) and large Froude numbers ($F > 2$), the vortex becomes more unstable with respect to another helical radiative mode which is localized in a ring. Moreover, we have shown that the instability for large Froude numbers is boosted by a mechanism of resonance. We have demonstrated that the radiative mode can enter in resonance with vortex Kelvin modes for particular frequencies in a specific range of Froude numbers. This mechanism selects particular wavenumbers which were found to be independent of the Froude number and makes the vortex unstable up to $F \approx 10$. Unstable perturbations with larger azimuthal wavenumbers were also found. All these modes are less unstable than the helical ring mode and exhibit a larger critical Reynolds number. The mechanism of resonance has also been shown to be present for $m = 2$ but not for larger azimuthal wavenumbers.

The results obtained in this paper could have important consequences for geophysical applications. We have shown that a generic vortex model as the Lamb-Oseen vortex is unstable for large Reynolds numbers in a very large range of Froude numbers. The strong small-scale cyclonic vortices sometimes observed in the atmosphere and the coherent vortical structures generated by the tide in the oceans could therefore be affected by this instability. Note also that for Froude numbers larger than 1, these vortical structures are also affected by another instability mechanism as soon as they are slightly tilted with respect to direction of stratification (Boulanger *et al.*, 2007, 2008).

It is worth mentioning that background rotation has not been considered in the present

work. Weak negative background rotation is known to be destabilising: the vortex becomes unstable with respect to the centrifugal instability. Positive background rotation could by contrast have an opposite effect if we believe in the inviscid theoretical predictions (Schecter & Montgomery, 2004; Le Dizès & Billant, 2009). It will therefore be interesting to quantify this stabilizing effect and determine whether it can suppress the present instability.

It is important to emphasize the radiative nature of the unstable modes. We have demonstrated that the geostrophic motion associated with the Lamb-Oseen vortex is able to emit spontaneously internal gravity waves. This phenomenon is a clear illustration that balanced geostrophic motions and unbalanced oscillating motions are strongly coupled and that the evolution of the vortex could not have been predicted by filtering out the unbalanced motions associated with internal gravity waves. Similar interactions between balanced and unbalanced motions have been documented in several recent studies (Molemaker *et al.*, 2005; Williams *et al.*, 2005; Vanneste & Yavneh, 2007; Gula *et al.*, 2009).

References

Balmforth, N. J. 1999 Shear instability in shallow water. *J. Fluid Mech.* **387**, 97–127.

Billant, P. & Gallaire, F. 2005 Generalized rayleigh criterion for non-axisymmetric centrifugal instabilities. *J. Fluid Mech.* **542**, 365–379.

Billant, P. & Le Dizès, S. 2009 Waves on a columnar vortex in a strongly stratified fluid (in preparation).

Boubnov, B., Gledzer, E. & Hopfinger, E. 1995 Stratified circular Couette flow: instability and flow regimes. *J. Fluid Mech.* **292**, 333–358.

Boulanger, N., Meunier, P. & Le Dizès, S. 2007 Structure of a tilted stratified vortex. *J. Fluid Mech.* **583**, 443–458.

Boulanger, N., Meunier, P. & Le Dizès, S. 2008 Instability of a tilted vortex in stratified fluid. *J. Fluid Mech.* **596**, 1–20.

Broadbent, E. & Moore, D. W. 1979 Acoustic destabilization of vortices. *Phil. Trans. Roy. Soc.* A **290**, 353–371.

Eloy, C. & Le Dizès, S. 1999 Three-dimensional instability of Burgers and Lamb-Oseen vortices in a strain field. *J. Fluid Mech.* **378**, 145–166.

Esch, R. E. 1957 The instability of a shear layer between two parallel streams. *J. Fluid Mech.* **3**, 289–303.

Fabre, D. & Jacquin, L. 2004 Viscous instabilities in trailing vortices at large swirl numbers. *J. Fluid Mech.* **500**, 239–262.

Fabre, D., Sipp, D. & Jacquin, L. 2006 The Kelvin waves and the singular modes of the Lamb-Oseen vortex. *J. Fluid Mech.* **551**, 235–274.

Ford, R. 1994 The instability of an axisymmetric vortex with monotonic potential vorticity in rotating shallow water. *J. Fluid Mech.* **280**, 303–334.

Gula, J., Plougonven, R. & Zeitlin, V. 2009 Ageostrophic instabilities of fronts in a channel in a stratified rotating fluid. *J. Fluid Mech.* (in press).

Hayashi, Y.-Y. & Young, W. R. 1987 Stable and unstable shear modes of rotating parallel flows in shallow waters. *J. Fluid Mech.* **184**, 477–504.

Hodyss, D. & Nolan, D. S. 2008 The Rossby-inertia-buyancy instability in baroclinic vortices. *Phys. Fluids* **20**, 096602.

Knessl, C. & Keller, J. B. 1992 Stability of rotating shear flows in shallow water. *J. Fluid Mech.* **244**, 605–614.

Le Bars, M. & Le Gal, P. 2007 Experimental analysis of the stratorotational instability in a cylindrical Couette flow. *Phys. Rev. Lett.* **99**, 064502.

Le Dizès, S. 2004 Viscous critical-layer analysis of vortex normal modes. *Stud. Appl. Math.* **112** (4), 315–332.

Le Dizès, S. 2008 Inviscid waves on a lamb-oseen vortex in a rotating stratified fluid: consequences on the elliptic instability. *J. Fluid Mech.* **597**, 283–303.

Le Dizès, S. & Billant, P. 2006 Instability of an axisymmetric vortex in a stably stratified fluid. In *6th European Fluid Mechanics Conference*, p. 143. Stockholm, Sweden.

Le Dizès, S. & Billant, P. 2009 Radiative instability in stratified vortices (submitted).

Le Dizès, S. & Lacaze, L. 2005 An asymptotic description of vortex Kelvin modes. *J. Fluid Mech.* **542**, 69–96.

Le Dizès, S. & Laporte, F. 2002 Theoretical predictions for the elliptic instability in a two-vortex flow. *J. Fluid Mech.* **471**, 169–201.

Lessen, M. & Paillet, F. 1974 The stability of a trailing line vortex. Part 2. Viscous theory. *J. Fluid Mech.* **65**, 769–779.

Luo, K. H. & Sandham, N. D. 1997 Instability of vortical and acoustic modes in supersonic round jets. *Phys. Fluids* **9**, 1003–13.

Meunier, P. & Leweke, T. 2005 Elliptic instability of a co-rotating vortex pair. *J. Fluid Mech.* **533**, 125–159.

Miyazaki, T. & Fukumoto, Y. 1991 Axisymmetric waves on a vertical vortex in a stratified fluid. *Phys. Fluids* A **3**, 606–616.

Molemaker, M. J., McWilliams, J. C. & Yavneh, I. 2001 Instability and equilibration of centrifugally stable stratified taylor-couette flow. *Phys. Rev. Lett.* **86**, 5270–5273.

Molemaker, M. J., McWilliams, J. C. & Yavneh, I. 2005 Baroclinic instability and loss of balance. *J. Phys. Oceanogr.* **35**, 1505–1517.

Narayan, R., Goldreich, P. & Goodman, J. 1987 Physics of modes in a differentially rotating system - analysis of the shearing sheet. *Mon. Not. R. Astr. Soc.* **228**, 1–41.

Papaloizou, J. C. B. & Pringle, J. E. 1984 The dynamical stability of differentially rotating discs with constant specific angular momentum. *Mon. Not. R. astr. Soc.* .

Sakai, S. 1989 Rossby-Kelvin instability: a new type of ageostrophic instability caused by a resonance between Rossby waves and gravity waves. *J. Fluid Mech.* **202**, 149–176.

Satomura, T. 1981 An investigation of shear instability in a shallow water. *J. Met. Soc. Japan* **59**, 148–167.

Schecter, D. A. 2008 The spontaneous imbalance of an atmospheric vortex at high Rossby number. *J. Atmos. Sci.* **65**, 2498–2521.

Schecter, D. A. & Montgomery, M. T. 2004 Damping and pumping of a vortex Rossby wave in a monotonic cyclone: Critical layer stirring versus inertia-buoyancy wave emission. *Phys. Fluids* **16**, 1334–48.

Schecter, D. A. & Montgomery, M. T. 2006 Conditions that inhibit the spontaneous radiation of spiral intertia-gravity waves from an intense mesoscale cyclone. *J. Atmos. Sci.* **63**, 435–456.

Vanneste, J. & Yavneh, I. 2007 Unbalanced instabilities of rapidly rotating stratified shear flows. *J. Fluid Mech.* **584**, 373–396.

Williams, P. D., Haine, T. W. N. & Read, P. L. 2005 On the generation mechaisms of short-scale unbalanced modes in rotating two-layer flows with vertical shear. *J. Fluid Mech.* **528**, 1–22.

Withjack, E. & Chen, C. 1974 An experimental study of Couette instability of stratified fluids. *J. Fluid Mech.* **66**, 725–737.

Withjack, E. & Chen, C. 1975 Stability analysis of rotational couette flow of stratified fluids. *J. Fluid Mech.* **68**, 157–175.

Yavneh, I., McWilliams, J. & Molemaker, M. 2001 Non-axisymmetric instability of centrifugally stable stratified Taylor–Couette flow,. *J. Fluid Mech.* **448**, 1–21.

Annexe 3

Articles sur la dynamique d'un fluide dans un cylindre en précession

P. Meunier, Ch. Eloy, R. Lagrange & F. Nadal (2008). "A rotating fluid cylinder subject to weak precession", *J. Fluid Mech* **599**, pp. 405-440.

R. Lagrange, P. Meunier, Ch. Eloy, & F. Nadal (2008). "Instability of a fluid inside a precessing cylinder", *Phys. Fluids* **20** (8).

J. Fluid Mech. (2008), *vol.* 599, *pp.* 405–440.
doi:10.1017/S0022112008000335 Printed in the United Kingdom

A rotating fluid cylinder subject to weak precession

PATRICE MEUNIER[1], CHRISTOPHE ELOY[1], ROMAIN LAGRANGE[1] AND FRANÇOIS NADAL[2]

[1]IRPHE, CNRS, Universités Aix Marseille I & II, 49 rue Joliot–Curie, 13013 Marseille, France
[2]Commissariat à l'Energie Atomique, CESTA, 33114 le Barp, France

(Received 4 July 2007 and in revised form 18 December 2007)

In this paper, we report experimental and theoretical results on the flow inside a precessing and rotating cylinder. Particle image velocimetry measurements have revealed the instantaneous structure of the flow and confirmed that it is the sum of forced inertial (Kelvin) modes, as predicted by the classical linear inviscid theory. But this theory predicts also that the amplitude of a mode diverges when its natural frequency equals the precession frequency. A viscous and weakly nonlinear theory has therefore been developed at the resonance. This theory has been compared to experimental results and shows a good quantitative agreement. For low Reynolds numbers, the mode amplitude scales as the square root of the Reynolds number owing to the presence of Ekman layers on the cylinder walls. When the Reynolds number is increased, the amplitude saturates at a value which scales as the precession angle to the power one-third for a given resonance. The nonlinear theory also predicts the forcing of a geostrophic (axisymmetric) mode which has been observed and measured in the experiments. These results allow the flow inside a precessing cylinder to be fully characterized in all regimes as long as there is no instability.

1. Introduction

In the field of aerospace, the stability of spinning spacecraft containing propellant liquids is still a topical question. For instance, the attitude of spinning satellites (see Stewartson 1958; Gans 1984; Garg, Furunoto & Vanyo 1986; Agrawal 1993; Bao & Pascal 1997) is likely to be disrupted by the hydrodynamics of the fluid inside. Consequently, a good understanding of the behaviour of such a fluid–structure coupled system requires a precise knowledge of the dynamics of the rotating contained fluid. Moreover, rotating fluid dynamics occurs far beyond the field of aerospace: many atmospheric phenomena (hurricanes, tornadoes) are closely connected with this class of problems, due to the dominant role played by the Coriolis force at low Rossby numbers (Vanyo 1993).

First experimental and theoretical studies on rotating fluids date from the end of the 19th century. Lord Kelvin (1880) suggested that the flow of a disturbed rotating fluid could be decomposed into a sum of so-called normal Kelvin modes (i.e. inertia waves), each of them corresponding to a well-defined frequency which is always less than twice the basic rotation frequency. The inviscid approach of Kelvin can be extended in the limit of large Reynolds numbers by taking into account viscous boundary layers on the walls of the container as shown by Kudlick (1966) and Greenspan (1968). A large set of experimental and numerical studies for the case of a completely filled

cylinder (see Fultz 1959; McEwan 1970; Kobine 1995; Kerswell & Barenghi 1995) has confirmed the values of the frequencies and viscous decay rates predicted by these theories.

An important aspect of these rotating flows is that Kelvin modes have been shown to become unstable for large Reynolds numbers. McEwan (1970) first showed that when a rotating fluid cylinder is forced at a given frequency on one of its ends, Kelvin modes are forced. One of these Kelvin modes can become resonant if its wavelength matches the height of the cylinder. This leads to a *resonant collapse* (i.e. a breakdown of the initial mode) degenerating into a fine-scale disordered flow. In some cases, this very disordered flow can relaminarize into solid-body rotation, again leading to a cycle of instability, breakdown and relaminarization. This behaviour has also been reported when the Kelvin modes are forced in a partly filled and tilted cylinder (Thompson 1970) or in a completely filled cylinder in precession (Manasseh 1992; Mahalov 1993) or when they are the natural modes of an instability such as the elliptic instability (Malkus 1989; Eloy, Le Gal & Le Dizès 2000; Kerswell 2002; Eloy, Le Gal & Le Dizès 2003). The physical mechanism leading to the breakdown is still unclear but several scenarios have been proposed. Kerswell (1999) proposed that a given Kelvin mode can trigger a triad resonance with two other Kelvin modes leading to an instability (this mechanism has similarity with the mechanism of the elliptic instability). The triggered modes can themselves be unstable leading to a secondary instability and eventually to a tertiary instability, and so on. This cascade of bifurcation may explain the transition to turbulence observed in these flows. When nonlinear effects are important, another aspect of these rotating flows is the generation of a geostrophic motion which slows down the main solid body rotation and modifies its radial profile. Kobine (1995, 1996) has proposed that, owing to this geostrophic motion, the main flow can be modified enough to cause a centrifugal instability responsible for the breakdown. Finally the observed breakdown could also be due to a boundary layer instability near the wall of the container. So far, there is no clear experimental evidence to support any of these scenarios.

The picture is different for an ellipsoidal container since there are no corners to prevent the azimuthal circulation. For an inviscid fluid, Poincaré (1910) showed that there exists a class of solution with uniform vorticity whose direction rotates around the precession axis. In a real fluid, the presence of viscous boundary layers selects a unique solution in which the viscous and pressure torques balance the precessional torque (Lorenzani & Tilgner 2001). However, some (conical) inertial waves are still generated by the breakdown of the Ekman layer at a critical latitude (Noir, Jault & Cardin 2001). This can lead to an instability consisting of cylindrical waves propagating around the axis of rotation of the fluid (Lorenzani & Tilgner 2001) and generates a strong turbulent flow (Goto *et al.* 2007). It is thus unclear if this flow will be unstable through local destabilization of the Ekman layers or through a global instability (such as a triadic resonance) for large Reynolds numbers.

In this paper, we address the basic laminar flow in the case of a precessing cylinder full of water. This flow can be decomposed into a sum of Kelvin modes which are resonant if their wavelength is equal to $2H$, $2H/3$, $2H/5$, etc. (where H is the cylinder height). By performing particle image velocimetry (PIV) measurements in the precessing frame, we investigate the primary inertial flow in both situations: far from a resonance, where the linear inviscid theory is valid; then close to a resonance, where viscous and nonlinear effects determine the amplitude of the resonant Kelvin mode. Gans (1970) first gave a theoretical interpretation of the amplitude saturation close to the resonance by taking into account the viscous effects only. In this paper,

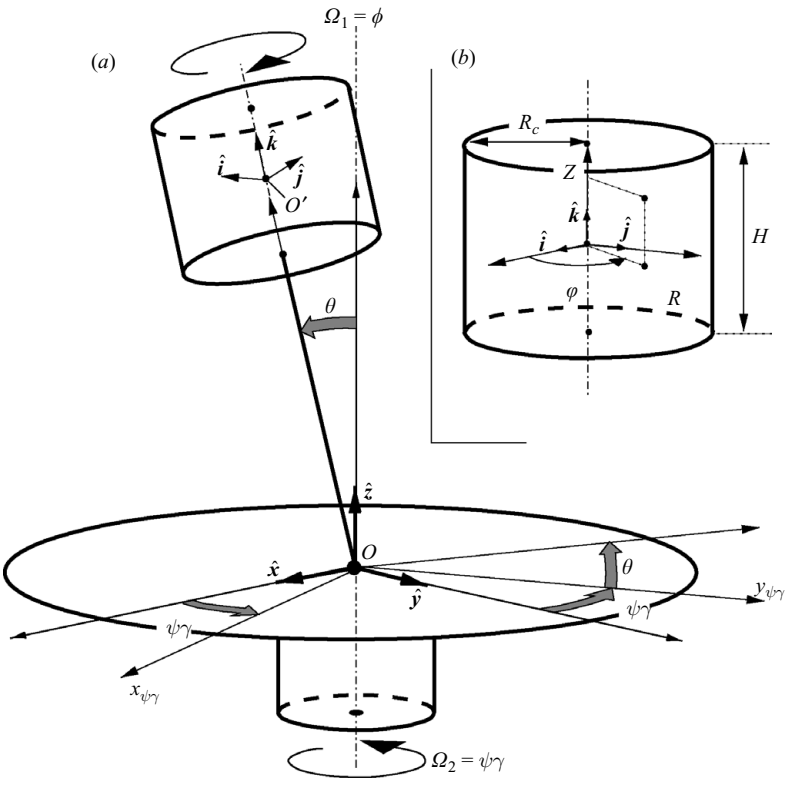

FIGURE 1. Sketch of the problem. (*a*) A cylinder of radius R_c and height H rotates about its axis at fixed angular frequency Ω_1. The precession rate Ω_2 and the nutation angle θ are also fixed. (*b*) Polar coordinates (R, φ, Z) defined in the cylinder rotating frame.

the amplitude equations are derived by considering both viscous and nonlinear terms. We have distinguished two different regimes of saturation. At low Reynolds numbers, the main mode amplitude is saturated by viscosity (which is consistent with Gans' results (Gans 1970), whereas the nonlinear effects prevail at higher Reynolds numbers (Wood 1965). Such nonlinear couplings of Kelvin modes have been mainly studied in the context of the elliptic instability (Waleffe 1989; Eloy *et al.* 2003; Mason & Kerswell 1999).

The paper is organized as follows. Section 2 is dedicated to the general problem formulation. The equations governing the fluid motion are first introduced then the whole experimental setup is presented in detail in § 2.2. In § 3, the linear inviscid theory is presented to express the Kelvin mode amplitudes when the flow is non-resonant. Experimental flow fields are then shown and compared to these theoretical predictions. In § 4 the viscous and nonlinear amplitude equations are derived and compared to the PIV velocity fields measured at the resonance. Finally our results are discussed in § 5.

2. Presentation of the problem

2.1. *Formulation*

We address the equations governing the flow inside a precessing cylinder full of fluid of density ρ and kinematic viscosity ν. This problem is illustrated in figure 1(*a*).

In the laboratory reference frame $(O, \hat{\boldsymbol{x}}, \hat{\boldsymbol{y}}, \hat{\boldsymbol{z}})$, we consider a turntable rotating at constant angular frequency $\Omega_2 = \dot{\psi}$ around the axis $(O, \hat{\boldsymbol{z}})$. In the reference frame of this turntable, a cylinder of radius R_c and height H rotates around its own axis $(O', \hat{\boldsymbol{k}})$ at the angular frequency $\Omega_1 = \dot{\phi}$. The angle between these two axes of rotation is the nutation angle θ. As shown in figure 1(*a*), the angles (ψ, θ, ϕ) are the classical Euler coordinates of the cylinder.

In the reference frame of the cylinder $(O', \hat{\boldsymbol{\imath}}, \hat{\boldsymbol{\jmath}}, \hat{\boldsymbol{k}})$, the radius vector $\boldsymbol{R}$ is located by its cylindrical coordinates (R, φ, Z) as shown in figure 1(*b*). The time-dependent rotation vector of the cylinder in the laboratory frame is

$$\boldsymbol{\Omega} = \Omega_1 \hat{\boldsymbol{k}} + \Omega_2 \hat{\boldsymbol{z}}. \tag{2.1}$$

Since the cylinder frame is non-Galilean, the Navier–Stokes equations satisfied by the velocity field $\boldsymbol{U}(\boldsymbol{R}, T)$ and the pressure field $P(\boldsymbol{R}, T)$ take the form

$$\frac{\partial \boldsymbol{U}}{\partial T} + (\boldsymbol{U} \cdot \nabla)\,\boldsymbol{U} + 2\boldsymbol{\Omega} \times \boldsymbol{U} + \boldsymbol{\Omega} \times (\boldsymbol{\Omega} \times \boldsymbol{R}) + \frac{\mathrm{d}\boldsymbol{\Omega}}{\mathrm{d}T} \times \boldsymbol{R} + \boldsymbol{\Gamma}_{O'} = -\frac{1}{\rho} \nabla P + \nu \Delta \boldsymbol{U}, \tag{2.2a}$$

$$\nabla \cdot \boldsymbol{U} = 0, \tag{2.2b}$$

with the boundary condition $\boldsymbol{U} = \boldsymbol{0}$ on the cylinder walls.

In the Navier–Stokes equation (2.2*a*), the first two terms are the usual inertial terms, the third and the fourth terms are the Coriolis and centrifugal acceleration respectively, the fifth term is due to the acceleration of the rotation vector and $\boldsymbol{\Gamma}_{O'}$ refers to the acceleration of the centroid O' of the cylinder. Note that this latter term is potential and corresponds to a hydrostatic pressure $\boldsymbol{\Gamma}_{O'} \cdot \boldsymbol{R}$.

The equations above are made dimensionless by using R_c and Ω^{-1} as characteristic length and time, where

$$\Omega = \boldsymbol{\Omega} \cdot \hat{\boldsymbol{k}} = \Omega_1 + \Omega_2 \cos\theta. \tag{2.3}$$

Using lowercase letters for the dimensionless quantities, the Navier–Stokes equations for the dimensionless velocity field $\boldsymbol{u}(\boldsymbol{r}, t)$ become

$$\frac{\partial \boldsymbol{u}}{\partial t} + 2\,\hat{\boldsymbol{k}} \times \boldsymbol{u} + \nabla p = -2\varepsilon\zeta\omega r \cos(\omega t + \varphi)\,\hat{\boldsymbol{k}} + \boldsymbol{u} \times (\nabla \times \boldsymbol{u}) - 2\varepsilon\zeta\,\boldsymbol{\delta} \times \boldsymbol{u} + \frac{1}{Re}\Delta \boldsymbol{u}, \tag{2.4a}$$

$$\nabla \cdot \boldsymbol{u} = 0, \tag{2.4b}$$

with

$$\omega = \frac{\Omega_1}{\Omega},\ \varepsilon = \left|\frac{\Omega_2 \sin\theta}{\Omega}\right|,\ \zeta = \operatorname{sgn}\left(\frac{\Omega_2 \sin\theta}{\Omega}\right),\ \boldsymbol{\delta} = \cos\omega t\,\hat{\boldsymbol{\imath}} - \sin\omega t\,\hat{\boldsymbol{\jmath}}, \tag{2.5a–d}$$

and $Re = \Omega R_c^2/\nu$ the Reynolds number. In this dimensionless form, $h = H/R_c$ is the aspect ratio of the cylinder. The dimensionless pressure field $p(\boldsymbol{r}, t)$ is constructed to include all the potential terms

$$p = \frac{P}{\rho\,\Omega^2 R_c^2} - \tfrac{1}{2}r^2 + \varepsilon\,|1 - \omega|\,rz\,\cos(\omega t + \varphi) + \boldsymbol{\gamma}_{O'} \cdot \boldsymbol{r} - \tfrac{1}{2}\varepsilon^2[z^2 + r^2 \sin^2(\omega t + \varphi)] + \tfrac{1}{2}\,\boldsymbol{u}^2, \tag{2.6}$$

where $\boldsymbol{\gamma}_{O'} = \boldsymbol{\Gamma}_{O'}/R_c\Omega^2$ is the dimensionless acceleration of the cylinder centroid. The boundary condition of the velocity field is

$$\boldsymbol{u} = \boldsymbol{0} \quad \text{at the walls } (r = 1 \text{ or } z = \pm h/2). \tag{2.7}$$

The Navier–Stokes equations (2.4 *a, b*) with the boundary condition (2.7) govern the flow inside a precessing cylinder. This set of equations has been obtained without any approximation and is thus valid for any value of the experimental parameters. It is clear from these equations that the problem is entirely governed by four dimensionless parameters: the forcing amplitude ε; the forcing frequency ω; the Reynolds number Re; and the cylinder aspect ratio h. However, these equations cannot be solved easily in the general case and we will limit ourselves hereinafter to the case of asymptotically small amplitude ε and large Reynolds number Re. This is the relevant limit if one is interested in the flow forced by the precession before it becomes unstable or at the onset of instability.

For the sake of clarity and brevity, a four-component formulation for the velocity–pressure field $\boldsymbol{v} = (\boldsymbol{u},\ p)$ expressed in cylindrical coordinates will be used. With this formulation the Navier–Stokes equations (2.4 *a, b*) take the form

$$\left(\frac{\partial}{\partial t}\mathscr{I} + \mathscr{M}\right)\boldsymbol{v} = \varepsilon\zeta\ \boldsymbol{F}_0 \mathrm{e}^{\mathrm{i}(\omega t+\varphi)} + \boldsymbol{N}(\boldsymbol{v},\boldsymbol{v}) + \varepsilon\zeta\ \mathscr{D}\,\mathrm{e}^{\mathrm{i}(\omega t+\varphi)}\boldsymbol{v} + \frac{1}{Re}\mathscr{L}\,\boldsymbol{v} + \text{c.c.}, \qquad (2.8)$$

where the operators $\mathscr{I}$, $\mathscr{M}$, $\mathscr{D}$, $\mathscr{L}$, the forcing vector $\boldsymbol{F}_0$ and the bilinear function $\boldsymbol{N}$ are defined in Appendix A. The symbol c.c. stands for the complex conjugate.

We will solve a linearized version of the above equation in § 3.1 and the weakly nonlinear and viscous solution corresponding to the saturated resonant flow will be given in § 4.1.

2.2. *Experimental setup*

The experimental setup is sketched in figure 2. It corresponds exactly to the configuration depicted in figure 1. A right-circular polymethyl methacrylate (PMMA) cylinder, filled with distilled water, rotates at the angular velocity Ω_1 around its axis and is mounted on a rotating platform. The cylinder axis is tilted relative to the axis of the platform with an angle θ. The platform, which ensures the precessing component of the motion, also rotates at a velocity Ω_2. The platform is mounted on a wide vertical axis in order to limit the vibrations of the structure at high precession velocities.

The angular frequency Ω_1 can be increased up to 60 rad s^{-1} and is measured with an accuracy of 0.1%. The precession frequency Ω_2 is limited to 6 rad s^{-1} and is measured with an accuracy of 0.2% when the precession frequency is larger than 0.2 rad s^{-1}. Each axis having its own driving motor, the angular velocities can be varied independently so that the dimensionless frequency ω can be varied over the whole range $[-2, 2]$. We used three different cylinders: a cylinder of aspect ratio $h = H/R_c = 1.989 \pm 0.3\%$ ($H = 9.14$ cm) was used first, but its principal resonance was found for a vanishing precessing frequency ($\omega \approx 1$). A second cylinder with aspect ratio $h = 1.8 \pm 0.7\%$ ($H = 8.27$ cm) was thus designed to study this resonance. Finally, a third cylinder with the same aspect ratio 1.8 but smaller dimensions ($H = 2.7$ cm) was been used to obtain data at smaller Reynolds numbers (by a factor almost 10). The thickness of the cylinder walls is extremely large (2 cm) in order to avoid shaded areas in the light sheet (because of refraction on the cylindrical wall).

The data acquisition computer is located on the rotating platform to limit the number of rotating electrical contacts and improve the quality of the data. The power is brought up to the platform by a rotating collector through the vertical axis and is used to supply the cylinder motor, the video camera and the electromagnet of the release device. The rotating collector also conveys the signal from the video camera

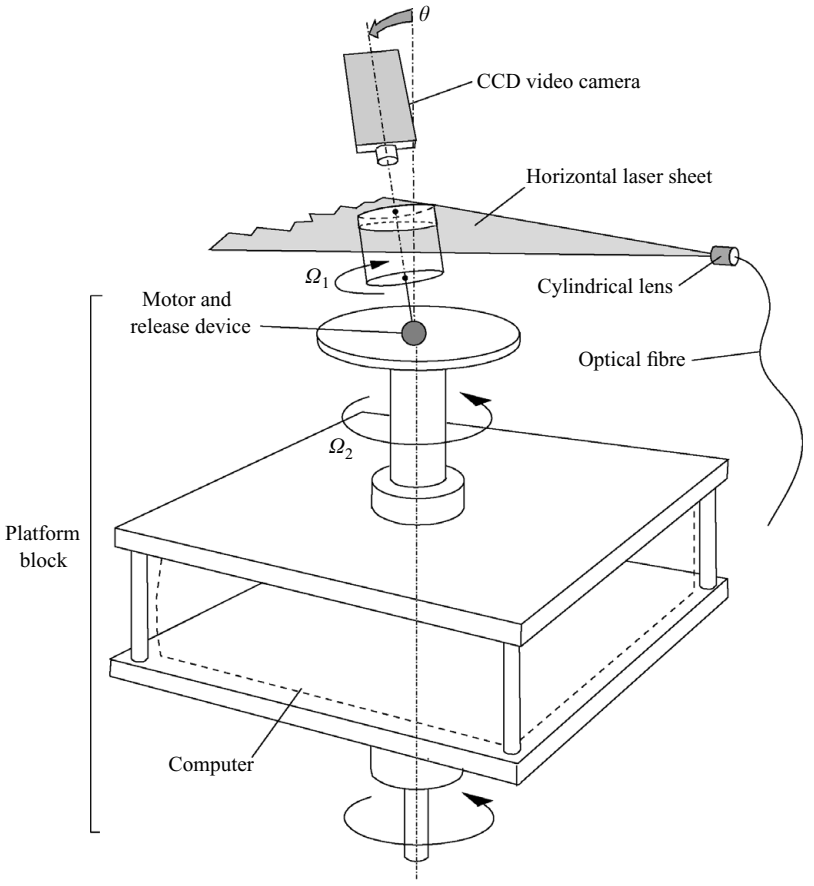

FIGURE 2. Sketch of the experimental setup. The cylinder is directly mounted on the axis of the motor which is located on the rotating platform, and can be tilted during the rotation of the platform. The camera, located above the cylinder is fixed in the platform frame of reference. The whole platform block, including the computer, rotates at angular frequency Ω_2.

back to an auxiliary screen, which is used for observation and optical adjustment of the PIV system.

A release device is mounted on the platform and is controlled externally, so that the cylinder can be tilted during the rotation of the platform. It allows the observation of the transient stage during which the observed Kelvin modes grow. The release device is composed of an electromagnet designed to keep the cylinder in a vertical position during the spin-up phase. Once the electromagnet is turned off, a drawback spring pulls the cylinder into its tilted position. The electromagnet is then turned on again to ensure the stability of the nutation angle θ during the experiment. This angle can be varied from 0 to 15°. Owing to the spring strength, we consider that the swing of the axis occurs in a duration (about half a second) much smaller than the duration of the transient stage (varying from 3 to 50 s).

The PIV measurement system is schematically presented in figure 2. The fluid is seeded with small reflecting particles (Optimage Ltd.) of mean diameter 50 μm and density $1000 \pm 20\,\mathrm{kg\,m^{-3}}$. They are illuminated with a light sheet of thickness 2 mm, created either by a Yag pulsed laser for large velocities or by an Argon Ion continuous laser (through an optical fibre) for small velocities. The laser beam goes through a cylindrical lens to provide the laser sheet. None of the lighting system is rotating so

the laser sheet is fixed relative to the laboratory frame. Provided the tilt angle θ is not too large (smaller than 5°), the laser sheet, due to its thickness, can be considered normal to the cylinder axis. This might introduce a bias at larger nutation angles and the laser sheet should then be created on the rotating platform with a set of mirrors. The height of the laser sheet can be varied along the height of the cylinder and was chosen in a subtle way, depending on the type of experiment. First, to examine the dependence of the amplitude on the frequency ω, we took a sheet close to the centre of the cylinder (in order not to be at a node of the Kelvin mode): a good compromise was taken as $z = 0.12h$. Then, to study the first (resp. second) resonance of a Kelvin mode, we took $z = h/4$ (resp. $z = h/6$) in order to measure a maximum transverse velocity.

The images of particles are recorded by a PIV camera (Kodak Megaplus ES 1.0, 1008×1018 pixels) mounted on the rotating platform and aligned with the axis of the cylinder. The time interval between two successive images is relatively large (from 5 ms to 1 s) such that the cylinder rotates by approximately 20° between the two images. This creates large displacements of the particles at the periphery of the cylinder (150 pixels), but the two images are rotated around the centre of the cylinder in order to remove the solid-body rotation of the particles. The PIV thus gives directly the velocity field in the cylinder reference frame. This procedure allows the measurement of very small velocities down to 1% of the velocity of the cylinder wall. Such measurements would not have been possible without the image rotation. The pairs of images are then treated by a cross-correlation algorithm detailed in Meunier & Leweke (2003) which gives velocity fields with 60×60 vectors.

For the acquisition of a PIV field, we proceed as follows. First the cylinder is kept vertical and rotates at Ω_1. The platform rotates at Ω_2 so that the angular velocity of the cylinder relative to the laboratory frame is $(\Omega_1 + \Omega_2)\,\hat{\boldsymbol{z}}$. Once the spin-up stage is completed, the cylinder is released to its tilted position. This allows the transient and the spin-up phase to be studied independently.

Some preliminary visualizations were also performed with Kalliroscope particles, in order to check that the resonances were in good agreement with the linear inviscid theory, and to validate our set-up by comparison of these visualizations with those from the literature (Manasseh 1992; Kobine 1995). However, no new quantitative results were obtained and we will not present any of these visualizations in this paper.

3. Flow inside a non-resonant cylinder

3.1. *Linear inviscid theory*

We assume an asymptotically small forcing amplitude ε and asymptotically large Reynolds number Re. In this limit, the velocity–pressure field $\boldsymbol{v}$ is $O(\varepsilon)$ and the Navier–Stokes equation (2.8) becomes at first order in ε

$$\left(\frac{\partial}{\partial t}\mathscr{I} + \mathscr{M}\right)\boldsymbol{v} = \varepsilon\zeta\ \boldsymbol{F}_0 \mathrm{e}^{\mathrm{i}(\omega t+\varphi)} + \text{c.c.} \tag{3.1}$$

For an inviscid fluid, the no-slip boundary condition (2.7) becomes a condition of no outward flow

$$\boldsymbol{u}\cdot\boldsymbol{n} = 0 \quad \text{at the walls } (r = 1 \text{ or } z = \pm h/2), \tag{3.2}$$

where $\boldsymbol{n}$ is a unitary vector normal to the wall.

Equations (3.1) and (3.2) form a linear system for the vector $\boldsymbol{v} = (\boldsymbol{u},\ p)$, with a forcing term. It admits a particular solution of the form

$$\boldsymbol{v}_{\text{part.}} = (0,\ 0,\ \varepsilon\,\zeta\,\mathrm{i}\,r\,\mathrm{e}^{\mathrm{i}(\omega t+\varphi)},\ 0) + \text{c.c.} \tag{3.3}$$

Unfortunately, this solution does not satisfy the boundary condition (3.2) at $z = \pm h/2$. Thus, one must complete this particular solution with a solution of the homogeneous equation (without forcing), so that the boundary condition at the upper and lower walls is satisfied. Owing to the time and azimuthal dependence of the forcing, the homogeneous solution is to be sought as a sum of Kelvin modes of azimuthal wavenumber $m = 1$ and angular frequency ω (see Greenspan 1968). Using (3.2) and (3.3) and such a form of the homogeneous solution, one finds

$$\boldsymbol{v} = \boldsymbol{v}_{\text{part.}} + \varepsilon\zeta \sum_{i=1}^{\infty} a_i \boldsymbol{v}_i(r,\, z)\mathrm{e}^{\mathrm{i}(\omega t+\varphi)} + \text{c.c.}, \tag{3.4}$$

where $\boldsymbol{v}_i(r,\, z)\mathrm{e}^{\mathrm{i}(\omega t+\varphi)}$ is a Kelvin mode of axial wavenumber k_i, azimuthal wavenumber $m = 1$ and frequency ω

$$\boldsymbol{v}_i(r,\, z) = \begin{pmatrix} u_i(r)\, \sin(k_i z) \\ v_i(r)\, \sin(k_i z) \\ w_i(r)\, \cos(k_i z) \\ p_i(r)\, \sin(k_i z) \end{pmatrix} \quad \text{with} \quad \begin{cases} u_i(r) = \mathrm{i}\dfrac{\omega r \delta_i\, J_1'(\delta_i r) + 2J_1(\delta_i r)}{r(\omega^2 - 4)} \\ v_i(r) = \dfrac{2r\delta_i\, J_1'(\delta_i r) + \omega J_1(\delta_i r)}{r(4 - \omega^2)} \\ w_i(r) = \dfrac{\mathrm{i}\, k_i}{\omega} J_1(\delta_i r) \\ p_i(r) = J_1(\delta_i r), \end{cases} \tag{3.5}$$

with $J_\nu(x)$ the Bessel function of the first kind and $J_\nu'(x)$ its x-derivative. The amplitude a_i of each Kelvin mode is

$$a_i = \frac{2\,\omega^2}{(\omega - 2)(k_i^2 + 1)\, k_i\, J_1(\delta_i)\cos(k_i\, h/2)}, \tag{3.6}$$

the axial wavenumber k_i is the positive root of the constitutive relation

$$\delta_i^2 = \frac{4 - \omega^2}{\omega^2} k_i^2, \tag{3.7}$$

and the radial wavenumber δ_i is solution of Kelvin's dispersion relation

$$\omega\, \delta_i\, J_1'(\delta_i) + 2J_1(\delta_i) = 0. \tag{3.8}$$

As long as $-2 < \omega < 2$, the dispersion relation admits an infinite, countable number of roots δ_i which are numbered in ascending order. A Kelvin mode can be associated with each root δ_i. The radial velocity $u_i(r)$ of the first Kelvin mode (corresponding to δ_1) is formed of one lobe and has no zero for $0 < r < 1$, the second Kelvin mode contains two lobes and one zero, the third contains three lobes and two zeros, and so on. The velocity field of the first Kelvin mode is shown in figure 3(*a*): it contains two counter-rotating vortices, due to the presence of a single lobe of radial velocity and an azimuthal wavenumber $m = 1$. In the general case, the ith Kelvin mode contains $2i$ vortices, and these Kelvin modes form a complete set. Their dispersion relation (3.7)–(3.8) is plotted on figure 4. The precession excites only the Kelvin modes with a given frequency ω corresponding to increasing wavenumbers k_i (as shown on figure 4 for $\omega = \omega_{3,4}$). When the wavenumber k_i of a Kelvin mode is equal to π/h, $3\pi/h$, $5\pi/h$... the mode 'fits' inside the height of the cylinder and becomes resonant. When ω is increased, each branch of the dispersion relation leads to an infinite number of resonances, with the wavenumber k_i of the Kelvin mode being equal to $\pi(2n - 1)/h$ (n being an integer). Strictly speaking, each resonance labelled (i, n) corresponds to a

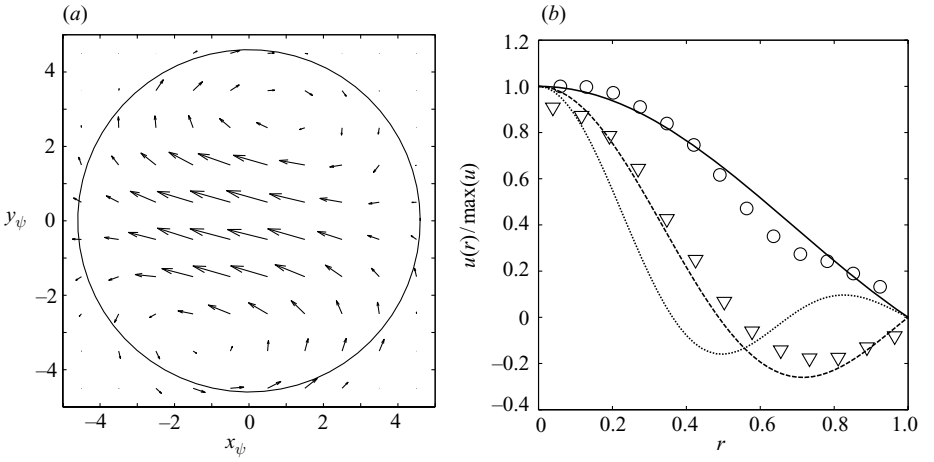

FIGURE 3. (*a*) Velocity field measured at $\omega = 0.9$, i.e. close to the first resonance $\omega_{1,1} = 0.996$ of mode $i = 1$ ($Re = 5500$, $h = 2$ and $\varepsilon = 1.7 \times 10^{-3}$). (*b*) Radial velocity along the x_ψ-axis. The circles ($\circ$) correspond to the field displayed in (*a*). The triangles ($\triangledown$) correspond to a velocity field at $\omega = 0.45$ with $\varepsilon = 9.6 \times 10^{-3}$, i.e. close to $\omega_{1,2} = 0.51$. The related linear theoretical profiles are plotted as solid and dashed lines. The dotted line corresponds to the theoretical profile for the third Kelvin mode.

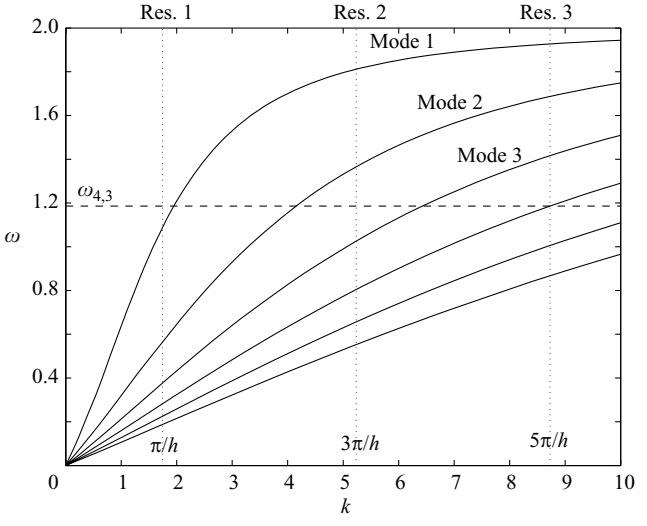

FIGURE 4. Dispersion relation of the Kelvin modes with azimuthal wavenumber $m = 1$, given by (3.7) and (3.8). The dotted lines correspond to the resonances for an aspect ratio $h = 1.8$.

different Kelvin mode. In the following, all modes corresponding to the same branch of the dispersion relation (same index i) will be collected into a family of modes which will be called the ith Kelvin mode (for the sake of simplicity).

Equation (3.6) gives the amplitudes of the Kelvin modes forced by the precession. This equation is valid as long as the cylinder aspect ratio is not resonant, i.e. $\cos(k_i h/2) \neq 0$. In other words, the present linear analysis predicts a divergent amplitude of the ith Kelvin mode if the forcing frequency ω is equal to one of the natural frequencies $\omega_{i,n}$ of the cylinder. Here, $\omega_{i,n}$ refers to the frequency obtained

through (3.7) and (3.8) by taking $k_i = \pi(2n - 1)/h$, with n an integer. One can show (Kudlick 1966) that the set of natural frequencies $\omega_{i,n}$ is dense in the interval $-2 < \omega < 2$. This means that there is always a Kelvin mode arbitrarily close to a resonance for any chosen forcing frequency ω. This emphasizes the need for a theoretical prediction of the Kelvin mode amplitude at the resonance, as will be done in § 4.1.

3.2. *Kelvin modes: PIV measurements*

We performed PIV measurements of the (u, v) transverse velocity field in the range $0.2 < \omega < 1.9$ and at Reynolds numbers between 2×10^3 and 2×10^5. The aim was to extract, from the averaged velocity field in the permanent regime, the linear amplitudes a_i of the main modes as defined by (3.6).

In figure 3(a) the horizontal-velocity field is shown at a frequency $\omega = 0.9$ close to the first resonance $\omega_{1,1} = 0.996$ of the mode $i = 1$, for $Re = 5500$ and $\theta = 1°$, the laser sheet being at a height $z = 0.29$. As previously mentioned, the flow in the reference frame of the cylinder mainly consists of two counter-rotating vortices corresponding to the first Kelvin mode described by the above inviscid theory. However, note that the mode is not exactly aligned with the x_ψ-axis. This tilt angle is due to the viscous and nonlinear effects appearing at the resonance and will be analysed in detail in the next section. Figure 3(b) shows the radial velocity profile along the x_ψ-axis of this velocity field, as circles. The normalized value of the velocity decreases monotonically between $r = 0$ and $r = 1$, and is very close to the curve found theoretically (solid line) for the first Kelvin mode at this value of ω. Figure 3(b) also shows the radial velocity profile obtained for $\omega = 0.45$, i.e. close to the resonance of the second mode. It exhibits a positive lobe for $r < 0.5$, a negative lobe for $r > 0.5$ and a zero for $r \simeq 0.5$. This is characteristic of the second Kelvin mode, whose theoretical radial velocity is plotted as a dashed line. The third Kelvin mode (plotted as a dotted line) has three lobes of opposite radial velocity, but in this case the experimental data are very noisy and have not been plotted.

The presence of these Kelvin modes is better visualized by plotting the mean vorticity fields as done in figure 5, since the small scatter in the velocity field (such as a translation or a rotation) is hidden by the differentiation of $\boldsymbol{u}$ and the modification of the colourbar. The Kelvin modes are thus clearly distinguished by plotting the vorticity fields at various ω: even the fifth Kelvin mode is discernible at its first resonance $\omega_{5,1} = 0.2$. However, the spatial structure is a double spiral for the highest modes, whereas the theory predicts a series of lobes since the vorticity is expected to vanish for $\varphi = \pi/2 - \omega t$. In fact, such a spiral structure has already been observed theoretically for the Kelvin modes of a Gaussian vortex by Fabre, Sipp & Jacquin (2006). We thus think that this discrepancy might be due to a slight differential rotation in the geostrophic motion, arising from nonlinear and viscous effects.

For each experiment outside the resonance, we have decomposed each velocity field into a sum of Kelvin modes. For this purpose, we use the fact that the Kelvin modes are orthogonal, such that the amplitude a_i of each Kelvin mode is simply given by the normalized scalar product $\langle \boldsymbol{u}_{\exp} | \boldsymbol{u}_i \rangle / \langle \boldsymbol{u}_i | \boldsymbol{u}_i \rangle$ (see Appendix B for the exact definition), where $\boldsymbol{u}_{\exp}$ (resp. $\boldsymbol{u}_i$) are the two transverse components of the measured (resp. theoretical) velocity field and the scalar product is defined as the average over the whole section. In fact, the method needs to be slightly improved since this average can only be calculated for $r \leqslant 0.9$ instead of $r \leqslant 1$ (due to spurious vectors at the cylinder wall) and because the mode can have a tilt angle α_i with respect to the x_ψ-axis. This

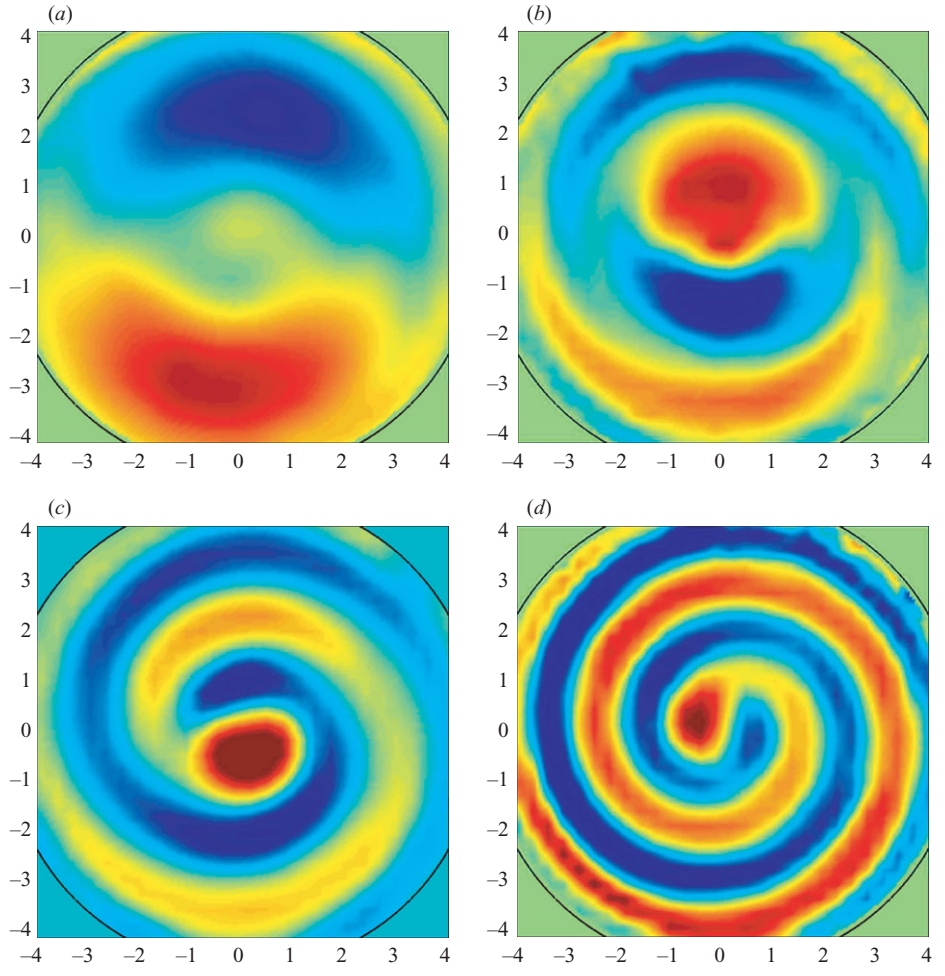

FIGURE 5. Vorticity fields of the first (*a*), second (*b*), third (*c*) and fifth (*d*) Kelvin mode, observed close to their first resonance (where k_i is close to π/h). Here, $h=2$ and the flows are observed respectively for $\omega=0.9$, 0.45, 0.3, 0.2. The Reynolds number is equal to 5500 (*a*), 11 800 (*b*), 17 700 (*c*) and 26 600 (*d*) and the small parameter ε is equal to 1.7×10^{-3} (*a*), 9.6×10^{-3} (*b*), 1.2×10^{-2} (*c*) and 1.4×10^{-2} (*d*).

method, which is detailed in Appendix B, allows the precise determination of the amplitude and tilt angle of the first two Kelvin modes for each instantaneous velocity field.

In the permanent regime, the amplitude of the Kelvin modes is stationary and depends only on the frequency ω. It is plotted in figure 6 for the first two Kelvin modes and for two different Reynolds numbers. Despite a large scatter, experimental results are clearly independent of the Reynolds number outside the resonances and very well predicted by the linear inviscid theory. As far as we know, this is the first exact measurement of the mode amplitudes forced by precession. The amplitudes measured at the resonances for the first two modes are large and cannot be predicted by the linear inviscid theory. A nonlinear and viscous theory is necessary to predict the finite value of the amplitude in this case; this is the subject of § 4.

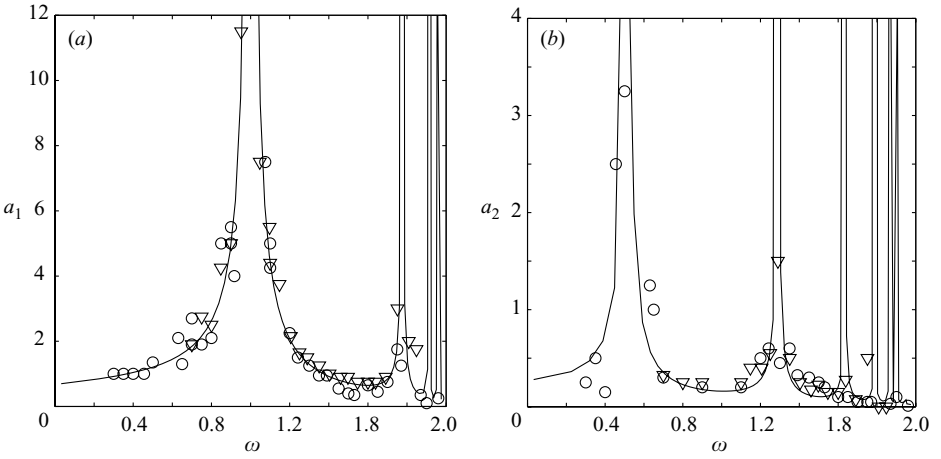

FIGURE 6. Amplitude of the first mode ($i=1$) (a) and second mode ($i=2$) (b) for a cylinder of radius $R_c=4.66$ cm and aspect ratio $h=2$. The angular velocity of the cylinder Ω_1 is equal to 2 rad s^{-1} ($\circ$) and 8 rad s^{-1} ($\triangledown$) so that the Reynolds number lies between 2×10^3 and 2×10^5. The solid line shows the prediction of the linear inviscid theory from § 3.1.

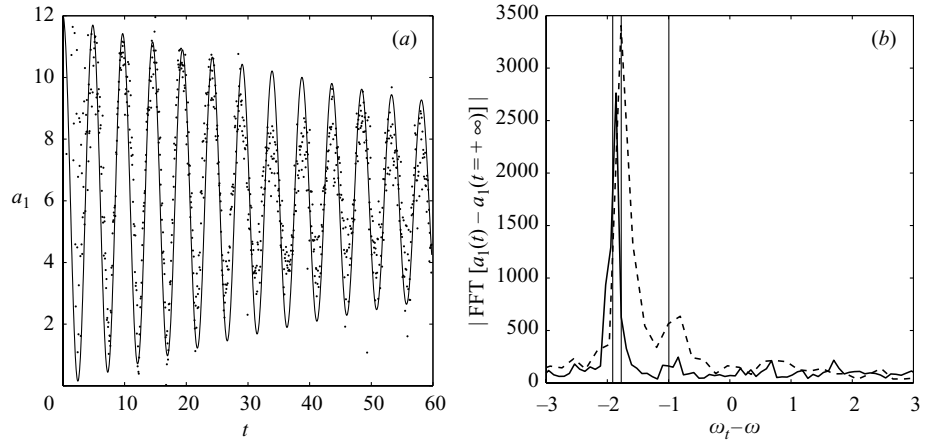

FIGURE 7. (a) Transient dynamics of the first mode amplitude for forcing frequency $\omega=0.8$ and Reynolds number $Re=6640$. (b) Spectrum of the amplitude for $\omega=0.8$ (solid line) and $\omega=1.1$ (dashed line). The corresponding Reynolds numbers are $Re=6640$ and $Re=4830$ respectively. The Fourier transform of the temporal signals is plotted as a function of the transient dimensionless frequency $(\Omega_t-\Omega_1)/\Omega$ (given in the cylinder frame). The thin solid lines correspond to the first three resonances of the Kelvin mode $i=1$: $\omega_{1,1}=0.996$, $\omega_{1,2}=1.774$, $\omega_{1,3}=1.912$. Here, $\varepsilon=3.5\times10^{-3}$ and $h=2$.

3.3. *Transient stage*

The experimental results can also give indications of the transient stage, since the amplitude a_i of each mode can be extracted for each instantaneous velocity field. Figure 7(a) shows the temporal evolution of the amplitude of the first Kelvin mode just after the onset of the precession forcing, far from its resonance. The amplitude oscillates very rapidly and converges toward its permanent value a_1^0 which is plotted in figure 6. This curve can be fitted by a decaying exponential $a_1(t)=a_1^0[1-\cos(\omega_t t)\mathrm{e}^{-t/t_s}]$ where ω_t corresponds to the frequency of the oscillation and t_s is the settling time.

Since ω_t corresponds to the frequency in the rotating-table reference frame, we have to subtract the dimensionalized angular velocity of the cylinder ω to obtain the frequency of the oscillation in the cylinder reference frame. By doing this, we find a non-dimensional frequency $\omega_t - \omega$ close to -1.8, and this was observed for any ω outside a resonance. This value is close to the frequency of the second resonance of the first Kelvin mode $\omega_{1,2} = 1.774$. This can be understood by the fact that, at $t = 0^+$, the velocity field which is equal to 0 in the bulk of the cylinder is the sum of the permanent solution (given by the inviscid theory) and a sum of free and decaying Kelvin modes with frequencies $-2 < \omega_{i,n} < 2$, n varying from 1 to infinity. Another method to evaluate experimentally the initial amplitude of each free Kelvin mode is to plot the Fourier transform of the amplitude as a function of the dimensionalized frequency $\omega_t - \omega$, as shown on figure 7(*b*). A small peak is discernible around -1 (for both values of ω), which corresponds to the free Kelvin mode $\omega_{1,1} = 0.996$ and which is indicated by a thin solid line on the figure. A large peak is located near -1.8, which is close to all the other free Kelvin modes (with $i = 1$), whose frequencies $(\omega_{1,n})_{n \geqslant 2}$ lie between 1.774 and 2. It is thus not clear whether this large peak is due to a large amplitude of the second free Kelvin mode $\omega_{1,2}$ or to the constructive interference of all these modes $(\omega_{1,n})_{n \geqslant 2}$.

4. Flow inside a resonant cylinder

4.1. *Nonlinear and viscous theory*

As seen in § 3.1, when the forcing frequency ω is equal to a natural frequency of the cylinder $\omega_{i,n}$, the linear inviscid theory predicts a divergent amplitude of the ith Kelvin mode. To predict correctly the mode amplitude in this case, one has to take into account the viscous effects or the nonlinear effects or both. As shown by Gans (1970), if A_i is the mode amplitude, the secondary flow in the core of the cylinder due to the viscous boundary layers is $O(A_i Re^{-1/2})$. If the nonlinear effects are negligible, the correct scaling is obtained when this secondary flow is of the order of the forcing amplitude ε. This gives a mode amplitude $A_i = O(\varepsilon Re^{1/2})$ which is factor $Re^{1/2}$ larger than the flow in the non-resonant case. On the other hand, if the viscous effects are negligible, the secondary flow is due to the nonlinear interaction of the Kelvin mode with itself. In this case, the secondary flow of the same Fourier components is obtained at third order and is $O(|A_i|^2 A_i)$. This gives a mode amplitude $A_i = O(\varepsilon^{1/3})$.

The distinguished scaling is obtained when the viscous and nonlinear effects are of the same order, that is $\varepsilon^{2/3} = O(Re^{-1/2})$. This leads to the definition of a viscous parameter η of order 1 and a slow time scale τ as follows:

$$\eta = Re^{-1/2} \varepsilon^{-2/3}, \quad \tau = \varepsilon^{2/3} t. \tag{4.1a,b}$$

We now assume that the forcing frequency ω is close to a resonant frequency $\omega_{i,n}$ for the ith Kelvin mode. The four-component velocity–pressure field corresponding to this Kelvin mode is expanded in powers of $\varepsilon^{1/3}$ as follows:

$$\boldsymbol{V}_i = \varepsilon^{1/3} \boldsymbol{V}_1 + \varepsilon^{2/3} \boldsymbol{V}_2 + \varepsilon \boldsymbol{V}_3 + \varepsilon^{4/3} \boldsymbol{V}_4 + \cdots . \tag{4.2}$$

The real velocity field is obtained by adding the complex conjugate to the above equation (the same is implicitly assumed in all the following equations). The nonlinear and viscous amplitude equations are obtained by injecting the above expansion (4.2) into the Navier–Stokes equation (2.8) and examining its different orders. The procedure is similar to the one used by Gans (1970) except that here the nonlinear effects are included and the forcing frequency ω is arbitrary, whereas Gans (1970)

considered only the special case $\omega = 1$ which corresponds to a nutation angle $\theta = \pi/2$. The present analysis has strong similarities with the weakly nonlinear analysis of parametric instabilities in rotating flows such as the elliptic instability (Waleffe 1989; Sipp 2000; Eloy *et al.* 2003) or the instability of a rotating gas that is periodically compressed (Racz & Scott 2007). Because this calculation is quite lengthy, most of its technical details are given in Appendices C, D and E.

4.1.1. *Order* $\varepsilon^{1/3}$

At order $\varepsilon^{1/3}$, the resonant flow satisfying the linear homogeneous equation

$$\left(\frac{\partial}{\partial t}\mathscr{I} + \mathscr{M}\right) \boldsymbol{V}_1 = \boldsymbol{0}, \tag{4.3}$$

is

$$\boldsymbol{V}_1 = A(\tau)\, \boldsymbol{v}_i\, \mathrm{e}^{\mathrm{i}(\omega t + \varphi)}, \tag{4.4}$$

where $\boldsymbol{v}_i$ is the ith Kelvin mode given by (3.5), as has been shown in § 3.1. The amplitude A of the Kelvin mode $\boldsymbol{v}_i$ is assumed to vary on the slow time scale τ and the other Kelvin modes (with $j \neq i$) are assumed to be non resonant so their amplitudes are given by (3.6).

The Kelvin mode $\boldsymbol{v}_i$ satisfies an inviscid boundary condition. In a viscous boundary layer of thickness $O(Re^{-1/2})$, the complete flow is obtained by adding the viscous flow $\widetilde{\boldsymbol{V}}_1$ such that $\boldsymbol{V}_1 + \widetilde{\boldsymbol{V}}_1$ satisfies the viscous boundary condition (2.7). This viscous flow takes the form

$$\widetilde{\boldsymbol{V}}_1 = A\, \widetilde{\boldsymbol{v}}_i\, \mathrm{e}^{\mathrm{i}(\omega t + \varphi)}, \tag{4.5}$$

where $\widetilde{\boldsymbol{v}}_i$ is the viscous counterpart of the Kelvin mode $\boldsymbol{v}_i$ located in a viscous boundary layer of thickness $O(Re^{-1/2})$ near the walls (its complete expression is given in Appendix D). At this order the viscous flow $\widetilde{\boldsymbol{v}}_i$ is parallel to the walls (it has to compensate $\boldsymbol{V}_1$ which is also parallel to the wall because of the inviscid boundary condition). However, this viscous flow gives rise to an Ekman pumping at order ε with a component perpendicular to the walls, $\widetilde{\boldsymbol{V}}_3^{\perp} = O(\eta \widetilde{\boldsymbol{V}}_1)$. This gives a boundary condition for the inviscid flow at order ε:

$$\boldsymbol{V}_3 \cdot \boldsymbol{n} = -\widetilde{\boldsymbol{V}}_3^{\perp} = -\eta A\, \widetilde{\boldsymbol{v}}_3 \cdot \boldsymbol{n}\, \mathrm{e}^{\mathrm{i}(\omega t + \varphi)} \quad \text{on the walls,} \tag{4.6}$$

where $\boldsymbol{n}$ is the unitary vector normal to the wall and $\widetilde{\boldsymbol{v}}_3 \cdot \boldsymbol{n}$ is a function of order 1 given in Appendix D.

4.1.2. *Order* $\varepsilon^{2/3}$

As shown by Greenspan (1969), the nonlinear interaction of a Kelvin mode with itself gives rise to two velocity components. For a Kelvin mode of wavenumbers–frequency (k, m, ω) (where m is the azimuthal wavenumber, in our case $m = 1$), these two components are of the form $(2k, 0, 0)$ and $(0, 2m, 2\omega)$. In other words, the geostrophic mode $(0, 0, 0)$ and the mode $(2k, 2m, 2\omega)$ are not forced by nonlinear interactions.

At order $\varepsilon^{2/3}$ the Navier–Stokes equation (2.8) becomes

$$\left(\frac{\partial}{\partial t}\mathscr{I} + \mathscr{M}\right) \boldsymbol{V}_2 = \boldsymbol{N}(\boldsymbol{V}_1, \boldsymbol{V}_1). \tag{4.7}$$

The solution of this equation is

$$\boldsymbol{V}_2 = |A|^2\,\boldsymbol{v}_{2k} + A^2\,\boldsymbol{v}_{2\omega}\mathrm{e}^{\mathrm{i}(2\omega t+2\varphi)} + \sum_{j=1}^{\infty} A_0^j(\tau)\boldsymbol{v}_0^j + \text{o.t.}, \tag{4.8}$$

where o.t. stands for 'other terms' of different Fourier components. The first two terms of (4.8) correspond to the particular solution of (4.7) (see Waleffe 1989). In agreement with Greenspan (1969), they are of the form $(2k, 0, 0)$ and $(0, 2, 2\omega)$ (these velocity fields are given explicitly in Appendix C).

The third term of (4.8) is the solution of (4.7) without forcing, where we have only retained the axisymmetric geostrophic modes of Fourier components $(k, m, \omega) = (0, 0, 0)$. It is easy to show that this flow is a stationary azimuthal velocity field whose components can be written as $\boldsymbol{v}_0^j = (0, v_0^j(r), 0, p_0^j(r))$ in cylindrical coordinates. At this point, the geostrophic flow is arbitrary and we choose to decompose it on the basis of the Bessel functions of the first kind such that

$$v_0^j(r) = -J_1(d_j r) \quad \text{with} \quad J_1(d_j) = 0, \tag{4.9}$$

with the roots d_j sorted in ascending order such that $d_j = j\pi + O(1)$. We chose to put a minus sign in the above expression such that a positive amplitude A_0^j corresponds to a slow down of the basic solid-body rotation. As we will see below, this geostrophic flow is forced at order $\varepsilon^{4/3}$ by the nonlinear interactions in the endwall boundary layers. Its saturation is due to viscous effects in the boundary layers and this geostrophic mode therefore appears at order $A_0 = O(\varepsilon^{4/3}Re^{1/2}) = O(\varepsilon^{2/3})$.

The velocity field $\boldsymbol{V}_2$ satisfies inviscid boundary conditions. As order $\varepsilon^{1/3}$, we have to add a viscous velocity field $\widetilde{\boldsymbol{V}}_2$ in a boundary layer of thickness $O(Re^{-1/2})$ in order to satisfy the viscous boundary condition at the walls. This viscous flow is decomposed into several components. First, the velocity fields $\boldsymbol{v}_{2k}$ and $\boldsymbol{v}_{2\omega}$ contribute to this viscous velocity field. Then the geostrophic flow corresponds to viscous corrections $\widetilde{\boldsymbol{v}}_0^j$ in the endwall boundary layers. And finally, the nonlinear interactions of $\boldsymbol{V}$ with $\widetilde{\boldsymbol{V}}$ and $\widetilde{\boldsymbol{V}}$ with itself act as a source term at order $\varepsilon^{2/3}$ and give rise to a nonlinear part of the viscous flow $\widetilde{\boldsymbol{V}}_2^{\mathrm{NL}}$. If we are only interested in the axisymmetric and stationnary part of this viscous flow, it can be written as

$$\widetilde{\boldsymbol{V}}_2 = |A|^2\,\widetilde{\boldsymbol{v}}_{2k} + |A|^2\widetilde{\boldsymbol{v}}_2^{\mathrm{NL}} + \sum_{j=1}^{\infty} A_0^j(\tau)\widetilde{\boldsymbol{v}}_0^j + \text{o.t.}, \tag{4.10}$$

where the details of these velocity fields are given in Appendices D and E. This viscous flow $\widetilde{\boldsymbol{V}}_2$ is parallel to the walls at this order but it gives rise to Ekman pumping at the endwalls at order $\varepsilon^{4/3}$ of the form $\widetilde{\boldsymbol{V}}_4^{\perp} = O(\eta\widetilde{\boldsymbol{V}}_2)$. This pumping gives a boundary condition for the inviscid flow of the form

$$\boldsymbol{V}_4\cdot\boldsymbol{n} = -\widetilde{\boldsymbol{V}}_4^{\perp} = -\eta|A|^2\widetilde{\boldsymbol{v}}_4^{\mathrm{NL}}\cdot\boldsymbol{n} - \eta\sum_{j=1}^{\infty} A_0^j(\tau)\widetilde{\boldsymbol{v}}_4^j\cdot\boldsymbol{n} + \text{o.t.} \quad \text{on the walls}, \tag{4.11}$$

where the details of these fields are given in Appendices D and E and where we have omitted the term due to $\widetilde{\boldsymbol{v}}_{2k}$ because it does not contribute to the forcing of the geostrophic mode at order $\varepsilon^{4/3}$, as will be shown below.

i,n	$\omega_{i,n}$	δ_i	f	μ	σ	ξ	ν
1,1	1.088	2.691	−0.467	$1.799-0.268\mathrm{i}$	−0.058	1.524	10.3
1,2	1.812	2.447	0.0328	$0.822-0.456\mathrm{i}$	11.37	170.2	33.4
1,3	1.927	2.420	−0.00522	$0.486-0.342\mathrm{i}$	76.03	1897	82.0
2,1	0.566	5.912	−0.0771	$1.707+0.041\mathrm{i}$	−9.13	2.736	38.0
2,2	1.366	5.602	−0.0187	$1.434-0.382\mathrm{i}$	15.35	75.51	58.8

TABLE 1. Values of the nonlinear and viscous parameters for aspect ratio $h=1.8$.

4.1.3. *Order* ε

At order ε, the Navier–Stokes equation becomes

$$\mathscr{I}\frac{\partial \boldsymbol{V}_1}{\partial \tau}+\left(\frac{\partial}{\partial t}\mathscr{I}+\mathscr{M}\right)\boldsymbol{V}_3=\zeta\,\boldsymbol{F}_0\mathrm{e}^{\mathrm{i}(\omega t+\varphi)}+\boldsymbol{N}(\boldsymbol{V}_1,\boldsymbol{V}_2)+\boldsymbol{N}(\boldsymbol{V}_2,\boldsymbol{V}_1)+\frac{\eta\mathscr{L}\boldsymbol{V}_1}{Re^{1/2}}. \tag{4.12}$$

The last term of this equation should not appear at this order but at order $\varepsilon^{5/3}$. However, we have decided to take it into account in the analysis because its importance in evaluating the viscous decay has been shown in several papers (Kerswell & Barenghi 1995; Eloy *et al.* 2003; Racz & Scott 2007). The integration of equation (4.12) is not needed. We introduce the scalar product

$$\boldsymbol{X}\odot\boldsymbol{Y}=\int_V(\overline{X}_rY_r+\overline{X}_\varphi Y_\varphi+\overline{X}_zY_z+\overline{X}_pY_p)\mathrm{d}^3V, \tag{4.13}$$

where the overbar stands for complex conjugation and V is the volume of the cylinder. A solvability condition for $\boldsymbol{V}_3$ is obtained by forming the scalar product of $\boldsymbol{v}_i\,\mathrm{e}^{\mathrm{i}(\omega t+\varphi)}$ with equation (4.12) and dividing by $\boldsymbol{v}_i\odot\mathscr{I}\boldsymbol{v}_i$. It yields the following amplitude equation for A:

$$\frac{\partial A}{\partial\tau}=\mathrm{i}f-\eta\left(\mu+\frac{\nu}{Re^{1/2}}\right)A+\mathrm{i}\left(\sigma|A|^2-\sum_{j=1}^{\infty}\xi_jA_0^j\right)A, \tag{4.14}$$

where the calculation of the different coefficients is detailed in Appendices D and C. Some useful numerical values are given in tables 1–3. In the above equation the term f comes from the forcing $\boldsymbol{F}_0$, and the term ν is linked to the volume viscous damping. The term σ originates from the nonlinear interaction of $\boldsymbol{V}_1$ with $\boldsymbol{v}_{2k}$ and $\boldsymbol{v}_{2\omega}$. The terms ξ_j come from the nonlinear interaction of $\boldsymbol{V}_1$ with the geostrophic modes $\boldsymbol{v}_0^j$. The surface viscous damping term μ comes from the relation

$$\boldsymbol{v}_i\,\mathrm{e}^{\mathrm{i}(\omega t+\varphi)}\odot\left(\frac{\partial}{\partial t}\mathscr{I}+\mathscr{M}\right)\boldsymbol{V}_3=\int_S\overline{p_i}\,\mathrm{e}^{-\mathrm{i}(\omega t+\varphi)}\boldsymbol{V}_3\cdot\boldsymbol{n}\,\mathrm{d}^2S=\eta\mu A\,(\boldsymbol{v}_i\odot\mathscr{I}\boldsymbol{v}_i), \tag{4.15}$$

where S is the surface of the cylinder. This relation is obtained by integrating by parts the scalar product and using the fact that $\boldsymbol{v}_i\,\mathrm{e}^{\mathrm{i}(\omega t+\varphi)}$ is in the kernel of the operator $(\partial\mathscr{I}/\partial t+\mathscr{M})$ by construction. Since $\boldsymbol{V}_3\cdot\boldsymbol{n}$ is known from relation (4.6) and is proportional to ηA, (4.15) leads to the evaluation of μ in (4.14). This term is a complex number whereas all the other coefficients of (4.14) are real. This means that the viscous boundary layers have two effects: the damping of the flow (the real part of μ is positive) and a detuning of the resonance (due to the non-zero imaginary part of μ).

i,n	$\omega_{i,n}$	δ_i	f	μ	σ	ξ	ν
1,1	0.996	2.737	0.469	$1.728-0.128\mathrm{i}$	−0.232	0.910	9.96
1,2	1.774	2.456	0.0418	$0.841-0.404\mathrm{i}$	7.799	94.28	28.2
1,3	1.911	2.424	−0.00696	$0.497-0.322\mathrm{i}$	50.93	1032	67.6
2,1	0.510	5.960	−0.0737	$1.579+0.112\mathrm{i}$	−10.69	1.921	38.0
2,2	1.285	5.618	−0.0209	$1.398-0.261\mathrm{i}$	9.962	45.70	53.8

TABLE 2. Values of the nonlinear and viscous parameters for an aspect ratio $h=2$.

i,n	h	ξ_1	ξ_2	ξ_3	ξ_4	ξ_5	χ_1	χ_2	χ_3	χ_4	χ_5
1,1	1.8	0.277	0.144	−0.052	0.031	−0.021	4.743	1.308	−0.314	0.139	−0.077
1,2	1.8	0.701	0.062	−0.017	0.009	−0.006	240.2	27.56	−7.231	3.253	−1.811
1,3	1.8	0.767	0.049	−0.011	0.005	−0.003	2458	244.3	−64.13	28.82	−16.03
2,1	2	−0.516	−0.132	0.316	0.127	−0.044	2.331	−1.044	7.969	3.388	−0.907

TABLE 3. Values of the first parameters ξ_i and χ_i for different resonances i,n and different aspect ratios h.

4.1.4. *Order* $\varepsilon^{4/3}$

At order $\varepsilon^{4/3}$, if we retain only the geostrophic terms, the Navier–Sokes equation becomes

$$\sum_{j=1}^{\infty} \frac{\partial A_0^j}{\partial \tau} \mathscr{I}\, \boldsymbol{v}_0^j + \mathscr{M} \boldsymbol{V}_4 = \sum_{j=1}^{\infty} \frac{\eta\, A_0^j}{Re^{1/2}} \mathscr{L}\, \boldsymbol{v}_0^j + \text{o.t.}, \tag{4.16}$$

where the volume viscous term on the right-hand side has been included for the same reason as in (4.12). The terms $\boldsymbol{N}(\boldsymbol{V}_2, \boldsymbol{V}_2)$ and $\boldsymbol{N}(\boldsymbol{V}_1, \boldsymbol{V}_3)$ do not appear in the above equation because they do not lead to geostrophic forcing.

The amplitude equation for the geostrophic mode can be found by forming the scalar product (as defined by (4.13)) of $\boldsymbol{v}_0^j$ with (4.16) and dividing by $\boldsymbol{v}_0^j \odot \mathscr{I}\, \boldsymbol{v}_0^j$. It yields the amplitude equations for the geostrophic modes

$$\frac{\partial A_0^j}{\partial \tau} = \eta \chi_j |A|^2 - \eta \left(\frac{2}{h} + \frac{d_j^2}{Re^{1/2}} \right) A_0^j. \tag{4.17}$$

The last term comes from volume viscous effects by using the equality

$$\boldsymbol{v}_0^j \odot \mathscr{L}\, \boldsymbol{v}_0^j = -d_j^2\, \boldsymbol{v}_0^j \odot \mathscr{I}\, \boldsymbol{v}_0^j. \tag{4.18}$$

The forcing term χ_j and the surface viscous damping $2/h$ originate from the relation

$$\boldsymbol{v}_0^j \odot \mathscr{M} \boldsymbol{V}_4 = \int_S p_0^j\, \boldsymbol{V}_4 \cdot \boldsymbol{n}\, \mathrm{d}^2 S = \eta \left(-\chi_j |A|^2 + \frac{2}{h} A_0^j \right) \left(\boldsymbol{v}_0^j \odot \mathscr{I}\, \boldsymbol{v}_0^j \right), \tag{4.19}$$

where we have integrated by parts the scalar product and used the fact that $\boldsymbol{v}_0^j$ is in the kernel of $\mathscr{M}$. The outward velocity $\boldsymbol{V}_4 \cdot \boldsymbol{n}$ is known from relation (4.11); it allows calculation of the coefficients χ_j and $2/h$ as is detailed in Appendices D and E. Here, the term due to $\widetilde{\boldsymbol{v}}_{2k}$ in $\boldsymbol{V}_4 \cdot \boldsymbol{n}$ has no influence since we have only retained the geostrophic part of the flow (independent of z) in (4.16). Physically, the forcing of the geostrophic mode appears through the coefficient χ_j and is due to the nonlinear interaction of the flow with itself in the endwall boundary layers. Therefore, to have a geostrophic flow, both nonlinear and viscous effects are needed near the endwalls.

4.2. *Discussion*

In this section, we will discuss the results of the nonlinear viscous theory presented in § 4.1 and compare them with experimental measurements.

4.2.1. *Amplitude equations*

The amplitude equations (4.14) and (4.17) give the time dependence of the Kelvin mode amplitude A and the amplitudes A_0^j of the geostrophic modes. A further simplification can be obtained by assuming that the Reynolds number is large when the nonlinear effects come into play. In this case, the volume viscous term $d_j^2 Re^{-1/2}$ in front of the surface viscous term $2/h$ can be neglected for the geostrophic modes. With this assumption, all geostrophic modes have the same natural decay time and one can define a single geostrophic amplitude $A_0 = A_0^j/\chi_j$ such that all amplitude equations for the geostrophic modes become identical. By defining a global parameter $\xi = \sum_{j=1}^{\infty} \chi_j \xi_j$, the final system can be reduced to two amplitude equations:

$$\frac{\partial A}{\partial \tau} = \mathrm{i} f \left(1 - \frac{A}{\varepsilon^{2/3} a_i}\right) - \eta \left(\mu + \frac{\nu}{Re^{1/2}}\right) A + \mathrm{i} \left(\sigma |A|^2 - \xi A_0\right) A, \tag{4.20a}$$

$$\frac{\partial A_0}{\partial \tau} = \eta \left(|A|^2 - \frac{2}{h} A_0\right). \tag{4.20b}$$

In these equations, we have assumed that the frequency ω is not exactly equal to the resonant frequency $\omega_{i,n}$, which introduces an additional axial velocity in the solvability condition at order ε, leading to the extra term $\mathrm{i} f A/(\varepsilon^{2/3} a_i)$, where a_i is the amplitude of the Kelvin mode given by (3.6). This term vanishes at the resonance since a_i diverges in this case. On the other hand, if the forcing frequency is far enough from the resonant frequency such that $a_i \ll \varepsilon^{2/3}$, we recover the inviscid solution $A = \varepsilon^{2/3} a_i$ of § 3.1.

The linear forcing parameter f and the nonlinear parameter σ (corresponding to the interaction of the Kelvin mode with itself) are given analytically in Appendix C. The surface and volume viscous parameters μ and ν are given in Appendix D. The term ξ is due to the nonlinear interaction of the Kelvin mode with the geostrophic modes and cannot be given analytically in a simple form. We thus show the variation of this parameter as a function of the aspect ratio h in figure 8 for five different resonances. It drastically decreases by ten decades when h increases from 0.1 to 10. This is due to the fact that the nonlinear forcing of the geostrophic mode is generated in the top and bottom boundary layers only, and is thus more efficient for small aspect ratios h.

The amplitude equations (4.20 *a*, *b*) describe the transient stage and the saturation of the mode amplitude A. They have been obtained for the distinguished scaling $\varepsilon^{2/3} = O(Re^{-1/2})$ which corresponds to $\eta = O(1)$. However, one can easily obtain simplified equations when viscous effects are dominant by taking the limit $\eta \gg 1$. In this case, the amplitude equation for the geostrophic mode (4.20*b*) is not needed anymore and the amplitude equation (4.20*a*) simplifies into a linear equation for A with a forcing term. Its solution is an exponential convergence toward a fixed point with a characteristic time scale which is the natural viscous decay time of the Kelvin mode. The fixed point corresponds to $A = O(\eta^{-1})$ which gives $\boldsymbol{V}_i = O(\varepsilon Re^{1/2})$ in agreement with the results of Gans (1970). In this case, it is easy to show that the mode amplitude is maximum when the detuning of the forcing frequency compensates exactly the viscous detuning, i.e. $f/(\varepsilon^{2/3} a_i) = -\eta \mathrm{Im}(\mu)$. When this is true, A is a pure

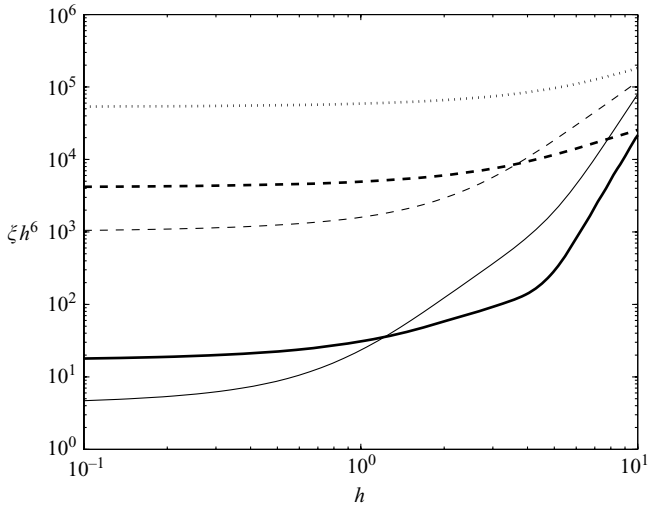

FIGURE 8. Numerical value of the nonlinear parameter ξ multiplied by h^6 quantifying the interaction of the resonant Kelvin mode with the geostrophic mode. The curves correspond to the first (thick lines) and second (thin lines) Kelvin modes at their first (solid line), second (dashed line) and third (dotted line) resonance.

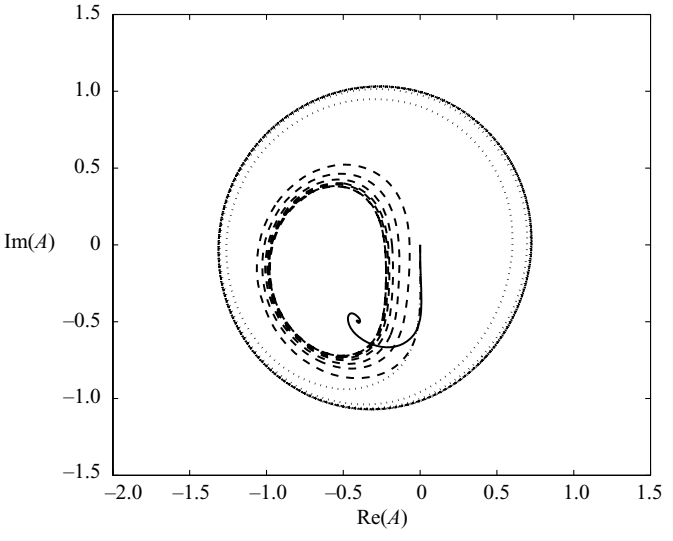

FIGURE 9. Phase portrait of the complex amplitude of the first Kelvin mode at its first resonance, obtained by integrating equations (4.20a, b). The Reynolds number is equal to 2.5×10^4 (solid line), 2.2×10^5 (dashed line) and 2.5×10^6 (dotted line) for a small parameter $\varepsilon = 0.003$ as in the experiments. This corresponds to η equal to 0.31, 0.10 and 0.03 respectively.

imaginary number, which means that the mode is oriented with an angle of $\pi/2$ compared to the non-resonant case of § 3.1.

When nonlinear effects are not negligible, the dynamics of the mode amplitude given by (4.20 a, b) becomes more complex. Some typical trajectories of A in the complex plane are shown in figure 9 for different values of the parameter η. If nonlinear effects are small, which corresponds to η large (or Re small compared to $\varepsilon^{-4/3}$), the

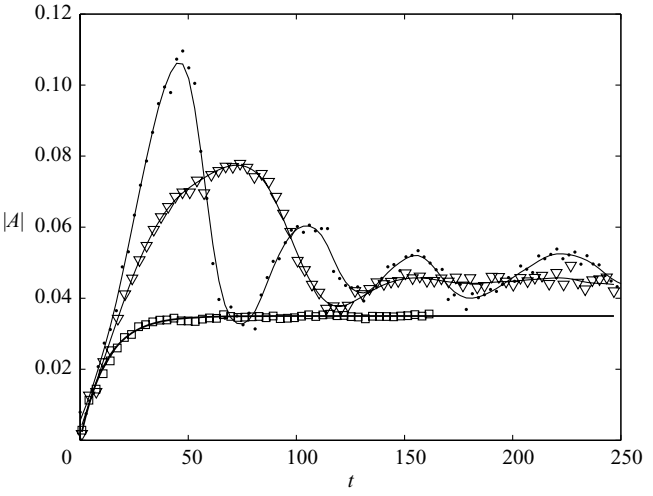

FIGURE 10. Time evolution of the amplitude of the first mode at the second resonance ($\omega = 1.812$ and $h = 1.8$) for $Re = 720$ (□), $Re = 2200$ (△) and $Re = 7400$ (•). The thick line corresponds to an exponential fit for $Re = 720$. The forcing amplitude is $\varepsilon = 2.8 \times 10^{-3}$.

amplitudes of the Kelvin mode A and geostrophic mode A_0 converge toward a fixed point. This fixed point is easily obtained by equating the time-derivative in (4.20 a, b) to zero. It is worth pointing out that the first effect of nonlinearities is to detune the Kelvin mode: the terms originating from the nonlinear interaction of the mode with itself and with the geostrophic mode are both expressed as a real number multiplying iA. This form is identical to that of the detuning term $\mathrm{i}Af/(\varepsilon^{2/3}a_i)$ and the viscous detuning term $-\eta \mathrm{Im}(\mu)\mathrm{i}A$.

For larger values of the Reynolds number (or smaller values of η), the fixed point may become unstable. In this case, the trajectory of A in the complex plane converges toward a limit cycle as shown on figure 9. However, this cycle could not be observed experimentally because it corresponds to experimental parameters leading to instability as shown in the next section.

As noted by Gans (1970) in the viscous regime, the resonances are important when the amplitude at the resonance (of the order of $\varepsilon\sqrt{Re}\, f/\mu$ in the viscous regime) is much larger than the linear amplitude (of the order of ε) outside of the resonance. Since the term f/μ decreases with the radial wavenumber δ as $\delta^{-7/2}$, we recover that the resonances are visible if $\delta < Re^{1/7}$ in the viscous regime. Doing the same analysis in the nonlinear regime, the resonance is visible only if the amplitude at the resonance, which scales as $(\varepsilon f/\sigma)^{1/3}$, is larger than the linear amplitude ε outside of the resonance. Since f/σ scales as $\delta^{-11/2}$, we find that the resonance is important when $\delta < \varepsilon^{-4/11}$. In the general case, the resonances are thus visible if the radial wavenumber δ is smaller than these two bounds scaling as $Re^{1/7}$ and $\varepsilon^{-4/11}$ respectively.

4.2.2. *Experimental amplitude at the resonance*

Figure 10 shows the experimental measurement of the amplitude of the first Kelvin mode at its second resonance for three different Reynolds numbers. For small Reynolds numbers, the temporal evolution of the amplitude is exponential, $A_f(1 - \mathrm{e}^{-t/t_s})$, with a final amplitude A_f and a settling time t_s which can be easily obtained by a least-square fit. However, for higher Reynolds numbers, the amplitude strongly oscillates before reaching a quasi-stationary final amplitude. This may be due

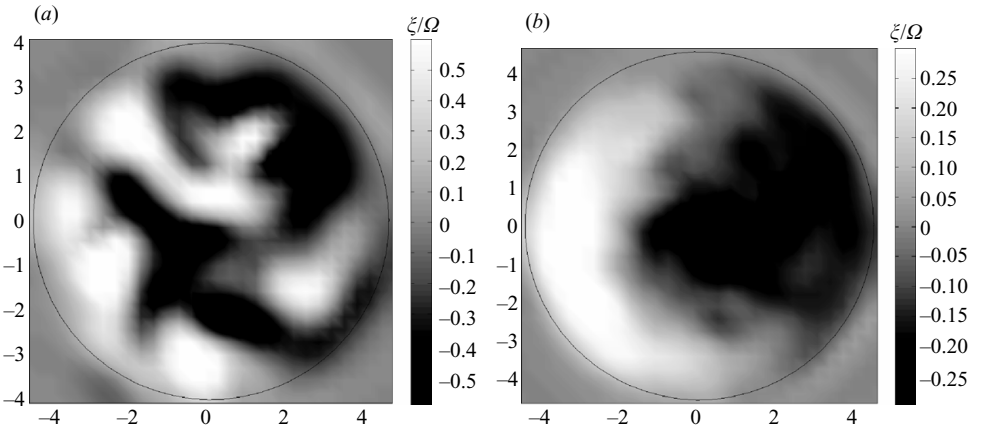

FIGURE 11. Instantaneous (a) and mean (b) vorticity field of the second resonance of the first Kelvin mode ($\omega = 1.812$ and $h = 1.8$) after destabilization of the flow ($Re = 7400$ and $\varepsilon = 2.8 \times 10^{-3}$).

to the nonlinear effects (which create a decaying oscillation of the amplitude), but in fact it mostly comes from the onset of a three-dimensional instability which is slowly growing during the transient stage. This oscillation prevents the correct determination of the final amplitude and introduces a large error, which is taken as the difference between the maximum and the local minimum of the amplitude. This error is shown in the following figures as error bars on the amplitude.

To clearly demonstrate that the flow has become three-dimensionally unstable at high Reynolds numbers, we have plotted in figure 11(a) the instantaneous vorticity field found in the cylinder for the second resonance of the first Kelvin mode. The vorticity is made up of several small vortices, which completely hide the organized structure of the initial Kelvin mode. However, this Kelvin mode is recovered (at a smaller amplitude) when plotting the mean vorticity field calculated on 100 fields (i.e. during 50 rotation periods), as in figure 11(b). It is striking to see that although the flow seems completely turbulent, the resonant Kelvin mode is still present with an amplitude only slightly oscillating in time. In this case, the current nonlinear theory no longer applies because other Kelvin modes have appeared because of an instability.

By plotting the transient regimes for each frequency ω, we were able to measure the final amplitude A decomposed on its norm $|A|$ and argument α such that $A = |A|e^{i\alpha}$. They are plotted in figure 12 as a function of the dimensionless frequency ω around the second resonance of the first Kelvin mode and for $\eta = 0.22$. This solution is compared to the theoretical viscous solutions (linear and nonlinear). What is intended here by viscous linear (respectively nonlinear) theory is the set of equations (4.20 a, b) in the limit $\eta \gg 1$ (respectively $\eta = O(1)$). Despite the large error bars, the comparison between experiment and theory clearly shows that both nonlinear and viscous effects are needed to predict the correct amplitude of the mode. The viscous effects saturate the amplitude of the mode at a finite value, and the nonlinear effects shift the maximum of the peak toward smaller frequencies ω. The overall agreement is excellent for the amplitude. However, the experimental determination of the orientation of the mode α is closer to the linear theory than to the nonlinear theory. This discrepancy may come from transient effects: the measurements can only be done for a small duration, due to the presence of an instability. When looking at the solid line of

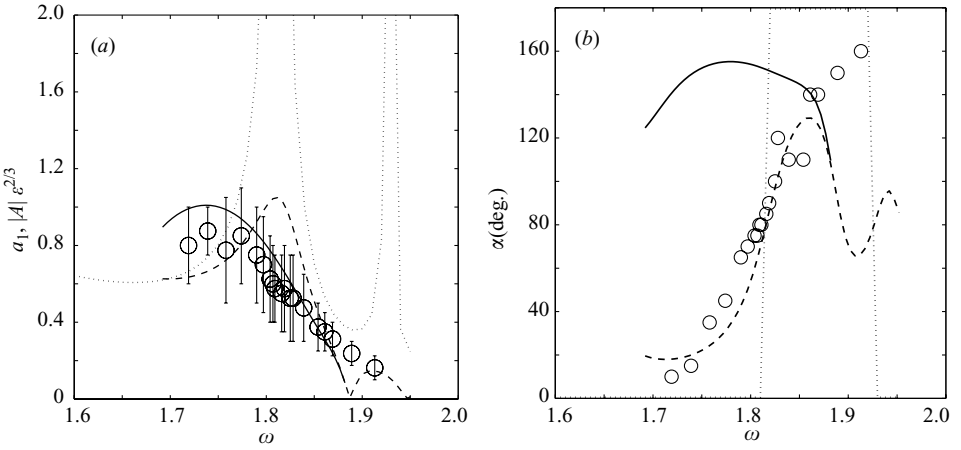

FIGURE 12. Amplitude (a) and orientation (b) of the first Kelvin mode around its second resonance. Experimental results ($\circ$) are obtained for an aspect ratio $h = 1.8$, Reynolds number $Re = 2500$ and ε varying between 2.3×10^{-2} and 3.3×10^{-2} . The solid line corresponds to the nonlinear viscous theory at the second resonance of the first mode, the dashed line to the linear viscous theory and the dotted line to the linear inviscid theory.

figure 9, we can see that the amplitude might be correctly predicted although the argument is not at its final value.

4.2.3. *Scaling at the resonance*

Five series of experiments were conducted to study the dependence of the amplitude on the Reynolds number when the frequency ω is exactly equal to the resonant frequency $\omega_{i,n}$. For this purpose, Ω_1 and Ω_2 were varied in each experiment, keeping a fixed dimensionless frequency ω. The experiments were done for the first three resonances of the first Kelvin mode and for the first two resonances of the second Kelvin mode. Figure 13 shows the final amplitude of the mode after the transient stage. The results are in excellent agreement with the present theoretical predictions, in view of there being no fitting parameters. They clearly show that the amplitude scales with $Re^{1/2}$ at low Reynolds numbers and saturates due to nonlinear effects at large Reynolds numbers. This saturation value decreases rapidly with the number of the resonance n. There is a large uncertainty in the nonlinear regime because of the onset of the three-dimensional instability as discussed above, which makes the validation of the nonlinear saturation more difficult. However, there is agreement up to 50%. It can be noted that the exact theory given by (4.14) and (4.17) and plotted as thin lines is so close to the approximate theory given by (4.20a, b) plotted as thick lines as to be almost in distinguishable: this means that it is justified to neglect the volume viscous damping of the geostrophic modes in the regime we have studied.

The dimensionless settling time t_s measured during the transient response is also plotted for these resonances in figure 14 as a function of the Reynolds number. It is compared to the viscous time $Re/(Re^{1/2}\mu + \nu)$. Although there is a large scatter, the agreement seems to be good. The settling time is only measured in the viscous regime since it is impossible to determine the settling time in the nonlinear regime when the transient response is no longer exponential (as shown in figure 10).

Figure 15 shows the argument α of the complex amplitude as a function of the Reynolds number for the same five resonances. At low Reynolds numbers, the angles are determined by the viscous theory and are equal to $\pm 90°$ (if viscous detuning is

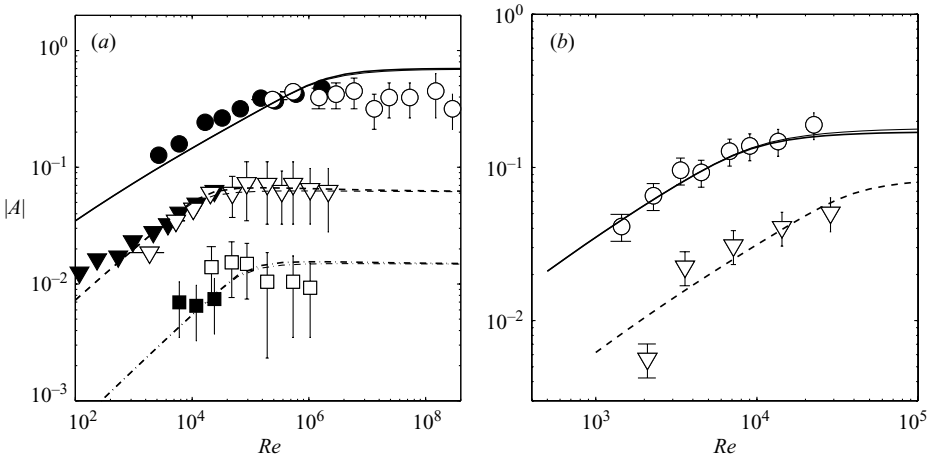

FIGURE 13. Amplitude of the first (a) and second (b) Kelvin modes as a function of the Reynolds number for the first (○, solid line), second (▽, dashed line), and third (□, dash-dotted line) resonances. Filled symbols correspond to a small cylinder $R_c = 1.5$ cm and open symbols to a large cylinder $R_c = 4.6$ cm. The thick lines correspond to the approximate theory (4.20) and the thin lines to the exact theory (4.14) and (4.17) (note that they are almost indistinguishable). For the first mode, $h = 1.8$; $\varepsilon = 3.1 \times 10^{-3}$, 2.8×10^{-3} and 3.2×10^{-2} for the first, second and third resonance respectively. For the second mode $h = 2$; $\varepsilon = 8.6 \times 10^{-3}$ and $\varepsilon = 5 \times 10^{-3}$ for the first and second resonance respectively.

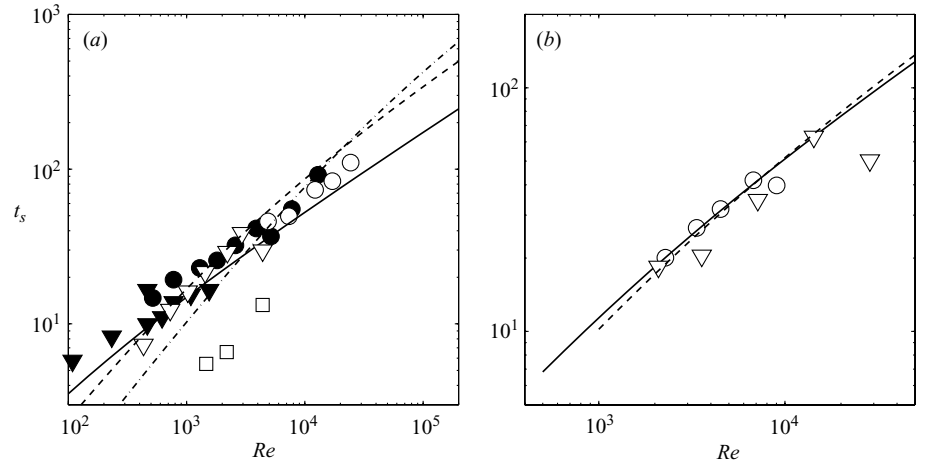

FIGURE 14. Settling time of the first (a) and second (b) modes as a function of the Reynolds number, obtained at the first (○, solid line), second (▽, dashed line) and third (□, dash-dotted line) resonances. Filled symbols correspond to a small cylinder and open symbols to a large cylinder. Same experimental parameters as in figure 13.

neglected). It means that, at the resonance, the mode is perpendicular to its direction in the linear inviscid theory (or far from the resonances). However, when the nonlinear effects become large, the phase shift occurs at a frequency different from $\omega_{i,n}$, and the angle is thus equal to 0° or 180° at $\omega = \omega_{i,n}$. The agreement with the experimental results is good for the first resonance of the first mode. However, there is a large

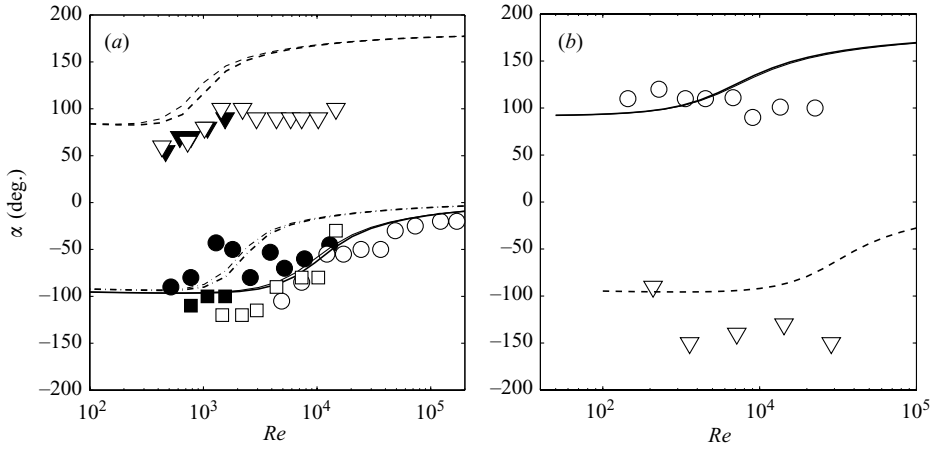

FIGURE 15. Orientation of the first (a) and second (b) modes as function of the Reynolds number, obtained at the first (○, solid line), second (▽, dashed line) and third (□, dash-dotted line) resonances. Filled symbols correspond to a small cylinder and open symbols to a large cylinder. The thick lines corresponds to the approximate theory (4.20) and the thin lines to the exact theory (4.14) and (4.17). Same experimental parameters as in figure 13.

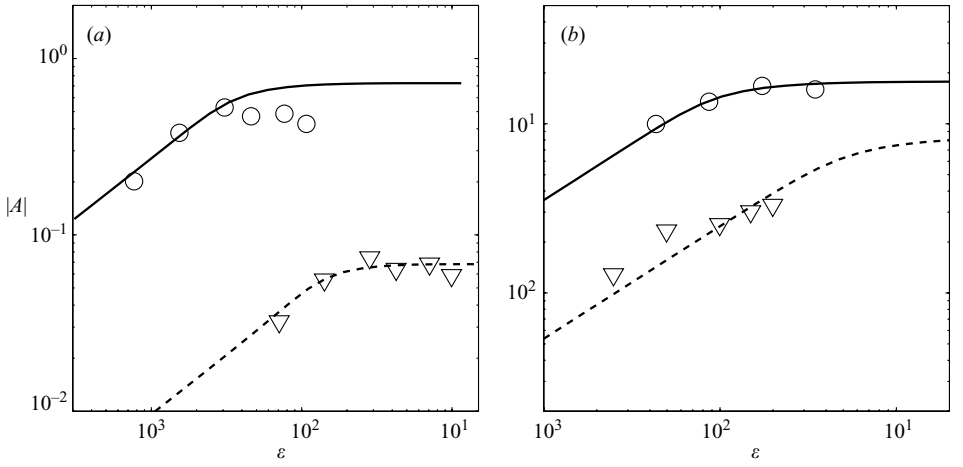

FIGURE 16. Amplitudes of the first (a) and second (b) modes as a function of the parameter ε (proportional to the precessing angle θ), obtained at the first (○, solid line) and second (▽, dashed line) resonances. For the first mode, $h = 1.8$ and $Re = 11900$ (resp. 2150) for the first (resp. second) resonance. For the second mode, $h = 2$ and $Re = 9000$ (resp. 3600) for the first (resp. second) resonance.

scatter for the other resonances, and it is hard to check the validity of the theoretical predictions.

Finally, we have measured the dependence of the amplitude A on the small parameter ε by varying the precession angle from 0.5° to 10°. The measured amplitudes are plotted in figure 16 and compared to the theoretical predictions. We recover that the amplitude scales as $\varepsilon^{2/3}$ in the viscous regime and then saturates at a fixed value for large precession angles. The agreement is again excellent in the viscous regime and fairly good in the nonlinear regime although the theory slightly overestimates the amplitude. This might be due once again to the appearance of a three-dimensional

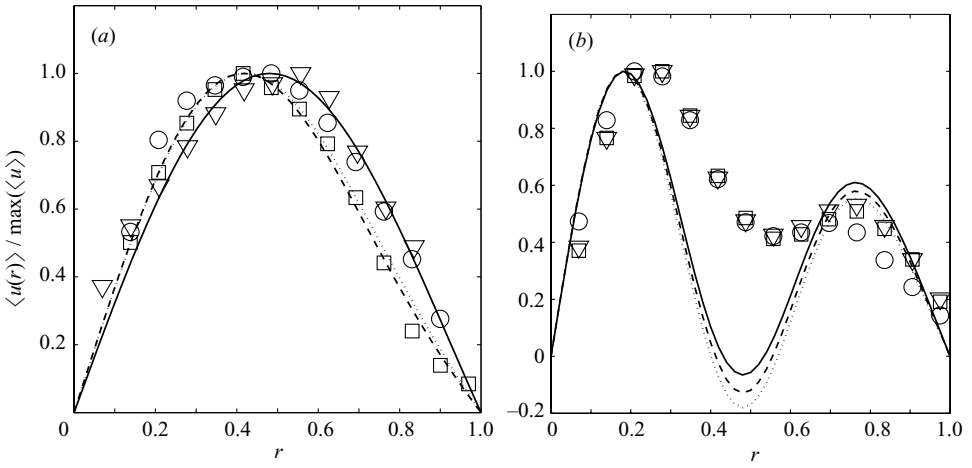

FIGURE 17. Velocity profile of the geostrophic mode ($m=0$) for the first resonance of (a) the first ($\omega=1.088,\ h=1.8,\ \varepsilon=3.1\times10^{-3}$) and ($b$) the second ($\omega=0.51,\ h=2,\ \varepsilon=8.6\times10^{-3}$) Kelvin mode. ($a$) $Re=1300$ (○, solid line), $Re=4900$ (▽, dashed line) and $Re=12\,200$, (□, dotted line); (b) $Re=3900$ (○, solid line), $Re=7800$ (▽, dashed line) and $Re=16\,000$ (□, dotted line).

instability before the final amplitude has been reached. This relative discrepancy could be also due to the fact that the theoretical derivation assumes that $\varepsilon^{1/3}$ is asymptotically small whereas it increases to 0.5 when the precession angle is large.

4.2.4. *Geostrophic modes*

As was previously stated in §4.2.1, the nonlinear and viscous effects lead to the generation of a geostrophic mode. This mode is mainly responsible for the saturation of the mode amplitude since the parameter ξ is generally larger than the parameter σ in (4.20a) as shown in tables 1 and 2. It is thus essential to check if the theory predicts an accurate amplitude of the geostrophic mode. Figure 17 shows the velocity profile of the geostrophic mode for the first and second modes. It has been obtained by taking an azimuthal average of the azimuthal velocity (in this way, the velocity of the Kelvin modes are conveniently removed). For the first mode, the measured profile is bell-shaped and depends very weakly on the Reynolds number. This is in excellent agreement with the nonlinear theory. For the second Kelvin mode, the geostrophic profile is more complex. It exhibits two velocity maxima, but still vanishes for $r=1$. This is due to the simultaneous presence of several components $J_1(d_j r)$ in the geostrophic mode. The experiments are again in fairly good agreement with the nonlinear theory, although the minimum is less pronounced in the former.

It is possible to decompose these profiles into the Bessel functions $J_1(d_j r)$(d_j being the roots of the Bessel function) in order to obtain the amplitudes A_0^j of the geostrophic mode as defined in (4.8) and (4.9). For the first Kelvin mode, the amplitude A_0^1 is much larger than the others since the geostrophic mode is mostly bell-shaped. We have thus plotted this amplitude A_0^1 as a function of the Reynolds number and the parameter ε. In the viscous regime, the amplitude A_0^1 roughly scales as the Reynolds number and as $\varepsilon^{4/3}$, since it scales as the square of the amplitude A, as shown in figure 18. This means that the total geostrophic motion $A_0\varepsilon^{2/3}v_0$ scales as the square of the forcing parameter ε. It can be noted that there are some small variations of the scaling exponent among the resonances, which are due to the volumic diffusion terms

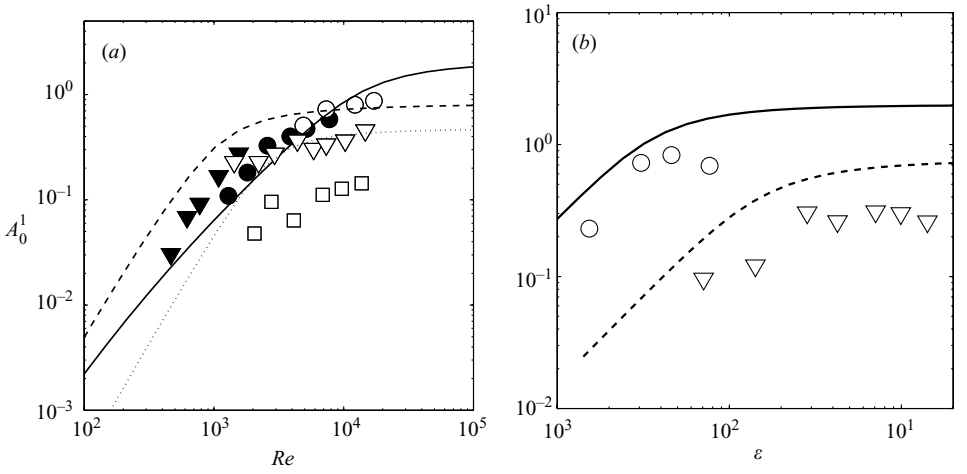

FIGURE 18. Amplitude of the geostrophic mode as a function of the Reynolds number (*a*) and the precession angle (*b*). The results are obtained with an aspect ratio $h = 1.8$ for the first mode at its first resonance (○, solid line, $\omega = 1.088$), its second resonance (▽, dashed line, $\omega = 1.812$) and its third resonance (□, dotted line, $\omega = 1.927$). Closed symbols correspond to a small cylinder and open symbols to a large cylinder. (*a*) $\varepsilon = 3.1 \times 10^{-3}$, 2.8×10^{-3} and 3.2×10^{-2} for the first, second and third resonance respectively; (*b*) $Re = 12\,200$ for the first resonance and $Re = 2200$ for the second resonance.

$d_j^2 Re^{-1/2}$. In the nonlinear regime, the geostrophic amplitude A_0^1 saturates because the amplitude A also saturates. This means that the geostrophic motion scales as $\varepsilon^{2/3}$ in this regime. The agreement between the experiment and the theory is good for the first two resonances: the scaling exponents and the multiplication factors are correct, although the theory slightly overestimates the amplitude of the first mode in the nonlinear regime. For the third resonance, the amplitude is much smaller in the experiments than in the theory, but the velocity of the geostrophic mode is very small in this case and the uncertainty is thus very high.

For the second Kelvin mode, the geostrophic profile contains more than one component and we thus need to plot the amplitudes A_0^j, j varying from 1 to 3. They are plotted in figure 19 and compared to the theory. It is surprising to see that here, the theory underestimates the amplitudes by a factor 10. Again this discrepancy could be due to the fact that $\varepsilon^{1/3}$ is not very small and thus the asymptotic decomposition may be no longer valid in this case.

5. Conclusion

In this paper we addressed both experimentally and theoretically the flow inside a rotating cylinder subject to a weak precession. We have shown that this flow can be expressed as a sum of Kelvin modes which have been measured for the first time using particle image velocimetry. We have distinguished two cases depending on the precession frequency. When this forcing frequency is not equal to a natural frequency of a Kelvin mode, the flow is said to be non-resonant and a linear inviscid theory can predict accurately the amplitude of the forced Kelvin modes in the limit of small precession amplitude and large Reynolds number. However, if the forcing frequency is resonant, this linear inviscid theory is unable to give the mode amplitude since it

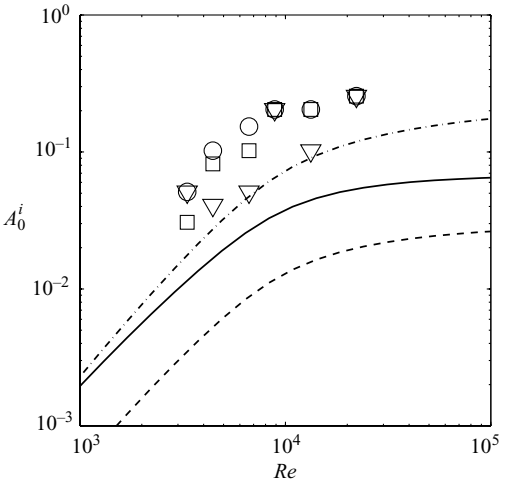

FIGURE 19. Amplitude of the geostrophic mode as a function of the Reynolds number, for the first resonance of the second mode. The different curves correspond to the first component A_0^1 (solid line, $\circ$), the second component A_0^2 (dashed line, ∇) and the third component A_0^3 (dash-dotted line, $\square$). The dimensionless parameters are $h = 2$, $\varepsilon = 8.6 \times 10^{-3}$.

diverges. In this case, a viscous and nonlinear theory has been introduced to predict the finite value of the mode amplitude.

In the resonant case, there are two different regimes depending on the value of the Reynolds number. For small enough Reynolds numbers, nonlinear effects are negligible and taking into account the effects of both the viscous boundary layers and the volume viscous damping is sufficient to predict the dynamics of the resonant Kelvin mode, as has already been shown by Gans (1970) in the particular case of a precession angle of 90°. It yields a saturation of the mode amplitude which scales as $Re^{1/2}$ in excellent agreement with the experimental results.

For larger Reynolds numbers, weakly nonlinear effects have to be taken into account together with viscous effects. It leads to the saturation of the mode amplitude at a value which scales as $\theta^{1/3}$, where θ is the precession angle, supposed small. It is thus independent of the Reynolds number. This scaling is correctly recovered experimentally. An interesting point is that experiments show the presence of a geostrophic motion, whose amplitude always scales as the square of the Kelvin mode amplitude, as can be predicted by the nonlinear and viscous theory. This small geostrophic motion has been observed and measured in the experiments and its amplitude has been shown to be correctly predicted by the theory for the first Kelvin mode.

We have characterized the stable flow inside a precessing cylinder in all regimes. In the future, these results could serve as a basis for a stability study of this flow; it is known from McEwan (1970) and Manasseh (1992) that Kelvin modes can become unstable and even turbulent for large Reynolds numbers. Such a breakdown of the flow has been observed in our experiments, and always appeared at the transition between the viscous and the nonlinear regime, i.e. when the nonlinear effects cease to be negligible. The instability of the Kelvin modes is probably due to a triadic resonance similarly to the elliptic instability (Kerswell 2002; Eloy *et al.* 2003). A theoretical and experimental study is currently underway to understand this instability better.

Finally, it would be interesting to know if the present theoretical framework would hold when the flow becomes unstable and eventually turbulent. The Kelvin modes

are still excited in this case, although they are hidden by the presence of a very disordered flow (which can still be expressed as a sum of Kelvin modes). This would have important consequences for industrial and geophysical applications, for which the Reynolds numbers are usually a few decades higher than in the laboratory experiments.

We would like to thank Laurie Devesvre for preliminary results during the setting-up of the laboratory experiment. This study has been carried out under the contract CEA-CNRS N° 004746.

Appendix A. Four-component formulation

The operators appearing in equation (2.8) are defined by

$$\mathscr{I} = \begin{pmatrix} 1 & 0 & 0 & 0 \\ 0 & 1 & 0 & 0 \\ 0 & 0 & 1 & 0 \\ 0 & 0 & 0 & 0 \end{pmatrix}, \tag{A 1}$$

$$\mathscr{D} = \begin{pmatrix} 0 & 0 & -\mathrm{i} & 0 \\ 0 & 0 & 1 & 0 \\ \mathrm{i} & -1 & 0 & 0 \\ 0 & 0 & 0 & 0 \end{pmatrix}, \tag{A 2}$$

$$\mathscr{L} = \begin{pmatrix} \Delta - \dfrac{1}{r^2} & -\dfrac{2}{r^2}\dfrac{\partial}{\partial\varphi} & 0 & 0 \\ \dfrac{2}{r^2}\dfrac{\partial}{\partial\varphi} & \Delta - \dfrac{1}{r^2} & 0 & 0 \\ 0 & 0 & \Delta & 0 \\ 0 & 0 & 0 & 0 \end{pmatrix}, \tag{A 3}$$

where

$$\Delta = \frac{1}{r}\frac{\partial}{\partial r} + \frac{\partial^2}{\partial r^2}\frac{1}{r^2}\frac{\partial^2}{\partial\varphi^2} + \frac{\partial}{\partial z^2}, \tag{A 4}$$

and

$$\mathscr{M} = \begin{pmatrix} 0 & -2 & 0 & \dfrac{\partial}{\partial r} \\ 2 & 0 & 0 & \dfrac{1}{r}\dfrac{\partial}{\partial\varphi} \\ 0 & 0 & 0 & \dfrac{\partial}{\partial z} \\ \dfrac{\partial}{\partial r} + \dfrac{1}{r} & \dfrac{1}{r}\dfrac{\partial}{\partial\varphi} & \dfrac{\partial}{\partial z} & 0 \end{pmatrix}. \tag{A 5}$$

The vectors $\boldsymbol{F}_0$ and $\boldsymbol{N}(\boldsymbol{v}_1, \boldsymbol{v}_2)$ are defined by

$$\boldsymbol{F}_0 = \begin{pmatrix} 0 \\ 0 \\ -r\omega \\ 0 \end{pmatrix}, \tag{A 6}$$

and

$$\boldsymbol{N}(\boldsymbol{v}_1,\ \boldsymbol{v}_2) = \begin{pmatrix} \boldsymbol{u}_1 \times (\nabla \times \boldsymbol{u}_2) + \overline{\boldsymbol{u}}_1 \times (\nabla \times \boldsymbol{u}_2) \\ 0 \end{pmatrix}. \tag{A 7}$$

Appendix B. Extraction of the mode amplitude a_i

The PIV measurements give the two components $\boldsymbol{u}_{\exp} = (u_{\exp}, v_{\exp})$ of the (real) transverse velocity field at a specific height z. We want to obtain the amplitudes a_i and the tilt angles α_i of the first five Kelvin modes whose transverse components are given in the reference frame of the rotating platform by $\boldsymbol{u}_i(r, \varphi, z) = \mathrm{e}^{\mathrm{i}\varphi}(u_i, v_i)\sin(k_i z)$ (u_i and v_i are given in (3.5)). We thus suppose that the experimental velocity field is given by

$$\boldsymbol{u}_{\exp}(r, \varphi, z) = \sum_i a_i \begin{pmatrix} -\mathrm{i}\sin(\varphi + \alpha_i)u_i(r) \\ \cos(\varphi + \alpha_i)v_i(r) \end{pmatrix}. \tag{B 1}$$

It can be noted that $\boldsymbol{u}_{\exp}$ is real since u_i is purely imaginary and v_i is purely real.

We introduce the scalar product $\langle \boldsymbol{X}|\boldsymbol{Y}\rangle = \int_0^{2\pi}\int_0^{0.9} (\overline{X}_r Y_r + \overline{X}_\varphi Y_\varphi)\, r\, \mathrm{d}r\, \mathrm{d}\varphi$ for which the Kelvin modes are almost orthogonal: they would be orthogonal if the integration were achieved over the whole section $0 < r < 1$. If we define the complex experimental velocity (which can be easily derived numerically)

$$\boldsymbol{u}^c_{\exp}(r, \varphi, z) = \boldsymbol{u}_{\exp}(r, \varphi, z) - \mathrm{i}\,\boldsymbol{u}_{\exp}(r, \varphi + \pi/2, z) \tag{B 2}$$

we find that the scalar product $\langle \boldsymbol{u}_i|\boldsymbol{u}^c_{\exp}\rangle$ is equal to

$$\langle \boldsymbol{u}_i|\boldsymbol{u}^c_{\exp}\rangle = \sum_j M_{ij} a_j \mathrm{e}^{\mathrm{i}\alpha_j}\sin(k_j z) \tag{B 3}$$

where $M_{ij} = 2\pi\int_0^{0.9}(\overline{u_i}u_j + \overline{v_i}v_j) r\, \mathrm{d}r$. If we consider only the five first Kelvin modes, we can invert numerically the 5×5 matrix M to obtain

$$\left(a_i \mathrm{e}^{\mathrm{i}\alpha_i}\sin(k_i z)\right)_{i=1,5} = M^{-1}\left(\langle \boldsymbol{u}_i|\boldsymbol{u}^c_{\exp}\rangle\right)_{i=1,5}. \tag{B 4}$$

The tilt angles α_i of the Kelvin modes are thus equal to the argument of this expression and the amplitudes a_i to the modulus of this expression divided by $(\sin(k_i z))_{i=1,5}$.

Appendix C. Calculation of the nonlinear coefficients

The aim of this Appendix is to calculate the coefficients f, σ and ξ_j appearing in the nonlinear amplitude equation (4.14).

C.1. *Order* $\varepsilon^{2/3}$

At order $\varepsilon^{2/3}$, the particular solution of (4.7) is given by (4.8) where

$$\boldsymbol{v}_{2k} = \begin{pmatrix} 0 \\ a_{2k}\cos(2k_i z) \\ 0 \\ p_{2k}\cos(2k_i z) \end{pmatrix}, \quad \boldsymbol{v}_{2\omega} = \begin{pmatrix} \dfrac{\mathrm{i}}{r}a_{2\omega} \\ -\dfrac{1}{2}\dfrac{\mathrm{d}a_{2\omega}}{\mathrm{d}r} \\ 0 \\ p_{2\omega} \end{pmatrix}, \tag{C 1a, b}$$

with

$$a_{2k} = \frac{\mathrm{i}k_i}{\omega}\left(v_i w_i - \frac{1}{2k_i}\frac{\partial(u_i v_i)}{\partial r}\right), \quad a_{2\omega} = \frac{\omega\delta_i^2}{(\omega^2-4)^2}\left[J_1^2(\delta_i r) - J_1^2(\delta_i)\, r^2\right]. \quad \text{(C 2}a,b\text{)}$$

C.2. *Order* ε

We first need to calculate the scalar product N, which is the norm of the velocity field

$$N = \boldsymbol{v}_i \odot \mathscr{I}\, \boldsymbol{v}_i = 2\pi h \frac{\omega^2\left(\omega + 2\delta_i^2 - 2\right) - 4\omega + 8}{\omega^2(4-\omega^2)^2} J_1^2(\delta_i) + \frac{\pi}{k_i}\sin(k_i h)\frac{\omega^2\left(\omega - \delta_i^2\omega - 2\right) - 4\omega + 8}{\omega^2(4-\omega^2)^2} J_1^2(\delta_i). \quad \text{(C 3)}$$

It can be noted that the last term vanishes at the resonance. The forcing term comes from

$$F = \boldsymbol{v}_i\, \mathrm{e}^{\mathrm{i}(\omega t+\varphi)} \odot \zeta\, \boldsymbol{F}_0 \mathrm{e}^{\mathrm{i}(\omega t+\varphi)} = 2\pi\zeta \frac{2\mathrm{i}}{\delta_i^2}\frac{\omega+2}{\omega}\sin\left(\frac{k_i h}{2}\right) J_1(\delta_i), \quad \text{(C 4)}$$

which is a pure imaginary number. The coefficient of forcing f appearing in the amplitude equation (4.14) is simply

$$f = \frac{F}{\mathrm{i}N}, \quad \text{(C 5)}$$

where N and F are given by (C 3) and (C 4).

The coefficient σ in (4.14) is separated into two parts. The first one comes from the nonlinear interaction of $\boldsymbol{V}_1$ with $\boldsymbol{v}_{2k}$

$$\sigma_{2k} = \boldsymbol{v}_i\, \mathrm{e}^{\mathrm{i}(\omega t+\varphi)} \odot \left[\boldsymbol{N}\left(\boldsymbol{v}_{2k}, \boldsymbol{v}_i\, \mathrm{e}^{\mathrm{i}(\omega t+\varphi)}\right) + \boldsymbol{N}\left(\boldsymbol{v}_i\, \mathrm{e}^{\mathrm{i}(\omega t+\varphi)}, \boldsymbol{v}_{2k}\right)\right], \quad \text{(C 6}a\text{)}$$

$$= 2\pi h \int_0^1 \left(2k_i\, a_{2k}\, v_i w_i - a_{2k}\frac{\partial(u_i v_i)}{\partial r}\right) r\,\mathrm{d}r, \quad \text{(C 6}b\text{)}$$

with a_{2k} given by (C 2a). The other term comes from the interaction of $\boldsymbol{V}_1$ with $\boldsymbol{v}_{2\omega}$

$$\sigma_{2\omega} = \boldsymbol{v}_i\, \mathrm{e}^{\mathrm{i}(\omega t+\varphi)} \odot \boldsymbol{N}\left(\boldsymbol{v}_{2\omega}\mathrm{e}^{2\mathrm{i}(\omega t+\varphi)}, \overline{\boldsymbol{v}_i}\, \mathrm{e}^{-\mathrm{i}(\omega t+\varphi)}\right), \quad \text{(C 7}a\text{)}$$

$$= 2\pi h \frac{\mathrm{i}k_i}{\omega}\int_0^1 \left(\frac{\mathrm{d}a_{2\omega}}{\mathrm{d}r}u_i w_i - \frac{2\mathrm{i}a_{2\omega}}{r} v_i w_i\right) r\,\mathrm{d}r, \quad \text{(C 7}b\text{)}$$

where the term associated with $\boldsymbol{N}(\boldsymbol{v}_i, \boldsymbol{v}_{2\omega})$ has been omitted because its scalar product with $\boldsymbol{v}_i\, \mathrm{e}^{\mathrm{i}(\omega t+\varphi)}$ is zero. The final coefficient σ used in the amplitude equation (4.14) is

$$\sigma = \frac{\sigma_{2k} + \sigma_{2\omega}}{\mathrm{i}N}, \quad \text{(C 8)}$$

where N, σ_{2k} and $\sigma_{2\omega}$ are given by (C 3), (C 6b) and (C 7b). The integrals appearing in the coefficients σ_{2k} and $\sigma_{2\omega}$ can be evaluated numerically. It is easy to see that σ_{2k} and $\sigma_{2\omega}$ are pure imaginary and therefore σ is real.

Finally the coefficients ξ_j describe the nonlinear interaction of the Kelvin mode with the jth geostrophic mode

$$X_j = \boldsymbol{v}_i\, \mathrm{e}^{\mathrm{i}(\omega t+\varphi)} \odot \left[\boldsymbol{N}\left(\boldsymbol{v}_0^j, \boldsymbol{v}_i\, \mathrm{e}^{\mathrm{i}(\omega t+\varphi)}\right) + \boldsymbol{N}\left(\boldsymbol{v}_i\, \mathrm{e}^{\mathrm{i}(\omega t+\varphi)}, \boldsymbol{v}_0^j\right)\right], \quad \text{(C 9}a\text{)}$$

$$= -2\pi h \int_0^1 \left(\frac{2\mathrm{i}k_i}{\omega} v_0^j u_i w_i + \frac{1}{r}\frac{\mathrm{d}\left(r v_0^j\right)}{\mathrm{d}r} u_i v_i\right) r\,\mathrm{d}r, \quad \text{(C 9}b\text{)}$$

where v_0^j is given by (4.9). The coefficient ξ_j of (4.14) is

$$\xi_j = -\frac{X_j}{\mathrm{i}N}, \tag{C 10}$$

where N and X_j are given by (C 3) and (C 9b). Again, the integral in (C 9b) is calculated numerically.

Some numerical values of the coefficients f, σ and ξ_j whose analytical expressions are given by (C 5), (C 8) and (C 10) are given in tables 1, 2 and 3.

Appendix D. Linear viscous boundary layers (Ekman pumping)

In this Appendix we derive the viscous correction to the main flow $\boldsymbol{V}$ in the boundary layers. This correction can be written as

$$\widetilde{\boldsymbol{V}} = \varepsilon^{1/3} A(\widetilde{\boldsymbol{v}}_i + Re^{-1/2}\,\widetilde{\boldsymbol{v}}_3)\mathrm{e}^{\mathrm{i}(\omega t+\varphi)} + \text{o.t.}, \tag{D 1}$$

with the boundary conditions $\boldsymbol{V} + \widetilde{\boldsymbol{V}} = 0$ on the walls and $\widetilde{\boldsymbol{V}}$ tending to zero far from the walls. In (D1), $\widetilde{\boldsymbol{v}}_i = (\widetilde{u}_i,\ \widetilde{v}_i,\ \widetilde{w}_i,\ \widetilde{p}_i)$ and $\widetilde{\boldsymbol{v}}_3 = (\widetilde{u}_3,\ \widetilde{v}_3,\ \widetilde{w}_3,\ \widetilde{p}_3)$ are of order 1. The added corrective flow (Ekman pumping) is denoted $\widetilde{\boldsymbol{v}}_3$ because, as we shall see below, this flow constitutes the normal boundary condition for the bulk flow $\boldsymbol{V}_3$ at order ε. This calculation is classical and can be found in several sources (e.g. Greenspan 1968; Gans 1970).

D.1. *Lateral wall*

First, let us focus on the lateral wall $r = 1$. By taking into account the viscous effects in (2.8) and considering the rescaled coordinate

$$\widetilde{r} = Re^{-1/2}(1 - r), \tag{D 2}$$

one can write the linear Navier–Stokes equation valid close to the lateral wall as

$$\left(\mathrm{i}\omega\mathscr{I} - Re^{1/2}\,\frac{\partial}{\partial\widetilde{r}}\mathscr{R}_l + \mathscr{M}_l - \frac{\partial^2}{\partial\widetilde{r}^2}\mathscr{I}\right)\widetilde{\boldsymbol{V}} = O(Re^{-1}\widetilde{\boldsymbol{V}}), \tag{D 3}$$

where the tensors $\mathscr{R}_l$ and $\mathscr{M}_l$ are defined as follows:

$$\mathscr{R}_l = \begin{pmatrix} 0 & 0 & 0 & 1 \\ 0 & 0 & 0 & 0 \\ 0 & 0 & 0 & 0 \\ 1 & 0 & 0 & 0 \end{pmatrix} \quad \text{and} \quad \mathscr{M}_l = \begin{pmatrix} 0 & -2 & 0 & 0 \\ 2 & 0 & 0 & \mathrm{i} \\ 0 & 0 & 0 & \dfrac{\partial}{\partial z} \\ 1 & \mathrm{i} & \dfrac{\partial}{\partial z} & 0 \end{pmatrix}. \tag{D 4}$$

At order $Re^{1/2}$,

$$\frac{\partial}{\partial\widetilde{r}}(\mathscr{R}_l\,\widetilde{\boldsymbol{v}}_i) = \boldsymbol{0}, \tag{D 5}$$

which leads to $\widetilde{u}_i = \widetilde{p}_i = 0$.

At order 1, (D 3) gives

$$\frac{\partial}{\partial\widetilde{r}}(\mathscr{R}_l\,\widetilde{\boldsymbol{v}}_3) = \left(\mathrm{i}\omega\mathscr{I} + \mathscr{M}_l - \frac{\partial^2}{\partial\widetilde{r}^2}\mathscr{I}\right)\widetilde{\boldsymbol{v}}_i. \tag{D 6}$$

The solution of this linear system with the boundary conditions $\boldsymbol{v}_i + \widetilde{\boldsymbol{v}}_i = 0$ at $\widetilde{r} = 0$ and $\widetilde{\boldsymbol{v}}_i$ vanishing to zero for $\widetilde{r} \gg 1$ is

$$\widetilde{v}_i(\widetilde{r},\, z) = -v_i(1)\, \sin(k_i z)\, \mathrm{e}^{-\kappa \widetilde{r}}, \quad \widetilde{w}_i(\widetilde{r},\, z) = -w_i(1)\, \cos(k_i z)\, \mathrm{e}^{-\kappa \widetilde{r}}, \tag{D 7}$$

where κ is given by

$$\kappa = \frac{1+\mathrm{i}}{\sqrt{2}} \sqrt{\omega}. \tag{D 8}$$

and

$$\widetilde{u}_3 = \widetilde{\boldsymbol{v}}_3 \cdot \boldsymbol{n} = -\alpha_i\, J_1(\delta_i)\, \sin k_i z \quad \text{at } r = 1, \tag{D 9}$$

where

$$\alpha_i = \frac{1+\mathrm{i}}{\sqrt{2}} \frac{(\delta_i^2 - 1)\, \omega^2 + 4}{(4-\omega^2)\, \omega^{3/2}}. \tag{D 10}$$

D.2. *Endwalls*

An equivalent derivation can be done for the upper wall (the flow in the lower wall boundary layer is formally identical). Using the local rescaled coordinate

$$\widetilde{z} = Re^{1/2} \left(\frac{h}{2} - z \right), \tag{D 11}$$

one can rewrite the Navier–Stokes equation valid close to the upper wall as

$$\left(\mathrm{i}\omega \mathscr{I} - Re^{1/2} \frac{\partial}{\partial \widetilde{z}} \mathscr{R}_u + \mathscr{M}_u - \frac{\partial^2}{\partial \widetilde{z}^2} \mathscr{I} \right) \widetilde{\boldsymbol{V}} = O(Re^{-1} \widetilde{\boldsymbol{V}}), \tag{D 12}$$

where the tensors $\mathscr{R}_u$ and $\mathscr{M}_u$ are defined as follows:

$$\mathscr{R}_u = \begin{pmatrix} 0 & 0 & 0 & 0 \\ 0 & 0 & 0 & 0 \\ 0 & 0 & 0 & 1 \\ 0 & 0 & 1 & 0 \end{pmatrix} \quad \text{and} \quad \mathscr{M}_u = \begin{pmatrix} 0 & -2 & 0 & \dfrac{\partial}{\partial r} \\ 2 & 0 & 0 & \dfrac{\mathrm{i}}{r} \\ 0 & 0 & 0 & 0 \\ \dfrac{1}{r} + \dfrac{\partial}{\partial r} & \dfrac{\mathrm{i}}{r} & 0 & 0 \end{pmatrix}. \tag{D 13}$$

At order $Re^{1/2}$, one finds $\widetilde{w}_i = \widetilde{p}_i = 0$. At order 1, the projection of (D 12) onto the radial, azimuthal and pressure directions with the proper boundary conditions gives

$$\widetilde{u}_i(r,\, \widetilde{z}) = \mathrm{i}\, S(r)\, \mathrm{e}^{-\kappa_s \widetilde{z}} - \mathrm{i}\, D(r)\, \mathrm{e}^{-\kappa_d \widetilde{z}}, \tag{D 14a}$$

$$\widetilde{v}_i(r,\, \widetilde{z}) = S(r)\, \mathrm{e}^{-\kappa_s \widetilde{z}} + D(r)\, \mathrm{e}^{-\kappa_d \widetilde{z}}, \tag{D 14b}$$

where κ_s and κ_d are given by

$$\kappa_s = \frac{1+\mathrm{i}}{\sqrt{2}} \sqrt{\omega + 2}, \quad \kappa_d = \frac{1-\mathrm{i}}{\sqrt{2}} \sqrt{2 - \omega}, \tag{D 15}$$

and where S and D are given by

$$S(r) = \frac{\mathrm{i}\, u_i - v_i}{2} \sin(k_i h/2), \quad D(r) = \frac{-\mathrm{i}\, u_i - v_i}{2} \sin(k_i h/2). \tag{D 16}$$

The projection of (D 12) onto the vertical direction gives

$$\widetilde{w}_3 = \left(\frac{2\mathrm{i}S}{r} + \mathrm{i} \frac{\mathrm{d}S}{\mathrm{d}r} \right) \frac{\mathrm{e}^{-\kappa_s \widetilde{z}}}{\kappa_s} - \mathrm{i} \frac{\mathrm{d}D}{\mathrm{d}r} \frac{\mathrm{e}^{-\kappa_d \widetilde{z}}}{\kappa_d}, \tag{D 17}$$

such that

$$\widetilde{w}_3 = \widetilde{\boldsymbol{v}}_3 \cdot \boldsymbol{n} = -\beta_i \sin(k_i h/2)\, J_1(\delta_i r) \quad \text{at } \widetilde{z} = 0 \quad \text{i.e.} \quad z = h/2, \tag{D 18}$$

where

$$\beta_i = \frac{1-\mathrm{i}}{2\sqrt{2}}\delta_i^2 \left[\frac{1}{(2-\omega)^{3/2}} + \frac{\mathrm{i}}{(2+\omega)^{3/2}}\right]. \tag{D 19}$$

D.3. *Geostrophic flow*

For the geostrophic flow, the viscous flow in the endwall boundary layers can be calculated with a similar method as for the Kelvin mode in § D.2. This viscous flow is of the form

$$\widetilde{\boldsymbol{V}} = \varepsilon^{2/3} \sum_{j=1}^{\infty} A_0^j(\tau)\left(\widetilde{\boldsymbol{v}}_0^j + Re^{-1/2}\widetilde{\boldsymbol{v}}_4^j\right) + \text{o.t.}, \tag{D 20}$$

where $\widetilde{\boldsymbol{v}}_0^j = (\widetilde{u}_0^j, \widetilde{v}_0^j, \widetilde{w}_0^j, \widetilde{p}_0^j)$. One finds $\widetilde{w}_0^j = \widetilde{p}_0^j = 0$ and

$$\widetilde{u}_0^j = \frac{\mathrm{i}}{2} v_0^j(-\mathrm{e}^{-\kappa_1\widetilde{z}} + \mathrm{e}^{-\kappa_2\widetilde{z}}), \quad \widetilde{v}_0^j = -\frac{1}{2} v_0^j(\mathrm{e}^{-\kappa_1\widetilde{z}} + \mathrm{e}^{-\kappa_2\widetilde{z}}), \tag{D 21}$$

where $\kappa_1 = 1 + \mathrm{i}$ and $\kappa_2 = 1 - \mathrm{i}$. This leads to

$$\widetilde{w}_4^j = \widetilde{\boldsymbol{v}}_4^j \cdot \boldsymbol{n} = \widetilde{w}_4^j = \frac{1}{2}\left(\frac{\mathrm{d}v_0^j}{\mathrm{d}r} + \frac{v_0^j}{r}\right) \quad \text{at } z = h/2. \tag{D 22}$$

D.4. *Viscous coefficients*

The surface viscous coefficients appearing in (4.14) and (4.17) can now be calculated. If the surface of the cylinder is separated into two parts $S = S_l + S_e$, where S_l is the lateral wall and S_e the endwalls, we have

$$\mu_l = \int_{S_l} p_i \sin(k_i z)\, \widetilde{\boldsymbol{v}}_3 \cdot \boldsymbol{n}\, \mathrm{d}^2 S = -\pi\,[h - \sin(k_i h)/k_i)]\, \alpha_i J_1^2(\delta_i), \tag{D 23a}$$

$$\mu_e = \int_{S_e} p_i \sin(k_i z)\, \widetilde{\boldsymbol{v}}_3 \cdot \boldsymbol{n}\, \mathrm{d}^2 S = -2\pi\beta_i \frac{(\delta_i^2 - 1)\omega^2 + 4}{\delta_i^2 \omega^2} J_1^2(\delta_i) \sin^2\left(\frac{k_i h}{2}\right), \tag{D 23b}$$

where we have used the formulation of $\widetilde{\boldsymbol{v}}_3 \cdot \boldsymbol{n}$ found in (D 9) and (D 18). Now using the relation (4.15) the viscous coefficient μ in (4.14) is simply

$$\mu = -\frac{\mu_l + \mu_e}{N}, \tag{D 24}$$

where N is given by (C 3).

For the geostrophic flow, we obtain by integrating by parts

$$\mu_0 = \int_{S_e} p_0^j\, \widetilde{\boldsymbol{v}}_4^j \cdot \boldsymbol{n}\, \mathrm{d}^2 S = -4\pi \int_0^1 {v_0^j}^2 r\, \mathrm{d}r, \tag{D 25}$$

where we have used $\widetilde{\boldsymbol{v}}_4^j \cdot \boldsymbol{n}$ as given by (D 22) and

$$N_0 = \boldsymbol{v}_0^j \odot \mathscr{I}\, \boldsymbol{v}_0^j = 2\pi h \int_0^1 {v_0^j}^2 r\, \mathrm{d}r, \tag{D 26}$$

which leads to a surface viscous coefficient $\mu_0/N_0 = -2/h$ which appears in the amplitude equation (4.17).

The volume viscous coefficient ν is simply

$$\nu = \frac{-\boldsymbol{v}_i \odot \mathscr{L}\, \boldsymbol{v}_i}{\boldsymbol{v}_i \odot \mathscr{I}\, \boldsymbol{v}_i} = \left(k_i^2 + \delta_i^2\right). \tag{D 27}$$

Some useful numerical values of the viscous coefficients μ and ν obtained through (D 24) and (D 27) are given in tables 1 and 2.

Appendix E. Nonlinear viscous boundary layers

To calculate the forcing of the geostrophic flow by the Kelvin mode, we need to perform a weakly nonlinear analysis in the endwall boundary layer. We choose to focus on the upper-wall boundary layer $z = h/2$ (the calculation is symmetric for the bottom wall) using the rescaled vertical coordinate $\widetilde{z}$ as defined by (D 11). Taking into account the nonlinear effects and considering only the forcing of geostrophic modes of angular frequency $\omega = 0$, the Navier–Stokes equation is

$$\left(-Re^{1/2}\,\frac{\partial}{\partial \widetilde{z}}\mathscr{R}_u + \mathscr{M}_u - \frac{\partial^2}{\partial \widetilde{z}^2}\mathscr{I}\right)\widetilde{\boldsymbol{V}} = \boldsymbol{N}_u(\widetilde{\boldsymbol{V}}, \widetilde{\boldsymbol{V}}) + \boldsymbol{N}_u(\boldsymbol{V}, \widetilde{\boldsymbol{V}}) + \boldsymbol{N}_u(\widetilde{\boldsymbol{V}}, \boldsymbol{V}) + \text{o.t.}, \tag{E 1}$$

where the operators $\mathscr{R}_u$ and $\mathscr{M}_u$ are defined in (D 13) and $\boldsymbol{N}_u$ is similar to the bilinear function $\boldsymbol{N}$ defined in (C 3) but adapted to the rescaled variable $\widetilde{z}$.

We now need to evaluate the right-hand side of (E 1) at order $\varepsilon^{2/3}$, focusing on the geostrophic component (independent of t and ϕ). This leads to

$$\boldsymbol{N}_u(\widetilde{\boldsymbol{V}}, \widetilde{\boldsymbol{V}}) = \varepsilon^{2/3}|A|^2 \begin{pmatrix} \gamma_1(r, \widetilde{z}) \\ \kappa_1(r, \widetilde{z}) \\ 0 \\ 0 \end{pmatrix} + \text{o.t.} + O(\varepsilon), \tag{E 2}$$

where

$$\gamma_1 = \overline{\widetilde{v}}_i \left(\frac{\widetilde{v}_i}{r} - \frac{\mathrm{i}}{r}\widetilde{u}_i\right) - \overline{\widetilde{u}}_i \frac{\partial \widetilde{u}_i}{\partial r} - \overline{\widetilde{w}}_3 \frac{\partial \widetilde{u}_i}{\partial \widetilde{z}}, \tag{E 3a}$$

$$\kappa_1 = \overline{\widetilde{u}}_i \left(\frac{\widetilde{v}_i}{r} - \frac{\partial \widetilde{v}_i}{\partial r}\right) - \overline{\widetilde{v}}_i \frac{\mathrm{i}\widetilde{v}_i}{r} - \overline{\widetilde{w}}_3 \frac{\partial \widetilde{v}_i}{\partial \widetilde{z}}, \tag{E 3b}$$

where $\widetilde{u}_i$ and $\widetilde{v}_i$ are given by (D 14 a, b) and $\widetilde{w}_3$ is given by (D 17). The other two terms are

$$\boldsymbol{N}_u(\boldsymbol{V}, \widetilde{\boldsymbol{V}}) = \varepsilon^{2/3}|A|^2 \begin{pmatrix} \gamma_2(r, \widetilde{z}) \\ \kappa_2(r, \widetilde{z}) \\ 0 \\ 0 \end{pmatrix} + \text{o.t.} + O(\varepsilon), \tag{E 4a}$$

$$\boldsymbol{N}_u(\widetilde{\boldsymbol{V}}, \boldsymbol{V}) = \varepsilon^{2/3}|A|^2 \begin{pmatrix} \gamma_3(r, \widetilde{z}) \\ \kappa_3(r, \widetilde{z}) \\ 0 \\ 0 \end{pmatrix} + \text{o.t.} + O(\varepsilon), \tag{E 4b}$$

where

$$\gamma_2 = \sin\frac{k_i h}{2}\left[v_i\left(-\frac{\mathrm{i}}{r}\widetilde{u}_i + \frac{\widetilde{v}_i}{r}\right) + u_i\frac{\partial\widetilde{u}_i}{\partial r} - \overline{w}_3\frac{\partial\widetilde{u}_i}{\partial\widetilde{z}} - k_i\widetilde{z}\,\overline{w}_i\frac{\partial\widetilde{u}_i}{\partial\widetilde{z}}\right], \tag{E 5a}$$

$$\kappa_2 = \sin\frac{k_i h}{2}\left[u_i\left(\frac{\widetilde{v}_i}{r} + \frac{\partial\widetilde{v}_i}{\partial r}\right) - \frac{\mathrm{i}}{r}v_i\widetilde{v}_i - \overline{w}_3\frac{\partial\widetilde{v}_i}{\partial\widetilde{z}} - k_i\widetilde{z}\,\overline{w}_i\frac{\partial\widetilde{v}_i}{\partial\widetilde{z}}\right], \tag{E 5b}$$

$$\gamma_3 = \sin\frac{k_i h}{2}\left[\widetilde{v}_i\left(-\frac{\mathrm{i}}{r}u_i + \frac{v_i}{r}\right) + \widetilde{u}_i\frac{\partial u_i}{\partial r}\right], \tag{E 5c}$$

$$\kappa_3 = \sin\frac{k_i h}{2}\left[-\widetilde{u}_i\left(\frac{v_i}{r} + \frac{\partial v_i}{\partial r}\right) + \frac{\mathrm{i}}{r}v_i\widetilde{v}_i\right], \tag{E 5d}$$

where $w_3 = -\widetilde{w}_3(\widetilde{z}=0)$.

The solution of (E 1) forced by the right-hand side is sought at order $\varepsilon^{2/3}$ of the form

$$\widetilde{\boldsymbol{V}} = \varepsilon^{2/3}|A|^2\left(\widetilde{\boldsymbol{v}}_2^{\mathrm{NL}} + Re^{-1/2}\,\widetilde{\boldsymbol{v}}_4^{\mathrm{NL}}\right). \tag{E 6}$$

Examinion of (E 1) at order $\varepsilon^{2/3}Re^{1/2}$ leads to $\widetilde{w}_2^{\mathrm{NL}} = \widetilde{p}_2^{\mathrm{NL}} = 0$. At order $\varepsilon^{2/3}$, it leads to

$$\left(\frac{\partial^4}{\partial\widetilde{z}^4} + 4\right)\widetilde{u}_2^{\mathrm{NL}} = 2(\kappa_1+\kappa_2+\kappa_3) - \frac{\partial^2}{\partial\widetilde{z}^2}(\gamma_1+\gamma_2+\gamma_3), \tag{E 7a}$$

$$\widetilde{v}_2^{\mathrm{NL}} = -\frac{1}{2}\left(\gamma_1+\gamma_2+\gamma_3 + \frac{\partial^2\widetilde{u}_2^{\mathrm{NL}}}{\partial\widetilde{z}^2}\right). \tag{E 7b}$$

The solution of the above system is a sum of the particular solution of (E 7 *a*) and the solution of the homogeneous system of the form $\widetilde{u}_2^{\mathrm{NL}} = a_1\exp(-1+\mathrm{i})\widetilde{z} + a_2\exp(-1-\mathrm{i})\widetilde{z}$. The particular solution is found with a symbolic calculation software where the coefficients a_1 and a_2 are adjusted to satisfy the boundary conditions $\widetilde{u}_2^{\mathrm{NL}} = \widetilde{v}_2^{\mathrm{NL}} = 0$ in $\widetilde{z}=0$ (the boundary condition of vanishing $\widetilde{\boldsymbol{v}}_2^{\mathrm{NL}}$ for $\widetilde{z}\gg 1$ is ensured by the selection of the vanishing exponential in the particular solution).

Taking (E 1) at order $\varepsilon^{2/3}$ also gives the form of the flow orthogonal to the wall at order $\varepsilon^{2/3}Re^{-1/2}$ which satisfies

$$\frac{\partial}{\partial\widetilde{z}}\widetilde{w}_4^{\mathrm{NL}} = -\left(\frac{1}{r} + \frac{\partial}{\partial r}\right)\widetilde{u}_2^{\mathrm{NL}}. \tag{E 8}$$

Once this is integrated, the normal flow is $\widetilde{\boldsymbol{v}}_4^{\mathrm{NL}}\cdot\boldsymbol{n} = \widetilde{w}_4^{\mathrm{NL}}(\widetilde{z}=0)$. The coefficients χ_j needed for the amplitude equation (4.17) can now be obtained as

$$\chi_j = \frac{4\pi}{N_0}\int_0^1 p_0^j\left(\widetilde{\boldsymbol{v}}_4^{\mathrm{NL}}\cdot\boldsymbol{n} - \widetilde{w}_4^{\mathrm{SB}}\right)r\,\mathrm{d}r + \mathrm{c.c.}, \tag{E 9}$$

where N_0 is given by (D 26), and

$$\widetilde{w}_4^{\mathrm{SB}} = \int_0^1 \widetilde{\boldsymbol{v}}_4^{\mathrm{NL}}\cdot\boldsymbol{n}\,r\,\mathrm{d}r + \mathrm{c.c.}, \tag{E 10}$$

corresponds to the flow associated with a modification of the solid-body rotation frequency.

REFERENCES

Agrawal, B. N. 1993 Dynamics characteristics of liquid motion in partially filled tanks of a spinning spacecraft. *J. Guid. Control Dyn.* **16**, 636–640.

Bao, G. W. & Pascal, M. 1997 Stability of a spinning liquid filled spacecraft. *Arch. Appl. Mech.* **67**, 407–421.

Eloy, C., Le Gal, P. & Le Dizès, S. 2000 Experimental study of the multipolar vortex instability. *Phys. Rev. Lett.* **85**, 3400–3403.

Eloy, C., Le Gal, P. & Le Dizès, S. 2003 Elliptic and triangular instabilities in rotating cylinders. *J. Fluid Mech.* **476**, 357–388.

Fabre, D., Sipp, D. & Jacquin, L. 2006 Kelvin waves and the singular modes of the Lamb–Oseen vortex. *J. Fluid Mech.* **551**, 235–274.

Fultz, D. 1959 A note on overstability and elastoid-inertia oscillations of Kelvin, Solberg and Bjerknes. *J. Met.* **16**, 199–208.

Gans, R. F. 1970 On the precession of a resonant cylinder. *J. Fluid Mech.* **476**, 865–872.

Gans, R. F. 1984 Dynamics of a near-resonant fluid-filled gyroscope. *AIAA J.* **22**, 1465–1471.

Garg, S. C., Furunoto, N. & Vanyo, J. P. 1986 Spacecraft nutational instability prediction by energy dissipation measurments. *J. Guid. Control Dyn.* **9**, 357–361.

Goto, S., Ishii, N., Kida, S. & Nishioka, M. 2007 Turbulence generator using a precessing sphere. *Phys. Fluids* **19**, 061705.

Greenspan, H. P. 1968 *The Theory of Rotating Fluids*. Cambridge University Press.

Greenspan, H. P. 1969 On the non-linear interaction of inertial modes. *J. Fluid Mech.* **36**, 257–264.

Kelvin, Lord 1880 Vibrations of a columnar vortex. *Phil. Mag.* **10**, 155–168.

Kerswell, R. R. 1999 Secondary instabilities in rapidly rotating fluids: inertial wave breakdown. *J. Fluid Mech.* **382**, 283–306.

Kerswell, R. R. 2002 Elliptical instability. *Annu. Rev. Fluid Mech.* **34**, 83–113.

Kerswell, R. R. & Barenghi, C. F. 1995 On the viscous decay rates of inertial waves in a rotating cylinder. *J. Fluid Mech.* **285**, 203–214.

Kobine, J. J. 1995 Inertial wave dynamics in a rotating and precessing cylinder. *J. Fluid Mech.* **303**, 233–252.

Kobine, J. J. 1996 Azimuthal flow associated with inertial wave resonance in a precessing cylinder. *J. Fluid Mech.* **319**, 387–406.

Kudlick, M. 1966 On the transient motions in a contained rotating fluid. PhD thesis, Massachussets Institute of Technology.

Lorenzani, S. & Tilgner, A. 2001 Fluid instabilities in precessing spheroidal cavities. *J. Fluid Mech.* **447**, 111–128.

Mahalov, A. 1993 The instability of rotating fluid columns subjected to a weak external coriolis-force. *Phys. Fluids* A **5**, 891–900.

Malkus, W. V. R. 1989 An experimental study of global instabilities due to tidal (elliptical) distortion of a rotating elastic cylinder. *Geophys. Astrophys. Fluid Dyn.* **48**, 123–134.

Manasseh, R. 1992 Breakdown regimes of inertia waves in a precessing cylinder. *J. Fluid Mech.* **243**, 261–296.

Mason, D. M. & Kerswell, R. R. 1999 Nonlinear evolution of the elliptical instability: an example of inertial breakdown. *J. Fluid Mech.* **396**, 73–108.

McEwan, A. D. 1970 Inertial oscillations in a rotating fluid cylinder. *J. Fluid Mech.* **40**, 603–640.

Meunier, P. & Leweke, T. 2003 Analysis and minimization of errors due to high gradients in particule image velocimetry. *Exps. Fluids* **35**, 408–421.

Noir, J., Jault, D. & Cardin, P. 2001 Numerical study of the motions within a slowly precessing sphere at low Ekman number. *J. Fluid Mech.* **437**, 283–29.

Poincaré, H. 1910 Sur la précession des corps déformables. *Bull. Astron.* **27**, 257–264.

Racz, J.-P. & Scott, J. F. 2007 Parametric instability in a rotating cylinder of gas subject to sinusoidal axial compression. Part 2. Weakly nonlinear theory. *J. Fluid Mech.* **595**, 291–321.

Sipp, D. 2000 Weakly nonlinear saturation of short-wave instabilities in a strained Lamb-Oseen vortex. *Phys. Fluids* **12**, 1715–1729.

Stewartson, K. 1958 On the stability of a spinning top containing liquid. *J. Fluid Mech.* **5**, 577–592.

Thompson, R. 1970 Diurnal tides and shear instabilities in a rotating cylinder. *J. Fluid Mech.* **40**, 737–751.

Vanyo, J. P. 1993 *Rotating Fluids in Engineering and Science*. Dover.

Waleffe, F. 1989 The 3d instability of a strained vortex and its relation to turbulence. PhD thesis, Massachusetts Institute of Technology.

Wood, W. W. 1965 Properties of inviscid, recirculating flows. *J. Fluid Mech.* **22**, 337–346.

Instability of a fluid inside a precessing cylinder

Romain Lagrange,[1,a)] Christophe Eloy,[1] François Nadal,[2] and Patrice Meunier[1]
[1]*IRPHE, CNRS, and Aix-Marseille Université, 49 rue Joliot-Curie, 13013 Marseille, France*
[2]*Commissariat à l'Énergie Atomique, CESTA, 33114 Le Barp, France*

(Received 4 April 2008; accepted 6 July 2008; published online 12 August 2008)

In this letter, we report experimental results on the stability of a fluid inside a precessing and resonant cylinder. Above a critical Reynolds number, the Kelvin mode forced by precession triggers an instability which saturates at intermediate Re and which leads to a turbulent flow at high Reynolds numbers. Particle image velocimetry measurements in two different sections of the cylinder have revealed the three-dimensional structure of this instability. It is composed of two free Kelvin modes whose wavenumbers and frequencies respect the conditions for a triadic resonance with the forced Kelvin mode, as is obtained for the elliptical instability. Moreover, an experimental diagram of stability has been established by varying both the precessing angle and the Reynolds number. It shows a good agreement with a scaling analysis based on a triadic resonance mechanism. © *2008 American Institute of Physics*. [DOI: 10.1063/1.2963969]

The knowledge of the flow forced by a precessional motion is of critical importance in several domains. In aeronautics, the liquid propellant contained in a flying object can be forced by precession. The resulting flow can create a destabilizing torque on the object and thus modify its trajectory dangerously. In geophysics the Earth's precession modifies the flow of its liquid core and is therefore of significant importance in understanding the geodynamo (among other effects such as convection, boundary layers, and elliptic or tidal instability[1]). The flow inside a cylinder subjected to precession can be decomposed as a sum of a shear along the cylinder axis and a superposition of Kelvin modes which become resonant for particular precession frequencies. McEwan[2] first observed that this flow can become unstable and even turbulent for large Reynolds numbers. This behavior has also been reported by Manasseh,[3–5] and Kobine.[6] Several scenarios have been proposed to explain this instability. Studying the case of an infinite cylinder, Mahalov[7] proposed a mechanism of triadic resonance between the flow shear and two Kelvin modes. Kerswell[8] suggested that a given Kelvin mode can trigger a triadic resonance with two other Kelvin modes leading to an instability. Another scenario, suggested by Kobine,[6,9] is that the main flow could be modified by a geostrophic mode (due to nonlinear effects) eventually leading to a centrifugal instability.

An experimental setup has been built to study the precession of a cylinder of height H along its axis $\hat{\mathbf{z}}$ and radius R, full of water of kinematic viscosity ν. More details about the setup can be found in Ref. 10. The cylinder rotates at the angular frequency Ω_1 (measured with an accuracy of 0.1%) around its axis. It is mounted on a platform which rotates at the angular frequency Ω_2 (measured with an accuracy of 0.2%). Once the spin-up stage is completed, the cylinder is tilted with an angle α (determined with an absolute accuracy of $\pm 0.1°$) with respect to the rotation axis of the platform. Particle image velocimetry (PIV) measurements in transverse sections of the cylinder are made. To perform the acquisition of a PIV field, we use small markers illuminated with a thin light sheet created by a yttrium aluminum garnet (YAG) pulsed laser. The particle images are recorded by a camera mounted on the rotating platform. The horizontal velocity and the axial vorticity fields in the cylinder frame of reference are thus measured. More details about PIV treatment can be found in Ref. 11.

In the following, variables are made dimensionless by using R and $\Omega=\Omega_1+\Omega_2\cos\alpha$ as characteristic length and characteristic frequency. The dynamics of this precessing system depends on four dimensionless numbers: the aspect ratio $h=H/R$, the frequency ratio $\omega=\Omega_1/\Omega$, the Rossby number $\mathrm{Ro}=\Omega_2\sin\alpha/\Omega$, and the Reynolds number $\mathrm{Re}=\Omega R^2/\nu$. The cylindrical coordinates are used in the reference frame of the cylinder and noted (r,θ,z), where $z=0$ corresponds to the midheight section of the cylinder.

Figure 1 shows the axial and instantaneous flow vorticity for a small precessing angle ($\alpha=1°$) and different Reynolds numbers. The laser sheet is at an altitude $z\simeq h/4$. For $\mathrm{Re}=3500$ [Fig. 1(a)], the flow mainly consists of two stationary counter-rotating vortices. A classical linear and inviscid theory is sufficient to explain this observation. By assuming a small Rossby number (weak precession, negligible nonlinear effects) and a large Reynolds number (negligible viscous effects), the linearized Euler equation at order $O(\mathrm{Ro})$ is

$$\frac{\partial \mathbf{v}}{\partial t}+2\hat{\mathbf{z}}\times\mathbf{v}+\nabla p=-2\mathrm{Ro}\,\omega r\cos(\omega t+\theta)\hat{\mathbf{z}}, \tag{1}$$

where $2\hat{\mathbf{z}}\times\mathbf{v}$ is the dimensionless Coriolis force and p the dimensionless pressure including all potential terms. The right-hand side of Eq. (1) is the precession forcing which forces a particular solution of Eq. (1): $\mathbf{v}_{\mathrm{part}}=-2\mathrm{Ro}\,r\sin(\omega t+\theta)\hat{\mathbf{z}}$. This solution does not satisfy the boundary conditions of no outward flow at $z=\pm h/2$. Thus, we must complete this solution with a solution of the homogeneous equation [Eq. (1) without forcing], so that the boundary condition at the

a)Electronic mail: lagrange@irphe.univ-mrs.fr.

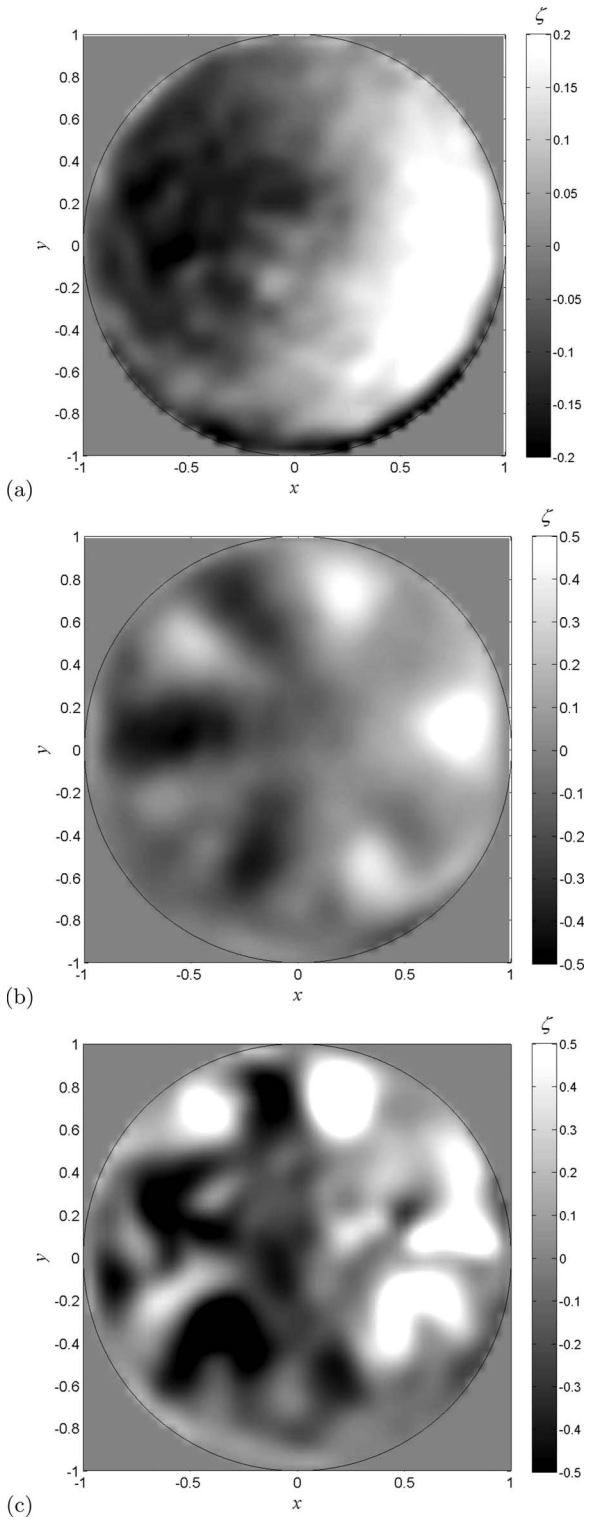

FIG. 1. Axial vorticity ζ of the flow for different Reynolds numbers at $z=h/4$. (a) For Re=3500 the stable flow exhibits the forced Kelvin mode. (b) For Re=6000 the flow is unstable and exhibits a free Kelvin mode with $m_1=5$ superimposed to the forced Kelvin mode. The temporal evolution of the instability can be observed in the corresponding movie. (c) For Re=24 400 the flow is turbulent. For these three cases $h=1.62$, $\omega=1.18$, and Ro=0.0031 (enhanced online).

upper and lower walls is satisfied. Due to time and azimuthal dependence of the forcing, the homogeneous solution is a sum of Kelvin modes of azimuthal wavenumber $m=1$ and angular frequency ω. Finally the solution of Eq. (1) is

$$\mathbf{v} = \mathbf{v}_{\text{part}} + \sum_{i=1}^{\infty} a_i \mathbf{v}_i(m=1,\omega,k_i), \tag{2}$$

where $\mathbf{v}_i(m,\omega,k_i)$ is a Kelvin mode of amplitude a_i and whose axial wavenumber k_i depends on ω by the dispersion relation,

$$\omega k_i \sqrt{4/\omega^2 - 1} J_m'(k_i \sqrt{4/\omega^2 - 1}) + 2J_m(k_i \sqrt{4/\omega^2 - 1}) = 0, \tag{3}$$

where J_m is the Bessel function of the first kind and J_m' its derivative. The axial vorticity ζ_i of the ith Kelvin mode is

$$\zeta_i = J_m(k_i \sqrt{4/\omega^2 - 1}\, r)\sin(k_i z)\cos(\omega t + m\theta). \tag{4}$$

When k_i is equal to $(2n+1)\pi/h$, with n an integer number, the ith Kelvin mode "fits" inside the height of the cylinder and becomes resonant. In our experiments (i.e., for $h=1.62$ and $\omega=1.18$) the first Kelvin mode (which is theoretically characterized by two lobes of vorticity) is resonant (its axial wavenumber, noted k, is equal to π/h). Because the amplitude a_1 is predicted to diverge by a linear analysis it is necessary to include viscous[12] and nonlinear effects. We have shown in Ref. 10 that a_1 scales as $\text{RoRe}^{1/2}$ for low Reynolds numbers (viscous regime, $\text{Re}^{1/2}\text{Ro}^{2/3} \ll 1$) and as $\text{Ro}^{1/3}$ for large Reynolds numbers (nonlinear regime, $\text{Re}^{1/2}\text{Ro}^{2/3} \gg 1$). Since the nonresonant mode amplitudes scale as Ro, the resonant mode is always predominant.

Figure 1(b) is a PIV measurement of the axial and instantaneous vorticity field for Re=6500. For such a value of Re the flow seen in Fig. 1 is unstable and the unstable mode exhibits a ring with ten lobes of vorticity with alternate sign. It corresponds to a free Kelvin mode [i.e., a solution of Eq. (1) without forcing] whose azimuthal wavenumber, noted m_1, equals 5. This mode $m_1=5$ is superimposed to the forced Kelvin mode $m=1$ shown in Fig. 1(a). [As seen on Fig. 1(b) the average vorticity is negative for $x<0$ and positive for $x>0$]. Such a flow, which is three-dimensional and nonstationary, corresponds to the instability discovered by McEwan[2] and studied by Manasseh[3] using visualizations, which was called "resonant collapse" since it decreases the amplitude of the forced Kelvin mode. Indeed, the same structure has been observed for other aspect ratios ($h=1.8$ and $h=2$) and it also leads to the decrease of the forced Kelvin mode's amplitude. The visualization of a sequence of instantaneous PIV fields shows that the free Kelvin mode rotates as a function of time at a dimensionless frequency $\omega_1=-0.34\pm11\%$ in the cylinder frame of reference. For this Reynolds number, the unstable mode beats probably due to a nonlinear coupling with the geostrophic mode. However, the amplitude of this unstable mode is stationary close to the threshold (i.e., $\text{Re}\simeq4600$).

Figure 1(c) represents the axial and instantaneous vorticity field for even larger Reynolds numbers (Re=24 400). For such a value of Re the flow is disordered and seems to be turbulent. As suggested by Kerswell,[8] this disordered flow could be the result of successive instabilities: a cascade of bifurcations could lead to a turbulent state. It can be noted

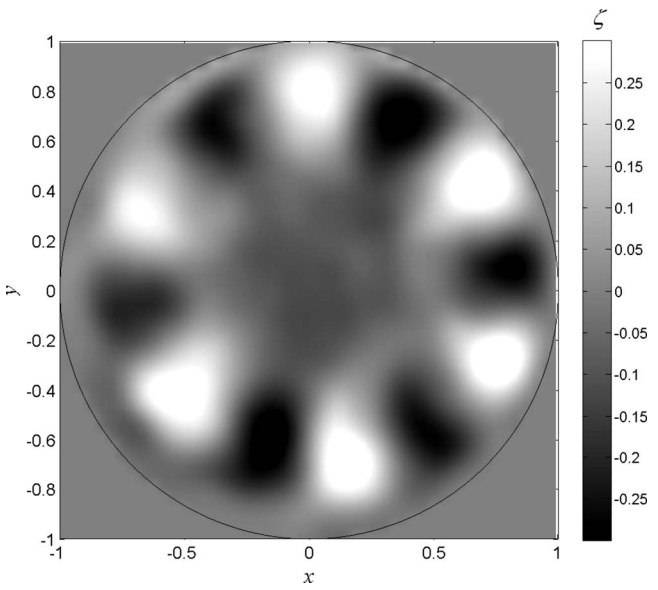

FIG. 2. Vorticity field of the unstable flow at midheight of the cylinder for the same parameters as in Fig. 1(b) ($h=1.62$, $\omega=1.18$, Ro=0.0031, and Re=6500).

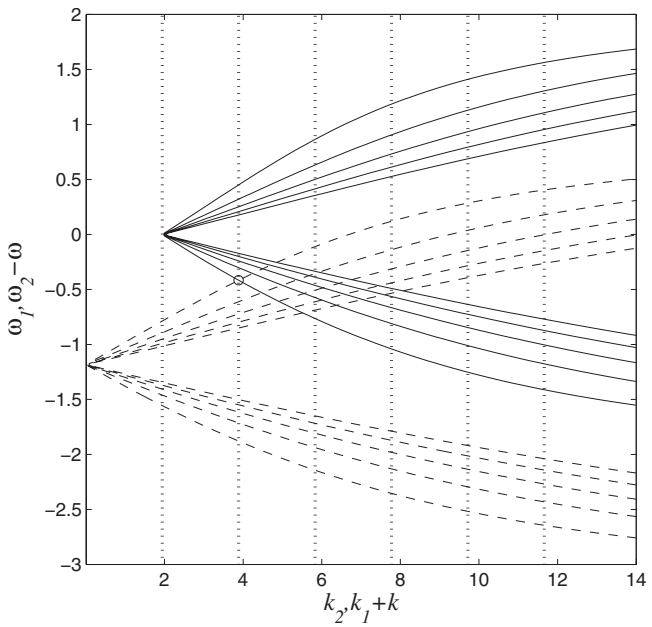

FIG. 3. Dispersion relations of the Kelvin modes. The solid lines (resp. dashed lines) correspond to the first five branches of the Kelvin modes with azimuthal wavenumber $m_1=5$ (resp. $m_2=6$). The solid lines have been translated by $k=\pi/h$ and the dashed lines have been translated by $\omega=1.18$. The vertical dotted lines correspond to $k=n\pi/h$, with n an integer, ($h=1.62$, $\omega=1.18$).

that the Kelvin mode $m=1$ forced by precession is still present since the average vorticity is still negative for $x<0$ and positive for $x>0$.

Figure 2 is a PIV measurement of the axial and instantaneous vorticity field measured in a section of the cylinder lower than in Fig. 1. The laser sheet is at midheight of the cylinder ($z=0$). According to Eq. (4) the vorticity of the forced Kelvin mode $m=1$ and of the free Kelvin mode $m_1=5$ is equal to 0. At this altitude a structure with 12 lobes of alternate vorticity is clearly observed. It corresponds to a free Kelvin mode whose azimuthal wavenumber, noted m_2, is equal to 6. Because it does not vanish at $z=0$ its axial vorticity is given by Eq. (4), where $\sin(k_2 z)$ has been changed in $\cos(k_2 z)$. This free Kelvin mode rotates at a dimensionless angular frequency $\omega_2=0.79\pm2.5\%$ in the cylinder frame of reference.

The axial velocity [which is in quadrature with respect to the axial vorticity given by Eq. (4)] of the free Kelvin mode $m_1=5$ (resp. $m_2=6$) is a cosine (sine) function of z. Boundary conditions of no outward flow at $z=\pm h/2$ imply that the axial wavenumber of the free Kelvin mode $m_1=5$ (resp. $m_2=6$) is discretized as follows: $k_1=(2n_1+1)\pi/h$ (resp. $k_2=2n_2\pi/h$), n_1 (resp. n_2) being an integer.

Furthermore, Figs. 1(b) and 2 show that the unstable Kelvin modes correspond to the first branch of the dispersion relation since there is only one ring of vortices. We can thus infer that $k_1=\pi/h$ (resp. $k_2=2\pi/h$) since the point ($k_1=\pi/h$, $\omega_1\approx-0.34$) (resp. $k_2=2\pi/h$, $\omega_1\approx0.79$) then falls very close to the first branch of the dispersion relation (3) for $m_1=5$ (resp. $m_2=6$) (Fig. 3).

These experiments have allowed to determine the structure of the instability of a fluid inside a precessing and resonant cylinder. We have found that the unstable flow is the sum of three Kelvin modes: the forced one and two free modes. The azimuthal wavenumber and the angular frequency of these free modes have been measured and satisfy the conditions for a triadic resonance with the forced Kelvin mode,

$$m_2 - m_1 = 1, \quad \omega_2 - \omega_1 \approx \omega, \quad k_2 - k_1 = k, \tag{5}$$

where $k=\pi/h$ is the axial wavenumber of the forced Kelvin mode. This suggests that the nonlinear coupling of the three Kelvin modes can trigger an instability, in a similar way as for the elliptical instability.[13,14]

The resonant condition given in Eq. (5) corresponds to the crossing points of the dashed and solid lines in Fig. 3, where the two dispersion relations are plotted in the same plane; the dispersion relation with $m_1=5$ (resp. $m_2=6$) being horizontally (vertically) translated of k (resp. translated of $-\omega$). It can be noted that there is an infinite and denumerable number of possible resonances. However, the free Kelvin modes observed experimentally correspond to the crossing point surrounded by a circle on Fig. 3. These modes satisfy exactly the boundary conditions at $z=\pm h/2$ (i.e., the crossing point lies on a vertical dotted line in Fig. 3). This exact resonance is only valid for $h=1.62$. For $h\approx1.62$ "detuning" effects shall come into play and thus decrease the instability growth rate.

For $h\simeq1.62$ two free Kelvin modes involving different branches of the dispersion relations or different azimuthal wavenumbers m_1 and m_2 can exactly resonate with the forced Kelvin mode. Nevertheless, it can be shown that there cannot be exact resonances for $m_1\leqslant4$ for the first branches of the dispersion relations. Thus, the aspect ratio $h=1.62$ corresponds to the exact resonance of the Kelvin modes with the smallest wavenumbers. Since the volume viscous effects increase with the wavenumbers of the free Kelvin modes, $h=1.62$ is expected to be the aspect ratio for which the flow

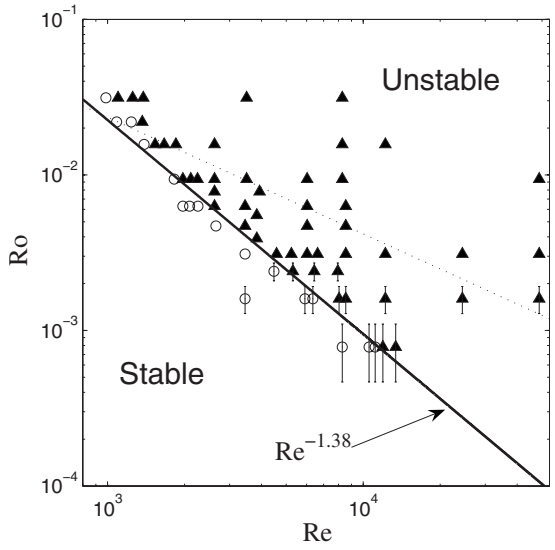

FIG. 4. Stability diagram of the flow inside a precessing cylinder for ($h=1.62$, $\omega=1.18$). The circles represent stable experiments. The black triangles represent unstable experiments. The solid line is an experimental fit of the threshold. The dashed line separates the viscous and the nonlinear domains of the base flow.

is the most unstable. However, the previous observations are very general and do not depend on the fact that the triadic resonance is exact or not. Indeed, experiments with an arbitrary aspect ratio ($h=1.8$) have shown exactly the same instability.

Finally we have plotted in Fig. 4 the stability diagram of this instability in the Re-Ro plane. The majority of the experiments close to threshold are in the viscous domain for the base flow. This means that the amplitude of the forced mode scales as $a_1 \sim \mathrm{RoRe}^{1/2}$.[10] Based on similarities with the elliptic instability, the inviscid growth rate σ of the present triadic instability is expected to scale as the amplitude of the forced Kelvin mode: $\sigma \sim a_1$. The natural decay rate of Kelvin modes is due both to the boundary viscous layers and volume viscous effects. The surface (volume) decay rate σ_{surf} (σ_{vol}) scales as $\sigma_{\mathrm{surf}} \sim -\mathrm{Re}^{-1/2}$ (resp. $\sigma_{\mathrm{vol}} \simeq -[m_1 + k_1^2(4/\omega^2 - 1)]\mathrm{Re}^{-1}$). In our experiments, $\sigma_{\mathrm{surf}} \simeq \sigma_{\mathrm{vol}}$ for $\mathrm{Re} \simeq 3000$. When the instability is saturated by volume (i.e., $\mathrm{Re} < 3000$) (resp. boundary, i.e., $\mathrm{Re} > 3000$), viscous effects, the amplitude of the forced Kelvin mode at which the flow becomes unstable satisfies $a_{1c} \sim \mathrm{Re}^{-1}$ (resp. $a_{1c} \sim \mathrm{Re}^{-1/2}$). Thus the Rossby number at which the flow becomes unstable scales as $\mathrm{Ro}_c \sim \mathrm{Re}^{-3/2}$ (resp. $\mathrm{Ro}_c \sim \mathrm{Re}^{-1}$). A "fit" of the experimental threshold gives $\mathrm{Ro}_c \sim \mathrm{Re}^{-1.38}$ (solid line), which is coherent with the theoretical scalings.

In this letter we studied experimentally the flow inside a precessing and resonant cylinder. At a given Rossby number the flow is stable for small enough Reynolds numbers and exhibits a Kelvin mode forced by the precessional motion. Increasing the Reynolds number above a critical value the flow becomes unstable (and even turbulent for high Re). Measurements in two different cylinder sections have revealed the presence of two Kelvin modes with high azimuthal wavenumbers. Their frequencies and their wavenumbers satisfy the conditions for a triadic resonance with the forced Kelvin mode. Thus, this letter has confirmed the scenario suggested by Kerswell[8] that a Kelvin mode can be destabilized by a triadic resonance mechanism. So, the precessional instability is very general since it appears as soon as a Kelvin wave has been excited (through precession, compression, in the nonlinear stages of the elliptical instability, or in the turbulent flow of a rotating cylinder). A stability diagram has also been established and showed that the scaling of the critical Ro as a function of Re is coherent with standard scaling laws in triadic resonances.

A linear stability analysis based on a mechanism of triadic resonance between Kelvin modes is currently under progress and will be the subject of a foregoing paper.

This study has been carried out under CEA-CNRS Contract No. 012171.

[1] W. V. R. Malkus, "An experimental study of global instabilities due to tidal (elliptical) distortion of a rotating elastic cylinder," Geophys. Astrophys. Fluid Dyn. **48**, 123 (1989).
[2] A. D. McEwan, "Inertial oscillations in a rotating fluid cylinder," J. Fluid Mech. **40**, 603 (1970).
[3] R. Manasseh, "Breakdown regimes of inertia waves in a precessing cylinder," J. Fluid Mech. **243**, 261 (1992).
[4] R. Manasseh, "Distortions of inertia waves in a rotating fluid cylinder forced near its fundamental mode resonance," J. Fluid Mech. **265**, 345 (1994).
[5] R. Manasseh, "Nonlinear behaviour of contained inertia waves," J. Fluid Mech. **315**, 151 (1996).
[6] J. J. Kobine, "Azimuthal flow associated with inertial wave resonance in a precessing cylinder," J. Fluid Mech. **319**, 387 (1996).
[7] A. Mahalov, "The instability of rotating fluid columns subjected to a weak external Coriolis force," Phys. Fluids A **5**, 891 (1993).
[8] R. R. Kerswell, "Secondary instabilities in rapidly rotating fluids: Inertial wave breakdown," J. Fluid Mech. **382**, 283 (1999).
[9] J. J. Kobine, "Inertial wave dynamics in a rotating and precessing cylinder," J. Fluid Mech. **303**, 233 (1995).
[10] P. Meunier, C. Eloy, R. Lagrange, and F. Nadal, "A rotating fluid cylinder subject to weak precession," J. Fluid Mech. **599**, 405 (2008).
[11] P. Meunier and T. Leweke, "Analysis and minimization of errors due to high gradients in particle image velocimetry," Exp. Fluids **35**, 408 (2003).
[12] R. F. Gans, "On the precession of a resonant cylinder," J. Fluid Mech. **41**, 865 (1970).
[13] C. Eloy, P. Le Gal, and S. Le Dizès, "Elliptic and triangular instabilities in rotating cylinders," J. Fluid Mech. **476**, 357 (2003).
[14] R. R. Kerswell, "Elliptical instability," Annu. Rev. Fluid Mech. **34**, 83 (2002).

Annexe 4

Articles sur le mélange d'un scalaire passif dans un écoulement

P. Meunier & E. Villermaux (2003). "How vortices mix", *J. Fluid Mech.* **476**, pp. 213-222.

P. Meunier & E. Villermaux (2007). "Van Hove singularities in Probability Density Functions of scalars", *C. R. Mecanique*, **335**, pp. 162-167.

P. Meunier & E. Villermaux (2009). "The Diffusive Strip Method as a tool for scalar mixing in two-dimensions.", *en prép. pour J. Fluid Mech.*.

How vortices mix

By P. Meunier and E. Villermaux

IRPHE, Université de Provence, Aix–Marseille 1
Technopôle de Château-Gombert
49, rue Frédéric Joliot-Curie 13384 Marseille Cedex 13, France

(Received 29 October 2002)

The advection of a passive scalar blob in the deformation field of an axisymmetric vortex is a simple mixing protocol for which the advection-diffusion problem is amenable to a near-exact description. The blob rolls-up in a spiral which ultimately fades away in the diluting medium. The complete transient concentration field in the spiral is accessible from the Fourier equations in a properly chosen frame. The concentration histogram of the scalar wrapped in the spiral presents unexpected singular transient features and its long time properties are discussed in connection with mixtures from the real world.

1. Introduction

A central question in scalar mixing consists in offering a satisfactory description of the histogram, or Probability Density Function (PDF) $P(c)$ of the concentration levels c of the substance being mixed. The question is particularly interesting, and relevant to many applications when the substrate is stirred since in that case molecular diffusion is altered, and in most cases enhanced, by the underlying substrate motions.

The interplay between molecular diffusion and simple deformation fields is a classical problem. It is solved in a closed form in a variety of situations such as the saddle point flow, the simple shear in two dimensions (Ranz(1979), Moffatt(1983)), in three dimensions (Villermaux & Rehab(2000)), and in the axisymmetric point vortex (Rhines & Young(1983), Flohr & Vassilicos(1997)) or spreading vortex flow (Marble(1988), Bajer et al. (2001)).

Most of the attention has focussed on the kinetics of the diffusion process in the presence of stirring motion, particularly its dependence on the substrate rate of deformation γ, and diffusion properties of the scalar (diffusivity D). Regarding the characteristic time t_s after which fluctuations start to decay from an initial scalar spatial distribution, of crucial importance is the rate at which material lines grow in time due to the substrate motions (Villermaux(2002)). If material lines grow like γt, as it is the case in a point vortex flow, the mixing time of, say, a scalar blob of initial size s_0 is $t_s \sim \gamma^{-1} Pe^{1/3}$; if material surfaces in three dimensions grow like $(\gamma t)^2$, then $t_s \sim \gamma^{-1} Pe^{1/5}$ and if material lines are exponentially stretched like $e^{\gamma t}$, then $t_s \sim (2\gamma)^{-1} \log Pe$ where $Pe = \gamma s_0^2/D$ is a Péclet number.

The times t_s given above are the relevant mixing times as soon as the inverse of the elongation rate γ^{-1} is smaller than the diffusive time of the blob constructed on its initial size s_0^2/D, that is for $Pe > 1$. In the limit $Pe \gg 1$, t_s is essentially given by the time needed to deform the blob γ^{-1} and molecular diffusion, although a crucial step in the ultimate uniformization, plays only a weak correction role in the kinetics of the process.

Experiments or numerical simulations addressing this problem quantitatively are scarce,

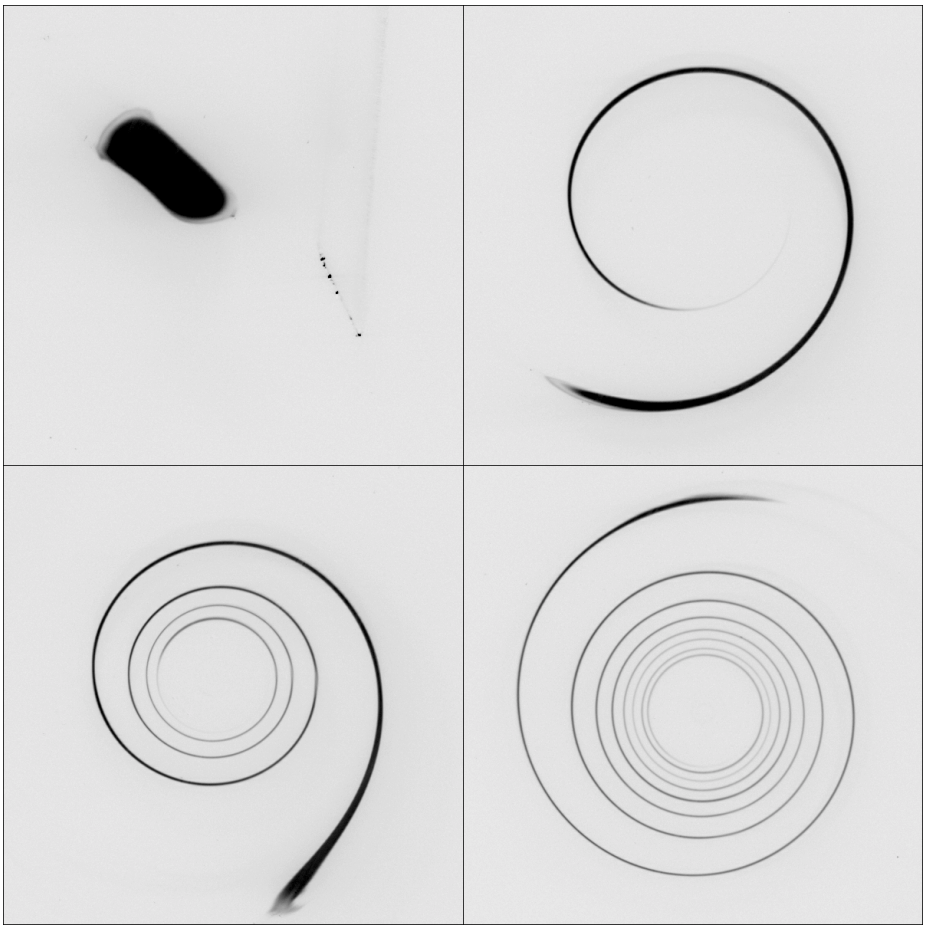

Figure 1. Roll-up of a blob of fluorescent dye in a point vortex at $t = 0$ (upper left), $t = 2$ sec (upper right), $t = 5$ sec (lower left) and $t = 10$ sec (lower right). Each picture covers a field 4.8×4.8 cm^2 wide and the circulation of the vortex is 14.2 cm^2/s. The data come from experiments described in section 2.

and are mostly limited to short times (i.e. $t \lesssim t_s$), therefore reflecting more the kinematics of the flow than its mixing properties (see, however Cetegen & Mohamad(1993) and Verzicco & Orlandi(1995)).

Based on a spatially and temporally resolved experiment, we study the mixing chronology of a blob of dye embedded in the displacement field of a diffusing, Lamb–Oseen type vortex. The process is described, from the initial segregation of the blob to a state where it is almost completely diluted in the surrounding medium, through the evolution of the spatial scalar field, and associated transient evolution of the overall concentration distribution $P(c)$.

2. A diffusive spiral

2.1. *Chronology*

The phenomenon we analyze is illustrated on Figure 1. A uniform blob of dye (the dark patch shown on Fig. 1(a))is deposed in a still transparent medium. Then a vortex is formed by the roll-up of a vortex sheet in the vicinity of the blob, which wraps around

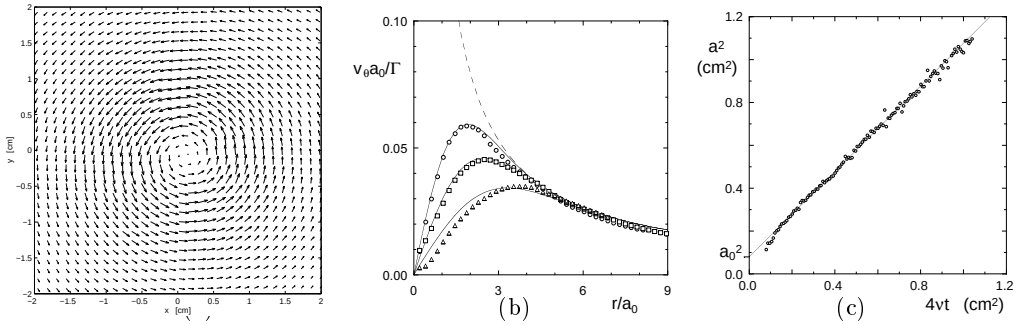

FIGURE 2. (a) Velocity field in the plane of the vortex at $t = 10$ sec. (b) Radial profiles of the azimuthal velocity measured at $t = 5$ sec ($\circ$), $t = 10$ sec ($\square$) and $t = 20$ sec ($\triangle$). Solid lines correspond to the profiles expected from a Lamb-Oseen vortex defined by (2.1) with $\Gamma = 14.2$ cm^2/s and $a_0 = 0.3$ cm. The dashed line corresponds to a point vortex defined by (3.1). (c) Core size of the Lamb-Oseen vortex measured by a least-square fit of the two-dimensional measured velocity field and compared to Eq. (2.2) (solid line).

the vortex as seen on Figure 1(b). Although it has been brought to a thin transverse size, most of the fluid particles constitutive of the blob still bear the initial concentration. The blob deforms in a spiral shape and after four turns (Fig. 1(c)), the dye concentration is no more uniform along the spiral: it is weaker near the center of the vortex where the spiral is very thin, and still close to the injection concentration in the outer region of the spiral which is thicker there. On Fig. 1(d), the spiral has made more than seven turns and is about to vanish in the diluting medium. The thickness of the spiral is fairly constant.

Molecular diffusion has clearly been enhanced by the vortex motion. The time lapse between figures 1(a) and 1(d) is 10 seconds, when the timescale of pure diffusion based on the initial size s_0 of the blob s_0^2/D is about 10^3 seconds.

2.2. *Flow field*

The vortex is formed by the impulsive flap motion of a long flat plate in a large tank of water initially at rest. The vorticity layer formed at the surface of the plate rolls-up and detaches at the plate end, producing an axisymmetric vortex which remains two-dimensional long after the dye has been mixed. A thin uniform Argon-Ion laser sheet is shed through the tank perpendicular to the plate, and the two-dimensional motion of the vortex is analyzed by Particle Image Velocimetry (PIV) using a Kodak 1008×1018 pixels digital camera aimed perpendicular to the laser sheet. Further information on the set-up and PIV techniques can be found in Meunier & Leweke(2002a) and Meunier & Leweke(2002b) respectively.

The dye is introduced, prior to the formation of the vortex, by a small tube positioned below the laser sheet, and forming a slowly ascending column of dye, aligned with the vortex axis. The dye concentration field (disodium Fluoresceine with initial concentration $c_0 \approx 10^{-3}$ mol/l) is recorded with the same camera and stored on a disk. The overall framing rate allows a complete roll-up sequence to be temporally resolved. The images are digitized on 8 bits and the resulting background subtracted grey levels are proportional to the dye concentration.

Figure 2(a) shows an example of the axisymmetric velocity field obtained by PIV after the vortex creation. The radial profiles of azimuthal velocity v_θ shown on Fig. 2(b) agree well with that of a Lamb-Oseen vortex, defined in the cylindrical coordinates $(r\,,\theta\,,z)$ by

$$v_\theta = \frac{\Gamma}{2\pi r}\left(1 - \mathrm{e}^{-r^2/a^2}\right) \tag{2.1}$$

Here, $\Gamma = 14.2\,\mathrm{cm}^2/\mathrm{s}$ is the circulation of the vortex, and a its core size. This vortex is an exact solution of the Navier-Stokes equations provided that

$$a^2 = a_0^2 + 4\nu t \tag{2.2}$$

where ν is the kinematic viscosity of the fluid, a law in close agreement with the observed growth (Fig. 2(c)), a_0 being the initial vortex radius equal to 0.3 cm.

The dashed line in Fig. 2(b) is the velocity profile of a point vortex with the same circulation, defined by (3.1). It is tangent to the measured velocity profiles for large radii ($r/a_0 > 3$).

Willing to decouple the problem of mixing from the (trivial) problem of the temporal evolution of the velocity field itself, we have systematically deposed the blob of dye far enough from the vortex core so that the velocity field remains that of a steady, point vortex, throughout the whole mixing process.

3. Concentration field along the spiral

We consider the evolution of a blob of dye of initial size s_0, in the two-dimensional, incompressible flow of a point vortex of circulation Γ (see Fig. 3a), whose azimuthal velocity is

$$v_\theta = \frac{\Gamma}{2\pi r} \tag{3.1}$$

We first describe the kinematics of the blob deformation. A fluid particle of the blob located at a distance r from the center of the vortex turns during time t by an angle θ

$$\theta(r,t) = \int_0^t \frac{v_\theta}{r}\,\mathrm{dt} = \frac{\Gamma t}{2\pi r^2} \tag{3.2}$$

A scalar strip of initial length dr, located at a distance r from the vortex center (Fig. 3(a)) is stretched so that its length equals at time t

$$\mathrm{dX} = \sqrt{\mathrm{d}r^2 + (r\mathrm{d}\theta)^2} = \mathrm{d}r\sqrt{1 + r^2\left(\frac{\mathrm{d}\theta}{\mathrm{d}r}\right)^2} = \mathrm{d}r\sqrt{1 + \frac{\Gamma^2 t^2}{\pi^2 r^4}} \tag{3.3}$$

Meanwhile, the transverse, or striation thickness $s(t)$ of the strip, in the absence of diffusion, decreases so that the surface $s(t)\mathrm{dX}$ remains constant in this two dimensional flow

$$s(t) = \frac{s_0\,\mathrm{dr}}{\mathrm{dX}} = \frac{s_0}{\sqrt{1 + \frac{\Gamma^2 t^2}{\pi^2 r^4}}} \tag{3.4}$$

We now describe the scalar dissipation of the blob. The displacement field results locally in a compression perpendicular to the strip, and in an extension along the strip. It is convenient to introduce a frame of reference (O, X, Y) whose X-axis is locally aligned

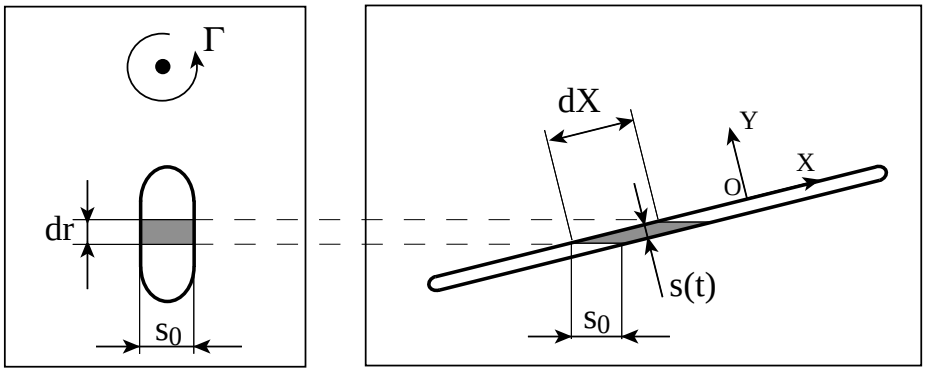

FIGURE 3. Schematic of the scalar blob elongation. (a) initial state and (b) at time t

with the spiral as shown on Fig. 3(b). In that frame, the velocity field is prescribed by the temporal evolution of the striation thickness $s(t)$ as

$$U = -\frac{X}{s}\frac{\mathrm{d}s}{\mathrm{d}t} \qquad \text{and} \qquad V = \frac{Y}{s}\frac{\mathrm{d}s}{\mathrm{d}t} \tag{3.5}$$

The evolution equation for the dye concentration c is the convection–diffusion equation in the (X, Y) coordinates

$$\frac{\partial c}{\partial t} + U\frac{\partial c}{\partial X} + V\frac{\partial c}{\partial Y} = D\left(\frac{\partial^2 c}{\partial X^2} + \frac{\partial^2 c}{\partial Y^2}\right) \tag{3.6}$$

The ratio of the two convective terms $V\partial c/\partial Y$ and $U\partial c/\partial X$ is in magnitude proportional to the strip aspect ratio $1 + (\Gamma^2 t^2)/(\pi^2 r^4)$: the concentration varies more slowly along the spiral than in its transverse direction for $\Gamma t/r^2 > 1$ so that Eq. (3.6) becomes

$$\frac{\partial c}{\partial t} + \frac{Y}{s}\frac{\mathrm{d}s}{\mathrm{d}t}\frac{\partial c}{\partial Y} = D\,\frac{\partial^2 c}{\partial Y^2} \tag{3.7}$$

A change of variables (see e.g. Ranz(1979), Marble(1988), Villermaux & Rehab(2000)) consisting in counting transverse distances in units of the striation thickness $s(t)$ and time in units of the current diffusion time $s(t)^2/D$ transforms Eq. (3.7) into a simple diffusion equation

$$\text{with} \quad \xi = \frac{Y}{s(t)} \quad \text{and} \quad \tau(r) = \int_0^t \frac{D\mathrm{d}t'}{s(t')^2} = \frac{Dt}{s_0^2} + \frac{D\Gamma^2 t^3}{3\pi^2 r^4 s_0^2} \quad \text{giving} \quad \frac{\partial c}{\partial \tau} = \frac{\partial^2 c}{\partial \xi^2} \tag{3.8}$$

If c_0 is the initial concentration of the dye, the initial conditions at $\tau = 0$ are

$$\begin{cases} c = c_0 & \text{for} \quad |\xi| < 1/2 \\ c = 0 & \text{for} \quad |\xi| > 1/2 \end{cases} \tag{3.9}$$

The concentration profile at any time and radial position along the spiral is

$$c(\xi, \tau) = \frac{c_0}{2}\left[\mathrm{erf}\left(\frac{\xi + 1/2}{2\sqrt{\tau}}\right) - \mathrm{erf}\left(\frac{\xi - 1/2}{2\sqrt{\tau}}\right)\right] \tag{3.10}$$

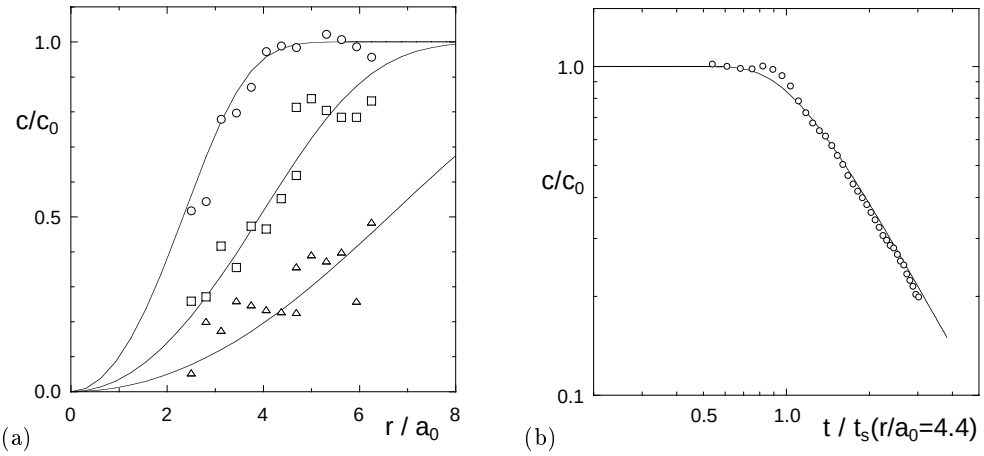

FIGURE 4. Comparison of the maximal dye concentrations obtained experimentally (symbols) and theoretically (solid lines) by Eq.(3.11). (a) Radial dependence at $t = 5\,\mathrm{sec}$ ($\circ$), $t = 10\,\mathrm{sec}$ ($\Box$) and $t = 20\,\mathrm{sec}$ ($\triangle$). (b) Temporal dependence for $r/a_0 = 4.4$

The maximal concentration is obtained at the profile center $\xi = 0$

$$c_M(r,t) = c_0\,\mathrm{erf}\left(\frac{1}{4\sqrt{\tau}}\right) = c_0\,\mathrm{erf}\left(\frac{1}{4\sqrt{\frac{Dt}{s_0^2}+\frac{D\Gamma^2t^3}{3\pi^2r^4s_0^2}}}\right) \tag{3.11}$$

This relation can be examined from the experiment ($\Gamma = 14.2\ \mathrm{cm}^2/\mathrm{s}$, $D = 5\times10^{-6}$ cm^2/s and $s_0 \approx 0.22$ cm). Figure 4(a) shows the maximal dye concentrations as a function of the radius r at a fixed time, for three different times. The concentration falls to zero more rapidly closer to the spiral center since the rate of elongation is higher there (see Eq. (3.3)).

Conversely, the temporal evolution of the concentration at a fixed $r-$location is constant (Fig. 4(b)) up to the mixing time $t_s(r)$. This time makes the argument of the error function in Eq. (3.11) of order unity i.e. $\tau = O(1)$

$$t_s(r) = \frac{r^2}{\Gamma}\left(\frac{3\pi^2}{16}\right)^{1/3}\left(\frac{s_0}{r}\right)^{2/3}\left(\frac{\Gamma}{D}\right)^{1/3} \tag{3.12}$$

and displays the expected Péclet number dependence $Pe^{1/3}$, with $Pe = \Gamma/D$ characteristic of flows where material lines grow asymptotically linearly in time (see Eq. (3.3)). After the mixing time, the maximal concentration c_M decreases like $t^{-3/2}$, in close agreement with the trend shown on Fig. 4(b).

4. Probability Density Function

If A is the total surface area of the spiral bearing a non-zero concentration level, the Probability Density Function (PDF) of the scalar $P(c)$ is the fraction of the total area whose concentration lies in the interval $[c,\ c+\mathrm{d}c]$. It is convenient to compute $P(c)$ in the (r,ξ) coordinates where ξ is defined in (3.8) so that with $\mathrm{d}X = \sqrt{1+(\Gamma^2t^2)/(\pi^2r^4)}\ \mathrm{d}r$ and $\mathrm{d}Y = s\,\mathrm{d}\xi = s_0\,\mathrm{d}\xi/\sqrt{1+(\Gamma^2t^2)/(\pi^2r^4)}$, one has

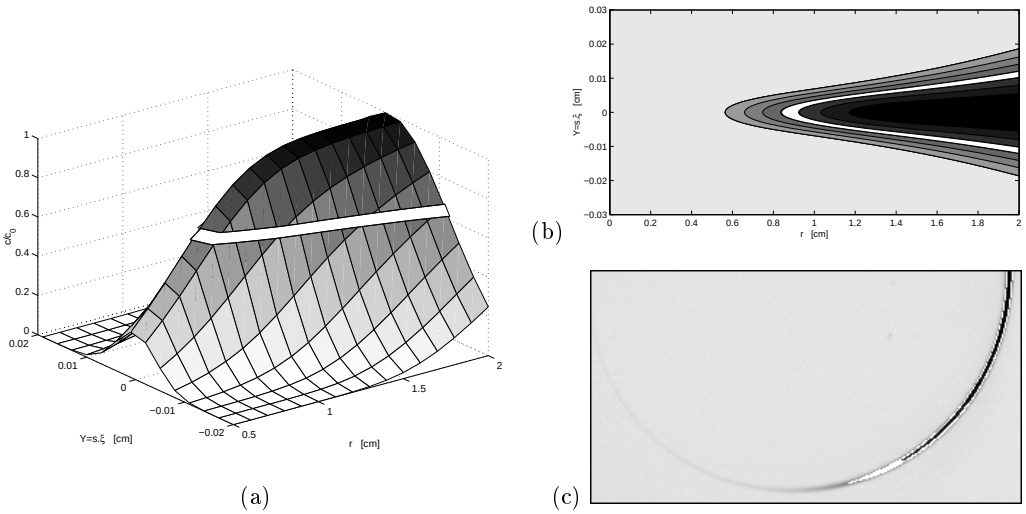

FIGURE 5. (a) Perspective view and (b) contour plot of the concentration profile given in Eq. (4.2). The white band corresponds to an iso-concentration $c/c_0 = 0.6$. (c) Zoom of the end of the spiral on Fig. 1 and same construction.

$$P(c)\mathrm{dc} = \iint_{c(X,Y)\in[c,\ c+\mathrm{dc}]} \frac{\mathrm{dX\ dY}}{A} = \iint_{c(r,\xi)\in[c,\ c+\mathrm{dc}]} \frac{s_0\ \mathrm{dr\ d}\xi}{A} \tag{4.1}$$

The scalar spatial distribution is given in Eq. (3.10) as the difference of two error functions. However, after the mixing time, that is when the spiral thickness is very thin, this difference approximates the derivative of the error function, providing a Gaussian concentration profile

$$c(\xi, r) = c_0\ \mathrm{erf}\left(\frac{1}{4\sqrt{\tau(r)}}\right) \mathrm{e}^{-\xi^2/2\sigma_\xi^2} \tag{4.2}$$

where $\tau(r)$ is given by Eq. (3.8) and $\sigma_\xi(r)$ is the standard deviation of the original profile $c(Y)$ given in Eq. (3.10)

$$\sigma^2 = \frac{\int Y^2 c(Y)\ \mathrm{dY}}{\int c(Y)\ \mathrm{dY}} = s^2(t)\frac{\int \xi^2 c(\xi)\ \mathrm{d}\xi}{\int c(\xi)\ \mathrm{d}\xi} = s^2(t)\frac{1+24\tau(r)}{12}, \quad \text{or} \quad \sigma_\xi^2 = \frac{1+24\tau(r)}{12} \tag{4.3}$$

Note that the 'spiral thickness' σ first decreases as t^{-1}, reaches a minimum at $t = t_s$ and re-increases as $t^{1/2}$ after the mixing time, when the spiral is locally nearly parallel to the vortex streamlines.

The shape of the iso-concentration lines $c(r\,, \xi) = c$ in the $(r,\ \xi)$ plane is shown in Fig. 5

$$\xi(r, c) = \pm\sigma_\xi(r)\sqrt{2\log\left[\mathrm{erf}\left(1/4\sqrt{\tau(r)}\right)\right] - 2\log(c/c_0)} \tag{4.4}$$

This curve is defined for $r > r_1^*(c)$ only, that is above the smallest radius bearing the concentration c at time t

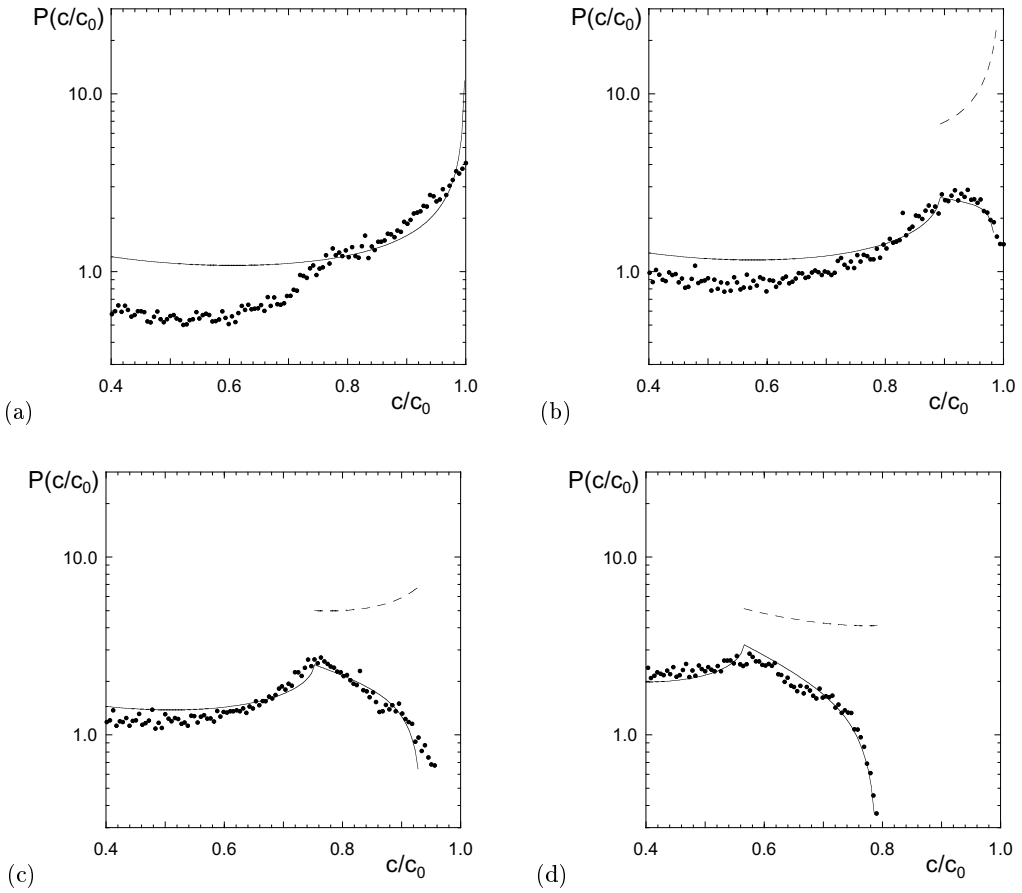

FIGURE 6. Probability Density Functions at (a) $t = 5\,\mathrm{sec}$, (b) $t = 8\,\mathrm{sec}$, (c) $t = 10\,\mathrm{sec}$ and (d) $t = 13\,\mathrm{sec}$. Solid lines correspond to the theoretical prediction given by Eq. (4.6) and dashed lines correspond to the PDF of the spatial maxima of concentration, defined by Eq. (4.7).

$$r_1^*(c) = \left[\frac{16}{3\pi^2}\,\frac{D\Gamma^2 t^3}{s_0^2\left[\mathrm{erf}^{-1}(c/c_0)\right]^{-2} - 16Dt}\right]^{1/4} \tag{4.5}$$

If the scalar blob was initially delimited between the radii r_1 and r_2, the concentration PDF is

$$P(c) = \frac{2s_0}{A}\int_{\max[r_1, r_1^*(c)]}^{r_2} \left|\frac{\partial c}{\partial \xi}\right|^{-1} \mathrm{dr} \tag{4.6}$$

The concentration profile across the spiral, and the evolution of the maximal concentration along the spiral set the global PDF.

The above relation is compared on Fig. 6 with the experimental histograms recorded with a blob initially located between $r_1 = 1.65\,\mathrm{cm}$ and $r_2 = 2.1\,\mathrm{cm}$. At early stages, (Fig. 6a), as long as most of the fluid particles constitutive of the spiral have not reached the mixing time yet, the PDF is that of a Gaussian spatial profile $1/c\sqrt{\log(c/c_M)}$ with $c_M = c_0$ displaying a characteristic $\cup$ shape.

As soon as diffusion becomes effective, the PDF nucleates a cusp located at the maximal concentration $c_M(r_1)$ obtained at the inner end of the spiral. The shape of the PDF for $c_M(r_1) < c < c_M(r_2)$ results from the superposition of the right branches of the $\cup$ shaped distributions parameterized by $c_M(r)$ with $r_1 < r < r_2$ (Fig. 6b,c,d) and weighted by the probability of finding the maximal concentration c_M, namely $Q(c_M)$. This distribution is the fraction of the spiral length dX whose concentration is in the interval $[c_M,\ c_M + \mathrm{dc_M}]$

$$Q(c_M) = \frac{1}{L}\left|\frac{\mathrm{dc_M}}{\mathrm{dX}}\right|^{-1} \tag{4.7}$$

where L is the spiral length $L = \int_{r_1}^{r_2} \mathrm{dX}$. It is defined in the range $[c_M(r_1),\ c_M(r_2)]$ and shown as the dotted line on Fig. 6. At short times, $P(c)$ and $Q(c_M)$ are very different because the low concentration levels at a small radii r and $\xi = 0$ are as numerous as the same levels at the edges of the Gaussian transverse profile ($\xi \neq 0$) at a higher r. The spatial distribution $c(\xi)$ contaminates the whole distribution $P(c)$, inducing the characteristic $\cup$ shape. At later stages (Fig. 6d), the low levels of concentration from the edges of the Gaussian profile at large radii are rare in comparison to those at the center of the spiral and $\xi = 0$. Therefore, $Q(c_M)$ becomes a decreasing function of c and gets closer to $P(c)$. In the final stages, when $\Gamma t/r^2 \gg 1$ and for $t_s(r) > 1$ for all r, these two distributions are both given by

$$P(c) \approx Q(c_M = c) \sim \left(\frac{\tilde{r}^4 s_0^2}{D\Gamma^2 t^3}\right)^{1/4} \frac{1}{c^{3/2}} \tag{4.8}$$

where $\tilde{r}$ stands for $(1/r_1 + 1/r_2)^{-1}$.

5. Conclusions and implications

In the simple displacement field of a two-dimensional vortex, a direct connection exists between the microscopic equations of diffusion, and the resulting global statistics of the mixture through the scalar concentration PDF $P(c)$ which, therefore, appears as a reformulation of the microscopic convection–diffusion problem.

This one-to-one connection is possible because the flow solely results in a spatial mapping of the fluid particles with no interaction between the particles themselves. The concentration of a given fluid element evolves due to molecular diffusion and not because it interacts with a nearby element; indeed, the arms of the spiral never reconnect. This situation would lead to a completely different route for the evolution of $P(c)$. It is, to this respect, useful to learn that the distribution $Q(c_M)$ tends asymptotically towards $P(c)$, a hidden assumption made when considering mixtures evolution by particle interaction (Curl(1963), Pope(1985), Pumir et al. (1991), Villermaux(2002)).

The simple stirring protocol considered here also provides an exact estimation of the scalar dissipation rate $\chi = -\frac{\mathrm{d}}{\mathrm{dt}}\langle c^2\rangle = 2D\langle(\nabla c)^2\rangle$, a quantity sometimes modeled in an ad-hoc way. Here $\langle\cdot\rangle$ denotes a spatial integration, therefore

$$\chi = 2D\int_{r_1}^{r_2}\frac{\mathrm{dX}}{s(t)}\int_{-\infty}^{+\infty}\left(\frac{\partial c}{\partial \xi}\right)^2 \mathrm{d}\xi \tag{5.1}$$

With $c(\xi)$ given in Eq. (3.10) and $\int_{-\infty}^{+\infty}\left(\frac{\partial c}{\partial \xi}\right)^2 \mathrm{d}\xi \sim \frac{1-e^{-1/8\tau(r)}}{\sqrt{\tau(r)}}$, one sees that as soon as $\Gamma t/r^2 > 1$

$$\begin{cases} \chi \sim \frac{\Gamma}{s_0}\sqrt{Dt} & \text{when} \quad t < t_s(r) \quad \text{for all } r \\ \chi \sim \frac{s_0}{\sqrt{D\Gamma}} t^{-5/2} & \text{when} \quad t > t_s(r) \quad \text{for all } r \end{cases} \tag{5.2}$$

As long as most of the fluid particles constitutive of the spiral have not reached the mixing time (i.e. while $t < t_s(r)$ and $\tau(r) \ll 1$), χ reflects both the diffusive smoothing ($\sim 1/\sqrt{Dt}$) at the edges of the concentration profile $c(\xi)$, and the increase of the concentration support length ($\sim \Gamma t$). When the mixing time has been reached all along the spiral (i.e. when $t > t_s(r)$ and $\tau(r) > 1$), the maximal concentration c_M decays as $t^{-3/2}$, the profile thickness σ re-increases by pure diffusion like $t^{1/2}$ and the spiral length still increases like Γt, thus, since $\chi \sim (c_M/\sigma)^2 \sigma \Gamma t$, providing the $t^{-5/2}$ time dependence in Eq. (5.2).

Acknowledgments: We thank Dr. Thomas Leweke for encouragements, and useful discussions.

REFERENCES

BAJER, K., BASSOM, A. P. & GILBERT, A. D. 2001 Accelerated diffusion in the centre of a vortex. *J. Fluid Mech.* **437**, 395–411.

CETEGEN, B. M. & MOHAMAD, N. 1993 Experiments on liquid mixing and reaction in a vortex. *J. Fluid Mech.* **249**, 391–414.

CURL, R. L. 1963 Dispersed phase mixing: I. theory and effect in simple reactors. *AIChE J.* **9**, 175–181.

FLOHR, P. & VASSILICOS, J. C. 1997 Accelerated scalar dissipation in a vortex. *J. Fluid Mech.* **348**, 295–317.

MARBLE, F. E. 1988 Mixing, diffusion and chemical reaction of liquids in a vortex field. In *Chemical Reactivity in Liquids: Fundamental Aspects* (ed. M. Moreau & P. Turq), pp. 581–596. Plenum.

MEUNIER, P. & LEWEKE, T. 2002a Elliptic instability of a co-rotating vortex pair. Submitted to *J. Fluid Mech.*

MEUNIER, P. & LEWEKE, T. 2002b Analysis and optimization of the error caused by high velocity gradients in PIV. Submitted to *Exp. Fluids.*

MOFFATT, H. K. 1983 Transport effects associated with turbulence with particular attention to the influence of helicity. *Rep. Prog. Phys.* **46**, 621–664.

POPE, S. B. 1985 Pdf methods for turbulent reacting flows. *Prog. Energy Combust. Sci.* **11**, 119–192.

PUMIR, A., SHRAIMAN, B. I. & SIGGIA, E. D. 1991 Exponential tails and random advection. *Phys. Rev. Letters* **66**, 2984–2987.

RANZ, W. E. 1979 Application of a stretch model to mixing, diffusion and reaction in laminar and turbulent flows. *AIChE J.* **25**, 41–47.

RHINES, P. B. & YOUNG, W. R. 1983 How rapidly is a passive scalar mixed within closed streamlines. *J. Fluid Mech.* **133**, 133–145.

VERZICCO, R. & ORLANDI, P. 1995 Mixedness in the formation of a vortex ring. *Phys. Fluids* **7** (6), 1513–1515.

VILLERMAUX, E. 2002 Mixing as an aggregation process. In *Turbulent Mixing and Combustion* (ed. A. Pollard & S. Candel), pp. 1–21. Kluwer Academic Publishers.

VILLERMAUX, E. & REHAB, H. 2000 Mixing in coaxial jets. *J. Fluid Mech.* **425**, 161–185.

Available online at www.sciencedirect.com
ScienceDirect
C. R. Mecanique 335 (2007) 162–167
COMPTES RENDUS MECANIQUE
http://france.elsevier.com/direct/CRAS2B/

Van Hove singularities in Probability Density Functions of scalars

Patrice Meunier [a,*], Emmanuel Villermaux [a,b]

[a] *Université de Provence and CNRS, institut de recherche sur les phénomènes hors équilibre, 49, rue Frédéric-Joliot-Curie, 13384 Marseille cedex 13, France*
[b] *Institut Universitaire de France*

Received 26 September 2006; accepted after revision 23 January 2007

Available online 21 March 2007

Presented by Paul Clavin

Abstract

A general theory for the Probability Density Function (PDF) of a scalar stirred in an axisymmetric time-dependent flow is derived. This theory reveals singularities, discontinuities and cusps occurring as soon as the spatial gradient of the scalar concentration vanishes somewhere in the field. These singularities are similar to the Van Hove singularities obtained in the density of vibration modes of a crystal. This feature, ubiquitous in convection–diffusion problems, is documented experimentally for the mixing of a dye in a Lamb–Oseen vortex. ***To cite this article: P. Meunier, E. Villermaux, C. R. Mecanique 335 (2007).***

Résumé

Singularités de Van Hove dans les densités de probabilité d'un scalaire. Nous dérivons une théorie générale pour la Densité de Probabilité (PDF) d'un scalaire étiré dans un champ de vitesse axisymmétrique et dépendant du temps. Cette théorie révèle des singularités (discontinuités et cusps), qui apparaissent dès lors que le gradient spatial du scalaire s'annule en un endroit du champ. Ces singularités sont similaires aux singularités de Van Hove obtenue pour la densité des modes de vibration d'un cristal. Ce phénomène, omniprésent dans les problèmes de diffusion–convection, est documenté expérimentalement pour le mélange d'un colorant dans un vortex de Lamb–Oseen. ***Pour citer cet article : P. Meunier, E. Villermaux, C. R. Mecanique 335 (2007).***

Keywords: Computational fluid mechanics; Mixing; Singularities; PDF

Mots-clés : Mécanique des fluides numérique ; Mélange ; Singularités ; PDF

The interplay between molecular diffusion and simple deformation fields is a classical problem. It is solved in closed form in a variety of situations such as the saddle point flow, the simple shear in two dimensions [1–3], in three dimensions [4], and in the axisymmetric point vortex [5,6] or spreading vortex flow [7,8]. In particular, simple situations are liable of a complete description of the overall Probability Density Function (PDF) of the scalar concentration from the Fourier equation [9].

* Corresponding author.
E-mail address: meunier@irphe.univ-mrs.fr (P. Meunier).

1631-0721/$ – see front matter
doi:10.1016/j.crme.2007.02.001

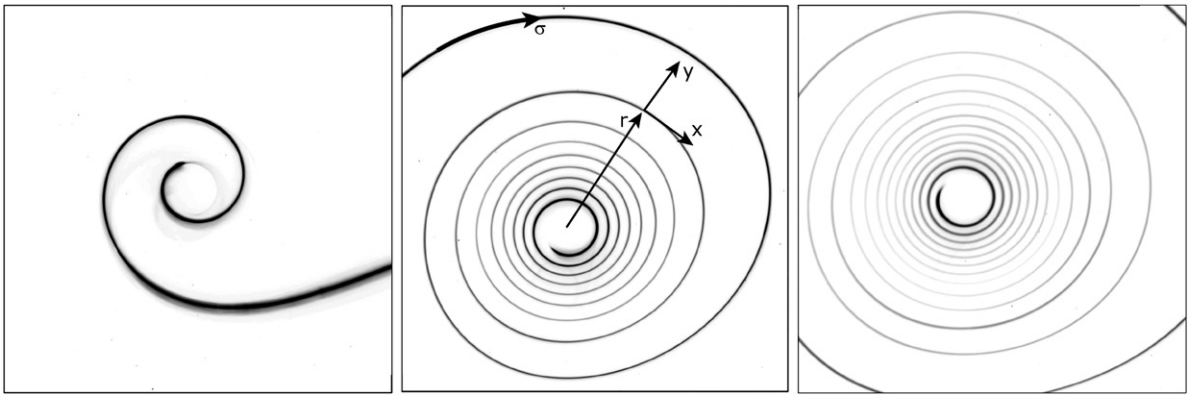

Fig. 1. Visualisation of the spiral formed by a dye lamellae wrapping around a Gaussian vortex. Images are obtained at $t = 5$ s, $t = 50$ s and $t = 95$ s and cover 10×10 cm^2 for a vortex of circulation $\Gamma = 17$ cm^2 s^{-1}.

Here, we discuss the condition under which the PDF presents a *singularity*. The phenomenon we analyse first is illustrated on Fig. 1. A lamellae of weakly diffusive dye ($D = 10^{-9}$ m^2 s^{-1}) with initial concentration c_0 and width $s_0 \approx 2$ mm is deposited in the velocity field of an axisymmetric, time-dependent vortex. The azimuthal velocity profile is Gaussian, that of a Lamb–Oseen vortex [10]

$$v_\theta(r,t) = \frac{\Gamma}{2\pi r}\left[1 - \exp\left(\frac{-r^2}{a_0^2 + 4\nu t}\right)\right] \tag{1}$$

with a circulation $\Gamma = 17$ cm^2 s^{-1} and initial core size $a_0 = 1.3$ cm. The lamellae first rolls-up around the vortex (Fig. 1(a)), stretches and, conversely, gets thinner in its transverse direction. Diffusion is hasten by this stretching motion [9] and indeed, Fig. 1(b) shows that the dye concentration is smaller where the elongation is higher, i.e. at intermediate radii. Close to the vortex center in solid body rotation, and far from the vortex center where the velocity magnitude is small and so is the stretching rate, the dye still bears a concentration close to the initial one. The process goes on until at late stages (Fig. 1(c)), the dye has vanished in the diluting medium.

Compared to our first contribution on the topic [9], the set-up has been modified to allow the study of the late stages. Previously, the vortex would experience an axial destabilization 15 seconds after its formation due to the end effects. Here, the fluid is linearly stratified, stabilizing the vortex for 2 to 3 minutes. The dye is now injected by slowly translating a thin iron wire coated with fluoresceine, forming a vertical sheet of dye aligned with the vortex axis. A horizontal laser sheet allows the visualisation of a field cross-section, which is imaged from below (Fig. 1) using a Kodak 8 bits 2048^2 pixels CCD array providing a 12 pixels/mm resolution. While our theory was limited to a stationary point vortex $v_\theta = \Gamma/2\pi r$, we extend it here to the general case of a time-dependent axisymmetric flow as in Eq. (1). Computing the stretching of a length element dr and using incompressibility, the distance between two material points in the direction perpendicular to the lamellae (striation thickness) is

$$s(r,t) = s_0\left[1 + \left(r\int_0^t \mathrm{d}t\,\frac{\partial(v_\theta/r)}{\partial r}\right)^2\right]^{-1/2}$$

where s_0 is the initial lamellae thickness. In a frame of reference (O, x, y) tangent to the lamellae with y pointing outwards, the convection–diffusion equation for the dye concentration c amounts to a pure diffusion equation $\partial c/\partial\tau = \partial^2 c/\partial\xi^2$, when the transverse coordinate y has been rescaled by the current striation thickness ($\xi = y/s(t)$) and time t has been rescaled by the current diffusion time ($\mathrm{d}\tau = D\,\mathrm{d}t/s^2$). The dimensionless time τ is

$$\tau(r,t) = \frac{Dt}{s_0^2} + \frac{Dr^2}{s_0^2}\int_0^t\left(\int_0^{t'}\frac{\partial(v_\theta/r)}{\partial r}\,\mathrm{d}t''\right)^2\mathrm{d}t' \tag{2}$$

At late stages, the dye concentration has a Gaussian profile in the transverse direction, with a maximum concentration $c_M(r,t) = c_0 \operatorname{erf}(1/4\sqrt{\tau})$ depending on τ only

$$c(r,\xi,t) \approx c_0 \operatorname{erf}\left(\frac{1}{4\sqrt{\tau(r)}}\right) \exp\left(\frac{-6\,\xi^2}{1+24\tau(r)}\right) \tag{3}$$

The PDF of such a spatial profile is easily obtained by integration over r in the range where the maximum concentration $c_M(r)$ is larger than a given concentration level c:

$$P(c) = 2s_0 \int\limits_{c_M(r)>c} |\partial c/\partial \xi|^{-1}\,\mathrm{d}r/A$$

where A is a normalising constant equal to the surface area on which the PDF is calculated. Expressing $\partial c/\partial\xi = -12\xi c/(1+24\tau)$, and inverting the function $c(\xi)$, we find the general solution

$$P(c) = \frac{2s_0}{cA} \int \max\left(0, \frac{\tau(r)+1/24}{\log[\operatorname{erf}(1/4\sqrt{\tau(r)})] - \log[c/c_0]}\right)^{1/2} \mathrm{d}r \tag{4}$$

The function 'max(0, .)' stands for the integrand to vanish when the maximum concentration $c_M(r)$ is smaller than c; this allows the integration to be performed on the entire lamellae length at any time.

Defining the curvilinear abscissa σ along the lamellae (Fig. 1), this formula is extended to any two-dimensional flow provided the stretching rate $\gamma(\sigma,t) = -[\mathrm{d}s(\sigma)/\mathrm{d}t]/s(\sigma)$ of all the lamellae elements is known at any time along their Lagrangian trajectory. The integral is computed over σ instead of r for axisymmetric flows, giving

$$\tau(\sigma,t) = \frac{D}{s_0^2} \int\limits_0^t \exp\left(2\int\limits_0^{t'} \gamma(\sigma,t'')\,\mathrm{d}t''\right)\mathrm{d}t' \tag{5}$$

Prediction (4) is plotted in Fig. 2 and shows good agreement with the measured distribution. The general solution (4) can be further simplified when $\tau(r)$ is rapidly varying with r. By a change of variable $u = c_M(r)/c$, the integral is modified into $\int_1^\infty c\,\mathrm{d}u\,\sqrt{\tau+1/24}/\sqrt{\log(u)}\,\partial c_M/\partial r$. Since this function diverges for $u=1$, the other terms can be replaced by their values in $u=1$, which corresponds to $c_M(r)=c$, giving

$$P(c) \approx \frac{\sqrt{\tau+1/24}}{\partial c_M/\partial r} \tag{6}$$

a result easily obtained by retaining the maximum of the concentration at each radius only in computing the PDF, with a weight equal to the transverse size of the Gaussian profile $\sqrt{\tau+1/24}$, giving $P(c_M)\,\mathrm{d}c_M = \sqrt{\tau+1/24}\,\mathrm{d}r$. This ansatz, also plotted in Fig. 2, reproduces the shape of the PDF correctly, and is off by a factor 2 in amplitude. This

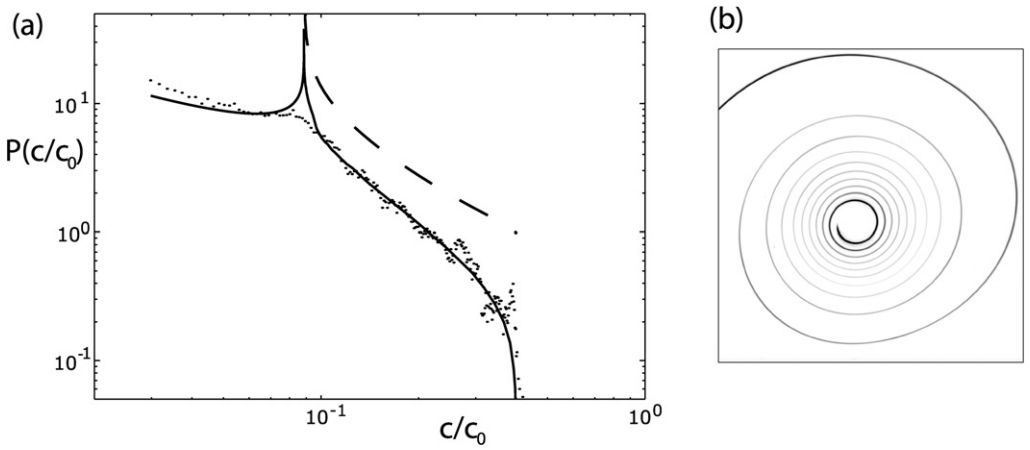

Fig. 2. (a) Probability density function of the concentration c and (b) concentration field at $t = 60$ s. The solid line corresponds to the full model (4) and the dashed line to the approximation (6) using the maximal concentration.

discrepancy is a normalization artifact due to the fact that the PDF of the maximal concentration in Eq. (6) does not represent levels smaller than the minimum of $c_M(r)$. This PDF is thus restricted to $c > 0.09c_0$, where the minimum of the maximal concentration over the dye lamellae is at that instant of time. This approximation is thus all the more valid that the lamellae is deposited initially far from the vortex center, in a region where $\tau(r)$ is systematically decreasing with r. There, this ansatz moreover predicts that $P(c) \sim t^{-3/4}c^{-3/2}$, asymptotically [9].

These predictions seem to be good enough when $\tau(r)$ and thus $c_M(r)$ are monotonic functions of the radius. However, both predictions reveal a singularity when $\tau(r)$ has an extremum, since formulas (4) and (6) diverge when $\partial c_M/\partial r$ vanishes. We now focus on these critical points.

Fig. 2 shows that the theoretical PDF presents a singularity at $c^*/c_0 = 0.09$. Before commenting on the experimental distribution, let us first recognize that such a phenomenon will obviously appear as soon as the gradient of the scalar $\partial c/\partial \mathbf{r}$ vanishes somewhere in the concentration field. This was already noted by Van Hove [11] for the density of the elastic vibration frequencies of a crystal (density of modes). Depending on the shape of the dispersion relation $\omega(k)$ in the crystal, the density of modes $D(\omega)$ has a singularity where the group velocity $\partial\omega/\partial k$ vanishes. We recall here the different types of singularities, corresponding in our case to the different topologies of the concentration profile where these events occur. Let us examine first concentration fields in two dimensions:

(i) First, consider a lamellae whose concentration profile presents a 2D saddle point: locally, the scalar concentration is equivalent to $c(x, y) = c^* + \alpha x^2 - \beta y^2$ with α and β positive. This case is shown schematically on Fig. 3(a) and can be obtained if the stretching is maximum somewhere along the lamellae. For $c < c^*$ the PDF is computed by integrating on a square surface of size $(R/\sqrt{\alpha}, R/\sqrt{\beta})$: $P(c) = 4\int_0^{R/\sqrt{\alpha}} |\partial c/\partial y|^{-1}\,\mathrm{d}x$, and by expressing y as a function of c and x: $P(c) = 2\,\mathrm{Arcsinh}(R/\sqrt{c^* - c})/\sqrt{\alpha\beta}$. The PDF is thus equivalent to $-\log(c^* - c)$ close to the critical level c^*. The same scaling can be obtained for $c > c^*$ and the PDF thus presents a logarithmic singularity at $c = c^*$ in that case.

(ii) Second, consider the opposite case where the concentration has a local maximum on the lamellae, as can be realized if there is a minimum of stretching along the lamellae, as shown schematically on Fig. 3(b). The scalar concentration is locally equivalent to $c(x, y) = c^* - \alpha x^2 - \beta y^2$. The PDF is equal to zero for $c > c^*$ and equal to $\pi/\sqrt{\alpha\beta}$ for $c < c^*$. The PDF is thus discontinuous as soon as the scalar concentration profile has a maximum.

(iii) Third, the concentration profile presents a local minimum. This is not likely to happen in two dimensions since the topology is rather that of an elongated lamellae, with a transverse concave concentration profile. However, the PDF can be computed in this case also and is found to be discontinuous (0 for $c < c^*$ and $\pi/\sqrt{\alpha\beta}$ for $c > c^*$).

The PDF of a concentration field in two-dimensions can thus present *logarithmic singularities* or *discontinuities* at finite times i.e. as soon as the concentration profiles are affected by diffusion. One understands now why this divergence is rendered on the experimental distribution (Fig. 2) as a weak cusp only. This is primarily due to the finite size resolution of the digital images from which the concentration field is extracted. The logarithmic singularity comes from a very restricted area around a single point, the one with $c = c^*$. The second reason comes from the finite binning of the concentration levels, which enlarges and smooths the singularity. However, this singularity, which comes from

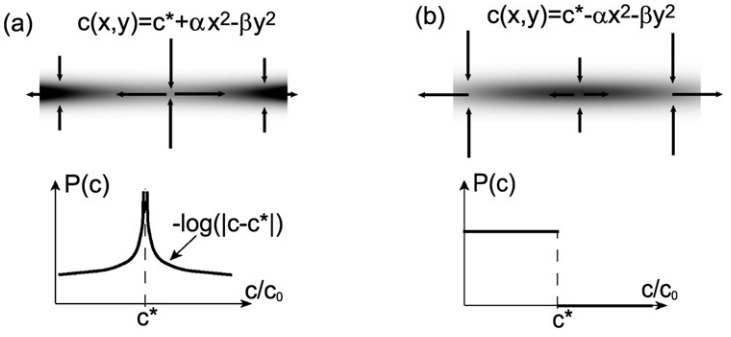

Fig. 3. Schematic of the singularities occurring in the scalar PDF of a 2D flow. (Top) Pseudo-color plot of the scalar distribution $c(x, y)$. (Bottom) The PDF is computed using $P(c) = 4\int_0^{R/\sqrt{\alpha}} |\partial c/\partial y|^{-1}_{y_0(x)}\,\mathrm{d}x$, with $y_0(x) = \sqrt{c^* - c + \alpha x^2}/\sqrt{\beta}$ for (a) and $y_0(x) = \sqrt{c^* - c - \alpha x^2}/\sqrt{\beta}$ for (b).

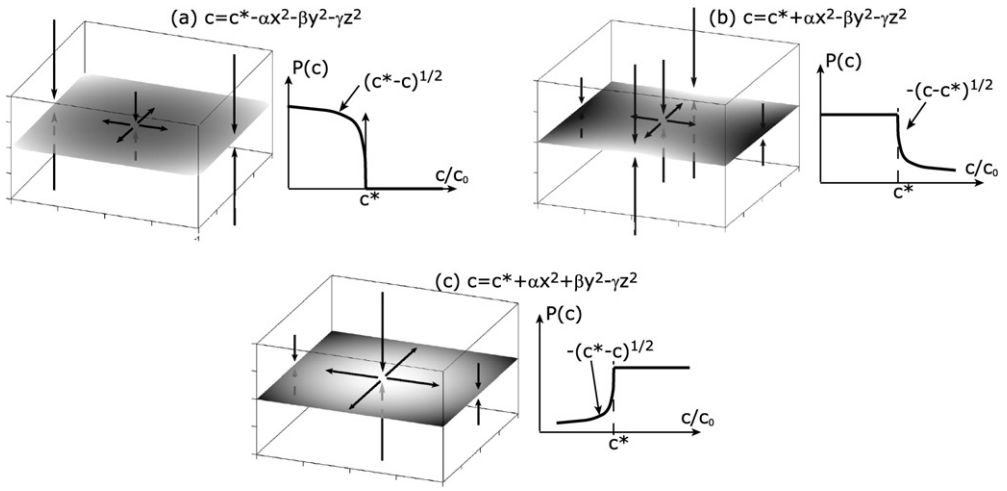

Fig. 4. Schematic of the singularities occurring in the scalar PDF of a 3D flow. (Left) Pseudo-color plot of the scalar distribution at the center of the 3D sheet. (Right) The PDF is calculated using $P(c) = 8 \int_0^{R/\sqrt{\alpha}} \int_0^{R/\sqrt{\beta}} |\partial c/\partial z|^{-1}_{z_0(x,y)} \,\mathrm{d}x\,\mathrm{d}y$, with $z_0(x, y)$ defined such that $c(x, y, z_0) = c$.

a maximum of the stretching along the spiral does exist (as clearly seen on Fig. 1(b)) and would be all the more resolved that the uncertainty in the definition of the concentrations, and the spatial resolution are sharp enough.

Consider now three-dimensional flows, where the scalar is usually found in the form of sheets as a result of various turbulent or chaotic motions [12–14]. These are shown schematically in Fig. 4 lying in the (x, y) plane. A singularity in the corresponding concentration PDF may again appear when the concentration gradient $\partial c/\partial \mathbf{r}$ vanishes. There are thus four different cases depending on whether the concentration profile has a maximum or a minimum in each direction:

(i) The first case corresponds to a concentration profile with a maximum of concentration: it is locally equivalent to $c(x, y, z) = c^* - \alpha x^2 - \beta y^2 - \gamma z^2$ (with α, β and γ positive). This can be obtained if the stretching has a local minimum (see Fig. 4(a)). The PDF, computed on a volume of radius R is equal to $\pi\sqrt{c^* - c}/\sqrt{\alpha\beta\gamma}$ for $c < c^*$ and vanishes for $c > c^*$. The PDF presents a cusp with an infinite (negative) slope for $c < c^*$, as indicated on Fig. 4(a).

(ii) The second case corresponds to a concentration profile locally equivalent to $c(x, y, z) = c^* + \alpha x^2 - \beta y^2 - \gamma z^2$, which is obtained if the stretching of the sheet is maximum along y and minimum along x (see Fig. 4(b)). The PDF is equal to $\pi(\sqrt{\gamma}R - \sqrt{c - c^*})/\sqrt{\alpha\beta\gamma}$ for $c > c^*$ and to $\pi R/\sqrt{\alpha\beta}$ for $c < c^*$. The PDF presents a cusp with an infinite slope for $c > c^*$, as indicated on Fig. 4(b).

(iii) The third case corresponds to a concentration profile locally equivalent to $c(x, y, z) = c^* + \alpha x^2 + \beta y^2 - \gamma z^2$, which is obtained if the stretching of the sheet has a maximum (see Fig. 4(c)). The PDF is equal to $\pi(\sqrt{\gamma}R - \sqrt{c^* - c})/\sqrt{\alpha\beta\gamma}$ for $c < c^*$ and to $\pi R/\sqrt{\alpha\beta}$ for $c > c^*$. The PDF presents a cusp with an infinite slope for $c < c^*$, as indicated on Fig. 4(c).

(iv) Finally, the fourth case would correspond to a local minimum concentration as $c(x, y, z) = c^* + \alpha x^2 + \beta y^2 + \gamma z^2$. It is not likely to be very frequent in 3D flows where the scalar has rather the topology of a sheet with a transverse concave concentration profile. However, the PDF can be calculated in that case too and is equal to $\pi\sqrt{c - c^*}/\sqrt{\alpha\beta\gamma}$ for $c > c^*$ and vanishes for $c < c^*$. The PDF again presents a cusp with an infinite slope for $c > c^*$.

As in two dimensions and for the same reason, the PDF of a concentration field in three-dimensions can thus present a cusp with an infinite slope each time the gradient of the scalar vanishes. This algebraic divergence is weaker than the logarithmic one in two dimensions.

The singularities are prominent in simple fields, as the one generated by a Gaussian vortex in the present experiment, where the concentration gradient vanishes at one location in the field only. In a complex flow stirred randomly, the number of these singularities should increase with time as the scalar field is distorted by the underlying motion.

Indeed, the more complex the spatial scalar distribution, the more likely it will contain saddle points and maxima. However, these singularities will occur at an increasing number of different critical concentration levels c^*, at an increasing number of spatial locations in the flow [15]. The scalar PDF, initially presenting one, then two, then a large collection of singular cusps will progressively built-up in a continuous distribution, made of a continuous spectrum of singularities. Being rooted in the local topology of the field, these singularities are, as noted above, robust and may be found in 3D flows as well.

References

[1] M.A. Lévêque, Les lois de la transmission de la chaleur par convection, Ann. Mines 13 (1928) 201–239.
[2] W.E. Ranz, Application of a stretch model to mixing, diffusion and reaction in laminar and turbulent flows, AIChE J. 25 (1979) 41–47.
[3] H.K. Moffatt, Transport effects associated with turbulence with particular attention to the influence of helicity, Rep. Prog. Phys. 46 (1983) 621–664.
[4] E. Villermaux, H. Rehab, Mixing in coaxial jets, J. Fluid Mech. 425 (2000) 161–185.
[5] P.B. Rhines, W.R. Young, How rapidly is a passive scalar mixed within closed streamlines, J. Fluid Mech. 133 (1983) 133–145.
[6] P. Flohr, J.C. Vassilicos, Accelerated scalar dissipation in a vortex, J. Fluid Mech. 348 (1997) 295–317.
[7] F.E. Marble, Mixing, diffusion and chemical reaction of liquids in a vortex field, in: M. Moreau, P. Turq (Eds.), Chemical Reactivity in Liquids: Fundamental Aspects, Plenum, New York, 1988, pp. 581–596.
[8] K. Bajer, A.P. Bassom, A.D. Gilbert, Accelerated diffusion in the centre of a vortex, J. Fluid Mech. 437 (2001) 395–411.
[9] P. Meunier, E. Villermaux, How vortices mix, J. Fluid Mech. 476 (2003) 213–222.
[10] P. Meunier, T. Leweke, Analysis and optimization of the error caused by high velocity gradients in PIV, Exp. Fluids 35 (2003) 408–421.
[11] L. Van Hove, The occurrence of singularities in the elastic frequency distribution of a crystal, Phys. Rev. 89 (6) (1953) 1189–1193.
[12] B.J. Cantwell, On the behavior of velocity gradient tensors invariants in direct numerical simulations of turbulence, Phys. Fluids A 5 (8) (1993) 2008–2013.
[13] K.A. Buch Jr, W.J.A. Dahm, Experimental study of the fine-scale structure of conserved scalar mixing in turbulent shear flows. Part 1. $Sc \gg 1$, J. Fluid Mech. 317 (1996) 21–71.
[14] G.O. Fountain, D.V. Khakhar, J.M. Ottino, Visualization of three-dimensional chaos, Science 281 (1998) 683–686.
[15] C.H. Gibson, Fine structure of scalar fields mixed by turbulence. i. Zero-gradient points and minimal gradient surfaces, Phys. Fluids 11 (11) (1968) 2305–2315.

The Diffusive Strip Method as a tool for scalar mixing in two-dimensions

By P. MEUNIER AND E. VILLERMAUX†

IRPHE, CNRS and Aix-Marseille Université, 13384 Marseille Cedex 13, France

(Received 18 May 2009)

We introduce a new numerical method for the study of scalar mixing in 2D advection fields. The position of an advected material strip is computed kinematically, and the associated convection-diffusion problem is solved using the computed local stretching rate along the strip, assuming that the diffusing strip thickness is smaller than its local radius of curvature. This widely legitimate assumption reduces the numerical problem to the computation of a single variable along the strip, thus making the method extremely fast and applicable to any Péclet number. The method is then used to document the mixing properties of a chaotic Sine Flow, for which we relate the global quantities (spectra, concentration PDFs, increments) to the distributed stretching of the strip convoluted by the flow, possibly overlapping with itself. The numerical results indicate that the PDF of the strip elongation is log-normal, a signature of random multiplicative processes. This property leads to exact analytical predictions for the spectrum of the field and for the PDF of the scalar concentration of a solitary strip. The present simulations offer a unique way of discovering the interaction rule building complex mixtures which are made of a random superposition of overlapping strips leading to concentration PDFs stable by convolution.

1. Introduction

Fluid mechanics has for a long time relied on observations, experiments, data collection rationalized by first principles theories or ad-hoc models and correlations. The output was a corpus of formulas, abacus and charts made available to the engineer, meteorologist, physicist etc... for helping him to solve practical problems. Originally motivated by weather forecasting issues, and since the basic equation describing fluids were known, the idea of re-creating natural phenomena by artificial means using automatic calculations arose, probably first formalized in this form by Lewis Fry Richardson (Richardson (1922)). Since then, the numerical simulation of fluid flows has undergone a dramatic growth. And the methods are continuously improving to make the computations faster and more faithful to reality.

As for scalar mixing, namely the equalization of a dye, or impurity in a prescribed flow field, the existing methods can be roughly grouped into two main categories:

Lagrangian methods follow the position $\mathbf{x}_i$ of passive tracers in the flow by integrating the equation of motion

$$\frac{\mathrm{d}\mathbf{x_i}}{\mathrm{d}t} = \mathbf{v}(\mathbf{x}_i, t) \tag{1.1}$$

in a velocity field $\mathbf{v}(\mathbf{x}_i, t)$ given a-priori. This method is useful to study trajectories,

† Also at: Institut Universitaire de France

the flow kinematics and stirring properties; it is widely used in the context of chaos, maps and ergodic theory for instance (e.g. Jones (1994); Phelps & Tucker (2006); Sturman *et al.* (2006); Robinson *et al.* (2008)). It does not, however, incorporate explicitly diffusion effects, those which are nevertheless ultimately responsible for mixing.

Eulerian methods on the other hand deal with the markers concentration field c (the number density of the markers coarse-grained on a grid) by solving a partial differential equation, namely the diffusion-advection equation

$$\frac{\partial c}{\partial t} + \mathbf{v} \cdot \nabla c = D \triangle c \tag{1.2}$$

where D is the tracers diffusivity. The method provides the whole concentration field accounting explicitly for diffusion, but needs a discretization grid of space to compute gradients, and remains therefore limited to smooth concentration fields with not too sharp gradients for reasonable computation times and cost (Sukhatme & Pierrehumbert (2002); Fereday & Haynes (2004); Perugini *et al.* (2004); Shankar & Kidambi (2009)).

Many other specific methods exist, particularly for turbulent flows, with possibly an admixture of models to represent small unsolved sub-grid scales, and/or additional effects such as buoyancy, chemical reactions, heat release etc... (see e.g. Yeung (2002); Fox (2004)).

The Diffusive Strip Method we introduce here is an extension of ideas developed to handle scalar diffusion on a moving substrate. The method amount to reduce the full convection–diffusion problem in (1.2) to a simpler, analytically tractable diffusion equation in suitably chosen coordinates as

$$\frac{\partial c}{\partial \tau} = \frac{\partial^2 c}{\partial \tilde{n}^2} \tag{1.3}$$

where τ and $\tilde{n}$ are functions of space, time, scalar diffusivity and of the structure of the velocity field. The method for going from equation (1.2) to equation (1.3) and find closed form, nearly exact solutions has been used in the context of heat transfer (Levèque (1928)), turbulence (Batchelor (1959); Villermaux & Duplat (2003)), combustion (Marble & Broadwell (1977); Marble (1988)), engineering and process industry (Mohr *et al.* (1957), Ranz (1979), Villermaux & Rehab (2000); Meunier & Villermaux (2003)), geophysics (Rhines & Young (1983), Allègre & Turcotte (1986)), chaos (Ottino (1989), Beigie *et al.* (1991)), physics (Moffatt (1983); Meunier & Villermaux (2007)) or mathematics (Fannjiang *et al.* (2004)).

In all of these works, the method has been successfully used for computing mixing times and length scales. However, the method can potentially provide more since it gives access to the evolution of the whole concentration field, with a direct, nearly exact link with the initial Fourier equation (1.2). For instance, in the simple case of a strip wrapping around a vortex (Meunier & Villermaux (2003, 2007)), the position and the stretching rate of the strip are known explicitly from the velocity field in a straightforward manner, which allows to derive the whole concentration field analytically, at any time. Building on this elementary step, we generalize here the method to a-priori any velocity field, as complicated as it may be. We first present the method, its numerical implementation and validation in section 2, and then apply it to study the mixing properties (internal structure, interaction rule, concentration distribution, spectra, increments, kinetics) of a prototype flow, namely the Sine Flow in sections 3 to 7. The details of the numerics and the computational cost of the method are discussed in Appendix A.

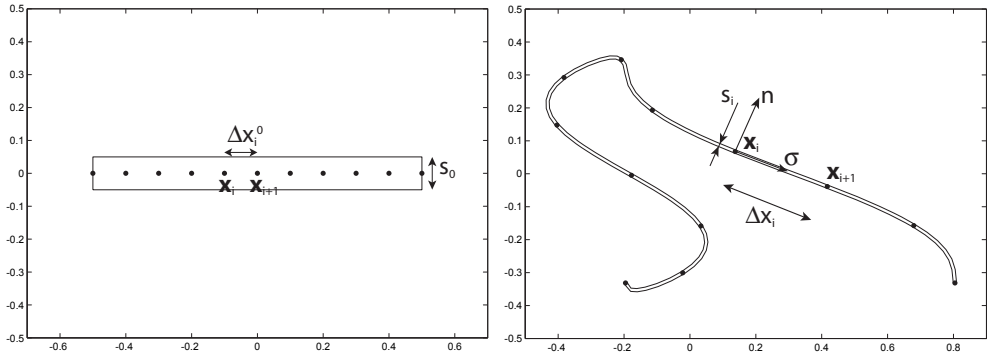

(a) (b)

FIGURE 1. Schematic drawing of the evolution of a strip defined by the points $\mathbf{x}_i$ and a striation thickness s_i initially equal to s_0.

2. The Diffusive Strip: a new numerical method

2.1. *The method*

The flow field $\mathbf{v}(\mathbf{x}, t)$ is assumed to be given analytically, decoupled from the concentration field itself (passive scalar), but not necessarily integrable. It is incompressible and two-dimensional. A scalar strip is described by the position of tracers located in $\mathbf{x}_i$, which are advected by solving numerically the equation of motion (1.1). The tracers are initially separated by a length Δx_i^0, as shown in Fig. 1. We then suppose that the strip contains a scalar c, whose concentration has initially a Gaussian transverse profile with a striation thickness s_0

$$c(n) = c_0 \, \mathrm{e}^{-n^2/s_0^2} \quad \text{at } t = 0$$

Here, n is the local coordinate normal to the strip (see Fig. 1). The particular choice of a Gaussian is not restrictive. It simply expresses that the strip is localized in space, and has a typical width s_0 initially. We wish to know how the transverse profile evolves when the strip is advected by the flow. The evolution equation for the scalar $c(\mathbf{x}, t)$ is the standard diffusion-advection equation (1.2).

In the absence of diffusion, the strip is stretched and thus experiences a contraction in the transverse direction due to incompressibility. Its striation thickness $s_i(t)$ decreases with time and can be calculated numerically by applying the conservation of areas

$$s_i = s_0 \Delta x_i^0 / \Delta x_i \tag{2.1}$$

Here $\Delta x_i = ||\mathbf{x}_{i+1} - \mathbf{x}_i||$ is the distance between two consecutive tracers. Around a tracer x_i, the velocity field in a local frame of reference (σ, n) aligned with the strip is given by

$$v_\sigma = \frac{\sigma}{s_i} \frac{\mathrm{d}s_i}{\mathrm{d}t} + \frac{\partial v_\sigma}{\partial n} n \tag{2.2}$$

$$v_n = -\frac{n}{s_i} \frac{\mathrm{d}s_i}{\mathrm{d}t} \tag{2.3}$$

It is a Taylor expansion at first order of the flow around $\mathbf{x}_i$. The velocity field at the position of the tracer $\mathbf{x}_i$ vanishes because the frame of reference is centered in $\mathbf{x}_i$. The velocity gradient $\partial v_\sigma / \partial \sigma$ is equal to $\mathrm{d}s_i/\mathrm{d}t$ by definition of the striation thickness. The velocity gradient $\partial v_n / \partial \sigma$ vanishes because the frame of reference is aligned with the strip at any time. The velocity gradient $\partial v_n / \partial n$ is equal to $-\mathrm{d}s_i/\mathrm{d}t$ due to incompressibility. The velocity gradient $\partial v_\sigma / \partial n$ is unknown. However, as time evolves, the lengthscale

in the transverse direction gets much smaller than the lengthscale along the strip. The transverse scalar gradient $\partial c/\partial n$ is thus much larger than the scalar gradient along the strip $\partial c/\partial \sigma$. We can thus neglect the term $v_\sigma \partial c/\partial \sigma$ in front of the term $v_n \partial c/\partial n$ in the advection term of equation (1.2) (Dimotakis & Catrakis (1999)). The same reasoning holds for the diffusion term such that the advection-diffusion equation (1.2) close to $\mathbf{x}_i$ becomes

$$\frac{\partial c}{\partial t} + \frac{n}{s_i}\frac{ds_i}{dt}\frac{\partial c}{\partial n} = D\frac{\partial^2 c}{\partial n^2} \tag{2.4}$$

This asymptotic partial differential equation has already been used in this form in the works mentioned in the Introduction. The impact of the flow is all concentrated in the rate of change of the striation thickness $d\ln s_i/dt$. This equation holds in flows which tend to form *elongated* structures (strips in two dimensions), as it is the case for most flows in nature, may they be random, or deterministic (see the early drawings of Welander (1955), and more recent observations, including in three dimensions, where the flow form *sheets* Buch Jr & Dahm (1996); Fountain *et al.* (1998)). It does not describe, however, regions of folded strips whose radius of curvature is of the order of their thichness. We will come back to this (negligible in practice) point in section 2.5. Equation (2.4) can be simplified by using a change of variable where the transverse distance n is non-dimensionalized by the striation thickness $\tilde{n} = n/s_i(t)$ and the time is counted in units of the current diffusion time $s_i(t)^2/D$ as

$$\frac{d\tau_i}{dt} = \frac{D}{s_i(t)^2} \tag{2.5}$$

The dimensionless time τ_i for the tracer $\mathbf{x}_i$ can be easily calculated numerically during the integration of the equation of motion (1.1) since the striation thickness s_i is known through (2.1). Using these new variables, the equation for the scalar c becomes a simple diffusion equation

$$\frac{\partial c}{\partial \tau} = \frac{\partial^2 c}{\partial \tilde{n}^2} \tag{2.6}$$

The initial condition at $\tau = 0$ (corresponding to $t = 0$) is $c(\tilde{n}) = c_0 \exp(-\tilde{n}^2)$. The solution is a Gaussian profile at any time, which can be rewritten as a function of the dimensional coordinate n as

$$c(n,t) = \frac{c_0}{\sqrt{1+4\tau_i(t)}} \exp\left(\frac{-n^2/s_i(t)^2}{1+4\tau_i(t)}\right) \tag{2.7}$$

It is thus sufficient to compute numerically the position of the tracers $\mathbf{x}_i$, the striation thickness s_i and the dimensionless time τ_i as a function of time by integrating equations (1.1), (2.1) and (2.5) to know the transverse profile of the scalar $c(n,t)$ across the strip, and thus to have access to the spatial distribution of the scalar initially contained in the strip. We will see in section 2.4 how to reconstruct numerically the scalar field $c(\mathbf{x},t)$ knowing these quantities.

The dimensionless time τ is proportional to the diffusivity D. It is thus sufficient to make a single numerical calculation with $D = 1$ to get the result for any diffusivity by multiplying τ_i by the desired value D at the end of the computation. The initial striation thickness s_0 can also be changed easily a posteriori since the striation thickness s_i is proportional to s_0 and the dimensionless time is proportional to s_0^{-2}.

2.2. *An example*

Let us take the simple example of a strip of initial thickness s_0 and length L_0, uniformly stretched at a rate γ. Its current length is $L(t) = L_0 e^{\gamma t}$ while its striation thickness

decreases as $s_0 e^{-\gamma t}$. According to equation (2.7), the maximal concentration in the strip (in $\tilde{n} = 0$) will start to decay when $\tau(t)$ becomes of order unity. From equation (2.5), one has

$$\tau(t) = \frac{D}{2\gamma s_0^2}\left(e^{2\gamma t} - 1\right) \tag{2.8}$$

and the condition $\tau(t_s) = \mathcal{O}(1)$ defines the *mixing time* t_s depending on a Péclet number Pe as

$$t_s = \frac{1}{2\gamma}\ln Pe \qquad \text{with} \qquad Pe = \frac{\gamma s_0^2}{D} \tag{2.9}$$

From this critical time, it is seen from equation (2.7) that the maximal concentration in the strip decays exponentially as

$$c(0,t) \sim e^{-\gamma(t-t_s)} \tag{2.10}$$

and that the strip transverse size remains constant and equal to

$$s(t_s) = \sqrt{\frac{D}{\gamma}} = s_0\, Pe^{-1/2} \tag{2.11}$$

the lengthscale equilibrating substrate compression and diffusion broadening. It is called the Batchelor scale (Batchelor (1959)).

2.3. *Strip refinement*

The strip diffusion method is based on the property that the strip will be stretched by the flow and thus becomes ever thinner and elongated. The main advantage is that it allows to neglect diffusion along the strip since concentration gradients in that direction essentially vanish. However, a direct consequence is that the distance between two consecutive tracers increases with time. We will see below that the total length of the strip increases linearly in time for the case of a vortex (section 2.6) and exponentially in time for the Sine flow (section 3). It is thus necessary to refine the strip such that it is always well represented geometrically. This refinement was implemented every ten time steps, and was thus very weakly time consuming.

The first idea would be to increase the number of points at each refinement such that the distance between two tracers $||\mathbf{x}_{i+1} - \mathbf{x}_i||$ is equal to a constant, say Δl. However, disordered flows bend the strip and create cusps with a very high curvature, as can be seen in Fig. 2 for the Sine flow. The refinement must then be denser in the regions with high curvatures. A good criterion is to refine the strip such that the distance between two consecutive points is equal to:

$$||\mathbf{x}_{i+1} - \mathbf{x}_i|| = \frac{\Delta l}{1 + \alpha\kappa} \tag{2.12}$$

where κ is the curvature of the strip and Δl and α are numerical constants. Δl corresponds to the distance between two tracers in the regions with low curvature. α governs the number of tracers in the regions with high curvature: the algorithm adds a number of points equal $\pi\alpha/\Delta l$ if the cusps makes a 180° turn. This refinement is illustrated on Fig. 2, where the distance between two consecutive points is much smaller at the cusp than in the other regions with low curvatures. The numerical method to do so is presented in appendix B.

This refinement has shown to be very efficient, even in the case of the Sine flow, which streches the strip exponentially in time and has thus a strong sensitivity to initial conditions. The main disadvantage is that the size of the variables ($\mathbf{x}_i$, s_i, τ_i) increases

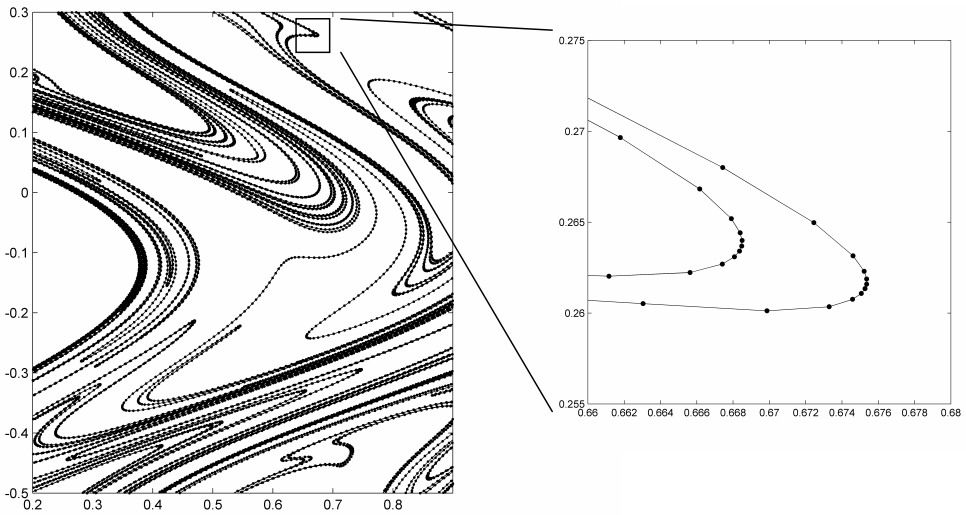

FIGURE 2. Example of the position of the strip in a disordered flow (Sine flow), showing the appearance of cusps along the strip. A zoom of a cusp shows that the distribution of points along the strips is denser at the cusp, i.e. when the curvature increases. The numerical constants defined by (2.12) are: $\Delta l = 0.01$ and $\alpha = 10\Delta l/\pi$.

with time and the algorithm gets slower and slower at late stages, although the algorithm is extremely fast to compute the early stages. However, we will see in the following that it is sufficient to reach the mixing time even for Péclet number up to 10^{10}. This allows to get very interesting properties of the diffusion process at these Péclet numbers, which would otherwise be impossible using standard algorithms.

2.4. *Reconstruction of the scalar field*

We have shown in section 2.1 how to calculate numerically the transverse profile $c(n)$ of a strip of scalar given by equation (2.7) by integrating a simple equation (2.5) for the dimensionless times τ_i during the integration of the motion of the tracers $\mathbf{x}_i$. We wish to reconstruct the spatial distribution of scalar using this information. The easiest method is to draw a line, with a color corresponding to the maximum of the transverse profile. This means that each segment $[\mathbf{x}_i\, \mathbf{x}_{i+1}]$ is plotted with a color corresponding to $c_0/\sqrt{1+4\tau_i}$. An example is plotted in Fig. 3(a) and shows that it gives a very good information on the position and concentration of the scalar. This method is extremely useful for large Péclet numbers, when the strip is so thin that its thickness get smaller than the resolution of the figure. Moreover, it is very fast and allows to draw a field of scalar almost instantaneously. However, this technique is not suitable as soon as several strips get so close to each other that their concentration profiles overlap.

We thus need to reconstruct the distribution of scalar on a 2D grid. This task is much more tedious than the previous technique. It is very demanding in memory since the grid must be as narrow as possible. And it is also very unstable at the cusps, where the model fails. The correct treatment of the cusps is detailed in section 2.5.

The first step is to reinterpolate the strip such that the distance between two tracers is constant and equal to Δl. In the reconstruction process, Δl was chosen equal to the mean thickness of the strip which is easily calculated numerically as $\langle s_i\sqrt{1+4\tau_i}\rangle$, with s_i the striation thickness. Once the tracers are equally spaced, the distribution of scalar

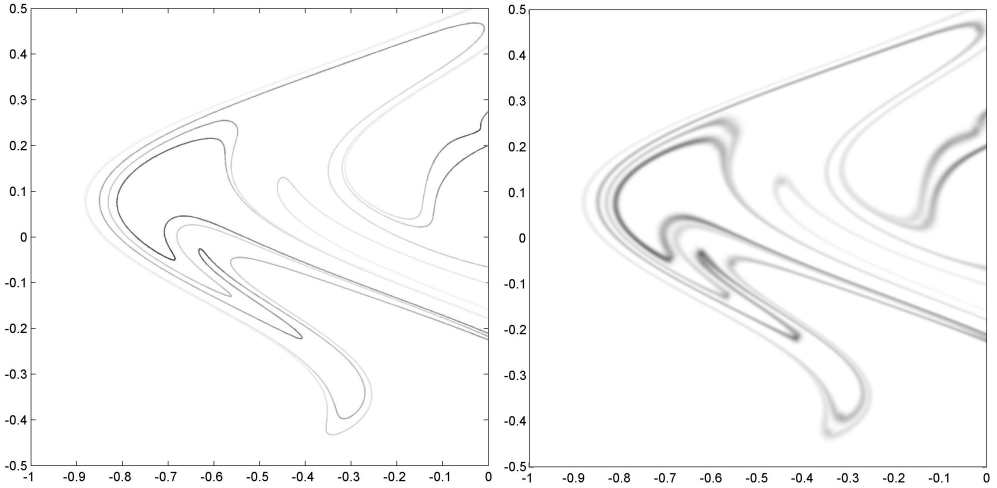

(a) (b)

FIGURE 3. Examples of the distribution of scalar obtained by plotting a line (a) and by reconstructing the scalar on a grid using Eq. (2.13). The distance Δl between two tracers during the reconstruction is equal to 0.0065 and the mesh size is equal to 0.001. The flow is a Sine flow at $t = 4$ and $Pe = 10^5$ and initial thickness of the strip is $s_0 = 0.05$.

can be reconstructed by adding small Gaussian ellipses centered on each tracer

$$c(\mathbf{x}) = \sum_i \frac{c_0/1.7726}{\sqrt{1+4\tau_i}} \exp\left\{ -\frac{[(\mathbf{x}-\mathbf{x}_i)\cdot\widehat{\sigma}_i]^2}{\Delta l^2} - \frac{[(\mathbf{x}-\mathbf{x}_i)\cdot\widehat{\mathbf{n}}_i]^2}{s_i^2(1+4\tau_i)} \right\} \tag{2.13}$$

Here, $\widehat{\sigma}_i$ and $\widehat{\mathbf{n}}_i$ are the unit vectors tangent and normal to the strip. The ellipses have a major axis oriented along the strip, with a parameter of the Gaussian profile equal to Δl. Their minor axis is normal to the strip with a parameter $s_i\sqrt{1+4\tau_i}$ as prescribed by the model. The constant 1.7726 is due to the overlap of the ellipses: since they are separated by Δl and have a Gaussian profile along the strip with a parameter Δl, the maximal concentration is overestimated by a factor $\sum_{j=-\infty}^{j=+\infty} \mathrm{e}^{-j^2} = 1.7726$. It can be noted that it is easier numerically to center the ellipses around the middle point of $[\mathbf{x}_i\,\mathbf{x}_{i+1}]$ since the unit vectors $\widehat{\sigma}_i$ and $\widehat{\mathbf{n}}_i$ are then easier to calculate.

An example of such a reconstruction is plotted in Fig. 3(b). The picture is similar to the one of Fig. 3(a). But here, the strip has a Gaussian transverse profile with the correct thickness. The overlap of the ellipses along the strip is not visible although they are separated by 5 times the mesh size. Different parts of the strip can mix together, for example at $\mathbf{x} = (-0.55, 0.15)$, which shows that the model is still valid in the case of strip overlap, or aggregation (see section 6.3 for a precise definition of this notion).

The strip is well defined in the regions with low curvatures. Its thickness is usually small when its concentration is small. This is consistent with the diffusion process since it corresponds to high stretching rates. The model thus describes well the diffusion of the strip although its calculation was not implemented on a 2D grid but only modeled assuming that the strip is thin. This assumption fails when the radius of curvature gets of the order of the thickness of the strip, i.e. at the cusps. These regions are treated separately in the next section.

2.5. *Post-treatment of cusps*

In regions with high curvature, the model fails because the thickness becomes of the order of the radius of curvature. There, the diffusion problem is no more essentially

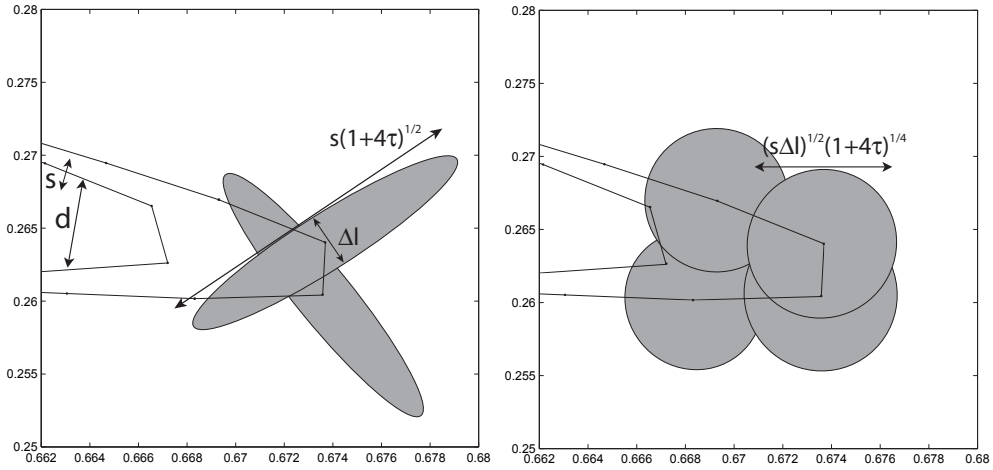

FIGURE 4. Regularisation of the scalar field around a cusp during the reconstruction process.

one dimensional, contrary to the assumption leading to equation (2.4). This poses two numerical problems in the reconstruction of the distribution of scalar. The first one arises even in the absence of diffusion, and comes from the superposition of the strip from both sides of the cusp. As shown in Fig. 4(a), if the distance d between these two sides of the cusp is smaller than twice the thickness s_i of the strip, there will be some overlap of these two parts of the strip and the concentration c of the scalar can be twice higher than the initial concentration c_0, which is not physical. The best way to prevent these overlaps is to reduce the thickness of the strip by reducing the initial thickness s_0. In our simulation, an initial thickness $s_0 = 0.05$ would lead to only 0.1% of the tracers where the distance d is smaller than twice s_i. For these points, the algorithm modifies the initial thickness only locally by decreasing s_i to $d/2$ and also changing the dimensionless time τ_i accordingly: it is multiplied by a factor $4s_i^2/d^2$ (since τ is proportional to s_0^{-2}). It is true that this procedure does not conserve the total quantity of scalar, but the loss was usually less than 0.1 %. This procedure does not modify at all the PDF of scalar or the spectra since these problems are localized in very small areas and do not contribute appreciably to the global quantities. This treatment is only necessary to prevent small dots of high concentration to appear in the spatial concentration distribution.

A second problem arises in the presence of diffusion. Indeed, for rather large diffusivities ($Pe < 10^5$), we observed some lines of high concentration of scalar centered around the cusps. They are represented schematically on Fig. 4(a) by the two gray ellipses centered around the two tracers of the cusp. Such a numerical problem arises when the thickness of the strip, equal to $s_i\sqrt{1+4\tau_i}$, is larger than the distance Δl between two consecutive tracers. We observed this phenomenon at only a few points of the scalar field (usually less than 10 cusps in the simulation of the Sine Flow in section 3), but these ellipses would contaminate the whole field. We thus treated them by replacing the ellipses by circles with the same area, such that the total quantity of scalar is conserved. This procedure was very efficient to solve this numerical problem, although it is not a clean treatment of theses cusps. However, as was said previously, these problems arise in very small areas and do not contribute appreciably to the global quantities such as PDF and spectra. It is thus sufficient to use these basic procedures. To properly treat these cusps, it might be possible to modify the model such that the diffusion is calculated numerically on a 2D mesh in the neighborhood of the cusp.

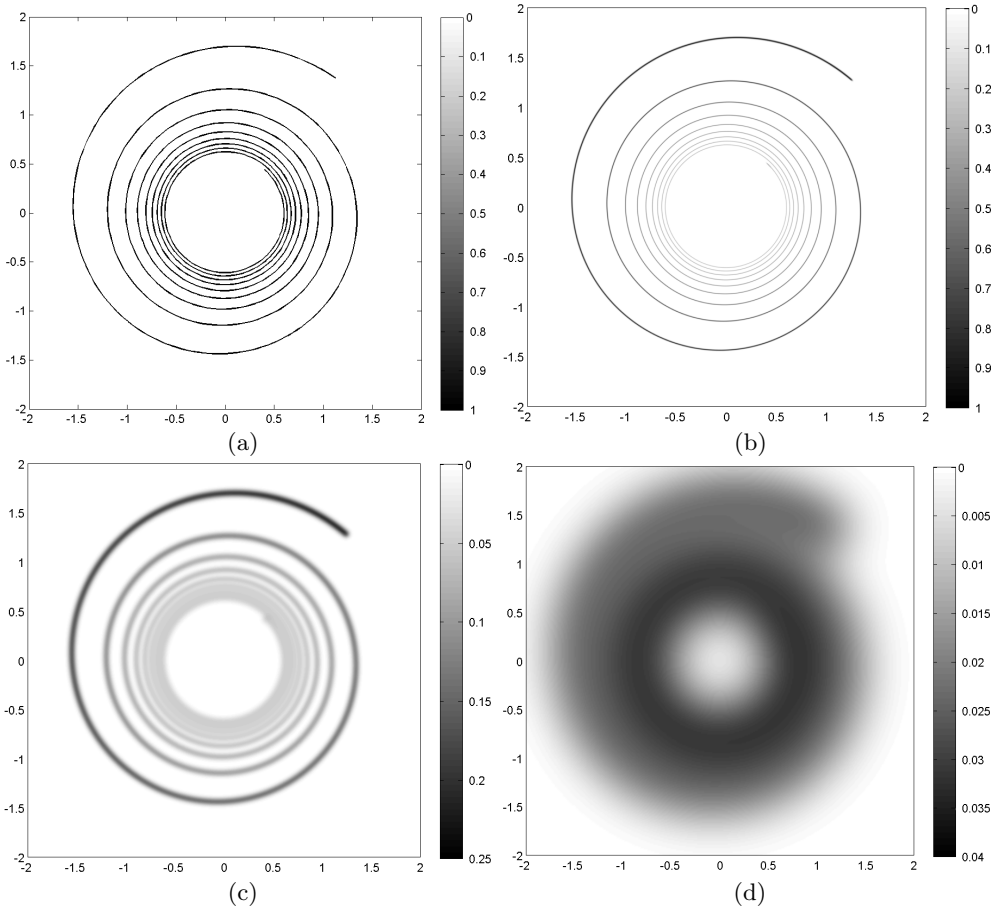

FIGURE 5. Spiral of scalar created by the roll-up of a strip around a point vortex with a circulation $\Gamma = 14.2$ cm^2/s at $t = 10$s. The diffusivity is equal to (a) $D = 10^{-8}$cm^2/s, (b) $D = 10^{-6}$cm^2/s, (c) $D = 10^{-4}$cm^2/s and (d) $D = 10^{-2}$cm^2/s. The scalar is injected initially along the x-axis with 0.6cm$< x <$ 1.8cm. The initial thickness of the strip is $s_0 = 0.11$cm. In (a), the strip is plotted as a line, whereas in (b,c,d), it is reconstructed on a 2D mesh.

2.6. *Validation: Flow in a point vortex*

In this section, meant to validate our method, we present the results of the strip diffusion method for the case of a point vortex with circulation $\Gamma = 14.2$ cm^2/s located in $\mathbf{x} = 0$, for which an experiment exists (Meunier & Villermaux (2003)). The scalar is injected initially along the x-axis in order to mimic the experiment. The initial thickness $s_0 = 0.11$ cm is chosen twice smaller than the experimental one ($s_0 = 0.22$ cm) such that the final theoretical profiles are equal. Indeed, in the original study of Meunier & Villermaux (2003), s_0 is the width of a square profile, whereas here, s_0 is the parameter of a Gaussian profile. Initially, the scalar is injected along the x-axis between $x = 0.6$ cm and $x = 1.8$ cm.

Figure 5 shows the distribution of scalar at $t = 10$ s for various diffusivities. As observed experimentally, the strip rolls up around the vortex center and creates a spiral. For a very small diffusivity ($D = 10^{-8}$ cm^2/s), the scalar has not yet reached the mixing time and the maximal concentration across the strip is equal to the initial concentration c_0 almost everywhere (Fig. 5a). For a slightly larger diffusivity ($D = 10^{-6}$cm^2/s), the

scalar has started to diffuse and its maximal concentration has decreased at some locations close to the vortex center. Since the stretching is larger at the center than at the periphery, the diffusion is faster and the concentration smaller there. This is very similar to the experimental result of Meunier & Villermaux (2003) except that here the strip contains more turns because the scalar is located closer to the vortex center. For even larger diffusivities ($D = 10^{-4}\mathrm{cm}^2/\mathrm{s}$), the scalar has a much lower concentration (note the change in the colorbar) and the strip starts to mix with itself at the center of the vortex. At a very high diffusivity ($D = 10^{-2}\mathrm{cm}^2/\mathrm{s}$), the aggregation of the strip is generalized to the whole area, which creates a ring of scalar. The scalar has a higher concentration close the center, since it is spread on an area smaller that at the periphery (proportional to the radius). It can be noted that the numerical simulation describes well (at least qualitatively at this stage) the aggregation of the strip. However, we expect the ring to become a single circular patch at even larger diffusivities (without a hole at the center), but this case cannot be described by the model since it corresponds to a thickness of the strip of the order of the curvature radius.

To compare the numerical results quantitatively with the experiment, we have plotted the maximal concentration as a function of the radius in Fig. 6. The numerical values (plotted as small black symbols) are in excellent agreement with the experimental and theoretical data taken from Fig. 4(a) of Meunier & Villermaux (2003). However, for this figure, the maximal concentration has been taken equal to $c_0\mathrm{erf}(1/\sqrt{4\tau})$ instead of $c_0/\sqrt{1+4\tau}$ as in equation (2.7) since it is the solution for a square initial transverse profile with a width $2s_0$. The numerical values are slightly smaller than the theory at large r and slightly larger for small r. But this error remains smaller than 3% and might be due to numerical errors during the advection of the tracers $\mathbf{x}_i$. We now use this method to study a more complex flow, where no analytical solution is available.

3. Mixing in a Sine flow

In the rest of the paper, we will analyze a case study of mixing at high Péclet number, taking advantage of the new numerical technique of strip diffusion. The aim is to link the local properties of stretching enhanced diffusion of a strip well captured by the numerical technique, to the global properties of the mixture such as spectra and Probability Distribution Functions (PDF) for a prototype chaotic flow to understand, using this new tool, how the complex mixture at a given stage of its development has been built from elementary objects (the stretched strips) and an appropriate interaction rule.

3.1. *Definition of the Sine flow*

We have chosen to analyse the case of a Sine flow, since it has been commonly studied using several numerical methods (tracking of tracers and spectral methods). Moreover, it is well known for its chaotic mixing behavior at high enough velocities. The Sine flow (or random wave flow, Zeldovich (1982)) consists of alternating vertical and horizontal sinusoidal shear flows. The randomness of the flow is introduced via phases χ^x and χ^y, which are chosen randomly at each period, as introduced by Jean-Luc THIFFEAULT & GIBBON (2004). The flow is defined as:

$$(v_x, v_y) = V_0\ [0, \sin(2\pi x + \chi^x_m)] \quad \text{for } m < t < m + 1/2 \tag{3.1}$$

$$(v_x, v_y) = V_0\ [\sin(2\pi y + \chi^y_m), 0] \quad \text{for } m + 1/2 < t < m + 1 \tag{3.2}$$

where the integer m is the period number, t is time and the amplitude of the flow V_0 is chosen equal to $1/\sqrt{2}$ in order to be in a chaotic regime (see Alvarez *et al.* 1998). The phases are chosen randomly between 0 and 2π. Their values are given in table 1. By

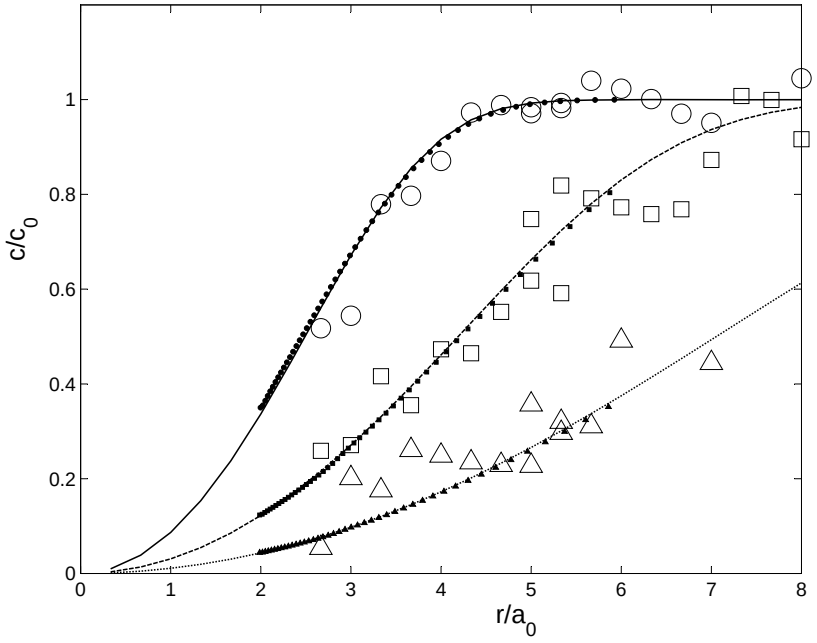

FIGURE 6. Maximal concentration of the scalar along the strip as a function of the radius at $t = 5$s (circles), $t = 10$s (squares) and $t = 20$s (triangles). Experimental data (open symbols) and theoretical predictions (lines) are taken from Meunier & Villermaux (2003). Numerical results (black filled symbols) are obtained with a diffusivity ($D = 5\ 10^{-6}\text{cm}^2/\text{s}$). The experimental vortex core size a_0 is equal to 0.3cm.

m	0	1	2	3	4	5	6
χ^x	1.2154	4.2865	1.9023	3.4034	0.9480	4.3850	2.3774
χ^y	3.1199	5.6534	5.1624	4.0521	5.1395	4.1483	2.1487

TABLE 1. Phases of the Sine flow in the x and y direction at each period m.

'chaotic', we mean that the flow will not leave place for segregated, unmixed islands at long times and that, although the flow will generate a non-trivial concentration distribution $P(c)$ (defined in section 6), that distribution will ultimately converge toward a Dirac Delta centered around the average concentration $\langle c \rangle$

$$P(c) \xrightarrow[t\to\infty]{} \delta(c - \langle c \rangle) \tag{3.3}$$

that is, in the language of Ergodic Theory, toward a measure of uniform probability over the whole domain. In that sense, the flow in equation (3.2) is 'mixing' (Arnold & Avez (1967)).

A strip of scalar is introduced at $t = 0$ along the x-axis between $x = -0.5$ and $x = +0.5$. The initial transverse profile is supposed to be Gaussian ($c(y) = c_0 \mathrm{e}^{-y^2/s_0^2}$) with an initial thickness equal to $s_0 = 0.05$. The evolution of the scalar is governed by the advection-diffusion equation (1.2) where the diffusivity D defines the Péclet number as

$$Pe = 1/D, \tag{3.4}$$

meaning that the lengthscale is chosen equal to the wavelength (equal to 1), and the typical velocity is chosen equal to $V_0\sqrt{2}$.

3.2. *Temporal evolution*

Figure 7 shows the distributions of scalar at various times for a moderate Péclet number ($Pe = 10^5$). The strip, initially straight, is bent and stretched by the flow. After one period, its thickness has decreased due to the compression in its transverse direction. However, the maximal concentration is still equal to the initial concentration c_0 since the mixing time has not yet been reached. After two periods, the scalar has started to diffuse, leading to a grey color of the strip. This diffusion is a proof that the mixing time has been reached, i.e. that the dimensionless time τ is of the order of one or larger. The strip is thinner than after one period, and several parts of the strip get closer to each other. However, there is no reconnection of the strip with itself.

After 4 periods (Fig. 7c), the strip has a very disordered shape. It is bent in many places and contains a few cusps. Different parts of the strip are so close that they have mixed because of diffusion. It is almost invisible except at the locations where the different parts separate, as can be seen at the upper left loop ($x = -0.7$, $y = 1.2$). The concentration of the scalar becomes smaller and smaller, and there is no remaining parts still bearing the initial concentration c_0. The thickness of the strip remains blocked at the Batchelor scale $\sqrt{D/\gamma}$ (see equation (2.11)), γ being the stretching rate of the strip, as soon as the diffusion has started.

After 7 periods (Fig. 7d), the strip has been bent and reconnected many times. It spreads on a large domain and very well shows the chaotic behavior of the flow. The concentration is very small, such that the scalar is almost completely diluted in the surrounding medium.

3.3. *Influence of the Péclet number*

The main advantage of the strip diffusion method is that the diffusivity can be varied a posteriori by simply tuning the dimensionless time τ accordingly. It is thus extremely easy to plot the distributions of scalar at any diffusivity (as high as wished in particular). Two examples are given in Fig. 8 for $Pe = 10^7$ and $Pe = 10^{10}$. Such numerical simulations are impossible to do using a spectral code, since the number of points needed would be too high. Indeed, it was impossible to reconstruct the scalar field on a 2D mesh, and the strip has only been plotted as a line in Fig. 8. However, it is possible to reconstruct the scalar field in 2D on a smaller area. This is shown in the insets of Fig. 8 and proves that the results are correct although it is impossible to visualize them on the whole field.

At a Péclet number equal to 10^7, the strip has reached the mixing time in some places, but some parts of the strip seem to have a concentration equal to c_0. The inset shows that the strip has reconnected with itself, leading to a rather blurry picture. On the contrary, for $Pe = 10^{10}$, the different parts of the strip remain separate, even at the upper left corner of the inset, where two lines are extremely close, but also extremely thin. This is in agreement with the fact that the mixing time has not been reached there, which prevents the reconnection of the strip (due to the flow incompressibility). At such a high Péclet number, the mixing time has not been reached almost everywhere, and the concentration is equal to c_0 almost everywhere. It is clear on this figure that the spatial distribution of scalar is very complex and contains a lot of information, which is why the numerical simulation gets very slow at these late stages. We are using in the following these informations to analyse the mixing properties of the flow and relate them to the stretching of the strip.

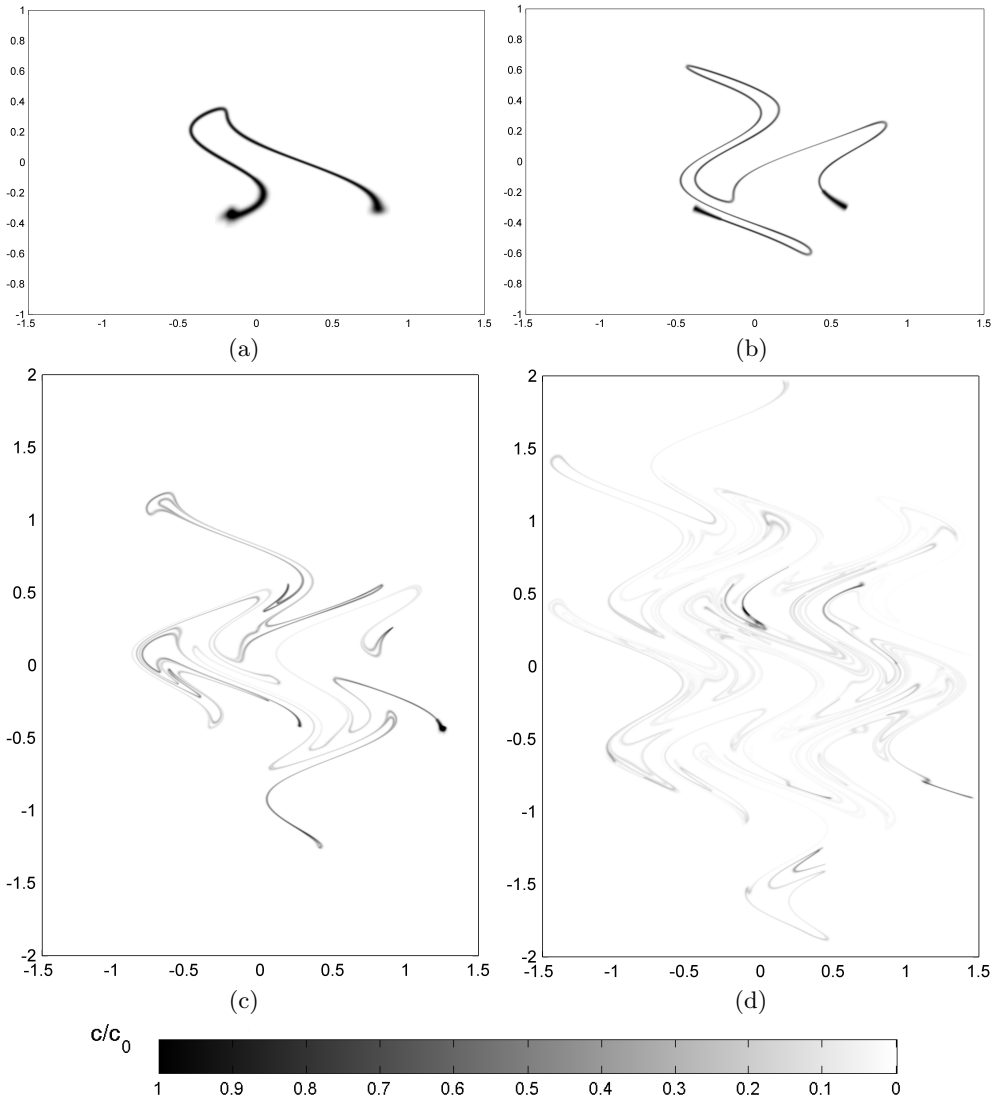

FIGURE 7. Temporal evolution of a strip of scalar in a Sine flow for a Péclet number equal to 10^5. The fields of the scalar are given at (a) $t = 1$, (b) $t = 2$, (c) $t = 4$ and (d) $t = 7$.

4. A simple model of stretching

4.1. *Temporal evolution of the strip length*

It is well known that in a chaotic stirring flow sustaining a series of stretchings an foldings, a strip of scalar is stretched exponentially in time; this is the paradigm of the Baker Transform (Ottino (1989)). More generally, a succesion of random motion distributed in intensity and direction results in a global exponential lengthening of material lines (Kraichnan (1974); Duplat & Villermaux (2000)). This is very well confirmed in the present Sine flow, where the total length L of the strip increases as $\mathrm{e}^{\gamma t}$, as shown in Fig. 9. The numerical value of the mean stretching rate can be obtained accurately $\gamma = 0.91 \pm 2\%$. This value will be the only constant needed for the theory developed in the following.

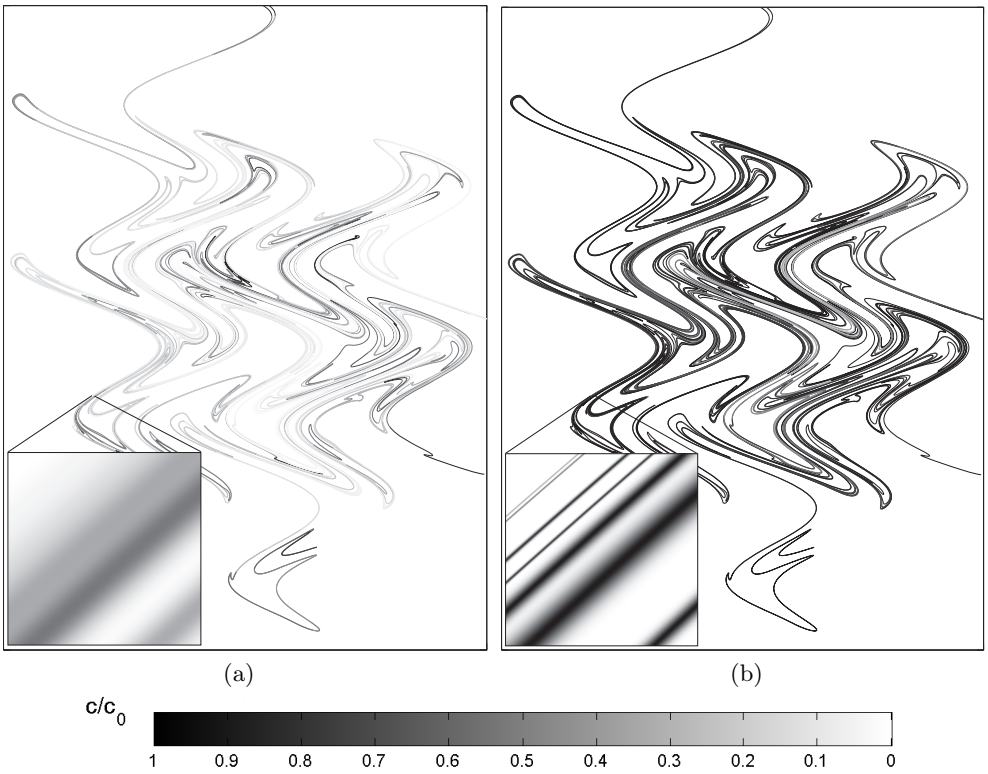

FIGURE 8. Distribution of a scalar in a Sine flow at $t = 7$ for (a) $Pe = 10^7$ and (b) $Pe = 10^{10}$. Due to a lack of printing resolution, the thickness of the strip has not been respected: the strip has been plotteed as a line. However, the image has been zoomed 200 times in the inset to show the correct thickness of the strips.

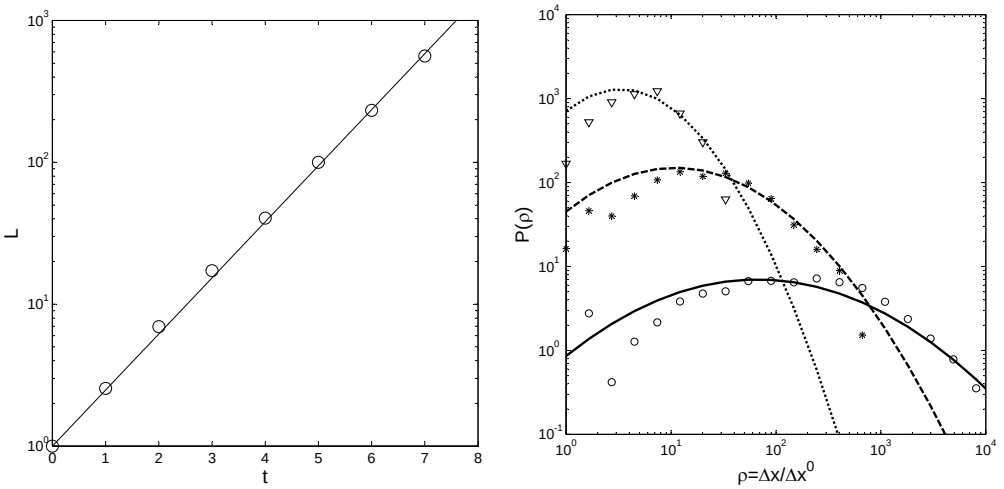

FIGURE 9. Left: Total length of the strip as a function of time. The solid line corresponds to an exponential growth with a mean stretching rate $\gamma = 0.91$. Right: PDF of elongation of the strip for $t = 2$ ($\bigtriangledown$, dotted line), $t = 4$ ($\star$, dashed line) and $t = 7$ ($\circ$, solid line). Lines correspond to the theoretical prediction of Eq. (4.7).

4.2. *PDF of stretching factors*

The total length of the strip is a global characteristic which does not give any information about the variation of the elongation ρ along the strip, which are distributed according to a well defined Probability Distribution Function (PDF) $P(\rho)$. It is defined as the probability to find a point on the final strip, where the strip has been stretched by a factor $\rho = \Delta x/\Delta x^0$. Since the final refinement is done such that the tracers are equally spaced along the strip, $P(\rho)$ is easily calculated as the number of tracers for which $\Delta x/\Delta x^0$ is in the interval $[\rho,\, \rho + \mathrm{d}\rho]$ divided by $\mathrm{d}\rho$. These PDF are plotted for $t = 2$, 4 and 7 in Fig. 9. The numerical results seem to be parabolic in this logarithmic scale, which means that $P(\rho)$ is a Gaussian function of $\log(\rho)$. It is clear that the parabola get wider as time increases. Moreover, $\log(\rho_M)$ increases linearly in time, where ρ_M is the most probable stretching.

4.3. *Multistep stretching*

The above result and shape of $P(\rho)$ is readily understood. Let us split the stretching of the strip at one point into N successive random stretching operations. We assume that a given tracer of the strip experiences a stretching ρ_1 between $t = 0$ and $t = \delta t$, a stretching ρ_2 between $t = \delta t$ and $t = 2\delta t$... The total stretching ρ of the strip after N operations is thus the product of the elementary stretchings: $\rho = \prod \rho_i$. If we assume that the stretching operations are random and independent, the stretching rate ρ has a log-normal law in virtue of the central limit theorem. This means that the probability $Q(\rho)$ that a point on the **initial** strip is stretched by a factor ρ is given by $Q(\rho) = \exp[-(\log(\rho) - N\mu)^2/2N\sigma^2]/\rho\sigma\sqrt{2\pi N}$. where μ and θ are the mean and the variance of $\log(\rho)$. However, the probability $P(\rho)$ that a point on the **final** strip has experienced a stretching ρ is proportional to $\rho Q(\rho)$ because the elementary length of such an interval has been multiplied by ρ, thus weighting the probability by a factor ρ. Since the number N of elementary stretchings is proportional to the time t in a permanently stirred flow, one can rewrite the probability $P(\rho)$ as

$$P(\rho) = A \exp\left[-\frac{(\log\rho - \gamma_p t)^2}{4\kappa t}\right] \tag{4.1}$$

where $\gamma_p = N\mu/t$ is the most probable stretching rate, $\kappa = N\theta/t$ corresponds to a diffusion of the stretching factors, and A is a normalising constant. This result has been derived, also assuming that the stretching is operated in multiple discrete steps by Kalda (2000), who showed that the probability $P(\log\rho)$ is the solution of a diffusion-advection equation

$$\frac{\partial P}{\partial t} + \gamma_p \frac{\partial P}{\partial \log\rho} = \kappa \frac{\partial^2 P}{(\partial \log\rho)^2} \tag{4.2}$$

The advective term $\gamma_p \partial P/\partial(\log\rho)$ corresponds to a constant average stretching of the strip meaning that the average length of the the strip ρ increases with time as $\mathrm{e}^{\gamma_p t}$. The diffusive term $\kappa\partial^2 P/(\partial\log\rho)^2$ comes from the distribution of the stretching intensities in the flow, which is progressively explored by the strip as time progresses. Indeed, a subpart of the strip can be stretched at a rate slower or faster than γ_p, and this alternatively and randomly as time evolves. The net result is a diffusion of an initial stretching $\log\rho$ to neighboring stretchings, with an apparent rate κ reflecting the width of the distribution of the stretching rates.

4.4. *Link with Richardson's dispersion*

An interesting analogy can also be drawn with Richardson's vision of pair dispersion in random flows (Richardson (1926)). Richardson proposed that the distribution of the distance r between pairs of particles (tracers) $P(r,t)$ at time t is ruled by a diffusion equation with an effective diffusion coefficient $\mathcal{D}(r)$ depending solely on r as

$$\frac{\partial P(r,t)}{\partial t} = \frac{1}{r}\frac{\partial}{\partial r}\left[\mathcal{D}(r)\, r \frac{\partial P(r,t)}{\partial r}\right] \tag{4.3}$$

in two dimensions. Equation (4.3) can also be written

$$\frac{\partial P(r,t)}{\partial t} = \frac{1}{r}\frac{\partial \mathcal{D}(r)}{\partial r}\frac{\partial P}{\partial \log r} + \frac{\mathcal{D}(r)}{r^2}\frac{\partial^2 P}{(\partial \log r)^2} \tag{4.4}$$

Now, for smooth flows (also called the Batchelor régime, a régime in which the Sine flow is likely to fall), those for which the velocity gradient $|\nabla \mathbf{v}|$ is constant and thus where typical velocity difference $|\delta v(r)|$ is expected to increase in proportion of r itself as, say, $|\delta v(r)| = \kappa r$, the diffusion coefficient is $\mathcal{D}(r) = |\delta v(r)|\, r = \kappa r^2$. In that case, equation (4.4) coincides formally with equation (4.2) provided

$$\gamma_p = 2\,\kappa \tag{4.5}$$

since the probability $P(r,t)$ to have a distance r between two particles corresponds to the probability $P(\rho,t)$ that a strip has been stretched by a factor ρ at time t. This result is consistent in smooth flows where stirring is dominated by a single lengthscale and where no small scale activity in the underlying velocity field contributes to the wrinkling of an advected material line. This result is no more true in rough, multiscale flows (Villermaux & Gagne (1994)). The result (4.5) above is easily generalized to any dimensions of space d and one has (Falkovich *et al.* (2001))

$$\gamma_p = d\,\kappa \tag{4.6}$$

a relationship which has the interesting consequence that the parameters describing the stretching field of the flow (γ_p, κ) reduce to a single parameter†.

4.5. *Conclusion*

A direct consequence of the stretching model above is that the length of the strip increases exponentially in time (since $L(t) = L_0 \int \rho Q(\rho,t)\mathrm{d}\rho$), with a mean stretching rate equal to $\gamma = \gamma_p + \kappa$. Using this relation and the link between γ_p and κ in equation (4.5), one can give explicitly the constants of the model as a function of the mean stretching rate γ, which has been determined numerically accurately. The model does not contain any fitting parameter any more, since the normalising constant A can also be calculated explicitly. The probability $P(\rho)$ that a point on the **final** strip has been stretched by a factor ρ is given by

$$P(\rho) = \frac{\mathrm{e}^{-\gamma t}}{\sqrt{4\pi\gamma t/3}} \exp\left[-\frac{(\log\rho - 2\gamma t/3)^2}{4\gamma t/3}\right] \tag{4.7}$$

This law is plotted in Fig. 9 at various times. The agreement with the numerical simulations is fair. In particular, the most probable stretching factor is correctly predicted as a function of time, although a best fit would give a most probable stretching rate

† Jaan Kalda (Private communication, 2008) has given a straightforward way to derive (4.6) by considering a space-filling stationary flow in a closed box for which $P(r) \sim r^d$ and relating it to the stationary solution $P(r) \sim r^{\gamma_p/\kappa}$ of (4.2).

$\gamma_p = 0.7$ instead of $\gamma_p = 2\gamma/3 = 0.6$ as expected from the model. The broadening of the PDF is also fairly well predicted, although a best fit would give a diffusivity $\kappa = 0.22$ instead of $\kappa = \gamma/3 = 0.3$ from the model. This result suggests that the hypothesis of a Richardson's pair dispersion of section 4.4 (which we have not checked directly) is fairly consistent with the data.

We now use this model to infer global quantities of the concentration field, which we compare to the simulation.

5. Spectrum of the scalar

We analyze the energy spectra of the scalar advected by the Sine flow presented in section 3, and relate them to known results and issues.

5.1. *Construction of the spectrum*

The one-dimensional energy spectrum $\Gamma(k)$ of the scalar is defined (see, e.g. Batchelor 1959) as the total 2D spatial spectrum $\Phi(\mathbf{k}')/2$ contained in an annulus of width $\mathrm{d}k$ divided by $\mathrm{d}k$

$$\Gamma(k)\mathrm{d}k = \int\int_{k<||\mathbf{k}'||<k+\mathrm{d}k} \frac{1}{2}\Phi(\mathbf{k}')\mathrm{d}\mathbf{k}' \tag{5.1}$$

The spatial spectrum $\Phi(\mathbf{k})$ is usually defined as the Fourier transform of the auto-correlation function of the scalar $\langle c(\mathbf{x})c(\mathbf{x}+\mathbf{r})\rangle_{\mathbf{x}}$. However, it is also equal to the squared modulus of the Fourier transform $\tilde{c}(\mathbf{k})$ of the scalar, due to the properties of the auto-correlation function

$$\Phi(\mathbf{k}) = \frac{1}{4\pi^2}\int\int_{-\infty}^{+\infty} \mathrm{e}^{-\mathrm{i}\mathbf{k}\cdot\mathbf{r}}\langle c(\mathbf{x})c(\mathbf{x}+\mathbf{r})\rangle_{\mathbf{x}}\mathrm{d}\mathbf{r} = \frac{4\pi^2}{\mathcal{A}}|\tilde{c}(\mathbf{k})|^2 \tag{5.2}$$

where $\mathcal{A}$ is the total area of the domain of the simulation. Numerically, it is easy to compute the 2D energy spectrum $\Phi(\mathbf{k})$ from the FFT of the scalar distribution $c(\mathbf{x})$, which has been reconstructed on a 2D grid. The 1D spectrum is then calculated by integration on an annulus of width $\mathrm{d}k$. However, this method is very demanding in memory since it creates a 2D matrix of the scalar, whereas the strip is defined on a 1D vector.

An alternative way is to use the fact that the scalar distribution is defined as a sum of ellipses with a Gaussian shape as can be seen in Eq. (2.13). Since the Fourier transform of a Gaussian is Gaussian, one can calculate directly $\tilde{c}(k)$ from (2.13) as a sum over the tracers $\mathbf{x}_i$ (using a change of variable $\mathbf{x}' = \mathbf{x} - \mathbf{x}_i$ in the integral over $\mathbf{x}$):

$$\tilde{c}(\mathbf{k}) = \sum_i \frac{c_0 \Delta l s_i}{4\pi \times 1.7726}\ \mathrm{e}^{-(\mathbf{k}\cdot\tilde{\sigma_i})^2\Delta l^2/4}\ \mathrm{e}^{-(\mathbf{k}\cdot\tilde{n_i})^2 s_i^2(1+4\tau_i)/4}\ \mathrm{e}^{-\mathrm{i}\mathbf{k}\cdot\mathbf{x}_i} \tag{5.3}$$

We recall that $\tilde{\sigma_i}$ and $\tilde{n_i}$ are the unit vectors tangent and normal to the strip, Δl is the distance between two tracers, s_i is the striation thickness and τ_i the dimensionless time. Since $\tilde{c}(\mathbf{k})$ is here given by an analytical expression (and not a matrix), it is very simple to calculate the spectrum at a given wavenumber k by integrating on a circle in the 2D wavevector coordinates

$$\Gamma(k) = k\int_{\theta=0}^{\theta=2\pi} |\tilde{c}(k\cos\theta, k\sin\theta)|^2 \mathrm{d}\theta \tag{5.4}$$

In our simulations, this formula is discretized on 20 or 50 angles θ, depending on the accuracy needed. The main advantage of this method is that it calculates the energy

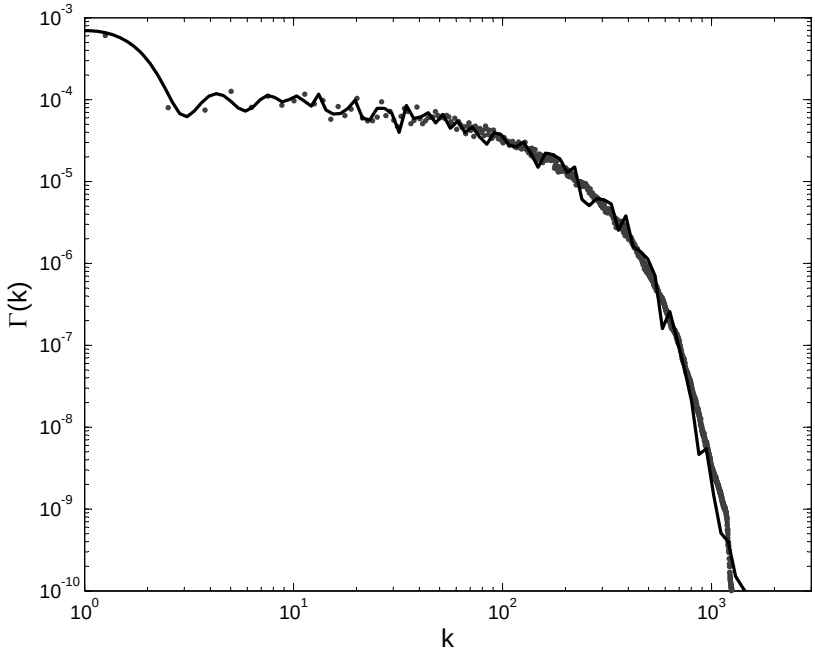

FIGURE 10. Energy spectrum of the scalar at $t = 7$ for $Pe = 10^5$. The spectrum is calculated by FFT of the scalar spatial distribution (grey symbols) and directly by integration along the strip using Eq.(5.3) (black solid line).

spectrum at each wave number k independently, unlike the method using a numerical FFT of the scalar distribution. The needs in memory is thus very low and the spectra can be calculated on as many decades as wanted. Moreover, the distribution of wave numbers can be chosen exponential, which is very interesting for spectra in logarithmic scale.

An example of a spectrum is plotted in Fig. 10 using the two numerical methods described previously. The method using an FFT of the reconstructed 2D scalar field (plotted as symbols) is particularly good at large wavenumbers, since the integration over the annulus of width dk contains many numerical data at large k (leading to an efficient averaging). However, this method gives very few points at low wave number, since k is a multiple of $2\pi/\mathcal{L}$, where the size of the domain $\mathcal{L}$ cannot be taken too large. This method can only give the spectrum over 3 decades, since the maximum size of a 2D matrix is 4096^2.

The method based on an analytical value of $\tilde{c}(k)$ is very efficient at low wave number: it gives an almost continuous description of the spectrum, due to the very dense number of data at low k. At high wavenumber, there seem to be some numerical oscillation of the spectrum compared to the other method. This comes from the limited number of angles θ in the discretization of the integration over an annulus, and can be reduced by using more angles (up to 200 angles). The agreement between the two methods is excellent, which validates the second method. In the following, we will use this alternative method only since it is faster and more accurate.

5.2. *Spectrum of a forced scalar*

Figure 11 shows the energy spectrum of a scalar in a Sine flow for three different Péclet numbers. A new strip of scalar has been injected at each period of the Sine flow to

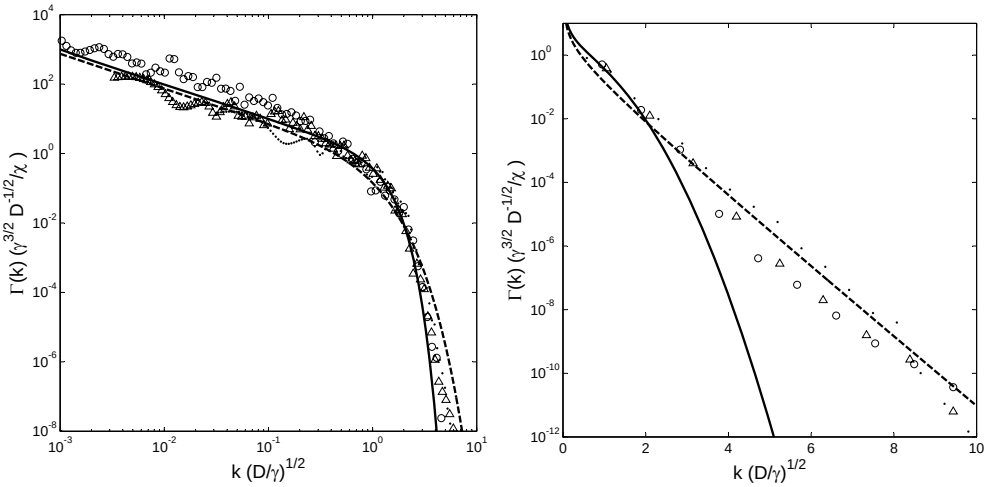

FIGURE 11. Energy spectrum of the scalar at $t = 7$, in a simulation where a new strip of scalar is injected at $t = 0, 1, 2, 3, 4, 5, 6$, to mimic sustained turbulence. The Péclet number is equal to $Pe = 10^3$ (•), $Pe = 10^5$ (△) and $Pe = 10^7$ (◯). The solid line corresponds to the Batchelor spectrum (5.5) and the dashed line corresponds to the solution (5.8) proposed by Kalda (2000) for sustained turbulence. The scale for the wavenumber is (a) logarithmic and (b) linear.

mimic forced turbulence and reach a stationary state. In this way, there is a constant injection of energy at low wavenumber, which is transferred to high wavenumbers by a direct cascade. This is consistent with the mechanism presented by Batchelor (1959): the wavenumbers increase, due to the stretching of the strip, up to the scale where the scalar is dissipated (equation (2.11)). In this picture where the scalar variance is conserved as k increases, the spectrum of a scalar is given by

$$\Gamma(k) = \frac{\chi}{\gamma k} \mathrm{e}^{-Dk^2/\gamma} \tag{5.5}$$

a result which holds for smooth flows characterized by a single mean stretching rate γ and the dissipation rate χ

$$\chi = 2D \int_0^\infty k^2 \Gamma(k) \mathrm{d}k \tag{5.6}$$

This prediction is plotted in Fig. 11 as a solid line. It is in excellent agreement with the numerical results, which present a k^{-1} spectrum on three decades in the so-called 'viscous-convective' subrange (above the Batchelor scale). This clear evidence is possible since the Péclet number is high (up to 10^7). It is less clear on the simulations made at small Péclet number ($Pe = 10^3$), where the slope k^{-1} is hardly visible on one decade.

At high wavenumbers, the spectrum presents a cut-off around the Batchelor wavenumber $\sqrt{\gamma/D}$. However, the numerical results lie above the Batchelor spectrum (5.5) at high wavenumber. This disagreement is even more visible when plotting the spectrum using a linear scale for the wavenumber (Fig. 11a). The numerical results show that the spectrum has an exponential decay e^{-k} instead of e^{-k^2}. This exponential behavior is consistent with Kraichnan (1974) who generalized the result of Batchelor (1959) to the case of a random stretching field, leading to an exponential decay of the spectrum (see also Toussaint *et al.* (2000) and Yeung *et al.* (2002)). This is qualitatively understood by the fact that a distribution of stretching rates γ leads to a distribution of Batchelor scales $\sqrt{D/\gamma}$, thus broadening the spectrum at high wavenumbers in a continuous fash-

ion, and stretching the cut-off from e^{-k^2} to e^{-k}. This result can be recovered in a simple way by using the equation (4.2) for the PDF of stretching rate $P(\rho)$, as proposed by Kalda (2000). Indeed, in the absence of diffusion, the quantity $k\Gamma(k)$ remains unchanged during the stretching by the flow, whereas the wave-number is multiplied by the same amount as the stretching factor ρ. The PDF of stretching rate and $k\Gamma$ are thus governed by the same differential equation (4.2). However, the presence of diffusion adds a decaying term in the equation for $k\Gamma$ with a decay rate equal to $-2Dk^2$, which leads to the following equation for $k\Gamma$

$$\frac{\partial(k\Gamma)}{\partial t} + \frac{2\gamma}{3}\frac{\partial(k\Gamma)}{\partial(\log k)} = \frac{\gamma}{3}\frac{\partial^2(k\Gamma)}{\partial(\log k)^2} - 2Dk^2(k\Gamma) \tag{5.7}$$

As explained in section 4, γ is the mean stretching rate of the strip, and has been calculated numerically very accurately for the Sine flow ($\gamma = 0.91$). The stationary solution of this equation is given by a Hankel function of order 1 (Kalda 2000)

$$\Gamma(k) = AH_1^{(1)}\left(\mathrm{i}k\sqrt{6D/\gamma}\right) \tag{5.8}$$

where $A = H_1^{(1)}(\mathrm{i}\sqrt{6D/\gamma})^{-1}$. This solution scales as $k^{-1}\mathrm{e}^{-k\sqrt{6D/\gamma}}$ at high wavenumbers, i.e. for $k \ll \sqrt{\gamma/D}$. This exponential decay corresponds to the result predicted by Kraichnan (1974) and is now tightly linked to the distribution of stretchings itself. This solution (5.8) is plotted in Fig. 11 as a dashed line. It is, as expected, in very good agreement with the numerical results at small wavenumbers (since it decays as k^{-1} like the Batchelor spectrum). It is also in excellent agreement at higher wavenumbers, as can be seen in Fig. 11(b), where the scale of the wavenumber is linear.

It might be surprising that the spectrum has an exponential decay at late stages. Indeed, the PDF of stretching factors $P(\rho)$ becomes more and more peaked as time evolves, since the variance $\langle(\log\rho - \langle\log\rho\rangle)^2\rangle^{1/2}$ increases slower (as $\sqrt{t}$) than the mean stretching factor $\langle\log\rho\rangle$ (which increases as t). The spectrum should thus tend toward the Batchelor spectrum at late stages (with a cut-off as e^{-k^2}). However, even if a strip is stretched by a factor ρ over a period t, it does not mean that the stretching rate is constant and equal to $\gamma = (\log\rho)/t$. The variation of the stretching rate with time induces a variation of the Batchelor scale $\sqrt{D/\gamma}$, which broadens the final spectrum although the stretching factors (integrated over time) are all equal.

5.3. *Spectrum of a decaying scalar*

We now turn to the case of the energy spectrum of the scalar when the strip is injected at $t = 0$ only, as was described in section 3. This is now a decaying field. Figure 12 shows the spectrum of the scalar field at $t = 7$ for three different Péclet numbers. It is clear that the numerical results are below the Batchelor spectrum (5.5) at low wavenumbers. This comes from the fact that the energy present at small wavenumbers at $t = 0$ has moved toward the large wavenumbers, thus creating a defect of energy at low wavenumbers since there is no injection of energy there. The disagreement is especially visible at high Péclet number ($Pe = 10^7$) since the spectrum is resolved on three decades in k.

For a decaying scalar, the differential equation (5.7) is still valid, but we don't look for a stationary solution which respects a boundary condition at $k = 0$. We instead look for a decaying solution which respects an initial condition at $k\Gamma(k, t = 0) = \delta(\log k)$, meaning that all the energy is in the initial lengthscale ($k = 1$) at $t = 0$. Kalda (2000) showed that the solution tends toward a Hankel function of order 0 at late stages

$$\Gamma(k) = \mathrm{i}\mathrm{e}^{-\gamma t/3}H_0^{(1)}\left(\mathrm{i}k\sqrt{6D/\gamma}\right) \tag{5.9}$$

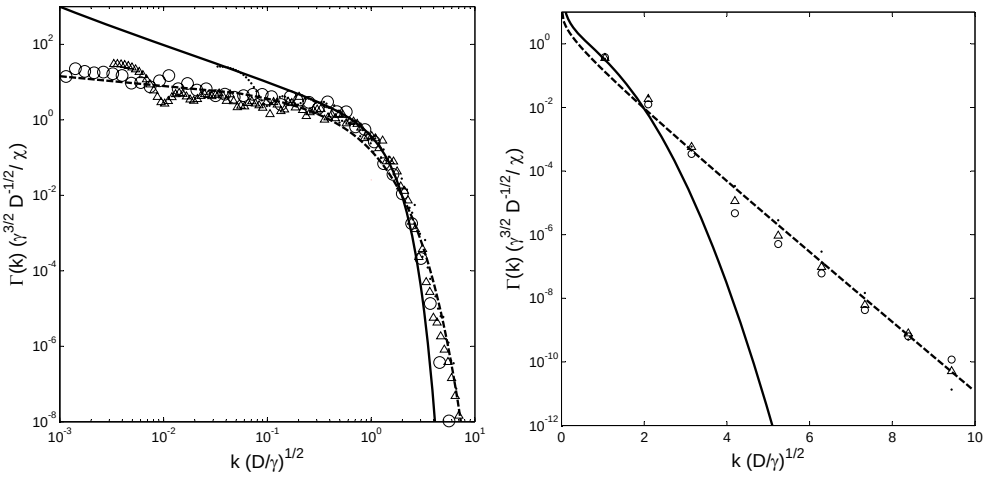

FIGURE 12. Energy spectrum of the scalar at $t = 7$ obtained by direct integration along the strip. The Péclet number is equal to $Pe = 10^3$ (•), $Pe = 10^5$ (△) and $Pe = 10^7$ (◯). The solid line corresponds to the Batchelor spectrum (5.5) and the dashed line corresponds to the solution (5.9) proposed by Kalda (2000) for decaying turbulence. The scale for the wavenumber is (a) logarithmic and (b) linear.

This solution is plotted as a dashed line in Fig. 12 and is in fairly good agreement with the numerical result at low wavenumbers. This solution is not a pure power law at low wavenumbers. Figure 5.9(b) shows that the solution is in excellent agreement with the numerical results at high wavenumbers, with an exponential decay e^{-k} as in the Kraichnan model, due to distributed stretching rates.

To conclude, the model for the stretching rate allows to predict the energy spectra of the scalar through a differential equation which is directly connected to the differential equation of the PDF of stretching factors. The solutions do not contain any fitting parameter and are in excellent agreement with the numerical results on 4 decades in k. The simulation clearly makes the distinction between a stationary, and a decaying scalar field on their respective spectral signature.

6. Probability Distribution Function (PDF) of the scalar.

6.1. *Two methods to calculate the PDF*

The central question in scalar mixing is to provide a description of the concentration content $P(c)$ of the mixture. $P(c)\mathrm{d}c$ is defined as the normalized number of pixels (in the simulation, otherwise, regions of space) whose concentration is in the interval $[c,\ c + \mathrm{d}c]$. Numerically, it can be computed by calculating the histogram of the scalar spatial distribution $c(\mathbf{x})$ and renormalize it such that $\int P(c)\mathrm{d}c = 1$. For the same reason than in the previous section for the spectrum, this method is tedious since it needs a reconstruction of the scalar distribution (very demanding in memory because c is a 2D matrix).

However, there is, as for the spectrum, an alternative way to compute the PDF $P(c)$. Using the fact that the strip has a Gaussian profile defined by (2.7), each segment

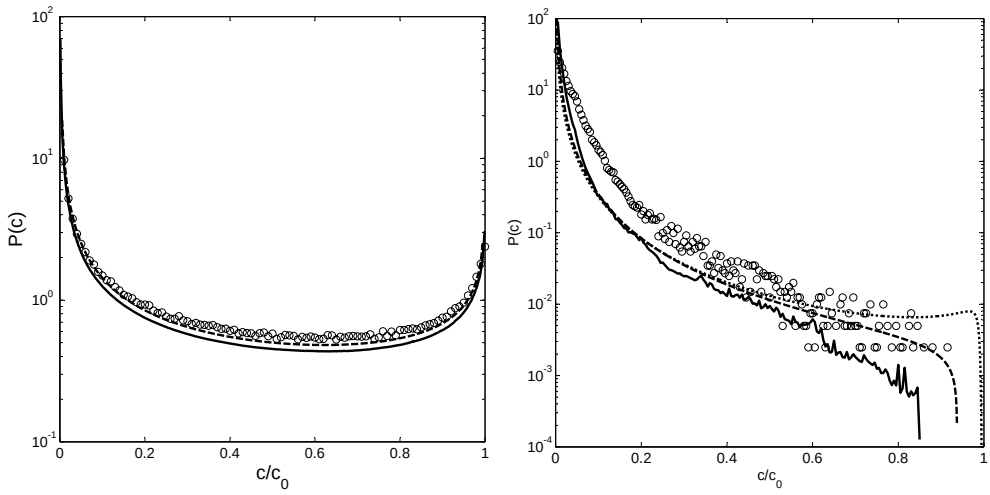

FIGURE 13. PDF of the scalar distribution for a strip in a Sine flow at $t = 7$ as in Fig. 7(d). The Péclet number is equal to $Pe = 10^{10}$ (a) and $Pe = 10^5$ (b). The true PDF ($\circ$) are computed by doing a histogram of the spatial distribution of scalar. Solid lines correspond to approximate PDF, computed by doing an integration of the Gaussian profile along the strip using Eq.(6.1). Dashed lines correspond to the prediction (6.3) using the log-normal model of stretching. Dotted line is the PDF of maximal concentration given by (6.4) for the log-normal model of stretching.

$[\mathbf{x}_i\ \mathbf{x}_{i+1}]$ has a histogram of concentration given by

$$N_{[\mathbf{x}_i\ \mathbf{x}_{i+1}]}(c) = \frac{s_i \Delta l}{c} \sqrt{\frac{1+4\tau_i}{-\log(\sqrt{1+4\tau_i}\ c/c_0)}} \tag{6.1}$$

where Δl is the length of the interval $[\mathbf{x}_i\ \mathbf{x}_{i+1}]$. In our simulations, the set of tracers $\mathbf{x}_i$ is reinterpolated before computing the PDF, such that the tracers are equally spaced (see section 2). This histogram has a well known U-shape, with a divergence as $1/c$ at low concentrations and a logarithmic divergence at the maximal concentration $c_0/\sqrt{1+4\tau_i}$. It comes from the 'large number of pixels' with $c = 0$ (far from the strip), and the 'large number of pixels' close to the maximum of the Gaussian at the maximal concentration (at the center of the strip, i.e. at $n = 0$). A major problem of this histogram is that it cannot be renormalised since $\int P(c)\mathrm{d}c$ diverges because of the divergence in $c = 0$. This property comes from the fact that a Gaussian profile extends on an infinite domain. It is intrinsic to the diffusion equation, which is in fact an ill-posed problem in an infinite domain. The consequence is that the PDF are defined with a normalising constant which cannot be calculated analytically.

The total PDF is obtained as the sum of the histograms of each segment $P(c) = A\sum_i N_{[\mathbf{x}_i\ \mathbf{x}_{i+1}]}(c)$ if the different intervals do not interfere between each other (A being a normalising constant). This is the case at large Péclet number and/or at early stages (see section 3). However, unlike the calculation of the spectrum, this method becomes invalid if there is some overlap between different parts of the strip, because the PDF is a nonlinear function of the concentration c. But, it is still interesting to use this method and to compare its result to the exact PDF, since it precisely quantifies the amount of self-overlap of the strip.

6.2. *PDF of a solitary strip*

Figure 13 shows the PDF of concentration for a strip advected by the Sine flow presented in section 3. The PDF is plotted at $t = 7$, which corresponds to the scalar distribution shown in Fig. 8. At high Péclet number ($Pe = 10^{10}$), the strip has not yet reached the mixing time so that the maximal concentration is almost everywhere equal to the initial concentration c_0. The logarithmic divergence of each interval's histogram is located at $c = c_0$. The total PDF is thus a U-shaped PDF between $c = 0$ and $c = c_0$. It can be recovered easily by assuming $\tau_i \ll 1$ in equation (6.1), leading to a PDF proportional to $1/c\sqrt{-\log(c/c_0)}$ (see also Meunier & Villermaux (2003)). There is a good agreement between the two methods used to calculate the PDF since there is no aggregation at this high Péclet number (as visible in the inset of Fig. 8b).

At moderate Péclet number ($Pe = 10^5$), the strip has started to diffuse, filling the low levels of concentrations in the PDF. The logarithmic divergence disappears, because there is no point on the strip where the maximal concentration is equal to c_0. The PDF becomes a decreasing function of c, with an inverted-S shape characteristic of flows with a broad distribution of stretchings (Duplat *et al.* (2009)). There is, moreover, a slight discrepancy between the two methods used to compute the PDF. This means that some aggregation of the strip with itself has occured. The exact PDF (plotted as symbols) is slightly above the ideal PDF that would be obtained if the strip was not overlapping with itself (plotted as a solid line).

In order to understand these PDF, we use the model of multiple step stretching, which leads to a log-normal law (4.7) for the PDF of stretching factors. The strip can thus be modeled as a sum of segments of length $P(\rho)\mathrm{d}\rho$, which have been stretched by a factor ρ in a time t. For a stretching rate assumed constant in time (equal to $\log(\rho)/t$), the striation thickness decreases exponentially in time and the dimensional time τ can be calculated by integration of (2.5) as

$$\tau(\rho) = \frac{Dt}{2s_0^2}\,\frac{\rho^2-1}{\log(\rho)} \tag{6.2}$$

Equation (6.1) then leads to an analytical formula for the PDF of concentration, if Δl is replaced by $P(\rho)\mathrm{d}\rho$ and s by s_0/ρ:

$$P(c) = \frac{A}{c}\int_{\tau(\rho)<\left(\frac{c_0^2}{4c^2}-\frac{1}{4}\right)} \sqrt{\frac{1+4\tau(\rho)}{-\log(\sqrt{1+4\tau(\rho)}\,c/c_0)}}\,\mathrm{e}^{-\frac{(\log\rho-2\gamma t/3)^2}{4\gamma t/3}}\,\frac{\mathrm{d}\rho}{\rho} \tag{6.3}$$

where A is a normalizing constant, and the mean stretching rate γ has been calculated numerically for the Sine flow ($\gamma = 0.91$).

This solution is plotted in Fig. 13 as a dashed line. It is in very good agreement with the numerical results at high Péclet number ($Pe = 10^{10}$). This is not a surprise because the dimensionless time τ is much smaller than 1 for the stretching factors which have a high probability $P(\rho)$, such that the integral in (6.3) simplifies into $1/\sqrt{-\log(c/c_0)}$, leading to a U-shaped PDF.

For a moderate Péclet number ($Pe = 10^5$), the theoretical prediction is still in fairly good agreement with the PDF obtained if there was no aggregation of the strip (plotted as a solid line), especially at low concentrations. For such a moderate Péclet number (where the mixing time has been reached everywhere), it is common to calculate the PDF of maximal concentration $Q(c)$, which is obtained by assuming that the strip has a square profile of width $s\sqrt{1+4\tau}$ instead of a Gaussian profile. The PDF is then defined

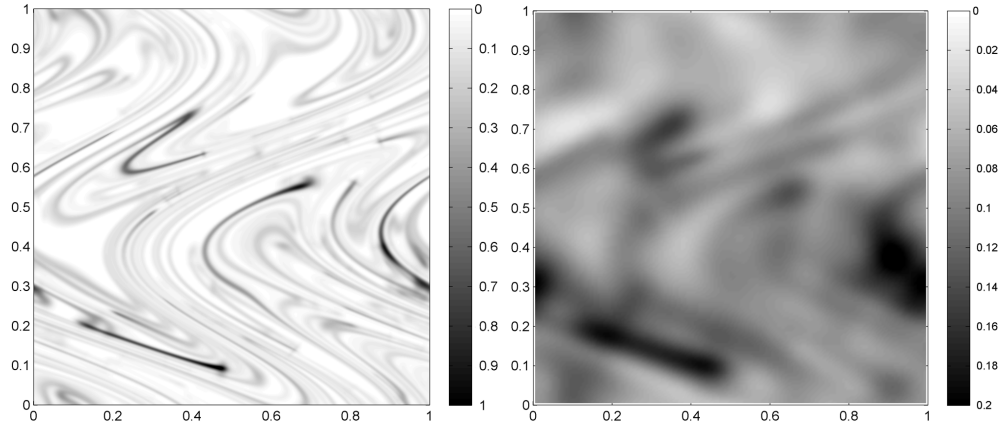

(a) (b)

FIGURE 14. Spatial distribution of a strip of scalar in a Sine flow at $t = 7$ for a Péclet number equal to (a) 10^5 and (b) 10^3. All points of the strip have been translated into the unit square in order to model a periodic initial condition (and flow) composed of a column of strips infinite in x and located at $y = ... - 2, -1, 0, 1, 2...$

by $Q(c)\mathrm{d}c = s\sqrt{1+4\tau(\rho)}P(\rho)\mathrm{d}\rho$ which gives an analytical expression for the PDF:

$$Q(c) \sim \frac{P(\rho)\log(\rho)^2}{c^4(1-\rho^2+2\rho^2\log\rho)} \quad \text{with } \rho = \tau^{-1}\left[\frac{c_0^2-c^2}{4c^2}\right] \tag{6.4}$$

Here, τ^{-1} is the inverse function of $\tau(\rho)$ defined in (6.2). This solution is plotted in Fig. 13(b) as dotted line. It is in fair agreement with the previous theoretical PDF at low concentrations, because the PDF is there a decreasing function of c. However, there is a small deviation at high concentrations. This reasoning would not work at high Péclet number ($Pe = 10^{10}$) because the PDF $Q(c)$ is then the sum of two Dirac functions at $c = 0$ and $c = c_0$, whereas the exact PDF is U-shaped, corresponding to a Gaussian profile.

6.3. *PDF of a strip with reconnection*

We have seen in the previous section that the PDF calculated by integrating along the strip the histogram of a Gaussian profile (6.1) is not equal to the exact PDF (calculated directly as a histogram of the scalar distribution) at late stages, and at moderate Péclet numbers. This originates from the aggregation of different parts of the strip, which occurs when the thickness of the strip (in the presence of diffusion) becomes of the order of the distance between two adjacent elements of the folded strips. To understand better how these reconnections modify the PDF, we have increased the number of reconnections by placing initially several long strips in the Sine flow instead of a single short strip. This can be done very easily (without further computation) if the strips are along the x-axis and infinite at $t = 0$. Indeed, if the computation was done for a strip $\mathbf{x}_i$ initially located between $x = -0.5$ and $x = 0.5$, an initially infinite strip is obtained as the sum of strips located in ... (x_i-3, y_i), (x_i-2, y_i), (x_i-1, y_i), (x_i, y_i), (x_i+1, y_i), (x_i+2, y_i), (x_i+3, y_i) ... because the Sine flow is periodic with a wavelength equal to 1 in the x-direction. The same argument can be used in the y direction: an initial column of strips separated by 1 in the y direction is obtained as a sum of strips located in ... (x_i, y_i-3), (x_i, y_i-2), (x_i, y_i-1), (x_i, y_i), (x_i, y_i+1), (x_i, y_i-2), (x_i, y_i+3) ... because the Sine flow is periodic in the y direction with a wavelength equal to 1.

The distribution of scalar obtained for such an initial condition is plotted in Fig 14

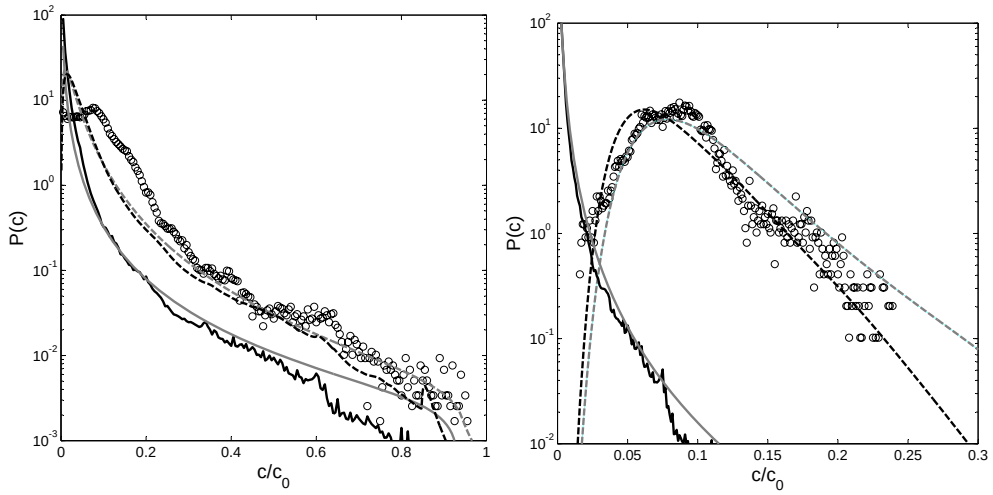

FIGURE 15. PDF of the scalar distribution for a strip in a Sine flow at $t = 7$, where the flow has been made periodic as in Fig.14. The Péclet number is equal to $Pe = 10^5$ (a) and $Pe = 10^3$ (b). Symbols are calculated by doing a histogram of the spatial distribution of scalar. Black solid lines are calculated by doing an integration of the Gaussian profile along the strip using Eq.(6.1). Grey solid lines correspond to the prediction (6.3) obtained using the log-normal model of stretching. The dashed lines are computed by self-convolving N times the solid lines, with (a) $N = 4$ and (b) $N = 43$, as predicted by Eq.(6.7).

for various Péclet numbers. It is only plotted for $0 < x < 1$ and $0 < y < 1$ because the distribution is periodic. While the strips are still discernible for $Pe = 10^5$, the field is almost homogeneous for the lowest Péclet number ($Pe = 10^3$). The density of strips is so large that the mean distance between two strips is smaller than their mean width.

The PDF of concentration corresponding to these scalar fields are plotted in Fig. 15 as symbols. For $Pe = 10^5$, the PDF is decreasing at large concentrations but it presents a plateau with a small maximum at $c = 0.1c_0$. For $Pe = 10^3$, this maximum is clearly visible, which corresponds to the fact that the field tends to be homogeneous with a mean concentration equal to the total quantity of scalar $\int c_0 L_0 \mathrm{e}^{-n^2/s_0^2} \mathrm{d}n$ divided by the area of the periodic domain (here, $\langle c \rangle = \sqrt{\pi} s_0 c_0 = 0.0886 c_0$).

These PDF are very different from those obtained by assuming that the strip has evolved on its own, independently of its neighbors (calculated in equation (6.1)), which are plotted as black solid lines. This strong difference is not surprising, since the PDF is a highly nonlinear function of c, while the concentration levels of overlapping strips interact in an additive fashion, owing to the linearity of the Fourier equation (Villermaux & Duplat (2003)). Precisely, if two strips with concentrations c_1 and c_2 such that $c = c_1 + c_2$ overlap, the total scalar field c has a PDF given by

$$P(c) = \int_{c=c_1+c_2} P_1(c_1) P_2(c_2) \mathrm{d}c_2 \tag{6.5}$$

where $P_1(c_1)$ is the PDF of the first strip and $P_2(c_2)$ that of the second. If the concentration levels c_1 and c_2 in (6.5) are chosen at random among those available in the original distributions P_1 and P_2, with no particular correlation or constraint, then equation (6.5) defines a *convolution* of the original distributions. The consequence of this interaction rule on the structure of $P(c)$ itself has been discussed in several random flows (Viller-

maux & Duplat (2003); Duplat & Villermaux (2008); Villermaux *et al.* (2008)), leading to a family of distributions stable by self-convolution.

The present simulations offer a unique way of testing the relevance of this interaction rule: In the case of a single strip which aggregates with itself, the PDF in the presence of aggregation should be obtained as the convolution of the PDF without aggregation, which we know from the solitary PDF $P_{\text{single}}(c)$ discussed in section 6.2. If the strip reconnects several times with itself, the PDF must be convolved as many times. Let us call this number of convolutions N, we thus expect

$$P(c) = P_{\text{single}}(c)^{\otimes N} \tag{6.6}$$

The result of this convolution is plotted in Fig. 15 as dashed lines and compared to the true PDF characterizing the true field (plotted as symbols). The agreement is fair for $Pe = 10^5$ and it is very good for $Pe = 10^3$: the self-convolved PDF indeed presents a plateau around $c = 0.1c_0$ and the width of the peak is well predicted. This actually means that the aggregation of the strip with itself is indeed the process by which the complex mixture has been built, and is well described by a self-convolution of the solitary PDF with itself.

The number of convolutions N needed to adjust the self-convolved solitary PDF onto the exact PDF is plotted in Fig. 16(a). It has been calculated in two different ways by taking either the theoretical prediction (6.3) for the PDF of the solitary strip, corresponding to the grey lines of Fig. 15, or by taking for the solitary strip the PDF obtained numerically by integration of (6.1), corresponding to the black lines of Fig. 15. The number of convolutions N increases exponentially with an exponent very close to $2\gamma/3$. This is surprising because the total length of the strip (and thus its surface) increases as $e^{\gamma t}$ and we would expect the number of convolutions to be proportional to the surface of the strip, leading to an exponent γ and not $2\gamma/3$. Theses simulations reveal that the number of convolutions is governed by the most probable stretching rate $2\gamma/3$ and not by the mean stretching rate γ.

This number of convolutions can be calculated in the simplified case where all strips are subject to the same stretching rate $\gamma_p = 2\gamma/3$. In this situation, all strips have a Gaussian normal profile $c(n) \sim e^{-\gamma_p n^2/2D}$. By definition, two strips reconnect if their levels are larger than a minimum level dc on a common area, which is achieved if their distance is smaller than a minimum distance $\Delta = 2\sqrt{-2D \log dc/\gamma}$ for Gaussian profiles. Since the mean distance between two strips decreases as $d_0 e^{-\gamma_p t}$ (d_0 being the initial mean distance between two strips), each strip reconnects with a number of strips equal to:

$$N = 2\Delta/(d_0 e^{-\gamma_p t} = \frac{4}{d_0}\sqrt{-\frac{3D}{\gamma}\log(dc)}e^{2\gamma t/3} \tag{6.7}$$

In our simulations, d_0 is equal to 1 in the periodic case and dc is a numerical constant for the scalar step, which is taken equal to 5×10^{-4}. It can be noted that this analytical formula diverges when dc tends to 0, but this divergence is very slow (scaling as $\log(dc)^{1/2}$, which makes it very weakly dependent on this numerical constant. This is in fact a consequence of the fact that a Gaussian profile extends to infinity and has thus a non-normalised PDF. This prediction is plotted in Fig. 16(a) as a solid line and is in excellent agreement with the empirical determination of the number of convolutions.

To conclude, it is possible to use the theoretical prediction of the PDF (6.3) in the absence of aggregation and to convolve it N times according to (6.7), giving a prediction for the PDF expected in the presence of aggregation. These PDF are plotted in Fig. 16(b) at various times. It predicts correctly the shape of the PDF in the three different regimes:

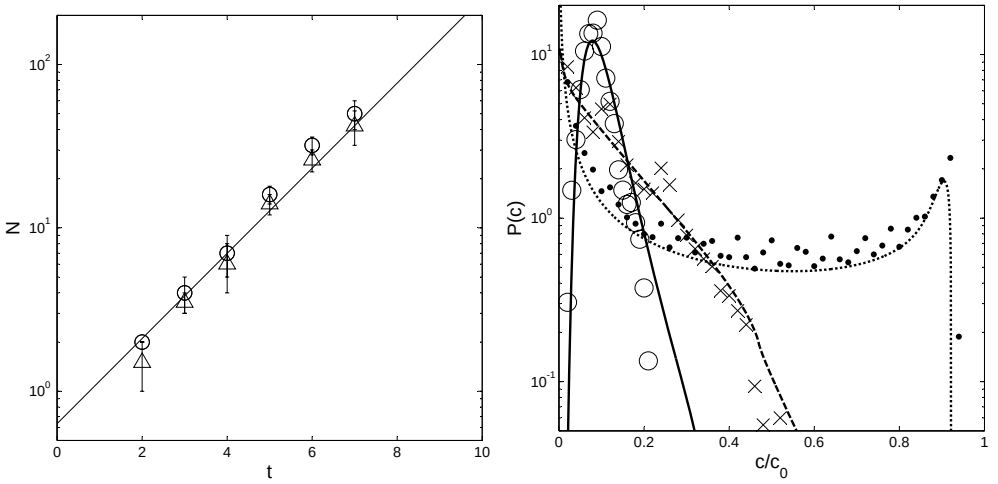

(a) (b)

FIGURE 16. (a) Temporal evolution of the number of self-convolutions N needed to transform the PDF of a solitary strip (i.e. in the absence of reconnection) into the exact PDF (with reconnections) obtained numerically by doing a histogram of the spatial distribution of scalar. The PDF of the solitary strip is either ($\bigcirc$) calculated numerically by integrating Eq. (6.1) along the strip or ($\bigtriangledown$) given by the theoretical prediction (6.3). The solid line corresponds to the theoretical prediction (6.7) for the number of convolutions. (b) PDF of scalar obtained for $Pe = 10^3$ at $t = 0.1$ (dotted line,$\bullet$), at $t = 2$ (dashed line,$\times$) and at $t = 7$ (solid line,$\bigcirc$). Symbols correspond to the exact numerical result. Lines correspond to the PDF given by (6.3) and self-convolved N times with N given by (6.7).

a U-shaped PDF at early stages, a decreasing PDF at intermediate times and a peaked PDF at late stages. The agreement is also quantitatively correct although it is not perfect. It should be noted however that this analytical solution does not contain any fitting parameter, since the mean stretching rate γ is known. It bridges a microscopic description of diffusion on a stretched substrate with a global quantity such as the scalar PDF in a non-trivial flow, from first principles.

6.4. *Why does the convolution rule work so well ?*

An interesting question to ask is why the convolution rule, which assumes the absence of correlation between the concentration levels adding at random, works so well. A possible justification is as follows: we have shown in section 5 that the Sine flow, like all smooth random flows, has a spatial concentration field $c(\mathbf{x})$ with a $\Gamma(k) \sim k^{-1}$ spectrum. This means that the correlation function of the field $\langle c(\mathbf{x})c(\mathbf{x}+\mathbf{r})\rangle_{\mathbf{x}}$ is equal to a constant $\langle c^2\rangle$ minus a rapidly varying function of r scaling as $\log(\gamma\, r^2/D)$, the inverse Fourier transform of k^{-1}, making the correlation function essentially zero for $r \gg \sqrt{D/\gamma}$. Distant concentration levels are thus *very weakly* correlated. The role of the large scale advection of the flow is to bring close to each other (i.e. at distances smaller than $\sqrt{D/\gamma}$) these distant concentration levels, which there merge under the blurring action of diffusion, defining a new concentration level equal to their sum. But since these concentration levels were basically uncorrelated, their addition is made at random, with a probability equal to the product of their respective probability of occurrence in the current distribution $P(c)$. The proper interaction rule is thus indeed of a pure convolution type, expressing an effective maximal randomness in the flow. We will have a confirmation of this fact in section 7.

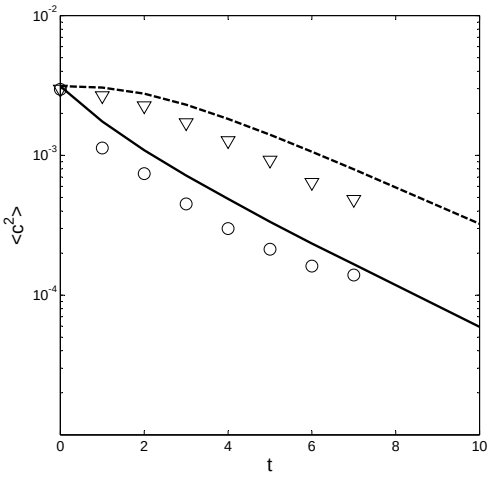

FIGURE 17. Variance of the field of scalar as function of time for $Pe = 10^3$ ($\bullet$) and $Pe = 10^5$ ($\bigtriangledown$). Lines correspond to the theoretical prediction of equation (6.9).

6.5. *Variance of the scalar*

The knowledge of the full PDF $P(c)$ solves the mixing problem. However, a traditional way since Corrsin (1952) and Danckwerts (1952) of characterizing the progress of a mixture towards uniformity, is to concentrate on the second moment of the PDF, namely the variance of the scalar $\langle c^2 \rangle$. In a confined mixture with conserved average concentration $\langle c \rangle$, the variance decays and relaxes toward $\langle c \rangle^2$ at late stages. The decay is prescribed by that of the maximal concentration in the strips, and is therefore exponential in time after the mixing time.

We have computed the scalar variance for the Sine flow directly using the Diffusive Strip Method by reconstructing the scalar field on the domain $-2 < x < 2$ and $-2.5 < y < 2.5$ (with an area $\mathcal{A} = 20$), where the scalar is initially introduced for $-0.5 < x < 0.5$ as in section 3. The variance is plotted in Fig. 17 as a function of time for two different Péclet numbers. It is indeed decaying exponentially after $t = 2$. The variance is smaller for smaller Péclet numbers, for which the mixing time is smaller. The late evolution is nevertheless independent in law of the Péclet number (i.e. exponential with the same decay rate).

It is fairly easy to give an analytical solution for the variance for a solitary strip. Indeed, the log-normal model for the strip stretching indicates that the length of the strip which has been stretched by a factor ρ is equal to $P(\rho, t)L(t)$ where $L(t) = L_0 \mathrm{e}^{\gamma t}$ is the total length of the strip and $P(\rho, t)$ is given by (4.7). For a given stretching factor ρ, the transverse profile is Gaussian with a parameter $s_0\sqrt{1+4\tau}/\rho$ and a maximal concentration equal to $c_0/\sqrt{1+4\tau}$, where the dimensionless time τ is given by (6.2). This leads to an integral of the squared concentration profile in its transverse direction as

$$\int_{-\infty}^{+\infty} c^2(n)\mathrm{d}n = \frac{c_0^2 s_0 \sqrt{\pi/2}}{\rho\sqrt{1+4\tau}} \tag{6.8}$$

The variance is then obtained as the sum along the strip of this integral multiplied by the length $P(\rho, t)L(t)\mathrm{d}\rho$ and divided by the total area $\mathcal{A}$ of the domain

$$\langle c^2 \rangle = \frac{c_0^2 L_0 s_0}{\mathcal{A}\sqrt{8\gamma t/3}} \int_0^{+\infty} \exp\left[\frac{-(\log\rho - 2\gamma t/3)^2}{4\gamma t/3}\right] \frac{\mathrm{d}\rho}{\rho\sqrt{1+4\tau(\rho)}} \tag{6.9}$$

This prediction is plotted in Fig. 17 for two different Péclet numbers. It overestimates the numerical result, which may come from the aggregation of the strip with itself. However, the theory recovers an exponential decay at late stages, with a correct decay rate. An asymptotic formula can be obtained for $\tau \gg 1$ by cutting the integral at $\log \rho = (\gamma t)^{1/4}$ showing that at late stages the variance tends to

$$\langle c^2 \rangle = \frac{c_0^2 L_0 s_0^2 \mathrm{e}^{-\gamma t/3}}{2\mathcal{A}\sqrt{D}} \left(\frac{\gamma}{6t}\right)^{1/4} \int_0^{+\infty} \sqrt{x} \mathrm{e}^{-x^2/2} \mathrm{d}x,$$

with $\int \sqrt{x} \mathrm{e}^{-x^2/2} \mathrm{d}x = 1.0304$. At leading order, the variance thus decays exponentially with time, as seen in Fig. 17 with a decay rate $\gamma/3$ indeed correctly predicted.

It is curious to see that the variance, the number of convolutions N and the total length of the strip have three different exponents. This is due to the log-normal law $P(\rho)$ which is very broad and contains large and small stretching factors ρ at the same time. The total length of the strip is more sensitive to large stretching factors since they create a larger interval on the final strip. The total length thus increases with a rate γ which is larger than the most probable stretching rate $2\gamma/3$. On the contrary, the variance is more sensitive to the least elongated parts of the strip, since they have higher levels of concentration. The variance thus decreases with a rate $\gamma/3$ smaller than the most probable stretching rate. The number of convolutions N is sensitive to both concentration levels and length of the strip. It thus increases at the most probable stretching rate.

7. Probability Distribution Function of scalar increments

As a complement, it is useful to study the PDF of scalar increments because it gives further insights into the spatial structure of the scalar distribution, and also because it legitimates the use of the 'maximal randomness' property made in section 6.3.

We define the PDF of the increment $\Delta c = c(\mathbf{x}) - c(\mathbf{x} + \Delta x\ \mathbf{e})$ of scalar concentration between two points separated by a distance Δx ($\mathbf{e}$ being a unit vector which has been taken along x and along y in the simulations). These PDF are plotted in Fig. 18 for two different Péclet numbers and aggregation conditions. In Fig 18(a), the initial scalar distribution is a unique strip and the Péclet number is relatively high ($Pe = 10^5$) such that there is basically no aggregation of the strip with itself at $t = 7$. In Fig 18(b), on the contrary, the scalar is injected initially as a dense periodic pattern and the Péclet number is smaller $Pe = 10^3$ so that reconnections of the strip with itself are more frequent.

In the case of a solitary strip (no aggregation), the PDF of increments is extremely peaked around 0 and has strong non-Gaussian tails. These large increments correspond to the high values of scalar located on the unmixed regions of the strip. When the distance Δx increases, the PDF gets wider up to a certain distance $\eta = 0.014$ above which it remains invariant whatever the value of Δx. This is a direct proof that above this distance, the concentration $c(\mathbf{x})$ and $c(\mathbf{x}+\Delta x)$ are uncorrelated. Indeed, in this large Δx limit, the probability to have an increment Δc can be calculated as the probability $P(c_1)$ that the concentration equals c_1 in $\mathbf{x}$ multiplied by the probability $P(c_2)$ that the concentration equals c_2 in $\mathbf{x} + \Delta x$, with $c_1 + c_2 = \Delta c$. When summing over c_2 and assuming that the probabilities are independent, one gets that the PDF of increments $P(\Delta c)$ is equal to the convolution product of the PDF of scalar $P(c)$ with $P(-c)$

$$P_{\Delta x}(\Delta c) = P(c) \otimes P(-c), \quad \text{for } \Delta x > \eta \tag{7.1}$$

This solution is plotted as a thick solid line in Fig 18(a), where the PDF of concentra-

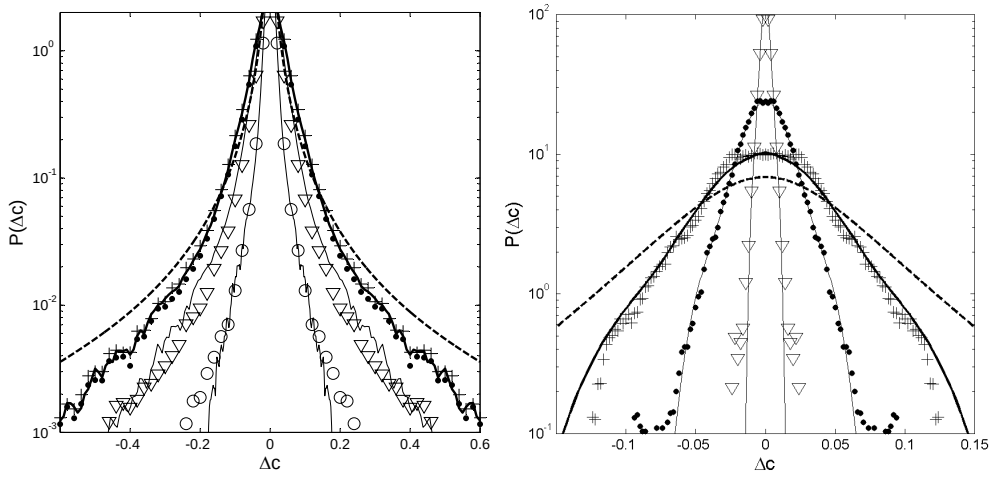

FIGURE 18. PDF of increments of scalar Δc for a strip in a Sine flow at $t = 7$. In (a) The Péclet number is equal to $Pe = 10^5$ and the scalar is initially injected between $-.5 < x < 0.5$, which leads to the distribution of scalar of Fig. 7(d). In (b), the Péclet number is equal to $Pe = 10^3$ and the scalar is initially periodic in both x and y direction, which leads to the distribution of scalar of Fig. 14(b). The increment Δc is taken between two points separated by $\Delta x = 0.003$ ($\bigcirc$), $\Delta x = 0.01$ ($\triangledown$), $\Delta x = 0.05$ ($\bullet$) and $\Delta x = 0.2$ (+). Thick solid lines are obtained as the convolution $P(c) * P(-c)$ of the numerical PDF of scalar with its symmetric part. Thin solid lines are deduced from this PDF by a dilatation with a factor $\Delta x/\eta$ where the Batchelor scale η is equal to 0.014 in (a) and 0.12 in (b). Dashed lines correspond to the convolution $P(c) * P(-c)$ of the theoretical PDF of scalar given by (6.3) and convolved with itself N times with N given by (6.7): in (a) $N = 1$ and in (b) $N = 48$.

tion $P(c)$ is given by the numerical simulation (the corresponding symbols are those of Fig. 13b). There is an excellent agreement with the PDF of increments for Δx larger than $\eta = 0.014$, an agreement even better than the one achieved using for the field PDF $P(c)$ obtained in (6.3) convoluted N times and transformed according to (7.1).

For small distances Δx, the PDF of increments becomes narrower. This is easily understood by the fact that the concentration $c(\mathbf{x})$ is now correlated with the concentration $c(\mathbf{x} + \Delta x)$ since now Δx explores the internal structure of the strip, or of a bundle of strips in the process of merging. An easy way to calculate the PDF of increment is then to assume that all the strips have the same thickness η. For $\Delta x < \eta$, the increment Δc is then proportional to Δx (assuming that a triangle is a good caricature of the strip transverse concentration profile), and the PDF of increment is squeezed by a factor $\Delta x/\eta$

$$P_{\Delta x<\eta}(\Delta c) = \frac{\eta}{\Delta x} P_{\Delta x>\eta}\left(\frac{\eta}{\Delta x}\ \Delta c\right) \tag{7.2}$$

This prediction is plotted as thin solid lines in Fig 18(a) with $\eta = 0.014$, and shows a good agreement with the numerical values of the PDF of increments.

In the case of a strip with many aggregations (as in Fig 18b), the PDF is closer to Gaussian at its center, but still presents substantial wings at large increments Δc. As in the case of the solitary strip, it gets wider when the distance Δx increases, but it now saturates at a larger value equal to $\eta = 0.12$ (the Péclet number is lower). As previously discussed, this means that for large distances $\Delta x > \eta$, the concentrations $c(\mathbf{x})$ and $c(\mathbf{x} + \Delta x)$ are uncorrelated and the PDF is given by (7.1) as the convolution of $P(c)$ and $P(-c)$. This prediction is plotted as a thick solid line in Fig 18(b), where $P(c)$ is determined numerically (the corresponding symbols are those of Fig. 15b). There is

an excellent agreement with the numerical result of $P(\Delta c)$. However, the same remark applies as for the solitary strip: the theoretical prediction of $P(c)$ given by (6.3) convolved N times and transformed according to (7.1), plotted as a thick dashed line, leads to a less good agreement.

For small distances $\Delta x < \eta$, the PDF of increment is again found by squeezing the PDF of increment at large distances by a factor $\Delta x/\eta$, as defined by (7.2). This prediction is plotted in Fig. 18(b) by thin solid lines and show an excellent agreement with the numerical results.

We have seen that the PDF of increment can be predicted using (7.1) for large distances ($\Delta x > \eta$) and using (7.2) for small distances ($\Delta x < \eta$). The question thus remains to determine what controls this critical distance η. It reflects the distance over which $c(\mathbf{x})$ correlates with itself. It thus scales as the distance over which diffusion has blurred the concentration differences. That distance is larger than the Batchelor scale $\sqrt{D/\gamma}$ itself since a bundle of elementary strips (whose width is $\sqrt{D/\gamma}$) in the process of aggregating realize a smooth ensemble at the scale of the bundle itself. This *coarse grained scale* is thus larger than the typical size of the concentration gradient in the flow (larger than the spectrum diffusive cut-off) and has been found to decreases like $Pe^{-1/2}$ as well in exponential flows, like the Sine flow (Villermaux & Duplat (2006)). Fig. 18 shows that $\eta \approx 4\sqrt{D/\gamma}$ in the present simulations.

8. Conclusion

We have introduced a new numerical method for the study of scalar mixing in 2D advection fields. This method is inspired by the empirical observation that natural flows tend to form elongated structures, making a mixture a collection of adjacent strips (sheets in three dimensions), more or less diffuse and overlapping.

As explained in section 2, the position of an advected material strip is computed kinematically, and the associated convection-diffusion problem is solved using the computed local stretching rate along the strip, assuming that the diffusing strip thickness is smaller than its local radius of curvature. This widely legitimate assumption reduces the numerical problem to the computation of a single variable along the strip, thus making the method extremely fast and applicable to any Péclet number. Since it is grounded on the use of a near-exact solution of the Fourier equation, this method is also extremely precise.

The method has then been used to document the mixing properties of a chaotic Sine Flow (sections 3 to 7), for which we have related the global quantities (spectra, concentration PDFs, increments) to the distributed stretching of the strip convoluted by the flow, possibly overlapping with itself. The numerical results indicate that the PDF of the strip elongation is log-normal, a signature of random multiplicative processes. This property lead to exact analytical predictions for the spectrum of the field and for the PDF of the scalar concentration of a solitary strip, in good agreement with the numerical results. An interesting result is that if the total strip is stretched at a rate γ, the most probable stretching rate is equal to $2\gamma/3$ and the variance decreases as $e^{-\gamma t/3}$.

The present simulations, since they keep track of both the contribution of a solitary strip, and of the global concentration PDF (as opposed to presently available experiments where these two information are mingled) offer a unique way of discovering the interaction rule building complex mixtures. That rule, formalized in equations (6.5) and (6.6), expresses that a random mixture is made of a superposition of overlapping strips

leading to concentration PDFs stable by convolution. Sections 6.4 and 7 make precise what 'random' means.

A natural extension of this method would be to consider chemically reacting scalars, in the spirit of the 'Flamelet models' used for turbulent diffusion flames (Peters (1984)). The generalization of the method to three dimensional flows would, also, be welcome.

This work has been supported by the Agence Nationale de la Recherche (ANR) through grant ANR-05-BLAN-0222-01. We thank Jérôme Duplat for numerous enlightening discussions on scalar mixing.

Appendix A. Numerics, Computational Time and Cost

• Numerics: In the MATLAB code of the Strip Diffusion Method, the equation of motion (1.1) is integrated using an explicit Runge-Kutta (4,5) formula, given by Matlab under the instruction 'ode45'. The time step δt was chosen equal to 10^{-3} for the vortex and a Sine flow with a period equal to 1 and a velocity equal to 0.5 (see section 3). Equation (2.5) for the dimensionless time τ is integrated in the most simple manner ($\tau_i(t+\delta t) = \tau_i(t) + \kappa \delta t / s_i(t)^2$), since it proved to be completely converged. Indeed, the striation thickness $s_i(t)$ usually decreases exponentially, making the integration of (2.5) very stable.

• Computational time: The Strip Diffusion Method has been implemented on MATLAB, in order to use standard instructions for the resolution of ordinary differential equations, and spline interpolation. This choice made the computation slower than using FORTRAN or C, but that was unnecessary since the method is extremely fast: The Vortex in section 2.6 lasted one hour on a PC at 1.1GHz and 1.24Go of RAM. The Sine flow computations (with $\Delta l = 0.005$, a number of points per cusps given by $\alpha = 25\Delta l/\pi$ and a time interval $\delta t = 0.001$) took 4 hours to calculate the field up to $t = 4$, and a week to extend it to $t = 7$ due to the exponentially large number of tracers generated by the method.

• Computational cost: The Strip Diffusion Method consists in following tracers along a strip advected by a flow. In an exponential flow like the Sine flow, the number of tracers defining the strip need to increase in proportion of the strip length, that is exponentially fast in time. This might look as a drawback of the method. It is not in fact since in spite of this, it remains competitive with grid-based methods computing the scalar gradients directly: a standard Direct Numerical Simulation of equation (1.2) will need a number of grid points of the order of

$$N_p = \left(\frac{L}{\sqrt{D/\gamma}} \right)^2 \sim Pe \tag{A 1}$$

for a domain size L in two dimensions, in order to resolve properly the concentration gradients whose size scales as the Batchelor scale (2.11).
Now the Strip Diffusion Method has already characterized the mixing properties of the flow (Spectrum, shape of PDF's, presence or absence of aggregation etc...) at the mixing time t_s, or after a few mixing times. After that, the field is completely mixed and close to uniformity (see e.g. Fig. 7). The maximal number of tracers needed to keep in memory is thus given by the amount of line stretching at the mixing time

$$N_p = e^{\gamma t_s} \sim \sqrt{Pe} \tag{A 2}$$

with t_s given by equation (2.9) a number which can be substantially smaller than the

number of grid points needed for the same Péclet number, when Pe becomes large. This, in addition to the advantage presented by the method that only one computation is needed per flow, the Péclet number being varied at will a posteriori, as mentioned in section 2.

Appendix B. Refinement numerical method

We detail here the technique used to add dynamically tracers on the strip during the calculation, in order to respect the criterion (2.12). The best method to do so was to calculate numerically the function $F_i = \int_0^{\sigma_i}(1 + \alpha\kappa(\sigma))\mathrm{d}\sigma$, where σ_i is the curvilinear abscissa at the tracer $\mathbf{x}_i$ (obtained numerically as the cumulative sum of the distance Δx_i between two consecutive points). The new set of tracers $\mathbf{x}_j$ were then interpolated such that the corresponding F_j are equally spaced with Δl. In our algorithm, this reinterpolation was done separately on each component of the position $\mathbf{x}_i = (x_i, y_i)$, by using a natural cubic spline interpolation provided by Matlab under the instruction 'csape' of the Spline ToolboxHowever, the best results were obtained when the interpolation was made with the position defined as a function of the curvilinear abscissa σ_j instead of F_j ($x_j = \mathrm{interp}(\sigma_i, x_i, \sigma_j)$). The reinterpolated abscissa σ_j were calculated using a basic linear interpolation corresponding to F_j: $\sigma_j = \mathrm{interp}(F_i, \sigma_i, F_j, '\,\mathrm{linear}')$.

To calculate the curvature κ_i at the tracer $\mathbf{x}_i$, the algorithm uses the formula:

$$\kappa = \frac{|x'y'' - x''y'|}{(x'^2 + y'^2)^{3/2}} \tag{B 1}$$

where x' (resp. y') is the derivative of the first (resp. second) component of $\mathbf{x}$ with respect to the curvilinear abscissa, which is calculated numerically using the smoothing cubic spline provided by Matlab under the instruction 'csaps'. This allowed to calculate in a stable way the curvature. It may not be exact since it is a smoothing algorithm, but this did not modify the position of the strip but only the density of tracers along the strip. It was also necessary to bound the curvature to 10^5 such that the number of points would not diverge. This criterion did not seem to modify the final position of the strip, even in the regions of the cusps.

During the refinement, the dimensional time τ_i needs also to be reinterpolated into τ_j (corresponding to the refined positions $\mathbf{x}_j$). This was done using a simple linear interpolation. However, some care had to be taken for the reinterpolation of the striation thickness s_i. Indeed, the striation thickness is linked to the initial length between two tracers Δx_i^0 due to incompressibility. A major constraint is then to respect numerically the conservation of the total quantity of scalar $C = c_0 s_0 \sum \Delta x_i^0$. For this purpose, the algorithm stores the initial length Δx_i^0 between the tracer $\mathbf{x}_i$ and the tracer $\mathbf{x}_{i+1}$, instead of the striation thickness s_i since they are related by (2.1). During the refinement from $\mathbf{x}_i$ into $\mathbf{x}_j$, the initial length Δx_i^0 is divided into the corresponding intervals Δx_j^0 such that the total quantity of scalar between $\mathbf{x}_i$ and $\mathbf{x}_{i+1}$ is conserved. In this way, the total quantity of scalar is constant within the numerical accuracy. For example, in the schematinc drawing of Fig. 19, the interval $[\mathbf{x}_i\, \mathbf{x}_{i+1}]$ is divided into 3 intervals from $\mathbf{x}_j$ to $\mathbf{x}_{j+3}$. The quantity of scalar $c_0 s_0 \Delta x_i^0$ must be equal to $c_0 s_0 \Delta x_j^0 + c_0 s_0 \Delta x_{j+1}^0 + c_0 s_0 \Delta x_{j+2}^0$. Moreover, the intervals Δx_j^0 must be proportional to the Δx_j, which allows to calculate $\Delta x_j^0 = \Delta x_i^0 \Delta x_j / (\Delta x_j + \Delta x_{j+1} + \Delta x_{j+2})$. The algorithm is sligthly more complex, because x_j does not correspond in fact to x_i.

The numerical values of Δl and α were chosen depending on the flow, such that the final position of the strip is independent of these constants. For the vortex, a large $\Delta l = 0.05$ was sufficient since the lengthscale of the vortex is rather large. Moreover,

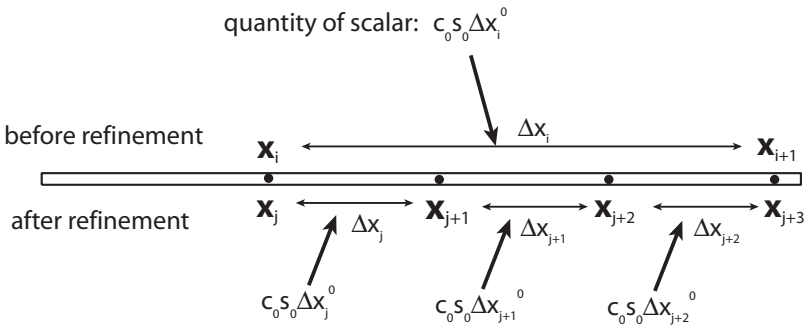

FIGURE 19. Schematic drawing explaining the calculation of the initial separation Δx_i^0 during the refinement. The set of tracers $\mathbf{x}_i$ is reinterpolated during the refinement into $\mathbf{x}_j$. The quantity of scalar between $\mathbf{x}_i$ and $\mathbf{x}_{i+1}$ is spread into the three corresponding intervals.

since the vortex does not create any cusps, the constant α could be taken very small ($\alpha = 5\Delta l/20\pi$ was chosen). For the Sine flow, a very small $\Delta l = 0.005$ was necessary, for the PDF of scalar to be converged. It might come from the sensitivity to initial conditions of this flow, linked to its well known chaotic behavior. The constant α had also to be taken very large since the flow creates many cusps. We needed to increase it up to $\alpha = 25\Delta l/\pi$.

REFERENCES

ALLÈGRE, C. J. & TURCOTTE, D. L. 1986 Implications of a two-component marble-cake mantle. *Nature* **323**, 123–127.

ALVAREZ, M. M., MUZZIO, F. J., CERBELLI, S., ADROVER, A. & GIONA, M. 1998 Self-similar spatiotemporal structure of intermaterial boundaries in chaotic flows. *Physical Review Letters* **81** (16), 3395–3398.

ARNOLD, V. I. & AVEZ, A. 1967 *Problèmes ergodiques de la mécanique classique*. Gauthier-Villars Editeur, Paris.

BATCHELOR, G. K. 1959 Small-scale variation of convected quantities like temperature in a turbulent fluid. part 1. general discussion and the case of small conductivity. *J. Fluid Mech.* **5**, 113–133.

BEIGIE, D., LEONARD, A. & WIGGINS, S. 1991 A global study of enhanced stretching and diffusion in cahotic tangles. *Phys. Fluids A* **3** ((5)), 1039–1050.

BUCH JR, K. A. & DAHM, W. J. A. 1996 Experimental study of the fine-scale structure of conserved scalar mixing in turbulent shear flows. part 1. sc $\gg$ 1. *J. Fluid Mech.* **317**, 21–71.

CORRSIN, S. 1952 Simple theory of an idealized turbulent mixer. *AIChE Journal* **3** (3), 329–330.

DANCKWERTS, P. V. 1952 The definition and measurement of some characteristics of mixtures. *Appl. Sci. Res.* **A3**, 279.

DIMOTAKIS, P. E. & CATRAKIS, H. J. 1999 Turbulence, fractals and mixing. In *Mixing Chaos and Turbulence* (ed. H. Chaté, E. Villermaux & J. M. Chomaz). Kluwer Academic/Plenum Publishers, New York.

DUPLAT, J., INNOCENTI, C. & VILLERMAUX, E. 2009 A non-sequential turbulent mixing process. *Submitted* .

DUPLAT, J. & VILLERMAUX, E. 2000 Persistency of material element deformation in isotropic flows and growth rate of lines and surfaces. *Eur. Phys. J. B* **18**, 353–361.

DUPLAT, J. & VILLERMAUX, E. 2008 Mixing by random stirring in confined mixtures. *J. Fluid Mech.* **617**, 51–86.

FALKOVICH, G., GAWEDZKI, K. & VERGASSOLA, M. 2001 Particles and fields in fluid turbulence. *Rev. Mod. Phys.* **73** ((4)), 913–975.

Fannjiang, A., Nonnenmacher, S. & Wolonski, L. 2004 Dissipation time and decay of correlations. *Nonlinearity* **17**, 1481–1508.

Fereday, D. R. & Haynes, P. H. 2004 Scalar decay in two-dimensional chaotic advection and batchelor-regime turbulence. *Phys. Fluids* **16** (12), 4359–4370.

Fountain, G. O., Khakhar, D. V. & Ottino, J. M. 1998 Visualization of three-dimensional chaos. *Science* **281**, 683 –686.

Fox, R. O. 2004 *Computational Models for Turbulent Reacting Flows*. Cambridge University Press.

Jean-Luc THIFFEAULT, C. R. D. & GIBBON, J. D. 2004 A bound on mixing efficiency for the advectionñdiffusion equation. *J. Fluid Mech.* **521**, 105–114.

Jones, S. V. 1994 Interaction of chaotic advection and diffusion. *Chaos Solitons & Fractals* **4** (6), 929–940.

Kalda, J. 2000 Simple model of intermittent passive scalar turbulence. *Physical Review Letters* **84** (3), 471–474.

Kraichnan, R. H. 1974 Convection of a passive scalar by a quasi-uniform random straining field. *J. Fluid Mech.* **64**, 737–732.

Levèque, M. A. 1928 Les lois de la transmission de la chaleur par convection. *Ann. Mines* **13**, 201–239.

Marble, F. E. 1988 Mixing, diffusion and chemical reaction of liquids in a vortex field. In *Chemical Reactivity in Liquids: Fundamental Aspects* (ed. M. Moreau & P. Turq). Plenum Press.

Marble, F. E. & Broadwell, J. E. 1977 The coherent flame model for turbulent chemical reactions. *Project SQUID, Tech. Rep. TRW-9-PU* .

Meunier, P. & Villermaux, E. 2003 How vortices mix. *J. Fluid Mech.* **476**, 213–222.

Meunier, P. & Villermaux, E. 2007 Van hove singularities in probability density functions of scalars. *C.R. Mécanique* **335**, 162–167.

Moffatt, H. K. 1983 Transport effects associated with turbulence with particular attention to the influence of helicity. *Rep. Prog. Phys.* **46**, 621–664.

Mohr, W. D., Saxton, R. L. & Jepson, C. H. 1957 Mixing in laminar-flow systems. *Industrial and Engineering technology* **49** ((11)), 1855–1856.

Ottino, J. M. 1989 *The Kinematics of Mixing: Stretching, Chaos, and Transport*. Cambridge University Press.

Perugini, D., Ventura, G., Petrelli, M. & Poli, G. 2004 Kinematic significance of morphological structures generated by mixing of magmas: a case study from salina island (southern italy). *Earth and Planetary Sci. Lett.* **222**, 1051–1066.

Peters, N. 1984 Laminar diffusion flamelet models in non-premixed turbulent combustion. *Prog. Energy Combust. Sci.* **10** (3), 319–339.

Phelps, J. H. & Tucker, C. 2006 Lagrangian particle calculations of distributive mixing: Limitations and applications. *Chem. Eng. Sci.* **61**, 6826–6836.

Ranz, W. E. 1979 Application of a stretch model to mixing, diffusion and reaction in laminar and turbulent flows. *AIChE Journal* **25** ((1)), 41–47.

Rhines, P. B. & Young, W. R. 1983 How rapidly is a passive scalar mixed within closed streamlines. *J. Fluid Mech.* **133**, 133–145.

Richardson, L. F. 1922 *Weather Prediction by Numerical Process*. Cambridge University Press.

Richardson, L. F. 1926 Atmospheric diffusion shown on a distance-neighbour graph. *Proc. R. Soc. Lond. A* **110**, 709–737.

Robinson, M., Cleary, P. & Monaghan, J. 2008 Analysis of mixing in a twin cam mixer using smoothed particle hydrodynamics. *AIChE J.* **54** (8), 1987–1998.

Shankar, P. N. & Kidambi, R. 2009 Mixing in internally stirred flows. *Proc. Roy. Soc. A* **465**, 1271–1290.

Sturman, R., Ottino, J. M. & Wiggins, S. 2006 *The Mathematical Foundations of Mixing*. Cambridge University Press.

Sukhatme, J. & Pierrehumbert, R. T. 2002 Decay of passive scalars under the action of single scale smooth velocity fields in bounded two-dimensional domains: From non-self-similar probability distribution functions to self-similar eigenmodes. *Phys. Rev. E* **66**, 056302.

Toussaint, V., Carrière, P., Scott, J. & Gence, J. N. 2000 Spectral decay of a passive scalar in chaotic mixing. *Phys. Fluids* **12** (11), 2834–2844.

Villermaux, E. & Duplat, J. 2003 Mixing as an aggregation process. *Phys. Rev. Letters* **91** (18), 184501.

Villermaux, E. & Duplat, J. 2006 Coarse grained scale of turbulent mixtures. *Phys. Rev. Letters* **97**, 144506.

Villermaux, E. & Gagne, Y. 1994 Line dispersion in homogeneous turbulence: Stretching, fractal dimensions and micromixing. *Phys. Rev. Letters* **73** ((2)), 252–255.

Villermaux, E. & Rehab, H. 2000 Mixing in coaxial jets. *J. Fluid Mech.* **425**, 161–185.

Villermaux, E., Stroock, A. D. & Stone, H. A. 2008 Bridging kinematics and concentration content in a chaotic micromixer. *Phys. Rev. E* **77** (1, Part 2).

Welander, P. 1955 Studies on the general development of motion in a two-dimensional, ideal fluid. *Tellus* **7** ((2)), 141–156.

Yeung, P. K. 2002 Lagrangian investigations of turbulence. *Annu. Rev. Fluid Mech.* **34**, 115–142.

Yeung, P. K., Xu, S. & Sreenivasan, K. R. 2002 Schmidt number effects on turbulent transport with uniform mean scalar gradient. *Phys. Fluids* **14** (12), 4178–4191.

Zeldovich, Y. B. 1982 Exact solution of the diffusion problem in a periodic velocity field and turbulent diffusion. *Doklady AN SSSR* **226** (4), 821–826.